Measurement-Altered Quantum Criticality

Thesis by
Yue Liu

In Partial Fulfillment of the Requirements for the
Degree of
Doctor of Philosophy

CALIFORNIA INSTITUTE OF TECHNOLOGY
Pasadena, California

2026
Defended May 29, 2026

Yue Liu
ORCID: 0000-0002-5965-0644

To Hongwen Shen, my high school physics teacher.

ACKNOWLEDGEMENTS

I would like to express my deepest gratitude to my advisor, Jason Alicea, who constantly supports me throughout my PhD. Jason is one of my role models in research, and I feel fortunate to have him as my advisor. This thesis would not be possible without his guidance. I also want to thank my committee members, Lesik Motrunich, Xie Chen, and David Hsieh for providing valuable feedback.

I am grateful to many professors and former postdocs for their guidance and mentorship. I want to thank Kevin Slagle for his kind help on both my research and my career. He always comes up with novel ideas and is one of the smartest people I've ever seen. I'm grateful to Sara Murciano for teaching me a lot on conformal field theories. I believe she has the best memory in the world. I also thank David Mross for his insight into many of my projects. He taught me a lot on Luttinger liquids and I'm always inspired by his comments. I also want thank Di Luo for bringing me to the world of AI. He has inspired my interest in large language models (LLM) for science.

I have also had the great pleasure to work with many wonderful collaborators in physics including Pablo Sala, Nandu Manoj, Stephen Naus, Zack Weinstein, Nathanan Tantivasadakarn, Kai Klocke, Gábor Halász, Abhijat Sarma, Cenke Xu, Ken Burch, Manuel Endres, Roger Mong. My PhD journey would not be so enriched without them. I want to thank Yinggan Xu and Chaorui Yao for discussions on LLMs. I am also grateful to Prof. Yaser Abu-Mostafa for his lectures on learning systems.

This journey of PhD is not easy. I am grateful to my family for their love and support, and my badminton friends who brought me so much joy. I also want to thank a sea otter, Luna, and her mom Toola, for teaching me the meaning of life.

I have been hoping to become a theoretical physicist since high school. I would say it has partly come true. This thesis is dedicated to my high school physics teacher, Ms. Hongwen Shen, who sparked this dream.

ABSTRACT

Measurements are usually introduced as probes of quantum systems, but they can also act as a powerful, intrinsically nonunitary control knob for manipulating quantum states. This thesis develops the theory, experimental realization, and detection of measurement-altered quantum criticality in one-dimension: the phenomenon where local measurements on critical wave functions reshape universal long-distance correlations, entanglement, and other scaling behaviors. We show that measurements generate defect or boundary perturbations in the underlying conformal field theory, producing new measurement-induced fixed points and new universal observables that are often invisible to the pristine theory.

In transverse-field Ising chains, we design measurement-altered criticality protocols in which correlated ancillas are entangled with the critical system and then projectively measured. This setting shows that measurement basis, entangling gate, measurement outcome, and ancilla correlations can qualitatively change correlations in the system and induce outcome-dependent order-parameter condensation. We also develop nonstandard probes — including higher moments and symmetry-resolved averages — that retain nontrivial signatures of the post-measurement ensemble.

These ideas are then connected to quantum information by studying imperfect teleportation of critical many-body wavefunctions. Teleportation errors can be reinterpreted as effective weak measurements acting on an otherwise faithfully teleported critical state. This perspective yields a classification of protocols in which imperfections either preserve universal correlations and entanglement scaling, continuously deform them, or destroy long-range entanglement while leaving altered power-law correlations behind. Measurement-altered criticality therefore becomes not only a fundamental phenomenon, but also a tool for understanding and optimizing noisy quantum-information protocols.

We also broaden the framework to measurement-induced boundary physics. In a gapless parent of the one-dimensional cluster state, a single round of measurements can generate boundary conformal field theories with distinct universal properties. Rotating the measurement basis drives transitions between these boundary fixed points, producing measurement-induced boundary transitions that have no analogue in the descendant gapped cluster state. Extensions to tricritical Ising and three-state Potts criticality show that such transitions arise generally in 1+1D conformal field

theories.

Finally, the thesis addresses experimental access. We propose practical protocols for observing measurement-altered criticality in Rydberg atom arrays tuned to Ising and tricritical-Ising transitions, where projective measurements of selected atoms can controllably modify critical correlations with experimentally favorable post-selection probabilities.

We also develop a post-selection-free framework for extracting nonlinear observables from raw measurement records using statistical learning. By recasting higher moments of conditioned observables as supervised learning objectives, the method replaces exponentially costly sector-by-sector postselection with regression whose sample complexity is controlled by decoder capacity. In critical Ising chains, linear, logistic, and convolutional decoders recover measurement-altered scaling and correlations from simulated unpostselected data.

Together, these results establish measurements as a pratical and universal route to engineering, diagnosing, and exploiting new forms of quantum critical behavior.

PUBLISHED CONTENT AND CONTRIBUTIONS

[1] Yue Liu, Nandagopal Manoj, Stephen Naus, Zack Weinstein, Sara Murciano, David F. Mross, and Jason Alicea. "Post-Selection-Free Measurement-Altered Criticality via Statistical Learning". In preparation. 2026.
Y. L. participated in the conception of the project, theoretical calculations, numerics, and manuscript preparation.

[2] Yue Liu, Sara Murciano, David F. Mross, and Jason Alicea. "Boundary Transitions from a Single Round of Measurements on Gapless Quantum States". In: *Physical Review Research* 7 (2025), p. 023293. DOI: `10.1103/l4b7-h5cd`. arXiv: `2412.07830`.
Y. L. participated in the conception of the project, theoretical calculations, numerics, and manuscript preparation.

[3] Stephen Naus, Yue Liu, Sara Murciano, Pablo Sala, Manuel Endres, and Jason Alicea. "Practical Roadmap to Measurement-Altered Criticality in Rydberg Arrays". arXiv preprint. 2025. DOI: `10.48550/arXiv.2506.21963`. arXiv: `2506.21963`.
Y. L. participated in theoretical calculations and manuscript preparation.

[4] Pablo Sala, Sara Murciano, Yue Liu, and Jason Alicea. "Quantum Criticality Under Imperfect Teleportation". In: *PRX Quantum* 5 (2024), p. 030307. DOI: `10.1103/PRXQuantum.5.030307`. arXiv: `2403.04843`.
Y. L. participated in theoretical calculations, numerics, and manuscript preparation.

[5] Sara Murciano, Pablo Sala, Yue Liu, Roger S. K. Mong, and Jason Alicea. "Measurement-Altered Ising Quantum Criticality". In: *Physical Review X* 13 (2023), p. 041042. DOI: `10.1103/PhysRevX.13.041042`. arXiv: `2302.04325`.
Y. L. participated in theoretical calculations, numerics, and manuscript preparation.

“You know what I say? A table of contents is just an index without spoilers, maaan.”

— Pascal, *Animal Crossing: New Horizons*

TABLE OF CONTENTS

LIST OF ILLUSTRATIONS

LIST OF TABLES

Part I

Foundations of Measurement-Altered Quantum Criticality

"If you wanna get ahead in life, you gotta pick a direction first, maaan!"

— Pascal, *Animal Crossing: New Horizons*

Chapter 1

MEASUREMENTS AS PERTURBATIONS OF CRITICAL WAVEFUNCTIONS

1.1 From measurement as readout to measurement as control

A measurement is often introduced as the final step of an experiment: the state is prepared, allowed to evolve, and then read out. In a many-body quantum system this viewpoint is incomplete. Measurement is itself an operation. It extracts classical information, but it also transforms the quantum state by a generally non-unitary map. When the measured degrees of freedom are coupled to unmeasured degrees of freedom, this non-unitary backaction can reshape the state that remains. The central idea of this thesis is that, in quantum critical systems, such reshaping is not merely a microscopic disturbance. It can change universal long-distance properties.

The phrase *measurement-altered quantum criticality* refers to this situation. One begins with a wavefunction whose long-distance behavior is governed by a critical fixed point. A measurement protocol is then applied to part of the system, to auxiliary degrees of freedom entangled with the system, or to a selected sublattice. Conditioned on the measurement record, the remaining state is described by a new wavefunction or density matrix. The question is whether its universal properties such as correlation exponents, entanglement structure, or scaling functions are the same as those of the original critical state or are instead altered by the measurement.

This question is distinct from asking whether measurements create a new dynamical phase in a monitored quantum circuit. In monitored dynamics, a state is repeatedly evolved and measured, and the competition between unitary scrambling and measurement-induced purification can yield measurement-induced phase transitions [1, 2]. The focus here is different. We usually begin with a nontrivial critical state already prepared. A *single* measurement layer or a teleportation protocol then acts as a structured perturbation of that state. The resulting phenomena are therefore closer in spirit to perturbing a conformal field theory than to generating a phase transition through long-time hybrid dynamics.

The five projects combined in this thesis develop this idea from several angles. The canonical example is the critical Ising chain coupled to correlated ancilla that are subsequently measured [3]. Imperfect teleportation of a critical wavefunction provides a quantum-information realization of the same physics, with gate imperfections acting as effective weak measurements [4]. Measurements on gapless parent states reveal that measurement basis can tune boundary conformal fixed points [5]. Rydberg arrays provide a practical ancilla-free route to observing altered criticality experimentally [6]. Finally, statistical-learning decoders address the post-selection bottleneck by estimating nonlinear conditioned observables from unpostselected measurement records [7].

1.2 Why quantum critical states are sensitive to measurement

Quantum critical states are natural amplifiers of measurement backaction. Away from criticality, a local perturbation of a gapped one-dimensional system generally has effects that decay beyond the correlation length. At criticality there is no intrinsic correlation length. Local and subdimensional perturbations can therefore influence observables at long distances if they couple to relevant or marginal fields of the low-energy theory.

A one-dimensional quantum critical ground state can be represented, after analytic continuation, by a two-dimensional Euclidean field theory. Equal-time wavefunction correlations are governed by scaling operators. If O is a primary field with scaling dimension Δ_O, then in an infinite translation-invariant system one expects

$$\langle O(x)O(0)\rangle \sim \frac{1}{|x|^{2\Delta_O}}. \tag{1.1}$$

This power law is universal in the sense that microscopic details affect amplitudes but not the exponent. Measurements can change the exponent if the corresponding post-measurement state flows to a different fixed point or is governed by a nonstandard replicated theory.

It is useful to think of a measurement layer as a perturbation localized at a single imaginary-time slice. If the initial state is the ground state of a Hamiltonian H, it can be formally represented as imaginary-time evolution from the far past. A measurement operator $M_{\mathbf{s}}$ inserted at the end of this evolution produces an unnormalized conditioned state

$$\left|\widetilde{\psi}_{\mathbf{s}}\right\rangle = M_{\mathbf{s}}\left|\psi_0\right\rangle, \tag{1.2}$$

where $\mathbf{s}$ denotes the measurement record. In a continuum description, $M_{\mathbf{s}}$ may be expanded in operators of the critical theory. Relevant terms can grow under coarse graining, marginal terms can continuously deform scaling data, and irrelevant terms may leave universal long-distance behavior unchanged. This is the first major organizing principle of the thesis.

The second organizing principle is symmetry. Measurements may preserve or break microscopic symmetries, and the particular measurement outcome may break additional symmetries even when the measurement protocol does not. Symmetry determines which low-energy fields can be generated. In the Ising examples, for instance, whether a measurement induces a spin-field perturbation, an energy-density perturbation, or only higher-order operators determines whether the outcome produces ordering, modified power laws, or essentially pristine critical behavior.

1.3 Measurement-altered criticality versus measurement-induced criticality

Because the terminology is close, it is worth separating measurement-altered criticality from measurement-induced phase transition at the outset. In a typical measurement-induced phase transition problem, a state evolves through a circuit or Hamiltonian dynamics interspersed with measurements. As the measurement rate or strength changes, the long-time entanglement structure can switch between volume-law and area-law behavior. The transition is dynamical and ensemble-defined: it concerns trajectories, monitored evolution, and often the fate of quantum information under repeated measurements.

In measurement-altered criticality, by contrast, the input state is itself critical. The central issue is not whether measurements prevent entanglement from building up dynamically, but rather how they alter the universal correlations already present in a critical wavefunction. A single layer can suffice. The resulting state may still exhibit power-law correlations, but with exponents that differ from those of the unmeasured state. It may acquire long-range order coexisting with critical fluctuations. It may flow to a new boundary fixed point. Or, after averaging over outcomes, it may reveal its altered character only through nonlinear observables.

This difference does not imply that the subjects are unrelated. Both rely on the fact that measurement is a non-unitary operation and that trajectory-resolved information matters. Both often require nonstandard observables because ordinary density matrices can obscure the relevant physics. Still, the conceptual starting points are different. This thesis uses the prepared critical wavefunction as the raw material and asks what universal structures measurement can engineer or reveal.

1.4 The post-selection problem

The cleanest theoretical object is often the state conditioned on a specific measurement record. If the measurement operators are $\{M_{\mathbf{s}}\}$, the Born probability of outcome $\mathbf{s}$ is

$$p(\mathbf{s}) = \mathrm{Tr}\big(M_{\mathbf{s}}\rho_0 M_{\mathbf{s}}^{\dagger}\big), \tag{1.3}$$

and the conditioned state is

$$\rho_{\mathbf{s}} = \frac{M_{\mathbf{s}}\rho_0 M_{\mathbf{s}}^{\dagger}}{p(\mathbf{s})}. \tag{1.4}$$

For a fixed $\mathbf{s}$, one can ask whether $\rho_{\mathbf{s}}$ has a modified order parameter, altered correlations, or a new entanglement structure. However, in an experiment with many measured sites, the number of possible records grows exponentially with system size. A particular long record usually occurs with exponentially small probability. Directly repeating the same record enough times to estimate conditioned observables is therefore generally impractical.

This obstacle is the "post-selection problem". It appears in all five parts of the thesis, but it takes different forms. In the Ising chapter, post-selecting special ancilla outcomes reveals clean altered exponents, while measurement-averaged and symmetry-resolved diagnostics provide more accessible alternatives. In the teleportation chapter, the measurement record is tied to the teleportation protocol, and some averages implement a built-in decoding of correlations. In the boundary-transition chapter, post-selection and decoding expose distinct boundary fixed points. In the Rydberg chapters, favorable outcome sectors occur with unexpectedly large probabilities because of microscopic blockade constraints, but post-selection remains a central practical issue. In the decoder chapters, the problem is recast as statistical learning: rather than selecting one record, one learns conditioned responses from the full distribution of records.

A useful identity shows why ordinary averages usually fail to expose the desired physics. For an observable O, the linear Born average over conditioned expectation values gives

$$\sum_{\mathbf{s}} p(\mathbf{s})\ \mathrm{Tr}(\rho_{\mathbf{s}}O) = \mathrm{Tr}(\rho_0 O) \tag{1.5}$$

whenever the measurement is complete and no additional reweighting is applied. Thus a linear average can reproduce the pre-measurement expectation value even when every typical conditioned state is strongly altered. The information about measurement-induced variation lives in the dependence of $\rho_{\mathbf{s}}$ on $\mathbf{s}$, not merely in the Born-averaged density matrix.

This observation motivates nonlinear quantities, such as

$$A_q[O] = \sum_{\mathbf{s}} w(\mathbf{s})\ \langle O \rangle_{\mathbf{s}}^q\,, \tag{1.6}$$

where $w(\mathbf{s})$ may be the Born weight or a deliberately chosen alternative ensemble. Such moments retain information about outcome-to-outcome fluctuations. They also naturally lead to replica descriptions, because powers of conditioned expectation values correspond to multiple copies sharing the same measurement record. This point becomes central in the decoder part of the thesis.

1.5 Three complementary viewpoints: weak perturbations, boundary conditions, and decoders

The projects collected here repeatedly return to three viewpoints. The first is the weak-perturbation viewpoint. A weak measurement produces a Kraus operator close to the identity, which can often be written as an exponential of local operators. Expanding this operator and matching to the low-energy theory reveals which CFT fields are generated. This is the natural language for the ancilla-assisted Ising protocol and for imperfect teleportation.

The second is the boundary-condition viewpoint. A post-measurement wavefunction can be represented as a Euclidean path integral with a defect or boundary at the measurement time slice. Measurements often impose strong boundary conditions rather than weak perturbations. In this language, changing the measurement basis changes the boundary condition, and universal transitions can occur when the boundary RG flow changes character. The gapless-parent and boundary-transition chapters develop this perspective systematically.

The third is the decoder viewpoint. If the measurement record is random and high dimensional, then the conditioned expectation value $\langle O \rangle_{\mathbf{s}}$ is a function of the record. Instead of estimating it separately for each $\mathbf{s}$, one can learn this function from data. The machine-learning chapters show that nonlinear probes of measurement-altered criticality can be estimated without brute-force post-selection when the conditioned response lies in, or is well approximated by, a restricted function class.

These viewpoints are not competing theories. They are different descriptions of the same physical phenomenon at different stages of abstraction. The weak-perturbation viewpoint identifies the relevant operators. The boundary viewpoint classifies the universal endpoints. The decoder viewpoint asks how those endpoints can be inferred from experimentally available data.

1.6 Roadmap of the thesis

Part I establishes the common language. Chapter 1 introduces measurement as a non-unitary perturbation of a critical wavefunction and explains why post-selection is the central practical obstruction. Chapter 2 reviews the critical, measurement, boundary, numerical, and statistical-learning tools used throughout the thesis.

Part II develops the canonical Ising mechanism. Chapter 3 introduces the ancilla-assisted weak-measurement protocol, derives the post-measurement wavefunction, and explains the effective-action approach. Chapter 4 uses this machinery to analyze altered Ising fixed points, nonlinear averages, symmetry-resolved diagnostics, and post-selection probabilities.

Part III interprets imperfect teleportation as measurement-altered criticality in a quantum-information protocol. Chapter 5 introduces teleportation of critical wavefunctions and maps imperfections to weak measurements. Chapter 6 classifies the resulting perturbations as relevant, marginal, or disguised and studies their consequences for correlations, entanglement, full counting statistics, and mixed-state averages.

Part IV develops the boundary-CFT perspective. Chapter 7 explains how measurements become boundary conditions, especially in gapless parents of cluster states. Chapter 8 studies measurement-induced boundary transitions driven by rotating the measurement basis. Chapter 9 generalizes the lessons to tricritical Ising, three-state Potts, and related universality classes.

Part V moves toward experiment. Chapter 10 introduces Rydberg arrays as an ancilla-free platform for measurement-altered criticality. Chapter 11 analyzes altered Ising and tricritical-Ising criticality in Rydberg chains. Chapter 12 addresses post-selection probabilities, restricted averages, finite temperature, off-critical preparation, and experimental imperfections.

Part VI treats post-selection-free access through statistical learning. Chapter 13 formulates nonlinear conditioned observables as a learning problem. Chapter 14 describes decoder architectures and training protocols. Chapter 15 applies those tools to learn measurement-altered fixed points and compare learned observables with reference simulations. Chapter 16 gives a full proof of sample complexity. Chapter 17 shows the numerical implementation of the decoders.

Part VII synthesizes the picture. Chapter 18 organizes the five case studies into a unified theory of measurement-altered quantum criticality. Chapter 19 discusses open directions, including higher dimensions, other universality classes, monitored dynamics, adaptive measurements, and experimental platforms beyond Rydberg arrays.

Chapter 2

CRITICAL WAVEFUNCTIONS, MEASUREMENTS, AND UNIVERSAL DIAGNOSTICS

2.1 One-dimensional quantum critical ground states

A one-dimensional quantum critical point describes the state of a diverging correlation length. On the lattice, it is often reached by tuning a Hamiltonian parameter until a gap closes in the thermodynamic limit. At long distances the microscopic lattice description is replaced by a continuum quantum field theory. For the systems considered in this thesis, the continuum theory is usually a two-dimensional conformal field theory after identifying imaginary time as the second coordinate [8, 9, 10].

The transverse-field Ising model is the simplest recurring example,

$$H_{\text{Ising}} = -J \sum_j Z_j Z_{j+1} - h \sum_j X_j . \tag{2.1}$$

At $h = J$ it realizes the Ising critical point [11]. Its long-distance theory has central charge $c = 1/2$ and contains three primary fields: the identity $\mathbf{1}$, the spin field σ, and the energy-density field ε. Their scaling dimensions are

$$\Delta_{\mathbf{1}} = 0, \qquad \Delta_\sigma = \frac{1}{8}, \qquad \Delta_\varepsilon = 1. \tag{2.2}$$

The spin field is odd under the Ising symmetry, while the energy-density field is even. This simple symmetry distinction is crucial throughout the book because it determines which perturbations can be generated by certain measurement protocols.

The tricritical Ising CFT is a second minimal model that appears in the later boundary-transition and Rydberg parts. It has central charge $c = 7/10$ and more relevant fields than the ordinary Ising CFT. This richer operator content allows more varied boundary fixed points and intermediate flows. The thesis uses the tricritical Ising point not as an isolated special case, but as a test of whether the measurement-altered framework extends beyond the Ising universality class.

2.2 Conformal data: scaling dimensions, central charge, and operator content

The central data of a two-dimensional CFT include the central charge c, the spectrum of scaling dimensions, and the operator product coefficients. For an operator O with scaling dimension $\Delta_{\mathcal{O}}$, the bulk two-point function in an infinite system behaves as

$$\langle \mathcal{O}(x)\mathcal{O}(0)\rangle \sim |x|^{-2\Delta_{\mathcal{O}}}. \tag{2.3}$$

On a periodic chain of length L, the chord distance replaces $|x|$,

$$d_L(x) = \frac{L}{\pi} \sin\left(\frac{\pi x}{L}\right), \tag{2.4}$$

so that a finite-size fit often uses

$$\langle \mathcal{O}(x)\mathcal{O}(0)\rangle \sim d_L(x)^{-2\Delta_{\mathcal{O}}}. \tag{2.5}$$

This form is repeatedly used to extract scaling dimensions before and after measurement.

The central charge can be obtained from entanglement scaling. For a periodic critical chain, the entanglement entropy of an interval of length ℓ scales as [12]

$$S(\ell) = \frac{c}{3} \log\left[\frac{L}{\pi a} \sin\left(\frac{\pi \ell}{L}\right)\right] + s_0, \tag{2.6}$$

where a is a microscopic cutoff and s_0 is nonuniversal. For an open chain the coefficient is halved,

$$S(\ell) = \frac{c}{6} \log\left[\frac{2L}{\pi a} \sin\left(\frac{\pi \ell}{L}\right)\right] + s_0'. \tag{2.7}$$

Measurement-altered states can have altered effective entanglement coefficients even when they retain power-law correlations. This is one reason why both correlation and entanglement diagnostics are needed.

2.3 The Ising conformal field theory

The Ising CFT provides the common technical language for much of the thesis. In the transverse-field Ising chain, the lattice order parameter Z_j maps to the spin field σ, while the deviation of the local energy density from its expectation value maps to ε. Schematically,

$$Z_j \sim a_\sigma\, \sigma(x) + \cdots, \tag{2.8}$$

$$X_j - \langle X_j \rangle \sim a_\varepsilon\, \varepsilon(x) + \cdots, \tag{2.9}$$

where the ellipses denote descendants and less relevant fields. The amplitudes a_σ and a_ε depend on microscopic conventions, but the scaling dimensions do not.

The Ising symmetry acts as $Z_j \to -Z_j$ and leaves X_j invariant. Consequently, a perturbation proportional to σ explicitly breaks the Ising symmetry and is strongly relevant. A perturbation proportional to ε preserves the symmetry and tunes the system through the thermal direction. Measurement protocols that generate these two fields can therefore have qualitatively different effects even if they look similar microscopically.

In the measurement-altered Ising protocol, the measured ancilla pattern determines whether the post-measurement critical chain sees a spatially structured spin-field perturbation, an energy-density-like perturbation, or a symmetry-constrained combination. In the Rydberg protocol, occupation measurements select patterns that can similarly couple to spin-like or energy-like fields of the emergent Ising theory. Ising notation is therefore introduced here once and reused throughout the book.

2.4 The tricritical Ising conformal field theory

The tricritical Ising CFT is a minimal model with central charge $c = 7/10$. It has a larger set of relevant operators than the Ising CFT and admits a richer set of conformal boundary conditions. In the Rydberg-array setting, tricritical Ising behavior arises where a line of Ising transitions terminates at a tricritical point. In the boundary-transition setting, tricritical Ising theory provides a stringent test of the idea that measurements can tune between universal boundary fixed points.

The most important conceptual distinction from the ordinary Ising case is that more than one relevant symmetry-allowed direction may be present. This means that a measurement protocol can generate flows with multiple competing relevant perturbations. Consequently, the endpoint of a measurement-altered flow need not be simply "ordered" or "thermal." It may approach a fixed boundary condition, a free boundary condition, or an intermediate boundary fixed point, depending on the microscopic measurement sector and the boundary operator content.

Later chapters will give the full lattice-to-CFT dictionaries for the tricritical Ising examples. The role of this section is only to flag why the tricritical theory is not a decorative generalization: it tests whether measurement-altered quantum criticality is governed by universal operator and boundary data rather than by accidental features of the Ising chain.

2.5 Boundary and defect conformal field theory

Boundary CFT enters whenever a system has an actual spatial boundary, an impurity, a defect line, or a Euclidean time slice with special conditions [13]. Measurements naturally create such structures. A weak measurement can be represented as a defect-line perturbation inserted at a time slice. A projective measurement can impose a stronger boundary condition. A post-selected measurement outcome can explicitly select one boundary sector, while averaging over outcomes can correspond to a replicated or disordered boundary ensemble.

For a half-plane or open chain, a bulk primary field O may acquire a one-point function,

$$\langle O(x)\rangle_{\mathrm{bdy}} \sim x^{-\Delta_O}, \tag{2.10}$$

where x is the distance to the boundary. This form is useful for extracting scaling dimensions in open-chain DMRG calculations and in Rydberg protocols with open boundaries. Boundary-condition-changing operators and boundary RG flows further classify how one boundary fixed point can flow to another under perturbations.

The boundary fixed point chapters use this language to interpret a single round of measurements on a gapless parent state. Rotating the measurement basis tunes the effective boundary perturbation. When that perturbation changes sign or relevance, the system can undergo a measurement-induced boundary transition. This viewpoint also clarifies why such transitions are universal: they depend on boundary operator content rather than on microscopic details of the measurement apparatus.

2.6 Weak measurements, projective measurements, and Kraus maps

A general measurement is described by Kraus operators $M_{\mathbf{s}}$ satisfying

$$\sum_{\mathbf{s}} M_{\mathbf{s}}^{\dagger} M_{\mathbf{s}} = \mathbf{1}. \tag{2.11}$$

Given an initial density matrix ρ_0, the outcome probability and conditioned state are those in Eqs. (1.3) and (1.4). For a pure state $\rho_0 = |\psi_0\rangle\langle\psi_0|$, the unnormalized conditioned wavefunction is $M_{\mathbf{s}}|\psi_0\rangle$.

Weak measurements are close to the identity. A common schematic form is

$$M_{\mathbf{s}} \propto \exp\left[\lambda \sum_j s_j O_j\right], \tag{2.12}$$

with small measurement strength λ. Such a measurement inserts a source coupled to the lattice operator O_j. In the continuum limit, the source couples to whichever

CFT fields appear in the lattice expansion of O_j. The source pattern s_j can be uniform, staggered, random, correlated, or selected by post-selection; each case leads to different long-distance behavior.

Projective measurements correspond to a strong limit in which the Kraus operator projects onto an eigenspace. They are harder to treat perturbatively but often simpler experimentally. The Rydberg roadmap uses projective occupation measurements on a subset of sites, while the boundary-transition work studies projective measurements on a subset of gapless states. In both cases, the strong-measurement limit is interpreted through boundary conditions rather than through a small-λ expansion.

2.7 Measurement-conditioned states and Born ensembles

The full set of conditioned states $\{\rho_{\mathbf{s}}\}$ forms an ensemble weighted by Born probabilities $p(\mathbf{s})$. Several inequivalent averages over this ensemble appear throughout the thesis.

The ordinary Born average is the density matrix

$$\rho_{\mathrm{Born}} = \sum_{\mathbf{s}} p(\mathbf{s})\rho_{\mathbf{s}} = \sum_{\mathbf{s}} M_{\mathbf{s}}\rho_0 M_{\mathbf{s}}^{\dagger}. \tag{2.13}$$

This object is natural if the measurement record is discarded. However, it often misses measurement-altered physics because it linearly averages over sectors with different signs, symmetries, or effective boundary conditions.

A post-selected ensemble restricts to a chosen subset $\mathcal{S}$ of outcomes,

$$\rho_{\mathcal{S}} = \frac{1}{P_{\mathcal{S}}} \sum_{\mathbf{s}\in\mathcal{S}} p(\mathbf{s})\rho_{\mathbf{s}}, \qquad P_{\mathcal{S}} = \sum_{\mathbf{s}\in\mathcal{S}} p(\mathbf{s}). \tag{2.14}$$

If $\mathcal{S}$ contains one record, this is strict post-selection. If it contains a symmetry-related family of records, it becomes symmetry-resolved or restricted averaging. Much of the practical challenge lies in choosing $\mathcal{S}$ large enough to be experimentally accessible but structured enough to retain the altered critical behavior.

A reweighted ensemble replaces $p(\mathbf{s})$ by another weight $w(\mathbf{s})$. Uniform-outcome averages, restricted averages, and replica-motivated nonlinear moments all fall into this broader category. They are not generally represented by a physical density matrix obtained from ignoring measurement outcomes, but they can be meaningful diagnostics of the post-measurement ensemble.

2.8 Nonlinear measurement averages

Suppose $O(\mathbf{z})$ is an observable measured in a final system snapshot $\mathbf{z}$, and $\mathbf{s}$ is the earlier measurement record. The conditioned expectation value is

$$f_O(\mathbf{s}) = \mathbb{E}[O(\mathbf{z}) \mid \mathbf{s}] = \langle O \rangle_{\mathbf{s}} \,. \tag{2.15}$$

The linear expectation $\mathbb{E}[f_O(\mathbf{s})] = \langle O \rangle_0$ is the ordinary pre-measurement expectation value. Nonlinear moments such as

$$A_q[O] = \mathbb{E}_{\mathbf{s}}\left[f_O(\mathbf{s})^q\right] \tag{2.16}$$

instead ask how strongly the measurement record predicts the system response.

The case $q = 2$ has a useful variational representation. For bounded observables,

$$A_2[O] = \sup_f \mathbb{E}\left[2O(\mathbf{z})f(\mathbf{s}) - f(\mathbf{s})^2\right], \tag{2.17}$$

where the unrestricted optimizer is $f^\star(\mathbf{s}) = \mathbb{E}[O \mid \mathbf{s}]$. This identity is the conceptual bridge from nonlinear observables to statistical learning. Estimating A_2 no longer requires resolving every post-selected sector separately; it requires learning the conditional response within an appropriate function class.

This perspective will be developed much more carefully in Chapters 13–15. Here it suffices to note that nonlinear observables are not optional technical complications. They are often the observables in which measurement-altered criticality survives after averaging over random outcomes.

2.9 Extracting scaling dimensions from correlation functions

The simplest diagnostic of altered criticality is a changed power-law exponent. In a periodic chain, the standard procedure is to measure or compute a correlation function $C(r)$ and fit it to

$$C(r) = A\, d_L(r)^{-2\Delta} + \cdots \,, \tag{2.18}$$

where $d_L(r)$ is the chord distance and the ellipses denote subleading corrections. In an open chain, one-point functions can be fit to boundary forms like Eq. (2.10), while two-point functions require boundary-dependent scaling functions.

For measurement-altered states one must decide which ensemble is being probed before fitting. A fixed-outcome correlator, a Born-averaged correlator, a symmetry-resolved correlator, a uniform-outcome correlator, and a learned nonlinear moment can all scale differently. Thus the exponent is not a property of the measurement protocol alone. It is a property of the protocol together with the ensemble and observable used to analyze it.

This point recurs throughout the book. The Ising chapters compare fixed-outcome and averaged diagnostics. The boundary chapters compare post-selected and decoded correlations. The Rydberg chapters emphasize restricted averages accessible from full measurement records. The decoder chapters learn nonlinear moments whose scaling reveals altered fixed points without explicit post-selection.

2.10 Entanglement diagnostics and effective central charge

Correlation functions diagnose operator scaling dimensions. Entanglement diagnoses the organization of many degrees of freedom. In an unmeasured one-dimensional critical ground state, the coefficient of logarithmic entanglement growth is fixed by the central charge. In a post-measurement state, entanglement can behave in more varied ways. It may retain the original coefficient, acquire an effective coefficient, or be destroyed even while some power-law correlations remain.

This separation between correlation and entanglement is especially visible in imperfect teleportation. Some teleportation errors preserve power-law correlations but eliminate the long-range entanglement structure of the original critical state. Boundary transitions also exhibit entanglement signatures associated with boundary fixed points and defect lines. For this reason, this thesis treats entanglement and correlation exponents as complementary diagnostics.

2.11 Numerical toolkit: exact methods, MPS, DMRG, and finite-size scaling

Most examples in this thesis require both field-theory predictions and numerical checks. Exact free-fermion methods are available for some Ising-chain calculations. Matrix-product-state (MPS) methods and density matrix renormalization group (DMRG) are used more broadly to prepare critical ground states and evaluate post-measurement observables [14, 15]. Finite-size scaling is then used to extract exponents and compare with CFT expectations.

Several numerical issues recur. Critical systems require large bond dimension because entanglement grows logarithmically. Post-measurement states can have stronger finite-size corrections than the original ground state. Open boundaries simplify some calculations but introduce boundary effects that must be fit carefully. Post-selected sectors may have small probabilities, so numerical sampling and exact contraction must be matched to the ensemble being studied.

2.12 Machine-learning decoders as conditional-response estimators

The statistical-learning chapters use a simple conceptual setup. Each experimental or simulated run produces a pair $(\mathbf{z}, \mathbf{s})$, where $\mathbf{s}$ is the measurement record and $\mathbf{z}$ is a final system snapshot. For an observable $O(\mathbf{z})$, the best possible decoder predicts

$$f_O^{\star}(\mathbf{s}) = \mathbb{E}[O(\mathbf{z}) \mid \mathbf{s}]. \tag{2.19}$$

A trained model $\widehat{f}$ approximates this conditional expectation. Once $\widehat{f}$ is learned, nonlinear observables such as $A_2[O]$ can be estimated from all available data rather than from repeated occurrences of the same post-selected record.

The relevant question is not whether an arbitrary function of $\mathbf{s}$ can be learned. The question is whether the physically important conditioned responses lie in function classes of manageable complexity: linear functions, multiscale convolutional networks, or symmetry-constrained models. Criticality complicates this question because long-range correlations are important, but it also imposes structure that suitable architectures can exploit.

This decoder viewpoint closes the loop begun in Chapter 1. Measurements alter criticality at the level of conditioned states. Experiments produce random measurement records. Nonlinear observables reveal the altered physics. Statistical learning offers a route from the raw records to those nonlinear observables without exponential costly post-selection.

Part II

The Canonical Ising Mechanism

"Rule of thumb, maaan. Spend more time <doing random hobby> than you do thinkin' about work."

— Pascal, *Animal Crossing: New Horizons*

Chapter 3

ANCILLA-ASSISTED MEASUREMENTS OF THE CRITICAL ISING CHAIN

This chapter develops the canonical microscopic mechanism for measurement-altered quantum criticality. Chapter 2 introduced the shared CFT and measurement language; here we specialize that language to an explicit two-chain protocol in which a critical Ising chain is entangled with a correlated ancilla chain and the ancilla are then projectively measured. The central lesson is that the measured ancilla induce a non-unitary, outcome-dependent perturbation of the critical-chain wavefunction. The form of that perturbation is controlled by the entangling gate, the measurement basis, the outcome string, and the ancilla correlations.

3.1 Overview

The protocol and main outcomes are summarized in Fig. 3.1. The upper chain is tuned to the critical transverse-field Ising point. The lower chain supplies correlated ancilla degrees of freedom. After the two chains are coupled locally, measuring the ancilla prepares an outcome-resolved critical-chain state. The remainder of this chapter derives an effective action for that state and analyzes the couplings that appear in it. Chapter 4 then uses the same machinery to classify the resulting altered Ising correlations and experimentally accessible diagnostics.

3.2 Microscopic Ising chain and ancilla protocol

Ising-chain conventions used in this part

Throughout this chapter we explore the effect of measurements on an Ising quantum critical point realized microscopically in the canonical transverse field Ising model,

$$H = \sum_j (-J Z_j Z_{j+1} - h X_j). \tag{3.1}$$

Here Z_j and X_j are Pauli operators acting on site j of a chain with periodic boundary conditions (unless specified otherwise). Additionally, we assume ferromagnetic interactions, $J > 0$, and a positive transverse field, $h > 0$. Equation (3.1) preserves both time reversal symmetry $\mathcal{T}$, which leaves X_j and Z_j invariant but enacts complex conjugation, and global $\mathbb{Z}_2$ spin flip symmetry generated by $G = \prod_j X_j$. At $h > J$, the system realizes a symmetry-preserving paramagnetic phase. For

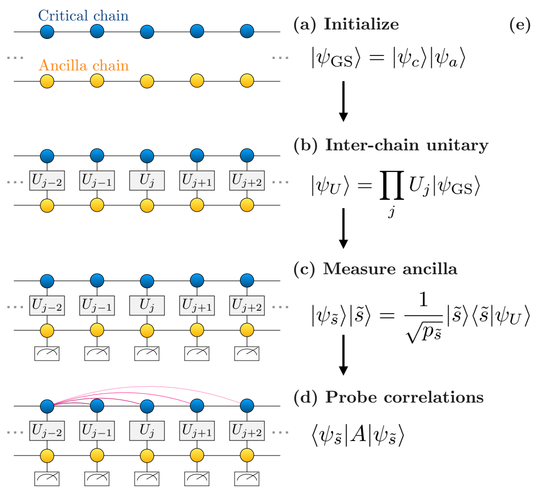

(e)

Symmetry of $\lvert\psi_{\tilde{s}}\rangle$	$\mathbb{Z}_2$ or $\mathbb{Z}_2 \times \mathcal{T}$	None
predictions for $\tilde{Z}$-basis measurements	modified scaling behavior of $\langle\psi_{\tilde{s}}\lvert Z_j Z_k\rvert\psi_{\tilde{s}}\rangle$ given a generic $\tilde{s}$	order parameter $\langle\psi_{\tilde{s}}\lvert Z_j\rvert\psi_{\tilde{s}}\rangle \neq 0$ given a generic $\tilde{s}$ and $\sum_{\tilde{s}} p_{\tilde{s}}\langle\psi_{\tilde{s}}\lvert Z_j\rvert\psi_{\tilde{s}}\rangle^2 \neq 0$
predictions for $\tilde{X}$-basis measurements	modified scaling behavior of $\langle\psi_{\tilde{s}}\lvert Z_j Z_k\rvert\psi_{\tilde{s}}\rangle$ given the most likely $\tilde{s}$	order parameter $\langle\psi_{\tilde{s}}\lvert Z_j\rvert\psi_{\tilde{s}}\rangle \neq 0$ given the most likely $\tilde{s}$ and $\sum_{\tilde{s}} p_{\tilde{s}}\langle\psi_{\tilde{s}}\lvert Z_j\rvert\psi_{\tilde{s}}\rangle^2 \neq 0$
	Symmetry-resolved average $r(A)$ [Eq.(76)]	
	modified scaling dimension of $r(Z_j Z_k)$	order parameter $r(Z_j) \neq 0$

Figure 3.1: **Protocol used to explore measurement-altered Ising criticality (left) and summary of the main results (right).** (a) The upper chain is always prepared in the ground state $|\psi_c\rangle$ of the critical transverse-field Ising model. The ancilla chain is initialized into the ground state $|\psi_a\rangle$ of the Ising model either in the paramagnetic phase or at criticality. (b) After a unitary that entangles the two chains followed by (c) ancilla measurements, the ancilla chain enters a product state $|\tilde{s}\rangle$ while the upper chain enters a state $|\psi_{\tilde{s}}\rangle$ dependent on the measurement outcome $\tilde{s}$. (d) Physical operators A for the top chain are then probed in the state $|\psi_{\tilde{s}}\rangle$. The table (e) summarizes our predictions for the four cases that we explore, distinguished by the ancilla measurement basis and symmetry of the post-measurement wavefunction $|\psi_{\tilde{s}}\rangle$.

$h < J$, a ferromagnetic phase emerges, characterized by a non-zero order parameter $\langle Z_j\rangle \neq 0$ that indicates spontaneously broken $\mathbb{Z}_2$ symmetry. The paramagnetic and ferromagnetic phases are related under a duality transformation that interchanges $J \leftrightarrow h$.

Ising criticality appears at the self-dual point $J = h$ to which we specialize hereafter. The low-energy critical theory is most easily accessed via a Jordan-Wigner transformation to Majorana fermion operators

$$\gamma_{Aj} = \left(\prod_{k<j} X_k\right) Z_j, \quad \gamma_{Bj} = \left(\prod_{k<j} X_j\right) iX_j Z_j. \tag{3.2}$$

In this basis the $J = h$ Hamiltonian becomes

$$H_c = iJ\sum_j (\gamma_{Aj+1} - \gamma_{Aj})\gamma_{Bj}. \tag{3.3}$$

Focusing on long-wavelength Fourier components of γ_{Aj} and γ_{Bj}, which comprise the important degrees of freedom at criticality, yields the continuum Hamiltonian

$\mathcal{H}_c = iv\int_x(\partial_x\gamma_A)\gamma_B$ with $v \propto J$. Upon changing basis to $\gamma_A = \gamma_R + \gamma_L$ and $\gamma_B = \gamma_R - \gamma_L$, we arrive at

$$\mathcal{H}_c = -iv\int_x(\gamma_R\partial_x\gamma_R - \gamma_L\partial_x\gamma_L), \tag{3.4}$$

which describes kinetic energy for right- and left-moving Majorana fermions γ_R and γ_L.

Equation (3.4) corresponds to an Ising conformal field theory (CFT) with central charge $c = 1/2$ [9]. The Ising CFT exhibits three primary fields: the identity $\mathbb{1}$, the 'spin field' σ (scaling dimension $\Delta_\sigma = 1/8$), and the 'energy field' ε (dimension $\Delta_\varepsilon = 1$). The spin field is odd under $\mathbb{Z}_2$ symmetry and represents the continuum limit of the ferromagnetic order parameter. Consequently, only correlators containing an even number of spin fields can be non-zero at criticality. For instance, one- and two-point spin-field correlators read

$$\langle\sigma(x)\rangle = 0, \quad \langle\sigma(x)\sigma(x')\rangle \sim \frac{1}{|x-x'|^{1/4}}. \tag{3.5}$$

The energy field is a composite of right- and left-movers, $\varepsilon = i\gamma_R\gamma_L$; this field is odd under duality and hence represents a perturbation that moves the system off of criticality. The operator product expansion for two fields at different points determine the following fusion rules:

$$\begin{cases} \sigma\times\sigma = \mathbb{1} + \varepsilon, \\ \varepsilon\times\varepsilon = \mathbb{1}, \\ \sigma\times\varepsilon = \sigma. \end{cases} \tag{3.6}$$

Local microscopic spin operators admit straightforward expansions in terms of the above CFT fields and their descendants. In particular, we have

$$Z_j \sim \sigma + \cdots \tag{3.7}$$

$$X_j - \langle X\rangle \sim \varepsilon + \cdots, \tag{3.8}$$

where the ellipses denote fields with subleading scaling dimension. Equation (3.7) follows from $\mathbb{Z}_2$ symmetry together with translation invariance of the ferromagnetic phase (for the antiferromagnetic case, $J < 0$, an additional $(-1)^j$ factor would appear on the right side). In Eq. (3.8), $\langle X\rangle$ denotes the (position-independent) ground-state expectation value of X_j—which is generically non-zero due to the transverse field. In the thermodynamic limit at criticality one finds $\langle X\rangle = 2/\pi$. Subtracting off this expectation value from the left-hand side removes terms proportional to the identity field on the right-hand side. One can understand the appearance of ε in Eq. (3.8) by noting that perturbing the microscopic Hamiltonian with a term $\propto \sum_j X_j$ moves the system off of criticality, corresponding to the generation of the energy field in the continuum theory. (The same conclusion follows by expressing X_j in terms of Majorana fermions and taking the continuum limit [1].)

With the aid of relations like Eqs. (3.7) and (3.8), standard techniques relate ground-state expectation values of microscopic operators to averages of CFT fields expressed in path-integral language. We illustrate the approach in a way that will be useful for exploring the influence of measurements in Section 3.3. The ground-state expectation value of a microscopic operator A in the critical chain's ground state $|\psi_c\rangle$,

$$\langle A\rangle = \langle\psi_c|\, A\, |\psi_c\rangle\,, \tag{3.9}$$

can always be expressed as

$$\langle A\rangle = \lim_{\beta\to\infty}\frac{1}{Z}\operatorname{Tr} e^{-\beta H_c/2} A e^{-\beta H_c/2}. \tag{3.10}$$

The $e^{-\beta H_c/2}$ factors in the numerator project away excited state components from the bra and ket in each element of the trace, and the partition function $Z = \lim_{\beta\to\infty}\operatorname{Tr} e^{-\beta H_c}$ in the denominator ensures proper normalization. Next we take the continuum limit of both sides:

$$\langle A\rangle \sim \langle\mathcal{A}\rangle = \lim_{\beta\to\infty}\frac{1}{\mathcal{Z}}\operatorname{Tr} e^{-\beta\mathcal{H}_c/2}\mathcal{A} e^{-\beta\mathcal{H}_c/2}. \tag{3.11}$$

Calligraphic fonts indicate low-energy expansions of the corresponding quantities in Eq. (3.10). For instance, if $A = Z_j Z_{j'}$ then Eq. (3.7) gives $\mathcal{A} = \sigma(x_j)\sigma(x_{j'})$ for x_i a continuum coordinate corresponding to site i. Finally, Trotterizing the exponentials and inserting resolutions of identity in the fermionic coherent state basis yields

$$\langle\mathcal{A}\rangle = \lim_{\beta\to\infty}\frac{1}{\mathcal{Z}}\int \mathcal{D}\gamma_R\mathcal{D}\gamma_L e^{-\mathcal{S}_c}\mathcal{A}(\tau=0) \tag{3.12}$$

with the Euclidean Ising CFT action

$$\mathcal{S}_c = \int_x\int_{-\beta/2}^{\beta/2} \mathrm{d}\tau\, [\gamma_R(\partial_\tau - iv\partial_x)\gamma_R + \gamma_L(\partial_\tau + iv\partial_x)\gamma_L]. \tag{3.13}$$

Note that in our convention imaginary time τ runs from $-\beta/2$ to $+\beta/2$ with $\beta\to\infty$; the operator ordering in Eq. (3.11) then naturally gives $\mathcal{A}$ evaluated at $\tau = 0$ in Eq. (3.12).

[1] Notice that $\langle i\gamma_R\gamma_L\rangle = 0$ when evaluated in the critical Ising CFT

Protocol

Performing local projective measurements to all sites of the critical chain reviewed above would simply collapse the corresponding wave function into a trivial product state, thereby destroying all existent correlations. Hence, we introduce a second, ancillary transverse-field Ising chain that enables us to enact different types of generalized measurements on the critical Ising chain and characterize their non-trivial effect on its entanglement structure. Specifically, the ancilla Hamiltonian is

$$H_{\rm anc} = \sum_j (-J_{\rm anc}\tilde{Z}_j\tilde{Z}_{j+1} - h_{\rm anc}\tilde{X}_j), \tag{3.14}$$

where $\tilde{Z}_j$ and $\tilde{X}_j$ are Pauli operators for the ancilla spins and we assume $J_{\rm anc}, h_{\rm anc} > 0$. Throughout we work in the regime $h_{\rm anc} \geq J_{\rm anc}$—i.e., the ancilla are either critical or realize the gapped paramagnetic phase, so that the spin-flip symmetry generated by $\tilde{G} = \prod_j \tilde{X}_j$ is always preserved in the ground state.

Inspired by Ref. [16], we consider the following protocol (see Fig. 3.1 for a summary):

(a) Initialize the system into the wavefunction

$$|\psi_{\rm GS}\rangle = |\psi_c\rangle\,|\psi_a\rangle\,, \tag{3.15}$$

where $|\psi_c\rangle$ is the ground state of the top (critical) chain and $|\psi_a\rangle$ is the ground state of the bottom (ancilla) chain.

(b) Apply a unitary gate U_j to each pair of adjacent sites from the critical and ancilla chains, sending

$$|\psi_{\rm GS}\rangle \to |\psi_U\rangle = \left(\prod_j U_j\right)|\psi_c\rangle\,|\psi_a\rangle\,. \tag{3.16}$$

The unitaries we apply generally consist of single-spin ancilla rotations followed by a two-spin entangling gate, and are always implemented in a translationally invariant manner.

(c) Projectively measure all ancilla spins in some fixed basis, e.g., $\tilde{Z}$ or $\tilde{X}$, yielding measurement outcome

$$\tilde{s} \equiv \{\tilde{s}_j\} \tag{3.17}$$

with $\tilde{s}_j \in \pm 1$. The wavefunction correspondingly collapses to $|\psi_{\tilde{s}}\rangle\,|\tilde{s}\rangle$; here $|\psi_{\tilde{s}}\rangle$ denotes the post-measurement state for the top chain, which depends on the outcome

$\tilde{s}$. More precisely, this step sends

$$\begin{aligned} |\psi_U\rangle &\xrightarrow{\text{measure}} |\psi_{\tilde{s}}\rangle |\tilde{s}\rangle \\ &= \frac{1}{\sqrt{p_{\tilde{s}}}} \left(\prod_j \left|\tilde{s}_j\right\rangle \left\langle\tilde{s}_j\right| U_j \right) |\psi_c\rangle |\psi_a\rangle , \end{aligned} \tag{3.18}$$

where the normalization

$$p_{\tilde{s}} = \langle\psi_a| \langle\psi_c| \left(\prod_j U_j^\dagger \left|\tilde{s}_j\right\rangle \left\langle\tilde{s}_j\right| U_j \right) |\psi_c\rangle |\psi_a\rangle \tag{3.19}$$

specifies the probability for obtaining measurement outcome $\tilde{s}$.

(d) Probe correlations on the top chain for the post-measurement state $|\psi_{\tilde{s}}\rangle$.

Inspection of Eq. (3.18) reveals that the ancilla measurements can nontrivially impact correlations in the critical chain only if the measurement basis and unitaries are chosen such that $[\left|\tilde{s}_j\right\rangle \left\langle\tilde{s}_j\right|, U_j] \neq 0$ [2]. Even in this case, however, extracting measurement-induced changes in correlations poses a subtle problem. For an arbitrary critical-chain observable A, performing a standard average of $\langle\psi_{\tilde{s}}| A |\psi_{\tilde{s}}\rangle$ over ancilla measurement outcomes simply recovers the expectation value $\langle\psi_U| A |\psi_U\rangle$ taken in the pre-measurement state. Indeed, using Eqs. (3.16) and (3.18) yields

$$\begin{aligned} \sum_{\tilde{s}} p_{\tilde{s}} \langle\psi_{\tilde{s}}| A |\psi_{\tilde{s}}\rangle &= \sum_{\tilde{s}} \langle\psi_U| \left(\prod_j \left|\tilde{s}_j\right\rangle \left\langle\tilde{s}_j\right| \right) \\ &\quad \times A \left(\prod_j \left|\tilde{s}_j\right\rangle \left\langle\tilde{s}_j\right| \right) |\psi_U\rangle \\ &= \sum_{\tilde{s}} \langle\psi_U| \left(\prod_j \left|\tilde{s}_j\right\rangle \left\langle\tilde{s}_j\right| \right) A |\psi_U\rangle = \langle\psi_U| A |\psi_U\rangle . \end{aligned} \tag{3.20}$$

The second equality follows from the fact that the projectors $\left|\tilde{s}_j\right\rangle \left\langle\tilde{s}_j\right|$ commute with A (because they act on different chains) and square to themselves, while the third follows upon removing a resolution of the identity for the ancilla chain.

Our protocol performs a particular physical implementation of generalized measurements that combines additional degrees of freedom provided by the ancilla chain, a unitary entangling transformation, and projective measurements (see, e.g., Ref. [17]). More importantly, it allows us to assess how quantum correlations among

[2] Otherwise the measurement translates into a control unitary on the top chain depending on the measurement outcome of the bottom chain.

the ancilla, tunable via the ratio $h_{\mathrm{anc}}/J_{\mathrm{anc}}$, impact the measurement-induced changes in the critical chain's properties. Let us make this connection more explicit. The post-measured state $|\psi_{\tilde{s}}\rangle$ given in Eq. (3.18) can be written as

$$|\psi_{\tilde{s}}\rangle = \frac{1}{\sqrt{p_{\tilde{s}}}} M_{\tilde{s}} |\psi_c\rangle, \tag{3.21}$$

where, given measurement outcome $\tilde{s}$, $M_{\tilde{s}} \equiv \langle \tilde{s}| \prod_j U_j |\psi_a\rangle$ denotes the measurement operator acting on the critical chain. The full set of measurement operators satisfy the completeness relation $\sum_{\tilde{s}} M_{\tilde{s}}^\dagger M_{\tilde{s}} = \mathbb{1}_c$. If $|\psi_a\rangle$ was a product state, then we could factorize $M_{\tilde{s}} = \prod_j M_{\tilde{s}_j}$ in terms of on-site measurement operators M_{s_j}. However, for nontrivially entangled $|\psi_a\rangle$—which we always consider below—this exact factorization no longer holds, though an approximate factorization can nevertheless suffice to capture the essential influence of measurement, depending on the precise form of $M_{\tilde{s}}$ and the range of ancilla correlations. We return to this point in Section 4.4.

Subsequent sections investigate the protocol with different classes of unitaries and measurement bases using a combination of field-theoretic and numerical tools. The latter combine covariant-matrix techniques for Gaussian states (explained in Chapter 3.6) when characterizing a single chain; exact diagonalization (ED) to exactly evaluate averages over measurement outcomes; and tensor network methods [18], using the density matrix renormalization group (DMRG) method [14] and its infinite variant (iDMRG) [19] to evaluate correlations on specific measurement outcomes. As a prerequisite, next we develop a perturbative formalism that we use extensively to distill measurement effects into a perturbation to the Ising CFT action.

3.3 Effective action formalism

Table 3.1 lists the four classes of unitaries U_j that we examine, together with the corresponding ancilla measurement basis taken for each case. In the second column, $\langle X\rangle = \langle\psi_c| X_j |\psi_c\rangle$ as defined previously, C is a constant, and u characterizes the strength of the unitary—i.e., how far U_j is from the identity. As we will see later, the symmetry of U_j depends on whether $C = 0$ or $C \neq 0$ in a manner that qualitatively affects critical-chain correlations after measurement. Throughout our analytical treatment, we assume small $u \ll 1$ that does not scale with system size. Our goal in Chapter 3.3 is to recast the post-measurement state in the form

$$|\psi_{\tilde{s}}\rangle = \frac{1}{\sqrt{\mathcal{N}}} U' e^{-H_m/2} |\psi_c\rangle. \tag{3.22}$$

Here U' is a unitary operator acting solely on the critical chain, while H_m is a Hermitian operator, organized systematically in powers of u, that encodes the

Case	Unitary U_j	Ancilla measurement basis
I	$\exp[iu(X_j - \langle X\rangle)\tilde{X}_j]$	$\tilde{Z}$
II	$\exp[iu(Z_j - C)\tilde{X}_j]$	$\tilde{Z}$
III	$\exp[iu(X_j - \langle X\rangle)\tilde{Z}_j]$	$\tilde{X}$
IV	$\exp[iu(Z_j - C)\tilde{Z}_j]$	$\tilde{X}$

Table 3.1: Four classes of unitaries used in our protocols, along with the corresponding ancilla measurement basis. In cases II and IV, C is a constant that controls whether or not the post-measurement state $|\psi_{\tilde{s}}\rangle$ preserves global spin-flip symmetry for the critical chain.

non-unitary change in $|\psi_U\rangle$ imposed by the measurement. One can view this representation of $|\psi_{\tilde{s}}\rangle$ as arising from a polar decomposition of the measurement operator $M_{\tilde{s}}$ in Eq. (3.21), up to an overall constant (dependent on $\tilde{s}$) that is absorbed into the normalization factor $\mathcal{N}$. Chapter 3.3 uses the form in Eq. (3.22) to develop a continuum-limit CFT framework for characterizing observables given a fixed ancilla measurement outcome.

Perturbative framework

All four unitaries in Table 3.1 take the form

$$U_j = e^{iu(O_j - \theta)\tilde{O}_j}. \tag{3.23}$$

The constant θ is either $\langle X\rangle$ (cases I, III) or C (cases II, IV), while O_j and $\tilde{O}_j$ denote Pauli matrices that respectively act on the critical chain and ancilla. We refer to Chapter 3.5 for a detailed derivation of the post-measurement state, providing here the final expression of U' and H_m appearing in Eq. (3.22). Defining $U' = e^{iH'}$, we obtain to $O(u^2)$

$$H' = u \sum_j a(j)(O_j - \langle O\rangle), \tag{3.24}$$

$$\begin{aligned} H_m &= u^2 \sum_j m_j (O_j - \langle O\rangle) \\ &\quad + u^2 \sum_{j \neq k} V_{jk}(O_j - \langle O\rangle)(O_k - \langle O\rangle). \end{aligned} \tag{3.25}$$

For later convenience we have organized the contributions in terms of $O_j - \langle O\rangle$, where $\langle O\rangle = \langle\psi_c| O_j |\psi_c\rangle$ is the expectation value of O_j in the initialized state, prior to applying the unitary and measuring. Equation (3.25) contains coefficients

$$V_{jk} = a(j,k) - a(j)a(k) \tag{3.26}$$

$$m_j = -2\theta[1 - a(j)^2] + 2(\langle O\rangle - \theta)\sum_{k\neq j} V_{jk}. \tag{3.27}$$

where

$$a(j) = \frac{\langle\tilde{s}|\tilde{O}_j|\psi_a\rangle}{\langle\tilde{s}|\psi_a\rangle}, \quad a(j,k) = \frac{\langle\tilde{s}|\tilde{O}_j\tilde{O}_k|\psi_a\rangle}{\langle\tilde{s}|\psi_a\rangle}. \tag{3.28}$$

We stress that $U' = e^{iH'}$ factorizes into a product of operators acting on a single site j—i.e., one can always decompose $U' = \prod_j U'_j$ at order $O(u^2)$—whereas $e^{-H_m/2}$ admits no such factorization due to the V_{jk} term. The leading corrections to H' and H_m arise at $O(u^3)$ and $O(u^4)$, respectively.

The derivation of the post-measurement state assumed $\langle\tilde{s}|\,\psi_a\rangle \neq 0$, which holds provided measurement outcome $\tilde{s}$ can arise even at $u = 0$, where the unitary applied in our protocol reduces to the identity. As we will see below, however, symmetry can constrain $\langle\tilde{s}|\,\psi_a\rangle = 0$ for a class of $\tilde{X}$-basis measurement outcomes. In the latter case our expansion for H_m and H' breaks down [as evidenced by the vanishing denominator in $a(i_1,\cdots,i_{N_f})$ from Eq. (3.50)]. Nevertheless, even without an action-based framework, in Section 4.3 we will use a non-perturbative technique to constrain correlations resulting from such measurement outcomes. For now we neglect this case and continue to assume $\langle\tilde{s}|\,\psi_a\rangle \neq 0$ in the remainder of this section.

Continuum limit

Using Eq. (3.22), the expectation value of a general critical-chain observable A in the state $|\psi_{\tilde{s}}\rangle$ associated with measurement outcome $\tilde{s}$ reads

$$\langle A\rangle_{\tilde{s}} = \frac{1}{\mathcal{N}}\langle\psi_c|\,e^{-H_m/2}A_{U'}e^{-H_m/2}\,|\psi_c\rangle\,, \tag{3.29}$$

where $A_{U'} = U'^{\dagger}AU'$. The numerator on the right-hand side of Eq. (3.29) has the same form as the right side of Eq. (3.9), but with $A \to e^{-H_m/2}A_{U'}e^{-H_m/2}$ as a consequence of the unitary and measurement applied in our protocol. Furthermore, the normalization constant $\mathcal{N} = \langle\psi_c|\,e^{-H_m}\,|\psi_c\rangle$ also has the form of Eq. (3.9) with $A \to e^{-H_m}$. Following exactly the logic below Eq. (3.9) for both the numerator and demoninator leads to the continuum expansion

$$\begin{aligned}\langle A\rangle_{\tilde{s}} &\sim \langle\mathcal{A}\rangle_{\tilde{s}}\\ &= \lim_{\beta\to\infty}\frac{1}{\mathcal{Z}'}\int\mathcal{D}\gamma_R\mathcal{D}\gamma_L e^{-(S_c+S_m)}\mathcal{A}_{U'}(\tau=0)\end{aligned} \tag{3.30}$$

that generalizes Eq. (3.12). The new partition function is

$$\mathcal{Z}' = \int \mathcal{D}\gamma_R \mathcal{D}\gamma_L e^{-(\mathcal{S}_c + \mathcal{S}_m)}. \tag{3.31}$$

Most crucially, the Ising CFT action $\mathcal{S}_c$ from Eq. (3.13) has been appended with a 'defect line' acting at all positions x but only at imaginary time $\tau = 0$, encoded through

$$\mathcal{S}_m = \int_x \mathcal{H}_m(\tau = 0) \tag{3.32}$$

with $\mathcal{H}_m$ the continuum expansion of H_m. The explicit form of the defect line action $\mathcal{S}_m$ depends on the unitary U and measurement basis, and will be explored in depth in Chapters 4.1 and 4.2 for cases I through IV in Table 3.1. Specifically, we seek to understand its impact on observables $\mathcal{A}_{U'}$—which are also evaluated at $\tau = 0$ in the path integral description, thereby potentially altering critical properties of the original Ising CFT in a dramatic manner. (Technically, $\mathcal{A}_{\tilde{U}}$ is sandwiched between two factors of $e^{-\mathcal{S}_m/2}$ evaluated at slightly different imaginary times. We approximated this combination as $\mathcal{A}_{\tilde{U}} e^{-\mathcal{S}_m}$ since the leading scaling behavior is unchanged by this rewriting.) It is important, however, to first understand the conditions under which the perturbative expansion developed above is expected to be controlled. To this end we now study the properties of the V_{jk} and m_j couplings in Eq. (3.25).

3.4 Properties of V_{jk} and m_j couplings

In general, both V_{jk} and m_j vary nontrivially with the site indices in a manner dependent on the measurement outcome. The couplings V_{jk} control the interaction range in H_m, and exhibit a structure reminiscent of a connected correlator. That is, V_{jk} specifies how the overlap between the initial ancilla wavefunction and the measured state changes under a *correlated* flip of spins at sites j, k. It is thus natural to expect that V_{jk} statistically averaged over measurement outcomes, denoted $\bar{V}_{jk}$, decays with $|j - k|$—either exponentially if the ancilla are initialized into the ground state of the gapped paramagnetic phase, or as a power-law if the ancilla are critical. We confirm this expectation below. The statistically averaged m_j coefficients, denoted $\bar{m}_j$, would then not suffer from a divergence in the presence of the $\sum_{k\neq j} V_{jk}$ term in Eq. (3.27), so long as $\bar{V}_{jk}$ decays faster than $1/|j - k|$ (which does not always hold as we will see later).

For a *particular* measurement outcome $\tilde{s}$, control of the expansion leading to H_m in the previous subsection requires, at a minimum, that V_{jk} and m_j for this outcome are similarly well-behaved. For example, if the amplitude of m_j for a particular $\tilde{s}$

grows with system size N, then $u \ll 1$ does not suffice to control the expansion (assuming that u does not also scale with system size). Additionally, if V_{jk} for a given $\tilde{s}$ does not decay to zero with $|j-k|$, then the correspondingly infinite-range interaction in Eq. (3.25) makes the expansion suspect. Thus it is crucial to quantify not only the mean but also the variances $\text{Var}(V_{jk})$ and $\text{Var}(m_j)$ of the couplings in H_m—which will inform which set of measurement outcomes we analyze later on. Next, we address this problem for the four classes of unitaries/ancilla measurement bases listed in Table 3.1.

In all four cases we statistically average using the $u = 0$ distribution for the ancilla measurement outcomes,

$$p_{\tilde{s}} = \langle \tilde{s}|\psi_a\rangle^2 \left\langle \psi_c|e^{-H_m}|\psi_c\right\rangle \sim \langle \tilde{s}|\psi_a\rangle^2 \equiv p_{\tilde{s}}^{(0)}, \tag{3.33}$$

since m_j and V_{jk} already come with u^2 prefactors. In Eq. (3.33) and many places below, we take advantage of the fact that the overlaps $\langle \tilde{s}|\psi_a\rangle$ are non-negative, which follows because the transverse-field Ising model [Eq. (3.14)] is *stoquastic* [20]. That is, on a given computational basis state $|v\rangle$—in this case the $\tilde{Z}$ or $\tilde{X}$ local basis—$\langle v|\, H_{\text{anc}}\, |w\rangle \leq 0$ for $v \neq w$, from which it follows that $\langle v|\, |\psi_a\rangle \geq 0$ for arbitrary basis states v. Hence, all elements $a(i_1, \cdots, i_{N_F})$ from Eq. (3.50) are also non-negative. Finally, since the fermionized H_{anc} is quadratic in Majorana fermion fields, we exploit the Gaussianity of both $|\psi_a\rangle$ and $|\tilde{s}\rangle$ to evaluate the elements $a(i_1, \cdots, i_{N_F})$ using covariance-matrix techniques; see Chapter 3.6. These tools, along with standard results for transverse-field Ising chain correlators, allow us to compute the probabilities $p_{\tilde{s}}^{(0)}$ as well as the mean and variance of m_j and V_{jk} below.

$\tilde{Z}$ measurement basis

When the ancilla are measured in the $\tilde{Z}$ basis, the mean and variance of V_{jk} evaluate to

$$\bar{V}_{jk} = \sum_{\tilde{s}} p_{\tilde{s}}^{(0)} V_{jk} = 0 \tag{3.34}$$

$$\begin{aligned}\text{Var}(V_{jk}) &= \sum_{\tilde{s}} p_{\tilde{s}}^{(0)} V_{jk}^2 - (\bar{V}_{jk})^2 \\ &= 1 + \sum_{\tilde{s}} p_{\tilde{s}}^{(0)} a(j)a(k)[a(j)a(k) - 2a(j,k)].\end{aligned} \tag{3.35}$$

Figure 3.2 illustrates $\text{Var}(V_{jk})$ versus $|j-k|$ determined numerically at $N = 20$, for both (a) paramagnetic ancilla and (b) critical ancilla ($h_{\text{anc}}/J_{\text{anc}} = 1$). In Fig. 3.2(a) and all subsequent simulations that use paramagnetic ancilla, we take $h_{\text{anc}}/J_{\text{anc}} = 1.5$.

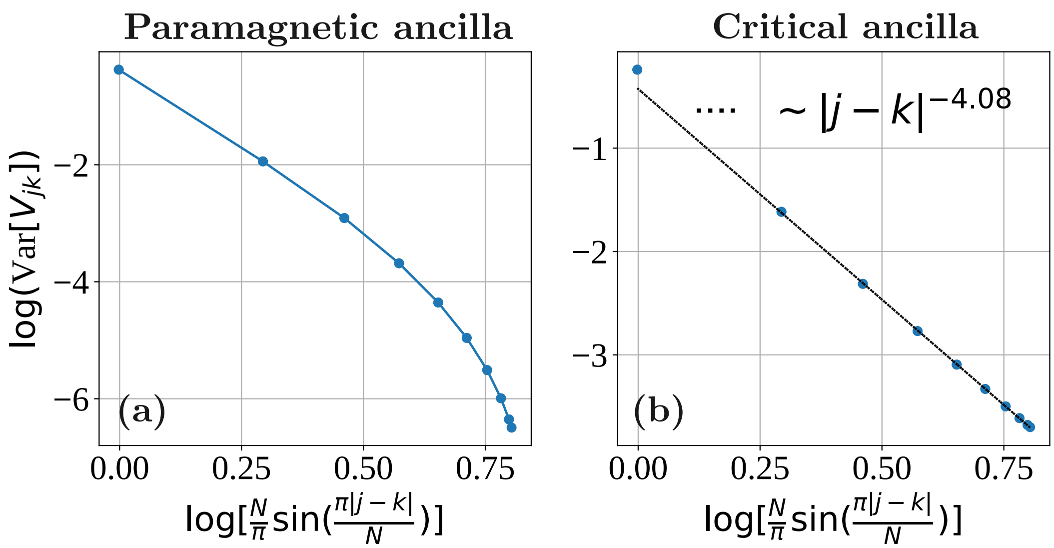

Figure 3.2: (Color online). **Variance of V_{jk} for $\tilde{Z}$-basis measurements.** Panels (a) and (b) respectively correspond to paramagnetic and critical ancilla. The variance decays exponentially with $|j-k|$ in the former but decays approximately as $|j-k|^{-4}$ in the latter. Data were obtained using the methods in Chapter 3.6 with a system size $N = 20$.

Additionally, when using periodic boundary conditions we present numerical results for correlations as a function of $\frac{N}{\pi}\sin(\frac{\pi|j-k|}{N})$ to reduce finite-size effects [21]. The variances in Fig. 3.2 clearly tend to zero at large $|j-k|$, exponentially with paramagnetic ancilla and as a power-law (with decay exponent ≈ 4) for critical ancilla. This decay suggests that typical $\tilde{Z}$-basis measurement outcomes yield well-behaved, decaying interactions in the second line of Eq. (3.25).

Due to the dependence on θ and $\langle O\rangle$ in Eq. (3.27), the mean and variance of m_j depend on the unitary applied in the protocol. For case I in Table 3.1 we have $\theta = \langle O\rangle = \langle X\rangle = 2/\pi$ while case II corresponds to $\theta = C, \langle O\rangle = 0$. For these cases we find

$$\bar{m}_j^{\mathrm{I}} = \bar{m}_j^{\mathrm{II}} = 0 \tag{3.36}$$

$$\mathrm{Var}(m_j^{\mathrm{I}}) = 4\langle X\rangle^2 \left[-1 + \sum_{\tilde{s}} p_{\tilde{s}}^{(0)} a(j)^4\right] \tag{3.37}$$

$$\mathrm{Var}(m_j^{\mathrm{II}}) = 4C^2 \left\{-1 + \sum_{\tilde{s}} p_{\tilde{s}}^{(0)} \left[a(j)^2 - \sum_{k\neq j} V_{jk}\right]^2\right\}. \tag{3.38}$$

Figure 3.3 illustrates the numerically evaluated standard deviation $\sqrt{\mathrm{Var}(m_j^{\mathrm{I,II}})}$ versus

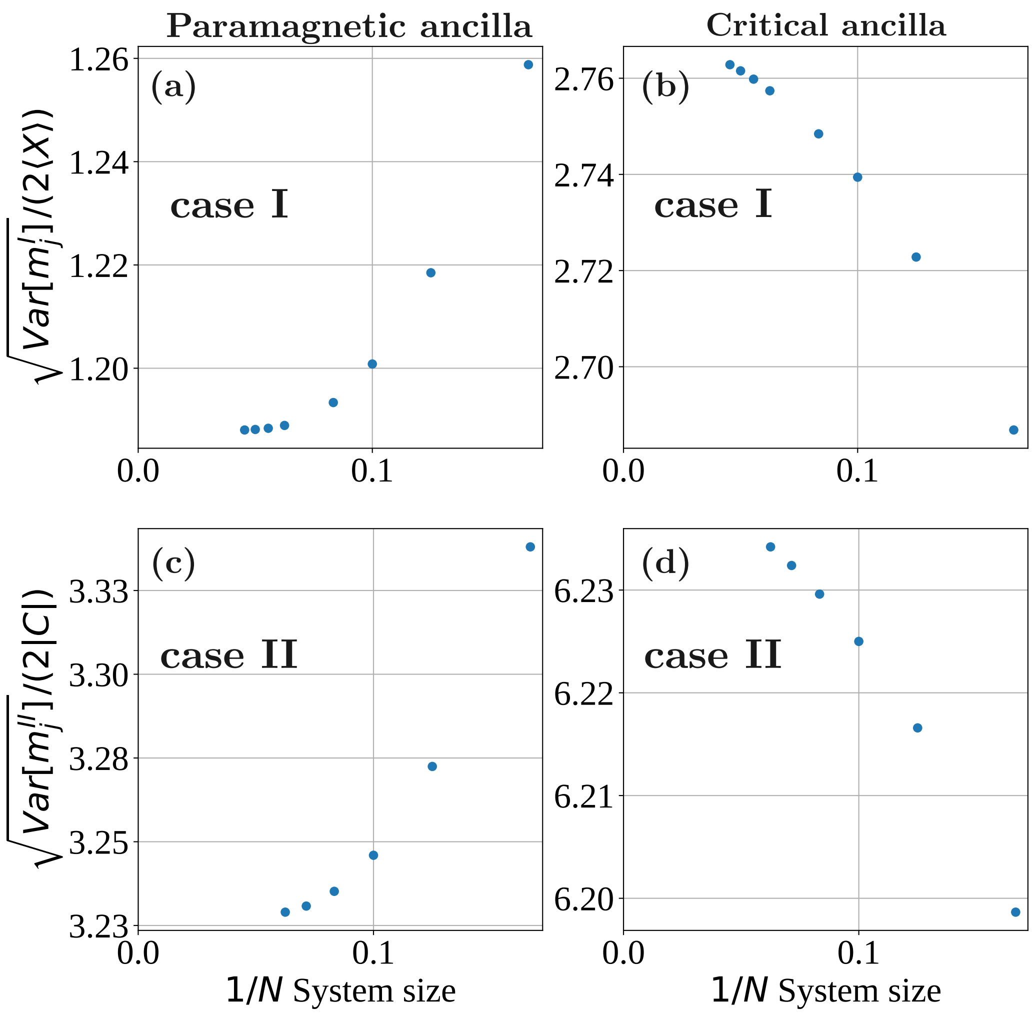

Figure 3.3: (Color online). **Standard deviation of m_j for $\tilde{Z}$-basis measurements.** For paramagnetic ancilla (panels (a, c)) in either case I or case II, the standard deviation decreases with N, with the trend suggesting saturation to a finite value in the thermodynamic limit. With critical ancilla (panels (b, d)) the standard deviation increases extremely slowly with N in both cases but remains comparable to the values with paramagnetic ancilla. Data were obtained using results from Chapter 3.6.

inverse system size $1/N$, again for both paramagnetic and critical ancilla. (For case II we assume $C \neq 0$ here, since otherwise m_j simply vanishes.) With paramagnetic ancilla, the standard deviation clearly converges at large N to a finite value for both case I and case II. With critical ancilla, in both cases the standard deviation is modestly larger for the system sizes shown, albeit showing *very* slow, potentially saturating, growth with N. Although here we can not ascertain the trend for the thermodynamic limit, we expect that for experimentally relevant N values the variance of m_j remains of the same order of magnitude as for the paramagnetic case.

The behavior of the variances discussed above suggests that, at least for paramagnetic ancilla, any typical string outcome yields a well-behaved defect-line action amenable to our perturbative formalism. To support this expectation, we illustrate V_{jk} and m_j for select measurement outcomes. First, Fig. 3.4 displays V_{jk} for a uniform measurement outcome with $|\tilde{s}\rangle = |\cdots\uparrow\uparrow\uparrow\cdots\rangle$—which, along with its all-down partner, occurs with highest probability $p_{\tilde{s}}^{(0)}$ (as confirmed numerically for systems as large as $N = 26$). Panels (a) and (b) correspond to paramagnetic and critical ancilla, respectively. In the former, V_{jk} decays exponentially with $|j-k|$, while in the latter it decays as $|j-k|^{-4}$. In both cases m_j is translational invariant, as dictated by uniformity of the measurement outcome. Moreover, we have numerically verified that m_j saturates to a constant value with increasing system size in the paramagnetic case, whereas it slowly grows (at the level of the third decimal digit) for critical ancilla. The V_{jk} and m_j values discussed here can be combined to infer the (also uniform) m_j profile for case II, which at $N \to \infty$ will simply differ from m_j for case I by a finite value given the 'fast' decay in V_{jk}.

The next-most-probable set of measurement outcomes correspond to configurations with isolated spin flips introduced into the uniform $\tilde{s}$ string considered above. Rather than consider such outcomes, we next examine a lower-probability configuration with two maximally separated domain walls: $|\tilde{s}\rangle = |\cdots\uparrow\uparrow\uparrow\downarrow\downarrow\downarrow\cdots\rangle$. (Due to periodic boundary conditions considered here, domain walls come in pairs.) Figure 3.5 displays both V_{jk} and m_j for this measurement outcome with domain walls at $j = 0, 100$ for a system with $N = 200$ assuming case I. Since V_{jk} now depends on j and k due to non-uniformity of the measurement outcome, in (a,b) we show V_{jk} versus k for three different j values. Overall decay with $|j-k|$ similar to that for the uniform measurement outcome persists here. For fixed j, a relative bump appears when k sits close to a domain walls, but the height of the bump is nonetheless orders of magnitude smaller than when k is close to j (see insets). In (c,d), the m_j profiles resemble those for the uniform case, but with dips that tend to zero from below in the thermodynamic limit for j's on either end of a given domain wall. We have also verified that still-lower-probability random $\tilde{s}$ strings also yield well-behaved V_{jk} and m_j couplings.

$\tilde{X}$ measurement basis

Switching the ancilla measurement basis from $\tilde{Z}$ to $\tilde{X}$ qualitatively changes the statistical properties of m_j and V_{jk}. By construction, the initialized ancilla wavefunction $|\psi_a\rangle$ is an eigenstate of the $\mathbb{Z}_2$-symmetry generator $\tilde{G} = \prod_j \tilde{X}_j$ with eigenvalue $+1$.

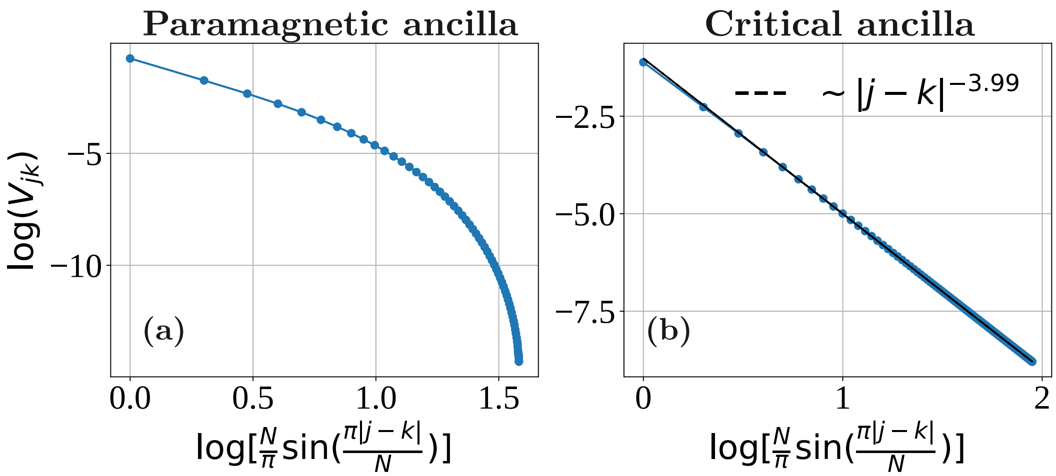

Figure 3.4: (Color online). V_{jk} **profiles for a uniform measurement outcome in case I of Table 3.1.** Translation invariance of the uniform string outcome implies that V_{jk} depends only on $|j-k|$. Decay in V_{jk} is exponential with paramagnetic ancilla (panel (a)) but power-law ($\sim |j-k|^{-4}$) with critical ancilla (panel (b)). The data were obtained for $N = 280$ for critical ancilla using results from Chapter 3.6.

For $\tilde{X}$-basis measurements, a given ancilla state $|\tilde{s}\rangle$ obtained after a measurement can also be classified by its $\tilde{G}$ eigenvalue; we refer to measurement outcomes with $\tilde{G}|\tilde{s}\rangle = +|\tilde{s}\rangle$ as 'even strings' and outcomes with $\tilde{G}|\tilde{s}\rangle = -|\tilde{s}\rangle$ as 'odd strings'. (Due to the form of the unitary U applied prior to measurement in this case, both sectors can still arise despite the initialization.) Consider now an even-string measurement outcome with $\langle\tilde{s}|\psi_a\rangle \neq 0$—as assumed in the perturbative expansion developed in Section 3.3. Crucially, due to mismatch in $\tilde{G}$ eigenvalues, $\langle\tilde{s}(i_1\cdots i_{N_f})|\psi_a\rangle$ then vanishes for *any* odd number of flipped spins N_f. It follows that $a(j) = 0$ in Eqs. (3.26) and (3.27), leaving

$$V_{jk} = a(j,k), \quad m_j = -2\theta + 2(\langle O\rangle - \theta)\sum_{k\neq j} V_{jk}. \tag{3.39}$$

Notice that V_{jk} here is always non-negative [recall the discussion below Eq. (3.33)].

The mean and variance of V_{jk} then reduce to simple ground-state ancilla correlation functions:

$$\bar{V}_{jk} = \langle\psi_a|\tilde{Z}_j\tilde{Z}_k|\psi_a\rangle, \quad \mathrm{Var}(V_{jk}) = 1 - \langle\psi_a|\tilde{Z}_j\tilde{Z}_k|\psi_a\rangle^2. \tag{3.40}$$

At large $|j-k|$, the mean always decays to zero: for ancilla initialized in the paramagnetic phase with correlation length ξ we have $\bar{V}_{jk} \sim e^{-|j-k|/\xi}$, while if the ancilla are critical $\bar{V}_{jk} \sim 1/|j-k|^{1/4}$. The variance of V_{jk}, by contrast, grows

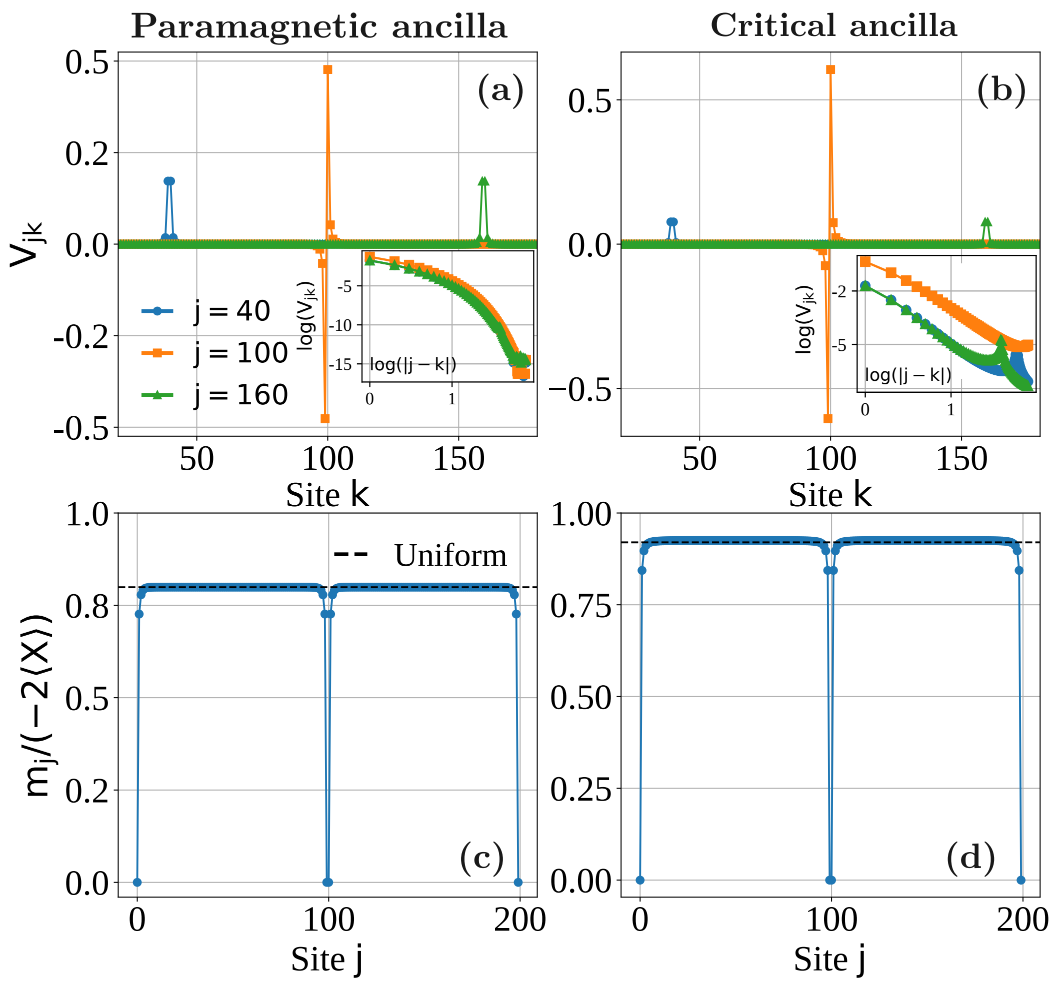

Figure 3.5: (Color online). V_{jk} **and** m_j **profiles for a two-domain-wall measurement outcome in case I of Table 3.1**. Domain walls reside near sites 0 and 100 in a system with $N = 200$. Left and right columns show data for paramagnetic and critical ancilla, respectively. Due to loss of translation symmetry, we show V_{jk} versus k for several j values. As shown in the insets, V_{jk} decays with the distance $|j - k|$, although we find a relative bump close to the domain walls. The corresponding m_j profiles (panels (c, d)) exhibit dips near zero in the immediate vicinity of the domain walls, but are otherwise roughly uniform matching the values obtained for a uniform string outcome (black dashed lines). Data obtained using results from Chapter 3.6.

towards unity at large $|j - k|$. Correspondingly, the V_{jk}'s for particular measurement outcomes can differ wildly from the mean, and in particular need not decay with $|j - k|$.

Remarkably, for case III in Table 3.1 m_j takes on the same j-independent value for *any* even-sector measurement outcome:

$$m_j^{\mathrm{III}} = -2\langle X \rangle. \tag{3.41}$$

For case IV, however, m_j depends nontrivially on V_{jk} and hence the measurement outcome; here we find

$$\bar{m}_j^{\mathrm{IV}} = -2C\left(1 + \sum_{k\neq j} \bar{V}_{jk}\right) \tag{3.42}$$

$$\mathrm{Var}(m_j^{\mathrm{IV}}) = (2C)^2 \sum_{k,k'\neq j} (\bar{V}_{kk'} - \bar{V}_{jk}\bar{V}_{jk'}) \tag{3.43}$$

with $\bar{V}_{jk}$ given in Eq. (3.40). Suppose that the ancilla are paramagnetic. Exponential decay of $\bar{V}_{jk}$ with $|j-k|$ yields a finite mean $\bar{m}_j^{\mathrm{IV}}$, though the variance diverges linearly with system size, $\mathrm{Var}(m_j^{\mathrm{IV}}) \sim N$, due to contributions from the $\bar{V}_{kk'}$ term with k' near k. With critical ancilla, power-law decay of $\bar{V}_{jk}$ generates divergent mean and variance: $\bar{m}_j^{\mathrm{IV}} \sim N^{3/4}$ and $\mathrm{Var}(m_j^{\mathrm{IV}}) \sim N^{7/4}$. In both scenarios the fluctuations of m_j increase with system size faster than the average value.

We therefore can only apply the perturbative formulation developed in Section 3.3 to a restricted set of $\tilde{X}$-basis measurement outcomes that lead to a well-behaved, decaying interaction term in H_m, and correspondingly well-behaved m_j couplings. Fortunately, the most probable measurement outcomes do indeed satisfy these criteria.

Figure 3.6 plots V_{jk} for the highest-probability outcome, corresponding to the uniform string $|\tilde{s}\rangle = |\cdots \rightarrow\rightarrow\rightarrow \cdots\rangle$ [3]. For (a) paramagnetic ancilla V_{jk} decays to zero with $|j-k|$ exponentially, while for (b) critical ancilla it decays as $\sim |j-k|^{-1}$. In case IV with $C \neq 0$, Eq. (3.39) implies that the associated m_j converges to a finite value as N increases for paramagnetic ancilla, but diverges as $\ln N$ with critical ancilla. (For $C = 0$, m_j again simply vanishes.) Therefore, modulo this possible logarithmic factor, the uniform string presents a 'good' $\tilde{X}$-basis measurement outcome.

As an example of a 'bad' measurement outcome, consider next the domain-wall configuration $|\tilde{s}\rangle = |\cdots \rightarrow\rightarrow\rightarrow\leftarrow\leftarrow\leftarrow \cdots\rangle$. Figure 3.7 shows that here V_{jk} becomes highly non-local. More precisely, V_{jk} takes on sizable values whenever both j and k reside in the '$\leftarrow$' domain, regardless of their separation. One can gain intuition for this observation by considering the ancilla ground state deep in the paramagnetic regime. Here the ground state takes the form $|\psi_a\rangle = |\rightarrow\rightarrow \cdots \rightarrow\rangle + \cdots$, where

[3] The high probability of this measurement outcome becomes intuitive in the $h_{\mathrm{anc}}/J_{\mathrm{anc}} \gg 1$ regime.

the ellipsis denotes perturbative corrections induced by small $J_{\text{anc}}/h_{\text{anc}}$. To leading order, these corrections involve spin flips on nearest-neighbor sites induced by J_{anc}, i.e., admixture of $|\cdots \rightarrow\rightarrow\leftarrow\leftarrow\rightarrow\rightarrow \cdots\rangle$ components into the wavefunction. Now consider the domain-wall outcome $|\tilde{s}\rangle$. Flipping two spins at sites j, k in the energetically unfavorable $\leftarrow$ domain tends to increase the overlap with the ground state—naturally leading to $V_{jk} = \frac{\langle \tilde{s}(j,k)|\psi_a\rangle}{\langle \tilde{s}|\psi_a\rangle}$ that can exceed unity even for distant j, k as seen in our simulations. Flipping one spin within each of the two domains takes the energetically favorable '$\rightarrow$' domain and introduces a *single* $\leftarrow$ spin. That domain then no longer resembles the ground state, which always harbors an even number of flipped spins. The coupling V_{jk} is therefore generically small with j and k in opposite domains, also as borne out in our numerics. Finally, flipping two spins in the $\rightarrow$ domain again decreases the resemblance with the ground state—more so as the separation between the flipped sites j and k increases. The corresponding V_{jk} diminishes with $|j - k|$ in line with simulations yet again.

More generally, 'good' measurement outcomes are those for which flipping two far away spins invariably decreases overlap with the ground state such that $V_{jk} \rightarrow 0$ as $|j - k|$ increases. In addition to the highest-probability uniform string, the next-highest-probability set of strings—which contain dilute sets of nearest-neighbor flipped spins relative to the uniform background—also satisfy this property. Indeed, starting from such configurations, flipping spins at well-separated sites always locally produces regions with an odd number of flipped spins in a background of energetically favorable $\rightarrow$ spins, thereby obliterating the overlap with the ancilla ground state and hence V_{jk}.

3.5 Derivation of the post-measurement wavefunction

Here we provide technical details leading to the post-measurement state specified in Eqs. (3.22), (3.24), and (3.25). We start by observing that the ancilla measurement basis is always orthogonal to $\tilde{O}_j$; hence if measurement projects ancilla site j to $|\tilde{s}_j\rangle$, then $\tilde{O}_j$ simply flips that measured spin: $\tilde{O}_j |\tilde{s}_j\rangle = |-\tilde{s}_j\rangle$. For the unitary in Eq. (3.23), we can then use properties of Pauli operators to express the post-measurement state defined in Eq. (3.18) as

$$|\psi_{\tilde{s}}\rangle = \frac{1}{\sqrt{p_{\tilde{s}}}} \left\{ \left[\prod_j \left(C_j \langle \tilde{s}_j| + S_j \langle -\tilde{s}_j| \right) \right] |\psi_a\rangle \right\} |\psi_c\rangle . \quad (3.44)$$

Equation (3.44) uses the short-hand notation

$$C_j = \cos[u(O_j - \theta)], \quad S_j = i \sin[u(O_j - \theta)], \quad (3.45)$$

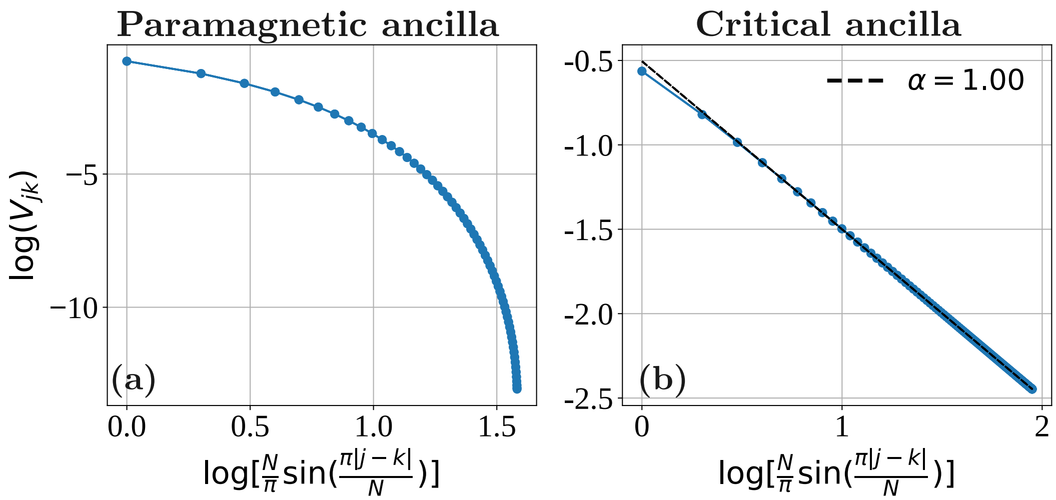

Figure 3.6: (Color online). V_{jk} **profile for a uniform $\tilde{X}$-basis measurement outcome.** Decay of V_{jk} is exponential with paramagnetic ancilla and power-law ($\sim |j-k|^{-1}$) with critical ancilla. In the critical case, note the significantly smaller exponent compared to Fig. 3.4. Data obtained using results from Chapter 3.6 with system size $N = 280$ for critical ancilla.

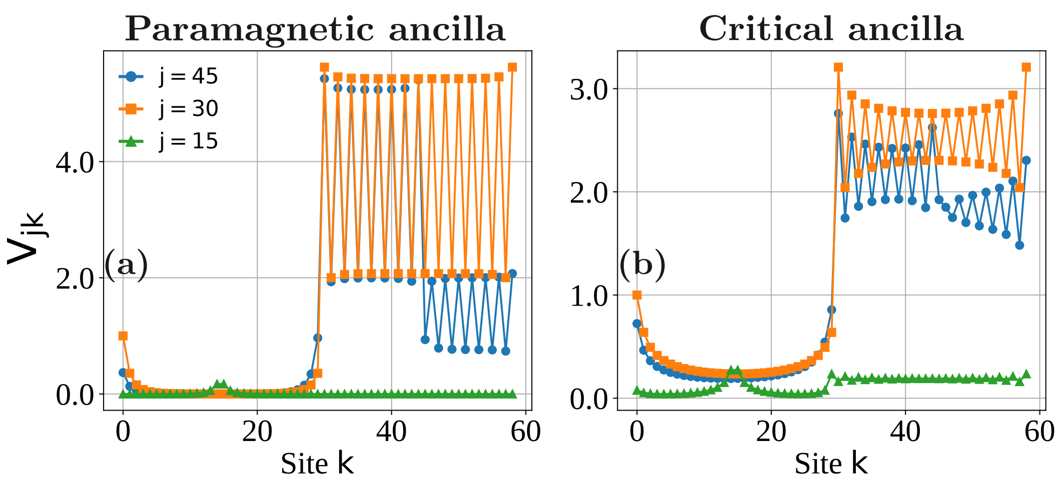

Figure 3.7: (Color online). V_{jk} **profile for a two-domain-wall $\tilde{X}$-basis measurement outcome.** The first 30 sites point in the energetically favorable $\longrightarrow$ direction, while the remaining 30 sites point in the unfavorable $\longleftarrow$ direction. Non-decaying behavior of V_{jk} occurs when j, k both reside in the unfavorable domain. Data obtained using results from Chapter 3.6 for system size $N = 60$.

which satisfy standard trigonometric identities even including the Pauli operators in the arguments.

Observe that multiplying all elements in the product from Eq. (3.44) yields a sum of terms with anywhere from $N_f = 0$ to N flipped ancilla spins (N is the total number of ancilla sites), and that these flipped spins can occur at arbitrary sites $i_1 < i_2 < \cdots < i_{N_f}$. Let $\left|\tilde{s}(i_1, \cdots, i_{N_f})\right\rangle$ be the state with N_f flipped ancilla spins at these sites, and let $F(i_1, \cdots, i_{N_f})$ denote a product of C_j's for the unflipped sites and S_j's for the flipped sites. For example,

$$\begin{aligned} |\tilde{s}(i_1, i_2)\rangle &= \tilde{O}_{i_1}\tilde{O}_{i_2}\,|\tilde{s}\rangle\,, \\ F(i_1, i_2) &= C_1 \cdots C_{i_1-1}S_{i_1}C_{i_1+1}\cdots C_{i_2-1}S_{i_2}C_{i_2+1}\cdots\,. \end{aligned} \tag{3.46}$$

We can then explicitly write

$$|\psi_{\tilde{s}}\rangle = \frac{1}{\sqrt{p_{\tilde{s}}}}\sum_{N_f=0}^{N}\sum_{i_1<i_2<\cdots<i_{N_f}}\left\langle\tilde{s}(i_1, \cdots, i_{N_f})\right|\left|\psi_a\right\rangle F(i_1, \cdots, i_{N_f})\left|\psi_c\right\rangle \tag{3.47}$$

which, en route to the form in Eq. (3.22), can be trivially re-expressed as

$$\begin{aligned} |\psi_{\tilde{s}}\rangle = \frac{1}{\sqrt{p_{\tilde{s}}}}\exp\Bigg\{\ln\Bigg[&\langle\tilde{s}|\,\psi_a\rangle F_0 + \sum_i\langle\tilde{s}(i)|\,\psi_a\rangle F(i) \\ &+\sum_{i_1<i_2}\langle\tilde{s}(i_1,i_2)|\,\psi_a\rangle F(i_1,i_2)+\cdots\Bigg]\Bigg\}\,|\psi_c\rangle \end{aligned} \tag{3.48}$$

with $F_0 \equiv C_1 \cdots C_N$.

Suppose now that $\langle\tilde{s}|\,\psi_a\rangle$ is non-zero. In this case we can factor out the first term in the log from Eq. (3.48) to obtain, after some manipulation and absorbing an $\tilde{s}$-dependent constant into a new normalization factor $\mathcal{N}$,

$$\begin{aligned} |\psi_{\tilde{s}}\rangle &= \frac{1}{\sqrt{\mathcal{N}}}e^{-H_{\text{temp}}/2}\,|\psi_c\rangle\,, \\ H_{\text{temp}} &= -2\ln\left[1+\sum_i a(i)T_i + \sum_{i_1<i_2}a(i_1,i_2)T_{i_1}T_{i_2}+\cdots\right] - 2\sum_i\ln(C_i). \end{aligned} \tag{3.49}$$

In the second and third lines we introduced the quantities

$$a(i_1, \cdots, i_{N_f}) = \frac{\left\langle\tilde{s}(i_1\cdots i_{N_f})\right|\psi_a\rangle}{\langle\tilde{s}|\,\psi_a\rangle}, \quad T_i = C_i^{-1}S_i, \tag{3.50}$$

which are a generalization of Eq. (3.28) of the main text. At this point one can expand H_{temp} to the desired order in $u \ll 1$. To proceed it is convenient to decompose H_{temp} via

$$H_{\text{temp}} = -2iH' + H_m, \tag{3.51}$$

where H', H_m are commuting Hermitian operators; $U' = e^{iH'}$ is the unitary transformation from Eq. (3.22) while H_m contains the crucial non-unitary effects from measurement. Upon absorbing constants into the normalization $\mathcal{N}$, to $O(u^2)$ one obtains Eqs. (3.24) and (3.25) in the main text.

3.6 Gaussian overlaps for ancilla amplitudes

Throughout this chapter, we are interested in the evaluation of correlation functions like the ones appearing in Eq. (3.50). To establish the main ideas, consider the case in which the unitary involves $\tilde{X}$, we measure in the $\tilde{Z}$-basis, and we want to evaluate

$$a(i_1, \cdots, i_{N_F}) = \frac{\langle \tilde{s}| \prod_{j=1}^{N_F} \tilde{X}_{i_j} |\psi_a\rangle}{\langle \tilde{s}|\psi_a\rangle}. \tag{3.52}$$

Here $\tilde{s}$ is an arbitrary string outcome and N_F denotes the number of flipped spins generated by $\tilde{X}_i$ operators in the product above. The ket $|\psi_a\rangle$ is the ground state of the transverse-field Ising model in Eq. (3.14) or, equivalently, of its fermionic representation obtained via the Jordan-Wigner transformation. We can collect the Majorana operators appearing in the latter form of the Hamiltonian into a vector $\vec{\gamma}$ defined by

$$\vec{\gamma} = \begin{pmatrix} \gamma_{A,1} \\ \gamma_{A,2} \\ \vdots \\ \gamma_{A,N} \\ \gamma_{B,1} \\ \vdots \\ \gamma_{B,N} \end{pmatrix}, \tag{3.53}$$

where N is the system size and $\{\vec{\gamma}_i, \vec{\gamma}_j\} = 2\delta_{ij}$. To simplify notation, in this section we suppress tildes on the Majorana fermion operators for the ancilla, and also replace $h_{\text{anc}} \to h$ and $J_{\text{anc}} \to 1$. The Hamiltonian is quadratic in the fermionic operators, and any fermionic Gaussian state can be described through the covariance matrix

$$\Gamma_{jk} = \frac{i}{2}\langle[\gamma_j, \gamma_k]\rangle, \tag{3.54}$$

with $[\gamma_j, \gamma_k]$ the commutator of the two Majorana operators γ_j and γ_k. From the definition, we observe that Γ is a real and skew-symmetric matrix. For the transverse field Ising chain, the covariance matrix is known analytically [22]. In particular it has a Toeplitz structure given by

$$\Gamma_{jk} = \frac{1}{N} \sum_{k \in \Omega_{\text{gs}}} e^{-\frac{2\pi i k}{N}(j-k)} \begin{pmatrix} 0 & \frac{h-\cos(\frac{2\pi k}{N})-i\sin(\frac{2\pi k}{N})}{\sqrt{(h-\cos(\frac{2\pi k}{N}))^2+\sin(\frac{2\pi k}{N})^2}} \\ -\frac{h-\cos(\frac{2\pi k}{N})-i\sin(\frac{2\pi k}{N})}{\sqrt{(h-\cos(\frac{2\pi k}{N}))^2+\sin(\frac{2\pi k}{N})^2}} & 0 \end{pmatrix}, \tag{3.55}$$

where Ω_{gs} is the set of occupied momenta in the ground state. In the limit $N \to \infty$, the Eq. above simplifies as

$$\Gamma_{jk} = \frac{1}{2\pi} \int_0^{2\pi} d\phi e^{-i\phi(j-k)} \begin{pmatrix} 0 & \frac{h-\cos(\phi)-i\sin(\phi)}{\sqrt{(h-\cos(\phi))^2+\sin(\phi)^2}} \\ -\frac{h-\cos(\phi)+i\sin(\phi)}{\sqrt{(h-\cos(\phi))^2+\sin(\phi)^2}} & 0 \end{pmatrix}, \quad (3.56)$$

We can also use an alternative approach to determine the covariance matrix. First, rewrite Eq. (3.3) as $H = \frac{1}{2}\sum_{j,k} h_{jk}\gamma_j\gamma_k$ with h a matrix encoding the free-fermion Hamiltonian. We proceed by finding the fermionic transformation U that diagonalizes h; in this diagonal basis, the correlation matrix associated to the ground state, Γ_{diag}, is simply obtained by substituting -1 $(+1)$ for any positive (negative) eigenvalue [23]. To obtain Γ, we just need to move back to the original basis, i.e., $\Gamma = U^\dagger \Gamma_{\mathrm{diag}} U$.

When we measure in the $\tilde{Z}$-basis, $|\tilde{s}\rangle$ is not a Gaussian state, but noticing that $\langle\tilde{s}|\,\tilde{X}_j\,|\psi_a\rangle = \langle\tilde{s}|\,\tilde{X}_j\tilde{G}\,|\psi_a\rangle = \langle -\tilde{s}|\,\tilde{X}_j\,|\psi_a\rangle$, we find

$$\langle\tilde{s}|\,\tilde{X}_j\,|\psi_a\rangle = \frac{1}{\sqrt{2}}\langle\psi_+|\,\tilde{X}_j\,|\psi_a\rangle, \qquad |\psi_+\rangle = \frac{|\tilde{s}\rangle + |-\tilde{s}\rangle}{\sqrt{2}}. \quad (3.57)$$

The advantage of using the cat state $|\psi_+\rangle$ is that now it is Gaussian and corresponds to the ground state of a quadratic Hamiltonian

$$H_{\tilde{s}} = -\sum_j \tilde{s}_j\tilde{s}_{j+1}\tilde{Z}_j\tilde{Z}_{j+1} \quad (3.58)$$

that, after a Jordan-Wigner transformation, reads

$$H_{\tilde{s}} = i\sum_j \tilde{s}_j\tilde{s}_{j+1}\gamma_{A,j+1}\gamma_{B,j} \equiv \frac{1}{2}\sum_{jk} h^{\tilde{s}}_{jk}\gamma_j\gamma_k. \quad (3.59)$$

By applying the procedure described above, we can find the covariance matrix $\Gamma_{\tilde{s}}$ describing the Gaussian ground state of Eq. (3.59). Once we know the covariance matrix both for the ground state of the ancilla and for the Hamiltonian $H_{\tilde{s}}$, we can apply a result found in Ref. [20]: the absolute value of the inner product $\langle\tilde{s}|\psi_a\rangle$ is

$$|\langle\tilde{s}|\psi_a\rangle| = \sqrt{2^{-N-1}\,\mathrm{Pf}(\Gamma+\Gamma_{\tilde{s}})}, \quad (3.60)$$

where Pf is the Pfaffian of $\Gamma + \Gamma_{\tilde{s}}$.

Evaluation of Eq. (3.52) follows straightforwardly from the above results since we know explicitly the action of $\prod_j \tilde{X}_{i_j}$ on $|\tilde{s}\rangle$. For instance, if $N_F = 1$, $\tilde{X}_j\,|\tilde{s}\rangle = |\tilde{s}(j)\rangle$, i.e., the action of $\tilde{X}_j$ simply flips the spin at site j. We therefore have to also compute the covariance matrix for the Hamiltonian associated with the outcome $\tilde{s}(j)$, and then extract the corresponding overlap with the ancilla ground state using Eq. (3.60) with $\tilde{s} \to \tilde{s}(j)$. This procedure yields

$$a(j) = \sqrt{\frac{\mathrm{Pf}(\Gamma + \Gamma_{\tilde{s}(j)})}{\mathrm{Pf}(\Gamma + \Gamma_{\tilde{s}})}}, \qquad a(j,k) = \sqrt{\frac{\mathrm{Pf}(\Gamma + \Gamma_{\tilde{s}(j,k)})}{\mathrm{Pf}(\Gamma + \Gamma_{\tilde{s}})}}; \tag{3.61}$$

other $a(i_1, \cdots, i_{N_F})$ coefficients from Eq. (3.52) follow similarly. Importantly, the absolute value in Eq. (3.60) is superfluous for the model we consider in this manuscript due to the stoquasticity of the transverse-field Ising model.

When we measure in the $\tilde{X}$-basis, $|\tilde{s}\rangle$ is automatically a Gaussian state, corresponding to the ground state of the quadratic Hamiltonian

$$H_{\tilde{s}} = -\sum_j \tilde{s}_j \tilde{X}_j = -i \sum_j \tilde{s}_j \gamma_{A,j} \gamma_{B,j}. \tag{3.62}$$

Therefore, computing the corresponding covariance matrix, we can again apply Eq. (3.60) to evaluate

$$\langle \tilde{s} | \psi_a \rangle = \sqrt{2^{-N} \, \mathrm{Pf}(\Gamma + \Gamma_{\tilde{s}})}, \tag{3.63}$$

as well as correlation functions like $\frac{\langle \tilde{s} | \prod_{j=1}^{N_F} \tilde{Z}_{i_j} | \psi_a \rangle}{\langle \tilde{s} | \psi_a \rangle}$. We remark here that if $|\tilde{s}\rangle$ is the uniform measurement outcome, $\Gamma + \Gamma_{\tilde{s}}$ is still a block-Toeplitz matrix because the system preserves its translational invariance. Indeed, for large N, it can be written as

$$\begin{aligned} (\Gamma + \Gamma_{\tilde{s}})_{jk} &= \frac{1}{2\pi} \int_0^{2\pi} d\phi \, e^{-i\phi(j-k)} \mathcal{G}(\phi, h), \\ \mathcal{G}(\phi, h) &= \begin{pmatrix} 0 & \dfrac{h - \cos\phi - i \sin\phi}{\sqrt{(h - \cos\phi)^2 + \sin^2\phi}} + 1 \\ -\dfrac{h - \cos\phi + i \sin\phi}{\sqrt{(h - \cos\phi)^2 + \sin^2\phi}} - 1 & 0 \end{pmatrix}. \end{aligned} \tag{3.64}$$

In order to evaluate $p^{(0)}_{\tilde{s}}$ in Eq. (3.33) for a uniform measurement outcome, we need to evaluate the Pfaffian (therefore the determinant) of $\Gamma + \Gamma_{\tilde{s}}$ using Eq. (3.63). One of the main results on the theory of block Toeplitz determinants is the Widom-Szegö theorem [24]. According to it, the determinant of a block Toeplitz matrix, like $\Gamma + \Gamma_{\tilde{s}}$, with symbol $\mathcal{G}(\phi, h)$, behaves for large N as

$$\begin{aligned} \log\det(\Gamma + \Gamma_{\tilde{s}}) &\sim N \int_0^{2\pi} \frac{d\phi}{2\pi} \log\det \mathcal{G}(\phi, h) \\ &= N \int_0^{2\pi} \frac{d\phi}{\pi} \log\left[\frac{\sqrt{h^2 - 2h\cos\phi + 1} + h - \cos\phi}{\sqrt{h^2 - 2h\cos\phi + 1}} \right]. \end{aligned} \tag{3.65}$$

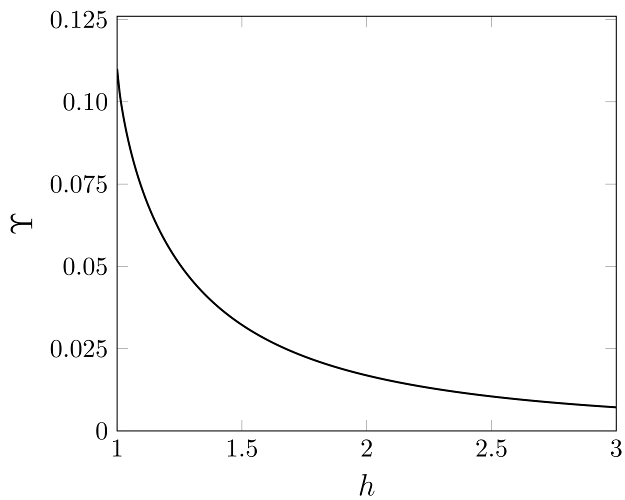

Figure 3.8: **Coefficient Υ in Eq.** (3.66)**.** The plot shows the behavior of the coefficient describing the exponential growth with system size of the probability $p^{(0)}_{\mathrm{uni}}$ for obtaining the uniform measurement outcome at $u = 0$.

This results allows us to compute explicitly the probability $p^{(0)}_{\mathrm{uni}}$ for finding the uniform measurement outcome at $u = 0$:

$$p^{(0)}_{\mathrm{uni}} \sim e^{-\Upsilon N}, \tag{3.66}$$

$$\Upsilon = \log 2 - \int_0^{2\pi} \frac{d\phi}{2\pi} \log\left[\frac{\sqrt{h^2 - 2h\cos\phi + 1} + h - \cos\phi}{\sqrt{h^2 - 2h\cos\phi + 1}}\right]. \tag{3.67}$$

In particular the integral above can be explicitly solved for $h = 1$, i.e., when the ancilla chain becomes critical, and we obtain

$$\Upsilon = \log 2 - 2\mathrm{Catalan}/\pi, \tag{3.68}$$

where Catalan's constant is $\simeq 0.92$. As Fig. 3.8 shows, Υ monotonically decreases to zero for $h \geq 1$.

Chapter 4

MEASUREMENT-ALTERED ISING FIXED POINTS AND OBSERVABLE DIAGNOSTICS

This chapter applies the effective-action machinery of Chapter 3 to the four principal Ising measurement protocols. First, fixed outcome sectors are analyzed for $\tilde{Z}$- and $\tilde{X}$-basis measurements; second, nonlinear and symmetry-resolved measurement averages are developed as experimentally useful diagnostics; finally, the scaling of post-selection and symmetry-resolved protocols is compared.

The purpose of this chapter is to make the canonical Ising example into a reusable template. Later parts of the thesis reinterpret the same ideas as teleportation errors, measurement-induced boundary flows, Rydberg-array protocols, and statistical-learning observables.

4.1 $\tilde{Z}$-basis measurements and outcome sectors

We now use our perturbative formalism to examine how correlations in the critical chain are modified by particular outcomes of $\tilde{Z}$-basis ancilla measurements in our protocol. In Section 3.4 we saw that for this measurement basis both the mean and variance of V_{jk} vanish as $|j-k| \to \infty$, suggesting that generic measurement outcomes yield well-behaved decaying interactions in H_m [Eq. (3.25)]. Moreover, with paramagnetic ancilla the variance of m_j trended to a finite value at large system sizes, suggesting that the single-body piece in H_m is also well-behaved for generic measurement outcomes. Thus for paramagnetic ancilla, below we proceed with confidence considering unrestricted measurement outcomes from the lens of the continuum defect-line action obtained in Section 3.3. For critical ancilla we saw that the variance of m_j grew slowly with system size, warranting more caution in this scenario.

Let us illustrate an example for case I where $m_j \propto 1 - a(j)^2$ with $a(j) = \frac{\langle \tilde{s}(j)|\psi_a\rangle}{\langle \tilde{s}|\psi_a\rangle}$. After the uniform strings, the next most likely measurement outcomes are those containing a single spin flip. Consider one such state $|\tilde{s}\rangle$ with a single flipped spin at site j_{flip}. Subsequently flipping the spin at j_{flip} converts $|\tilde{s}\rangle$ back into the most probable, uniform string. We thereby obtain $a(j_{\text{flip}}) > 1$ and hence $m_{j_{\text{flip}}} < 0$ for this measurement outcome. With paramagnetic ancilla, this negative $m_{j_{\text{flip}}}$ value saturates to a small constant as the system size increases. With critical ancilla, by contrast, we find that the magnitude of this negative value continues to increase over accessible system sizes—but *very* slowly similar to the standard deviation shown in the right panels of Fig. 3.3. We thus expect our formalism to apply also to general $\tilde{Z}$-basis measurement outcomes even for critical ancilla, at least over system sizes relevant for experiments.

We now consider the unitaries in cases I and II from Table 3.1 in turn.

Case I

We start with case I where the unitary reads $U_j = e^{iu(X_j - \langle X \rangle)\tilde{X}_j}$. This form of U_j preserves the $\mathbb{Z}_2$ symmetries G and $\tilde{G}$ for the critical and ancilla chains, but does not preserve time reversal symmetry $\mathcal{T}$ (which sends $U_j \to U_j^\dagger$). Thus although the $\tilde{Z}$-basis measurements break $\tilde{G}$ symmetry, the post-measurement state $|\psi_{\tilde{s}}\rangle$ remains invariant under G. These considerations tell us that, for case I, $U' = e^{iH'}$ in Eq. (3.22) is generically nontrivial [as one can indeed see from Eq. (3.24)] while H_m and hence $\mathcal{S}_m$ must preserve G symmetry. Indeed, Eq. (3.25) now takes the manifestly G-invariant form

$$\begin{aligned} H_m &= u^2 \sum_j m_j (X_j - \langle X \rangle) \\ &+ u^2 \sum_{j \neq k} V_{jk} (X_j - \langle X \rangle)(X_k - \langle X \rangle) \end{aligned} \tag{4.1}$$

with

$$m_j = -2\langle X \rangle [1 - a(j)^2]. \tag{4.2}$$

and V_{jk} given (as for all cases) by Eq. (3.26). The defect-line action, using the low-energy expansion from Eq. (3.8), then reads

$$\begin{aligned} \mathcal{S}_m &= u^2 \int_x m(x) \varepsilon(x, \tau = 0) \\ &+ u^2 \int_{x,y} V(x, y) \varepsilon(x, \tau = 0) \varepsilon(y, \tau = 0). \end{aligned} \tag{4.3}$$

Here $m(x)$ and $V(x, y)$ represent the coarse-grained, continuum-limit counterparts of m_j and V_{jk}.

Provided $V(x, y)$ scales to zero faster than $1/|x - y|$—which is indeed generally the case both for paramagnetic and critical ancilla—we can approximate the second line of Eq. (4.3) as a local interaction obtained upon fusing the two ε fields according to the fusion rules summarized in Eq. (3.6). The leading nontrivial fusion product is $-i\gamma_R\partial_x\gamma_R + i\gamma_L\partial_x\gamma_L$, which is a descendent of the identity that, crucially, has a larger scaling dimension compared to the ε field appearing in the first line of Eq. (4.3) [9]. It follows that for capturing long-distance physics we can neglect the $V(x,y)$ term altogether and simply take

$$\mathcal{S}_m \approx u^2 \int_x m(x)\varepsilon(x, \tau = 0). \tag{4.4}$$

We are primarily interested in computing the two-point correlator

$$\langle Z_j Z_{j'}\rangle_{\tilde{s}} \sim \langle \sigma(x_j)\sigma(x_{j'})\rangle_{\tilde{s}} \tag{4.5}$$

in the presence of Eq. (4.4). Technically, according to Eq. (3.29) we need to conjugate the Z_j operators with the unitary U', which in case I rotates Z about the X direction. Such a rotation only mixes in operators in the low-energy theory with (much) larger scaling dimension compared to σ [1]. Hence Eq. (4.5)—which is the same as what one would obtain by ignoring U' altogether—continues to provide the leading decomposition for the correlator.

When $m(x)$ is independent of x, as arises for uniform measurement outcomes, the above defect line action is marginal, though for general measurement outcomes $m(x)$ retains nontrivial x dependence. References [25, 26, 27] employed non-perturbative field-theory methods to study the effects of this type of defect line on spin-spin correlation functions in the two dimensional Ising model. In particular, Ref. [27] derived the spin-spin correlation function for an ε line defect whose coupling is an arbitrary function of position. We report here their main result:

$$\langle \sigma(x)\sigma(x')\rangle_{\tilde{s}} \sim |x - x'|^{-\frac{1}{4} - \frac{\kappa u^2}{8}[m(x)+m(x')]} e^{\frac{\kappa u^2}{16}\mathcal{F}(x,x')}, \tag{4.6}$$

where

$$\begin{aligned}\mathcal{F}(x,x') = &\int_x^{x'} \mathrm{d}y\, m(y) \frac{\mathrm{d}}{\mathrm{d}y} \ln \frac{[(y-x')^2 + a^2]^{1+\kappa u^2 m(x')}}{[(y-x)^2 + a^2]^{1+\kappa u^2 m(x)}} \\ &- \int_x^{x'} \mathrm{d}y\, \mathrm{d}y'\, [1 + \kappa u^2 m(y')] \left[\frac{\mathrm{d}}{\mathrm{d}y} m(y)\right] \\ &\times \frac{\mathrm{d}}{\mathrm{d}y'} \ln[(y-y')^2 + a^2]. \end{aligned} \tag{4.7}$$

[1]Explicitly, after dropping terms that vanish by time-reversal symmetry, one finds $\left\langle (U')^\dagger Z_j Z_{j'} U'\right\rangle_{\tilde{s}} = \cos(2ua(j))\cos(2ua(j'))\left\langle Z_j Z_{j'}\right\rangle_{\tilde{s}} + \sin(2ua(j))\sin(2ua(j'))\left\langle Y_j Y_{j'}\right\rangle_{\tilde{s}}$. Given that (i) Y_j maps to a CFT operator with larger scaling dimension than that for Z_j ($Y_j \sim i\partial_\tau\sigma$, $\Delta_{\partial_\tau\sigma} = 9/8$ [11]) and (ii) our perturbative expansion focuses on the $u \ll 1$ regime, the U' unitary can be safely neglected.

Above, a is a short-distance cutoff, and κ is a dimensionless parameter that captures an overall constant neglected on the right side of Eq. (3.8) as well as difference in normalization conventions between our work and Ref. [27]. We simply view κ as a fitting parameter in our analysis. Since $\mathcal{F}(x,x')$ in Eq. (4.6) already contains an $O(u^2)$ prefactor, to the order we are working it suffices to simply set $u = 0$ in Eq. (4.7). Some algebra then gives the far simpler expression

$$\langle \sigma(x)\sigma(x')\rangle_{\tilde{s}} \sim |x-x'|^{-\frac{1}{4}-\frac{\kappa u^2}{4}[m(x)+m(x')]} e^{\frac{\kappa u^2}{8} f(x,x')} \tag{4.8}$$

with

$$f(x,x') = \int_x^{x'} \mathrm{d}y \ln\left[\frac{(y-x)^2+a^2}{(y-x')^2+a^2}\right]\frac{\mathrm{d}}{\mathrm{d}y}m(y). \tag{4.9}$$

Eqs. (4.8) and (4.9) capture coarse-grained spin-spin correlations for general measurement outcomes, though for deeper insight we now explicitly examine some special cases.

For a uniform measurement outcome (e.g., $s_j = +1$ for all j) giving constant $m(x) \equiv m_{\text{const}}$, Eq. (4.8) simplifies to

$$\langle \sigma(x)\sigma(x')\rangle_{\tilde{s}} \sim \frac{1}{|x-x'|^{2\Delta_\sigma(u)}}, \quad (\text{uniform } \tilde{s}) \tag{4.10}$$

$$\Delta_\sigma(u) = \frac{1}{8}(1+2\kappa u^2 m_{\text{const}}), \tag{4.11}$$

consistent with the result found in Refs. [25] and [26] in the limit $|x-x'| \gg a$ and to $O(u^2)$. Remarkably, the defect line in this post-selection sector yields an $O(u^2)$ change in the scaling dimension of the σ field compared to the canonical result in Eq. (3.5). We confirm this change using infinite DMRG simulation reported in Fig. 4.1(a,b): with both paramagnetic and critical ancilla, the scaling dimension of the σ field, $\Delta_\sigma(u)$, exceeds $1/8$ when $u \neq 0$, as is particularly clear at $u \geq 0.3$. The fact that the scaling dimension increases (rather than decreases) with u is consistent with the fact that in this case the $e^{-H_m/2}$ non-unitary implements weak measurement in the X basis—thereby naturally suppressing Z correlations. The scaling-dimension enhancement is quite similar for the paramagnetic and critical cases, as expected given that m_j is only slightly larger in the latter [see black dashed line in Fig. 3.5(c,d)]. Figure 4.2 shows the dependence of the numerically extracted power-law exponent α as a function of u^2, revealing a linear dependence in agreement with Eq. (4.11). The linear fit also allows us to extract a value $\kappa = -1.12$; note that $\kappa m_{\text{const}} > 0$—ensuring that $\Delta_\sigma(u)$ increases with u in the presence of the defect line as observed in our numerical simulations.

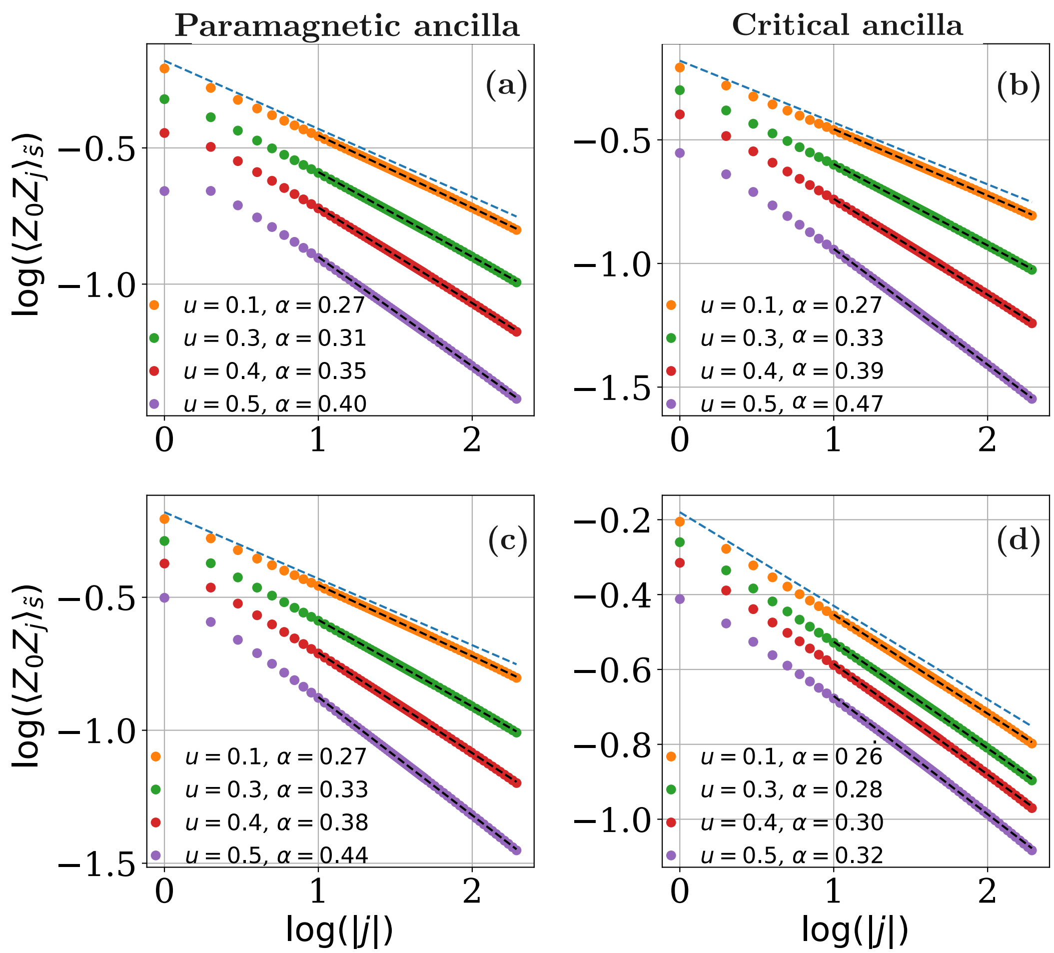

Figure 4.1: (Color online). **Correlation function $\langle Z_0 Z_j\rangle_{\tilde{s}}$ for uniform measurement outcomes.** The first row corresponds to case I from Table 3.1 while the second corresponds to case III. At $u = 0$ the curves exhibit an exponent $1/4$ that follows from the pristine Ising CFT. Turning on $u \neq 0$ yields a measurement-induced *increase* in the scaling dimension in all panels—as predicted by Eq. (4.11) for case I and (4.25) for case III. Data were obtained using infinite DMRG with bond dimension 1000 for paramagnetic ancilla and 2000 for critical.

Next we examine a measurement outcome $|\tilde{s}\rangle = |\cdots\uparrow\uparrow\uparrow\downarrow\downarrow\downarrow\cdots\rangle$ with a domain wall. This outcome yields nearly uniform m_j—see black dashed lines in Figs. 3.5(c, d)—except for a window around the domain wall where it approximately vanishes. We model the associated continuum $m(x)$ profile as

$$m(x) = m_{\text{const}}\{\Theta[(x_0 - d) - x] + \Theta[x - (x_0 + d)]\}, \tag{4.12}$$

where x_0 is the domain-wall location, d is the spatial extent of suppressed $m(x)$ region on either side and Θ is the Heaviside function. Adequately capturing detailed behavior near the domain wall likely requires incorporating short-distance physics,

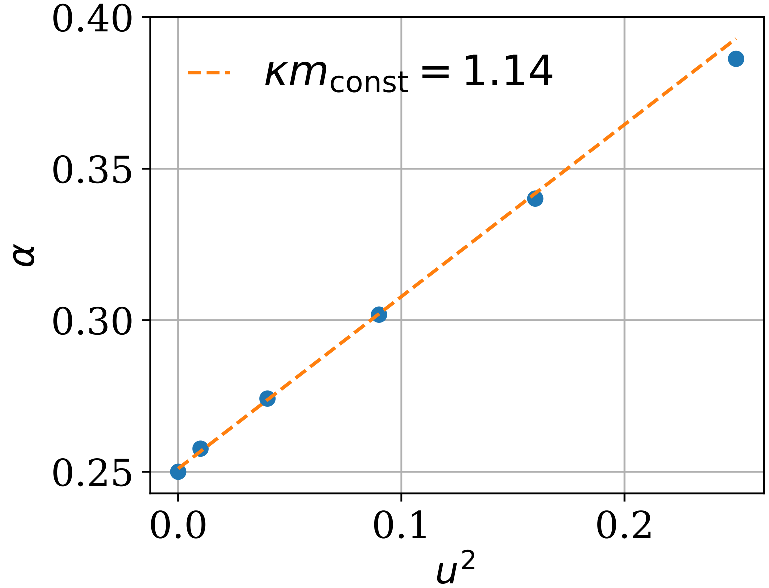

Figure 4.2: (Color online). **Scaling of the power-law exponent for $\langle Z_0 Z_j \rangle_{\tilde{s}}$ with a uniform measurement outcome.** Data correspond to case I in Table 3.1 assuming paramagnetic ancilla, and were obtained using iDMRG. The numerically extracted exponent α scales approximately linearly with u^2 at small u, in quantitative agreement with $2\Delta_\sigma(u)$ predicted by Eq. (4.11). A linear fit to Eq. (4.11) yields $\kappa m_{\mathrm{const}} = 1.14$.

though we expect that our low-energy framework can describe correlations among operators sufficiently far from x_0. With this restriction in mind, we consider the two-point correlator $\langle \sigma(x)\sigma(x')\rangle_{\tilde{s}}$ with x far to the left of the domain wall ($x \ll x_0$) and $x' > x$. If x' also sits to the left of the domain wall, then $f(x, x') = 0$ and the correlator retains—within our approximation—exactly the same form as in Eq. (4.10). If, however, x' sits to the right of the domain wall with $x' \gg x_0$, then we obtain

$$f(x, x') \approx 4dm_{\mathrm{const}} \left(\frac{1}{x_0 - x} + \frac{1}{x' - x_0} \right), \tag{4.13}$$

resulting in a modest enhancement of the correlator amplitude compared to the domain-wall-free case. Summarizing, for the single-domain-wall measurement outcome we get

$$\langle \sigma(x)\sigma(x')\rangle_{\tilde{s}} \sim \begin{cases} \frac{1}{|x-x'|^{2\Delta_\sigma(u)}}, & x' \ll x_0 \\ \frac{e^{\frac{1}{2}\kappa u^2 dm_{\mathrm{const}}\left(\frac{1}{x_0 - x} + \frac{1}{x' - x_0}\right)}}{|x-x'|^{2\Delta_\sigma(u)}}, & x' \gg x_0 \end{cases}. \tag{4.14}$$

To test Eq. (4.14), we performed DMRG simulations for a system of size $N = 256$ system with open boundary conditions, so that we can accommodate a single-domain-wall measurement outcome. Figure 4.3 plots the numerically determined function

$$\delta\langle Z_j Z_{j'}\rangle \equiv \frac{\langle Z_j Z_{j'}\rangle_{\tilde{s},\mathrm{DW}} - \langle Z_j Z_{j'}\rangle_{\tilde{s},\mathrm{unif}}}{\langle Z_j Z_{j'}\rangle_{\tilde{s},\mathrm{unif}}}, \tag{4.15}$$

i.e., the difference in the microscopic two-point correlator with and without a domain wall, normalized by the correlator for the uniform measurement outcome. Quite remarkably, the figure reveals the main qualitative features predicted by our result in Eq. (4.14): When both j and j' sit to the left of the domain wall, the difference in correlators approaches zero, while the correlator in the presence of a domain wall exhibits a small enhancement when j and j' sit on opposite sides of the domain wall. Moreover, the enhancement factor modestly increases as j approaches the domain wall—also in harmony with Eq. (4.14). The agreement between numerics and analytics here provides a very nontrivial check on our formalism.

In the presence of multiple well-separated dilute domain walls, the behavior of the correlator $\langle\sigma(x)\sigma(x')\rangle_{\tilde{s}}$ follows from a straightforward generalization of Eq. (4.14). For x and x' within the same domain, the correlator again reproduces that in a uniform measurement outcome, whereas moving x' rightward leads to a relative uptick in the correlator upon passing successive domain walls. For dense domain walls, the m_j pattern changes significantly, necessitating a separate analysis.

Case II

The unitary in case II, $U_j = e^{iu(Z_j - C)\tilde{X}_j}$, is invariant under $\tilde{G}$ but preserves neither G nor $\mathcal{T}$. Thus the post-measurement state generically breaks all microscopic symmetries. A special case arises, however, when $C = 0$: here U_j and hence the post-measurement state preserve the composite operation $G\mathcal{T}$. In line with these symmetry considerations, case II yields

$$H_m = u^2 \sum_j m_j Z_j + u^2 \sum_{j\neq k} V_{jk} Z_j Z_k \tag{4.16}$$

with

$$m_j = -2C\left[1 - a(j)^2 + \sum_{k\neq j} V_{jk}\right]. \tag{4.17}$$

Indeed, the m_j term—which is odd under G—appears as long as $C \neq 0$. The unitary $U' = e^{iH'}$, by contrast, is generically nontrivial even for $C = 0$ and always preserves $G\mathcal{T}$: H' in Eq. (3.24) is odd under G in case II, but in U' the minus sign is undone by $i \to -i$ from time reversal. Nevertheless, we only consider Z_j correlators below, which here are invariant under conjugation by U'.

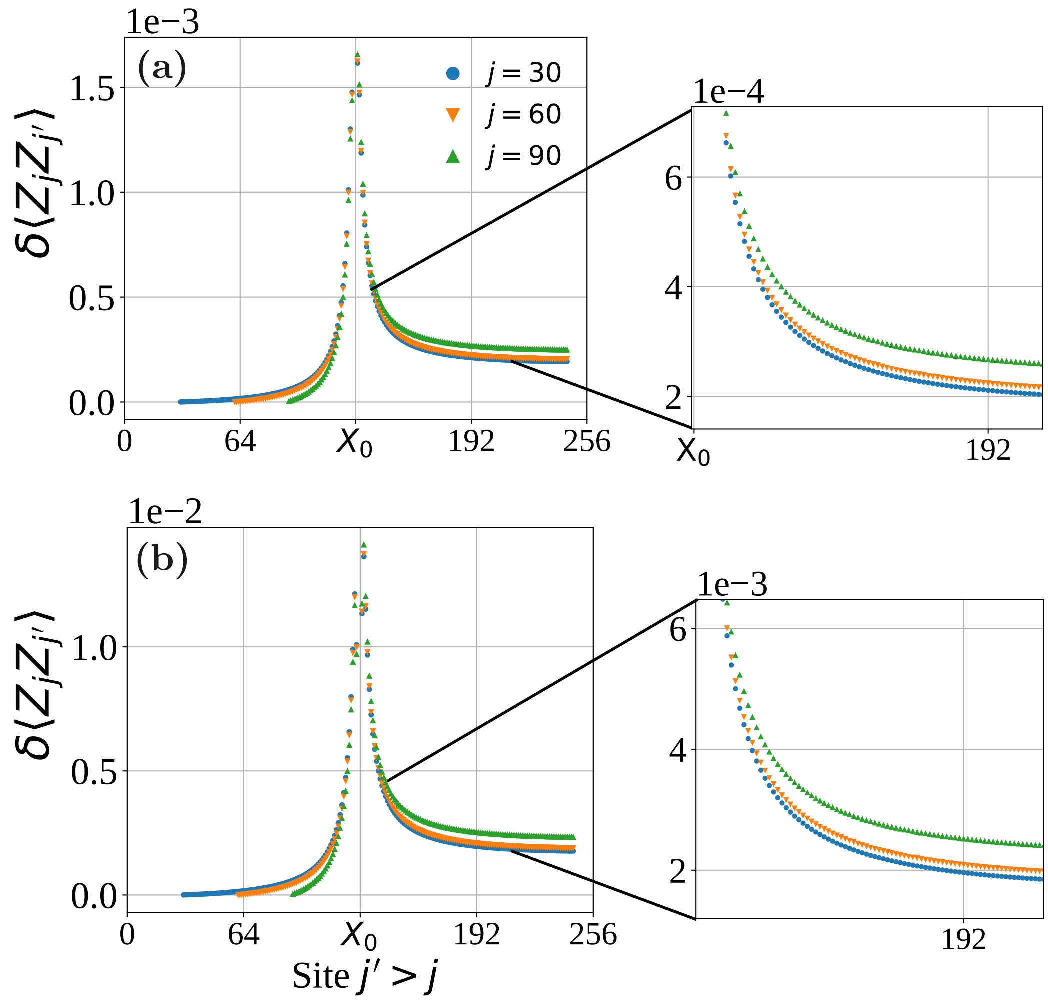

Figure 4.3: (Color online). **Relative correlation function** $\delta\langle Z_j Z_{j'}\rangle$ **[Eq.** (4.15)**] for a domain-wall measurement outcome in case I from Table 3.1.** Main panels illustrate the relative change in the two-point function resulting from insertion of a domain wall. Panel (a) corresponds to $u = 0.1$, and panel (b) to $u = 0.3$. The domain wall resides near site $x_0 = 128$ in an $N = 256$ system with open boundary conditions. When j and j' both sit on one side of the domain wall, the change in correlations is negligible. When they sit on opposite sides, however, the correlations *increase* relative to the uniform measurement outcome. As discussed in the main text, the behavior captured here reproduces the main qualitative features of the analytical prediction in Eq. (4.14). Data were obtained using DMRG with paramagnetic ancilla.

The associated continuum defect-line action, now using Eq. (3.7), is

$$\begin{aligned} \mathcal{S}_m &= u^2 \int_x m(x)\sigma(x,\tau=0) \\ &\quad + u^2 \int_{x,y} V(x,y)\sigma(x,\tau=0)\sigma(y,\tau=0). \end{aligned} \tag{4.18}$$

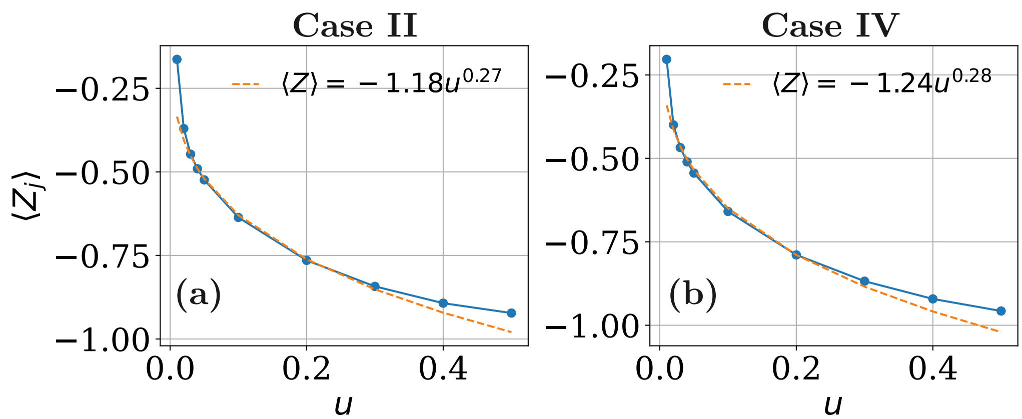

Figure 4.4: (Color online). **One-point function $\langle Z_j\rangle$ with a uniform measurement outcome.** Panels (a) and (b) respectively correspond to cases II and IV from Table 3.1. Results were obtained using infinite DMRG with $C = -1$, assuming paramagnetic ancilla. The non-zero value generated by measurement at $u \neq 0$ validates analytic predictions, e.g., Eq. (4.21). Moreover, the fits shown by the dashed lines exhibit excellent agreement with the u dependence extracted using renormalization group arguments.

As in case I, $V(x, y)$ decays fast enough that we can approximate the second line with a local interaction, obtained here by fusing the pair of σ fields. The leading nontrivial fusion product is ε [see Eq. (3.6)]. For $C = 0$, where the $m(x)$ term drops out by symmetry, Eq. (4.18) then reduces to the form

$$\mathcal{S}_m = u^2 \int_x M(x)\varepsilon(x, \tau = 0), \quad (C = 0) \tag{4.19}$$

studied in the previous subsection with $M(x) = \int_y V(x, y)$. One-point correlators $\langle Z_j\rangle_{\tilde{s}}$ vanish by symmetry (to all orders in u due to preservation of $G\mathcal{T}$ symmetry) while two-point correlators $\langle Z_j Z_{j'}\rangle_{\tilde{s}}$ can be computed using the methods deployed above. For the remainder of this subsection we therefore take $C \neq 0$. In this regime the σ field arising from first line of Eq. (4.18) has a smaller scaling dimension compared to the ε field emerging from the second line. We can therefore neglect the latter term, yielding

$$\mathcal{S}_m \approx u^2 \int_x m(x)\sigma(x, \tau = 0), \quad (C \neq 0). \tag{4.20}$$

Physically, $m(x)$ plays the role of a longitudinal magnetic field that acts only at $\tau = 0$.

For uniform strings where $m(x) = m_{\text{const}}$, the defect-line action in Eq. (4.20) constitutes a strongly relevant perturbation. Clearly then $\sigma(x, \tau = 0)$ and hence Z_j

take on uniform, non-zero expectation values in this post-selection sector:

$$\langle Z_j \rangle_{\tilde{s}} \sim \langle \sigma(x_j) \rangle_{\tilde{s}} = g(u), \quad (\text{uniform } \tilde{s}), \tag{4.21}$$

where the function $g(u)$ vanishes as $u \to 0$ but tends to a non-zero constant at $u \neq 0$ in the thermodynamic limit. In sharp contrast, prior to measurements we have $\langle \psi_U | Z_j | \psi_U \rangle = 0$ for all u. Infinite DMRG results for $\langle Z_j \rangle_{\tilde{s}}$ presented in Fig. 4.4 confirm the qualitative behavior predicted by Eq. (4.21).

For a more quantitative treatment, we apply the renormalization group (RG) technique to obtain the dependence of $\langle \sigma(x_j) \rangle_{\tilde{s}}$ on u. Rescaling the spatial coordinate x by a factor b and defining $x' = x/b$, the σ field transforms as $\sigma(x) = b^{-1/8} \sigma'(x')$. The defect-line action $S_m = u^2 m_{\text{const}} \int \mathrm{d}x\, \sigma(x)$ is then rewritten as $S_m = u^2 m_{\text{const}} b^{1-1/8} \int \mathrm{d}x'\, \sigma'(x')$ and in particular exhibits a renormalized coupling strength $u^2 b^{7/8}$. Suppose now that at some coupling strength u^2_{ref}, the magnetization is a fixed constant $\langle \sigma'(0) \rangle_{\tilde{s}} = M_{\text{ref}}$. We can back out the observables at arbitrary u by finding the RG map that takes $u \to u_{\text{ref}}$. First, choose the scaling parameter b such that $u^2 b^{7/8} = u^2_{\text{ref}}$, i.e., $b = (u/u_{\text{ref}})^{-16/7}$. We then obtain $\langle \sigma(0) \rangle_{\tilde{s}} = b^{-1/8} M_{\text{ref}} \propto u^{2/7}$. Despite the simplicity of this argument, a fit of $\langle Z_j \rangle$ in Fig. 4.4 yields a scaling $\sim u^{0.27}$ with an exponent that agrees well with our prediction of $2/7 \approx 0.29$. It is also interesting to ask about two-point connected spin correlations in the presence of the uniform relevant defect-line action from Eq. (4.20). In Ref. [28] we explain that, for arbitrary u, power-law correlations persist with rigid exponents that are distinct from those of the pristine Ising theory.

We are not aware of works that compute the one-point function in the presence of arbitrary position-dependent $m(x)$'s that arise with generic measurement outcomes. Nevertheless, we expect that, at least for smoothly varying $m(x)$ profiles, $\langle \sigma(x) \rangle_{\tilde{s}}$ polarizes for each x with an orientation determined by the sign of $m(x)$. Since m_j averages to zero as shown in Section 3.4, averaging $\langle Z_j \rangle_{\tilde{s}}$ over measurement outcomes then naturally erases the effects of measurements as must be the case on general grounds. In contrast, such cancellation need not arise when averaging $\langle Z_j \rangle_{\tilde{s}}^2$ over measurement outcomes. We thus anticipate that

$$\sum_{\tilde{s}} p_{\tilde{s}} \langle Z_j \rangle_{\tilde{s}}^2 \neq 0. \tag{4.22}$$

Very crudely, if for a random measurement outcome $\langle Z_j \rangle_{\tilde{s}} \sim u^2 m_j$, then the nonlinear average above would be proportional to $u^4 \mathrm{Var}(m_j)$. Our exact diagonalization results presented in Fig. 4.5 support these predictions. The top panels show $\langle Z_j \rangle_{\tilde{s}}^2$ averaged

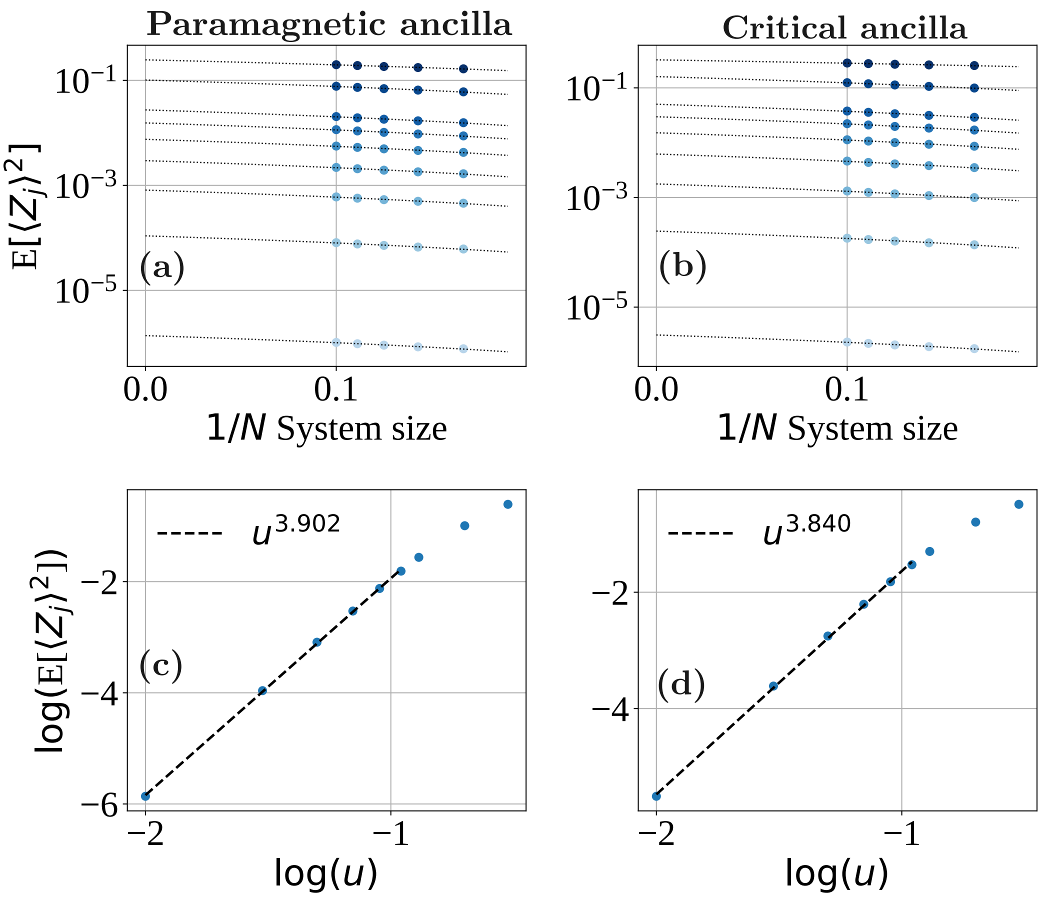

Figure 4.5: (Color online). **Average of $\langle Z_i \rangle_{\tilde{s}}^2$ over measurement outcomes in case II of Table 3.1.** Data were obtained using exact diagonalization for two chains of length $N = 6, 7, 8, 9, 10$ with $C = -1$. Panels (a, b) reveal well-behaved scaling with system size; larger values of u correspond to darker blue, with the darkest color corresponding to $u = 0.13$. Panels (c, d) show the extrapolated dependence of $\mathrm{E}(\langle Z_j \rangle_{\tilde{s}}^2)$ with u. For small u, we find $\sim u^4$ scaling, consistent with the crude expectation that $\langle Z_j \rangle_{\tilde{s}} \sim u^2 m_j$ for a particular measurement outcome.

over all $\tilde{Z}$-basis measurement outcomes versus $1/N$ for several values of u. For both paramagnetic and critical ancilla, extrapolation to $N \to \infty$ yields nonzero values for all $u \neq 0$ cases; additionally, the lower panels show that the extrapolated values indeed scale very nearly as u^4 for small u.

4.2 $\tilde{X}$-basis measurements and outcome sectors

Recall that for $\tilde{X}$-basis measurements, our perturbative formalism applies only to the highest probability subset of even-string ($\tilde{G} |\tilde{s}\rangle = +|\tilde{s}\rangle$) measurement outcomes. These outcomes, to which we exclusively focus in this section, include the uniform state with $\tilde{s}_j = +1$ on every site, and descendant states containing a dilute set of adjacent spin flips. Interestingly, even in this restricted space of measurement outcomes, we will encounter qualitative differences between paramagnetic versus critical ancilla in our protocol.

For both cases III and IV, the unitary $U' = e^{iH'}$ is trivial in the even-string measurement sector. This result immediately follows from Eq. (3.24) using the fact that $a(j) = 0$ for any even-string $\tilde{s}$. Hence in the ensuing analysis we need only consider H_m and the associated defect-line action $\mathcal{S}_m$. Note also that the U_j unitaries for cases III and IV explicitly violate $\tilde{G}$ symmetry; nevertheless, ancilla measurements project onto an even-string $\tilde{s}$ (by assumption), so that both the initial and post-measurement states are $\tilde{G}$ eigenstates with eigenvalue $+1$. The situation is reversed compared to the protocol with $\tilde{Z}$-basis measurements, where the U_j unitaries preserved $\tilde{G}$ while measurements produced a wavefunction that was not a $\tilde{G}$ eigenstate.

Case III

The case-III unitary $U_j = e^{iu(X_j - \langle X \rangle)\tilde{Z}_j}$ yields a defect-line action

$$\begin{aligned}\mathcal{S}_m = u^2 m \int_x \varepsilon(x, \tau = 0) \\ + u^2 \int_{x,y} V(x,y)\varepsilon(x, \tau = 0)\varepsilon(y, \tau = 0).\end{aligned} \tag{4.23}$$

Equation (4.23) has the same form as Eq. (4.3) from case I—with the crucial difference that here $m(x)$ is replaced with a *constant* $m = -2\langle X \rangle$ that is the same for all of the (restricted) strings that we consider. For paramagnetic ancilla, results from Section 3.4 imply that $V(x,y)$ decays exponentially with $|x - y|$, allowing us to once again fuse the ε's in the second line into a subleading term compared to the first. More care is needed for critical ancilla, since for the uniform string outcome $V(x,y)$ decays like $1/|x - y|$. The second line then represents an inherently long-range, power-law-decaying interaction. Such a term is, however, still less relevant by power counting compared to the first line. Thus, similar to case I, we can approximate the defect-line action as simply

$$\mathcal{S}_m \approx u^2 m \int_x \varepsilon(x, \tau = 0). \tag{4.24}$$

In this case one-point $\langle Z_j \rangle$ correlators again vanish by symmetry, while two-point correlators correspondingly behave as

$$\langle\sigma(x)\sigma(x')\rangle_{\tilde{s}} \sim \frac{1}{|x-x'|^{2\Delta_\sigma(u)}},\ \Delta_\sigma(u) = \frac{1}{8}(1+2\kappa u^2 m). \tag{4.25}$$

At least within the approximations used here, a pristine power-law with $O(u^2)$ enhanced scaling dimension occurs for any even-string measurement outcome conforming to our perturbative formalism, even if the outcome is not translationally invariant. Surely additional ingredients beyond those considered here would restore dependence on the measurement outcome; such terms, however, reflect subleading contributions, e.g., the neglected $V(x,y)$ term above. By contrast, for case I the dependence on measurement outcome was already encoded in the leading $m(x)\varepsilon$ term in the defect-line action.

The lower panels of Fig. 4.1 confirm the modified power-law behavior for the uniform measurement outcome, which again is especially clear at $u \geq 0.3$. Notice that for $u = 0.1$, the fitted scaling dimension is nearly the same for cases I and III, and for both paramagnetic and critical ancilla. This similarity is expected from our perturbative framework given that the leading defect-line actions [Eqs. (4.4) and (4.24)] take the same form with similar coupling strengths in the uniform measurement outcome sector. At the larger value of $u = 0.3$, the extracted scaling dimensions in case III differ for paramagnetic and critical ancilla—even though our $O(u^2)$ theory predicts precisely the same exponent in both scenarios. Such a correction is not surprising, given that at higher orders in u, even the leading term in the defect-line action can discriminate between paramagnetic and critical ancilla. Indeed, we have checked that in the paramagnetic case $\Delta_\sigma(u)$ scales like u^2 over a wider range of u compared to the case with critical ancilla.

Case IV

For case IV, with unitary $U_j = e^{iu(Z-C)\tilde{Z}}$, the defect-line action reads

$$\begin{aligned}\mathcal{S}_m &= u^2 \int_x m(x)\sigma(x,\tau=0) \\ &+ u^2 \int_{x,y} V(x,y)\sigma(x,\tau=0)\sigma(y,\tau=0),\end{aligned} \tag{4.26}$$

which has identical structure to that of case II but with modified couplings $m(x)$ and $V(x,y)$ due to the shift in ancilla measurement basis. As in case II, the special limit $C = 0$ still yields $m(x) = 0$, as required by symmetry.

Let us first take $C \neq 0$. Following the logic used for case III above, the second line is always subleading compared to the first, independent of whether the ancilla

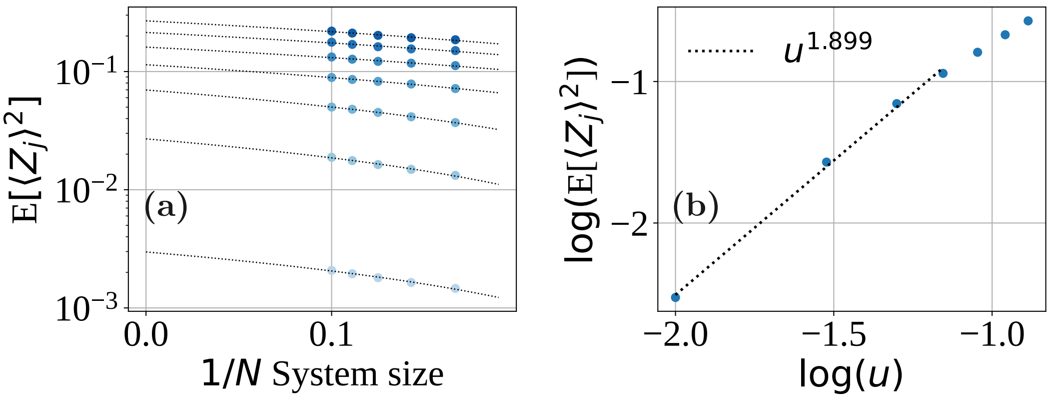

Figure 4.6: (Color online). **Average of $\langle Z_i \rangle_{\tilde{s}}^2$ over measurement outcomes in case IV of Table 3.1.** All parameters are the same as in Fig. 4.5, except here we consider only paramagnetic ancilla. The scaling of $\mathrm{E}[\langle Z_j \rangle_{\tilde{s}}^2]$ with u in panel (b) is much steeper ($\sim u^2$) compared to the scaling found in Fig. 4.5.

are paramagnetic or critical. (Technically, however, $m(x)$ diverges logarithmically with system size when the ancilla are critical, so extra care is warranted when applying our perturbative formalism in this scenario.) For the uniform or nearly uniform measurement outcomes that we can treat here, the strongly relevant $m(x)\sigma$ perturbation leads once again to a non-zero one-point function $\langle \sigma \rangle_{\tilde{s}} \neq 0$ that scales as $u^{2/7}$, as reproduced in DMRG simulations [Figure 4.4(b)]. Similar to our previous discussion in case II, we numerically find that $\langle Z_j \rangle_{\tilde{s}}^2$ averaged over all measurement outcomes also appears to yield a non-zero value at large N (at least for paramagnetic ancilla), even though our perturbative formulation now only applies to a restricted set of measurement outcomes. See Fig. 4.6 and notice the rather different scaling with u compared to Fig. 4.5. The results for critical ancilla, however, did not show an obvious trend and so we do not report them.

When $C = 0$, the approximation invoked above no longer applies, and the defect-line action instead becomes

$$\mathcal{S}_m = u^2 \int_{x,y} V(x,y)\sigma(x,\tau=0)\sigma(y,\tau=0), \quad (C=0). \tag{4.27}$$

Here the nature of the initial ancilla state becomes pivotal. For gapped ancilla, exponential decay in $V(x,y)$ enables fusing the σ fields into a single ε field. One then obtains the form in Eq. (4.19) that, for uniform or nearly uniform measurement outcomes, modifies the power-law correlations in $\langle \sigma(x)\sigma(x') \rangle_{\tilde{s}}$ as described previously. For critical ancilla this prescription breaks down since $V(x,y)$ scales like $1/|x-y|$. The resulting power-law-decaying interaction between σ's in Eq. (4.27) is strongly relevant by power counting; the system's fate then depends on whether the power-law interaction is ferromagnetic or antiferromagnetic. On one hand, ferromagnetic $\sigma(x, \tau = 0)\sigma(y, \tau = 0)$ interaction would promote order-parameter correlations at $\tau = 0$—possibly replacing power-law decay in the spin-spin correlation function with true long-range order, i.e., turning the critical chain into a cat state [2]. On the other, antiferromagnetic interaction would produce frustration, leading to a subtle interplay with ferromagnetic order-parameter correlations built into the pre-measurement critical theory.

Since $V(x, y)$ is always non-negative in case IV, $\mathcal{S}_m$ in Eq. (4.27) realizes the antiferromagnetic scenario. Figure 4.7 presents infinite DMRG simulations of $\langle Z_0 Z_j \rangle_{\tilde{s}}$ for this case [3]. For separations $|j|$ smaller than $O(10)$ we find signatures of faster-than-power-law decay induced by measurements. For larger separations, however, we find a possible revival of correlations (though in this regime the DMRG data continue to evolve over the bond dimensions simulated). While correlations might exhibit exponential decay at short distances, we expect algebraic decay to take over at long distances—which may be related to physics of antiferromagnetic long-range Ising chains analyzed in Refs. [29, 30]. This expectation is consistent with the fact that, as we will show in an upcoming work [28], when a short-range-correlated system entangles with critical ancilla, measuring the latter imprints long-range correlations into the former. Hence, it is natural to anticipate that tuning the short-range-correlated system to criticality only further enhances its long-range correlations.

With critical ancilla, the full two-chain system prior to measurement corresponds to a free-fermion problem with total central charge $c = 1/2 + 1/2$. Thus here the setup resembles a single-channel Luttinger-liquid in the special case with Luttinger parameter $K = 1$. For the Luttinger-liquid measurement protocol considered in Ref. [16], uniform measurement outcomes were shown to produce a marginal defect-line action. Our protocol, by contrast, yields a *relevant* defect-line action both for $C = 0$ and $C \neq 0$ in case IV—thereby qualitatively modifying correlations as discussed above. Interestingly, it follows that the total central charge alone does not dictate the impact of measurements on long-distance correlations. Additional factors including the allowed physical operators and details of the measurement protocol also play a role. For example, the protocol from Ref. [16] used an uncorrelated ancilla chain to mediate measurements on the Luttinger liquid, whereas in our effective

[2] Notice that for $C = 0$, $|\psi_{\tilde{s}}\rangle$ is an eigenstate of G, even though U breaks this symmetry explicitly.

[3] We show connected correlations, as for finite bond dimension $\langle Z \rangle_{\tilde{s}}$ gives non-zero values.

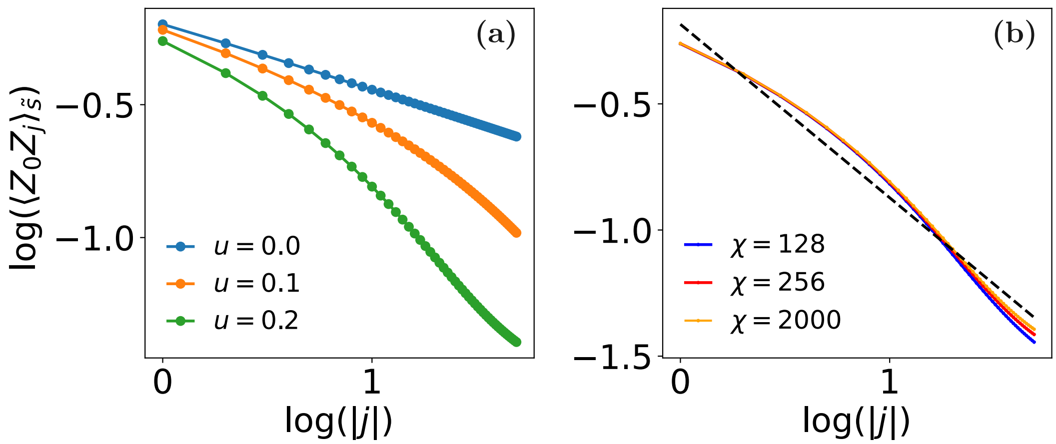

Figure 4.7: (Color online). **Correlation function $\langle Z_0 Z_j \rangle_{\tilde{s}}$ for case IV in Table 3.1 with $C = 0$ and critical ancilla.** (a) At $u > 0$ the correlator appears to decay faster than a power-law for $|j|$ less than $O(10)$ in response to the measurement-induced long-range interaction in Eq. (4.27). Data were obtained using iDMRG with bond dimension 2000. (b) Two-point correlator at $u = 0.2$ for a range of bond dimensions χ. Over the separations shown in (a), the data are well-converged. For larger separations, however, the data continue to evolve with bond dimension.

$c = 1/2 + 1/2$ setup measurements are enacted 'internally' without invoking an additional auxiliary chain.

4.3 Exact averaging over even/odd strings in $\tilde{X}$-measurement protocol

Symmetry-resolved averages

With $\tilde{X}$-basis measurements, outcomes $\tilde{s}$ can be divided into sectors according to whether $\tilde{G}\,|\tilde{s}\rangle = +\,|\tilde{s}\rangle$ or $-\,|\tilde{s}\rangle$. Here we exploit this neat even/odd-string dichomotomy to obtain illuminating, exact expressions for the average of critical-chain observables A over measurement outcomes confined to a particular $\epsilon = \pm 1$ parity sector. Using Eqs. (3.18) and (3.19), the average in sector ϵ reads

$$\begin{aligned}\langle A \rangle_\epsilon &= \sum_{\tilde{s}\in\epsilon} p_{\tilde{s}} \langle \psi_{\tilde{s}} | \, A \, | \psi_{\tilde{s}} \rangle \\ &= \sum_{\tilde{s}\in\epsilon} \langle \psi_a | \langle \psi_c | \, U^\dagger \left(\prod_j |\tilde{s}_j\rangle \langle \tilde{s}_j| \right) U A_U \, |\psi_c\rangle \, |\psi_a\rangle \\ &= \langle \psi_a | \langle \psi_c | \, U^\dagger \tilde{P}_\epsilon U A_U \, |\psi_c\rangle \, |\psi_a\rangle \,, \end{aligned} \tag{4.28}$$

where $U = \prod_j U_j$ represents the unitary applied prior to measurement and $A_U = U^\dagger A U$. In the last line

$$\tilde{P}_\epsilon = \sum_{\tilde{s}\in\epsilon} |\tilde{s}\rangle \langle \tilde{s}| = \frac{1}{2}\left(1 + \epsilon \tilde{G}\right) \tag{4.29}$$

projects onto the measurement-outcome sector with parity ϵ. For the unitaries in either case III or IV from Table 3.1, the anticommutation relation $\{\tilde{Z}_j, \tilde{G}\} = 0$ implies that $U^\dagger \tilde{G} = \tilde{G} U$. We can therefore express Eq. (4.28), after also using $\tilde{G} |\psi_a\rangle = |\psi_a\rangle$, as

$$\langle A\rangle_\epsilon = \frac{1}{2} \langle\psi_a| \langle\psi_c| A_U |\psi_c\rangle |\psi_a\rangle + \frac{\epsilon}{2} \langle\psi_a| \langle\psi_c| U^2 A_U |\psi_c\rangle |\psi_a\rangle . \quad (4.30)$$

Notice that the second term is real for any Hermitian operator A, since any imaginary parts vanish by parity constraints. Summing over the even and odd sectors yields $\langle A\rangle_+ + \langle A\rangle_- = \langle\psi_a| \langle\psi_c| A_U |\psi_c\rangle |\psi_a\rangle$—which, in agreement with Eq. (3.20), is simply the result one would obtain without performing any measurements. The difference between the even- and odd-sector correlators, by contrast, isolates the second term in Eq. (4.30),

$$\langle A\rangle_+ - \langle A\rangle_- = \langle\psi_a| \langle\psi_c| U^2 A_U |\psi_c\rangle |\psi_a\rangle , \quad (4.31)$$

and *does* retain nontrivial imprints of the measurements enacted in our protocol. Equation (4.31) is equivalent to the expectation value of the *non-local* operator $A\tilde{G}$ taken in the pre-measurement state $U |\psi_c\rangle |\psi_a\rangle$; crucially, measuring the ancilla in the $\tilde{X}$ basis provides access to such non-local information.

There is, however, no free lunch here: On general grounds the right side of Eq. (4.31) should decay to zero with system size N for any fixed $u \neq 0$. To see why, let $p_\epsilon = \sum_{\tilde{s}\in\epsilon} p_{\tilde{s}}$ denote the probability for obtaining parity sector ϵ after a measurement, and consider the difference

$$\Delta p \equiv p_+ - p_- = \langle\psi_a| \langle\psi_c| U^2 |\psi_c\rangle |\psi_a\rangle . \quad (4.32)$$

Equation (4.32) simply corresponds to Eq. (4.31) with A being the identity. At $u = 0$, where U also reduces to the identity, we obtain $\Delta p = 1$—reflecting the fact that the initial ancilla state $|\psi_a\rangle$ resides in the even-parity sector by construction. Turning on $u \ll 1$, the state $U^2 |\psi_c\rangle |\psi_a\rangle = \prod_j U_j^2 |\psi_c\rangle |\psi_a\rangle$ exhibits a small $O(u^2)$ probability for flipping a particular $\tilde{X}$-basis ancilla spin. Yet the net effect over a macroscopic number of sites N inevitably translates into a 'large' change in the probability for remaining in the even-parity sector. In terms of Eq. (4.32), this logic implies that $U^2 |\psi_c\rangle |\psi_a\rangle$ becomes orthogonal to $|\psi_c\rangle |\psi_a\rangle$ at fixed $u \neq 0$ with $N \to \infty$, leading to $\Delta p \approx 0$. The insertion of A_U in Eq. (4.31), assuming it represents physically relevant combinations of local operators, can not change this conclusion, implying that $\langle A\rangle_+ - \langle A\rangle_-$ vanishes with N as well. In Section 4.6 we numerically show that, with paramagnetic ancilla, these quantities decay exponentially with system size.

We propose the ratio

$$r(A) \equiv \frac{\langle A\rangle_+ - \langle A\rangle_-}{\Delta p} = \frac{\langle\psi_a|\,\langle\psi_c|\,U^2 A_U\,|\psi_c\rangle\,|\psi_a\rangle}{\langle\psi_a|\,\langle\psi_c|\,U^2\,|\psi_c\rangle\,|\psi_a\rangle} \tag{4.33}$$

as an appealing diagnostic of $\tilde{X}$-basis measurement effects on Ising criticality. Equation (4.33) need not vanish in the thermodynamic limit. Moreover, both the numerator and denominator comprise linear averages over experimentally accessible quantities. (But again there is no free lunch—the individually small numerator and denominator would need to be obtained with sufficient accuracy to yield a meaningful ratio as quantified further below.)

The formalism developed in Section 3.3 and Section 3.5 allows us to rewrite $r(A)$ in a more illuminating form that directly connects with the results from Section 4.2. For simplicity we focus for now on observables A that commute with U so that $U^2 A_U = AU^2$ (see below for a comment on the generic case). As detailed in Section 4.5, we can express the ratio in Eq. (4.33) as

$$r(A) = \frac{\langle\psi_c|\,Ae^{-H^r_m}\,|\psi_c\rangle}{\langle\psi_c|\,e^{-H^r_m}\,|\psi_c\rangle}, \tag{4.34}$$

where through our perturbative formalism we obtain at $O(u^2)$

$$\begin{aligned} H^r_m =& u^2 \sum_j m^r(O_j - \langle O\rangle) \\ &+ u^2 \sum_{j\neq k} V^r_{jk}(O_j - \langle O\rangle)(O_k - \langle O\rangle). \end{aligned} \tag{4.35}$$

Equation (4.35) is analogous to Eq. (3.25) but involves distinct couplings

$$V^r_{jk} = 2\langle\psi_a|\tilde{Z}_j\tilde{Z}_k|\psi_a\rangle \tag{4.36}$$

$$m^r = -4\theta + 2(\langle O\rangle - \theta)\sum_{k\neq 0} V^r_{0k}. \tag{4.37}$$

Most notably, compared to the V_{jk} and m_j couplings from cases III and IV of Table 3.1, V^r_{jk} here depends only on $|j-k|$ and follows from the expectation value of $\tilde{Z}_j\tilde{Z}_k$ in the initial ancilla ground state (rather than depending on some particular measurement outcome). For similar reasons m^r does not depend on position. If $[A, U] \neq 0$, then Eq. (4.34) holds together with an additional subleading term resulting from the commutator. For example, if we are interested in $A = Z_j Z_{j'}$ in case III from Table 3.1, then $[Z_j, U] = -2\,i\,Y_j \sin(u)[i\cos(u\,\theta)\tilde{Z}_j + \sin(u\,\theta)]\prod_{k\neq j} e^{iu(O_k-\theta)\tilde{Z}_k}$. Given that Y_j maps to a CFT operator with larger scaling dimension than that for

Z_j, we can already deduce that the additional term coming from the commutator involves subleading contributions that we can safely neglect. For further analysis see Section 4.5.

Taking the continuum limit, the ratio in Eq. (4.34) can be recast in terms of a path integral perturbed by a defect-line action akin to Eq. (3.32); recall the steps below Eq. (3.29). Let us now specialize to paramagnetic ancilla, where V^r_{jk} decays exponentially leading to a purely local action and finite m^r. We can then immediately import results from Section 4.2 to obtain $r(A)$ for spin correlators of interest. For case III we find

$$r(Z_j Z_k) \sim |j-k|^{-2\Delta^r_\sigma(u)} \quad \text{(case III)} \tag{4.38}$$

with nontrivially modified scaling dimension

$$\Delta^r_\sigma(u) = \frac{1}{8}(1 + 2\kappa u^2 m^r), \tag{4.39}$$

where $m^r = -4\langle X\rangle$. This result is, remarkably, nearly identical to the prediction for post-selected uniform measurement outcomes in case III; comparing with Eq. (4.25), the sole difference is that m^r is twice as larger as m, leading to a more pronounced upward shift in scaling dimension. For case IV with $C \neq 0$ we similarly find that

$$r(Z_j) \sim u^{2/7} \qquad \text{(case IV, } C \neq 0\text{)}, \tag{4.40}$$

which also emulates predictions for the corresponding post-selected uniform measurement outcome.

We performed a numerical experiment of Eqs. (4.38) and (4.40) using DMRG, focusing again on paramagnetic ancilla. Figure 4.8 presents the results for $r(Z_0 Z_j)$ in case III, which indeed reveals power-law decay with scaling dimension exceeding 1/8 at $u > 0$. In Fig. 4.9, we further contrast the data with the power-law exponents obtained for $\langle Z_0 Z_j\rangle_{\tilde{s}}$ with a uniform measurement outcome in case III. There we use finite DMRG for a system size of $N = 88$ to treat both quantities with a common numerical method. Our perturbative formalism predicts that, at small u, the measurement-induced change in the power-law for $r(Z_0 Z_j)$ should exceed that for $\langle Z_0 Z_j\rangle_{\tilde{s}}$ by a factor of 2. We indeed recover a more pronounced enhancement for the former—albeit by a factor smaller than 2. Note also that the $r(Z_0 Z_j)$ power-law exponent clearly exhibits more dramatic higher-order-in-u corrections that are beyond our leading perturbative treatment. Figure 4.10 reports the results for $r(Z_j)$ in case IV with non-zero C. Just as in Fig. 4.4 taken for uniform measurement outcomes in cases II and IV, we obtain good quantitative agreement with the prediction in

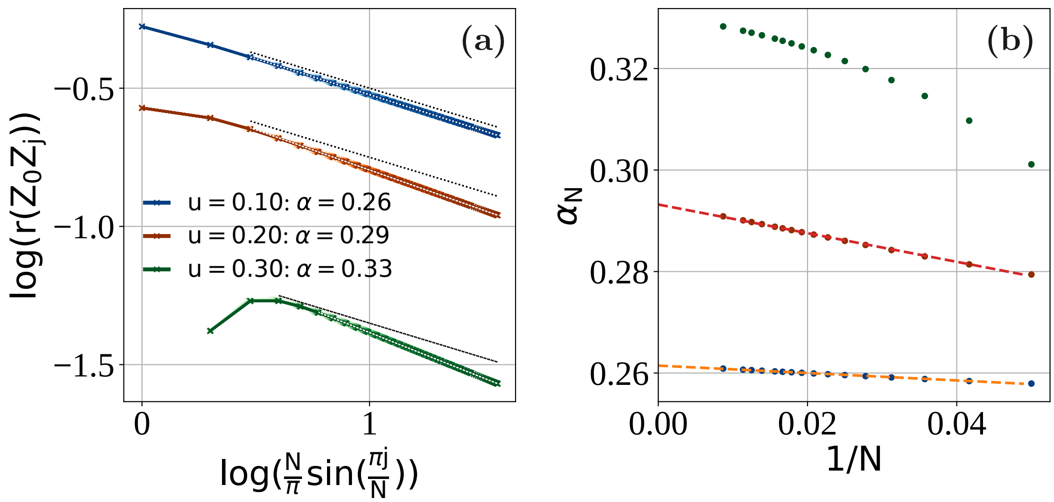

Figure 4.8: (Color online). **Ratio** $r(Z_0 Z_j)$ **in Eq.** (4.33) **involving symmetry-resolved measurement averages.** The data correspond to case III from Table 3.1 with paramagnetic ancilla, and different system sizes between $N = 20$ (light colors in (a)) and $N = 115$ (dark colors in (a)). At $u > 0$, the curves exhibit power-law decay with exponent exceeding $1/4$ in agreement with Eq. (4.38). The shift in scaling dimension becomes particularly clear for larger values of u when compared with the black dotted lines, corresponding to a power-law decay exponent 0.25. The tendency continues upon extrapolating to the thermodynamic limit, as shown in (b). The power-law exponents α displayed in panel (a) were obtained from fitting the data with the largest system size available. Data were obtained using finite DMRG with periodic boundary conditions and bond dimension 1000.

Eq. (4.40). Moreover, panel (b) shows that the $r(Z_j)$ values quickly saturate as N increases, at least for $u \geq 0.2$.

Despite the striking resemblance discussed above between $r(A)$ and correlators in post-selected uniform measurement outcomes, we stress that these quantities are not quite identical. The distinction becomes particularly apparent with critical ancilla—for which V^r_{jk} encodes a power-law interaction in the asssociated defect-line action with much slower decay (exponent $1/4$) compared to the decay found in cases III and IV (exponent 1). In case IV with $C = 0$, the inherently long-range $\sigma\sigma$ interaction mediated by V^r_{jk} is much more strongly relevant compared to the (also strongly relevant) interaction encountered in Eq. (4.27). Moreover, in case IV with $C \neq 0$, m^r correspondingly diverges rapidly with system size, signalling a clear breakdown of the perturbative expansion used above. By contrast, in Section 4.2 we saw that critical ancilla yield only a mild logarithmic divergence in m_j. We leave a detailed investigation of the properties of $r(A)$ with critical ancilla for future work.

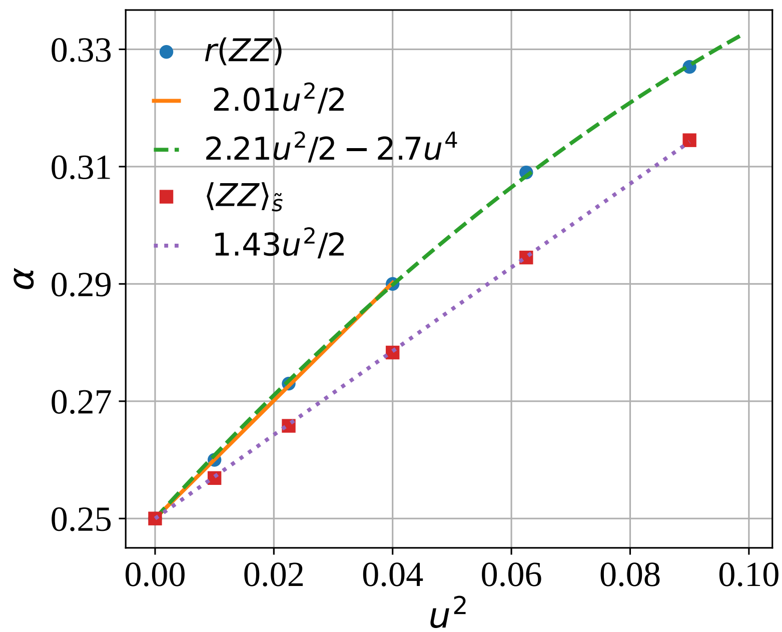

Figure 4.9: (Color online). **Comparison between power-laws for the $r(Z_0Z_j)$ ratio and $\langle Z_0Z_j \rangle_{\tilde{s}}$ correlator with a uniform measurement outcome in case III.** The measurement-induced shift in power-law exponent for $r(Z_0Z_j)$ exceeds that of $\langle Z_0Z_j \rangle_{\tilde{s}}$, in qualitative agreement with perturbative analytical predictions (though the enhancement is smaller than the predicted factor of 2). The green dashed line represents a quartic fit ($1/4 + \kappa m_{\text{const}} u^2/2 + bu^4$) in u of the exponent for the r ratio, while the orange and purple lines are the result of a quadratic fit ($1/4 + \kappa m_{\text{const}} u^2/2$). Data correspond to paramagnetic ancilla and were obtained with finite DMRG for a system of size $N = 88$ with periodic boundary conditions and bond dimensions 800 and 1000.

Comparison with post-selection

We now critically assess the experimental feasibility of probing measurement-altered criticality via symmetry-resolved averages and contrast with the alternative strategy of post-selection of an a priori specified measurement outcome [4]. For the latter, we focus in particular on post-selecting the uniform ancilla measurement string $\tilde{s}_{\text{uni}}$—which as we saw previously is the most likely measurement outcome and leads to clear measurement-induced changes of correlators that closely resemble symmetry-resolved averages. Quite different challenges accompany these two approaches. For the experimental extraction of symmetry-resolved averages, every protocol

[4]Notice that targeting a particular outcome is different from characterizing typical outcomes, for which our field theory results might not apply.

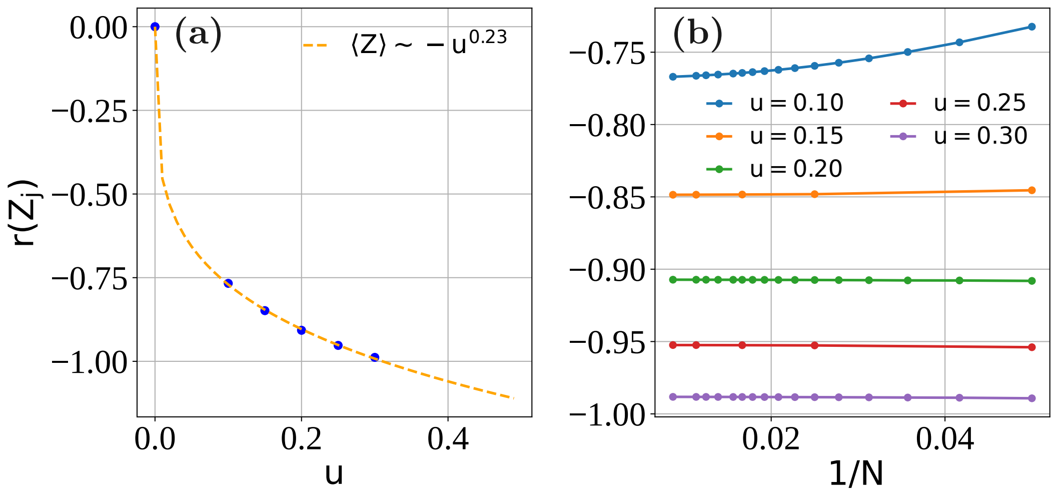

Figure 4.10: (Color online). **Ratio $r(Z_j)$ in Eq.** (4.33) **involving symmetry-resolved measurement averages.** The data correspond to case IV from Table 3.1 with paramagnetic ancilla, $C = -1$, and system sizes between $N = 20$ (light colors in(a)) and $N = 115$ (dark colors in (a)). Panel (a) shows that the small-u data are well-fit by a $\sim u^{0.23}$ scaling form—consistent with the prediction from Eq. (4.40). As shown in (b), increasing u suppresses the dependence on system size such that $r(Z_j)$ quickly saturates to a finite value. Data were obtained using finite DMRG with periodic boundary conditions and bond dimension 1000.

iteration—regardless of the specific ancilla measurement outcome—can in principle nontrivially inform evaluation of the ratio $r(A)$ in Eq. (4.33). As stressed above, however, the numerator and denominator both decay exponentially with system size, suggesting that obtaining sufficient statistics to reliably measure $r(A)$ requires a correspondingly large number of experimental trials. With post-selection, nearly all protocol iterations yield outcomes which differ from the target ancilla measurement outcome $\tilde{s}_{\text{uni}}$. But within the rare instances in which the target outcome emerges, evaluating $\langle \psi_{\tilde{s}_{\text{uni}}} | A | \psi_{\tilde{s}_{\text{uni}}} \rangle$ becomes relatively straightforward for two reasons. First, this expectation value generally does not decay exponentially with system size [contrary to Eq. (4.31)]. Second, due to translation invariance of $|\psi_{\tilde{s}_{\text{uni}}}\rangle$, one can interrogate all system spins in the post-measurement state to reduce the number of recurrences of $\tilde{s}_{\text{uni}}$ needed to resolve correlations to a desired accuracy; even a single successful trial suffices to approximate the expectation value of both one- and two-point correlations with an error scaling as $1/\sqrt{N}$, with N the system size. In what follows we quantify the number of trials required for both approaches.

Let us first assess symmetry-resolved averages and respectively write the numerator and denominator of $r(A)$ as

$$\mathcal{N} = \sum_{\tilde{s}} p_{\tilde{s}} \epsilon_{\tilde{s}} A_{\tilde{s}}, \quad \Delta p = \sum_{\tilde{s}} p_{\tilde{s}} \epsilon_{\tilde{s}}, \tag{4.41}$$

where $A_{\tilde{s}} = \langle \psi_{\tilde{s}} | A | \psi_{\tilde{s}} \rangle$ and $\epsilon_{\tilde{s}}$ denotes the parity for measurement outcome $\tilde{s}$. Both quantities decay exponentially with system size as

$$\mathcal{N}, \Delta p \sim e^{-\eta_{\mathrm{sra}}(u) N}. \tag{4.42}$$

The function $\eta_{\mathrm{sra}}(u)$ vanishes as $u \to 0$, reflecting the fact that, in the $u = 0$ limit, we obtain $\Delta p = 1$ exactly while $\mathcal{N}$ reduces to the critical correlator $\langle \psi_c | A | \psi_c \rangle$ that (at least for the few-body operators A of interest) does not decay exponentially with system size. For simplicity we will assume that in a given protocol iteration yielding a particular $\tilde{s}$, one can determine both $\epsilon_{\tilde{s}}$ and $A_{\tilde{s}}$ in a single shot. (In practice, each iteration would yield an eigenvalue of A, and determining $A_{\tilde{s}}$ would require multiple iterations yielding the same outcome $\tilde{s}$. Our assumption mods out these standard repetitions; moreover, since averaging over measurement outcomes restores translation invariance, here too one can probe all system spins to reduce the required number of repetitions, similar to the situation noted above for post-selection.) After M experimental protocol iterations yielding a set of outcomes $\tilde{s}_{i=1,\ldots,M}$ and associated parities $\epsilon_{\tilde{s}_i}$ and observables $A_{\tilde{s}_i}$, the quantities in Eq. (4.41) can be estimated by

$$\mathcal{N}_M = \frac{1}{M} \sum_{i=1}^{M} \epsilon_{\tilde{s}_i} A_{\tilde{s}_i}, \quad \Delta p_M = \frac{1}{M} \sum_{i=1}^{M} \epsilon_{\tilde{s}_i}. \tag{4.43}$$

In the limit $M \to \infty$ one obtains the exact results $\mathcal{N}_M \to \mathcal{N}$ and $\Delta p_M \to \Delta p$.

It is crucial to now understand the variance of the sampling distribution that quantifies the quality of these estimations at finite M. Given an estimator θ_M the sample variance is

$$\mathrm{Var}_M(\theta) = \frac{\mathrm{Var}(\theta)}{M}, \tag{4.44}$$

i.e., the population variance $\mathrm{Var}(\theta) = \sum_{\tilde{s}} p_{\tilde{s}} \theta_{\tilde{s}}^2 - \langle \theta \rangle^2$ divided by the sample size M. Intuitively, this quantity implies that the larger the sample size M, the smaller the variance of the sampling distribution of θ_M. For the $\mathcal{N}$ and Δp estimators we have

$$\mathrm{Var}_M(\mathcal{N}) = \frac{1}{M} \left(\sum_{\tilde{s}} p_{\tilde{s}} A_{\tilde{s}}^2 - \mathcal{N}^2 \right) \approx \frac{1}{M} \sum_{\tilde{s}} p_{\tilde{s}} A_{\tilde{s}}^2 \tag{4.45}$$

$$\mathrm{Var}_M(\Delta p) = \frac{1}{M}(1 - \Delta p^2) \approx \frac{1}{M}, \tag{4.46}$$

where on the rightmost sides we used the fact that both $\mathcal{N}$ and Δp decay exponentially with system size. Comparing to Eq. (4.42), we see here that accurately determining both the numerator and denominator of $r(A)$ requires a number of trials M that grows exponentially with N. The relative error $\sqrt{\mathrm{Var}_M\,(\Delta p)}/\Delta p$ in determining Δp, for instance, becomes smaller than one for $M \gtrsim e^{2\eta_{\mathrm{sra}}(u)N}$; similar reasoning applies to $\mathcal{N}$.

We are primarily interested in the number of trials required to reliably estimate $r(A)$ itself. The corresponding ratio estimator reads

$$r_M(A) = \frac{\mathcal{N}_M}{\Delta p_M}, \tag{4.47}$$

while to $\mathrm{O}(M^{-1})$ its variance is [31]

$$\mathrm{Var}_M[r(A)] \;\approx\; \frac{1}{\Delta p^2}\left[\mathrm{Var}_M(\mathcal{N}) + r(A)^2\mathrm{Var}_M(\Delta p)\; -2r(A)\mathrm{Covar}_M(\mathcal{N},\Delta p)\right]. \tag{4.48}$$

Evaluating the terms in brackets and neglecting contributions that are exponentially small in system size yields

$$\mathrm{Var}_M[r(A)] \approx \frac{1}{M\Delta p^2}\{\mathrm{Var}(A) + [r(A) - \langle A\rangle]^2\}. \tag{4.49}$$

The dominant remaining system-size dependence appears through Δp in the denominator. Consequently, accurate extraction of the symmetry-resolved average ratio $r(A)$ requires a number of trials satisfying [5]

$$M_{\mathrm{sra}} \gtrsim \frac{1}{\Delta p^2} \sim e^{2\eta_{\mathrm{sra}}(u)N} \tag{4.50}$$

(which is the same criterion for separately determining the numerator and denominator).

To diagnose a potential advantage of this approach with respect to post-selection, we next estimate the minimum sample size required to obtain the target measurement outcome $\tilde{s}_{\mathrm{uni}}$ with high likelihood. The probability to measure this string,

$$p_{\mathrm{uni}} = \langle\psi_U|\tilde{s}_{\mathrm{uni}}\rangle\langle\tilde{s}_{\mathrm{uni}}|\psi_U\rangle \sim e^{-\eta_{\mathrm{uni}}(u)N}, \tag{4.51}$$

[5] Equation (4.50) provides the leading N dependence needed to ensure that $\sqrt{\mathrm{Var}_M[r(A)]}/r(A)$ becomes smaller than one for the cases of interest. This conclusion follows from the fact that $r(A)$ decays at most as a power-law in system size, whereas the factor in braces in Eq. (4.49) is at most O(1).

also decreases exponentially with system size, as expected from the fact that it arises from the overlap of two very different many-body wave functions. Importantly, the function $\eta_{\text{uni}}(u)$, unlike $\eta_{\text{sra}}(u)$, generically does *not* vanish as $u \to 0$: At $u = 0$ exponential decay with N persists due to nontrivial overlap between $|\tilde{s}_{\text{uni}}\rangle$ and the initial ancilla wavefunction, except in the extreme limit $h_{\text{anc}}/J_{\text{anc}} \to \infty$. Since the probability of not measuring $\tilde{s}_{\text{uni}}$ after M trials is $(1 - p_{\text{uni}})^M$, the probability of finding this measurement outcome at least once is $p_{\text{success}} = 1 - (1 - p_{\text{uni}})^M$. The number of trials required for post-selecting the uniform measurement outcome with high success probability $p_{\text{success}} = 1 - \varepsilon$ (ideally 1) accordingly satisfies

$$M_{\text{uni}} = \frac{\log(\varepsilon)}{\log(1 - p_{\text{uni}})} \sim \frac{1}{p_{\text{uni}}} \sim e^{\eta_{\text{uni}}(u)N}. \tag{4.52}$$

Both the symmetry-resolved average and brute-force post-selection approaches thus require an exponentially large (in system size) number of measurements specified by Eqs. (4.50) and (4.52), respectively. It is crucial to observe, however, that the scaling with N is tunable via the choice of entangling gate and ancilla initialization in a manner that differs for the two methods. On very general grounds, since $\eta_{\text{sra}}(u = 0)$ vanishes whereas $\eta_{\text{uni}}(u = 0)$ is positive, there always exists a window of sufficiently small u for which symmetry-resolved averages can be probed more efficiently compared to post-selection. To be more quantitative, Section 4.6 provides numerical evidence that for small u these functions typically behave as

$$\eta_{\text{sra}}(u) \approx c_{\text{sra}} u^{\zeta}, \quad \eta_{\text{uni}}(u) \approx \Upsilon + c_{\text{uni}} u^{\zeta}. \tag{4.53}$$

Here $c_{\text{sra}}, c_{\text{uni}}$ are positive constants, ζ is a case-dependent exponent that we extract (see Fig. 4.14), and Υ determines the probability of finding the uniform measurement outcome at $u = 0$ (see Section 3.6 and Fig. 3.8). Equation (4.53) implies that when $2c_{\text{sra}} > c_{\text{uni}}$—which we find holds in practice—M_{sra} grows with system size exponentially but with a slower rate compared to M_{uni} for u between 0 and $u_* \equiv \left(\frac{\Upsilon}{2c_{\text{sra}} - c_{\text{uni}}}\right)^{1/\zeta}$. When u increases just beyond u_*, post-selection begins to become more efficient than symmetry-resolved averages. Intuitively, as the ancilla correlation length increases, the probability for obtaining the uniform measurement outcome decreases, thereby enhancing u_* and broadening the window in which symmetry-resolved averages are advantageous. In case IV with critical ancilla, we find that Δp does not decay monotonically to zero with N, but rather changes sign along the way. Equation (4.53) does not capture such non-monotonic behavior; similar conclusions nevertheless hold also in that case as we will see.

We validate the preceding picture by numerically analyzing the ratio $M_{\text{uni}}/M_{\text{sra}} \sim \Delta p^2/p_{\text{uni}}$, in particular by simulating the system-size dependence of $\Delta p^2/p_{\text{uni}}$ for different u values in cases III and IV. (When $uN \ll 1$ the unitary entangling gates are sufficiently close to the identity that they do not induce appreciable decay of either Δp or p_{uni}; hence we restrict the range of u such that the N values accessible in our simulations include regimes with $uN \gtrsim 1$. With this constraint we also avoid possible artificial phenomena appearing as a result of scaling u with system size.) Growth of $\Delta p^2/p_{\text{uni}}$ with N indicates more favorable scaling for symmetry-resolved averages, while decay with N indicates an advantage for post-selection. Figure 4.11 presents our results. For paramagentic ancilla (left panels), data for cases III and IV are consistent with post-selection becoming favorable for $u \gtrsim 0.1$. For critical ancilla (right panels), the data show that symmetry-resolved averages can remain advantageous out to larger values of u—consistent with the intuition above—especially in case III. Non-monotonic behavior evident in panel (d) arises because of the aforementioned sign changes in Δp arising in case IV with critical ancilla.

Assessing practicality of either scheme also requires quantifying the separate values M_{sra} and M_{uni} (as opposed to just their ratio) for experimentally reasonable system sizes. Relevant N values will certainly be platform dependent, as will the number of trials that one can feasibly conduct on laboratory timescales. For concreteness, we will focus on $N \sim O(100)$—which is relevant for present-day hardware—and postulate that trials up to $O(10^3)$ are accessible. Furthermore, we will simply take $M_{\text{sra}} = 1/(\Delta p)^2$ and $M_{\text{uni}} = 1/p_{\text{uni}}$ to roughly evaluate the trials required for symmetry-resolved averages and for post-selection, respectively; Fig. 4.12 displays the N dependence of these quantities for select u values. Remarkably, all four panels explored in the figure reveal regimes for which symmetry-resolved averages satisfy the experimental plausibility criteria laid out above. With paramagnetic ancilla, post-selection also enjoys regimes that require a surprisingly moderate number of trials even out to fairly large system sizes—ultimately because ancilla measurement outcomes obey a highly biased, controllable distribution. For reference, had all measurement outcomes been equally likely, one would obtain $M_{\text{uni}} = 2^N \sim 10^{24}$ in an $N = 80$ system! Figure 4.12 additionally reveals that M_{uni} increases relatively slowly with u (compared to M_{sra}), extending the experimentally plausible regime for post-selection to larger u's that display correspondingly stronger signatures of measurement-altered criticality.

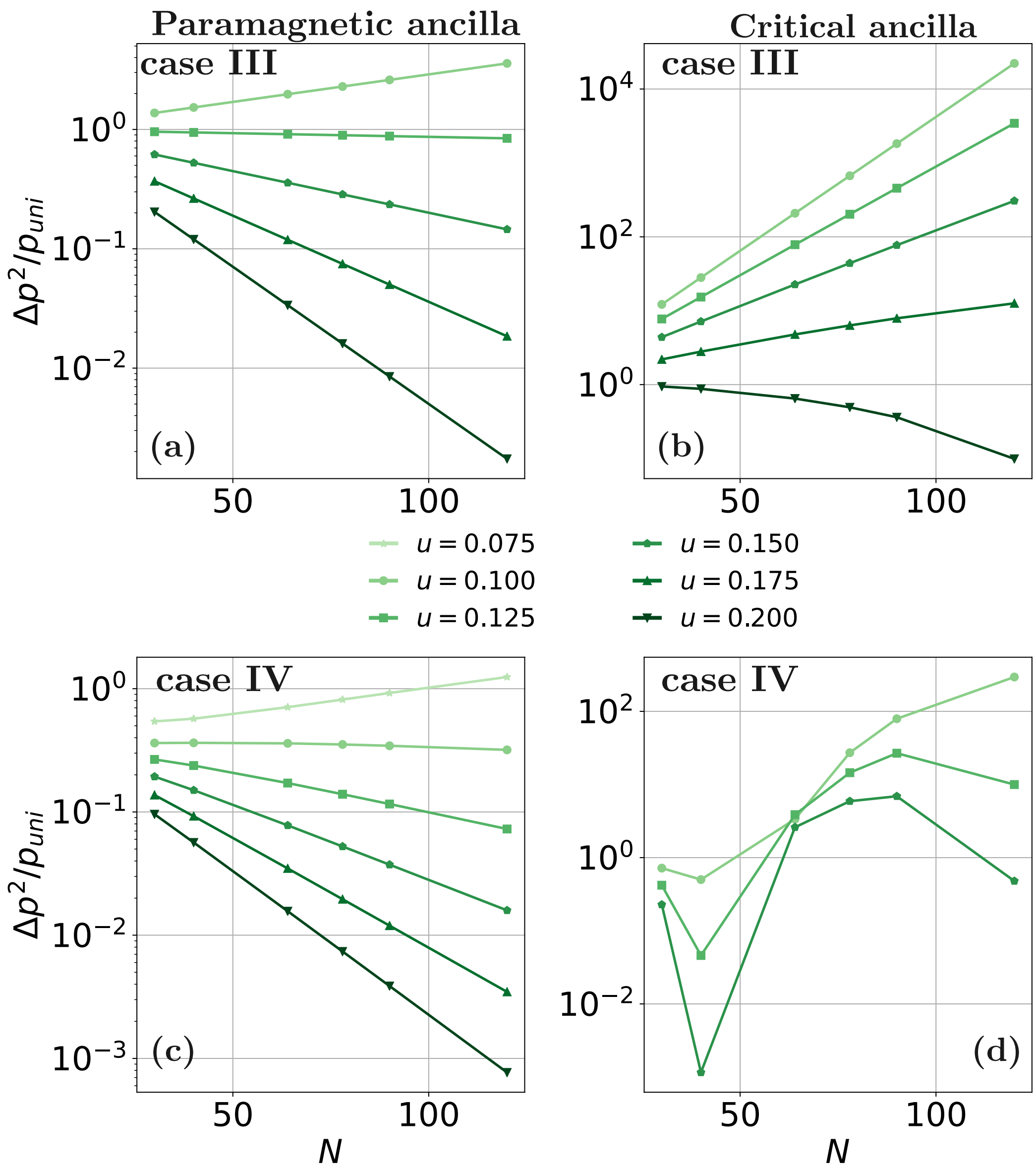

Figure 4.11: (Color online). **Comparison between symmetry-resolved averages and post-selection.** The vertical axis captures the ratio $M_{\text{uni}}/M_{\text{sra}} \sim \Delta p^2/p_{\text{uni}}$, where M_{uni} characterizes the number of trials needed for post-selection that targets the uniform measurement outcome and M_{sra} characterizes the number of trials required for evaluation of symmetry-resolved averages with order one variance. All panels are consistent with symmetry-resolved averages providing more favorable scaling with system size N over a window of small u—as argued on general grounds in the main text. Data were obtained using finite DMRG with bond dimension $\chi = 800$ and periodic boundary conditions; case IV results used $C = -1$.

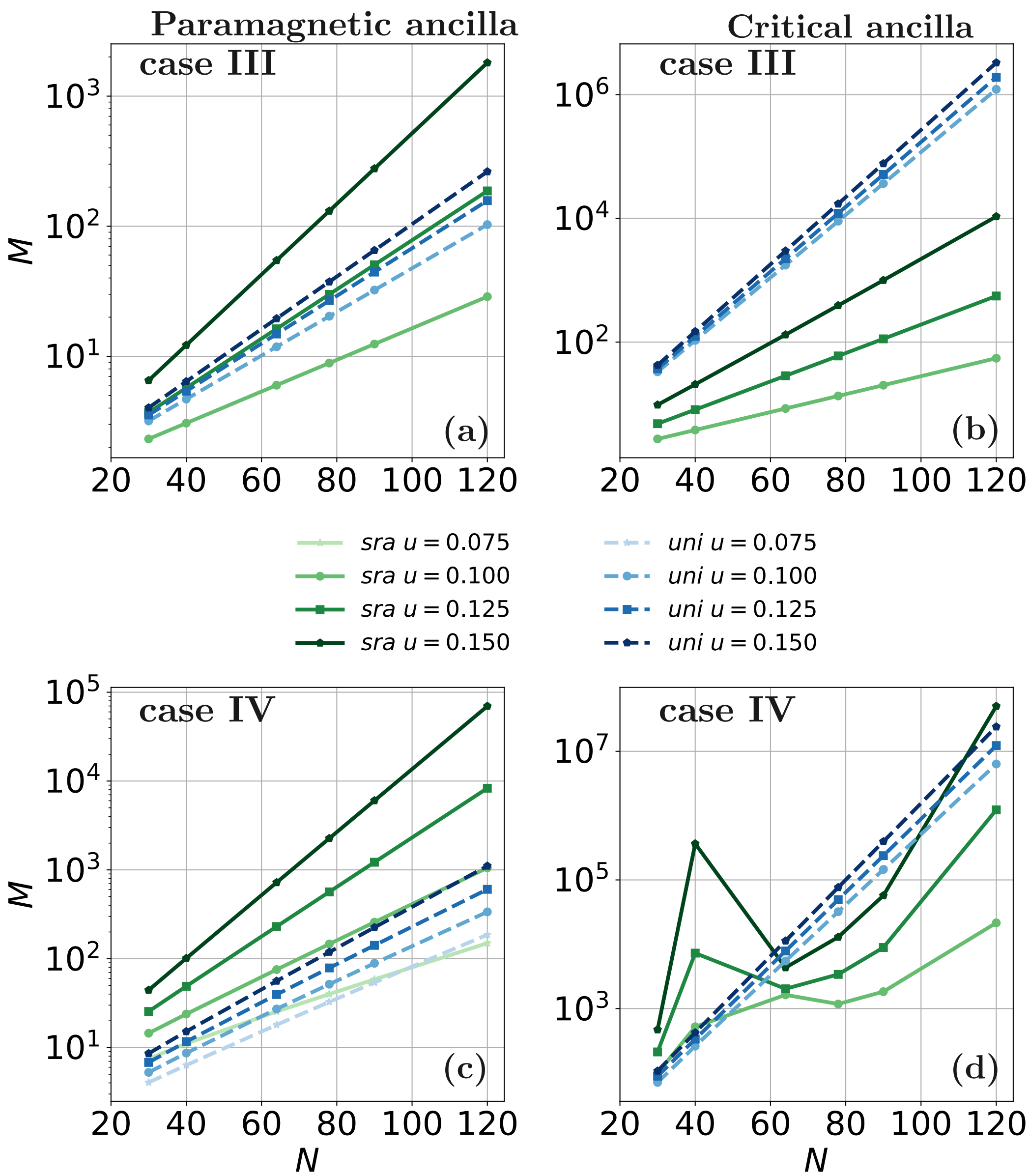

Figure 4.12: (Color online). **Scaling of M_{uni} and M_{sra} with system size N.** The number of trials needed for post-selection of the uniform measurement outcome and to extract symmetry-resolved averages are here estimated by $M_{\text{uni}} = 1/p_{\text{uni}}$ and $M_{\text{sra}} = 1/(\Delta p)^2$, respectively. Both approaches offer complementary regimes of experimental viability even at large systems with $N \sim O(100)$, as evidenced by a number of required trials of $O(10^3)$ or smaller. Data were obtained identically as in Fig. 4.11.

4.4 Lessons from the Ising example

We analyzed the initialize-entangle-measure-probe protocol summarized in Fig. 3.1 to investigate how measurements impact correlations in 1D Ising quantum critical points.

Specifically, we developed a perturbative formalism that allowed us to analytically study the outcome of our protocol applied with the four classes of unitaries and projective ancilla measurements listed in Table 3.1. Within this approach, long-distance correlations of microscopic spin operators were related to correlations of low-energy fields evaluated with respect to the usual Ising CFT action perturbed by a 'defect line'. The detailed structure of the defect line depends on the choice of entangling unitary, the initial ancilla state, and the outcome of ancilla measurements. We argued that, with $\tilde{Z}$-basis ancilla measurements, this formalism applies to general measurement outcomes; with $\tilde{X}$-basis ancilla measurements, however, well-behaved defect-line actions emerge only for a restricted set of (high-probability) measurement outcomes. In the latter context, we hope that future work can develop a more complete analytic theory capable of treating arbitrary measurement outcomes and assessing their probabilities for general ancilla initializations.

Various predictions follow from this framework—most of which we supported with numerical simulations. We recapitulate our main findings here (see also Fig. 3.1(e)):

Case I: unitary $U_j = e^{iu(X_j - \langle X\rangle)\tilde{X}_j}$, $\tilde{Z}$-basis measurements. Non-perturbative CFT results [27] allow one to formally compute the coarse-grained two-point spin correlation function $\langle Z_j Z_{j'}\rangle_{\tilde{s}}$ for general measurement outcomes $\tilde{s}$. For a uniform measurement outcome—which occurs with highest probability—the two-point function exhibits power-law decay with a measurement-induced change in the scaling dimension. Our formulation also captured subtle changes in correlations that arise with measurement outcomes featuring a domain wall. The agreement we found between analytical and numerical results here represents a highly nontrivial check for the validity of our approach.

Case II: unitary $U_j = e^{iu(Z_j - C)\tilde{X}_j}$, $\tilde{Z}$-basis measurements. With $C \neq 0$ the defect-line action includes a longitudinal-field term that explicitly breaks the $\mathbb{Z}_2$ symmetry enjoyed by the critical chain prior to measurement. Correspondingly, the one-point function $\langle Z_j\rangle_{\tilde{s}}$ becomes non-zero, with a spatial profile dependent on the measurement outcome. Averaging $\langle Z_j\rangle_{\tilde{s}}$ over measurement outcomes yields a vanishing one-point function as required on general grounds. By contrast, averaging $\langle Z_j\rangle_{\tilde{s}}^2$ retains memory of the measurements and yields a non-zero result that, based on our exact diagonalization results, appears to survive in the thermodynamic limit.

Case III: unitary $U_j = e^{iu(X_j - \langle X\rangle)\tilde{Z}_j}$, $\tilde{X}$-basis measurements. Just as for case I, the uniform string measurement outcome occurs with highest probability and yields a two-point function $\langle Z_j Z_{j'}\rangle_{\tilde{s}}$ with modified scaling dimension.

Case IV: unitary $U_j = e^{iu(Z_j - C)\tilde{Z}_j}$, $\tilde{X}$-basis measurements. As for case II, explicit breaking of $\mathbb{Z}_2$ symmetry induced by $C \neq 0$ yields a non-zero one-point function $\langle Z_j \rangle_{\tilde{s}}$ for the nearly uniform measurement outcomes amenable to our perturbative formalism. Taking $C = 0$ restores $\mathbb{Z}_2$ symmetry for the critical chain. Here, when the ancilla are *also* critical, the defect-line action hosts a long-range power-law decaying interaction among CFT spin-fields that, based on iDMRG simulations, appears to qualitatively alter $\langle Z_j Z_{j'} \rangle_{\tilde{s}}$ correlations (for uniform or nearly uniform measurement outcomes). That is, on short distances the correlations decay faster than power-law, though we argued that on longer-distances power-law correlations are likely to re-emerge. Further substantiating this scenario, possibly drawing connections to previous work on long-range-interacting Ising chains [29, 30], raises an interesting open problem.

In the cases with $\tilde{X}$-basis ancilla measurements, we further proposed a a new method for detecting non-trivial effects of measurements on Ising quantum criticality. Here we exploited the fact that $\tilde{X}$-basis measurement outcomes factorize into two symmetry sectors depending on the value of the generator $\tilde{G} = \prod_j \tilde{X}_j \in \pm 1$ of the global $\mathbb{Z}_2$ symmetry for the ancilla. Although $\tilde{G}$ is a non-local operator, its eigenvalue for any outcome $|\tilde{s}\rangle$ follows trivially given measurements of $\tilde{X}_j$ for each ancilla site; one can, in turn, average critical-chain observables over measurement outcomes separately within each symmetry sector. We found analytically that the *difference* in averages between the two sectors (normalized by the difference in probability for accessing the sectors) encodes measurement effects on Ising criticality that survive in the thermodynamic limit. Strikingly, such ratios evaluated for one- and two-point spin correlations mimic the behavior predicted for uniform post-selection outcomes by our perturbative defect-line framework, as recovered also in our simulations. The practical catch is that the ratio involves a numerator and denominator that individually decay to zero as the system size increases.

To address feasibility given this catch, we quantified the number of trials needed to meaningfully extract symmetry-resolved averages and contrasted with the alternative technique of post-selecting for the uniform measurement outcome. We established very generally that symmetry-resolved averages require exponentially fewer trials—although still exponentially many—compared to post-selection over a window of small entangling-gate strength u that widens as the ancilla become more correlated. Moreover, within this window symmetry-resolved averages necessitate a strikingly modest number of protocol runs—estimated to be on the scale of 10^2 to 10^3 for critical chains composed of $O(100)$ spins. Another important message of this work, however, is that post-selection poses a far less daunting challenge compared to the situation where all measurement outcomes are equally likely. With paramagnetic ancilla in particular, we found that in larger-u regimes where post-selection outperforms symmetry-resolved averages, the uniform measurement outcome can emerge with high probability after a similarly modest number of protocol runs in systems with as large as $O(100)$ spins. Apparent viability of post-selection here originates from the fact that measurement outcomes are far from random, but rather follow a highly biased distribution that one can control via u and the initial ancilla configuration. It would be valuable to understand the effects of measurement errors and decoherence on both symmetry-resolved averages and post-selection to further address their suitability for experimental application. More broadly, might factorization into symmetry sectors as exploited for symmetry-resolved averages prove fruitful for detecting measurement-induced phenomena in other contexts?

In much of this chapter, correlations in the initialized ancilla state played an important role. Cases I and II, for instance, become completely trivial if the ancilla are initialized into the (product-state) ground state of Eq. (3.14) at $h_{\text{anc}}/J_{\text{anc}} \to \infty$. In this extreme case $|\psi_a\rangle$ is an eigenstate of the U_j's used in our protocol for cases I and II. Hence those unitaries do not actually entangle the critical chain with the ancilla, and measurements of the latter do not affect the former. Case IV highlights a more striking example, where once again critical ancilla can produce a defect-line action exhibiting inherently long-range interaction among CFT fields, mediating physics qualitatively different from what we found with paramagnetic ancilla.

Outside of this last example, we invariably concluded that the defect-line action could be approximated by a single term linear in either the σ or ε field (depending on the protocol details under consideration). Microscopically, we showed that for the post-measurement state $|\psi_{\tilde{s}}\rangle = \frac{1}{\sqrt{N}} U' e^{-H_m/2} |\psi_c\rangle$ [Eq. (3.22)], the important non-unitary $e^{-H_m/2}$ part generically does not factorize into a product of operators acting at individual sites j due to the V_{jk} term in Eq. (3.25). An approximate factorized form,

$$|\psi_{\tilde{s}}\rangle \approx \frac{1}{\sqrt{p_{\tilde{s}}}} \prod_j M_j |\psi_c\rangle, \tag{4.54}$$

nevertheless captures the leading defect-line action linear in σ or ε that we typically obtained. When m_j is non-zero, the factorized measurement operators M_j follow by simply setting $V_{jk} = 0$ in H_m; with $m_j = 0$, one instead modifies the V_{jk} term by 'fusing' the constituent microscopic operators (mimicking the CFT-field fusion rules) to arrive at a factorizable form. Intuitively, the more highly entangled the ancilla are, the worse this approximation becomes—culminating in its complete breakdown in case IV with $C = 0$ when the ancilla are critical. The breakdown is anticipated to be especially stark in the case of symmetry-resolved averages due to the very slowly decaying longe-range interaction generated by measurement. It would be interesting to quantify the accuracy of Eq. (4.54) from a microscopic viewpoint, e.g., by studying the operator space entanglement of $M_{\tilde{s}}$ as a function of the ancilla wavefunction.

Chains of laser-excited Rydberg atoms trapped in optical tweezer arrays comprise a promising experimental platform for measurement-altered Ising criticality. A single Rydberg chain effectively realizes an antiferromagnetic spin model with power-law-decaying Ising interactions, supplemented by both transverse *and* longitudinal fields—though the latter can be tuned to zero by choosing an appropriate detuning from resonance. The phase diagram hosts a readily accessible Ising quantum phase transition (among other more exotic critical points) [32] that is well-understood also at the lattice level in this setting [21]. Moreover, a second Rydberg chain could furnish the ancilla degrees of freedom in our protocol. Devising concrete implementations of the requisite unitaries and ancilla measurements in this venue poses a nontrivial problem for future work. Additionally, the pursuit of measurement-altered criticality in Rydberg arrays highlights several fundamental open questions—including the impact of antiferromagnetic Ising interactions, a non-zero longitudinal field, integrability-breaking perturbations, etc. Erasure conversion developed for Rydberg arrays in Ref [33] is a promising tool for probing measurement-altered quantum criticality in this arena. Recent work in a quite different setting has also shown the possibility of creating the ground state of a critical transverse-field Ising chain using a quantum computer [34], highlighting tantalizing prospects for realization also in digital quantum hardware.

Finally, many other variations would be interesting to explore. Extension to strongly interacting CFTs—e.g., tricritical Ising, parafermionic, etc.—is particularly intriguing given their rich field content, and correspondingly rich set of possible measurement-induced defect-line actions. Measurements could also be performed in various alternative ways that add a new twist into the problem; for instance, one could contemplate joint measurements of operators on the critical and ancilla chains, or measure different quantities in different regions of space.

4.5 Effective-action derivation of the symmetry-resolved ratio $r(A)$

In this section, we show how the formalism developed in Section 3.3 and Section 3.5 allows us to rewrite $r(A)$ from Eq. (4.33) in a more illuminating form that immediately allows us to take advantage of the effective action formalism exploited throughout this chapter. Let us start from the case where $[A, U] = 0$. The numerator of Eq. (4.33) can be rewritten as

$$\langle\psi_c|A\langle\psi_a|\prod_j [C_j^r + S_j^r \tilde{Z}_j]|\psi_a\rangle|\psi_c\rangle, \tag{4.55}$$

where

$$C_j^r = \cos[2u(O_j - \theta)], \quad S_j^r = i\sin[2u(O_j - \theta)]. \tag{4.56}$$

Notice the extra factor of 2 in front of u compared to Eq. (3.45). The form of Eq. (4.55) resembles Eq. (3.44) and is therefore amenable to similar manipulations that led to Eqs. (3.49) and (3.51). Following these steps, we re-express the ratio in Eq. (4.33) as in Eq. (4.34), where now

$$H_m^r = -\ln\left[1 + \sum_{i_1<i_2}\langle\psi_a|\tilde{Z}_{i_1}\tilde{Z}_{i_2}|\psi_a\rangle T_{i_1}^r T_{i_2}^r + \cdots\right] - \sum_i \ln(C_i^r), \tag{4.57}$$

with $T_i^r = (C_i^r)^{-1}S_i^r$. Compared to Eq. (3.51), the argument of the log contains only terms with an even number of T_i^r operators. This difference results from the fact that $\tilde{G}\,|\psi_a\rangle = |\psi_a\rangle$, implying that only multi-point ancilla correlators with an even number of $\tilde{Z}$ operators give non-trivial contributions. It turn, $\langle\psi_c|\,Ae^{-H_m^r}\,|\psi_c\rangle$ does not contain a unitary contribution, even though $\langle\psi_a|\,\langle\psi_c|\,AU^2\,|\psi_c\rangle\,|\psi_a\rangle$ naively does. This conclusion can be understood by noticing that $\langle\psi_a|\,\langle\psi_c|\,AU^2\,|\psi_c\rangle\,|\psi_a\rangle = \langle\psi_a|\,\langle\psi_c|\,A\mathrm{Re}(U^2)\,|\psi_c\rangle\,|\psi_a\rangle$ with $\mathrm{Re}(U^2)$ a non-unitary operator. Upon expanding H_m^r to $O(u^2)$ and simplifying all constant terms between the numerator and denominator, we obtain Eq. (4.35) in the main text.

So far, we derived Eq. (4.34) assuming that $[A, U] = 0$. When $[A, U] \neq 0$ we obtain a modified form of H_m as follows. Consider case III from Table 3.1 and suppose that we are interested in observables $A = Z_j Z_{j'}$ with $j \neq j'$. We start by noticing that $U^2 A_U = AU^2 + [U, A]U$ which leads to

$$\langle\psi_a|\langle\psi_c|U^2 A_U|\psi_c\rangle|\psi_a\rangle = \langle\psi_a|\langle\psi_c|AU^2|\psi_c\rangle|\psi_a\rangle + \langle\psi_a|\langle\psi_c|[U, Z_j Z_{j'}]U|\psi_c\rangle|\psi_a\rangle. \tag{4.58}$$

Computing the commutator explicitly and using the notation $U_{\neq j} \equiv \prod_{k\neq j} e^{iu(X_k - \langle X\rangle)\tilde{Z}_k}$ then yields

$$\begin{aligned}
&\langle\psi_a|\langle\psi_c|U^2 A_U|\psi_c\rangle|\psi_a\rangle \\
&= \langle\psi_a|\langle\psi_c|AU^2|\psi_c\rangle|\psi_a\rangle \\
&\quad - 2i\sin u\ \langle\psi_a|\langle\psi_c|Y_j Z_{j'}\left[i\cos(u\langle X\rangle)\tilde{Z}_j + \sin(u\langle X\rangle)\right] \times U_{\neq j}U|\psi_c\rangle|\psi_a\rangle \\
&\quad - 2i\sin u\ \langle\psi_a|\langle\psi_c|Z_j Y_{j'}\left[i\cos(u\langle X\rangle)\tilde{Z}_{j'} + \sin(u\langle X\rangle)\right] \times U_{\neq j'}U|\psi_c\rangle|\psi_a\rangle \\
&\quad + 4\sin^2 u\ \langle\psi_a|\langle\psi_c|Y_j Y_{j'}\left[i\cos(u\langle X\rangle)\tilde{Z}_j + \sin(u\langle X\rangle)\right] \\
&\qquad\qquad \times \left[i\cos(u\langle X\rangle)\tilde{Z}_{j'} + \sin(u\langle X\rangle)\right]U_{\neq j,j'}U|\psi_c\rangle|\psi_a\rangle.
\end{aligned} \tag{4.59}$$

Let us focus on the second term on the right side, which can be recast into the form of Eqs. (4.55) in the main text but with $C_k^r = \sin(2u\langle X\rangle - uX_j)$, $S_k^r = i\cos(2u\langle X\rangle - uX_j)$ when $k = j$, and given by Eq. (4.56) otherwise. Hence, one recovers the Hamiltonian H_m^r in Eq. (4.57) although with local modifications for terms involving the j-th site. We denote the resulting Hamiltonian as $H_m^{(j)}$. All together, this procedure allows the second term on the right side to be compactly expressed as (up to constants that cancel when normalized by the denominator in $r(A)$),

$$-2i\sin(u)\,\langle\psi_c|\,Y_j Z_{j'} e^{-H_m^{(j)}}\,|\psi_c\rangle\,. \tag{4.60}$$

Compared to H_m^r in Eq. (4.35), $H_m^{(j)}$ and $H_m^{(j')}$ are very similar and differ only by some corrections involving sites j or j'. Importantly, both $\langle\psi_c|\,Y_j Z_{j'} e^{-H_m^{(j)}}\,|\psi_c\rangle$ and $\langle\psi_c|\,Z_j Y_{j'} e^{-H_m^{(j')}}\,|\psi_c\rangle$ contain Y operators, which map to a CFT operator with larger scaling dimension than that for Z. One can find an effective action also for the fourth term in Eq. (4.59), but since it contains operators $Y_j Y_{j'}$, its contribution will be even more subleading with respect to the previous ones. Therefore, as already mentioned in Section 4.3, we can neglect their subleading contributions at large distances.

4.6 System-size dependence of post-selection quantities

In Section 4.3, we argued that the symmetry-resolved differences $\langle A\rangle_+ - \langle A\rangle_- = \langle\psi_c|\langle\psi_a|U^2 A_U|\psi_a\rangle|\psi_c\rangle$, with A corresponding to correlators of local operators, vanish in the thermodynamic limit $N \to \infty$. Figure 4.13 numerically shows that with paramagnetic ancilla these quantities decay exponentially with system size for the values of u considered in the main text. In particular, panels (a,b) respectively show numerical results for case IV (at $C = -1$) with $A = \mathbb{1}$, i.e., the probability difference

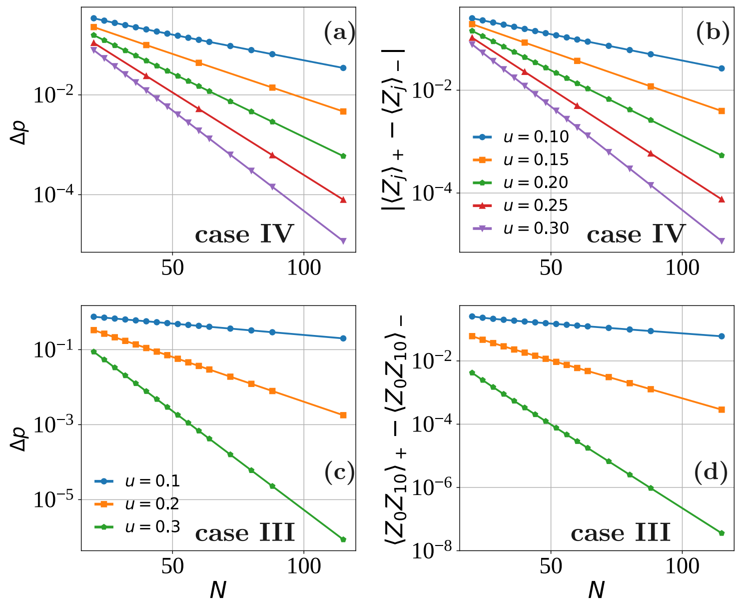

Figure 4.13: (Color online). **Exponential decay of symmetry-resolved differences $\langle A\rangle_+ - \langle A\rangle_-$ with system size.** (a) Probability difference Δp corresponding to $A = \mathbb{1}$. (b) One-point expectation value corresponding to $A = Z_j$. The result does not depend on the evaluated site j due to translation invariance. (c) Two-point correlator $A = Z_0 Z_{10}$ evaluated at a distance 10 from the reference site. Data were obtained using (finite) DMRG with periodic boundary conditions for case IV (with $C = -1$) in panels (a,b), and case III in panels (c,d) assuming paramagnetic ancilla.

$\Delta p = p_+ - p_-$, and $A = Z_j$. Panels (c,d) respectively show results in case III for Δp and $A = Z_0 Z_{10}$.

In Section 4.3, when comparing symmetry-resolved averages and post-selection, we used the scaling forms $\Delta p \sim e^{-\eta_{\rm sra}(u)N}$ and $p_{\rm uni} \sim e^{-\eta_{\rm uni}(u)N}$. Here we numerically establish that, for small u, these quantities in most cases conform well to the more precise scaling behavior $\Delta p \sim e^{-c_{\rm sra} u^\zeta N}$ and $p_{\rm uni}/p^{(0)}_{\rm uni} \sim e^{-c_{\rm uni} u^\zeta N}$ with $c_{\rm sra}, c_{\rm uni}$ constants, ζ an exponent that depends on the entangling gate U and on the initial ancilla wavefunction, and $p^{(0)}_{\rm uni} \sim e^{-\Upsilon N}$ given in Eq. (3.66). Equivalently, the prefactors determining the scaling with N obey $\eta_{\rm sra}(u) \approx c_{\rm sra} u^\zeta$ and $\eta_{\rm uni}(u) \approx \Upsilon + c_{\rm uni} u^\zeta$ at small u.

In agreement with the expressions above, Fig. 4.14 illustrates data collapse of both $p_{\rm uni}/e^{-\Upsilon N}$ (upper row) and Δp (lower row) when plotted versus $u^\zeta N$, with exponents ζ indicated on the horizontal axes. The range of u and N considered here are the same as those examined in the figures of Section 4.3. Panels (a,b) and (c,d) correspond to case III of Table 3.1 with paramagnetic ancilla and critical

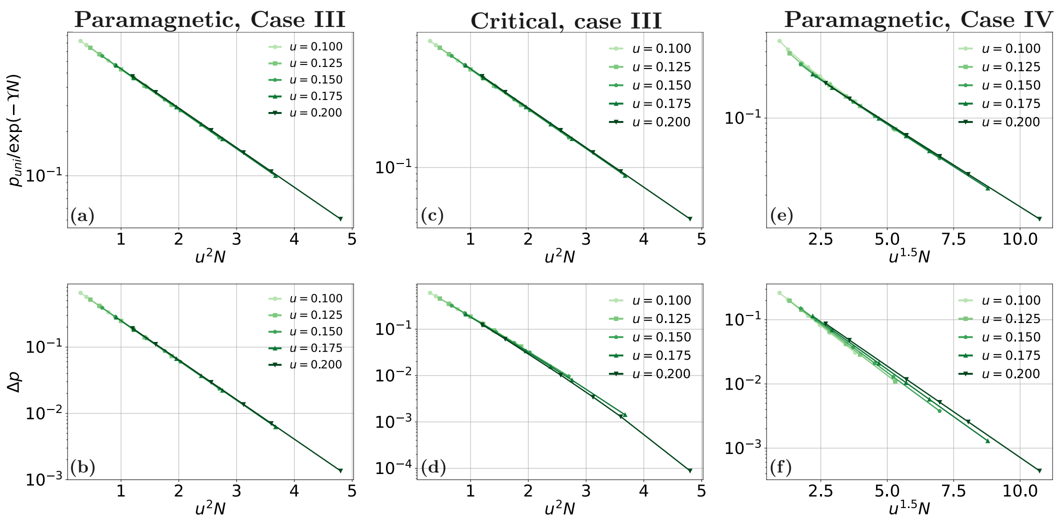

Figure 4.14: (Color online). **Scaling of Δp and p_{uni}.** Upper panels show that the ratio $p_{\mathrm{uni}}/p_{\mathrm{uni}}^{(0)}$ exhibits excellent data collapse when plotted versus $u^{\zeta}N$, with ζ exponents specified in the horizontal axes. Lower panels show similar data collapse for Δp. These results are consistent with scaling behavior $\Delta p \sim e^{-c_{\mathrm{sra}}u^{\zeta}N}$ and $p_{\mathrm{uni}}/p_{\mathrm{uni}}^{(0)} \sim e^{-c_{\mathrm{uni}}u^{\zeta}N}$. Data were obtained using finite DMRG with bond dimension $\chi = 800$ and periodic boundary conditions. Panels (e,f) for case IV correspond to $C = -1$.

ancilla, respectively. Panels (e) and (f) correspond to case IV with $C = -1$ and paramagnetic ancilla. The non-ideal data collapse in (f) possibly originates from neglected subleading corrections in u (but in any event does not matter for the conclusions drawn in Section 4.3). In case IV with critical ancilla, we find good data collapse for $p_{\mathrm{uni}}/e^{-\Upsilon N}$ with $\zeta = 0.25$ (data not shown); data collapse with our ansatz does not arise for Δp, however. The reason is that Δp undergoes sign changes in this case as a function of N for fixed u, thus no longer displaying monotonic behavior.

Part III

Measurement-Altered Criticality in Quantum Information Protocols

“Gold is just rocks with good makeup.”

— Pascal, *Animal Crossing: New Horizons*

Chapter 5

TELEPORTING CRITICAL WAVEFUNCTIONS

The preceding chapters developed measurement-altered criticality as a property of explicitly measured quantum critical wavefunctions. Teleportation provides a complementary route to the same structure: the measurement is built into the protocol, while the imperfection of the entangling or measurement stage determines the non-unitary deformation inherited by the teleported state. This chapter first reviews perfect and imperfect teleportation at the single-qubit level, then generalizes to many-body wavefunctions and the full-counting-statistics diagnostics that anticipate the Ising-critical analysis in Chapter 6.

5.1 Why teleportation is a probe of measurement-altered criticality

The groundbreaking 1993 work of Bennett et al. [35] elevated teleportation from science fiction to a key concept in modern quantum science. Quantum teleportation refers to the transfer of an unknown wavefunction from a sender, Alice, to a receiver, Bob, at a remote location. The protocol proceeds roughly as follows. First, Alice and Bob maximally entangle their qubits, e.g., by applying an appropriate unitary gate. Alice then performs a projective measurement that destroys the quantum state that she wishes to teleport, and communicates her measurement outcome to Bob. Finally, Bob applies an outcome-dependent unitary to his qubits to recover the target wavefunction. Aside from revealing a fundamental aspect of quantum mechanics—relevant for phenomena including black-hole evaporation [36]—teleportation admits potential applications in quantum communication, quantum networks, and quantum computation [37]; for reviews see Refs. [38, 39, 40]. To date, quantum teleportation has been demonstrated experimentally in numerous settings (e.g., Refs. [41, 42, 43, 44, 45]), including ground-to-satellite teleportation over distances of 1400 kilometers [46].

Teleportation protocols are far from unique. In fact there exists an infinite family of protocols—distinguished, for instance, by the choice of initialization for Bob's qubits, the particular entangling gate employed, and Alice's measurement basis—all of which yield perfect teleportation in the ideal case. Imperfections invariably occur, however, in experimental implementations due to decoherence, measurement and gate errors, etc. The generic presence of such imperfections raises many practically relevant questions, particularly in the context of teleporting *many-body* wavefunctions. To what extent do protocol imperfections modify universal aspects of correlations and entanglement in a teleported quantum state? Is there necessarily a sense in which one can regard imperfections as benign when assessing universal features, or can arbitrarily weak deviations from an ideal protocol qualitatively alter the teleported state's character? Among the infinite set of possible teleportation protocols, are some more resilient to certain types of imperfections than others? Can one optimize against expected errors with a judiciously chosen protocol? How do errors manifest after averaging over many imperfect teleportation runs?

We address these questions for the special case of imperfect teleportation of quantum critical wavefunctions. In particular, we focus on the ground state of the one-dimensional transverse-field Ising model tuned to the phase transition between paramagnetic and ferromagnetic phases, described by an Ising conformal field theory (CFT) with central charge $c = 1/2$. This setting offers an appealing test bed for diagnosing the influence of teleportation-protocol imperfections: First, the critical state exhibits universal power-law correlations among local observables, as well as universal long-range entanglement; both features provide useful diagnostics for assessing the quality of the teleported wavefunction. Second, the fact that the critical point is gapless implies sensitivity of physical properties to perturbations—in turn hinting that protocol imperfections can potentially drastically alter the character of the teleported quantum critical wavefunction.

We identify and analyze a class of protocol imperfections for which the teleported wavefunction received by Bob corresponds to Alice's original quantum critical state modified by the application of a *non-unitary* operator (that reduces to the identity in the ideal case). Such imperfections arise, for example, when Alice and Bob fall short of maximally entangling their qubits, or when Alice misaligns her measurement basis relative to the optimal protocol. One can profitably view the resulting non-unitary operator as effectively encoding the action of a weak measurement on the critical wavefunction. In other words, imperfectly teleporting the quantum critical wavefunction is formally equivalent to perfectly teleporting a weakly measured counterpart of that state. This perspective unites the problem of quantum criticality under imperfect teleportation with the developing theory of 'measurement-altered quantum criticality'.

The latter area has its roots in earlier works [47, 1, 48, 49, 50, 51, 52, 53] but came into sharp focus with Garratt et al.'s demonstration that even arbitrarily weak measurements can qualitatively alter long-distance correlations in a Luttinger liquid [16]. In particular, these authors established that weak measurements perturb the Luttinger-liquid action with an 'imaginary-time quantum impurity'—enabling a renormalization group analysis of their effects similar to the classic Kane-Fisher (real space) impurity problem [54]. Soon after, Ref. [55] showed that measurement-induced modifications of correlations are accompanied by qualitative changes in the Luttinger liquid's entanglement; see also Ref. [56]. These results have since been extended to quantum Ising spin chains [57, 58, 3, 59, 60, 61] and $(2+1)$-dimensional quantum critical points [62] (see also Ref. [63]). Various strategies have also been proposed for experimentally detecting measurement-altered criticality [16, 3, 64, 65, 66, 67]. In passing, we note that many recent works have explored measurement-induced phenomena in related contexts including entanglement phase transitions in monitored systems [1, 2, 68, 69, 70, 71, 72, 73], where unitary dynamics intertwines with local measurements, and for efficiently generating long-range entangled quantum states [74, 75, 76, 48, 77, 78, 79].

By leveraging and advancing the theory of measurement-altered criticality, we derive detailed predictions for the fate of Ising quantum critical states under imperfect teleportation. We explicitly obtain a family of imperfection-induced non-unitary operators—which indeed depend on the choice of protocol, as well as the measurement outcome that Alice communicates to Bob. These non-unitary operators apply to teleportation of generic many-body wavefunctions, as do some of the complementary tools that we employ to further analyze their impact on quantum critical states in both the limits of 'weak' and 'strong' imperfection. The weak regime admits a renormalization group analysis of imperfection-induced imaginary-time quantum impurities similar to Refs. [57, 58, 3, 60, 55]; in the strong regime we show that the character of the imperfectly teleported wavefunction relates deeply to 'strange correlators' [80]. Our main results are summarized in Fig. 5.1, and can be divided into three categories:

Relevant imperfection. Protocols yielding an imperfection-induced non-unitary operator that breaks $\mathcal{T} \times \mathbb{Z}_2$, where $\mathcal{T}$ denotes time reversal and $\mathbb{Z}_2$ is the spin-flip symmetry for the Ising spin system, are the least resilient to errors. Here, the associated imaginary-time quantum impurity comprises a relevant perturbation, and in the thermodynamic limit any amount of imperfection qualitatively alters both entanglement and correlations in the teleported wavefunction received by Bob. Long-range entanglement present in the original quantum critical state becomes

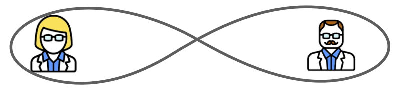

Measurement basis $\boldsymbol{n}$	Entanglement unitary $\prod_j U_j$	Teleported wavefunction		Entanglement	Correlations
$\hat{\boldsymbol{z}}$	$U_j = e^{iuX_j^A X_j^B}$	$e^{\frac{\alpha}{2}\sum_j a_j Z_j^B}\|\psi_c\rangle$	1	Area-law	Uniform order parameter condensation, power-law correlations w/ new exponents
			2	Area-law	Non-uniform order parameter condensation, average power-law correlations w/ new exponents
$\hat{\boldsymbol{x}}$	$U_j = e^{iuZ_j^A Z_j^B}$	$e^{\frac{\alpha}{2}\sum_j a_j X_j^B}\|\psi_c\rangle$	1	Long-range w/ modified eff. central charge	Power-law $\langle XX\rangle_c$ exponent unmodified $\langle YY\rangle, \langle ZZ\rangle$ exponents continuously variable
			2	Pristine	Pristine
$\hat{\boldsymbol{y}}$	$U_j = e^{iuZ_j^A Z_j^B}$	$e^{\frac{\alpha}{2}\sum_j a_j Y_j^B}\|\psi_c\rangle$	1	Long-range w/ modified eff. central charge	Power-law $\langle XX\rangle_c$,$\langle YY\rangle_c$ and $\langle ZZ\rangle$ exponents continuously variable
			2	Pristine	Pristine

$\alpha = -\ln[\tan(u)]$

1: Most-likely outcome
2: Typical outcome

Teleportation success: Good ⟶ Bad

Figure 5.1: **Executive summary.** The first two columns respectively indicate Alice's measurement basis and the imperfect entangling gate used in the protocol, leading to the teleported wavefunction in the third column. Here u denotes the entangling gate strength, with $u = \pi/4$ corresponding to the ideal protocol limit; a_j denotes Alice's measurement outcome for qubit j; and $|\psi_c\rangle$ is Alice's original critical wavefunction. The remaining columns summarize the entanglement and correlations in the imperfectly teleported state received by Bob. Colors (from good/green to bad/red) represent imperfections that we classify in the main text as irrelevant, disguised marginal, marginal, and relevant. Tools used to obtain these results include exact algebraic calculations of the resulting teleported states, analysis of an Ising CFT perturbed by an imperfection-induced 'impurity', parent Hamiltonians for imperfectly teleported states, analytical calculations of correlations and entanglement based on Gaussian states, and tensor network techniques.

downgraded to area-law behavior [57, 55], independent of Alice's measurement outcome. Moreover, power-law correlations nevertheless persist—with apparently rigid decay exponents distinct from those in the pristine Ising theory. We explain the coexistence of these properties through both the boundary CFT that incorporates the relevant perturbation [57, 16, 58], and by deriving a long-range-interacting parent Hamiltonian for the imperfectly teleported wavefunction. We further quantify how imperfection immediately and sharply modifies the distribution of order-parameter eigenvalues—i.e., full counting statistics—in that state. (See also Ref. [81] for a discussion of full counting statistics in a complementary setting with measurements.)

Marginal imperfection. In the weak-imperfection regime, teleportation protocols yielding non-unitary operators that preserve $\mathcal{T} \times \mathbb{Z}_2$ symmetry disrupt correlations and entanglement to a milder extent. For Alice's most likely measurement outcomes—which preserve translation symmetry, in some cases with an enlarged unit cell—the associated imaginary-time quantum impurity is generically marginal. Depending on the measurement basis used in the teleportation protocol, the marginal impurity can either arise at first order in the imperfection (in a sense made precise later on), or emerge as a higher-order effect under renormalization; we refer to the latter scenario as 'disguised marginal imperfection'. In either case, Bob inherits an imperfectly teleported wavefunction featuring both power-law correlations and long-range entanglement, though the power-law exponents [58, 57, 3, 16] and effective central charge [55, 57, 60] characterizing the long-range entanglement vary continuously as one moves away from the ideal protocol limit. The difference from relevant imperfection can be partly understood through the gentler impact of imperfection on full counting statistics. In the extreme limit of 'strong' imperfection—where the protocol transmits an asymptotically small amount of information from Alice's critical state—we recover the imperfectly teleported state's correlations and entanglement from a parent Hamiltonian (despite subtleties with convergence in the marginal case).

Irrelevant imperfection. Weak protocol imperfections yielding non-unitary operators that preserve $\mathcal{T} \times \mathbb{Z}_2$ symmetry generate irrelevant imaginary quantum impurities in two scenarios: (i) for Alice's 'typical' measurement outcomes (which we will define precisely) [16] and (ii) for translation-invariant measurement outcomes provided one fine-tunes the measurement basis in a way that cancels off the marginal contribution highlighted above. Irrelevant imperfections are optimal in the sense that Bob's wavefunction inherits Alice's universal correlations and entanglement, albeit at sufficiently long length scales; such imperfections still inevitably corrupt short-distance properties. In scenario (ii) above, we show that a fine-tuned, finite level of imperfection actually *revives* pristine universal properties in the imperfectly teleported state. We further conjecture that Bob can, remarkably, continue to inherit these universal features even arbitrarily deep in the regime of strong imperfection, where the imperfection-induced non-unitary operators corrupting Alice's original quantum critical state are far from the identity.

The hierarchy of imperfections that we identify—relevant, marginal, disguised marginal, and irrelevant—are associated with progressively greater resilience of the teleported quantum critical state to protocol errors. These results provide concrete guidelines for choosing teleportation protocols that most faithfully transfer universal quantum critical properties between parties. We stress that the imperfectly teleported wavefunction received by Bob can overlap negligibly with the original quantum critical wavefunction—while still (in the irrelevant case) displaying the same universal features. In essence, the metrics we study quantify the quality of teleporting within a family of quantum critical wavefunctions in the same universality class, rather than a specific many-body state. Wavefunction overlaps, by contrast, in no way isolate long-distance characteristics, and at least in this context do not appear to be the 'right' metric for assessing quality of the teleportation protocol. Finally, we address the fate of the teleported (mixed) state when a specific protocol is run many times, as would naturally occur when Bob wants to perform tomography of the teleported state with Alice obtaining different measurement outcomes sampled according to the Born rule. We find that power-law exponents encoded in the mixed state are faithfully teleported by virtue of the outcome-dependent unitary Bob applies in each teleportation run, which one can view as a 'decoding step' (as in, e.g., Ref. [82]) baked into the protocol. Imperfections can, nevertheless, nontrivially alter the entanglement structure of the mixed state as measured by the negativity. More broadly, our work highlights many open questions, ranging from studying imperfect teleportation of other classes of entangled many-body wavefunctions to identifying concrete applications of this family of problems.

We organize the remainder of this Part as follows. As a warm-up, Sec. 5.2 briefly reviews imperfect teleportation at the single-qubit level. Section 5.3 then discusses the imperfect many-body teleportation problem from a mostly general viewpoint that sets the stage for our subsequent analysis of imperfectly teleported quantum critical wavefunctions. Section 6.1 reviews the correlations, entanglement structure, and full counting statistics for the ground state of a critical quantum Ising chain; these properties provide the baseline that we compare against when exploring the fate of Ising criticality under imperfect teleportation in Sec. 6.2. Section 6.3 generalizes our imperfect teleportation protocols by allowing an additional error source with similar consequences. Section 6.4 diagnoses errors in mixed states describing an ensemble of imperfectly teleported critical wavefunctions. Conclusions and an outlook appear in Sec. 6.5.

5.2 Single-qubit teleportation primer

Canonical protocol

Imperfect teleportation of a single qubit [35] already contains ingredients essential for the many-body case of our interest, and hence we begin with this simpler problem. Following the standard protocol, consider a three-qubit Hilbert space $\mathcal{H}_{A_1} \otimes \mathcal{H}_{A_2} \otimes \mathcal{H}_B$; two qubits belong to Alice ($A_{1,2}$) and the third belongs to Bob

(B). In what follows X_q, Y_q, Z_q denote Pauli operators acting on qubit q.

Suppose that Alice wishes to transfer the state of qubit A_1 to Bob—without revealing her precise wavefunction. In the computational (Z) basis, the state to be teleported reads $\left|\psi_{A_1}\right\rangle = c_1 \left|\uparrow_{A_1}\right\rangle + c_2 \left|\downarrow_{A_1}\right\rangle$ with $c_1, c_2 \in \mathbb{C}$. Starting from a product state $\left|\uparrow_{A_2}\uparrow_B\right\rangle$ for the remaining two qubits, applying a Hadamard gate on qubit A_2 followed by a CNOT entangling gate [17] yields the maximally entangled state $|\phi^+\rangle = (\left|\downarrow_{A_2}\downarrow_B\right\rangle + \left|\uparrow_{A_2}\uparrow_B\right\rangle)/\sqrt{2}$ that provides a resource for teleportation. Next, Alice performs a Bell measurement on her two qubits. Adopting similar logic used to generate maximal entanglement, Alice can accomplish this measurement by performing a CNOT gate, then a Hadamard gate on A_2, and finally measuring her individual qubits in the computational basis with outcomes z_{A_1} and z_{A_2}. (All measurement outcomes appear with the same probability of $1/4$.) Bob's resulting unnormalized single-qubit state reads

$$\left|\psi_{z_{A_1} z_{A_2}}\right\rangle = \left\langle z_{A_1} z_{A_2}\right| U_{A_1 A_2 B} \left|\psi_{A_1} \uparrow_{A_2}\right\rangle |\uparrow_B\rangle . \tag{5.1}$$

Here $U_{A_1A_2B} \equiv H_{A_2}\text{CNOT}_{A_2A_1}\text{CNOT}_{A_2B}H_{A_2}$ incorporates the Hadamard and CNOT gates used for entanglement generation and Bell measurement [1]. Using the fact that H_{A_2} squares to the identity, one can equivalently express $U_{A_1A_2B} = \widetilde{\text{CNOT}}_{A_2A_1}\widetilde{\text{CNOT}}_{A_2B}$ as a product of two-qubit entangling unitaries

$$\widetilde{\text{CNOT}}_{ij} = e^{i\frac{\pi}{4}(1-X_i)(1-X_j)}. \tag{5.2}$$

After some algebra one finds that Bob's wavefunction becomes $\left|\psi_{A_1}\right\rangle$, up to a unitary $W_{z_{A_1}z_{A_2}}$ dependent on Alice's measurement outcomes $z_{A_{1,2}}$, i.e., $\left|\psi_{z_{A_1}z_{A_2}}\right\rangle = W_{z_{A_1}z_{A_2}}\left|\psi_{A_1}\right\rangle$. After Alice classically communicates these outcomes to Bob, he can 'undo' that unitary—completing the teleportation perfectly.

Notice that perfect teleportation can also arise upon replacing $\widetilde{\text{CNOT}}_{ij}$ by $U_{ij}^{\frac{\pi}{4}} = e^{i\frac{\pi}{4}X_iX_j}$, which mods out the single-qubit gates in Eq. (5.2) yet similarly generates maximal entanglement when acting on $\left|\uparrow_{A_2}\uparrow_B\right\rangle$. As before Alice's measurement outcomes remain equally likely, and one finds that, after she performs her measurement, Bob's state reduces to $\left|\psi_{A_1}\right\rangle$ up to a (different) measurement-outcome-dependent unitary $V_{z_{A_1}z_{A_2}}$ that he can undo. Below we consider the latter unitary entangling gate since it simplifies the analysis of imperfect protocols.

[1]In the standard teleportation protocol $U_{A_1A_2B} \equiv H_{A_1}\text{CNOT}_{A_1A_2}\text{CNOT}_{A_2B}H_{A_2}$. Nonetheless, our different choice of the controlled qubit (i.e., A_1 instead of A_2) only results in different measurement-dependent unitaries.

As alluded to in the introduction, failure to perform the preceding operations exactly yields imperfect fidelity of the teleported state. Such imperfections can arise from different error sources. We primarily focus on imperfection in the two-qubit entangling gate $U_{ij}^{\pi/4}$; that is, suppose that the protocol unintentionally implemented $U_{ij} = e^{iu_{ij}X_iX_j}$, with $u_{ij} \in [0, \pi/2]$. For $u_{ij} \neq \pi/4$ this unitary does *not* maximally entangle computational-basis eigenstates, and moreover leads to unequal probabilities for Alice's measurement outcomes. Hence, by repeatedly measuring, Alice can acquire some information about the unknown state $\left|\psi_{A_1}\right\rangle$. Following the measurement phase of the protocol, Bob's unnormalized state correspondingly becomes

$$\begin{aligned}\left|\psi_{z_{A_1}z_{A_2}}\right\rangle &= \left\langle z_{A_1}z_{A_2}\right| U_{A_1A_2}U_{A_2B}\left|\psi_{A_1}\uparrow_{A_2}\right\rangle\left|\uparrow_B\right\rangle \\ &= V_{z_{A_1}z_{A_2}}P_{z_{A_1}z_{A_2}}\left|\psi_{A_1}\right\rangle. \end{aligned} \tag{5.3}$$

On the second line, $V_{z_{A_1}z_{A_2}}$ is the same outcome-dependent unitary from the preceding paragraph, while crucially

$$P_{z_{A_1}z_{A_2}} = e^{\frac{1}{2}z_{a_1}(\alpha_{A_1A_2}+z_{A_2}\alpha_{A_2B})\hat{Z}_B} \tag{5.4}$$

is a non-unitary operator dependent on the amount of imperfection through the parameters

$$\alpha_{ij} = -\ln[\tan(u_{ij})]. \tag{5.5}$$

For a perfect protocol with $u_{ij} = \pi/4$, α_{ij} vanishes, and hence $P_{z_{A_1}z_{A_2}}$ reduces to the identity. For $u_{ij} \neq \pi/4$ the imperfect protocol generically teleports to Bob a non-unitarily modified cousin of Alice's A_1 qubit state [2]. In the extreme limit where u_{ij} approaches 0, α_{ij} diverges; here the non-unitary operator completely obliterates the content of Alice's original state, and Eq. (5.3) simply reduces to Bob's initial wavefunction. Incidentally, this limit shows why entangling-gate imperfections non-unitarily (as opposed to unitarily) corrupt the teleported state: When the protocol altogether fails to entangle Alice's and Bob's qubits, Bob's wavefunction before and after Alice measures her qubits must be unchanged for any choice of $\left|\psi_{A_1}\right\rangle$, which can only occur by modifying the latter with a non-unitary operator.

Imperfections in the initialization and measurement stages provide additional error sources that also non-unitarily corrupt the teleported state. Suppose, for instance,

[2] A loophole occurs when $u_{A_1A_2} = u_{A_2B}$. In this fine-tuned limit, even with a highly imperfect protocol for which the identical u's are far from $\pi/4$, perfect teleportation still arises in the measurement outcome sector with $z_{A_2} = -1$. The probability for accessing this measurement outcome vanishes in the extreme limit where the protocol fails to entangle Alice's and Bob's qubits. We neglect this non-generic limit in what follows.

that Alice inadvertently measures along a quantization axis tilted away from the Z direction and with a finite projection along X—thus no longer achieving a perfect Bell measurement. The first line of Eq. (5.3) would then be modified via $\langle z_{A_1} z_{A_2}| \to \langle z_{A_1} z_{A_2}| S_{A_1} S_{A_2}$, where S_{A_j} is a spin-rotation operator acting on qubit A_j that encodes the measurement misalignment. In the extreme case where the quantization axis rotates all the way to the X direction, $U_{A_1 A_2}$ entirely fails to entangle Alice's $A_{1,2}$ qubits, and once again no information about $|\psi_{A_1}\rangle$ can be transmitted to Bob. Following the above logic, $P_{z_{A_1} z_{A_2}}$ must again be a non-unitary operator that erases the content of Alice's A_1 qubit state. Similar reasoning holds for misalignment in the initialization of the A_1 and B qubits.

Next we will explore a simplified version of the teleportation protocol reviewed here. This simplification will turn out to greatly streamline explicit, closed-form derivation of imperfectly teleported quantum states both at the single- and many-qubit levels.

Simplified protocol

Let us retain the key ingredients underlying quantum teleportation—entanglement, measurement, and classical communication—while distilling the setup by reducing the number of degrees of freedom. Specifically, we replace the three-qubit Hilbert space ($\mathcal{H}_{A_1} \otimes \mathcal{H}_{A_2} \otimes \mathcal{H}_B$) with that of just two qubits ($\mathcal{H}_A \otimes \mathcal{H}_B$). Bob once again initializes his qubit into the state $|\uparrow_B\rangle$. Alice's now sole qubit, A, realizes some general state $|\psi_A\rangle = c_1 |\uparrow_A\rangle + c_2 |\downarrow_A\rangle$ that she would like to transfer to Bob in a similar vein as in the previous subsection. (Alice need not know her precise qubit state, e.g., she may have received it through a separate teleportation protocol.) An ideal protocol proceeds by entangling A and B via the unitary gate $U_{AB}^{\pi/4} = e^{i\frac{\pi}{4} X_A X_B}$ and then projectively measuring A in the computational basis. Importantly, as for the standard protocol, in this perfect implementation all measurement outcomes are equally likely. Upon Alice communicating her measurement outcome to Bob, he can perform an outcome-dependent unitary to perfectly recover Alice's qubit state.

Imagine, however, that the actual entangling gate employed had the form $U_{AB} = e^{iuX_A X_B}$ for some $u \in [0, \pi/2]$. With $u = \pi/4$ we recover the ideal case, but otherwise the protocol is imperfect. This unitary sends the initial state $|\psi_A\rangle |\uparrow_B\rangle$ to

$$
\begin{aligned}
|\psi_U\rangle = |\uparrow_A\rangle &[\cos(u) c_1 |\uparrow_B\rangle + i \sin(u) c_2 |\downarrow_B\rangle] \\
&+ |\downarrow_A\rangle [\cos(u) c_2 |\uparrow_B\rangle + i \sin(u) c_1 |\downarrow_B\rangle].
\end{aligned} \tag{5.6}
$$

Also as for the standard protocol, Alice's measurement outcomes become biased by imperfection. After Alice measures her qubit with outcome $z_A = \pm 1$, Bob's unnormalized wavefunction becomes

$$\begin{aligned} \left|\psi_{z_A=+1}\right\rangle &= \cos(u)c_1 \left|\uparrow_B\right\rangle + i\sin(u)c_2 \left|\downarrow_B\right\rangle \\ \left|\psi_{z_A=-1}\right\rangle &= \cos(u)c_2 \left|\uparrow_B\right\rangle + i\sin(u)c_1 \left|\downarrow_B\right\rangle . \end{aligned} \tag{5.7}$$

One can equivalently recast Eqs. (5.7), modulo an overall normalization, in the compact form

$$\left|\psi_{z_A}\right\rangle = V_{z_A} P_{z_A} \left|\psi_A\right\rangle . \tag{5.8}$$

Here

$$V_{z_A} = e^{i\frac{\pi}{4}(1-z_A)X_B} e^{-i\frac{\pi}{4}z_A Z_B} \tag{5.9}$$

is an outcome-dependent unitary operator present even in the optimal protocol, while imperfection is encoded through the non-unitary operator

$$P_{z_A} = e^{\frac{\alpha}{2}z_A Z_B} \tag{5.10}$$

dependent on u through the parameter

$$\alpha = -\ln[\tan(u)]. \tag{5.11}$$

Once Bob learns Alice's measurement outcome and undoes the W_{z_A} unitary, the final teleported wavefunction reads

$$\left|\psi_{z_A}^{\text{tele}}\right\rangle = P_{z_A} \left|\psi_A\right\rangle . \tag{5.12}$$

The above analysis closely parallels the results from Eqs. (5.3) through (5.5) for the canonical three-qubit teleportation protocol. Similar to the latter case, imperfection in our simplified protocol, encoded through the single parameter $u \neq \pi/4$, nonunitarily corrupts the teleported state, completely erasing the content of Alice's qubit in the extreme case where $u \to 0$ and $\alpha \to \infty$. This similarity is not accidental: In fact the upper line from Eq. (5.3) maps to Eq. (5.8) (modulo a unitary that does not depend on the state being teleported) in the limit where $u_{A_2B} = \pi/4$ and $u_{A_1A_2} = u$. Thus our simplified teleportation protocol captures the situation in which imperfection appears in only one of the two entangling gates employed in the canonical protocol.

5.3 Many-body teleportation

Next we turn to the richer problem of imperfectly teleporting a many-body wavefunction from Alice to Bob. Although we are primarily interested in teleporting quantum critical states, in much of this section we keep our discussion general. Many-body

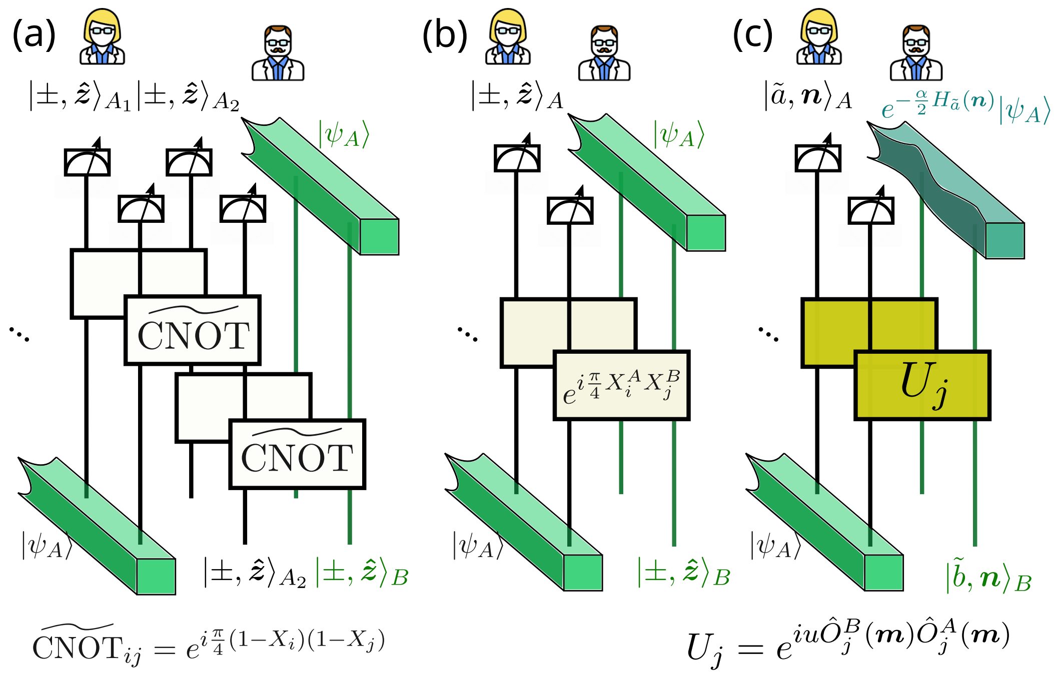

Figure 5.2: **Many-body quantum teleportation.** (a) Perfect quantum teleportation of an L-qubit wavefunction $|\psi_A\rangle$. After coupling Alice's qubits A_1, A_2 to Bob's B (via two consecutive entangling unitaries $\widetilde{\mathrm{CNOT}}$), performing properly aligned single-qubit measurements, and implementing an outcome-dependent unitary, $|\psi_A\rangle$ (light green prism) is perfectly teleported to Bob. (b) The same perfect setup can be simplified—see Sec. 5.2—by reducing Alice's number of degrees of freedom from $2L$ to L. (c) Errors in the 'strength' of the entangling unitary (deviations from $u = \pi/4$), or improper alignment of the measurement basis ($\boldsymbol{m}$ not parallel to $\boldsymbol{n}^\perp$), leads to imperfect teleportation where Bob receives a non-unitarily corrupted wavefunction $e^{-\frac{\alpha}{2}H_{\tilde{a}}}|\psi_A\rangle$ (deformed dark green solid) with $\alpha = -\ln[\tan(u)]$ and $H_{\tilde{a}}$ a Hermitian operator.

teleportation of an L-qubit state can proceed by running the protocol reviewed in Sec. 5.2 separately on each constituent qubit—respectively requiring a total of $3L$ and $2L$ qubits in the canonical and simplified teleportation protocols. Figures 5.2(a) and (b) sketch the corresponding protocols in the ideal case of perfect teleportation.

In the following we focus on the simplified protocol with imperfectly applied entangling gates and establish the formalism that we will use to assess the nature of the resulting teleported state. Once again, this scenario accounts for imperfection in one of the two entangling gates used in the canonical protocol (see Sec. 5.2). For a many-body state that breaks spin-rotation symmetry (always the case for the present paper), the impact of such protocol imperfections depends on the specific entangling gate used as we will emphatically see later in the context of teleporting

Ising criticality. We therefore generalize the teleportation protocol from Sec. 5.2 in a way that incorporates freedom in the intialization of Bob's qubits and the gate that entangles with Alice's qubits.

Suppose that Bob's initial wavefunction is a product state $|\psi_B\rangle = |\tilde{b}, \boldsymbol{n}\rangle$. On the right side we introduced short-hand notation $\tilde{b} = \{b_j\}$, where $b_k = \pm 1$ is the spin eigenvalue for qubit k along the quantization axis set by the unit vector $\boldsymbol{n}$; i.e., b_k is the eigenvalue for the Pauli operator $\hat{O}^B_k(\boldsymbol{n}) = \boldsymbol{n} \cdot \boldsymbol{\sigma}^B_k$. Alice's initial wavefunction—which we leave unspecified for now—can be expanded in the analogous basis as $|\psi_A\rangle = \sum_{\tilde{a}} c_{\tilde{a}} \left|\tilde{a}, \boldsymbol{n}\right\rangle$; as above $\tilde{a} = \{a_j\}$, and the $c_{\tilde{a}}$ coefficients encode Alice's entanglement and correlations. En route to teleportation, Alice and Bob employ the unitary

$$U = \prod_j e^{iu\hat{O}^A_j(\boldsymbol{n}^\perp)\hat{O}^B_j(\boldsymbol{n}^\perp)} \tag{5.13}$$

that pairwise entangles their respective qubits, transforming their combined state to $|\psi_U\rangle = U|\psi_A\rangle|\psi_B\rangle$. Here $\boldsymbol{n} \cdot \boldsymbol{n}^\perp = 0$ such that $\hat{O}_k(\boldsymbol{n}^\perp) = \boldsymbol{n}^\perp \cdot \boldsymbol{\sigma}_k$ acting on $|\tilde{s}, \boldsymbol{n}\rangle$ sends $s_k \to -s_k$ [3]; the A, B superscript designates whether the operator acts on Alice or Bob; and u specifies the strength of the entangling gate. Next, Alice projectively measures all of her spins along the same quantization axis $\boldsymbol{n}$ used for Bob's initial state—obtaining particular measurement outcomes $\tilde{a}$ with probability $p_{\tilde{a}}$. All measurement outcomes are equally likely in the ideal $u = \pi/4$ protocol limit—similar to single-qubit teleportation—but imperfection biases the distribution as we discuss further in Sec. 6.2. The wavefunction correspondingly evolves via $|\psi_U\rangle \to |\tilde{a}, \boldsymbol{n}\rangle|\psi_{\tilde{a}}\rangle$, where

$$|\psi_{\tilde{a}}\rangle = \frac{1}{\sqrt{p_{\tilde{a}}}} \langle \tilde{a}, \boldsymbol{n}| U |\psi_A\rangle |\tilde{b}, \boldsymbol{n}\rangle \tag{5.14}$$

is Bob's normalized wavefunction after the measurement stage of the protocol.

One can alternatively view Eq. (5.14) as the wavefunction resulting from weakly measuring Bob's initial qubit state. From this perspective, Alice's qubits constitute ancillary degrees of freedom that are entangled with Bob via the unitary U and then projectively measured—thereby mediating the weak measurement. Reference [3] indeed encountered expressions similar to Eq. (5.14) in the context of measurement-altered Ising criticality. There, both Alice's and Bob's initial wavefunctions exhibited nontrivial quantum correlations; analytical progress in treating the analogue of

[3] Notice that this choice is unique. Given $\boldsymbol{n} = (\sin(\theta)\cos(\phi), \sin(\theta)\sin(\phi), \cos(\theta))$, then the unique $\boldsymbol{n}^\perp$ satisfying these constraints is given by $\boldsymbol{n}^\perp = (-\cos(\theta)\cos(\phi), -\cos(\theta)\sin(\phi), \sin(\theta))$. Nonetheless, a similar result holds also when considering $U_{AB} = \prod_j e^{iu\hat{O}^A_j(\boldsymbol{n}\times\boldsymbol{n}^\perp)\hat{O}^B_j(\boldsymbol{n}\times\boldsymbol{n}^\perp)}$

Eq. (5.14) could then be carried out only perturbatively for entangling gates close to the identity. Here, by contrast, any entanglement in $|\psi_{\tilde{a}}\rangle$ descends exclusively from Alice's initial state $|\psi_A\rangle$—enabling further non-perturbative evaluation. As detailed in Section 6.6, using properties of Pauli operators for the unitary in Eq. (5.13), and the fact that Alice's and Bob's Hilbert spaces are isomorphic, Bob's wavefunction can be exactly recast as

$$|\psi_{\tilde{a}}\rangle = \frac{1}{\sqrt{\mathcal{N}}} e^{i\frac{\pi}{4}H_{\tilde{b}\leftarrow\tilde{a}}(\boldsymbol{n}^{\perp})} e^{i\frac{\pi}{4}H_{\tilde{a}}(\boldsymbol{n})} e^{-\frac{\alpha}{2}H_{\tilde{a}}(\boldsymbol{n})} |\psi_A\rangle . \tag{5.15}$$

Above α parametrizes the degree of protocol imperfection and once again depends on u through Eq. (5.11); we will often interchangeably refer to the entangling gate strength by quoting α and/or u depending on context. The exponentials acting on $|\psi_A\rangle$ involve Hermitian operators

$$H_{\tilde{b}\leftarrow\tilde{a}}(\boldsymbol{n}^{\perp}) = \sum_j (1 - a_j b_j)\hat{O}_j^B(\boldsymbol{n}^{\perp}) \tag{5.16}$$

$$H_{\tilde{a}}(\boldsymbol{n}) = -\sum_j a_j \hat{O}_j^B(\boldsymbol{n}). \tag{5.17}$$

Notice that $\{\hat{O}_j(\boldsymbol{n}^{\perp}), \hat{O}_j(\boldsymbol{n})\} = 0$. The normalization factor $\mathcal{N}$ relates to the probability $p_{\tilde{a}}$ according to

$$\mathcal{N} = [\sin(u)\cos(u)]^{-L} p_{\tilde{a}}. \tag{5.18}$$

For $u = \pi/4$ (perfect teleportation protocol), equal probability of all measurement outcomes implies $p_{\tilde{a}} = 2^{-L}$ and hence $\mathcal{N} = 1$, consistent with the fact that the non-unitary operator becomes trivial in that limit.

Equation (5.15) closely resembles Eq. (5.8) and similarly involves unitary and non-unitary operators acting on Alice's wavefunction $|\psi_A\rangle$. As in the one-qubit limit, knowledge of Alice's measurement outcome allows Bob to undo the unitaries—yielding the final teleported state

$$\left|\psi_{\tilde{a}}^{\text{tele}}\right\rangle = \frac{1}{\sqrt{\mathcal{N}}} e^{-\frac{\alpha}{2}H_{\tilde{a}}(\boldsymbol{n})} |\psi_A\rangle . \tag{5.19}$$

[Later we will examine both Eqs. (5.15) and (5.19) to analyze the impact of teleportation imperfections, since each form offers advantages in different regimes.] Also as in the one-qubit example, the measurement-outcome-dependent non-unitary factor $e^{-\frac{\alpha}{2}H_{\tilde{a}}(\boldsymbol{n})}$ becomes the identity at $u = \pi/4$ (aka $\alpha = 0$) but otherwise becomes nontrivial, spoiling perfect teleportation. See Fig. 5.2(c) for a sketch of the imperfect teleportation protocol discussed here.

As highlighted already in the introduction, subtle questions arise when specifically addressing imperfect teleportation of a quantum critical wavefunction. To what extent is Bob's final wavefunction $\left|\psi_{\tilde{a}}^{\text{tele}}\right\rangle$ the ground state of a critical chain? Under what conditions can one regard the imperfect teleportation as weak? That is, does small non-zero α perturbatively modify the structure of $\left|\psi_{\tilde{a}}^{\text{tele}}\right\rangle$ compared to the ideal $\alpha = 0$ case, or is the effect inherently non-perturbative? What is the relation between changes in entanglement and changes in critical correlations resulting from imperfect teleportation? In the thermodynamic limit where system size $L \to \infty$, does $\left|\psi_{\tilde{a}}^{\text{tele}}\right\rangle$ necessarily tend to a simple product state as α increases?

Imperfection-induced modification of full counting statistics

At $\alpha \neq 0$, the imperfection-induced non-unitary operator in Eq. (5.19) redistributes the weight on the elements of Alice's original wavefunction $|\psi_A\rangle$. This redistribution becomes particularly transparent upon expanding $|\psi_A\rangle$ in terms of $H_{\tilde{a}}(\boldsymbol{n})$ eigenstates, since the non-unitary operator acts very simply in that basis. Below we explore general properties of Alice's imperfectly teleported wavefunction from this vantage point—leading to additional metrics, complementary to correlations and entanglement, for diagnosing the quality of the teleported state. Our discussion here will additionally allow us to anticipate various scenarios for the impact of both weak and strong protocol imperfections.

Since $H_{\tilde{a}}(\boldsymbol{n})$ in Eq. (5.17) is just a sum of L commuting Pauli operators, $H_{\tilde{a}}(\boldsymbol{n})/2$ admits eigenvalues $m = -L/2, -L/2+1, \ldots, L/2-1, L/2$ with degeneracy $D_m = \binom{L}{m+L/2}$ [4]. The corresponding eigenvalue distribution in a many-body wavefunction is known as full counting statistics and, at least for quantum critical states, exhibits universal features [83, 84] (for a review see Sec. 6.1). Alice's initial state can always be decomposed into different m sectors via $|\psi_A\rangle = \sum_m c_m |\psi_m\rangle$. Here c_m denotes the amplitude for the normalized component $|\psi_m\rangle$ that has $H_{\tilde{a}}(\boldsymbol{n})/2$ eigenvalue m, and determines the full counting statistics through $|c_m|^2$. In terms of the intensive variable $f = m/L + 1/2$—which ranges from 0 to 1—the function $P(f, L) = L|c_{m=(f-1/2)L}|^2$ [5] gives the probability density for finding Alice's initial state with quantum number f in system size L. We stress that a quantum-critical initial state $|\psi_A\rangle$ will generically superpose all possible m sectors compatible with symmetries. Furthermore, given

[4] Notice that $H_{\tilde{a}}(\boldsymbol{n})$ is unitarily equivalent to the uniform Hamiltonian $H_{\text{uni}}(\boldsymbol{n}) = -\sum_j \hat{O}_j^B(\boldsymbol{n})$. Hence an eigenspace labeled by eigenvalue m shares the same degeneracy.

[5] The relation between $P(f, L)$ and c_m follows upon assuming that m and f can be treated as continuous variables. This assumption is expected to hold generally for sufficiently large system sizes, except for deep in the tails of the distribution near $f = 0, 1$, e.g., for f of order $1/L$.

that D_m grows combinatorially as $|m|$ decreases from $L/2$ towards zero, $P(f, L)$ is expected to invariably peak at some intermediate $O(1)$ value(s) of f and eventually decay to zero at both $f = 0$ and 1 in the thermodynamic limit.

Applying the non-unitary operator $e^{-\frac{\alpha}{2}H_{\tilde{a}}(\boldsymbol{n})}$ to $|\psi_A\rangle$ restructures the wavefunction by sending $c_m \to e^{-\alpha m}c_m$ and hence yields a modified probability density

$$P_{\text{modified}}(\alpha, f, L) \propto e^{-2\alpha L f} P(f, L). \tag{5.20}$$

In particular, the new exponential heavily favors f's in the interval 0 to $\sim (\alpha L)^{-1}$ (which for any fixed nonzero α becomes vanishingly small as $L \to \infty$) and exponentially suppresses weight for larger f's. That exponential suppression, however, competes with the growth in $P(f, L)$ as f increases from 0. Upon turning on α to nominally small values, one can then ask whether the most probable f values predicted by P_{modified} (w1) evolve smoothly with α or (w2) non-perturbatively shift, for any nonzero α, toward the interval near zero favored by the exponential in Eq. (5.20). We will encounter examples of both types later in this paper.

In either case (w1) or (w2), increasing α to large values shifts the probability weight captured by P_{modified} deep into the left tail of the distribution near $f = 0$. Taking $\alpha \to \infty$ at fixed L generically yields a product state. In particular, here we obtain $e^{-\frac{\alpha}{2}H_{\tilde{a}}(\boldsymbol{n})}|\psi_A\rangle \to |\psi_{m=-L/2}\rangle = |\tilde{a}, \boldsymbol{n}\rangle$, corresponding to Alice's measured state. Upon accounting also for the unitaries in Eq. (5.15), Bob's wavefunction $|\psi_{\tilde{a}}\rangle$ reduces to his initialized product-state wavefunction $|\tilde{b}, \boldsymbol{n}\rangle$. Since $\alpha \to \infty$ implies $u \to 0$, corresponding to the limit where Alice and Bob's entangling unitary approaches the identity, this result appears trivial—yet need not apply in the order of limits of interest here wherein $L \to \infty$ first, followed by $\alpha \to \infty$. The naively expected product state with $m = -L/2$ is non-degenerate, whereas the next $m = -L/2 + 1$ sector exhibits degeneracy L that diverges in the thermodynamic limit; hence we expect that corrections to the naively expected product state persist in the above order of limits. Similar in spirit to (w1) and (w2) above, two possible cases also appear in the regime of strongly imperfect teleportation: With $L \to \infty$, the teleported wavefunction at large α, aka small u, (s1) may be perturbatively accessible starting from the naively expected product state, and thus exhibit properties such as full counting statistics that evolve smoothly with u, or (s2) may undergo non-perturbative changes for any non-zero u.

The remainder of this section further explores the small-α and large-α regimes.

Small-α regime

To make analytical progress at small α, corresponding to u near $\pi/4$, we now specialize to the case where $|\psi_A\rangle$ is the ground state of a quantum critical chain governed by a CFT. We can then formulate a continuum field-theoretic description of correlations in the teleported state received by Bob that highlights universal consequences of protocol imperfections—similar to techniques employed for measurement-altered quantum criticality [16]. We will attack the final teleported state $\left|\psi_{\tilde{a}}^{\text{tele}}\right\rangle$ from Eq. (5.19); this form proves most illuminating in the weak-imperfection regime where comparison with Alice's initial state is natural.

Long-distance correlations in Alice's original quantum critical state can be extracted from a Euclidean path integral with accompanying CFT action $\mathcal{S}_{\text{CFT}}$. For an infinite chain, $\mathcal{S}_{\text{CFT}}$ describes fields living at spatial coordinate x and imaginary time τ each spanning the range $(-\infty, \infty)$. One can view imaginary-time evolution from $\tau = -\infty$ to 0 as preparing Alice's initial ket $|\psi_A\rangle$, while imaginary time evolution from $\tau = 0$ to $+\infty$ prepares the dual bra $\langle\psi_A|$. The measurement-induced non-unitary factor $e^{-\frac{\alpha}{2}H_{\tilde{a}}(\boldsymbol{n})}$ in Eq. (5.15) disrupts the pristine CFT action via a 'defect-line' perturbation acting at all spatial positions x but only at $\tau = 0$ [16]. *To leading order in* α, the defect-line action takes the form

$$\delta\mathcal{S} = \alpha \int_x \omega(x)\chi(x, \tau = 0). \tag{5.21}$$

Here $\omega(x)$ is a scalar function and $\chi(x)$ is a CFT field such that $\omega(x)\chi(x)$ represents the continuum limit of $a_j \hat{O}_j^B(\boldsymbol{n})$ appearing in $H_{\tilde{a}}(\boldsymbol{n})$ [Eq. (5.17)]. The detailed structure of ω and χ depends on Alice's measurement basis (i.e., the vector $\boldsymbol{n}$) and particular measurement outcome.

Within this continuum formulation, we can utilize renormalization group techniques to efficiently assess the extent to which the final teleported state $\left|\psi_{\tilde{a}}^{\text{tele}}\right\rangle$ obtained by Bob showcases the distinguishing features of Alice's critical behavior at $\alpha \ll 1$. More precisely, weakly imperfect teleportation yields profoundly different consequences depending on whether the defect-line action is relevant, marginal, or irrelevant. [We caution that, as we will encounter later, properly assessing relevance in some cases requires considering $\mathcal{O}(\alpha^2)$ corrections that are not displayed in Eq. (5.21).] The relevance or otherwise of the defect-line perturbation influences critical correlations and entanglement, as well as full counting statistics captured by the probability density P_{modified}, in a ways that we will later characterize in detail.

Large-α regime

At $\alpha \gg 1$ (equivalently $u \approx e^{-\alpha} \ll 1$), further analytical progress is possible without specifying Alice's initial wavefunction $|\psi_A\rangle$. Here it is more natural to examine Bob's wavefunction $|\psi_{\tilde{a}}\rangle$ given in Eq. (5.15). The reason is that at $u = 0$, for which Alice and Bob remain unentangled throughout, Eq. (5.15) reduces precisely to Bob's initial state $|\tilde{b}, \boldsymbol{n}\rangle$—whereas $\left|\psi_{\tilde{a}}^{\text{tele}}\right\rangle$ in Eq. (5.19) contains additional outcome-dependent unitary factors that somewhat mask the triviality of the teleportation protocol in this extreme limit. We will assume for the remainder of this subsection that at small nonzero u, Bob inherits only faint imprints of Alice's state that can be captured by applying a 'weak' entanglement-generating operator to $|\tilde{b}, \boldsymbol{n}\rangle$. In other words, we postulate that small u represents either a marginal or irrelevant perturbation to the trivial protocol that transmits no information about Alice's state.

As detailed in Ref. [3], assuming $\langle\tilde{a}, \boldsymbol{n}|\,\psi_A\rangle \neq 0$ we can exactly write $|\psi_{\tilde{a}}\rangle$ as

$$\begin{aligned} |\psi_{\tilde{a}}\rangle = \frac{1}{\sqrt{\mathcal{N}}}\langle\tilde{a}, \boldsymbol{n}|\psi_A\rangle \sum_{N_f=0}^{L} e^{-\alpha N_f} e^{i\frac{\pi}{2}N_f} \\ \times \sum_{i_1<\cdots<i_{N_f}} q(i_1, \ldots, i_{N_f}) \left(\prod_{j=1}^{N_f} \hat{O}_{i_j}^B(\boldsymbol{n}^\perp)\right)\left|\tilde{b}, \boldsymbol{n}\right\rangle . \end{aligned} \tag{5.22}$$

Here N_f counts the number of spin flips on Bob's initial state generated by a given piece of the entangling gate U, and we have defined the generalized 'strange correlator' [80]

$$q(i_1, \ldots, i_{N_f}) \equiv \frac{\left\langle\tilde{a}, \boldsymbol{n}\right| \prod_{j=1}^{N_f} \hat{O}_{i_j}^A(\boldsymbol{n}^\perp)|\psi_A\left.\right\rangle}{\langle\tilde{a}, \boldsymbol{n}|\psi_A\rangle} \tag{5.23}$$

involving normalized matrix elements between Alice's (generally very different) initial and post-measurement wavefunctions. Expanding about the $\alpha \to \infty$ ($u = 0$) limit allows one to recast the expression above as

$$\begin{aligned} |\psi_{\tilde{a}}\rangle \approx \frac{1}{\sqrt{\mathcal{N}}} \underbrace{\exp\left(iu\sum_j q(j)\hat{O}_j^B(\boldsymbol{n}^\perp)\right)}_{=U'} \\ \times \underbrace{\exp\left(-\frac{u^2}{2}\sum_{j\neq k} V_{jk}\hat{O}_j^B(\boldsymbol{n}^\perp)\hat{O}_k^B(\boldsymbol{n}^\perp)\right)}_{=e^{-\frac{u^2}{2}H'_{\tilde{a}}}}\left|\tilde{b}, \boldsymbol{n}\right\rangle . \end{aligned} \tag{5.24}$$

In the first line we absorbed constants into the normalization, and in the second line

$$V_{jk} = q(j,k) - q(j)q(k) \tag{5.25}$$

can be viewed as a connected strange correlator. Equation (5.24) is consistent with Ref. [3], where we performed a similar analysis but starting from a critical state for Bob, i.e., replacing $|\tilde{b}, \boldsymbol{n}\rangle$ with a quantum critical wavefunction. As we discussed there, the large-α, small-u expansion employed above is expected to hold provided V_{jk} is sufficiently local. In some cases Alice's measured state $|\tilde{a}, \boldsymbol{n}\rangle$ may yield V_{jk} that does not decay to zero sufficiently rapidly with $|j-k|$, spoiling the validity of the expansion in Eq. (5.24) (likely indicating that Bob's state $|\psi_{\tilde{a}}\rangle$ can not be obtained by perturbatively modifying his initial state, contrary to our assumption).

Equations (5.15) and (5.24) encode quantum correlations for Bob's wavefunction $|\psi_{\tilde{a}}\rangle$ in a very different manner. In Eq. (5.15) correlations are encoded primarily through Alice's initial state $|\psi_A\rangle$, while in Eq. (5.24) they are captured by the structure of $q(j)$ and V_{jk}—where information about Alice's state is embedded. One advantage of the latter representation is that, when the large-α expansion is valid, it permits using a variant of Witten's conjugation method [85] to find a parent Hamiltonian for which $|\psi_{\tilde{a}}\rangle$ is the unique ground state. Let us specialize to the case where $q(j)$ and V_{jk} are purely real, so that in Eq. (5.24) U' is a unitary operator and $H_m^{\tilde{a}}$ is Hermitian. (The case with imaginary parts can be treated by re-partitioning the exponentials to factor out a purely unitary component.) First observe that $|\tilde{b}, \boldsymbol{n}\rangle$ is the unique ground state of the commuting-projector Hamiltonian $H_0 = \sum_j \Gamma_j^\dagger \Gamma_j = \sum_j \Gamma_j$ with projectors $\Gamma_j = \frac{1}{2}[1 - b_j \hat{O}_j^B(\boldsymbol{n})]$. Physically, H_0 represents a position-dependent Zeeman field of uniform strength $1/2$ pointing along or against $\boldsymbol{n}$ such that Bob's initial state is energetically optimal. Using $e^{-\frac{u^2}{2}H'_{\tilde{a}}}(U')^\dagger\,|\psi_{\tilde{a}}\rangle \propto |\tilde{b}, \boldsymbol{n}\rangle$, the state $|\psi_{\tilde{a}}\rangle$ is annihilated by the new set of operators $\overline{\Gamma}_j = U' e^{\frac{u^2}{2}H'_{\tilde{a}}}\Gamma_j e^{-\frac{u^2}{2}H'_{\tilde{a}}}(U')^\dagger$, which satisfy $\overline{\Gamma}_j^2 = \overline{\Gamma}_j$ but are not Hermitian and do not commute at different sites. It follows that $|\psi_{\tilde{a}}\rangle$ is the unique ground state of the frustration-free parent Hamiltonian $H_{\text{parent}} = \sum_j \overline{\Gamma}_j^\dagger \overline{\Gamma}_j$, which explicitly reads (modulo a constant)

$$\begin{aligned} H_{\text{parent}} = \frac{1}{4}U' \Bigg[&\sum_j e^{2u^2 \hat{O}_j^B(\boldsymbol{n}^\perp)\sum_{k\neq j} V_{jk}\hat{O}_k^B(\boldsymbol{n}^\perp)} \\ -\sum_j b_j &\left\{ \hat{O}_j^B(\boldsymbol{n}), e^{-u^2 \hat{O}_j^B(\boldsymbol{n}^\perp)\sum_{k\neq j} V_{jk}\hat{O}_k^B(\boldsymbol{n}^\perp)} \right\} \Bigg] (U')^\dagger. \end{aligned} \tag{5.26}$$

Equation (5.26) in general is not a sum of local operators. Nonetheless, boldly expanding the terms in brackets to $O(u^2)$ yields the illuminating form

$$\begin{aligned} H_{\text{parent}} \approx U'\Big[-\frac{1}{2}\sum_j b_j \hat{O}^B_j(\boldsymbol{n})\Big](U')^\dagger \\ + u^2 \sum_{j\neq k} V_{jk}\hat{O}^B_j(\boldsymbol{n}^\perp)\hat{O}^B_k(\boldsymbol{n}^\perp). \end{aligned} \tag{5.27}$$

Nonzero u manifests in two ways at this order. First, already at order u the orientations of the local Zeeman fields in H_{parent} rotate slightly compared to their orientations in H_0—though their magnitudes remain fixed at $1/2$. This contribution originates entirely from the U' unitary in Eq. (5.24). Teleportation-wise, these rotations imprint information about Alice's initial state only at the single-qubit level, i.e., with this effect alone, Bob's wavefunction $|\psi_{\tilde{a}}\rangle$ would remain a product state and thus not inherit any of Alice's correlations and entanglement. Second, and much more importantly, the non-unitary piece $e^{-\frac{u^2}{2}H'_{\tilde{a}}}$ from Eq. (5.24) generates Ising spin-spin interactions of strength u^2V_{jk} in H_{parent}. These Ising interactions couple spin components that are orthogonal to the spin components appearing in the Zeeman field terms from the top line of Eq. (5.27), even when accounting for the U' rotations. One can therefore always (for any measurement outcome $\tilde{a}$ and any initialization $\tilde{b}$) unitarily transform the parent Hamiltonian to recast the Zeeman terms in the top line as spatially uniform without altering the bottom-line interactions. It follows that when the large-α expansion holds, Bob's wavefunction $|\psi_{\tilde{a}}\rangle$ is the ground state of a transverse-field Ising model with weak but long-range Ising interactions dependent on both Alice's initial state and her particular measurement outcome. The Ising interactions, albeit weak, enrich the structure of $|\psi_{\tilde{a}}\rangle$ beyond a simple product-state form and thus do impart some information about Alice's correlations and entanglement. We will later exploit such parent Hamiltonians to intuitively understand the character of teleported states in highly imperfect protocols.

Earlier we remarked that the large-α expansion is expected to be controlled provided V_{jk} decays sufficiently rapidly with $|j-k|$. The structure of Eq. (5.27) more quantitatively suggests that the expansion is controlled provided V_{jk} decays faster than $1/|j-k|$. In that case the Ising interaction term in H_{parent} is an extensive operator—just like the Zeeman term—with eigenvalues generically scaling linearly with system size. One can then always make the V_{jk} contribution a small perturbation by taking u sufficiently small (i.e., α sufficiently large). Conversely, if V_{jk} decays as or slower than $1/|j-k|$, then the Ising interactions are no longer extensive and may exhibit eigenvalues that grow *faster* than extensively with system size, thus potentially dominating over the Zeeman contribution for any nonzero u. The large-α expansion is expected to break down in the latter case.

Hereafter we specialize to imperfect teleportation of Ising quantum criticality realized in the transverse-field Ising chain (see next section for a review). Our specific goals include (1) characterizing the final teleported state received by Bob for different protocols, considering both Alice's most likely measurement outcomes as well as typical outcomes; (2) identifying optimal teleportation protocols in the sense of resilience to imperfections; and (3) characterizing the mixed state describing the average over a series of sequential runs of a specific teleportation protocol via correlations and the entanglement negativity.

Chapter 6

RELEVANT, MARGINAL, AND DISGUISED MARGINAL MEASUREMENT PERTURBATIONS

The Ising measurement protocols of Chapters 3 and 4 showed that weak measurements can reorganize universal critical correlations. The present chapter shows that imperfect teleportation realizes the same classification without explicitly engineering an ancilla-assisted measurement protocol: the imperfection parameter controls a weak non-unitary perturbation, and the measured outcome pattern decides whether the perturbation is relevant, marginal, or hidden inside a more benign channel.

6.1 Ising-critical input state and teleportation diagnostics

Suppose now that Alice's initial wavefunction $|\psi_A\rangle$ realizes the ground state $|\psi_c\rangle$ of a quantum Ising spin chain tuned to criticality, described by the Hamiltonian

$$H_c = -J \sum_j (Z_j Z_{j+1} + X_j). \tag{6.1}$$

We take $J > 0$ and consider a chain of length L with periodic boundary conditions; moreover, here and below we ease the notation by neglecting superscripts A/B on Pauli operators whenever the qubits that they act on is clear from context. In this section we briefly review the phenomenology of Ising criticality needed to investigate imperfect teleportation of Alice's quantum critical state.

Equation (6.1) preserves translation symmetry, global $\mathbb{Z}_2$ spin flip symmetry generated by $G \equiv \prod_j X_j$, and an antiunitary time reversal symmetry $\mathcal{T}$ that leaves X_j and Z_j invariant but sends $Y_j \to -Y_j$. By applying a Jordan-Wigner transformation to Majorana fermion operators

$$\gamma_{Aj} = \left(\prod_{k<j} X_k\right) Z_j, \quad \gamma_{Bj} = \left(\prod_{k<j} X_j\right) iX_j Z_j, \tag{6.2}$$

the Hamiltonian maps to a free-fermion problem:

$$H = iJ \sum_j (\gamma_{Aj+1} - \gamma_{Aj})\gamma_{Bj}. \tag{6.3}$$

One can correspondingly express all correlation functions in terms of two-point fermion correlators using Wick's theorem. Taking into account the non-local strings present in the Jordan-Wigner transformation, correlation functions of the physical spin operators X, Z and Y can be expressed in terms of Toeplitz matrices, whose entries only depend on the difference between the two indices of the matrix [86, 87]. Long-distance ground-state spin-spin correlations follow from the asymptotic behavior of Toeplitz determinants and are given by

$$\begin{gathered}\langle X_i X_j\rangle_c \sim \frac{1}{|i-j|^2}, \quad \langle Y_i Y_j\rangle \sim \frac{1}{|i-j|^{9/4}}, \\ \langle Z_i Z_j\rangle \sim \frac{1}{|i-j|^{1/4}}.\end{gathered} \tag{6.4}$$

The subscript c indicates a connected correlator and is only needed for X, given that one-point Y and Z expectation values vanish by symmetry. Note that Z correlations exhibit by the far the slowest decay, followed by X and then Y. For a general Pauli operator $\hat{O}_j(\boldsymbol{n}) = \boldsymbol{n}\cdot\boldsymbol{\sigma}_j$, its two-point correlation function $\langle \hat{O}_i(\boldsymbol{n})\hat{O}_j(\boldsymbol{n})\rangle$ will be dominated at long distances by the slowest-decaying contribution.

The free-fermion representation in Eq. (6.3) also enables an efficient computation of the entanglement entropy. Bipartitioning the system between a subregion R and its complement $\overline{R}$, the reduced density matrix in R is given by $\rho_R = \mathrm{Tr}_{\overline{R}}(|\psi_c\rangle\langle\psi_c|)$. Then the entanglement between R and its complement reads $S_R = -\mathrm{Tr}(\rho_R \ln \rho_R)$. A more general family of functions quantifying the entanglement—dubbed Rényi entropies—are given by $S_R^{(n)} = 1/(1-n)\ln \mathrm{Tr}\rho_R^n$. We notice the relation $S_R = \lim_{n\to 1} S_R^{(n)}$ known as the replica limit [12]. For the critical Ising chain, the leading-order contributions in the subsystem size $|R| = \ell$ for a single interval on the infinite line ($L \to \infty$) read [12]

$$S_R^{(n)} = \frac{c}{6}\left(\frac{n+1}{n}\right)\ln(\ell/\epsilon), \quad S_R = \frac{c}{3}\ln(\ell/\epsilon), \tag{6.5}$$

where ϵ is an ultraviolet cutoff. The logarithm prefactors are universal and are related to the central charge $c = 1/2$ of the underlying Ising CFT governing long-distance, low-energy properties at criticality.

The CFT description follows upon changing variables to left-moving (γ_L) and right-moving (γ_R) Majorana fermion fields via $\gamma_A = \gamma_R + \gamma_L$ and $\gamma_B = \gamma_R - \gamma_L$, and then taking the continuum limit of Eq. (6.3). This procedure yields the continuum Hamiltonian

$$\mathcal{H} = -iv\int_x(\gamma_R\partial_x\gamma_R - \gamma_L\partial_x\gamma_L) \tag{6.6}$$

with $v \propto J$; the associated Euclidean action describes precisely the $c = 1/2$ Ising CFT. The Ising CFT admits three primary fields: the identity $\mathbb{1}$, the spin field

σ (scaling dimension $\Delta_\sigma = 1/8$), and the energy operator $\varepsilon = i\gamma_R\gamma_L$ (scaling dimension $\Delta_\varepsilon = 1$). Physically, σ represents the continuum limit of the microscopic order parameter Z_j, while ε represents the perturbation generated by moving off of criticality in a $\mathbb{Z}_2$-preserving manner (e.g., by increasing or decreasing the transverse-field strength). Microscopic spin components relate to CFT fields according to the following dictionary:

$$\begin{aligned} X_j - \langle X \rangle &\sim \varepsilon + \cdots , \\ Y_j &\sim i\partial_\tau \sigma + \cdots , \\ Z_j &\sim \sigma + \cdots . \end{aligned} \tag{6.7}$$

On the left side, $\langle X \rangle = 2/\pi$ is the ground state expectation value of X_j; subtracting this factor merely removes a contribution proportional to the identity field $\mathbb{1}$. On the right side, the fields are evaluated on coarse-grained positions corresponding to lattice site j, τ denotes imaginary time, and the ellipses account for subleading terms with higher scaling dimension. Equation (6.7) is not only compatible with symmetries, but also immediately reproduces the scaling behavior in Eq. (6.4) given the scaling dimensions for the CFT fields provided above.

Finally, we briefly review the full counting statistics for the critical ground state of the Ising spin chain studied previously in Refs. [83, 84]. As anticipated in Sec. 5.3, this property will yield insight about the resilience of Ising criticality under imperfect teleportation protocols. We will first examine how eigenvalues for the global operator

$$M_X^{\tilde{a}} = \sum_j a_j X_j/2 \tag{6.8}$$

are distributed in the critical ground state. Here the a_j's take on ± 1 values, and hence $M_X^{\tilde{a}}$ admits eigenvalues $m = -L/2, -L/2+1, \ldots, L/2$; later we will associate a_j with Alice's measurement outcomes. In the special case where $a_j = +1$ for all j, $M_X^{\tilde{a}}$ reduces to the global transverse magnetization.

The mean $\langle M_X^{\tilde{a}} \rangle$ depends non-universally on the choice of a_j while the variance reads

$$\langle (M_X^{\tilde{a}})^2 \rangle - \langle M_X^{\tilde{a}} \rangle^2 = \frac{1}{4} \sum_{i,j} a_i a_j \langle X_i X_j \rangle_c . \tag{6.9}$$

Given that the connected two-point X correlator decays faster than $1/|i-j|$, the right-hand side is dominated by the short-distance region with i near j (for any pattern of a_j signs). One thus generically obtains $\langle (M_X^{\tilde{a}})^2 \rangle - \langle M_X^{\tilde{a}} \rangle^2 \propto L$, i.e., the variance grows linearly with system size. In terms of the intensive variable $f = m/L + 1/2$

used in Sec. 5.3, these properties are compatible with $M_X^{\tilde{a}}$ exhibiting full counting statistics of a Gaussian form

$$P(f, L) \propto e^{-\kappa L(f-\overline{f})^2}, \tag{6.10}$$

where κ and $\overline{f}$ are a_j-dependent constants. This conclusion is consistent with Ref. [83] in the limit of uniform a_j. Due to the even faster decay of two-point Y correlators, we expect $M_Y^{\tilde{a}} = \sum_j a_j Y_j/2$ to similarly exhibit Gaussian-like full counting statistics.

Next we consider the global longitudinal magnetization

$$M_Z^+ = \sum_j Z_j/2. \tag{6.11}$$

[Contrary to Eq. (6.8), we do not allow for unspecified a_j signs above since drawing conclusions about full counting statistics in the general case is not straightforward here.] The mean $\langle M_Z^+\rangle$ vanishes by symmetry while the variance is

$$\langle (M_Z^+)^2\rangle = \frac{1}{4}\sum_{i,j}\langle Z_i Z_j\rangle. \tag{6.12}$$

Slow decay of the two-point Z correlator implies that the right side, unlike Eq. (6.9), is dominated by the long-distance region with $|i-j| \gg 1$. This contribution yields a variance $\langle (M_Z^+)^2\rangle \propto L^{7/4}$ that diverges with system size faster than the linear growth obtained for $M_X^{\tilde{a}}$. Thus the longitudinal magnetization eigenvalues are distributed more broadly in the critical ground state relative to the transverse magnetization eigenvalues: the characteristic spread of the intensive variable f is $\delta f \sim 1/L^{1/8}$ for the former versus $\delta f \sim 1/L^{1/2}$ for the latter. Full counting statistics for the longitudinal magnetization is non-Gaussian, however, and exhibits a universal double-peak structure [84] discussed in more detail in Section 6.6.

6.2 Imperfect teleportation of Ising criticality

We are now in position to examine Bob's final wavefunction in Eq. (5.19) resulting from imperfect teleportation of Alice's Ising quantum critical state $|\psi_A\rangle = |\psi_c\rangle$. The non-unitary operator $e^{-\frac{\alpha}{2}H_{\tilde{a}}(\boldsymbol{n})}$ encoding imperfection depends on the quantization axis $\boldsymbol{n}$ defining Bob's initial wavefunction and Alice's measurement basis, her particular measurement outcome $\tilde{a}$, and the imperfection strength quantified by α. We will specifically address the extent to which the universal features of Ising criticality reviewed in the previous section survive with protocols employing different

$\boldsymbol{n}$ vectors, assuming for simplicity throughout this section that Bob initializes his qubits into the uniform state $|\psi_B\rangle = |\tilde{b}, \boldsymbol{n}\rangle$ with all $b_j = +1$. Sections 6.2 through 6.2 analyze the impact of protocol imperfections upon post-selecting for Alice's highest probability measurement outcomes; Sec. 6.2 then examines typical outcomes.

One can anticipate the hierarchy of protocol imperfections that we uncover by viewing the problem through the lens of full counting statistics. For $\boldsymbol{n} = \hat{\boldsymbol{x}}$, the non-unitary operator becomes $e^{-\frac{\alpha}{2}H_{\tilde{a}}(\boldsymbol{n})} = e^{\alpha M_X^{\tilde{a}}}$ and hence alters full counting statistics of the global operator $M_X^{\tilde{a}}$ defined in Eq. (6.8). In Sec. 6.1 we argued that, for any $\tilde{a}$, the distribution of $M_X^{\tilde{a}}$ eigenvalues in Alice's original quantum critical wavefunction obeys a Gaussian distribution, Eq. (6.10). Following Eq. (5.20), Bob's final wavefunction exhibits the modified eigenvalue distribution

$$P_{\text{modified}} \propto e^{-2\alpha L f} e^{-\kappa L (f - \overline{f})^2} \tag{6.13}$$

that remains Gaussian. Imperfection merely shifts the peak location via $\overline{f} \to \overline{f} - \alpha/\kappa$; L-independence of the shift descends from the fact that $\langle (M_X^{\tilde{a}})^2 \rangle - \langle M_X^{\tilde{a}} \rangle^2 \propto L$. The gradual change of full counting statistics with α in the thermodynamic limit implies that with $\boldsymbol{n} = \hat{\boldsymbol{x}}$, imperfections smoothly restructure the weight in Alice's original wavefunction, regardless of which measurement outcome she obtains during the teleportation protocol. This property, in turn, hints that correlations and entanglement in the imperfectly teleported state generically also evolve smoothly with α relative to the ideal case. (We caution that full counting statistics by itself does not reveal whether long-distance properties, e.g., scaling dimensions, evolve nontrivially with α, though short-distance properties certainly will.) Analogous conclusions apply to protocols utilizing $\boldsymbol{n} = \hat{\boldsymbol{y}}$.

Protocols with $\boldsymbol{n} = \hat{\boldsymbol{z}}$, by contrast, can behave qualitatively differently in this regard. Let us consider uniform $\tilde{a}$ with all $a_j = +1$—which, along with the all $a_j = -1$ state, corresponds to Alice's most probable measurement outcome (see below). In this case, the imperfection-induced non-unitary operator instead becomes $e^{-\frac{\alpha}{2}H_{\tilde{a}}(\boldsymbol{n})} = e^{\alpha M_Z^+}$, now modifying full counting statistics of M_Z^+ from Eq. (6.11). Recall that in this case the full counting statistics for Alice's original critical wavefunction exhibits a universal double-peak structure whose variance is parametrically broader with system size compared to the distribution for $M_X^{\tilde{a}}$. Full counting statistics for Bob's imperfectly teleported wavefunction is once again modified according to Eq. (5.20), though the broader variance now translates into a more effective reshaping of the distribution by the imperfection-induced exponential factor $e^{-2\alpha L f}$.

In Section 6.6 we introduce an analytical function that approximates the pristine double-peak distribution obtained in Ref. [84]; we then use that function to simply extract the imperfection-modified distribution that Bob inherits. This analysis reveals that in the thermodynamic limit arbitrarily small α obliterates the double-peak structure—yielding a single peak located in the distribution's tail near $f = 0$. (The precise peak location in this altered distribution nevertheless varies smoothly with α.) Consequently, such protocol imperfections non-perturbatively restructure the weights in Alice's original quantum critical state in a manner that, owing to the explicit breaking of $f \to 1 - f$ symmetry, yields a net non-zero magnetization in Bob's final state. The non-perturbative restructuring further strongly suggests that long-distance correlations and entanglement in Bob's state are no longer captured by the Ising CFT—even for arbitrarily weak imperfection.

Relevant imperfection

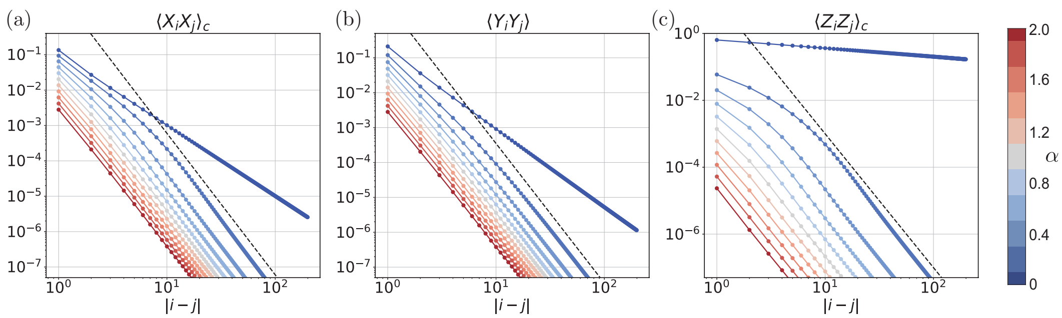

Figure 6.1: **Correlations with relevant imperfection.** Correlations in the teleported state received by Bob [Eq. (6.14)] following an imperfect protocol with $\boldsymbol{n} = \hat{\boldsymbol{z}}$ and with Alice's most probable measurement outcome. Data points were obtained using infinite DMRG for $\alpha \in [0, 2]$ in steps of 0.2. For all $\alpha \neq 0$ shown, we obtain non-perturbatively altered power-law correlations with apparently rigid exponents that agree well with the analytical predictions in Eqs. (6.17) and (6.20) (dashed lines).

We proceed by exploring protocols with $\boldsymbol{n} = \hat{\boldsymbol{z}}$, for which full counting statistics suggests the most dramatic impact of imperfection. Numerically, we find that whenever the entangling unitary $e^{iuX_j^A X_j^B}$ employed in the protocol is imperfect, i.e., with $u \neq \pi/4$, Alice's most probable measurement outcomes are uniform states $|\tilde{a}, \hat{\boldsymbol{z}}\rangle$ with all $a_j = +1$ or all $a_j = -1$. Focusing for concreteness on the $a_j = +1$ uniform outcome, Bob's final state explicitly reads

$$\left|\psi_{\tilde{a}}^{\mathrm{tele}}\right\rangle = \frac{1}{\sqrt{\mathcal{N}}} e^{\alpha M_Z^+} \left|\psi_c\right\rangle, \tag{6.14}$$

where M_Z^+ is the global longitudinal magnetization defined in Eq. (6.11). Neither correlation functions nor entanglement scaling are amenable to exact analytical computations since M_Z^+ does not map to a local operator under a Jordan-Wigner transformation. Nevertheless, below we pursue several strategies for diagnosing universal aspects of these quantities.

As a first approach we appeal to a parent Hamiltonian for the imperfectly teleported state $\left|\psi_{\tilde{a}}^{\text{tele}}\right\rangle$. Section 5.3 already previewed a parent Hamiltonian operative in the large-α limit—which we revisit shortly—but here we seek an alternate form valid at any α. While the existence of a general Hermitian parent Hamiltonian is not guaranteed, one can construct a *strictly local* non-Hermitian parent H_α which has $\left|\psi_{\tilde{a}}^{\text{tele}}\right\rangle$ as its unique (right) ground state:

$$\begin{aligned} H_\alpha &\equiv e^{\alpha M_Z^+} H e^{-\alpha M_Z^+} \\ &= -J \sum_j Z_j Z_{j+1} - \sum_j \left(h_x X_j - i h_y Y_j\right) \end{aligned} \tag{6.15}$$

with $h_x = J\cosh(\alpha)$ and $h_y = J\sinh(\alpha)$. Since H and H_α are related by a similarity transformation, they share the same (purely real) gapless energy spectrum for any value of α; their corresponding wavefunctions, however, are non-unitarily related to one another. This viewpoint suggests that imperfectly teleported critical states can exhibit atypical behavior inherited from non-Hermiticity of their parent Hamiltonians. In fact, Ref. [88] studied a non-unitarily perturbed free-fermion Hamiltonian that also features a gapless spectrum yet exhibits a finite 'non-Hermitian coherence length' ξ_{NH}, beyond which two striking features emerge: First, correlations remain power-law, albeit with enhanced exponents encoding faster decay, and second, the spatial entanglement entropy saturates to a finite value $S \sim \frac{c}{3}\ln(\xi_{\text{NH}})$ with increasing subsystem size. We will show that the state in Eq. (6.14) similarly exhibits anomalous power-law correlations coexisting with area-law entanglement.

Following Sec. 5.3, we can gain further quantitative insight at small α by translating the non-unitary operator in Eq. (6.14) into a defect-line action δS [Eq. (5.21)] perturbing the pristine Ising CFT at imaginary time $\tau = 0$. Using the continuum-limit expansion $M_Z^+ \sim \int_x \sigma$, one obtains

$$\delta S \sim \alpha \int_x \sigma(x, \tau = 0). \tag{6.16}$$

Equation (6.16) constitutes a strongly relevant perturbation that induces a flow to a new fixed point far from the Ising CFT [3, 57]. That is, arbitrarily weak teleportation imperfection of the type studied here—which we dub relevant imperfection—qualitatively alters the universal long-distance properties encoded in Alice's original quantum critical wavefunction, consistent with the dramatic restructuring of full counting statistics arising for any $\alpha \neq 0$.

The Ising CFT specifically flows to a fixed point that pins $\langle\sigma\rangle \neq 0$ along the defect line, yielding a boundary condition that chops the $1+1$-dimensional Euclidean spacetime into decoupled upper ($\tau > 0$) and lower ($\tau < 0$) halves. Scaling arguments [3] reveal that Bob's final wavefunction exhibits a net longitudinal magnetization that grows non-analytically with α: $\langle Z_j\rangle \sim \langle\sigma(x_j, \tau = 0)\rangle \sim \alpha^{1/7}$. Furthermore, using the dictionary in Eq. (6.7), connected two-point X and Z correlators in Bob's final state can be calculated by evaluating the correlators $\langle\sigma(x)\sigma(x')\rangle$ and $\langle\varepsilon(x)\varepsilon(x')\rangle$ along the boundary at the new fixed point. Section 6.6 details the boundary CFT calculation, which yields power-law correlations

$$\langle X_i X_j\rangle_c \sim \frac{1}{|i-j|^4}, \quad \langle Z_i Z_j\rangle_c \sim \frac{1}{|i-j|^4} \tag{6.17}$$

with entirely different exponents from those of the unperturbed Ising CFT. (As we show below, Y correlators also admit power-law exponent 4, again in contrast to the pure Ising CFT.)

The modified power-law correlations captured above assuming small α hold for any $\alpha \neq 0$ in the thermodynamic limit. In the opposite regime of large α we can exploit the asymptotic expansion developed in Sec. 5.3 to express the penultimate form of Bob's wavefunction (prior to applying the final outcome-dependent unitary) in the useful form [Eq. (5.24)]

$$|\psi_{\tilde{a}}\rangle \approx \frac{1}{\sqrt{\mathcal{N}}} e^{iu\sum_j q(j)X_j} e^{-\frac{u^2}{2}\sum_{j\neq k} V_{jk}X_jX_k} |\psi_B\rangle\,. \tag{6.18}$$

Recall that $u \approx e^{-\alpha}$ at $\alpha \gg 1$, $q(j)$ is defined in Eq. (5.23), V_{jk} is a connected strange correlator defined in Eq. (5.25), and $|\psi_B\rangle$ is Bob's initial state with all $Z_j = +1$. Due to translation symmetry $q(j)$ is just a constant; the strange correlator was evaluated in Ref. [3] and scales as $V_{jk} \sim 1/|j-k|^4$. As discussed in Section 6.6, one can equivalently express two-point X correlators evaluated in the wavefunction (6.18) as

$$\langle\psi_{\tilde{a}}| X_i X_j |\psi_{\tilde{a}}\rangle_c = \frac{1}{\mathcal{Z}} \sum_{\{x_k\}=\pm 1} x_i x_j e^{-\beta\mathcal{H}}, \tag{6.19}$$

where $\mathcal{Z}$ is a classical partition function corresponding to the classical power-law-interacting Hamiltonian $\mathcal{H} = \sum_{j\neq k} V_{jk}x_jx_k$ with inverse temperature $\beta = u^2$. The leading contribution in a high-temperature series expansion gives $\langle X_i X_j\rangle_c \approx u^2 V_{ij} \sim$

$1/|i-j|^4$ in harmony with Eq. (6.17) obtained at small α. We further argue in Section 6.6 that, given the fast decay of V_{jk} with separation, Z and Y correlators also display the same power law,

$$\langle Z_i Z_j \rangle_c \sim \frac{1}{|i-j|^4}, \quad \langle Y_i Y_j \rangle \sim \frac{1}{|i-j|^4}, \tag{6.20}$$

which for Z also agrees with Eq. (6.17).

Our DMRG simulations presented in Fig. 6.1 support universality of the anomalous power-laws captured above at small- and large-α. Curves in each panel cover $\alpha \in [0,2]$ in steps of 0.2, while, as a guide, the dashed black line represents the slope for a power law with exponent 4. (Details of our DMRG simulations presented here and below can be found in Section 6.6.) The simulations agree well with our predictions for X, Y, and Z correlators. To summarize, with any degree of imperfection in the protocol considered here, two-point correlators of an arbitrary Pauli operator display 'fast' algebraic decay with a common exponent that does not depend on α and differs strongly relative to pristine Ising CFT expectations.

Does logarithmic growth of entanglement entropy survive relevant imperfect teleportation? Reference [57] provided numerical results together with CFT arguments suggesting that even arbitrarily weak non-unitary operators of the form in Eq. (6.14) destroy logarithmic growth in favor of area-law entanglement entropy that saturates to a value dependent on α but not subsystem size. We can further justify this conclusion at the lattice level in the large-α regime. Consider again the state in Eq. (6.18). Upon further expanding this perturbative expression to order $O(u^2)$, which we expect is legitimate given the fast power-law decay of V_{jk}, we can explicitly obtain the reduced density matrix ρ_R and evaluate the second Rényi entropy $S_R^{(2)}$ at $O(u^4)$. The result (derived in Section 6.6) reads $S_R^{(2)} \propto u^4 \sum_{j\in R, k\in\overline{R}} V_{jk}^2$ and indeed saturates to a constant that does not depend on the subsystem size $|R|$. Figure 6.2 shows that this expansion is well-behaved in the large-α regime (as expected), with the difference between the entanglement entropies numerically computed from the exact wavefunction $\left|\psi_{\tilde{a}}^{\text{tele}}\right\rangle$ in Eq. (6.14) using DMRG, and from the preceding perturbative treatment, decreasing with increasing system size and with increasing α.

Therefore, the imperfectly teleported wavefunction $\left|\psi_{\tilde{a}}^{\text{tele}}\right\rangle$ showcases power-law decaying correlations yet exhibits short-range area-law entanglement, as hinted at earlier from our non-Hermitian parent Hamiltonian discussion. Additional insight into this unusual coexistence emerges by examining the Hermitian parent Hamiltonian derived in the large-α, small-u limit in Sec. 5.3 [Eq. (5.27)]. In the present context

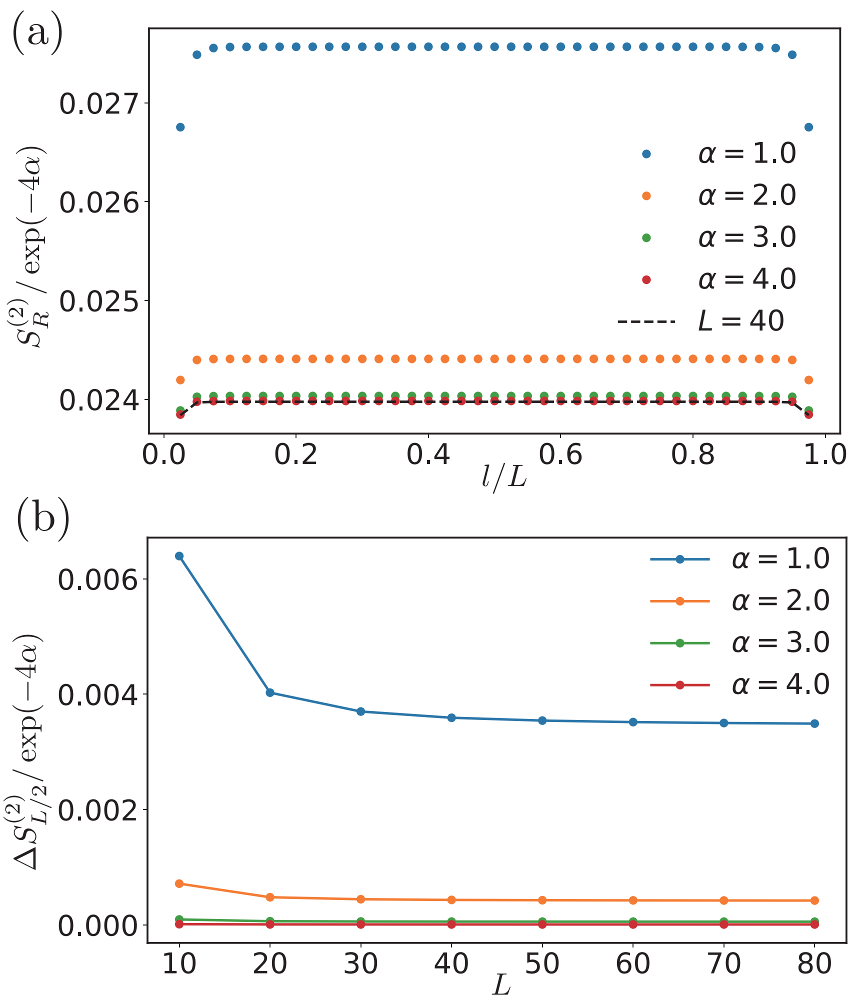

Figure 6.2: **Area-law entanglement for relevant imperfection.** (a) Second Rényi entropy of the teleported state in Eq. (6.14) for system size $L = 40$ with periodic boundary conditions and different α's obtained using finite DMRG. The dashed line refers to the perturbative analytical prediction in Eq. (6.89). (b) System-size dependence of the difference in the half-chain entanglement entropy between the perturbative analytical approach [as obtained by expanding Eq. (6.18)] and numerical evaluation of Eq. (6.14) using finite DMRG. The data show excellent agreement with area-law entanglement emerging from relevant imperfection as calculated analytically in the large-α limit.

the parent Hamiltonian (after applying a unitary to undo the unimportant U' rotation) explicitly reads

$$H_{\text{parent}} \approx -\sum_j Z_j + u^2 \sum_{j \neq k} V_{jk} X_j X_k. \tag{6.21}$$

The dominant Zeeman field in the first term reflects the fact that at $u = 0$, the protocol trivially returns Bob's initial state with all $Z_j = +1$; the subdominant second term is an $O(u^2)$ anti-ferromagnetic Ising-like interaction with power-law decay dictated by the strange correlator V_{jk} that encodes information about Alice's critical state. References [29, 30] analyzed the phase diagram of such long-range-interacting Hamiltonians for general power-law behavior of V_{jk}. In particular, for our Zeeman-field-dominated model with fast-decaying $V_{jk} \sim |j-k|^{-4}$, the ground state realizes an area-law-entangled paramagnetic gapped phase but with connected correlation functions displaying algebraic decay at long distances—precisely as found above. Given these atypical properties, it is interesting to ask whether the imperfectly teleported state received by Bob can be efficiently expressed as a matrix product state (MPS). Using the expression of the parent Hamiltonian in Eq. (6.21), and the proof in Ref. [89], one finds that this state can indeed be efficiently approximated by an MPS (see Section 6.6 for details).

Marginal imperfection

Here we examine protocols with $\boldsymbol{n} = \hat{\boldsymbol{x}}$. Similar to the previous subsection, we find numerically that Alice's most probable measurement outcome for any imperfect strength of the entangling unitary $e^{iuZ_j^A Z_j^B}$ is the uniform state $|\tilde{a}, \hat{\boldsymbol{x}}\rangle$ with all $a_j = +1$. Focusing on this measurement outcome, Bob's final state reads

$$\left|\psi_{\tilde{a}}^{\text{tele}}\right\rangle = \frac{1}{\sqrt{\mathcal{N}}} e^{\alpha M_X^+} |\psi_c\rangle \tag{6.22}$$

with $M_X^+ = \sum_j X_j/2$ the global transverse magnetization. In the weak-imperfection limit $\alpha \ll 1$ one can again map the non-unitary operator acting on Alice's pristine quantum critical state to a defect-line action perturbing the Ising CFT. Expanding $M_X^+ \sim \int_x \varepsilon$ yields

$$\delta S \sim \alpha \int_x \varepsilon(x, \tau = 0), \tag{6.23}$$

which is marginal (hence the name marginal imperfection). Marginality indicates that in this case imperfection in the teleportation protocol smoothly modifies universal aspects of correlations and entanglement as Refs. [3, 57, 58] established in the context of measurement-altered criticality. Specifically, Refs. [3, 58] exploited CFT calculations [26, 27] to compute two-point Z correlators in the presence of an ε line defect. Reference [57] evaluated Z correlators as well as the von Neumann entanglement entropy of the state in Eq. (6.22) for arbitrary α by mapping the problem to a single-bond-defect Ising model and using the results of Ref. [90]. We will pursue a complementary approach that allows explicit microscopic computation, for any α, of two-point X, Y, and Z correlators together with Rényi entropies with any index n.

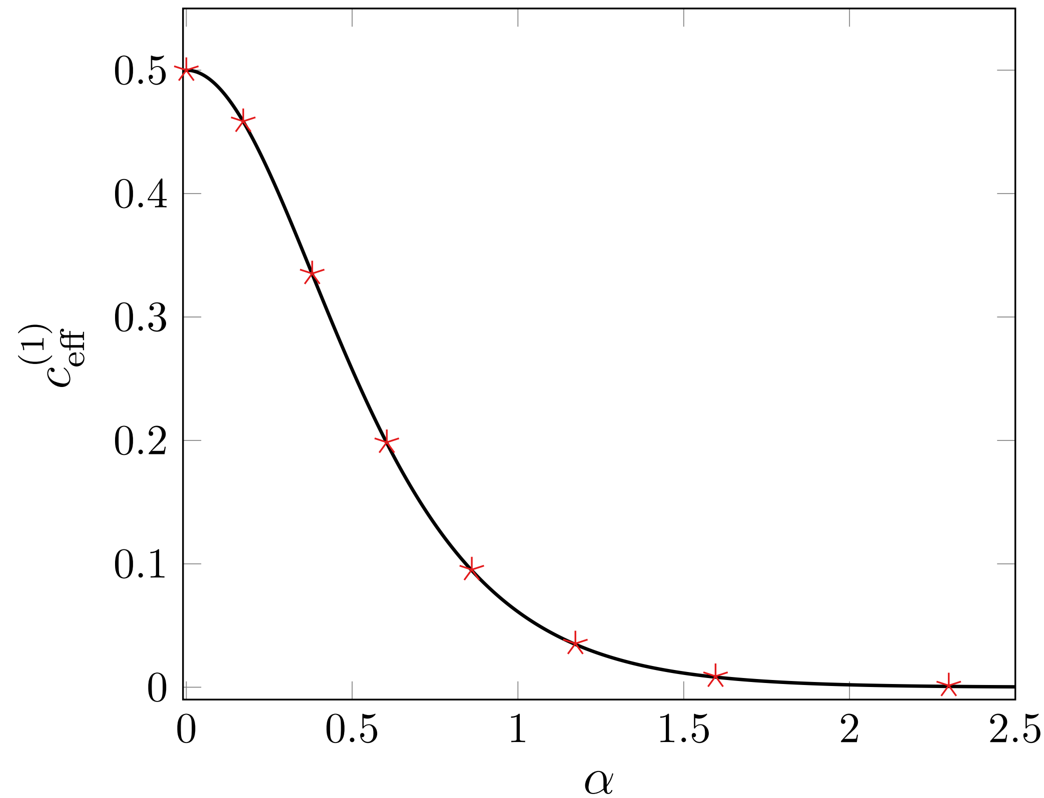

Figure 6.3: **Effective central charge resulting from marginal imperfection.** The solid line corresponds to the analytical prediction in Eq. (6.27) while the symbols are obtained using the numerical techniques described in Section 6.6. In particular, for each value of α, we calculated numerically $S_R^{(1)}$ for several values of the subsystem size ℓ up to 300; the results were fitted with $a \ln \ell + b$, and we plot here $c_{\text{eff}}^{(1)}$ extracted from the best fit of a as a function of α. These results imply that teleportation protocols corrupted by marginal imperfection preserve long-range entanglement of Alice's original critical state, but with a prefactor that decays smoothly to zero with the degree of imperfection.

Our approach views Bob's final state in Eq. (6.22) as the result of evolving the critical wavefunction $|\psi_c\rangle$ with a non-Hermitian Hamiltonian $i\alpha M_X^+$, similar to what has been done in Ref. [91]. As we show in Section 6.6, this time evolution can be exactly computed upon mapping the model to free fermions through the Jordan-Wigner transformation in Eq. (6.2), followed by a Fourier transform to momentum space. Both the von Neumann and Rényi entanglement entropies as well as all correlation functions of Bob's final state $\left|\psi_{\tilde{a}}^{\text{tele}}\right\rangle$ can be expressed as determinants of matrices with a special structure, known as Toeplitz matrices—just as for the ground state of the critical Ising model. The asymptotic behavior of block-Toeplitz determinants can be studied using a generalization of the Fisher-Hartwig conjecture [92]. We refer the interested reader to Section 6.6 for all technical details; here we simply report the main results.

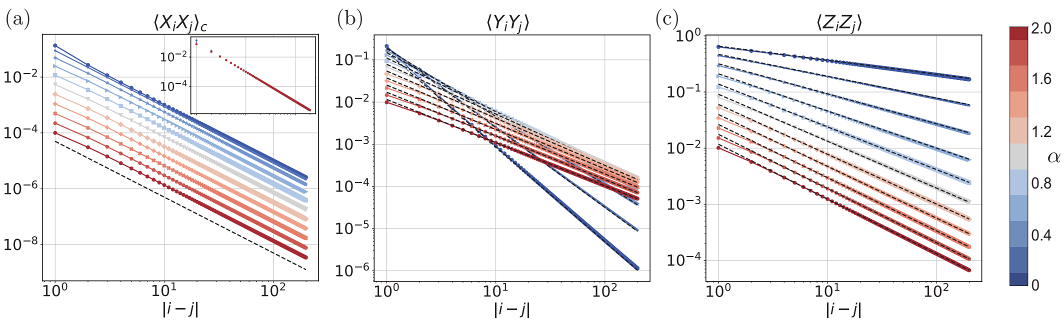

Figure 6.4: **Correlations with marginal imperfection.** Correlations in the teleported state received by Bob [Eq. (6.22)] following an imperfect protocol with $\boldsymbol{n} = \hat{\boldsymbol{x}}$ and with Alice's most probable measurement outcome. Data points were obtained using infinite DMRG for $\alpha \in [0, 2]$ in steps of 0.2. (a) Two-point X correlators exhibit unmodified power-law exponents (dashed line shows the slope arising with decay exponent 2), though imperfection suppresses the amplitude. *Inset:* Same correlations scaled by $\operatorname{sech}(2\alpha)^{-2}$; the collapse indicates that Eq. (6.28) indeed captures the amplitude's α dependence. (b,c) Two-point Y and Z correlators exhibit modified power-law exponents dependent on the imperfection strength. Dashed lines correspond to the analytical predictions in Eqs. (6.28), after fitting the overall scale from numerical data.

In the thermodynamic limit $L \to \infty$, the Rényi entropies for a large interval of size $\ell \gg 1$ read

$$S_R^{(n)} = \frac{c_{\text{eff}}^{(n)}}{6}\left(\frac{n+1}{n}\right)\ln \ell + O(1), \tag{6.24}$$

where $c_{\text{eff}}^{(n)}$ is given by the real integral

$$c_{\text{eff}}^{(n)} = \frac{12}{\pi^2}\int_{\tanh(2\alpha)}^{1} g_n(\lambda)\ln\frac{\sqrt{1-\lambda^2}}{\sqrt{\lambda^2-\tanh^2(2\alpha)}+\operatorname{sech}(2\alpha)}\,d\lambda \tag{6.25}$$

with

$$g_n(\lambda) = \frac{n^2}{1-n^2}\frac{(\lambda+1)(1-\lambda)^n+(\lambda-1)(\lambda+1)^n}{(\lambda^2-1)\left[(1-\lambda)^n+(\lambda+1)^n\right]}. \tag{6.26}$$

At $\alpha = 0$ one obtains $c_{\text{eff}}^{(n)} = 1/2$, i.e., the coefficients reduce to the central charge of the Ising CFT for any n in agreement with Eq. (6.5). In the limit $n \to 1$, where $S_R^{(n)}$ reduces to the von Neumann entanglement entropy, $c_{\text{eff}}^{(1)}$ defines an effective central charge. For this case the integral in Eq. (6.25) explicitly evaluates to

$$
\begin{aligned}
c_{\text{eff}}^{(1)} = -\frac{3}{\pi^2}\,\big[&(x+1)\mathrm{Li}_2(-x) + (1-x)\mathrm{Li}_2(x) + \\
&\ln(x)((1-x)\ln(1-x) + (x+1)\ln(x+1))\big]\,,
\end{aligned}
\tag{6.27}
$$

where $x = \cosh^{-1}(2\alpha)$ and Li_2 denotes the dilogarithm function [93]. Figure 6.3 shows the α-dependence of $c_{\text{eff}}^{(1)}$—which decays from the ideal value of 1/2 to zero as α increases (see caption for details). Consequently, while for any finite α the von Neumann entanglement entropy still follows a logarithmic-law, its coefficient—the effective central charge—is diminished by protocol imperfection relative to Alice's original critical state. This result agrees with that of Ref. [57], where the mapping to a single-bond-defect Ising model was used. To our knowledge, the general expression in Eq. (6.25) for $c_{\text{eff}}^{(n)}$ characterizing logarithmic growth of Rényi entropies with $n \neq 1$ for the state (6.22) has not been reported previously. These coefficients similarly decay smoothly to zero as the protocol imperfection increases in a manner that depends (somewhat weakly) on n and yields a finite α-dependent value at $n \to \infty$. The situation should be contrasted to Eq. (6.5) for the pristine Ising theory, where a single parameter c characterizes the logarithmic entanglement growth for any n. We will return to these general Rényi entropies shortly from the perspective of the $\alpha \gg 1$ limit.

We now report the results of two-point correlation functions arising from marginally imperfect teleportation. In the limit $|i-j| \gg 1$ they read

$$
\begin{aligned}
\langle X_i X_j\rangle_c &= \frac{\mathrm{sech}^2(2\alpha)}{\pi^2|i-j|^2},\\
\langle Y_i Y_j\rangle &\propto \frac{1}{|i-j|^{2\Delta_Y(\alpha)}}, \quad \Delta_Y(\alpha) = \frac{2[\arctan(e^{2\alpha})-\pi]^2}{\pi^2}\\
\langle Z_i Z_j\rangle &\propto \frac{1}{|i-j|^{2\Delta_Z(\alpha)}}, \quad \Delta_Z(\alpha) = \frac{2\arctan^2(e^{2\alpha})}{\pi^2}.
\end{aligned}
\tag{6.28}
$$

Compared to the correlations in Eq. (6.4) operative for perfect teleportation, the following salient features arise: The power-law exponent for the connected $\langle X_i X_j\rangle_c$ correlator does not vary upon turning on non-zero α, although the amplitude is suppressed and vanishes smoothly as $\alpha \to \infty$. Power-law exponents for two-point Y and Z correlators, by contrast, do depend on the degree of protocol imperfection: as α increases from 0 to ∞, Δ_Y decreases from $9/8$ to $1/2$ while Δ_Z increases from $1/8$ to $1/2$. DMRG simulations presented in Fig. 6.4 confirm the scaling behavior predicted by Eq. (6.28). As an aside, although we focus on $\alpha \geq 0$, our analytical results for both the $c_{\text{eff}}^{(n)}$ entanglement coefficients and the correlators in Eq. (6.28) apply for either sign of α; the $c_{\text{eff}}^{(n)}$ coefficients are invariant under $\alpha \to -\alpha$ while the scaling dimensions Δ_Z and Δ_Y are not.

Using the formalism from Sec. 5.3, we can approximate Bob's penultimate wavefunction (again prior to applying the final outcome-dependent unitary) as

$$|\psi_{\tilde{a}}\rangle \approx \frac{1}{\sqrt{\mathcal{N}}} e^{-\frac{u^2}{2}\sum_{j\neq k} V_{jk} Z_j Z_k} |\psi_B\rangle . \tag{6.29}$$

The unitary operator in Eq. (5.24) is absent here since $q(j)$ vanishes by symmetry. In the non-unitary operator, the strange correlator V_{jk} was evaluated in Ref. [3] and shown to scale as $V_{jk} \sim 1/|j-k|$. In Sec. 5.3 we argued that the perturbative expansion leading to Eq. (6.18)—and the associated Hermitian parent Hamiltonian from Eq. (5.27)—was expected to be controlled provided V_{jk} decays *faster* than $1/|j-k|$. Nevertheless, we can recover asymptotic features present in our earlier non-perturbative computations by boldly calculating correlations and entanglement using the above large-α form of Bob's penultimate state. Methods similar to Sec. 6.2 and detailed further in Section 6.6 show that $\langle Y_i Y_j\rangle$ and $\langle Z_i Z_j\rangle$ both scale as $u^2 V_{ij}$ whereas $\langle X_i X_j\rangle_c$ scale as $u^4 V_{ij}^2$. Power-law exponents for the Y and Z correlators agree with the asymptotic $\alpha \to \infty$ limit of Eq. (6.28); the X correlator recovers the exact exponent as well as the leading large-α dependence of the prefactor in Eq. (6.28) upon using $u \approx e^{-\alpha}$. We can, moreover, analytically calculate the $n = 2$ Rényi entropy upon Taylor expanding the exponential in Eq. (6.29) (see Section 6.6). To leading nontrivial order we obtain

$$S_R^{(2)} = \frac{4u^2}{\pi^2} \ln \ell + \mathcal{O}(1), \tag{6.30}$$

which agrees with Eq. (6.24) in the $\alpha \gg 1$ regime.

To summarize, compared with relevant imperfection treated in Sec. 6.2, in the imperfect protocol studied here Bob inherits a far more faithful version of Alice's critical wavefunction: power-law correlations and long-range entanglement both persist, albeit with modifications that vary smoothly with α. In the next subsection we will see how resilience to imperfection can be further improved by following a protocol that employs yet a different quantization axis $\boldsymbol{n}$—though, as we will see, the improvement is not quite to a degree that a naive analysis would initially suggest.

Disguised marginal imperfection

Consider now a teleportation protocol with $\boldsymbol{n} = \hat{\boldsymbol{y}}$. In this case we find that whenever the entangling gate $U = \prod_j e^{iuZ_j^A Z_j^B}$ is imperfect, Alice's most probable measurement

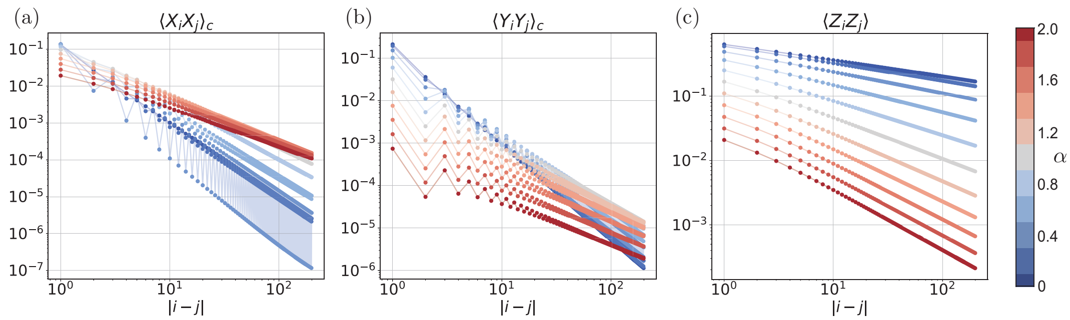

Figure 6.5: **Correlations with disguised marginal imperfection.** Correlations in the teleported state received by Bob [Eq. (6.31)] following an imperfect protocol with $\boldsymbol{n} = \hat{\boldsymbol{y}}$ and with Alice's most probable measurement outcome. Data points were obtained using infinite DMRG with for $\alpha \in [0, 2]$ in steps of 0.2. Setup with Bob's initial wavefunction as a product state in the $\hat{\boldsymbol{y}}$ basis. All correlators exhibit continuously modified power-law exponents as the imperfection strength increases—in agreement with naively irrelevant imperfections generating marginal corrections under renormalization.

outcomes are the two symmetry-related Néel states $|\tilde{a}, \hat{\boldsymbol{y}}\rangle$ with $a_j = \pm(-1)^j$ (at least for an even number of sites with periodic boundary conditions [1]). For these outcomes Bob's final wavefunction is

$$\left|\psi_{\tilde{a}}^{\text{tele}}\right\rangle = \frac{1}{\sqrt{\mathcal{N}}} e^{\alpha M_Y^s} \left|\psi_c\right\rangle, \tag{6.31}$$

where we defined the staggered Y magnetization $M_Y^s = \sum_j (-1)^j Y_j/2$. What is the appropriate defect-line perturbation δS generated by the non-unitary operator above at small α? Given that the low-energy expansion $Y_j \sim i\partial_\tau \sigma$ contains only smoothly varying field components, the $(-1)^j$ in the staggered magnetization M_Y^s appears to imply that only highly oscillatory—and thus strongly irrelevant—terms appear in δS. Actually, had we post-selected for (lower-probability) uniform outcomes rather than staggered measurement outcomes, the $(-1)^j$ oscillatory factor would disappear, yielding $\delta S \sim \alpha \int_x i\partial_\tau \sigma(x, \tau = 0)$—which is still irrelevant. One might be tempted to conclude then that, for either the uniform or staggered measurement outcomes, Bob faithfully inherits the universal features of Alice's critical correlations and entanglement over at least a finite window of protocol imperfection.

Such a conclusion would be incorrect, however. Under renormalization, additional symmetry-allowed terms will be generated that may be more relevant than those in the 'bare' theory (see, e.g., Ref. [94]). In our context, with either the uniform or

[1] With an odd number of sites, there are $O(L)$ degenerate states corresponding to Néel states with a single local ferromagnetic bond. We only consider even system sizes here.

staggered measurement outcomes, symmetry allows generation of the *marginal* term

$$\delta S' \sim \alpha^2 \int_x \varepsilon(x, \tau = 0) \tag{6.32}$$

at $\mathcal{O}(\alpha^2)$. For instance, one can view α in Eq. (6.31) as odd under time reversal $\mathcal{T}$, $\mathbb{Z}_2$ spin-flip symmetry, and single-site translations; α^2 is then invariant under all symmetries, so that $\delta S'$ is indeed symmetry-allowed. For another perspective on Eq. (6.32) let us examine further the uniform measurement outcome. Using Lorentz invariance of the unperturbed continuum theory, we can Wick rotate to interchange imaginary time and space to obtain a defect-line action that acts at one spatial position $x = 0$ but all τ. This Wick-rotated defect describes a conventional static quantum impurity that microscopically descends from a critical Hamiltonian with a Y perturbation of strength αJ at a single site:

$$H_{\text{imp}} = -J\left(\sum_j Z_j Z_{j+1} + \sum_{j\neq 0} X_j\right) - J(X_0 + \alpha Y_0). \tag{6.33}$$

Note that we grouped the transverse field and the Y perturbation at the impurity site, $j = 0$. Locally rotating the $j = 0$ spin about Z by an angle θ satisfying $\tan(2\theta) = \alpha$ yields the unitarily equivalent form

$$\begin{aligned} e^{i\theta Z_0} H_{\text{imp}} e^{-i\theta Z_0} &= -J\left(\sum_j Z_j Z_{j+1} + \sum_{j\neq 0} X_j\right) \\ &\quad - J\sqrt{1+\alpha^2} X_0 \approx H_c - \frac{J}{2}\alpha^2 X_0. \end{aligned} \tag{6.34}$$

On the bottom right we assumed $\alpha \ll 1$ to arrive at the uniform critical Ising Hamiltonian H_c from Eq. (6.1) perturbed solely by a local $\mathcal{O}(\alpha^2)$ shift in the transverse field. In this form it is clear that the original $\mathcal{O}(\alpha)$ Y perturbation indeed germinates an $\mathcal{O}(\alpha^2)$ ε perturbation in the low-energy theory, as previously deduced on symmetry grounds.

Because a marginal perturbation appears only upon a careful inspection that accommodates higher-order terms, we refer to this situation as 'disguised marginal imperfection'. Section 6.2 already analyzed the impact of a marginal defect-line action on the teleported state. Here we similarly expect that imperfection smoothly modifies long-distance entanglement and correlations away from their ideal universal forms, but to a still less dramatic degree at $\alpha \ll 1$ since corruption kicks in only at $\mathcal{O}(\alpha^2)$. Figure 6.5 presents two-point correlators obtained with DMRG assuming the most-likely staggered measurement outcome and confirms this expectation. Indeed, in the small-α regime, the correlations in Fig. 6.5 behave qualitatively similarly to those for the $\boldsymbol{n} = \hat{\boldsymbol{x}}$ protocol in Fig. 6.4. [The main difference arises for two-point X correlators, whose power-law exponent does now evolve nontrivially with α. This feature can be understood from the large-α limit. We observe that in the present case $q(j)$ is non-zero in Eq. (5.24), which produces different behavior with respect to measuring in the $\hat{\boldsymbol{x}}$-basis.]

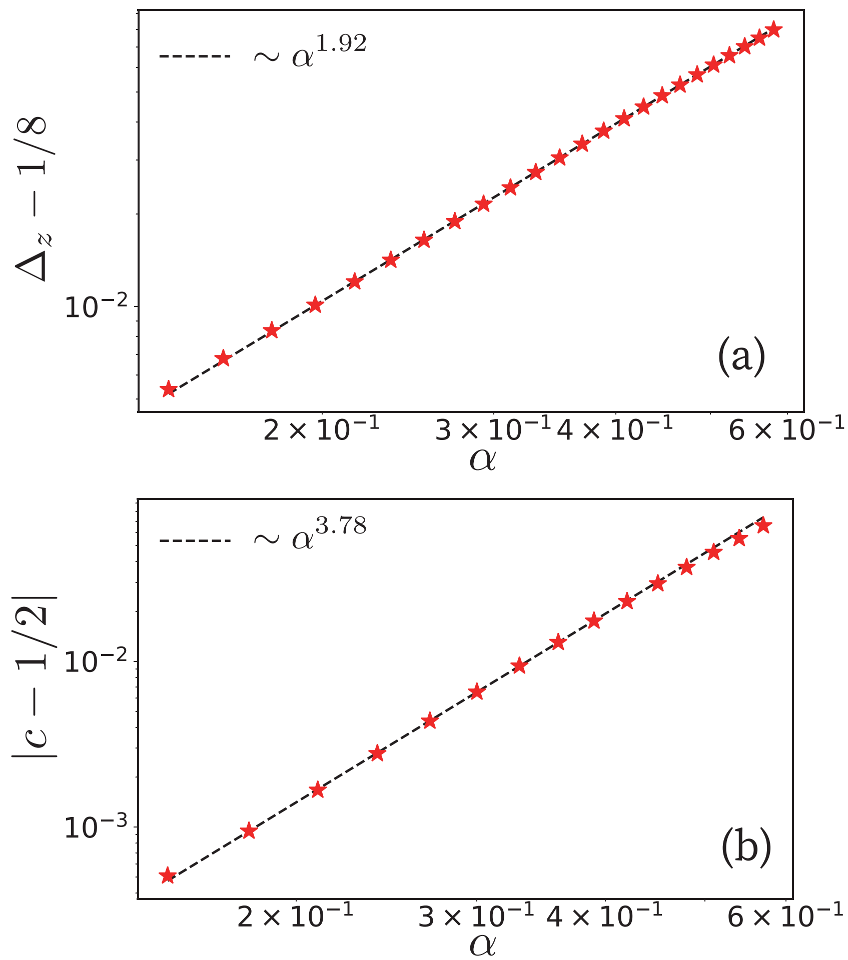

Figure 6.6: **Scaling dimension and effective central charge with disguised marginal imperfection.** (a) Power-law dependence of the scaling dimension of Z as a function of α. Red stars represent data obtained from infinite DMRG [Fig. 6.5(c)], while the dashed line is a power-law fit $\Delta_z(\alpha) - 1/8 \sim \alpha^{1.92}$. The fit agrees well with the α^2 scaling expected from the generation of a marginal term at second order in the imperfection strength α; see Eq. (6.32). (b) Dependence of the effective central charge on α. Red stars represent the data obtained using finite DMRG from fitting $S_{L/2}$ vs $\ln L$ for $L = [20, 40, 60, 80, 100, 150, 200]$. Dashed line represents a power-law fit $|c - 1/2| \sim \alpha^{3.78}$—which agrees reasonably well with α^4 scaling expected from an $O(\alpha^2)$ marginal imperfection term.

To further bolster our predictions, Fig. 6.6(a) presents the imperfection-induced change in the $\langle Z_i Z_j \rangle \sim 1/|i-j|^{2\Delta_Z}$ scaling dimension relative to the ideal value of $\Delta_Z = 1/8$. We numerically find the relation $\Delta_Z(\alpha) - 1/8 \sim \alpha^{1.92}$ at small α, in good agreement with the scaling $\Delta_Z(\alpha) - 1/8 \sim \alpha^2$ that follows from Eq. (6.32). One can also recover that scaling directly from Eq. (6.28) upon sending $\alpha \to \alpha^2$. Figure 6.6(b) shows that the change in the effective central charge characterizing logarithmic entanglement growth scales approximately as $|c^{(1)}_{\text{eff}} - 1/2| \sim \alpha^4$—as expected from Eq. (6.27) upon similarly replacing $\alpha \to \alpha^2$. Therefore, protocols with $\boldsymbol{n} = \hat{\boldsymbol{y}}$ yield additional resilience to weak imperfection when post-selecting for the highest-probability measurement outcomes, despite universal features still undergoing modifications.

Further improvement is technically possible even when post-selecting for similar measurement outcomes. Suppose that we generalize Eq. (6.31) to

$$\left|\psi^{\text{tele}}_{\tilde{a}}\right\rangle = \frac{1}{\sqrt{\mathcal{N}}} e^{\alpha_x M^+_X + \alpha_y M^s_Y} \left|\psi_c\right\rangle . \tag{6.35}$$

The above form of Bob's final state arises upon replacing $\boldsymbol{n} = \hat{\boldsymbol{y}}$ with a position-dependent quantization axis $\boldsymbol{n}_j = (-1)^j \sin\varphi \hat{\boldsymbol{x}} + \cos\varphi \hat{\boldsymbol{y}}$ and again post-selecting for a staggered outcome with $a_j = \pm(-1)^j$. In the weak-imperfection limit, we have seen that both M^+_X and M^s_Y generate marginal ε defect-line perturbations—the former at $\mathcal{O}(\alpha_x)$ and the latter at $\mathcal{O}(\alpha_y^2)$. When the two ε contributions come with opposite sign, one can cancel off the marginal term by fine-tuning $\alpha_{x,y}$ to values satisfying $|\alpha_x| \sim \alpha_y^2$. Here the imperfectly teleported state retains the quantized central charge $c = 1/2$ and power-law correlations characteristic of the pristine Ising theory. By continuity this fine-tuned limit must persist also in the limit where $\alpha_{x,y}$ are not necessarily weak. We support this scenario in Fig. 6.7, which shows the $\alpha_{x,y}$ dependence of the effective central charge of Eq. (6.35) obtained using DMRG. An extended region with $c = 1/2$ is clearly visible in agreement with our predictions. Although this limit is doubly fine-tuned in the sense of requiring both post-selection and tuning of α_x given some α_y, we learn two lessons: First, it serves as a nontrivial check on our theory of disguised marginal imperfection. And second, it shows that in principle one can teleport the ideal long-distance universal Ising criticality properties even with simple, spatially periodic measurement outcomes and with superficially 'large' protocol imperfections (the $c = 1/2$ line in Fig. 6.7 indeed persists to sizable $|\alpha_x|$ values where one might naively anticipate dramatically altered critical properties).

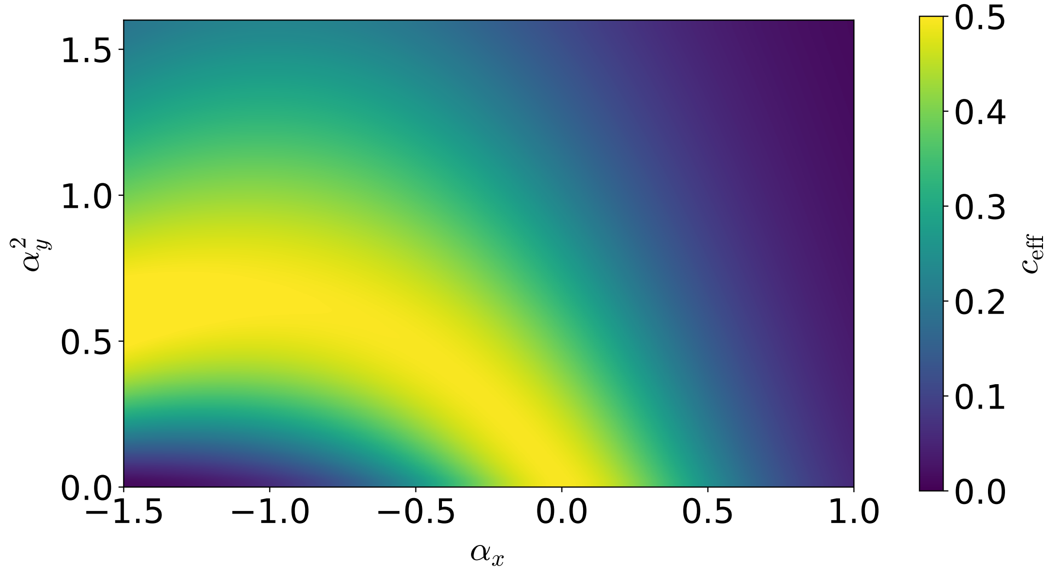

Figure 6.7: **Cancellation of marginal imperfections.** Effective central charge for the generalized teleported state in Eq. (6.35) as a function of α_x and α_y^2. Data were obtained using infinite DMRG (see Section 6.6 for details). The bright yellow arc highlights fine-tuned parameters for which imperfection-induced marginal terms cancel—in turn producing a teleported state with pristine central charge $c = 1/2$. Note the persistence of this fine-tuned arc even for sizable imperfection strengths $\alpha_{x,y}$.

Imperfect teleportation with typical measurement outcomes

Above we focused on the effects of an imperfect teleportation protocol when Alice obtains her most likely measurement outcomes. However, the probabilities for such outcomes, while maximal, are still exponentially small in the number of teleported qubits. Hence, it is important to investigate the quality of teleportation in the case of *typical* measurement outcomes $\tilde{a}$—i.e., those appearing when sampling according to the (α-dependent) Born probability distribution $p_{\tilde{a}}$ corresponding to the state $|\psi_U\rangle = U\,|\psi_c\rangle\,|\tilde{b}, \boldsymbol{n}\rangle$ obtained after Alice and Bob entangle their qubits. Reference [16] already addressed a related question when probing measurement-altered criticality in a Luttinger liquid. We will repeat and adapt their findings to our teleportation protocols with quantization axis/measurement basis $\boldsymbol{n}$.

Let $\tilde{a}$ now denote a typical outcome consisting of bits $a_j = \pm 1$ associated with the Pauli operators $O_j^A(\boldsymbol{n})$ that Alice measures. We would like to use a coarse-graining procedure to take the continuum limit of the non-unitary operator $e^{-\frac{\alpha}{2}H_{\tilde{a}}(\boldsymbol{n})}$ encoding teleportation-protocol imperfection, obtain a corresponding defect-line action in the $\alpha \ll 1$ regime, and analyze its effect on the long-distance properties of Bob's

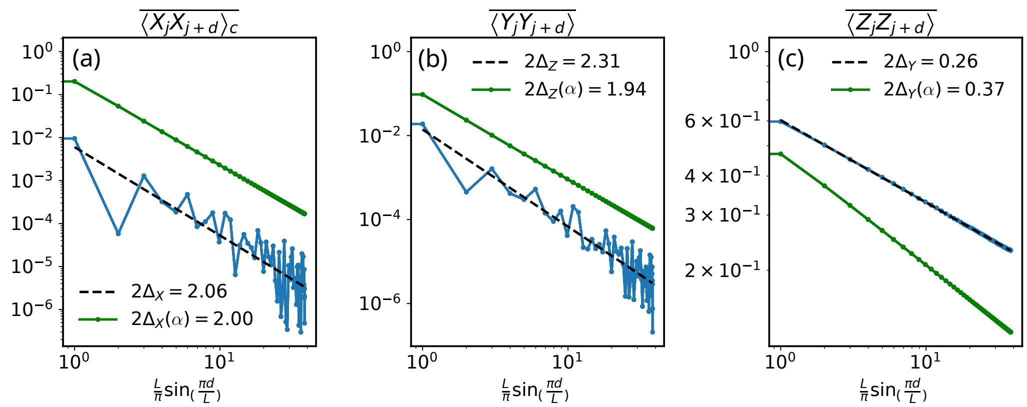

Figure 6.8: **Correlations with typical measurement outcomes.** Correlations in the teleported state received by Bob following an imperfect protocol with $\boldsymbol{n} = \hat{\boldsymbol{x}}$, now with a typical measurement outcome randomly sampled from Born's probability distribution as prescribed in Ref. [57]. Data were obtained using finite DMRG with bond dimension $\chi = 800$ and system size $L = 120$ with periodic boundary conditions. Results shown in blue correspond to $u = 0.7$ ($\alpha \approx 0.17$) after averaging the correlation functions over the center of mass coordinate, i.e., $\overline{\langle \hat{O}_j \hat{O}_{j+d}\rangle} = \sum_{j=1}^{L} \langle \hat{O}_j \hat{O}_{j+d}\rangle / L$. For comparison, the green points show correlations obtained with Alice's most probable measurement outcome for the same value of u. Contrary to the latter case, with typical outcomes imperfections are irrelevant, and hence the averaged correlators are consistent with power laws expected for pristine Ising criticality.

final wavefunction. For a perfect teleportation protocol with $\alpha = 0$, all outcomes are equally likely, and hence the a_j bits are completely uncorrelated. An imperfect protocol with $\alpha \neq 0$—which we assume hereafter—biases the measurement-outcome distribution, yielding correlations among the bits that are inherited from structure in the pre-measurement entangled state $|\psi_U\rangle$. For instance, averaging a given a_j over measurement outcomes gives

$$\overline{a}_j = \sum_{\tilde{a}} p_{\tilde{a}} a_j = \cos(2u) \langle \psi_c | \hat{O}^A_j(\boldsymbol{n}) | \psi_c \rangle , \tag{6.36}$$

while similarly averaging $a_j a_k$ for $j \neq k$ yields the connected correlation

$$\overline{a_j a_k} - \overline{a}_j \overline{a}_k = \cos^2(2u) \langle \psi_c | \hat{O}^A_j(\boldsymbol{n}) \hat{O}^A_k(\boldsymbol{n}) | \psi_c \rangle_c . \tag{6.37}$$

(Both quantities above vanish in the perfect protocol limit $u = \pi/4$ as required.) Equation (6.37) in particular limits the spatial extent of correlations among bit strings in a typical measurement outcome: on average, they decay at long distances according to the leading power-law contribution $\sim 1/|j-k|^{2\Delta_{\rm sl}}$ arising from the critical correlation of Alice's initial state on the right-hand side.

Following Kadanoff's decimation argument [95], next we analyze the block-spin variable $a(x;b) = 1/b\sum_{j=x-b/2}^{x+b/2} a_j$, which reduces the number of degrees of freedom by grouping the $\tilde{a}$ variables within a block of size $b \gg 1$. Intuitively, the more rapidly correlations among different a_j's decay with their separation, the faster the block-spin variable averages to zero as b increases. One can estimate the decay rate with b for a typical measurement outcome by examining the variance of $a(x;b)$:

$$\begin{aligned}\overline{[a(x;b)]^2} - [\overline{a}(x;b)]^2 &= \frac{1}{b^2}\sum_{j,k=x-b/2}^{x+b/2}(\overline{a_j a_k} - \overline{a}_j\overline{a}_k) \\ &\propto \frac{1}{b^2}\sum_{j,k=x-b/2}^{x+b/2}\langle\psi_c|\,\hat{O}_j^A(\boldsymbol{n})\hat{O}_k^A(\boldsymbol{n})\,|\psi_c\rangle_c\,. \end{aligned} \tag{6.38}$$

For large b, in the regime $\Delta_{\rm sl} < 1/2$ the second line scales as $\frac{1}{b^2}\times b^{2(1-\Delta_{\rm sl})} = 1/b^{2\Delta_{\rm sl}}$ due to the power-law contribution from the long-distance $|j-k| \gg 1$ part of the sums. With $\Delta_{\rm sl} > 1/2$, however, the long-distance part vanishes sufficiently quickly that the short-distance part dominates, yielding the faster scaling $\frac{1}{b^2}\times b = 1/b$. Thus we obtain

$$\overline{[a(x;b)]^2} - [\overline{a}(x;b)]^2 \sim \begin{cases} b^{-2\Delta_{\rm sl}}, & \Delta_{\rm sl} < 1/2 \\ b^{-1}, & \Delta_{\rm sl} > 1/2 \end{cases}. \tag{6.39}$$

Notice that the scaling with b in the lower line is the same as one would obtain at $\alpha = 0$, where all measurement outcomes are equally likely and the a_j's at different sites are completely uncorrelated. The key upshot is that $a(x;b)$ realizes a smoothly varying function whose scaling dimension follows from the square root of Eq. (6.39); i.e., the dimension is either $\Delta_a = \Delta_{\rm sl}$ (for $\Delta_{\rm sl} < 1/2$) or $\Delta_a = 1/2$ (for $\Delta_{\rm sl} > 1/2$).

We can now take the continuum limit of $e^{-\frac{\alpha}{2}H_{\tilde{a}}(\boldsymbol{n})}$. Recalling the definition of $H_{\tilde{a}}(\boldsymbol{n})$ in Eq. (5.17), the coarse-grained function $a(x;b)$ couples to the low-energy expansion of $\hat{O}_j(\boldsymbol{n})$ given by the dictionary in Eq. (6.7). Hence, if $\hat{O}_j(\boldsymbol{n}) \sim O_{\rm sl}$ is the leading contribution (which has the same scaling dimension $\Delta_{\rm sl}$ from earlier), then the corresponding defect-line action reads

$$\delta S \sim \alpha\int_x a(x;b)O_{\rm sl}(x,\tau=0). \tag{6.40}$$

For $\Delta_{\rm sl} < 1/2$, the integrand has scaling dimension $\Delta_{\rm sl} + \Delta_{\rm sl} < 1$—implying that δS constitutes a relevant perturbation. For $\Delta_{\rm sl} > 1/2$, in contrast, the dimension becomes $1/2 + \Delta_{\rm sl} > 1$ so that δS is then irrelevant.

Teleportation protocols with $\boldsymbol{n} = \hat{\boldsymbol{x}}$ yield $O_{\rm sl} = \varepsilon$ and $\Delta_{\rm sl} = 1$. Post-selecting for typical measurement outcomes thereby demotes the marginal defect-line action studied in Sec. 6.2 to an irrelevant perturbation. At least on sufficiently long length scales, Bob inherits Alice's universal correlations and entanglement despite imperfection in the protocol. We numerically tested this prediction by computing two-point X, Y, and Z correlators in Bob's final state obtained for an imperfect entangling gate with $u = 0.7$ and when Alice measures a typical outcome randomly sampled according to Born's probability distribution. Specifically, following Ref. [57] we measured one of Alice's qubit (sampled according to Born's rule), obtained the resulting post-measurement state, then moved on to measure her next qubit, and so on. Our results for the spatially averaged quantities $\sum_{j=1}^{L}\langle O_j O_{j+d}\rangle/L$ with $O_j = X, Y$ and Z are shown in the blue curves from Fig. 6.8; for reference, the green curves correspond to correlators obtained with Alice's most probable outcome (Sec. 6.2). The blue curves in the X and Y panels appear noisier than for Z. We attribute this behavior to their faster power-law decay, which in turn suppresses averaging out of the randomness from the measurement outcome. Nevertheless, in all three panels, power-law behavior for the typical outcome is indeed compatible with the results of Eq. (6.4) obtained for the pure Ising CFT.

Using similar logic, δS is also irrelevant for protocols with $\boldsymbol{n} = \hat{\boldsymbol{y}}$. In Sec. 6.2 we saw for the highest-probability outcome that an irrelevant term appearing at leading order in α generated a marginal ε term [Eq. (6.32)] at $O(\alpha^2)$. With typical outcomes, we also expect an ε term to be generated—but now with a prefactor $[\alpha a(x;b)]^2$. The appearance of $a(x;b)$ in particular renders that second-order term irrelevant as well. Thus protocols with $\boldsymbol{n} = \hat{\boldsymbol{y}}$ also enjoy resilience against imperfection in the case of typical measurement outcomes.

When $\boldsymbol{n} = \hat{\boldsymbol{z}}$, however, imperfection continues to yield dramatic consequences even for typical outcomes. Here $O_{\rm sl} = \sigma$ and $\Delta_{\rm sl} = 1/8$, and consequently δS is relevant (albeit less so compared to the case of uniform measurement outcomes). Here we expect $\langle Z_j\rangle$ to take on a non-zero, position-dependent expectation value that roughly follows the sign of the imperfection-induced longitudinal-field-like perturbation encoded in δS. Two-point correlators and entanglement can be attacked from the large-α limit using the parent Hamiltonian formalism from Sec. 5.3. We saw in Sec. 6.2 that this formalism captures both power-law correlations and area-law entanglement when post-selecting for the highest-probability measurement outcome; recall Eq. (6.21) and the accompanying discussion. With typical outcomes, the main difference stems from the form of the strange correlator V_{jk} that governs 'weak' long-range interactions in the parent Hamiltonian. At large separation $|j-k|$, the mean of V_{jk} is exactly 0, while the variance of V_{jk} vanishes as $\sim 1/|j-k|^4$ (see Ref. [3] for the computation). This relatively fast power-law decay suggests that (i) the perturbative treatment underlying the large-α analysis is valid, (ii) the entanglement entropy exhibits area-law behavior also for typical outcomes, and (iii) spatially averaged spin-spin correlations decay as the square root of the variance of V_{jk}, i.e., as $\sim 1/|j-k|^2$. (Verifying this power-law decay numerically, however, is challenging.) We conclude that regardless of whether Alice obtains the most probable measurement outcome or a typical outcome, even weak imperfection in protocols using $\boldsymbol{n} = \hat{\boldsymbol{z}}$ qualitatively alters the universal correlations and entanglement of the Ising critical state undergoing teleportation.

6.3 Generalized protocol

In our imperfect teleportation protocol treated so far we restricted to entangling on-site unitaries $U = \prod_j U_j$ with U_j generated by the tensor product of two Pauli operators $\hat{O}^A_j(\boldsymbol{n}^\perp)\hat{O}^B_j(\boldsymbol{n}^\perp)$. Recall that $\boldsymbol{n}^\perp$ is orthogonal to the vector $\boldsymbol{n}$ specifying the basis for Alice's measurement and Bob's initialization. We will now generalize the protocol to incorporate an additional possible imperfection by assuming that Alice and Bob entangle their qubits via

$$U_j = e^{iu\hat{O}^A_j(\boldsymbol{m})\hat{O}^B_j(\boldsymbol{m})}, \tag{6.41}$$

where $\boldsymbol{m}$ is now a general unit vector not necessarily orthogonal to $\boldsymbol{n}$. As in the previous, more restricted protocol, Bob is allowed to perform a unitary dependent on Alice's measurement outcome $\tilde{a}$ (as well as $\tilde{b}, \boldsymbol{n}$, and $\boldsymbol{m}$) to obtain the final teleported state. In what follows we discuss how the quality of teleportation is altered by imperfections in both the entangling gate strength (parametrized by u) and 'orientation' (parametrized by $\boldsymbol{m}$). Other error sources may of course also arise and can be studied similarly.

We first examine the structure of Bob's penultimate wavefunction $|\psi_{\tilde{a}}\rangle$, prior to applying the final outcome-dependent unitary. With details consigned to Section 6.6, the expression—valid for an arbitrary initial state $|\psi_A\rangle$ for Alice—can be written as

$$\begin{aligned} |\psi_{\tilde{a}}\rangle = {} & \frac{1}{\sqrt{\mathcal{N}}} e^{i\frac{\pi}{4}H_{\tilde{b}}(\boldsymbol{n})} e^{-\frac{\alpha}{2}H_{\tilde{b}}(\boldsymbol{n})} \\ & \times \mathcal{U}_{\tilde{b}}(\boldsymbol{m}\times\boldsymbol{n}^\perp) U_{\tilde{b}\leftarrow\tilde{a}} \mathcal{U}^\dagger_{\tilde{a}}(\boldsymbol{m}\times\boldsymbol{n}^\perp)\,|\psi_A\rangle\,. \end{aligned} \tag{6.42}$$

The first two exponentials involve the Hermitian operator $H_{\tilde{b}}(\boldsymbol{n}) = -\sum_j b_j \hat{O}_j(\boldsymbol{n})$, while $\mathcal{U}_{\tilde{d}}(\boldsymbol{m}\times\boldsymbol{n}^\perp)$ (for $d = a, b$) are on-site transformations that are in general non-unitary. They take the explicit form $\mathcal{U}_{\tilde{d}}(\boldsymbol{m}\times\boldsymbol{n}^\perp) = \prod_j [e^{i\theta\frac{(\boldsymbol{m}\times\boldsymbol{n}^\perp)}{||\boldsymbol{m}\times\boldsymbol{n}^\perp||}\cdot\boldsymbol{\sigma}_j}P^d_j + \mathbb{1}(1-P^d_j)]$, where θ is the angle between $\boldsymbol{m}$ and $\boldsymbol{n}^\perp$, and P_j^d are projectors defined as $P_j^d = \frac{1}{2}[1 - \tilde{d}_j \hat{O}_j(\boldsymbol{n})]$. Thus the $\mathcal{U}$ factors in Eq. (6.42) either act as the identity, or rotate the spins about the axis $\boldsymbol{m} \times \boldsymbol{n}^\perp$. Notice that these rotations become trivial if $\boldsymbol{m}$ was chosen parallel to $\boldsymbol{n}^\perp$ (as arose in our previously treated protocols). When they act nontrivially, the projectors P_j^d correct the 'mismatch' in Eq. (6.41) that prevents U_j from performing a full flip from $a_j \to -a_j$ and/or $b_j \to -b_j$. With these definitions, we can view the first three operators acting on $|\psi_A\rangle$ in Eq. (6.42) as follows: First, $\mathcal{U}_{\tilde{a}}^\dagger(\boldsymbol{m} \times \boldsymbol{n}^\perp)$ 'readjusts' the $\boldsymbol{m}$ direction such that it lies along $\boldsymbol{n}^\perp$. Next, $U_{\tilde{b}\leftarrow\tilde{a}} = e^{i\frac{\pi}{4}H_{\tilde{b}\leftarrow\tilde{a}}(\boldsymbol{n}^\perp)}$ is a unitary that flips the measurement outcome $\tilde{a}$ to $\tilde{b}$ as in Eq. (5.15). Finally, $\mathcal{U}_{\tilde{b}}(\boldsymbol{m} \times \boldsymbol{n}^\perp)$ readjusts $\boldsymbol{m}$ by rotating it into the $\boldsymbol{n}^\perp$ direction.

Deducing the fate of the imperfectly teleported wavefunction as written in Eq. (6.42) is nontrivial since a series of interspersed unitary and non-unitary operators acts on $|\psi_A\rangle$. A more useful form arises upon re-organizing the expression such that unitary factors act to the left of manifestly Hermitian, non-unitary factors. We will not attempt a completely general rewriting of this type, but rather examine the situation where $\boldsymbol{m}$ is weakly misaligned but close to $\boldsymbol{n}^\perp$. In this limit one can write, after dropping an unimportant overall phase,

$$\mathcal{U}_{\tilde{d}}(\boldsymbol{m} \times \boldsymbol{n}^\perp) \approx e^{\frac{i}{2}\sum_j \hat{O}_j(\boldsymbol{m}\times\boldsymbol{n}^\perp)} \times e^{\frac{(\boldsymbol{m}\cdot\boldsymbol{n})}{2}\sum_j d_j \hat{O}_j(\boldsymbol{n}^\perp)}. \tag{6.43}$$

Using this approximation and allowing Bob to undo an overall unitary operator, we obtain the final (unnormalized) teleported state

$$\left|\psi_{\tilde{a}}^{\text{tele}}\right\rangle = e^{-\frac{\alpha}{2}H_{\tilde{a}}(\boldsymbol{n}) + \frac{\alpha}{2}\sum_j \epsilon_{-,j}\hat{O}_j(\boldsymbol{n}^\perp)} \times e^{\frac{1}{2}\sum_j \epsilon_{+,j}\hat{O}_j(\boldsymbol{n}^\perp)} |\psi_A\rangle\,, \tag{6.44}$$

where $\epsilon_{\pm,j} = (b_j \pm a_j)(\boldsymbol{m} \cdot \boldsymbol{n})$ are small factors originating from the new source of imperfection that we have allowed.

Let us now specialize to the case $|\psi_A\rangle = |\psi_c\rangle$ so that $\left|\psi_{\tilde{a}}^{\text{tele}}\right\rangle$ forms an imperfectly teleported Ising critical wavefunction. Section 6.2 showed that, for our previously studied protocol, orienting $\boldsymbol{n}$ in the (x, y) plane optimized resilience to errors in the sense that imperfections were generically marginal (for the highest probability outcomes) or irrelevant (for typical outcomes). Equation (6.44) reveals that misaligning $\boldsymbol{m}$ away from $\boldsymbol{n}^\perp$—which importantly would orient along $\hat{\boldsymbol{z}}$ for such $\boldsymbol{n}$'s—supplements the non-unitary operator with a Z component that comprises a *relevant* imperfection. The heart of the issue is that misalignment of $\boldsymbol{m}$ with this otherwise optimal choice of $\boldsymbol{n}$ causes the entangling unitary to violate $\mathcal{T} \times \mathbb{Z}_2$ symmetry (contrary to the case where the unitary only involves Z operators). This symmetry reduction trickles down to the final teleported state via generation of a σ perturbation to the defect-line action that is no longer symmetry-forbidden. Zooming out, we anticipate that the effects of a still broader class of possible protocol imperfections can be analogously classified on symmetry grounds.

6.4 Average teleported mixed-state

The results of Sec. 6.2 quantify the character of an imperfectly teleported quantum critical state following a *single* protocol implementation. In particular, we saw that the role of imperfections depends on the quantization axis $\boldsymbol{n}$ used for initialization and measurement, as well as Alice's particular measurement outcome. Suppose now that Alice and Bob repeat an (identically) imperfect teleportation protocol many times, and that after each iteration, Bob measures observables with respect to the final teleported state $\left|\psi_{\tilde{a}}^{\text{tele}}\right\rangle$ in Eq. (5.19). Upon averaging over Alice's measurement outcomes $\tilde{a}$, are the nontrivial effects that we captured for a single implementation still observable? Or do imperfections average out, allowing Bob to sample Alice's pristine quantum critical state even if each implementation is flawed?

To address these questions, we examine the mixed-state density matrix

$$\rho^{\text{tele}} = \sum_{\tilde{a}} p_{\tilde{a}} \left|\psi_{\tilde{a}}^{\text{tele}}\right\rangle \left\langle\psi_{\tilde{a}}^{\text{tele}}\right| \tag{6.45}$$

describing an ensemble of imperfectly teleported states, where again $p_{\tilde{a}}$ is the probability of Alice obtaining outcome $\tilde{a}$. Using Eq. (5.18) and inserting resolutions of the identity allows us to write

$$\begin{aligned}\rho^{\text{tele}} = \sum_{\tilde{a},\tilde{a}'} &\left\{\prod_j [\sin(2u)]^{\frac{1-a_j a'_j}{2}}\right\} \langle\psi_c|\tilde{a}',\boldsymbol{n}\rangle\langle\tilde{a},\boldsymbol{n}|\psi_c\rangle \\ &\times |\tilde{a},\boldsymbol{n}\rangle\langle\tilde{a}',\boldsymbol{n}|\,.\end{aligned} \tag{6.46}$$

[Equation (6.46) actually holds for an arbitrary initial state $|\psi_A\rangle$ for Alice upon simply replacing $\psi_c \to \psi_A$ in the corresponding bra and ket.] In the perfect-protocol limit with $u = \pi/4$, the factor in braces becomes unity, and hence the density matrix reduces to the pure-state form $\rho^{\text{tele}} = |\psi_c\rangle\langle\psi_c|$. Here any correlations and entanglement probed by Bob exactly mirror the properties in Alice's original state.

Away from this limit ρ^{tele} describes a mixed state, and the extent to which Bob's correlations match those in Alice's original critical state depends on the operators under consideration. Defining a string of Bob's Pauli operators $\hat{O}_{\mathcal{K}}(\boldsymbol{d}) = \prod_{a=1}^{|\mathcal{K}|} \hat{O}_{j_a}(\boldsymbol{d})$

acting along quantization axis $\boldsymbol{d}$, we in particular find

$$\begin{aligned}
\mathrm{Tr}[\rho^{\mathrm{tele}}\hat{O}_{\mathcal{K}}(\boldsymbol{n})] &= \langle\psi_c|\,\hat{O}_{\mathcal{K}}(\boldsymbol{n})\,|\psi_c\rangle\,, \\
\mathrm{Tr}[\rho^{\mathrm{tele}}\hat{O}_{\mathcal{K}}(\boldsymbol{n}^{\perp})] &= [\sin(2u)]^{|\mathcal{K}|}\,\langle\psi_c|\,\hat{O}_{\mathcal{K}}(\boldsymbol{n}^{\perp})\,|\psi_c\rangle\,, \\
\mathrm{Tr}[\rho^{\mathrm{tele}}\hat{O}_{\mathcal{K}}(\boldsymbol{n}\times\boldsymbol{n}^{\perp})] &= [\sin(2u)]^{|\mathcal{K}|}\,\langle\psi_c|\,\hat{O}_{\mathcal{K}}(\boldsymbol{n}\times\boldsymbol{n}^{\perp})\,|\psi_c\rangle\,.
\end{aligned} \tag{6.47}$$

The first line indicates that Bob exactly recovers critical correlations of operators oriented along $\boldsymbol{n}$ *for any choice of* u. At $u = \pi/4$ this result is clear since the teleportation is perfect in every iteration as already highlighted above. For the opposite extreme, at $u = 0$—where Alice and Bob altogether fail to entangle—the same conclusion persists for the following reason: Upon receiving Alice's measurement outcome, the unitary that Bob implements simply converts his initial product state into Alice's post-measurement product state, i.e., he probes correlations in the wavefunction $\left|\psi^{\mathrm{tele}}\right\rangle = |\tilde{a}, \boldsymbol{n}\rangle$. In effect, Alice has simply farmed out the measurement of correlations in her state to Bob, and hence averaging over outcomes reproduces her critical correlations as captured by the first line of Eq. (6.47). The bottom two lines indicate that Bob also recovers critical correlations of Alice's state for Pauli operators oriented orthogonal to $\boldsymbol{n}$, but with a suppressed amplitude that eventually vanishes as u decreases from $\pi/4$ towards zero.

Consequently, averaging over sequential imperfect teleportation runs indeed allows Bob to measure Alice's pristine universal power-law exponents—even for $\boldsymbol{n} = \hat{\boldsymbol{z}}$ protocols where imperfection constitutes a relevant perturbation with both uniform and typical measurement outcomes. This conclusion relates deeply to the 'post-selection problem' commonly plaguing measurement-induced phenomena that manifest only when following specific measurement outcomes whose probability decays exponentially with system size. From the quantum teleportation perspective, however, the preceding results comprise a feature rather than a bug in that averaging over sequential imperfectly teleported states suppresses errors in correlations that appear in any particular implementation.

In this context, the Rényi entropies we discussed earlier cannot discern between classical and quantum correlations, and hence are not adequate measures of mixed-state entanglement. Instead we consider the entanglement negativity—which does provides a good metric [96, 97]. We refer the interested reader to Section 6.6 for more details about the behavior of entanglement negativity for the mixed-state density matrix ρ^{tele}. The main lesson we learn is that long-range entanglement encoded in the negativity in the pure-state $u = \pi/4$ limit persists with marginal or irrelevant imperfections but is spoiled by relevant imperfections—which is natural given that, in the latter case, individual protocols runs yield area-law entanglement with both uniform and typical measurement outcomes. Thus entanglement in the mixed state is less resilient to imperfections compared to correlations. These results are compatible with those in Ref. [63] regarding the effect of local quantum channels on quantum critical states. Indeed, by analyzing a proxy for the entanglement negativity, the authors find that when their channel corresponds to a relevant perturbation, the negativity obeys an area law.

It is instructive to consider an alternative averaging scheme wherein Bob does not implement the final outcome-dependent unitary in each protocol iteration, and instead directly probes the state $|\psi_{\tilde{a}}\rangle$ given in Eq. (5.15). In this scenario the relevant mixed-state density matrix reads

$$\rho = \sum_{\tilde{a}} p_{\tilde{a}} |\psi_{\tilde{a}}\rangle \langle\psi_{\tilde{a}}| , \tag{6.48}$$

which is simply the average of Bob's penultimate wavefunction. For an arbitrary observable $\hat{O}$ of Bob's qubits, we have $\mathrm{Tr}[\hat{O}\rho] = \langle\tilde{b}, \boldsymbol{n}| \langle\psi_c| U^\dagger \hat{O} U |\psi_c\rangle |\tilde{b}, \boldsymbol{n}\rangle$, where U is the entangling gate employed in the protocol [Eq. (5.13)]. That is, this alternative averaging scheme returns the expectation value of observables evaluated in Alice and Bob's entangled state before she measures her qubits. The analogue of Eq. (6.47) accordingly becomes

$$\begin{aligned}
\mathrm{Tr}[\rho \hat{O}_{\mathcal{K}}(\boldsymbol{n})] &= [\cos(2u)]^{|\mathcal{K}|} \prod_{a=1}^{|\mathcal{K}|} b_{j_a}, \\
\mathrm{Tr}[\rho \hat{O}_{\mathcal{K}}(\boldsymbol{n}^\perp)] &= \left\langle \tilde{b}, \boldsymbol{n} \right| \hat{O}_{\mathcal{K}}(\boldsymbol{n}^\perp) \left| \tilde{b}, \boldsymbol{n} \right\rangle = 0, \\
\mathrm{Tr}[\rho \hat{O}_{\mathcal{K}}(\boldsymbol{n} \times \boldsymbol{n}^\perp)] &= [\sin(2u)]^{|\mathcal{K}|} \prod_{a=1}^{|\mathcal{K}|} b_{j_a} \\
&\quad \times \langle\psi_c| \hat{O}_{\mathcal{K}}(\boldsymbol{n}^\perp) |\psi_c\rangle .
\end{aligned} \tag{6.49}$$

At $u = \pi/4$, only the bottom correlation returns a nonzero result, which we can understand as follows. In any given perfect-protocol implementation, Bob's state $|\psi_{\tilde{a}}\rangle$ corresponds to the pristine quantum critical wavefunction $|\psi_c\rangle$ modified by an outcome-dependent unitary. For the case of $\langle\psi_{\tilde{a}}| \hat{O}_{\mathcal{K}}(\boldsymbol{n} \times \boldsymbol{n}^\perp) |\psi_{\tilde{a}}\rangle$ correlations, the outcome-dependent unitary factors rotate $\hat{O}_{\mathcal{K}}(\boldsymbol{n} \times \boldsymbol{n}^\perp)$ in a manner that depends on the bits $\tilde{b}$ for Bob's initialization but *not* on Alice's outcome $\tilde{a}$. Hence averaging over measurement outcomes for such correlators does not 'scramble' the signal obtained from individual protocol implementations. In contrast, for $\langle\psi_{\tilde{a}}| \hat{O}_{\mathcal{K}}(\boldsymbol{n}) |\psi_{\tilde{a}}\rangle$

or $\langle\psi_{\tilde{a}}|\,\hat{O}_{\mathcal{K}}(\boldsymbol{n}^{\perp})\,|\psi_{\tilde{a}}\rangle$ correlators, the rotation depends on $\tilde{a}$, and averaging over outcomes therefore returns zero. The amplitude for the third correlation in Eq. (6.49) becomes suppressed for an imperfect protocol, while the first correlation actually gets revived (but in a way that reveals no information about Alice's critical correlations). Indeed in the trivial $u = 0$ protocol limit the upper line simply reveals a non-zero expectation value from Bob's initial product state.

Comparing Eqs. (6.47) and (6.49), we see that averaging observables measured after each full teleportation protocol run captures Alice's critical correlations far more completely compared to the scenario where Bob skips applying the final outcome-dependent unitary. One can view the former averaging scheme as amending the latter with a decoding protocol very similar to that studied recently in Ref. [82] (related frameworks are also common in adaptive circuits; see, e.g., Refs. [98, 76, 99, 48]). Interestingly, in the present context such decoding algorithms are automatically incorporated into the quantum teleportation protocols.

6.5 Lessons for robust teleportation of critical states

Quantum teleportation refers to a protocol that transmits an arbitrary, and in-principle unknown, quantum state from Alice to Bob over potentially long distances, enabled by entanglement, measurements, and classical communication. When the entangling and measurement stages are accomplished perfectly, Bob recovers Alice's precise original state up to a unitary transformation that he can decode (i.e., eliminate) upon receiving classical information corresponding to her measurement outcome. In retrospect, it is remarkable that combining entangling unitaries and projective measurements acting on just a subsystem does not yield a general transformation containing both unitary *and* non-unitary operators acting on Alice's original state. Quantum teleportation utilizes a set of fine-tuned operations that renders both the non-unitary and unitary (once the classical channel has been exploited) pieces trivial. From this perspective, it becomes natural that when these operations are subject to imperfections, Bob generically receives a non-unitarily corrupted cousin of Alice's original state—as we showed explicitly in many instances throughout this paper.

Understanding how general many-body wavefunctions behave under imperfect teleportation protocols defines a very broad and rich problem. Relative to the single-qubit case, many-body states exhibit vastly more structure characterized, e.g., by local observables, multi-body correlations, entanglement, symmetry quantum numbers, topological properties, etc. Our study establishes two broadly applicable principles in this realm: First, imperfect teleportation deeply relates to the survival of correlations and entanglement in many-body states subjected to weak measurements. The fact that an imperfect teleportation translates into an imaginary-time evolution holds in general, and applies to any many-body wavefunction, including those showcasing topological order. In fact, those types of imaginary-time evolutions have been previously studied in the literature (see e.g., Refs. [100, 101]), leading to conclusions regarding their robustness under teleportation protocols. The link between imperfect teleportation and the effects of weak measurements on many-body states identifies a potential quantum networking application (see below) for the growing body of literature on the latter topic.

Second, fidelity defined by the overlap between Alice's original wavefunction and the state Bob receives after decoding, while a natural metric for the single-qubit case, need not provide a useful measure for many-body wavefunctions. Fidelity based on wavefunction overlap blurs the distinction between unitary and non-unitary errors, which can be understood as a consequence of an Anderson orthogonality catastrophe: Consider a many-body wavefunction $|\psi\rangle$, and apply to each qubit j an on-site linear transformation $M_j(\epsilon)$ that reduces to the identity as $\epsilon \to 0$. Then the overlap $|\langle\psi| \prod_j M_j(\epsilon)|\psi\rangle|$ is expected to decay exponentially as the number of qubits L increases for any small but finite ϵ—regardless of whether $M_j(\epsilon)$ is unitary or non-unitary. Alternatively, one could consider the 'local fidelity', defined as the L-th root of the global fidelity; this quantity, however, still does not cleanly distinguish between unitary and non-unitary errors that can yield drastically different consequences on many-body states. It is crucial to instead focus on physically meaningful diagnostics of imperfectly teleported many-body wavefunctions that emphasize salient universal features over fine details. Ultimately, Bob may be content receiving an imperfectly teleported wavefunction that overlaps negligibly with Alice's original state, provided that his state belongs to the same phase of matter, exhibits the same symmetries, displays the same universal correlations and entanglement characteristics, and so on. This perspective becomes particularly essential in a scenario where Alice has limited information about her original wavefunction; for instance, she may know only that it is the ground state of some local Hamiltonian whose parameters are uncertain yet realizes a known phase or critical point. The performance of different teleportation protocols could be naturally assessed by exploring how universal features of the most sensitive regions in the phase diagram respond to imperfections.

With this last message in mind, rather than analyzing the detailed character of arbitrary many-body wavefunctions under imperfect teleportation, we specialized to Ising quantum critical states as an illuminating test case. Here universal power-law correlations and long-range entanglement encoded in Alice's original state provide well-motivated quantities for benchmarking the character of an imperfectly teleported wavefunction received by Bob. Moreover, as shown in a collection of recent works [16, 62, 57, 58, 3, 62], quantum critical points are expected to sensitively respond to even weak imperfections by virtue of their gaplessness. The dichotomy between unitary and non-unitary errors becomes especially sharp here: On-site unitary errors preserve both power-law exponents and long-range entanglement, albeit with locally scrambled manifestations. Non-unitary contributions, on the other hand, can qualitatively modify both properties in ways that we elucidated in detail for protocols employing different measurement bases and in different measurement outcome sectors. Specifically, we classified protocol imperfections as relevant, marginal, disguised marginal, or irrelevant depending on their impact on universal correlations and entanglement—though in all of these cases the wavefunction-overlap fidelity decreases exponentially with system size. In a nutshell, fidelity does not distinguish between corruption of short- versus long-distance physics arising from local errors.

En route to establishing these results, we nontrivially extended the theory of measurement-altered criticality by, e.g., relating measurement effects to modifications of full counting statistics; uncovering the phenomenon of disguised marginal perturbations generated under renormalization by naively irrelevant measurement-induced terms; adding a new perspective on decoding protocols put forward in Ref. [82], which quantum teleportation protocols automatically incorporate; and deriving parent Hamiltonians for non-unitarily corrupted states. The last item allowed us to make contact with the physics of long-range interacting chains—whose ground states resemble weakly measured/imperfectly teleported critical wavefunctions—as well as with non-Hermitian systems that even at criticality can display area-law entanglement and an emerging finite correlation length [88]. We hope that many of these tools can be directly exported to understand measurement effects on other systems such as those realizing strongly interacting CFTs and deconfined critical points.

We close with some questions related to future directions. Are there practical applications of teleporting *particular* many-body wavefunctions, e.g., Ising critical states? As one possibility, quantum critical wavefunctions, by virtue of their long-range entanglement, are nontrivial to prepare on quantum hardware. If Alice owns a special-purpose device that allows her to efficiently accomplish the task, she may (for a fee) quantum teleport critical wavefunctions to remote interested parties over quantum networks. To this end, it would be highly desirable to adopt a protocol that optimizes against imperfections following insights from this work. Among the infinite variety of possible many-body wavefunctions, which other classes are particularly interesting to examine through the lens of imperfect teleportation? Is it possible to teleport only a subset of qubits from a many-body wavefunction while still allowing the receiver to back out universal features of the complete state? Finally, can one devise near-term experiments for testing the resilience of various many-body teleportation protocols against errors?

6.6 Technical details and derivations from the teleportation paper

Derivation of imperfectly teleported many-body state

In this Section we derive the form of the imperfectly teleported wavefunction received by Bob, prior to application of the final outcome-dependent unitary. We will consider the generalized protocol from Sec. 6.6, recovering the main result of Sec. 5.3 as a limiting case. For clarity, let us recall the general setup. Alice and Bob prepare the initial wavefunction $|\psi\rangle_A |\psi\rangle_B$, where $|\psi\rangle_B = |\tilde{b}, \boldsymbol{n}\rangle$ is a product state along the common quantization axis $\boldsymbol{n}$. In most of the text we considered Alice's wavefunction is given by the critical state $|\psi_c\rangle$ although this is not necessary. Then, they couple their degrees of freedom via the on-site unitary $U = \prod_j U_j$ with $U_j = \exp(iu\hat{O}^A_j(\boldsymbol{m})\hat{O}^B_j(\boldsymbol{m}))$ with $\boldsymbol{m}$ a unit vector. Finally, Alice measures her qubits along $\boldsymbol{n}$ obtaining the outcome $\tilde{a} = \{a_j\}$ with probability $p_{\tilde{a}}$. All together, a generic setup is parametrized by the tuple $\{\tilde{a}, \tilde{b}, \boldsymbol{n}; \boldsymbol{m}\}$. Similar computations as those leading to Eq. (5.15) in the main text, allow us to write

$$|\psi_{\tilde{a}}\rangle = \frac{1}{\sqrt{p_{\tilde{a}}}} \sum_{N_f=0}^{N} \sum_{i_1<i_2<\cdots<i_N} i^{N_f} \cos^{N-N_f}(u) \sin^{N_f}(u) \prod_{j=1}^{N_f} \hat{O}^B_{i_j}(\boldsymbol{m}) |\tilde{b}, \boldsymbol{n}\rangle \langle \tilde{a}, \boldsymbol{n}| \prod_{j=1}^{N_f} \hat{O}^A_{i_j}(\boldsymbol{m}) |\psi_c\rangle . \tag{6.50}$$

Next, we explicitly include the flipping Pauli operators $\hat{O}^A_j(\boldsymbol{n}^\perp), \hat{O}^B_j(\boldsymbol{n}^\perp)$ mapping $a_j \to -a_j$, $b_j \to -b_j$ respectively by writing

$$\hat{O}^D_j(\boldsymbol{m}) = \hat{O}^D_j(\boldsymbol{m})\hat{O}^D_j(\boldsymbol{n}^\perp)^2 = \underbrace{(\boldsymbol{m}\cdot\boldsymbol{n}^\perp + i\boldsymbol{m}\times\boldsymbol{n}^\perp\cdot\boldsymbol{\sigma})}_{\equiv U^D_j(\boldsymbol{m}\times\boldsymbol{n}^\perp)} \hat{O}^D_j(\boldsymbol{n}^\perp) \tag{6.51}$$

with $D = A, B$. Notice that $U^D_j(\boldsymbol{m}\times\boldsymbol{n}^\perp) = \exp(i\theta\hat{O}_j(\boldsymbol{m}\times\boldsymbol{n}^\perp/||\boldsymbol{m}\times\boldsymbol{n}^\perp||))$ with $\cos(\theta) = \boldsymbol{m}\cdot\boldsymbol{n}^\perp$, $\sin(\theta) = ||\boldsymbol{m}\times\boldsymbol{n}^\perp||$. We also need to relate the product wavefunctions $\left|\tilde{b}, \boldsymbol{n}\right\rangle$, $|\tilde{a}, \boldsymbol{n}\rangle$ by applying a unitary that connects the string of numbers $\tilde{a}$ and $\tilde{b}$. This is achieved via

$$\left|\tilde{b}, \boldsymbol{n}\right\rangle = \underbrace{\left(\prod_{j:a_j\neq b_j} \hat{O}^B_j(\boldsymbol{n}^\perp)\right)}_{\equiv U^B_{\tilde{b}\leftarrow\tilde{a}}} |\tilde{a}, \boldsymbol{n}\rangle = U^B_{\tilde{b}\leftarrow\tilde{a}} |\tilde{a}, \boldsymbol{n}\rangle, \tag{6.52}$$

where we notice that this untary satisfies $(U^B_{\tilde{b}\leftarrow\tilde{a}})^2 = \mathbb{1}$. Bringing all together and up to an overall factor we find

$$\begin{aligned}|\psi_{\tilde{a}}\rangle = \frac{1}{\sqrt{\mathcal{N}}} \sum_{N_f=0}^{N} \sum_{i_1<\cdots<i_N} i^{N_f} \tan^{N_f}(u) \prod_{j=1}^{N_f} U^B_{i_j}(\boldsymbol{m}\times\boldsymbol{n}^\perp) U^B_{\tilde{b}\leftarrow\tilde{a}} \\ \times\left(\prod_{j=1}^{N_f} \hat{O}^B_{i_j}(\boldsymbol{n}^\perp) |\tilde{a}, \boldsymbol{n}\rangle \langle\tilde{a}, \boldsymbol{n}| \prod_{j=1}^{N_f} \hat{O}^A_{i_j}(\boldsymbol{n}^\perp)\right) \prod_{j=1}^{N_f} U^A_{i_j}(-\boldsymbol{m}\times\boldsymbol{n}^\perp) |\psi_c\rangle.\end{aligned} \tag{6.53}$$

where we have used that $[\hat{O}^B_{i_j}(\boldsymbol{n}^\perp), U^B_{\tilde{b}\leftarrow\tilde{a}}] = 0$. To move further we recall that Alice's and Bob's Hilbert spaces are isomorphic and as such, we can evaluate

$$\langle\tilde{a}, \boldsymbol{n}| \prod_{j=1}^{N_f} \hat{O}^A_{i_j}(\boldsymbol{n}^\perp) U^A_{i_j}(-\boldsymbol{m}\times\boldsymbol{n}^\perp) |\psi_c\rangle = \langle\tilde{a}, \boldsymbol{n}| \prod_{j=1}^{N_f} \hat{O}^B_{i_j}(\boldsymbol{n}^\perp) U^B_{i_j}(-\boldsymbol{m}\times\boldsymbol{n}^\perp) |\psi_c\rangle \tag{6.54}$$

on Bob's degrees of freedom. Finally, when summing over all possible values of N_f for any set of locations $i_1 < i_2 < \ldots i_N$, the state $|a', \boldsymbol{n}\rangle \equiv \prod_{j=1}^{N_f} \hat{O}^B_{i_j}(\boldsymbol{n}^\perp) |\tilde{a}, \boldsymbol{n}\rangle \in \mathcal{H}_B$ runs over all possible product states in the local $\boldsymbol{n}$ basis. This allows us to express the Bob's wavefunction as

$$|\psi_{\tilde{a}}\rangle = \frac{1}{\sqrt{\mathcal{N}}} \sum_{a'} (i\tan u)^{N_f(a',\tilde{b})} \prod_{j:a'_j\neq\tilde{b}_j} U^B_j(\boldsymbol{m}\times\boldsymbol{n}^\perp) U^B_{\tilde{b}\leftarrow\tilde{a}} |a', \boldsymbol{n}\rangle \langle a', \boldsymbol{n}| \prod_{j:a'_j\neq\tilde{a}_j} U^B_j(-\boldsymbol{m}\times\boldsymbol{n}^\perp) |\psi_c\rangle. \tag{6.55}$$

where the sum is over binary chains $a' = \{\pm 1\}$ of size N, and $N_f(a', \tilde{b}) = \sum_{j=1}^{N} \frac{1}{2}(1 - a'_j \tilde{b}_j)$ counts the number of entrees where $a'_j \neq \tilde{a}_j$ for a reference string $\tilde{a}$. This expression can be recast as

$$|\psi_{\tilde{a}}\rangle = \frac{1}{\sqrt{\mathcal{N}}} e^{i\frac{\pi}{4}H_{\tilde{b}}(\boldsymbol{n})} e^{-\frac{\alpha}{2}H_{\tilde{b}}(\boldsymbol{n})} \mathcal{U}_{\tilde{b}}(\boldsymbol{m}\times\boldsymbol{n}^\perp) U_{\tilde{b}\leftarrow\tilde{a}} \mathcal{U}^\dagger_{\tilde{a}}(\boldsymbol{m}\times\boldsymbol{n}^\perp) |\psi_c\rangle, \tag{6.56}$$

where the transformation $\mathcal{U}_{\tilde{b}}(\boldsymbol{m}\times\boldsymbol{n}^\perp), \mathcal{U}_{\tilde{a}}(\boldsymbol{m}\times\boldsymbol{n}^\perp)$ are defined via

$$\mathcal{U}_{\tilde{b}}(\boldsymbol{m}\times\boldsymbol{n}^\perp) = \prod_{j=1}^{N} \left[U^B_j(\boldsymbol{m}\times\boldsymbol{n}^\perp)\frac{1}{2}(1 - \tilde{b}_j \hat{O}^B_j(\boldsymbol{n})) + \mathbb{1}\frac{1}{2}(1 + \tilde{b}_j \hat{O}^B_j(\boldsymbol{n}))\right], \tag{6.57}$$

$$\mathcal{U}_{\tilde{a}}(\boldsymbol{m}\times\boldsymbol{n}^{\perp}) = \prod_{j=1}^{N}\left[U_j^B(\boldsymbol{m}\times\boldsymbol{n}^{\perp})\frac{1}{2}(1-\tilde{a}_j\hat{O}_j^B(\boldsymbol{n})) + \mathbb{1}\frac{1}{2}(1+\tilde{a}_j\hat{O}_j^B(\boldsymbol{n}))\right], \tag{6.58}$$

while $H_{\tilde{b}}(\boldsymbol{n}) = -\sum_j \tilde{b}_j\hat{O}_j^B(\boldsymbol{n})$ as defined in the main text. Finally, we can combine $\mathcal{U}_{\tilde{b}}(\boldsymbol{m}\times\boldsymbol{n}^{\perp})$ and $\mathcal{U}_{\tilde{a}}^{\dagger}(\boldsymbol{m}\times\boldsymbol{n}^{\perp})$ using that $\mathcal{U}_{\tilde{b}}(\boldsymbol{m}\times\boldsymbol{n}^{\perp})U_{\tilde{b}\leftarrow\tilde{a}}\mathcal{U}_{\tilde{a}}^{\dagger}(\boldsymbol{m}\times\boldsymbol{n}^{\perp}) = U_{\tilde{b}\leftarrow\tilde{a}}\mathcal{U}_{\tilde{a}}^{\dagger}(\boldsymbol{m}\times\boldsymbol{n}^{\perp})\mathcal{U}_{\tilde{a}}^{\dagger}(\boldsymbol{m}\times\boldsymbol{n}^{\perp})$, leading to the expression

$$|\psi_{\tilde{a}}\rangle = \frac{1}{\sqrt{\mathcal{N}}}U_{\tilde{b}\leftarrow\tilde{a}}e^{i\frac{\pi}{4}H_{\tilde{a}}(\boldsymbol{n})}e^{-\frac{\alpha}{2}H_{\tilde{a}}(\boldsymbol{n})}\left(\mathcal{U}_{\tilde{a}}^{\dagger}(\boldsymbol{m}\times\boldsymbol{n}^{\perp})\right)^2|\psi_c\rangle\,. \tag{6.59}$$

If we restrict to the case $\boldsymbol{m}=\boldsymbol{n}^{\perp}$, then $\mathcal{U}_{\tilde{a}}^{\dagger}(\boldsymbol{m}\times\boldsymbol{n}^{\perp})$ simply reduces to the identity and we recover Eq. (5.15) in the main text.

Probability distribution of the longitudinal field

The goal of this Section is to analyze the probability distribution of the longitudinal field $M_Z = \sum_j Z_j$ in the ground state of the critical Ising model, $P(f,L)$. This amounts to compute the probability density for finding Alice's initial state in a given magnetization sector in the Z-basis in a system of size L. Taking advantage of the results found in [84], we can introduce the scaling variable $r = m/s$, where $s^2 = \langle (M_Z^+)^2\rangle$ is the variance of the order parameter M_Z^+, and using $f = m/L + 1/2 = sr/L + 1/2$, we are able to compute the asymptotic expression for the universal scaling function $\mathcal{F}(r) = sP(sr/L+1/2, L)$. We remark that, in order to have an analytic prediction for $\mathcal{F}(r)$ which captures the main features of the probability distribution, we use the asymptotic result for the generating function of the moments of the distribution, and therefore our result is not very accurate for r close to 0. In particular, we found that

$$\mathcal{F}(r) = \begin{cases} \frac{1.05e^{0.05r^6-0.07r^8}}{|r|^{15/16}}, & |r|\geq 1.44, \\ e^{-0.29r^6+0.11r^4+1.48r^2-2.07} & \text{otherwise.}\end{cases} \tag{6.60}$$

In order to benchmark out this prediction, we have tested it by exact diagonalization of the lattice Hamiltonian (6.1) for system sizes $L = 18, 24, 32$ in Fig. 6.9. As we expected, we observe that the agreement is not perfect close to $r = 0$, but $\mathcal{F}(r)$ correctly captures the shape of the numerical data, which is enough for our purposes.

We numerically checked that $s = 1/2\,L^{7/8}$ and, from the expression of $\mathcal{F}(r)$, we can compute $P(f,L) = \frac{1}{\mathcal{N}}\mathcal{F}(2(f-1/2)L^{1/8})$, where $\mathcal{N}$ is fixed such that the probability

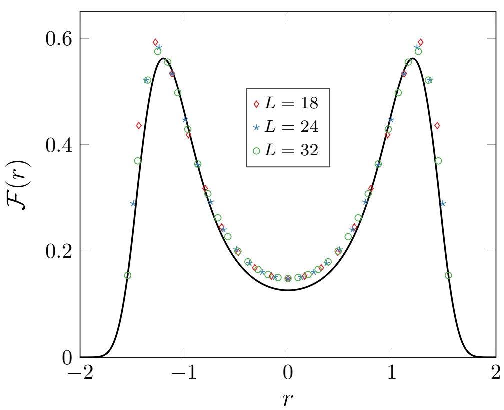

Figure 6.9: **Universal scaling function $\mathcal{F}(r)$.** The solid line in Eq. (6.60), while the symbols are the numerical data obtained using exact diagonalization for a system size $L = 18, 24, 32$.

distribution is correctly normalized. Once we have the result for $P(f, L)$, we can compute $P_{\text{modified}}(\alpha, f, L) = \frac{e^{-2\alpha f L}}{\mathcal{N}'} P(f, L)$ and also study its behavior as a function of α and L. We observe that, for $\alpha = 0$, $P(f, L)$ shows a double peak structure (see Fig. 6.9). As we slightly increase α, the right peak is suppressed, while the left peak drastically moves to the left until it falls outside the region $|r| \leq 1.44$. In particular, in the large L limit, the saddle point analysis reveals that we have a single saddle point at $f^* = 1/2 - \kappa' \alpha^{1/5} L^{1/20}$, which we can observe only until the condition $|r| \leq 1.44$ is satisfied, i.e. for small values of α, L (see the left panel of Fig. 6.10 for $L = 30, 60$). Here κ' is only a numerical prefactor. If we focus on the behavior of the tail of the distribution, i.e. $r < -1.44$, we can observe a peak for $f^* = 1/2 - \kappa'' \alpha$ (when f satisfies the condition $r < -1.44$), where κ'' is a constant, which is pushed towards $f = 0$ as we increase α, while its position does not change by varying L. This can be clearly observed in the middle panel of Fig. 6.10. In order to have a complete analysis of the behavior for f close to 0, we need to know the analytic behavior of $\mathcal{F}(r)$ for any real value of r, which is not accessible from Ref. [84]. However, with the data at our disposal, we can already capture the main qualitative features of the distribution $P_{\text{modified}}(\alpha, f, L)$, checking how the effect of a relevant perturbation can drastically spoil the double-peak structure, shifting the weight of the distribution towards $f^* = 0$.

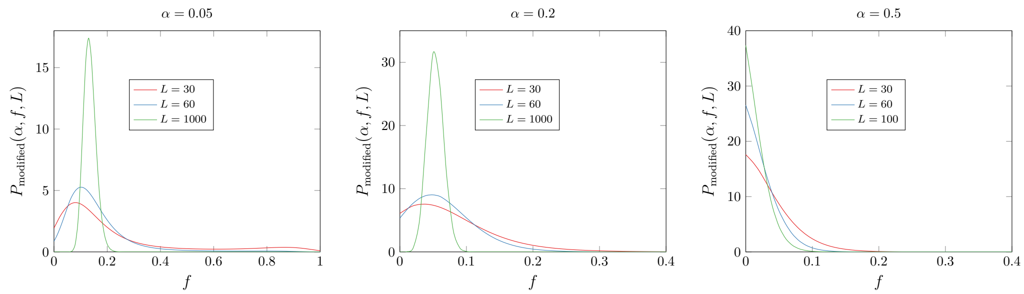

Figure 6.10: $P_{\text{modified}}(\alpha, f, L)$ **as a function of the intensive magnetization sector** f **for different** α **and** L**.** The left panel shows how, for small α and L (30,60) the left peak moves towards left and the double-peak structure is suppressed. As L increases ($L = 1000$), as well as α (middle panel), the peak we observe is due to the tail of the probability distribution $P(f, L)$. Indeed, for $\alpha = 0.2$, its position is not shifted. As we increase α (right panel) $P_{\text{modified}}(\alpha, f, L)$ becomes peaked around $f = 0$, even though the exact details of the probability distribution require a more accurate analytical prediction in Eq. (6.60).

Two-point correlators along the boundary

The goal of this Section is to derive the results in Eq. (6.17) through a field theoretical approach. We can perform a spacetime rotation such that Eq. (6.14) describes a different one-dimensional critical Ising spin chain everywhere in space except at a defect located in the middle point of the chain. Being the defect line relevant, we can think of it as a fixed boundary condition. In order to fix the ideas, we can focus on a system with spatial coordinate $x \in [-L/2, L/2]$ and we aim to study the behavior of the correlation functions of the critical Ising chain along the boundary denoted by $(x = 0, \tau)$, where τ is the imaginary time. We can take advantage of the results found in [102, 103] to write down the magnetization profile with fixed boundary conditions (e.g. spin up (+)) at $x = 0$ and at $x = L/2$, which reads

$$\langle \sigma(x) \rangle_+ = 2^{1/8} \left(\frac{L}{2\pi} \sin \frac{2\pi x}{L} \right)^{-1/8}. \tag{6.61}$$

Notice that here x denotes the distance from the boundary, while what we are really interested in are the correlation functions along the boundary. In the limit $x \to \epsilon$ (it plays the role of an ultra-violet cutoff), it turns out that, along the boundary the expectation value of the magnetic field is just a constant. Similarly, we can exploit the known results for the two-point correlation functions on the half-plane, which read [102]

$$\langle \sigma(1)\sigma(2) \rangle_+ = (4y_1 y_2)^{-1/8} (u + u^{-1})^{1/2}, \tag{6.62}$$

with $u = \left(1+4y_1y_2/r^2\right)^{1/4}$, $r = \sqrt{(v_1-v_2)^2+(y_1-y_2)^2}$. Since the half-space with fixed boundary conditions is transformed into a strip of width $L/2$ with boundary conditions on the edges under the conformal mapping $w = L/(2\pi)\ln z$, we find $z = v+iy = e^{2\pi/L(ix+\tau)} = e^{2\pi\tau/L}(\cos\frac{2\pi x}{L} + i\sin\frac{2\pi x}{L})$. Taking into account that under the conformal transformation $z \to w$, correlation functions of primary operators transform according to

$$\langle\prod_i \phi(z_i,\bar{z}_i)\rangle = \prod_i w'(z_i)^{\Delta_i}\overline{w'(z_i)}^{\bar{\Delta}_i}\langle\prod_i \phi(w_i,\bar{w}_i)\rangle, \tag{6.63}$$

in this way, we can map the result in Eq. (6.62) for the half-space into the strip geometry. It reads

$$\begin{aligned} \langle\sigma(1)\sigma(2)\rangle_+ &= \left(\frac{L}{\pi}\right)^{-1/4}\left(\sin\frac{2\pi x_1}{L}\sin\frac{2\pi x_2}{L}\right)^{-1/8}(u+u^{-1})^{1/2}, \\ u &= 1+4\frac{e^{\frac{2\pi}{L}(\tau_1+\tau_2)}\sin\frac{2\pi x_1}{L}\sin\frac{2\pi x_2}{L}}{D}, \\ D &= \left(e^{\frac{2\pi\tau_1}{L}}\sin\frac{2\pi x_1}{L} - e^{\frac{2\pi\tau_2}{L}}\sin\frac{2\pi x_2}{L}\right)^2 \\ &\quad + \left(e^{\frac{2\pi\tau_1}{L}}\cos\frac{2\pi x_1}{L} - e^{\frac{2\pi\tau_2}{L}}\cos\frac{2\pi x_2}{L}\right)^2. \end{aligned} \tag{6.64}$$

In this way, we get in the limit $x_1 \to x_2 \to \epsilon$ and $L \to \infty$

$$\langle\sigma(1)\sigma(2)\rangle_+ - \langle\sigma(1)\rangle_+\langle\sigma(2)\rangle_+ \simeq \frac{\epsilon^{15/4}}{|\tau_1-\tau_2|^4}. \tag{6.65}$$

Strictly speaking, the right-hand side vanishes when $\epsilon = 0$, which here plays the role of a ultra-violet cutoff. We can repeat the same analysis for the connected two-point correlator of the energy field ε. Its one-point correlation function in the presence of a boundary reads

$$\langle\varepsilon(x)\rangle_+ = \left(\frac{L}{2\pi}\sin\frac{2\pi x}{L}\right)^{-1}, \tag{6.66}$$

while the 2-point correlation function on the complex plane is

$$\begin{aligned} &\langle\varepsilon(1)\varepsilon(2)\rangle_+ = 4\left(\frac{1}{4y_1y_2} + \frac{1}{r^2} - \frac{1}{r^2+4y_1y_2}\right), \\ &\langle\varepsilon(1)\varepsilon(2)\rangle_{+,c} \equiv \langle\varepsilon(1)\varepsilon(2)\rangle_+ - \langle\varepsilon(1)\rangle_+\langle\varepsilon(2)\rangle_+ = 4\left(\frac{1}{r^2} - \frac{1}{r^2+4y_1y_2}\right). \end{aligned} \tag{6.67}$$

By applying the conformal transformation, we can evaluate the connected correlator in the original geometry, and in the limit $x_1 \to x_2 \to \epsilon$ and $L \to \infty$ we get

$$\langle\varepsilon(1)\varepsilon(2)\rangle_{+,c} \simeq \frac{\epsilon^2}{|\tau_1-\tau_2|^4}. \tag{6.68}$$

By doing a spacetime rotation back, both the results in Eqs. (6.65) and (6.68) state that the correlation function for the spin and energy field decay as $1/|x|^4$ along the boundary, which is the content of Eq. (6.17).

Correlators from the perturbative approach

Let us start from computing the correlator $\langle X_i X_{i'} \rangle$ in Eq. (6.18). It can be written as

$$\langle X_i X_{i'} \rangle_c \propto \mathrm{Tr}[e^{-u^2 \sum_{j\neq k} V_{jk} X_j X_k} X_i X_{i'}] \sim u^2 V_{ii'} \sim \frac{u^2}{|i-i'|^4}. \tag{6.69}$$

where the Tr denotes a sum over all possible spin configurations. By expanding the exponential in the limit $u \to 0$, the first non-vanishing contribution is

$$\langle X_i X_{i'} \rangle_c \sim u^2 V_{ii'} \sim \frac{u^2}{|i-i'|^4}. \tag{6.70}$$

If we now consider the correlator $\langle Y_i Y_{i'} \rangle_c$, we get (we denote $|Z\rangle \equiv |z\rangle^{\otimes L}$, $q(j) \equiv q$)

$$\begin{aligned}\langle Y_i Y_{i'} \rangle &= \langle Z| \, e^{-u^2 \sum_{j\neq k, \neq i,i'} V_{jk} X_j X_k} e^{\frac{u^2}{2} X_i \sum_{k\neq i} V_{jk} X_k} e^{\frac{u^2}{2} X_{i'} \sum_{k\neq i'} V_{jk} X_k} e^{2iuqX_i + 2iuqX_{i'}} Y_i Y_{i'} \, |Z\rangle \\ &\propto \mathrm{Tr}\left[e^{-u^2 \sum_{j\neq k, \neq i,i'} V_{jk} X_j X_k} e^{\frac{u^2}{2} X_i \sum_{k\neq i} V_{jk} X_k} e^{\frac{u^2}{2} X_{i'} \sum_{k\neq i'} V_{jk} X_k} e^{2iuqX_i + 2iuqX_{i'}} X_i X_{i'} \right] \sim u^2 V_{ii'}.\end{aligned} \tag{6.71}$$

where we have used that $Y = -iXZ$. Finally, using $Z_i Z_{i'} \, |Z\rangle = |Z\rangle$, we get

$$\begin{aligned}\langle Z_i Z_{i'} \rangle_c &= \langle Z| \, e^{-u^2 \sum_{j\neq k, \neq i,i'} V_{jk} X_j X_k} e^{\frac{u^2}{2} X_i \sum_{k\neq i} V_{jk} X_k} e^{\frac{u^2}{2} X_{i'} \sum_{k\neq i'} V_{jk} X_k} e^{2iuqX_i + 2iuqX_{i'}} Z_i Z_{i'} \, |Z\rangle \\ &\propto \mathrm{Tr}\left[e^{-u^2 \sum_{j\neq k, \neq i,i'} V_{jk} X_j X_k} e^{\frac{u^2}{2} X_i \sum_{k\neq i} V_{jk} X_k} e^{\frac{u^2}{2} X_{i'} \sum_{k\neq i'} V_{jk} X_k} e^{2iuqX_i + 2iuqX_{i'}} \right] \sim u^4 V_{ii'}.\end{aligned} \tag{6.72}$$

We can repeat the computations above starting from Eq. (6.29). The easiest correlator to compute is

$$\langle Z_i Z_{i'} \rangle = \mathrm{Tr}[e^{-u^2 \sum_{j\neq k} V_{jk} Z_j Z_k} Z_i Z_{i'}] \sim u^2 V_{ii'} \sim \frac{u^2}{|i-i'|}. \tag{6.73}$$

If we now consider the correlator $\langle X_i X_{i'} \rangle_c$, we get (we denote again $|X\rangle \equiv |x\rangle^{\otimes L}$)

$$\begin{aligned}\langle X_i X_{i'} \rangle_c = \langle X| \, & e^{-\frac{u^2}{2} \sum_{j\neq k} V_{jk} Z_j Z_k} X_i X_{i'} \\ & \times e^{-\frac{u^2}{2} \sum_{j\neq k} V_{jk} Z_j Z_k} \, |X\rangle \, .\end{aligned} \tag{6.74}$$

Observing that $X_j e^{-\frac{u^2}{2} Z_j \sum_{k\neq j} V_{jk} Z_k} = e^{\frac{u^2}{2} Z_j \sum_{k\neq j} V_{jk} Z_k} X_j$, we get

$$\begin{aligned}\langle X_i X_{i'} \rangle_c &= \langle X| \, e^{-u^2 \sum_{j\neq k, \, j,k\neq i,i'} V_{jk} Z_j Z_k} e^{\frac{u^2}{2} Z_i \sum_{k\neq i} V_{jk} Z_k} e^{\frac{u^2}{2} Z_{i'} \sum_{k\neq i'} V_{jk} Z_k} X_i X_{i'} \, |X\rangle \\ &= \mathrm{Tr}\left[e^{-u^2 \sum_{j\neq k, \, j,k\neq i,i'} V_{jk} Z_j Z_k} e^{\frac{u^2}{2} Z_i \sum_{k\neq i} V_{jk} Z_k} e^{\frac{u^2}{2} Z_{i'} \sum_{k\neq i'} V_{jk} Z_k} \right] \sim u^4 V_{ii'}^2.\end{aligned} \tag{6.75}$$

where we have used that $X_i X_{i'} |X\rangle = |X\rangle$. We remark that this result not only properly captures the algebraic behavior of $\langle X_i X_{i'}\rangle_c$ in Eq. (6.28), but also the amplitude, since by using that $\alpha = -\ln[\tan(u)]$, α behaves at leading order in u as $\mathrm{sech}(2\alpha)^2 = u^4$. The result in Eq. 6.75 refers to the connected correlator, since the disconnected part vanishes. Finally, in order to compute $\langle Y_i Y_{i'}\rangle$, we use that $Y_i Y_{i'} |X\rangle = -Z_i Z_{i'} |X\rangle$ and therefore we can exploit the result in Eq. (6.73), $\langle Y_i Y_{i'}\rangle \sim u^2 V_{ii'}$, in agreement with Eq. (6.28).

Entanglement entropy from the perturbative approach

We consider the entanglement entropy of the teleported wavefunction,

$$|\psi\rangle = \exp(\frac{\alpha}{2}\sum_j \hat{O}_j(\boldsymbol{n}))\,|\psi_A\rangle \quad \text{(up to normalization)}, \tag{6.76}$$

where $\hat{O}(\boldsymbol{n})$ is a Pauli operator along $\boldsymbol{n}$ axis and $|\psi_A\rangle$ is the initial state (which in this paper is the ground state of a critical Ising chain). In the $\alpha \to \infty$ limit, it becomes a product state for finite systems. However, the $\alpha < \infty$ case is non-trivial and we can compute the second Rényi entropy perturbatively.

Let us assume $\alpha > 0$ and define $|0\rangle \equiv \left|\tilde{b}, \boldsymbol{n}\right\rangle$ to be the product state of one-site eigenstates with $\hat{O}(\boldsymbol{n})$ eigenvalue $+1$. We denote by

$$|j, k, l, \ldots\rangle \equiv \hat{O}_j(\boldsymbol{n}^\perp)\hat{O}_k(\boldsymbol{n}^\perp)\hat{O}_l(\boldsymbol{n}^\perp)\ldots|0\rangle \tag{6.77}$$

the state with spin flips on the j-, k-, l-$\ldots$-th sites. The teleported state can be written as

$$|\psi\rangle = \exp\left(\frac{\alpha}{2}\sum_j \hat{O}_j(\boldsymbol{n})\right)|\psi_A\rangle \tag{6.78}$$

$$= \exp\left(\frac{\alpha}{2}L\right)\left[\langle 0|\psi_A\rangle|0\rangle + e^{-\alpha}\sum_j \langle j|\psi_A\rangle|j\rangle + e^{-2\alpha}\sum_{j<k}\langle j,k|\psi_A\rangle|j,k\rangle + \cdots\right]. \tag{6.79}$$

where L is the length of the system. In the nearly-projective measurement limit ($\alpha \gg 1$), one can neglect the terms in the ellipsis since they are exponentially suppressed by α. After keeping only the first three terms on the right-hand-side (RHS) and defining

$$q(j,k,l\ldots) = \frac{\langle j,k,l,\ldots|\psi_A\rangle}{\langle 0|\psi_A\rangle}, \tag{6.80}$$

we simplify the above form as

$$|\psi\rangle = |0\rangle + u\sum_j q(j)\,|j\rangle + u^2\sum_{j<k} q(j,k)\,|j,k\rangle + O(u^3), \tag{6.81}$$

$$|\psi\rangle_{\text{approx}} = H_{\text{eff}}\,|0\rangle\,, \tag{6.82}$$

$$H_{\text{eff}} = 1 + u\sum_j q(j)\hat{O}_j(\boldsymbol{n}^\perp) \tag{6.83}$$

$$+\, u^2\sum_{j<k} q(j,k)\hat{O}_j(\boldsymbol{n}^\perp)\hat{O}_k(\boldsymbol{n}^\perp). \tag{6.84}$$

where the first line is written up to normalization. The operator H_{eff} can be written as a matrix product operator (MPO) [104] with bond dimension $L+1$, $H_{\text{eff}} = W_1 W_2 \cdots W_L$, where W's are operator-valued matrices:

$$W_i = \begin{pmatrix} \mathbb{1} & 0 & \cdots & 0 & \hat{O}_i(\boldsymbol{n}^\perp) & uq(i)\hat{O}_i(\boldsymbol{n}^\perp) \\ 0 & \mathbb{1} & \cdots & 0 & 0 & u^2q(1,i)\hat{O}_i(\boldsymbol{n}^\perp) \\ \vdots & \vdots & \ddots & \vdots & 0 & u^2q(2,i)\hat{O}_i(\boldsymbol{n}^\perp) \\ 0 & 0 & \cdots & \mathbb{1} & 0 & u^2q(i-1,i)\hat{O}_i(\boldsymbol{n}^\perp) \\ 0 & 0 & \cdots & 0 & 0 & \mathbb{1} \end{pmatrix} \tag{6.85}$$

for $1 < i < L$ is an $(i+1)\times(i+2)$ matrix, and on the first and last sites

$$W_1 = \left(\mathbb{1},\quad \hat{O}_1(\boldsymbol{n}^\perp),\quad \mathbb{1} + uq(1)\hat{O}_1(\boldsymbol{n}^\perp)\right),\quad W_L = \begin{pmatrix} uq(L)\hat{O}_L(\boldsymbol{n}^\perp) \\ u^2q(1,L)\hat{O}_L(\boldsymbol{n}^\perp) \\ u^2q(2,L)\hat{O}_L(\boldsymbol{n}^\perp) \\ \vdots \\ u^2q(L-1,L)\hat{O}_L(\boldsymbol{n}^\perp) \\ \mathbb{1} \end{pmatrix}. \tag{6.86}$$

Therefore, the entanglement entropy of $|\psi\rangle_{\text{approx}}$ is upper bounded by $O(\ln(L))$; hence the following calculation of entanglement entropy only makes sense when u is small enough such that $S \lesssim \ln(L)$.

For a system bipartitioned into subsystems R and $\bar{R}$, the 2nd Rényi entanglement entropy is defined to be,

$$S_R^{(2)} \equiv -\ln\frac{\mathrm{Tr}(\rho_R^2)}{\mathrm{Tr}(\rho_R)^2} \tag{6.87}$$

where ρ_R is the reduced density matrix for subsystem R. From now on, for simplicity we assume all $q(j,k,l...)$ are real. One can then write down

$$\begin{aligned}\rho_R = &\left[1+u^2\sum_{k\in\bar{R}}q(k)^2+u^4\sum_{j<k\in\bar{R}}q(j,k)^2\right]|0\rangle\langle 0| + \sum_{j\in R}\left[uq(j)+u^3\sum_{k\in\bar{R}}q(k)q(j,k)\right](|0\rangle\langle j|+|j\rangle\langle 0|)\\ &+\sum_{j\in R}\sum_{j'\in R}\left[u^2q(j)q(j')+u^4\sum_{k\in\bar{R}}q(j,k)q(j',k)\right]|j\rangle\langle j'| + u^2\sum_{j<k\in R}q(j,k)(|0\rangle\langle j,k|+|j,k\rangle\langle 0|)\\ &+u^3\sum_{j'\in R}\sum_{j<k\in R}q(j')q(j,k)\left(|j'\rangle\langle j,k|+|j,k\rangle\langle j'|\right)+u^4\sum_{j<k\in R}\sum_{j'<k'\in R}q(j,k)q(j',k')\,|j,k\rangle\langle j',k'|\,.\end{aligned} \tag{6.88}$$

The second Rényi entropy takes a surprisingly simple form,

$$S_R^{(2)} = 2u^4\sum_{j\in R}\sum_{k\in\bar{R}}[q(j,k)-q(j)q(k)]^2+O(u^6). \tag{6.89}$$

When the subsystem R consists of ℓ consecutive sites and $a_{jk}-a_ja_k\sim|j-k|^{-\kappa}$ decays as a power law with exponent κ, one can show by replacing the summation by integrals (i.e. going to the continuous limit),

$$S_R^{(2)} \simeq 2u^4\sum_{1\le j\le\ell}\sum_{(\ell+1)\le k\le L}\frac{1}{|j-k|^{2\kappa}} \tag{6.90}$$

$$\approx 2u^4\int_0^\ell dx\int_{\ell+1}^L dy\,\frac{1}{|x-y|^{2\kappa}} = 2u^4\,F_\kappa(\ell,L). \tag{6.91}$$

where we consider an open chain, $R=[0,\ell]$, $\bar{R}=[\ell+1,L]$ and

$$F_\kappa(\ell,L)\equiv\frac{-1+\ell^{2-2\kappa}-L^{2-2\kappa}+(L-\ell+1)^{2-2\kappa}}{2(1-2\kappa)(\kappa-1)}. \tag{6.92}$$

For a segment in an infinite chain, one has $S_R^{(2)}\simeq 4u^4\sum_{1\le j\le\ell}\sum_{(\ell+1)\le k<\infty}\frac{1}{|j-k|^{2\kappa}}$, which is the case of Eq. 6.30.

We can then consider different cases:

1. For $\kappa>1$, the half-chain entropy

$$\max_\ell F_\kappa(\ell,L) = F_\kappa\left(\frac{L}{2},L\right) = \frac{L^{2-2\kappa}-2\left(\frac{L}{2}+\frac{1}{2}\right)^{2-2\kappa}+1}{2(2\kappa-1)(\kappa-1)} \tag{6.93}$$

converges to a finite value in the thermodynamic limit. Therefore the system satisfies the area law.

2. For $\kappa=1$, we find

$$F_1(\ell,L) = \left.\frac{\partial_\kappa[-1+\ell^{2-2\kappa}-L^{2-2\kappa}+(L-\ell+1)^{2-2\kappa}]}{\partial_\kappa[2(1-2\kappa)(\kappa-1)]}\right|_{\kappa=1} = \ln(\ell(L-\ell)/L), \tag{6.94}$$

indicating that the entanglement entropy grows logarithmically in the subsystem size.

3. For $0 < \kappa < 1$, we find

$$F_\kappa(L/2, L) = \frac{L^{2-2\kappa} - 2\left(\frac{L}{2} + \frac{1}{2}\right)^{2-2\kappa} + 1}{2(2\kappa - 1)(\kappa - 1)} \propto L^{2-2\kappa}, \tag{6.95}$$

and, for small ℓ,

$$F_\kappa(\ell, L) \approx \ell^{2-2\kappa} + (2 - 2\kappa)L^{1-2\kappa}\ell + \cdots . \tag{6.96}$$

This approximation is only valid when $S_2 \lesssim \ln(L)$; otherwise u must scale with system size as $u \lesssim L^{(\kappa-1)/2} \ln^{1/4}(L)$.

When $\boldsymbol{n} = \hat{\boldsymbol{x}}$, we have $\kappa = 1$. Using that $V_{jk} = \frac{1}{\pi|j-k|}$, we find that the entanglement scaling remains logarithmic but $c^{(2)}_{\text{eff}}$ for the 2nd Rényi entropy scales as u^4, which is consistent with the derivation in Section. 6.6 (see also Eq. (6.30) for the result in the thermodynamic limit). For the Z measurement, $\kappa = 4$. Therefore the teleported state satisfies entanglement area law at large α, although concomitant with power-law decaying 2-point correlations. In Fig. 6.11, we numerically computed the entanglement entropies in Eq. 6.76 by DMRG for $\boldsymbol{n} = \hat{\boldsymbol{z}}$ and $\hat{\boldsymbol{x}}$, and check that they are close to the prediction from perturbation theory in Eq. 6.89.

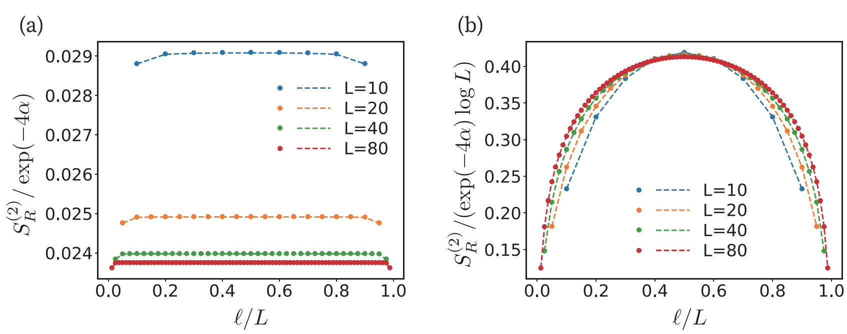

Figure 6.11: **Second Rényi entanglement entropy** for the state in Eq. 6.76 with $\alpha = 4$ and (a) $\boldsymbol{n} = \hat{\boldsymbol{z}}$ or (b) $\boldsymbol{n} = \hat{\boldsymbol{x}}$. The dots refer to the data obtained by DMRG on a periodic chain and dashed lines refer to the analytical prediction by Eq. 6.89.

MPS representation for a relevant imperfection

Given the atypical properties found in the presence of a relevant imperfection in Sec. 6.2, it is interesting to ask whether the imperfectly teleported state received by

Bob can be efficiently expressed as an MPS. An MPS with bond dimension χ on a Hilbert space $(\mathbb{C}^d)^{\otimes L}$ takes the form

$$\left|\psi_\chi\right\rangle = \sum_{s_1,s_2\ldots,s_L=1}^{d} \mathrm{tr}\left(A_1^{[s_1]}A_2^{[s_2]}\cdots A_L^{[s_L]}\right)|s_1,s_2\ldots,s_L\rangle\,, \tag{6.97}$$

where $\{A_j^{[s_j]}\}_{j,s_j}$ are $\chi\times\chi$ matrices. Hence, an MPS $\left|\psi_\chi\right\rangle$ has entanglement entropy less than $\ln\chi$ for any spatial cut. While arbitrary states can be described by an MPS with exponentially large (in L) bond dimension, one can only efficiently calculate expectation values of spatially local observables when such states can be approximated by an MPS with sufficiently small bond dimension. Hence, whether such an approximation exists poses a very relevant question.

For 1D systems with strictly local interactions and a finite excitation gap, it has been rigorously proven that correlations decay exponentially and that the entanglement entropy satisfies an area law [105]—the latter justifying efficient description of ground states for such systems using MPS's. One then wonders to which extent relaxing strict locality can modify these conclusions, as relevant, e.g., for systems with van der Waals interactions or, as we have shown here, imperfectly teleported quantum critical states. Reference [89] proved that the (non-degenerate) ground state $|\psi\rangle$ of generic 1D gapped systems with interactions decaying as a power law $\sim 1/|i-j|^n$ exhibits area-law entanglement for $n>2$. Evidently the gap condition imposes stronger constraints on the entanglement structure than on the decay of correlations. This important conclusion further implies that there exists an MPS $\left|\psi_\chi\right\rangle$ with bond dimension $\chi=\exp[c\ln^{5/2}(1/\delta)]$ and $c\sim O(1)$ such that

$$||\mathrm{tr}_{X^c}\left(\left|\psi_\chi\right\rangle\left\langle\psi_\chi\right|\right)-\mathrm{tr}_{X^c}\left(|\psi\rangle\langle\psi|\right)||_1\leq\delta|X| \tag{6.98}$$

for an arbitrary concatenated subregion of size $|X|$, with $||\cdot||_1$ the trace norm and δ the approximation error. Applying these results to our problem, we conclude that $|\psi_{\tilde a}\rangle$—which is the non-degenerate ground state of the gapped Hamiltonian in Eq. (6.21) with $\sim 1/|j-k|^4$ interactions—can be efficiently approximated by an MPS. (And since $|\psi_{\tilde a}\rangle$ is the same as Bob's final wavefunction $\left|\psi_{\tilde a}^{\mathrm{tele}}\right\rangle$ up to a product of local unitary operators, the same conclusion holds for the latter.)

Effective central charge calculation for x-basis measurement

Let us consider the teleported wavefunction in Eq. (6.22). We can study it as a quantum quench protocol in which the system at time $t=0$ is initialized in the ground state $|\psi_c\rangle$ of the critical Ising chain of length L with periodic boundary conditions and then is let evolve under the action of the non-Hermitian effective Hamiltonian

$$\left|\psi_{\tilde{a}}^{\text{tele}}\right\rangle = \frac{e^{-itH_+(x)}\,|\psi_c\rangle}{||e^{-itH_+(x)}\,|\psi_c\rangle\,||}, \quad H_+(x) = i\sum_j X_j, \tag{6.99}$$

with $t = \alpha/2$. As already mentioned in the main text, this time-evolution can be exactly computed once the model is mapped to free fermions $(c, c^\dagger)$ through Jordan-Wigner transformation, followed by Fourier transform into momentum space. Indeed, it can be written as

$$H_+(x) = \sum_k \left[\begin{pmatrix} c_k^\dagger & c_{-k} \end{pmatrix} M \begin{pmatrix} c_k \\ c_{-k}^\dagger \end{pmatrix} \right] = \sum_k H_k \tag{6.100}$$

where the momenta are semi-integer

$$k = -\frac{L}{2} + \frac{1}{2}, \ldots, -\frac{1}{2}, \frac{1}{2}, \ldots, \frac{L}{2} - \frac{1}{2}, \tag{6.101}$$

(even parity sector) and

$$M = 2\begin{pmatrix} i & 0 \\ 0 & -i \end{pmatrix} \tag{6.102}$$

Since the state $|\psi_c\rangle$ is translational invariant and with a well defined parity, then its dynamics can be decomposed in

$$\begin{gathered} |\psi_c\rangle = \prod_k |\psi_k(t=0)\rangle\,, \quad \left|\psi_{\tilde{a}}^{\text{tele}}\right\rangle = \prod_k |\psi_k(t=\alpha/2)\rangle \\ |\psi_k(t=\alpha/2)\rangle = \frac{\left|\tilde{\psi}_k(t=\alpha/2)\right\rangle}{||\left|\tilde{\psi}_k(t=\alpha/2)\right\rangle||}, \quad i\frac{d}{dt}\left|\tilde{\psi}_k(t)\right\rangle = H_k\left|\tilde{\psi}_k\right\rangle \end{gathered} \tag{6.103}$$

where the k-momentum states are expressed as $\left|\tilde{\psi}_k\right\rangle = u_k(t)\,|0\rangle + v_k(t) c_k^\dagger c_{-k}^\dagger\,|0\rangle$. Thus, we have to solve a differential equation

$$i\frac{d}{dt}\begin{pmatrix} u_k(t) \\ v_k(t) \end{pmatrix} = -M\begin{pmatrix} u_k(t) \\ v_k(t) \end{pmatrix} \tag{6.104}$$

with given initial conditions $u_k(0), v_k(0)$ fixed by $|\psi_c\rangle$. By solving it, we find

$$\begin{aligned} u_k(t=\alpha/2) &= -\frac{1}{2}e^{-\alpha}\sqrt{2 - 2|\sin(\pi k/L)|}, \\ v_k(t=\alpha/2) &= e^{\alpha}\frac{\sin(2\pi k/L)}{2\sqrt{(1-\cos(2\pi k/L))(1-|\sin(\pi k/L)|)}}. \end{aligned} \tag{6.105}$$

Exploiting the Guassianity of the state (6.99) and employing Wick's theorem, the correlation functions and the entanglement properties can be fully encoded in the two-point function of the Majorana fermions, which are given by the operators $\gamma_{A,j} = c_j + c_j^\dagger$, $\gamma_{B,j} = i(c_j^\dagger - c_j)$. Then, we find

$$\begin{aligned}
&\langle \gamma_{A,n}\gamma_{A,m}\rangle = \langle \gamma_{B,n}\gamma_{B,m}\rangle = 0 \\
&\langle \gamma_{A,n}\gamma_{B,m}\rangle = \langle \gamma_{B,m}\gamma_{A,n}\rangle^* = \frac{1}{L}\sum_k e^{2\pi i k/L(n-m)}\frac{u_k^2 - v_k^2 - 2iu_k v_k}{u_k^2 + v_k^2}
\end{aligned} \tag{6.106}$$

Taking the thermodynamic limit $L \to \infty$, the above sum is transformed into an integral, and we have

$$V \equiv \left\langle \begin{pmatrix} \gamma_{A,n} \\ \gamma_{B,n} \end{pmatrix} \begin{pmatrix} \gamma_{A,m} & \gamma_{B,m} \end{pmatrix} \right\rangle = \int_{-\pi}^{\pi} \frac{d\theta}{2\pi} e^{i\theta(n-m)} \begin{pmatrix} 0 & \frac{u_\theta^2 - v_\theta^2 - 2iu_\theta v_\theta}{u_\theta^2 + v_\theta^2} \\ \frac{u_\theta^2 - v_\theta^2 + 2iu_\theta v_\theta}{u_\theta^2 + v_\theta^2} & 0 \end{pmatrix}$$
$$\int_{-\pi}^{\pi} \frac{d\theta}{2\pi} e^{i\theta(n-m)} \mathcal{G}(\theta), \tag{6.107}$$

where we took $2\pi k/L \to \theta$ in Eq. (6.105). The quantity $\mathrm{Tr}(\rho_A^n)$ can be computed from the two-point correlation matrix V introduced in Eq. (6.107) [106]. More specifically,

$$\mathrm{Tr}\rho_A^n = \det\left[\left(\frac{I + V_A}{2}\right)^n + \left(\frac{I - V_A}{2}\right)^n\right], \tag{6.108}$$

where V_A denotes the restriction of V to the subsystem A. If we take into account that the eigenvalues of V_A lie on the real interval $[-1, 1]$ and we use the residue theorem, then the previous expression can be rewritten as the contour integral

$$\frac{1}{1-n}\ln \mathrm{Tr}_A^{(n)} = \frac{1}{2\pi i}\lim_{\varepsilon\to 1^+}\oint_C f_n(\lambda/\varepsilon)\frac{d}{d\lambda}\ln D_A(\lambda)d\lambda, \tag{6.109}$$

where the integration contour C encloses the interval $[-1, 1]$,

$$f_n(\lambda) = \frac{1}{1-n}\ln\left[\left(\frac{1+\lambda}{2}\right)^n + \left(\frac{1-\lambda}{2}\right)^n\right], \tag{6.110}$$

and $D_f(\lambda)$ denotes the characteristic polynomial of V_A, i.e. $D_f(\lambda) = \det(\lambda I - V_A)$.

Here we will focus on a single interval of ℓ contiguous sites. In this case, the restriction V_A is a $2\ell \times 2\ell$ block Toeplitz matrix with symbol the 2×2 matrix $\mathcal{G}(\theta)$ of Eq. (6.107). To deduce the large ℓ behaviour of $D_f(\lambda)$ and, therefore, of $\mathrm{Tr}\rho_A^n$, we will apply the results on the asymptotic behaviour of block Toeplitz determinants. In particular, if the symbol $\mathcal{G}_\lambda(\theta) = \lambda I - \mathcal{G}(\theta)$ satisfies $\det \mathcal{G}_\lambda(\theta) \neq 0$ and is a piecewise continuous function in θ with jump discontinuities at $\theta = \theta_1, \ldots, \theta_R$, then

$$\ln D_f(\lambda) = \frac{\ell}{4\pi}\int_{-\pi}^{\pi}\ln\det \mathcal{G}_\lambda(\theta)d\theta + \frac{\ln \ell}{4\pi^2}\sum_{r=1}^{R}\mathrm{Tr}[\ln \mathcal{G}_{\lambda,r}^-(\mathcal{G}_{\lambda,r}^+)^{-1}]^2 + O(1), \tag{6.111}$$

where $\mathcal{G}^{\pm}_{\lambda,r}$ are the lateral limits of $\mathcal{G}_\lambda(\theta)$ in the jump discontinuity at $\theta = \theta_r$,

$$\mathcal{G}^{\pm}_{\lambda,r} = \lim_{\theta\to\theta_r^{\pm}} \mathcal{G}_\lambda(\theta). \tag{6.112}$$

Eq. (6.111) is a generalisation of the Fisher-Hartwig conjecture for block Toeplitz determinants [107, 108]. If the symbol $\mathcal{G}_\lambda(\theta)$ has continuous entries in θ, then there is no logarithmic term in the asymptotic expansion of $\ln D_f(\lambda)$, and Eq. (6.111) simplifies to

$$\ln D_f(\lambda) = \frac{\ell}{4\pi}\int_{-\pi}^{\pi} \ln\det \mathcal{G}_\lambda(\theta) d\theta + O(1). \tag{6.113}$$

This is the Szegő-Widom theorem [24]. Now the source of discontinuities in the symbol $\mathcal{G}_\lambda(\theta)$ is around $\theta = 0$, with lateral limits

$$\mathcal{G}^{\pm}_{\lambda,0} = \lambda I + \tanh(2\alpha)X \pm \mathrm{sech}(2\alpha)Y, \tag{6.114}$$

where X and Y are the Pauli matrices. According to Eq. (6.111), this discontinuity gives rise to a logarithmic term in $\ln D_f(\lambda)$. If we plug Eq. (6.114) into Eq. (6.111), we find that

$$\ln D_f(\lambda) = \ln\left[\lambda^2 - 1\right] + b_0(\lambda)\ln\ell + O(1), \tag{6.115}$$

with

$$b_0(\lambda) = \frac{2}{\pi^2}\left(\ln\frac{\sqrt{\lambda^2 - \tanh^2(2\alpha)} + \mathrm{sech}(2\alpha)}{\sqrt{\lambda^2 - 1}}\right)^2. \tag{6.116}$$

The linear term is obtained from the integral

$$\lim_{\varepsilon\to 1^+}\oint_C f_n(\lambda/\varepsilon)\frac{\lambda}{\lambda^2 - 1}d\lambda, \tag{6.117}$$

which is zero by applying the Cauchy theorem, since $f_n(\pm 1) = 0$. Therefore, we obtain the following asymptotic behaviour for the Rényi entropies

$$S_R^{(n)} = \frac{c_{\text{eff}}^{(n)}}{6}\left(\frac{n+1}{n}\right)\ln\ell + O(1), \tag{6.118}$$

where the coefficient $c_{\text{eff}}^{(n)}$ is given by the contour integral

$$c_{\text{eff}}^{(n)} = \frac{6n}{4\pi i(1+n)}\lim_{\varepsilon\to 1^+}\oint_C f_n(\lambda/\varepsilon)\frac{db_0(\lambda)}{d\lambda}d\lambda, \tag{6.119}$$

which, following similar steps as in Ref.[92], can be reduced to the real integral in Eq. (6.25).

Beyond the computation of the entanglement entorpy, we are also interested in computing the spin-spin correlation functions, for which we have to take into account the non-local effects of the Jordan-Wigner transformation. Using them and Wick's Theorem, we can expand the spin expectation values in terms of two-point correlation. In particular, for the X correlators, we find

$$\langle X_0 X_j \rangle = H(0)^2 - H(j)H(-j), \quad H(j) = \langle \gamma_{B,n}\gamma_{A,m} \rangle. \tag{6.120}$$

Therefore the connected two-point function reads

$$\langle X_0 X_j \rangle_c = \int_{-\pi}^{\pi} \frac{d\theta}{2\pi} e^{ij\theta} \mathcal{M}(\theta,\alpha), \tag{6.121}$$

$$\mathcal{M}(\theta,\alpha) = \frac{\begin{array}{c}\left|\sin\left(\frac{k}{2}\right)\right| \left(4 + 4ie^{2\alpha}\cot\left(\frac{k}{2}\right)\right) - 2ie^{2\alpha}\sin k \\ + e^{4\alpha}(\cos k + 1) + \cos k - 3\end{array}}{4\left|\sin\left(\frac{k}{2}\right)\right| - e^{4\alpha}(\cos k + 1) + \cos k - 3}. \tag{6.122}$$

We can solve explicitly this integral and in the limit of large distances, j, we find

$$\langle X_i X_j \rangle_c = \frac{\operatorname{sech}^2(2\alpha)}{\pi^2 |i-j|^2}. \tag{6.123}$$

The other two correlators involve a non-local string of operators and their Wick expansion can be expressed as determinants of matrices with elements given by all nontrivial contractions,

$$\begin{aligned} \langle Z_l Z_m \rangle &= \det |H(i-j)|_{i=l\ldots m-1}^{j=l+1\ldots m}, \\ \langle Y_l Y_m \rangle &= \det |H(i-j)|_{i=l+1\ldots m}^{j=l\ldots m-1}. \end{aligned} \tag{6.124}$$

In order to derive the scaling behavior of these correlators, we can apply again the Fisher-Hartwig conjecture in Eq. (6.111); now our symbol $\mathcal{M}(k,\alpha)$ is not a matrix but a function. For our purpose we compute determinants of the matrices

$$M^Z_{kj} = \int_{-\pi}^{\pi} \frac{d\theta}{2\pi} e^{i(j-k)\theta} \mathcal{M}(\theta,\alpha), \tag{6.125}$$

$$M^Y_{kj} = \int_{-\pi}^{\pi} \frac{d\theta}{2\pi} e^{i(j-k)\theta} \widetilde{\mathcal{M}}(\theta,\alpha), \qquad k = l,\ldots,m-1, \quad j = l+1,\ldots,m. \tag{6.126}$$

with $\widetilde{\mathcal{M}}(\theta,\alpha) = \mathcal{M}(\theta,\alpha)e^{-2i\theta}$. The imaginary part of $\mathcal{M}(\theta,\alpha)$ has a discontinuity for $\theta \to 0$, and

$$\begin{aligned} \mathcal{M}_\pm(\alpha) &= \lim_{\theta\to 0^\pm} \mathcal{M}(\theta,\alpha) = \frac{e^{-2\alpha} \mp i}{e^{-2\alpha} \pm i}, \\ \widetilde{\mathcal{M}}_+(\alpha) &= \lim_{\theta\to 0^+} \widetilde{\mathcal{M}}(\theta,\alpha) = \frac{e^{-2\alpha} - i}{e^{-2\alpha} + i}, \\ \widetilde{\mathcal{M}}_-(\alpha) &= \lim_{\theta\to 0^-} \widetilde{\mathcal{M}}(\theta,\alpha) = e^{-4i\pi}\frac{e^{-2\alpha} + i}{e^{-2\alpha} - i}. \end{aligned} \tag{6.127}$$

The non-vanishing terms in the Fisher-Hartwig conjecture are then

$$\ln\det[M^Z] = \frac{1}{4\pi^2}\left(\ln[\mathcal{M}_-\mathcal{M}_+^{-1}]\right)^2 \ln|l-m| \tag{6.128}$$

$$= \frac{1}{\pi^2}\left(\ln\left[\frac{e^{-2\alpha}-i}{e^{-2\alpha}+i}\right]\right)^2 \ln|l-m|, \tag{6.129}$$

$$\ln\det[M^Y] = \frac{1}{4\pi^2}\left(\ln[\widetilde{\mathcal{M}}_-\widetilde{\mathcal{M}}_+^{-1}]\right)^2 \ln|l-m| \tag{6.130}$$

$$= \frac{1}{\pi^2}\left(\ln\left[\frac{e^{-2\alpha}-i}{e^{-2\alpha}+i}\right]+2i\pi\right)^2 \ln|l-m|. \tag{6.131}$$

We can now compare these results with the ones in Eq. (6.28). By using that

$$\begin{aligned}\left(\ln\left[\frac{e^{-2\alpha}-i}{e^{-2\alpha}+i}\right]\right)^2 &= -4\arctan^2(e^{2\alpha}),\\ \left(\ln\left[\frac{e^{-2\alpha}-i}{e^{-2\alpha}+i}\right]+2i\pi\right)^2 &= -4[\arctan(e^{2\alpha})-\pi]^2,\end{aligned} \tag{6.132}$$

and Eq. (6.128), we can derive the correct power-law behavior for the correlators $\langle Z_l Z_m\rangle$ and $\langle Y_l Y_m\rangle$ in Eq. (6.28).

Extracting the correlations and effective central charge from DMRG

In this Section, we provide details of DMRG simulations of correlation functions and how the effective central charges are extracted in Fig. 6.6(b). The critical Ising state (used for computing correlations in Figs. 6.1, 6.4 and 6.5 is obtained by infinite DMRG with bond dimension $\chi = 300$. In Fig. 6.12 we show that this bond dimension is enough to correctly extract the expected power-law exponent for distances up to $|j| \approx 500$ sites. We also used a bond dimension $\chi = 300$ in Figs. 6.2 and 6.6.

The effective central charge can be obtained using finite DMRG with different system sizes. In Fig. 6.6(b), we extract c_{eff} from

$$S_{L/2} \sim \frac{c_{\text{eff}}}{3}\ln(L), \tag{6.133}$$

where $S_{L/2}$ is the half-chain von Neumann entanglement entropy of the teleported wavefunction with periodic boundary and length L. In practice we take $L = [20, 40, 60, 80, 100, 150, 200]$ and fit $S(L/2)$ v.s. $\ln(L)$ for different imperfection strength α (see Fig. 6.13).

For the mixed X- and Y-basis measurement in Fig. 6.7, we make use of the relation between entanglement entropy and correlation length (as induced by a finite bond dimension) in infinite DMRG [109],

$$S \sim \frac{c_{\text{eff}}}{3}\ln(\xi) \tag{6.134}$$

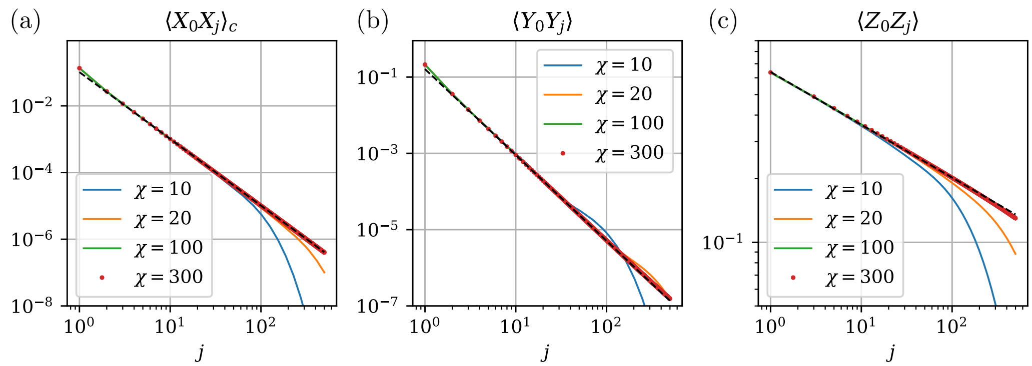

Figure 6.12: **Connected XX, YY and ZZ correlations of the pristine critical Ising chain.** Data obtained using infinite DMRG with different bond dimensions $\chi = 10, 20, 200, 300$. The black dashed lines represent the power-law decay with theoretical exponents, i.e., -2, $-9/4$, $-1/4$ in panels (a), (b) and (c) respectively.

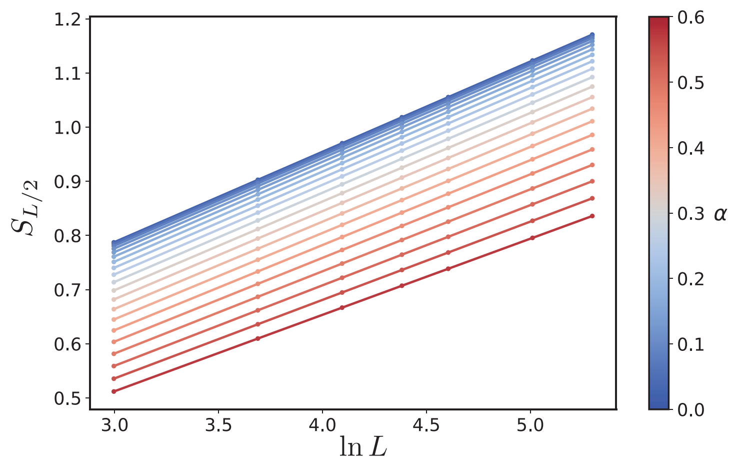

Figure 6.13: **Half-chain entanglement entropy for different system sizes and imperfection strength**. The effective central charges extracted from the slope of the lines are shown in Fig. 6.6(b)

where ξ is the correlation length computed from the transfer matrix of the infinite MPS. Practically, for a given set of (α_x, α_y) in Fig. 6.7, we use different bond dimensions $\chi \in [5, 100]$ and compute the entanglement entropy S. The curve $S(\ln(\xi))$ is expected to be a straight line in the large ξ limit for critical systems. We extract the effective central charge using 30 data points of each curve with the largest ξ. In Fig. 6.14 we show S vs $\ln \xi$ for some combinations of (α_x, α_y).

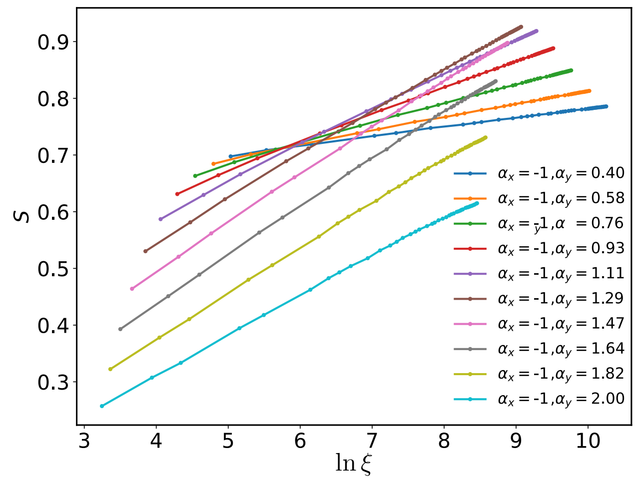

Figure 6.14: S-ln(ξ) curves for different (α_x, α_y) in Fig. 6.7.

Correlators of teleported mixed state

Using $|\tilde{a}, \boldsymbol{n}\rangle = \hat{O}(\boldsymbol{n})\,|\tilde{a}, \boldsymbol{n}\rangle$, it is easy to check that

$$\mathrm{Tr}\Big(\rho^{\text{tele}}\hat{O}(\boldsymbol{n})\Big) = \sum_{\tilde{a},\tilde{a}'}\prod_j [\sin(2u)]^{\frac{1-a_j a_j'}{2}} \langle\psi_c|\tilde{a}', \boldsymbol{n}\rangle\langle\tilde{a}, \boldsymbol{n}|\psi_c\rangle \tag{6.135}$$

$$\times \langle\tilde{a}', \boldsymbol{n}|\,\hat{O}_{\mathcal{K}}(\boldsymbol{n})\,|\tilde{a}, \boldsymbol{n}\rangle \tag{6.136}$$

$$= \langle\psi_c|\,\hat{O}(\boldsymbol{n})\left(\sum_{\tilde{a}}|\tilde{a}, \boldsymbol{n}\rangle\,\langle\tilde{a}, \boldsymbol{n}|\right)|\psi_c\rangle \tag{6.137}$$

$$= \langle\psi_c|\,\hat{O}(\boldsymbol{n})\,|\psi_c\rangle\,. \tag{6.138}$$

On the other hand, if we consider $\hat{O}(\boldsymbol{n}^{\perp})$, we need to take care of the fact that $\hat{O}(\boldsymbol{n}^{\perp})$ acting on $|\tilde{a}, \boldsymbol{n}\rangle$ sends $a_k \to -a_k$, which yields

$$\mathrm{Tr}\Big(\rho^{\text{tele}}\hat{O}_{\mathcal{K}}(\boldsymbol{n}^{\perp})\Big) = \sum_{\tilde{a},\tilde{a}'}\prod_j [\sin(2u)]^{\frac{1-a_j a_j'}{2}} \langle\psi_c|\tilde{a}', \boldsymbol{n}\rangle\langle\tilde{a}, \boldsymbol{n}|\psi_c\rangle \tag{6.139}$$

$$\times \langle\tilde{a}', \boldsymbol{n}|\,\hat{O}_{\mathcal{K}}(\boldsymbol{n}^{\perp})\,|\tilde{a}, \boldsymbol{n}\rangle \tag{6.140}$$

$$= \prod_{j\in\mathcal{K}}\sin(2u)\sum_{\tilde{a}}\langle\psi_c|\,\hat{O}_{\mathcal{K}}(\boldsymbol{n}^{\perp})\,|\tilde{a}, \boldsymbol{n}\rangle\,\langle\tilde{a}, \boldsymbol{n}|\,|\psi_c\rangle \tag{6.141}$$

$$= \sin(2u)^{|\mathcal{K}|}\,\langle\psi_c|\,\hat{O}_{\mathcal{K}}(\boldsymbol{n}^{\perp})\,|\psi_c\rangle\,. \tag{6.142}$$

where we have used that $\langle\tilde{a}', \boldsymbol{n}|\,\hat{O}(\boldsymbol{n}^{\perp})\,|\tilde{a}, \boldsymbol{n}\rangle = \prod_{j\notin\mathcal{K}}\delta_{a_j,a_j'}\prod_{j\in\mathcal{K}}\delta_{a_j,-a_j'}$ and $|-\tilde{a}, \boldsymbol{n}\rangle = \hat{O}(\boldsymbol{n}^{\perp})\,|\tilde{a}, \boldsymbol{n}\rangle$. Finally, in order to get the result for $\hat{O}_{\mathcal{K}}(\boldsymbol{n}\times\boldsymbol{n}^{\perp})$, we first notice that $\hat{O}(\boldsymbol{n}\times\boldsymbol{n}^{\perp}) = i\hat{O}(\boldsymbol{n}^{\perp})\hat{O}(\boldsymbol{n})$ and then we apply the same strategy as in Eq. (6.139).

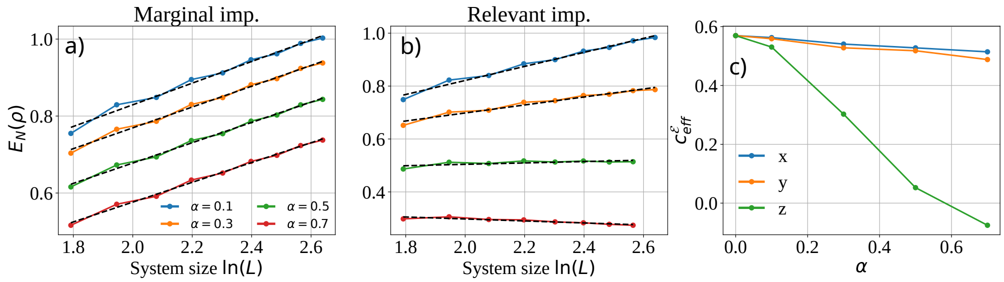

Figure 6.15: **Half-chain entanglement negativity as a function of system size for different deformations**. Scaling of the half-chain entanglement negativity of the teleported mixed state ρ^{tele} with system size in $L \in [6, 14]$ as a function of the deformation strength α along $\boldsymbol{x}$ (panel (a)) and $\boldsymbol{z}$ (panel (b)) axes. (c) Scaling of the effective central charge $c^{\mathcal{E}}_{\text{eff}}$ as a function of α with imperfections in the $\boldsymbol{x}$, $\boldsymbol{y}$ and $\boldsymbol{z}$ quantization axes.

Entanglement negativity of teleported mixed state

Since ρ^{tele} from Eq. 6.45 is a mixed state, the natural way to quantify its entanglement structure is using the entanglement negativity [96, 97], as we already pointed out in Sec. 6.4. Through a numerical study, the goal of this Section is to show how the negativity is affected by the imperfections of our teleportation protocol. Let us recall the definition of negativity. We consider a bi-partition of the system into a region R and its complement $R \cup \bar{R}$, and we then perform a partial transposition of the density matrix ρ^{tele} with respect to the system R, that we denote as ρ^{tele,T_R}. This operation is defined performing a standard transposition in the Hilbert space $\mathcal{H}_R$ associated to the region R, i.e. exchanging the matrix elements in R, $\rho^{\text{tele},T_R} = (T_R \otimes \mathbb{1}_{\bar{R}})\rho^{\text{tele}}$, leaving the rest untouched. The presence of negative eigenvalues of ρ^{tele,T_R} is a signature of mixed state entanglement [96], which can be quantified by the logarithmic negativity $\mathcal{E} = \ln \text{Tr}||\rho^{\text{tele},T_R}||_1$, where $||\cdot||_1$ denotes the trace norm. When $\alpha = 0$, the negativity of a single interval of size $|R| = \ell$, embedded in an infinite system, behaves as $\mathcal{E} = c/2 \ln(\ell/\epsilon)$, where c is the central charge of Alice's critical state $|\psi_c\rangle$ [110]. For $\alpha \neq 0$, we do not have any analytical prediction about the behavior of $\mathcal{E}$ and, for this reason, we focus on some specific examples.

In the following, we numerically compute the negativity of ρ^{tele} with Alice in the critical state, initializing Bob's wavefunction on a uniform product state on either the $\hat{\boldsymbol{x}}$ basis (Fig. 6.15a)) or on the $\hat{\boldsymbol{z}}$ basis (Fig. 6.15B)), as in Secs. 6.2 and 6.2 respectively. We have used exact diagonalization (ED) for finite systems of length up to $L = 14$ and computed the half-chain negativity of ρ^{tele}. We numerically find that

$\mathcal{E}$ approximately obeys the scaling form

$$\mathcal{E} = \frac{c_{\text{eff}}^{\mathcal{E}}}{2} \ln(L) + \Upsilon, \tag{6.143}$$

where Υ is an α-dependent term. From the plots in Fig. 6.15a)-c), we find that for $\alpha = 0$, $c_{\text{eff}}^{\mathcal{E}} \lesssim 0.6$, while we would expect $c_{\text{eff}}^{\mathcal{E}} = 1/2$ [110] and this is due to the small system sizes L we can study with ED (similarly to Ref. [82]). As α increases, we notice that $c_{\text{eff}}^{\mathcal{E}}$ smoothly decreases when we measure in the $\hat{\boldsymbol{x}}$ basis (Fig. 6.15b)-c)), in agreement with the discussion of Sec. 6.2 about a marginal imperfection, while it quickly drops to 0 in the $\hat{\boldsymbol{z}}$ basis (Fig. 6.15c)), in the same spirit of a relevant imperfection described in Sec. 6.2. This behavior suggests that the amount of long-range entanglement of Bob's wavefunction is maximal when Alice and Bob are maximally entangled (i.e. $u = \pi/4$), and it decreases otherwise. Finally, we comment that we do not report the plots of $\mathcal{E}$ as a function of $\ln(L)$ when measuring in the $\hat{\boldsymbol{y}}$ basis since its behavior is not different with respect to the one observed in Fig. 6.15a), consistently with the disguised marginal imperfection discussed in Sec. 6.2. This is confirmed by comparing the behavior of $c_{\text{eff}}^{\mathcal{E}}$ in Fig. 6.15c) measuring in the $\hat{\boldsymbol{x}}$ (blue line) and $\hat{\boldsymbol{y}}$-basis (green line).

Part IV

Measurement-Induced Boundary Transitions

"Sometimes a delivery guy in a pizza hat is so much better than a knight in shining armor, maaan."

— Pascal, *Animal Crossing: New Horizons*

Chapter 7

MEASUREMENTS AS BOUNDARY CONDITIONS

The Ising and teleportation chapters showed that measurements and teleportation imperfections can modify a critical wavefunction through non-unitary perturbations. In this part, we show how a single round of measurements on gapless quantum systems can, upon rotating the measurement basis, induce non-trivial transitions separating regimes displaying universal characteristics governed by distinct boundary conformal field theories. We develop the theory of such 'measurement-induced boundary transitions' by investigating a gapless parent of the one-dimensional cluster state, obtained by appropriately symmetrizing a commuting projector Hamiltonian for the latter. Projective measurements on the cluster state are known to convert the wavefunction, after post-selection or decoding, into a long-range-ordered Greenberger-Horne-Zeilinger (GHZ) state. Similar measurements applied to the gapless parent (i) generate long-range order coexisting with power-law correlations when post-selecting for uniform outcomes, and (ii) yield power-law correlations distinct from those in the pre-measurement state upon decoding. In the post-selection scenario, rotating the measurement basis preserves long-range order up until a critical tilt angle marking a measurement-induced boundary transition to a power-law-ordered regime. Such a transition—which does not exist in the descendant cluster state—establishes new connections between measurement effects on many-body states and non-trivial renormalization-group flows. We extend our analysis to tricritical Ising and three-state Potts critical theories, which also display measurement-induced boundary transitions, and propose general criteria for their existence in other settings.

7.1 Canonical cluster states and measurement intuition

To establish a baseline, we review known features of the canonical 1D $\mathbb{Z}_2 \times \mathbb{Z}_2$ cluster state SPT—including the structure of the ground state [111] as well as the influence of measurements [37, 78]. As noted in the introduction, we view the model as defined on a square ladder shown in Fig. 7.1(a), such that the two $\mathbb{Z}_2$ symmetries correspond to flipping spins on one leg or the other. In the zero-correlation-length limit, the cluster-state Hamiltonian on this geometry reads

$$H_{\text{cluster}} = -\sum_{j=1}^{N-1} (Z_{j,1}X_{j,2}Z_{j+1,1} + Z_{j,2}X_{j+1,1}Z_{j+1,2}), \tag{7.1}$$

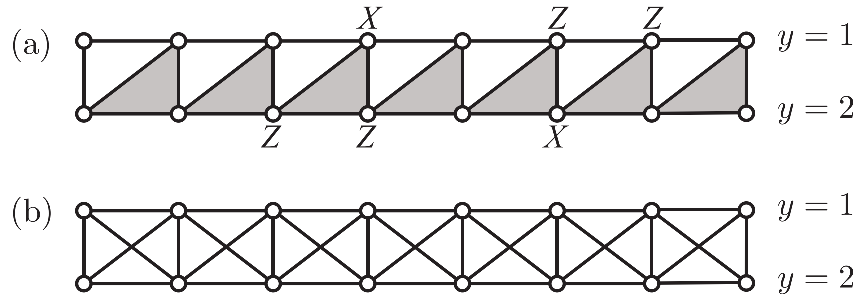

Figure 7.1: Canonical and symmetrized cluster-state constructions. Panel (a) shows the ladder representation of the canonical cluster state, while panel (b) shows the reflection-symmetric construction used to define the gapless parent. This figure is adapted from the boundary-transition source.

where $X_{j,y}, Z_{j,y}$ are Pauli operators acting on the site $j = 1, \ldots, N$ in chain $y = 1, 2$. The first and second terms respectively represent three-spin ZXZ interactions on the white and grey triangles in Fig. 7.1(a). Notice that H_{cluster} violates interchain reflection symmetry, since the orientation of these triangles flips upon swapping the legs. The two $\mathbb{Z}_2$ symmetries protecting SPT order in the ground state are generated by

$$G_1 = \prod_{j=1}^{N} X_{j,1} \quad \text{and} \quad G_2 = \prod_{j=1}^{N} X_{j,2}. \tag{7.2}$$

Exact solvability of Eq. (7.1) descends from the fact that all ZXZ terms commute with one another and square to the identity. Consequently, the ground state satisfies $Z_{j,1}X_{j,2}Z_{j+1,1} = Z_{j,2}X_{j+1,1}Z_{j+1,2} = +1$ for all j. Multiplying ZXZ terms on consecutive triangles with the same color in Fig. 7.1(a) defines $\mathbb{Z}_2 \times \mathbb{Z}_2$ SPT string order parameters, which are equal to one in the ground state of the above cluster state model. Taking the product on grey triangles, for instance, yields

$$\mathcal{S}_{j,k} \equiv \begin{bmatrix} & X_{j+1} & \cdots & X_{k-1} & X_k \\ Z_j & & & & Z_k \end{bmatrix} = 1 \tag{7.3}$$

for any $k > j$. On the left-hand side, all operators are multiplied, with the top and bottom rows corresponding to the upper and lower chain of the ladder. A second string order parameter similarly follows from the grey triangles. Beyond the zero-correlation-length limit, these string order parameters tend to a non-zero constant at $|j - k| \to \infty$ in the SPT phase.

Interestingly, measurements together with decoding convert the zero-correlation-length SPT ground state $|\psi_0\rangle$ into a GHZ state $|\text{GHZ}\rangle = \frac{1}{\sqrt{2}}(|\uparrow \cdots \uparrow\rangle + |\downarrow \cdots \downarrow\rangle)$.

Suppose that one projectively measures the local operators $\{X_{j,1}\}$ for all j on the upper chain, and denotes the outcome as $\boldsymbol{s} \equiv \{s_j\}$ and the corresponding Born probability as $p_{\boldsymbol{s}}$. The post-measurement state (up to normalization) is then

$$|\psi\rangle_{\boldsymbol{s}} \propto \mathcal{P}_{\boldsymbol{s}} |\psi_0\rangle \equiv \prod_{j=1}^{N} \left(\frac{1 + s_j X_{j,1}}{2}\right) |\psi_0\rangle\,, \tag{7.4}$$

where $\mathcal{P}_{\boldsymbol{s}}$ is the projector corresponding to the measurement. In the state $|\psi\rangle_{\boldsymbol{s}}$, two-point ZZ correlators for the unmeasured bottom chain readily evaluate to

$$\langle Z_{j,2} Z_{k,2}\rangle_{\boldsymbol{s}} = \frac{\langle\psi_0| \mathcal{P}_{\boldsymbol{s}} Z_{j,2} Z_{k,2} \mathcal{P}_{\boldsymbol{s}} \mathcal{S}_{j,k} |\psi_0\rangle}{\langle\psi_0|\mathcal{P}_{\boldsymbol{s}}|\psi_0\rangle} = s_{j+1} \cdots s_k. \tag{7.5}$$

[Using Eq. (7.3), in the middle, we benignly inserted an $\mathcal{S}_{j,k}$ factor to immediately obtain the result.] The above correlator remains non-zero even at $|j - k| \to \infty$—though the value depends on the measurement outcome. Correspondingly, performing a standard average over measurement outcomes gives

$$\sum_{\boldsymbol{s}} p_{\boldsymbol{s}} \left\langle Z_{j,2} Z_{k,2}\right\rangle_{\boldsymbol{s}} = \left\langle Z_{j,2} Z_{k,2}\right\rangle = 0 \tag{7.6}$$

for any $k \neq j$. We see here that Born-rule averaging effectively erases the measurement, yielding a two-point ZZ correlator for the pre-measurement state that naturally becomes trivial in the SPT phase.

One can nevertheless extract correlations characteristic of a GHZ state in several ways. By post-selecting for a uniform measurement outcome with all $s_j = +1$, Eq. (7.5) returns standard long-range ordered correlations characteristic of the wavefunction $|\mathrm{GHZ}\rangle$. Since the probability for the target measurement outcome decays exponentially with system size, however, this approach is non-ideal—but fortunately unnecessary. A post-measurement state $|\psi\rangle_{\boldsymbol{s}}$ associated with an arbitrary outcome $\boldsymbol{s}$ can be converted into a GHZ state via controlled unitary feedback: namely, $U_{\boldsymbol{s}} |\psi\rangle_{\boldsymbol{s}} = |\mathrm{GHZ}\rangle$ with $U_{\boldsymbol{s}} = \prod_j X_{j,2}^{(1-p_j)/2}$ a unitary dependent on the measurement outcome through $p_j = \cdots s_{j-2} s_{j-1} s_j$ [82]. An alternative, and closely related, perspective is to consider

$$\sum_{\boldsymbol{s}} p_{\boldsymbol{s}} \left\langle Z_{j,2} Z_{k,2}\right\rangle_{\boldsymbol{s}} s_{j+1} \cdots s_k = 1. \tag{7.7}$$

The left side averages the ZZ correlator weighted by a measurement-outcome-dependent sign structure that cancels the signs in Eq. (7.5); hence averaging over measurement outcomes returns 1 [instead of 0 as in Eq. (7.6)]. Equation (7.7) is equivalent to what one would obtain by evaluating ZZ in the unitarily modified state $U_s |\psi\rangle_s$ and then averaging over measurement outcomes. For a more general discussion of unitary feedback in related settings, see Ref. [82].

Sec. 7.5 discusses additional properties of the cluster state including the effects of finite correlation length, enacting weak vs projective measurements, and tilting the measurement basis away from X. As reviewed there, the emergence of a GHZ state requires both strict projective measurements *and* pristinely measuring X for the lower chain [78]. Weakening the measurement or tilting the measurement basis—even by arbitrarily small amounts—produces exponentially decaying ZZ correlations in the post-measurement state, rather than long-range-ordered GHZ-like correlations arising in the ideal case. We will later uncover qualitatively different resilience to such modifications in the context of the gapless parent of the 1D cluster state that we introduce next.

7.2 Gapless parent of the cluster state

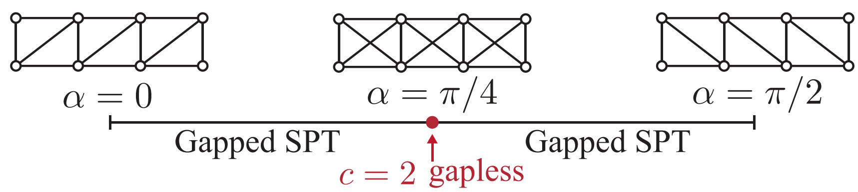

Figure 7.2: Phase diagram of Eq. (7.8). For $0 \leq \alpha < \pi/4$ and $\pi/4 < \alpha \leq \pi/2$, two cluster-state SPT regimes emerge that are related by interchain reflection symmetry. At $\alpha = \pi/4$, the system is gapless with central charge $c = 2$.

We introduce the gapless parent of the cluster state SPT by first considering the generalized Hamiltonian

$$\begin{aligned} H = -\sum_{j=1}^{N-1} [&\cos\alpha (Z_{j,1}X_{j,2}Z_{j+1,1} + Z_{j,2}X_{j+1,1}Z_{j+1,2}) \\ &+ \sin\alpha (Z_{j,2}X_{j,1}Z_{j+1,2} + Z_{j,1}X_{j+1,2}Z_{j+1,1})]. \end{aligned} \tag{7.8}$$

The ZXZ terms in the first line, which are the same as those in Eq. (7.1), correspond to the triangles in Fig. 7.1(a). The second line includes a new set of ZXZ terms on 'flipped' triangles. When $\alpha = 0$, H simply recovers the cluster state SPT reviewed in Sec. 7.1; $\alpha = \pi/2$ corresponds to an alternative cluster state SPT realization that relates to the former by interchain reflection. At $\alpha = \pi/4$ the Hamiltonian uniquely preserves interchain reflection symmetry [see Fig. 7.1(b) for a schematic].

We will show below that this limit realizes a gapless state that intervenes between the two gapped cluster state SPT regimes highlighted above. Figure 7.2 illustrates the phase diagram as a function of α for this model. We stress, however, that $\alpha < \pi/4$ and $\alpha > \pi/4$ do not represent distinct phases. In fact the cluster state SPT can harmoniously coexist with interchain reflection symmetry as shown explicitly in Ref. [112]. A reflection-symmetric SPT can also emerge as a descendent of our gapless parent state; see Sec. 9.3 for details.

Table 7.1: Dictionary between select operators in the original basis and in the new basis specified in Eq. (7.9).

Original	$\begin{bmatrix} Z_j & Z_{j+1} \\ X_j & \end{bmatrix}$	$\begin{bmatrix} Z_j & Z_{j+1} \\ & X_{j+1} \end{bmatrix}$	$\begin{bmatrix} X_j & \\ Z_j & Z_{j+1} \end{bmatrix}$	$\begin{bmatrix} & X_{j+1} \\ Z_j & Z_{j+1} \end{bmatrix}$	$\begin{bmatrix} Y_j & Z_{j+1} \\ Y_j & Z_{j+1} \end{bmatrix}$	$\begin{bmatrix} Z_j & Y_{j+1} \\ Z_j & Y_{j+1} \end{bmatrix}$	$\begin{bmatrix} X_j \\ \end{bmatrix}$	$\begin{bmatrix} \\ X_j \end{bmatrix}$
New	$\begin{bmatrix} \mathcal{Y}_j & \mathcal{Y}_{j+1} \\ & \end{bmatrix}$	$\begin{bmatrix} & \\ \tilde{\mathcal{Y}}_j & \tilde{\mathcal{Y}}_{j+1} \end{bmatrix}$	$\begin{bmatrix} \mathcal{X}_j & \mathcal{X}_{j+1} \\ & \end{bmatrix}$	$\begin{bmatrix} & \\ \tilde{\mathcal{X}}_j & \tilde{\mathcal{X}}_{j+1} \end{bmatrix}$	$-\begin{bmatrix} \mathcal{Z}_j & \mathcal{Z}_{j+1} \\ & \end{bmatrix}$	$-\begin{bmatrix} & \\ \tilde{\mathcal{Z}}_j & \tilde{\mathcal{Z}}_{j+1} \end{bmatrix}$	$\begin{bmatrix} \mathcal{X}_j \\ \tilde{\mathcal{X}}_j \end{bmatrix}$	$\begin{bmatrix} \mathcal{Y}_j \\ \tilde{\mathcal{Y}}_j \end{bmatrix}$

Gaplessness at $\alpha = \pi/4$ becomes manifest under a unitary non-local mapping—equivalent to a Kennedy-Tasaki transformation [113, 114, 115, 116]—to Pauli operators,

$$
\begin{aligned}
\mathcal{X}_j &= \begin{bmatrix} \cdots & X_{j-2} & X_{j-1} & \\ & & & Z_j \end{bmatrix}, \\
\tilde{\mathcal{X}}_j &= \begin{bmatrix} \cdots & X_{j-2} & X_{j-1} & X_j \\ & & & Z_j \end{bmatrix}, \\
\mathcal{Y}_j &= \begin{bmatrix} Z_j & & & \\ X_j & X_{j+1} & X_{j+2} & \cdots \end{bmatrix}, \\
\tilde{\mathcal{Y}}_j &= \begin{bmatrix} Z_j & & & \\ & X_{j+1} & X_{j+2} & \cdots \end{bmatrix}.
\end{aligned}
\tag{7.9}
$$

[Operators in each bracket are multiplied. The upper (lower) row of each bracket refers to the first (second) chain.] The structure of this transformation—attaching a string of X operators in one chain to a Z operator in the opposite chain—closely resembles the SPT string order parameters in Eq. (7.3). The new variables satisfy the usual Pauli algebra with $\mathcal{Z}_j = -i\mathcal{X}_j\mathcal{Y}_j$ and similarly for $\tilde{\mathcal{Z}}_j$. Table 7.1 provides a dictionary between select operators in the original basis and in the new basis above. In particular, the constituent ZXZ operators from Eq. (7.8) map to nearest-neighbor bilinears of the new Pauli operators in Eq. (7.9), yielding (after some rearrangement)

$$
\begin{aligned}
H = -\sum_{j=1}^{N-1} (&\sin\alpha \mathcal{X}_j\mathcal{X}_{j+1} + \cos\alpha \mathcal{Y}_j\mathcal{Y}_{j+1} \\
&+ \cos\alpha \tilde{\mathcal{X}}_j\tilde{\mathcal{X}}_{j+1} + \sin\alpha \tilde{\mathcal{Y}}_j\tilde{\mathcal{Y}}_{j+1}).
\end{aligned}
\tag{7.10}
$$

For general α, Eq. (7.10) describes two decoupled $\mathcal{XY}$ models, each of which is gapped due to anisotropy in the couplings. The limits $\alpha = 0$ and $\alpha = \pi/2$ correspond to two decoupled Ising chains in the spontaneous symmetry breaking phase. The Kennedy-Tasaki transformation mapping the cluster state SPT (7.1) to this symmetry-broken phase has been studied in [115]. The anisotropy disappears at $\alpha = \pi/4$—where each $\mathcal{XY}$ model manifestly exhibits an exact U(1) symmetry. Here the system is gapless with central charge $c = 2$ and admits the usual free-fermion representation.

Adding local, symmetry-preserving terms to Eq. (7.8) generates $\mathcal{ZZ}$ terms (see Table 7.1) that lead to interactions in the fermion picture and turn the system into a two-channel Luttinger liquid with nontrivial Luttinger parameters. Taking $\alpha = \pi/4$, dropping a grotesque factor of $\sqrt{2}$, and allowing for such interactions leads to the following Hamiltonian that we will study extensively in the remainder of this paper:

$$
\begin{aligned}
H_\Delta = -\sum_j \Big(&\mathcal{X}_j\mathcal{X}_{j+1} + \mathcal{Y}_j\mathcal{Y}_{j+1} + \Delta\mathcal{Z}_j\mathcal{Z}_{j+1} \\
&+\tilde{\mathcal{X}}_j\tilde{\mathcal{X}}_{j+1} + \tilde{\mathcal{Y}}_j\tilde{\mathcal{Y}}_{j+1} + \Delta\tilde{\mathcal{Z}}_j\tilde{\mathcal{Z}}_{j+1}\Big),
\end{aligned} \tag{7.11}
$$

which describes two decoupled $\mathcal{XXZ}$ models. Since we are interested in the gapless phase, we restrict our analysis to $\Delta \in [-1, 1)$ throughout. Next, we will study the effect of weak measurements on the gapless parent state realized by Eq. (7.11).

7.3 Uniform weak measurements and defect perturbations

Weak measurement on a Tomonaga-Luttinger liquid

As a primer let us discuss the impact of weak measurement on a single $\mathcal{XXZ}$ spin chain—described by just the first line of Eq. (7.11)—mainly following Refs. [16, 55, 56] but also adding some new insights. The $\mathcal{XXZ}$ model realizes a Tomonaga-Luttinger liquid (TLL) governed by the low-energy fixed-point action

$$
S_{\mathrm{TLL}} = \frac{1}{2\pi}\int_{x,\tau}\left[2i\partial_\tau\phi\partial_x\theta + K^{-1}(\partial_x\phi)^2 + K(\partial_x\theta)^2\right]. \tag{7.12}
$$

Here $\phi(x,\tau), \theta(x,\tau)$ are slowly varying bosonic fields dependent on a coarse-grained position x and imaginary time τ, while $K = \frac{\pi}{2\arccos\Delta}$ is the Luttinger parameter determined by the microscopic $\mathcal{ZZ}$ coupling Δ. In particular, since we consider only $\Delta \in [-1, 1)$, we always have $K \geq 1/2$. In the low-energy, long-distance limit, the Pauli operators at site j relate to the bosonic fields through [117]

$$\begin{aligned}\mathcal{X}_j - i\mathcal{Y}_j &\sim e^{i\theta} + ic_1(-1)^j\left[e^{i(\theta+2\phi)} - e^{i(\theta-2\phi)}\right]\\ \mathcal{Z}_j &\sim -\frac{2}{\pi}\partial_x\phi + c_2(-1)^j\cos(2\phi),\end{aligned} \tag{7.13}$$

where $c_1, c_2 \in \mathbb{R}$ are non-universal coefficients. (In the first line, we do not factor out an overall $e^{i\theta}$ factor to avoid subtle issues regarding commutation of θ and ϕ evaluated at microscopically separated positions. Symmetries are more readily accounted for in the form above.) Equation (7.12) implies equal-time correlators $\left\langle[\phi(x) - \phi(0)]^2\right\rangle = K\log(x)$ and $\left\langle[\theta(x) - \theta(0)]^2\right\rangle = \frac{1}{K}\log(x)$. Two-point correlators of the lattice Pauli operators follow as

$$\begin{aligned}&\left\langle\mathcal{X}_j\mathcal{X}_0\right\rangle = \left\langle\mathcal{Y}_j\mathcal{Y}_0\right\rangle \sim C_0|j|^{-\frac{1}{2K}} + C_1(-1)^j|j|^{-\frac{1}{2K}-2K},\\ &\left\langle\mathcal{Z}_j\mathcal{Z}_0\right\rangle \sim C_2|j|^{-2} + C_3(-1)^j|j|^{-2K}\end{aligned} \tag{7.14}$$

with C_i some other non-universal constants.

The weak measurements that we consider here and below are a softened version of the standard projective measurements used, e.g., in Eq. (7.4). In physical setups, weak measurements can be achieved by entangling the many-body wavefunction to ancillary degrees of freedom and then projectively measuring the latter. References [16, 55] previously investigated $\mathcal{Z}$-basis measurements in a Luttinger liquid; see especially the seminal study of Ref. [16] that established a connection to the classic Kane-Fisher impurity problem [118]. We will consider $\mathcal{X}$-basis weak measurements, as they illustrate the main points in a way that closely connects to measurements of interest in our gapless parent of the cluster state.

Upon weakly measuring all sites, the ground state $|\psi_c\rangle$ of the $\mathcal{XXZ}$ spin chain becomes

$$|\psi_{\boldsymbol{s}}\rangle = \frac{1}{\mathcal{N}}e^{\beta\sum_j s_j\mathcal{X}_j}\,|\psi_c\rangle \tag{7.15}$$

where $\boldsymbol{s} = \{s_j = \pm 1\}$ encodes the set of measurement outcomes (e.g., in a scheme utilizing ancillas), $\mathcal{N}$ is an overall normalization factor, and β sets the measurement strength [55, 57, 58, 62]. In particular, when acting on some initial state, the on-site operator $e^{\beta s_j\mathcal{X}_j}$ amplifies the contribution with $\mathcal{X}_j = s_j$ and suppresses the contribution with $\mathcal{X}_j = -s_j$; $\beta \to \infty$ recovers the projective limit where the latter is killed.

In the following, we post-select for the uniform outcome where $s_j = 1$ for all j. Using Eq. (7.15) and the bosonized expression in Eq. (7.13), such a post-selected weak measurement manifests as a boundary term acting at all spatial points but only at imaginary time $\tau = 0$ [1] :

$$S' = S_{\text{TLL}} + \beta b_1 \int_{x,\tau} \delta(\tau) \cos\theta, \tag{7.16}$$

where b_1 is a non-universal factor. We observe that the scaling dimension of $\cos\theta$ is $\Delta_{\cos\theta} = 1/(4K)$—implying that the measurement-induced boundary perturbation is marginal for $K = 1/4$, relevant for larger K and irrelevant for smaller K. Weak measurements do not qualitatively impact universal long-distance properties in the latter case.

In our setup, the Luttinger parameter is constrained by $K \geq 1/2$, and the $\tau = 0$ perturbation is always relevant. Even arbitrarily weak measurements will therefore eventually pin θ. Specifically, the flow of β implies a length scale $L_\beta(\tau) \sim \ell_\tau \beta^{-1/\Delta_{\cos\theta}}$ with ℓ_0 the UV cutoff and $\ell_\tau \approx \tau$ at large τ. Equal-time correlations at distances at $x \gtrsim L_\beta(\tau)$ feel the full impact of the measurement while those at $x \lesssim L_\beta(\tau)$ are only affected perturbatively. In this paper we are always interested in correlations of microscopic operators that are *not* time-evolved, which in the bosonized theory follow from correlations of fields evaluated at $\tau = 0$. For such cases the crossover length $L_\beta(0)$ depends only on β (and a UV cutoff).

We use BCFT formalism to efficiently compute various correlation functions. Specifically, we encode pinning of θ in the IR by a Dirichlet boundary condition (DBC) $\theta(\tau^*) = 0$ at all x and at a β-dependent time τ^*. The dual field, ϕ, consequently obeys free or Neumann boundary conditions (NBc), i.e., $\partial_\tau \phi|_{\tau=\tau^*} = 0$. The BCFT exhibits a crossover scale $L^{\text{BCFT}}_{\tau^*}(\tau)$ which depends on the distance $\tau - \tau^*$, and in the limit $\tau - \tau^* \to 0$ is set by a UV cutoff. To determine $\tau^*(\beta)$, we match the crossover length scales of Eq. (7.15) and the BCFT at $\tau = 0$, i.e., we require $L^{\text{BCFT}}_{\tau^*} = L_\beta(0)$. In particular, the correlations of Eq. (7.15) for a given β correspond to BCFT correlations evaluated at a specific distance from the boundary.

Combining relevance of the measurement-induced perturbation and the flow to a BCFT with DBC for θ, Sec. 8.4 evaluates two-point correlation functions $\left\langle e^{ia\theta(0,\tau)} e^{-ib\theta(x,\tau)} \right\rangle_{\text{DBC}}$ and $\left\langle e^{ia\phi(0,\tau)} e^{-ib\phi(x,\tau)} \right\rangle_{\text{NBC}}$ for general x, τ. The dictionary

[1] The post-measurement density matrix $|\psi_{\boldsymbol{s}}\rangle \langle \psi_{\boldsymbol{s}}|$ with $s_j = 1$ can be written as $\lim_{\mu\to\infty} \frac{e^{\beta\sum_j X_j} e^{-\mu H_\Delta} e^{\beta \sum_j X_j}}{\text{Tr}(e^{2\beta\sum_j X_j} e^{-\mu H_\Delta})}$, which, in the continuum limit, is described by a boson field theory governed by the action of Eq. (7.16). More intuitively, one can view imaginary times $\tau < 0$ as preparing a quantum critical ket while imaginary times $\tau > 0$ prepare a quantum critical bra; the measurement applies to those prepared states and hence acts only at $\tau = 0$

in Eq. (7.13) allows us to leverage this computation to evaluate two-point correlations of microscopic spin operators at spatial separation x but at the same imaginary time τ. To extract the characteristic scale τ^*, we need to also examine two-point spin correlations in an alternative way that directly incorporates the measurement strength β. We will do so by expanding around the projective measurement limit and using scaling arguments.

Consider first nearly projective measurements ($\beta \gg 1$); here correlations are expected to be governed by a scale τ^* close to 0. By exploiting the results reviewed in Sec. 8.4, in this regime we obtain up to $O(\tau^{*4}/x^4)$

$$\frac{\left\langle e^{ia\theta(0,0)} e^{-ib\theta(x,0)} \right\rangle_{\text{DBC}}}{\left\langle e^{ia\theta(0,0)} \right\rangle_{\text{DBC}} \left\langle e^{-ib\theta(x,0)} \right\rangle_{\text{DBC}}} = 1 + \frac{ab}{K}\left(\frac{\tau^*}{x}\right)^2 \tag{7.17}$$

at long distances $x \gg \tau^*$. Using Eq. (7.13), two-point $\mathcal{Y}$ correlators —which suffice for the present aims—are then given in the same regime by

$$\frac{\langle \mathcal{Y}_0 \mathcal{Y}_x \rangle_{\text{uni}}}{\langle \mathcal{X}_0 \mathcal{X}_x \rangle_{\text{uni}}} \sim \frac{\langle \sin[\theta(0)] \sin[\theta(x)] \rangle_{\text{DBC}}}{\langle \cos[\theta(0)] \cos[\theta(x)] \rangle_{\text{DBC}}} \sim \left(\frac{\tau^*}{x}\right)^2. \tag{7.18}$$

Above we normalized the two-point correlator $\langle \mathcal{Y}_0 \mathcal{Y}_x \rangle_{\text{uni}}$ by $\langle \mathcal{X}_0 \mathcal{X}_x \rangle_{\text{uni}}$ to eliminate dependence on the UV cutoff of the field theory. Sec. 8.2 alternatively finds

$$\frac{\langle \mathcal{Y}_0 \mathcal{Y}_x \rangle_{\text{uni}}}{\langle \mathcal{X}_0 \mathcal{X}_x \rangle_{\text{uni}}} \sim \left(\frac{e^{-2\beta}}{x}\right)^2 \tag{7.19}$$

by examining the ground-state wavefunction near the projective-measurement limit. Comparing the preceding two equations yields an exponentially small characteristic scale $\tau^* \sim e^{-2\beta}$ in the $\beta \gg 1$ limit.

For $\beta \ll 1$, we do not know how to explicitly compute the β dependence of the asymptotic long-distance correlations—but can nevertheless proceed using scaling arguments. In particular, prior to performing the weak measurement, the scaling dimension of β in Eq. (7.16) is $[\beta] = -1 + \frac{1}{4K}$, such that the overall action is dimensionless. Dimensional analysis then gives $\beta \sim (\tau^*)^{-1+1/(4K)}$, and hence long-distance correlations at $x \gg \tau^*$ should be obtained with $\tau^* \sim \beta^{4K/(1-4K)}$ in the $\beta \ll 1$ limit.

X-basis measurements

Analyzing the effects of measurements on a single-channel Luttinger liquid serves as a useful warm-up to study their consequences in the gapless parent of the cluster state. Let

$$|\psi_\Delta\rangle = |\psi_c\rangle |\tilde{\psi}_c\rangle \tag{7.20}$$

denote the ground state of Eq. (7.11); on the right side, $|\psi_c\rangle$ and $\left|\tilde{\psi}_c\right\rangle$ denote the ground states of the two decoupled $\mathcal{XXZ}$ spin chains that arise under the Kennedy-Tasaki mapping from Eq. (7.9). Weakly measuring all $X_{j,1} = \mathcal{X}_j \tilde{\mathcal{X}}_j$ operators from the upper chain and post-selecting for the uniform outcome $\boldsymbol{s} = \{s_j = +1\}$ modifies the wavefunction to $|\psi\rangle_{\text{uni}} = \frac{1}{N} M_X |\psi_\Delta\rangle$, where

$$M_X = e^{\beta \sum_j X_{j,1}} = e^{\beta \sum_j \mathcal{X}_j \tilde{\mathcal{X}}_j} \tag{7.21}$$

is the associated non-unitary measurement operator.

Following the previous subsection, long-distance properties of the weakly measured wavefunction can be extracted from the action

$$S = S_{\text{TLL}}[\theta, \phi] + S_{\text{TLL}}[\tilde{\theta}, \tilde{\phi}] + \delta S_{\text{meas}}[\theta, \tilde{\theta}]. \tag{7.22}$$

Here S_{TLL} is given in Eq. (7.12) and

$$\delta S_{\text{meas}} \propto \beta \int_{x,\tau} \delta(\tau) \cos\theta \cos\tilde{\theta} \tag{7.23}$$

encodes the measurement-induced perturbation that couples the Luttinger liquids at all x but only at $\tau = 0$. [2] It is useful to introduce symmetric and antisymmetric combinations of the bosonic fields via $\theta_\pm \equiv \theta \pm \tilde{\theta}$ and $\phi_\pm = (\phi \pm \tilde{\phi})/2$. [56]. In this basis the problem maps onto two independent Luttinger liquids for the + and − fields that remain decoupled for $\beta \neq 0$; indeed Eq. (7.23) becomes

$$\delta S_{\text{meas}} \propto \beta \int_{x,\tau} \delta(\tau)(\cos\theta_+ + \cos\theta_-). \tag{7.24}$$

The scaling dimension of $\cos\theta_\pm$ (and equivalently of $\cos\theta\cos\tilde{\theta}$) is $1/(2K)$. Consequently, for $K > 1/2$ any nonzero measurement strength generates a relevant perturbation that, at long distances, imposes DBC's that pin θ_+ and θ_- as described earlier. We assume this regime in what follows. Given the decoupling between the $\theta_\pm$ sectors, we can use boundary CFT calculations just like those in the previous section to extract correlation functions in the post-measurement wavefunction.

Inspecting the right side of Eq. (7.21), the post-measurement wavefunction clearly breaks the two U(1) symmetries associated with each $\mathcal{XXZ}$ chain. A subgroup

[2] It is known that for multichannel Luttinger liquids, higher order contribution coming from $4k_F$ osicillation can sometimes become more relevant than the $2k_F$ oscillation counterpart [117]. In our case we do not have such problem because the first two terms in (7.22) describe two identical and decoupled Luttinger liquids. In particular, the term $\cos\theta\cos\tilde{\theta}$ is more relevant than terms like $\cos(2\theta)$ or $\cos(2\tilde{\theta})$

that sends $\mathcal{X}_j \rightarrow -\mathcal{X}_j$ *and* $\tilde{\mathcal{X}}_j \rightarrow -\tilde{\mathcal{X}}_j$ is, however, preserved—implying that $\langle \mathcal{X}_j \rangle = \langle \tilde{\mathcal{X}}_j \rangle = 0$. In the bosonized description, one can account for the vanishing of these expectation values by observing that Eq. (7.23) exhibits two possible DBC's: either $\theta = \tilde{\theta} = 0$ or $\theta = \tilde{\theta} = \pi$ [56]. Democratically sampling both boundary conditions leads to $\langle \cos\theta \rangle = \langle \cos\tilde{\theta} \rangle = 0$ as dictated by symmetry. The measurement nevertheless catalyzes long-range order in both $\mathcal{X}_j$ and $\tilde{\mathcal{X}}_j$. For instance, for $\mathcal{X}$ we find that

$$\begin{aligned} &\langle \mathcal{X}_j \mathcal{X}_k \rangle_s \\ &\sim \left\langle \cos\left(\frac{\theta_+(j) + \theta_-(j)}{2}\right) \cos\left(\frac{\theta_+(k) + \theta_-(k)}{2}\right) \right\rangle_{\text{DBC}} \end{aligned} \tag{7.25}$$

tends to a non-zero constant at $|j - k| \rightarrow \infty$ due to pinning of $\theta_\pm$.

Consider next the two-point Z correlator

$$\left\langle Z_{j,2} Z_{k,2} \right\rangle_{\text{uni}} = \left\langle \begin{matrix} & \mathcal{X}_{j+1} & \mathcal{X}_{j+2} & \cdots & \mathcal{X}_k \\ \tilde{\mathcal{X}}_j & \tilde{\mathcal{X}}_{j+1} & \cdots & \tilde{\mathcal{X}}_{k-1} & \end{matrix} \right\rangle_{\text{uni}}. \tag{7.26}$$

In the projective measurement limit $\beta \rightarrow \infty$, we can use the post-selected measurement result $X_{j,1} = \mathcal{X}_j \tilde{\mathcal{X}}_j = 1$ for all sites to write

$$\left\langle Z_{j,2} Z_{k,2} \right\rangle_{\text{uni}} = \left\langle \mathcal{X}_j \mathcal{X}_k \right\rangle_{\text{uni}}, \tag{7.27}$$

i.e., in this limit long-range $\mathcal{X}$ order implies long-range Z order for the bottom chain. DMRG simulations presented in Fig. 7.3(a) (green points) confirm this prediction. Importantly, even though Eq. (7.27) is valid only in the projective-measurement limit, our DMRG results (not shown) reveal that long-range Z order persists for any finite β. According to Eq. (7.9), long-range order in $\mathcal{X}$ *also* implies a non-zero expectation value for two Z operators on the unmeasured bottom chain linked by a non-local product of X operators on the weakly measured top chain. We therefore conclude that the weak X measurement catalyzes long-range Z order in the bottom chain *and* long-range order in the disorder operator $\mu_{j,1} = \prod_{k \le j} X_{k,1}$ for the top chain. For reference, both quantities exhibit only power-law order in the pre-measurement state. Recall also that in the gapped descendant cluster-state SPT, long-range Z order emerges only with strict projective measurements.

Using Table 7.1 as well as calculations detailed in Sec. 8.4, we can further evaluate X correlations in the unmeasured bottom chain:

$$\left\langle X_{j,2} X_{k,2} \right\rangle_{\text{uni}} = \left\langle \mathcal{Y}_j \tilde{\mathcal{Y}}_j \mathcal{Y}_k \tilde{\mathcal{Y}}_k \right\rangle_{\text{uni}} \sim |j - k|^{-\min(4, 4K)} \tag{7.28}$$

for any finite measurement strength β. (Obtaining the above result requires incorporating irrelevant tunneling processes between saddle points with $\theta = \tilde{\theta} = 0$ and π into the boundary CFT analysis.) See Fig. 7.3(a) for numerical support of Eq. (7.28) at $\beta = \infty$. We are also interested in the behavior of the string operator $\prod_{i=j}^{k} X_{i,2}$. Our DMRG simulations reported in Sec. 8.5 and Fig. 7.3(a) suggest that, in the projective-measurement limit, the two-point correlations of the disorder operator $\mu_{j,2} = \prod_{k \leq j} X_{k,2}$ are

$$\langle \mu_{j,2} \mu_{k,2} \rangle \sim |j-k|^{-2K}. \tag{7.29}$$

Correlations that decay to zero with separation are natural given the long-range Z correlations identified above. The particular *power-law* decay, however, evident in Eq. (7.29) is nontrivial and reflects the gaplessness of the pre-measurement state. We can analytically recover this scaling relation by first using the post-selected projective measurement outcome to write

$$X_{j,2} = \mathcal{Y}_j \tilde{\mathcal{Y}}_j = -\mathcal{X}_j \tilde{\mathcal{X}}_j \mathcal{Z}_j \tilde{\mathcal{Z}}_j \xrightarrow{\mathcal{X}_j \tilde{\mathcal{X}}_j = 1} e^{i\frac{\pi}{2}(\mathcal{Z}_j + \tilde{\mathcal{Z}}_j)}. \tag{7.30}$$

Further applying the bosonization dictionary from Eq. (7.13) yields $\langle \prod_{i=j}^{k} X_{i,2} \rangle_{\text{uni}} \sim \left\langle e^{-i\int_j^k dx(\partial\phi + \partial\tilde{\phi})} \right\rangle_{\text{NBC}} \sim \langle e^{i[\phi(j)-\phi(k)]} e^{i[\tilde{\phi}(j)-\tilde{\phi}(k)]} \rangle_{\text{NBC}}$. Techniques from Sec. 8.4 then recover Eq. (7.29). For the weak measurement case with finite β, it is natural to expect the string operator to continue displaying power-law correlations, presumably with the same exponent.

Another important tool for characterizing many-body quantum systems is the entanglement entropy. Given a pure state, $|\psi\rangle$, and a bipartite system $A \cup B$, the crucial object to compute is the reduced density matrix $\rho_A = \text{Tr}_B |\psi\rangle \langle\psi|$. The entanglement entropy between A and B is given by $S = -\text{Tr}(\rho_A \log \rho_A)$. In Fig. 7.3(b), we present numerical evidence that the post-measurement state exhibits area-law entanglement, as expected in the presence of a relevant perturbation [55, 58, 57]. Weak X measurements therefore generate a state exhibiting a curious coexistence of long-range order, power-law correlations, and area-law entanglement. The combination of power-law correlations and area-law entanglement has been found in 2D systems such as wavefunctions constructed from Boltzmann weights of a classical model [119]. In 1D, such coexistence after weak measurement was also found in Ref. [4], where the post-measurement wavefunction can be approximated as a ground state of a non-local Hamiltonian with power-law-decaying interactions [29, 30, 89].

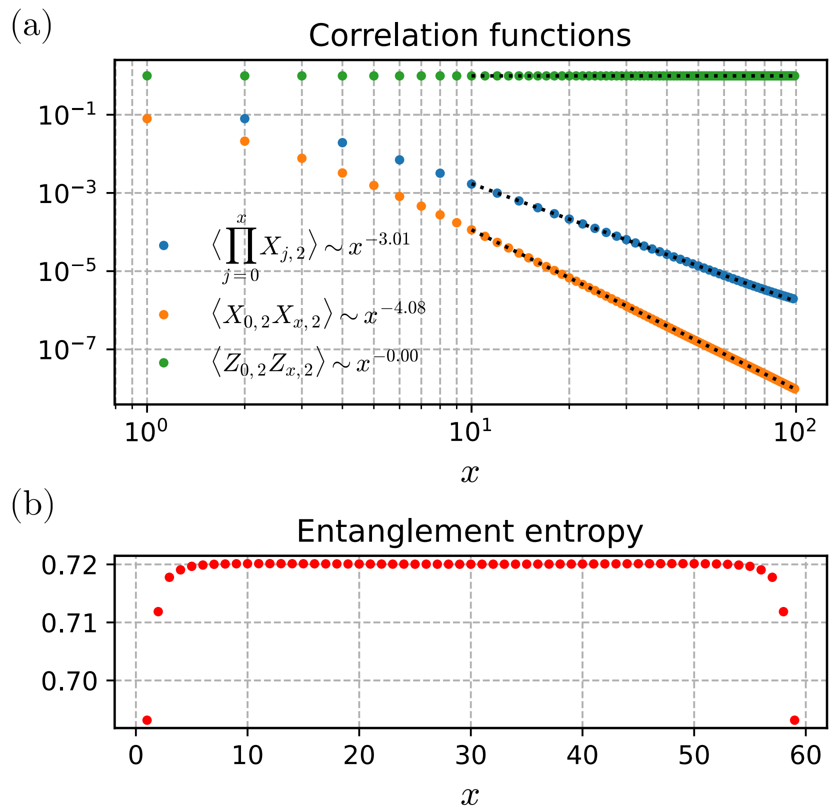

Figure 7.3: (a) Correlation functions and (b) entanglement entropy of the gapless parent of the cluster state with $K = 1.5$ after projective measurement of X in the upper chain with post-selection for a uniform outcome. The gapless parent state is obtained with bond dimension $\chi = 2000$ via infinite-size DMRG (iDMRG) in (a) and via finite DMRG with $L = 60$ and periodic boundary conditions in (b). Fitted power-laws in (a)—see black dotted lines and the legend—agree well with analytical predictions, e.g., from Eqs. (7.28) and (7.29). In (b) we show the entanglement entropy of the post-measurement wavefunction between subsystems $A = \{j \in [0, x], y \in \{1, 2\}\}$ and $B = \{j \in [x + 1, L], y \in \{1, 2\}\}$, supporting area-law behavior. For both (a) and (b), we have numerically checked that the results for finite measurement strength $\beta = 0.3, 0.5, 1$ are similar to the projective limit.

Z-basis measurement

Next we explore Z-basis weak measurements. Individual Z operators map to non-local combinations of the operators defined in Eq. (7.9),

$$Z_{j,1} = \begin{bmatrix} & \mathcal{Y}_{j+1} & \mathcal{Y}_{j+2} & \cdots \\ \tilde{\mathcal{Y}}_j & \tilde{\mathcal{Y}}_{j+1} & \tilde{\mathcal{Y}}_{j+2} & \cdots \end{bmatrix}, \tag{7.31}$$

which makes it difficult to apply bosonization techniques. Therefore, it proves enlightening to first examine measurement of nearest-neighbor products $Z_j Z_{j+1}$—

which according to Table 7.1 simply map to the local operators $\tilde{\mathcal{Y}}_j \mathcal{Y}_{j+1}$. Once again post-selecting for a uniform measurement outcome, we specifically consider the post-measurement wavefunction $|\psi\rangle_{\text{uni}} = \frac{1}{N} M_{ZZ} |\psi_\Delta\rangle$ with

$$M_{ZZ} = e^{\beta \sum_j Z_{j,1} Z_{j+1,1}} = e^{\beta \sum_j \tilde{\mathcal{Y}}_j \mathcal{Y}_{j+1}}. \tag{7.32}$$

In the $\beta \to \infty$ limit, the above non-unitary operator projects onto configurations for which the spins in the measured top chain point either all 'up' or all 'down'. Projectively measuring single-body Z operators (which we examine later) manifestly breaks the spin-flip symmetry and selects one of those two polarizations. It is thus plausible that the two types of measurements yield similar consequences—as we will indeed confirm.

Using Eq. (7.13), weak measurements encoded by Eq. (7.32) perturb the Luttinger liquid action via

$$\delta S_{\text{meas}} \propto \beta \int_{x,\tau} \delta(\tau) \sin\theta \sin\tilde{\theta}, \tag{7.33}$$

which has a very similar form to Eq. (7.23) and is also relevant for $K > 1/2$ (as usual, assumed hereafter). The microscopic Hamiltonian in Eq. (7.8) is invariant under the duality transformation

$$X_{j,y} \to Z'_{j,y} Z'_{j+1,y}, \quad Z_{j-1,y} Z_{j,y} \to X'_{j,y}. \tag{7.34}$$

Self-duality also persists when $\Delta \neq 0$ in Eq. (7.11). Consequently, measuring $Z_{j,1} Z_{j+1,1}$ is dual to measuring $X_{j,1}$, allowing us to adapt results for X-basis measurements in Sec. 7.3 to the present case. In particular, we immediately deduce the following properties of the post-measurement state in Eq. (7.32):

(i) The measured top chain exhibits long-range Z order.

(ii) The unmeasured bottom chain exhibits long-range order in the disorder operator $\mu_{j,2} = \prod_{k \le j} X_{k,2}$.

(iii) The bottom chain exhibits power-law Z correlations,

$$\langle Z_{j,2} Z_{k,2} \rangle_{\text{uni}} \sim |j-k|^{-2K} \tag{7.35}$$

and

$$\langle Z_{j,2} Z_{j+1,2} Z_{k,2} Z_{k+1,2} \rangle_{\text{uni}} \sim |j-k|^{-\min(4,4K)}. \tag{7.36}$$

(iv) The post-measurement state exhibits area-law entanglement.

Now we turn to single-Z weak measurements and consider the state

$$|\psi\rangle_{\text{uni}} = \frac{1}{\mathcal{N}} e^{\beta \sum_j Z_{j,1}} |\psi_\Delta\rangle \, . \tag{7.37}$$

Despite the non-locality of the right side of Eq. (7.31), we can make progress via numerics, analytics in limiting cases, and intuition from our results for ZZ measurements [i.e., Eq. (7.32)]. Sec. 8.5 reports DMRG simulations indicating that the scaling dimension of $Z_{j,1}$ is

$$[Z_{j,1}] = \frac{1}{4}, \tag{7.38}$$

for any $K \geq 1/2$; there we also provide an analytical derivation in the two special cases $K = 1/2$ and 1. Consequently, single-Z weak measurement in the uniform post-selection sector always comprises a strongly relevant perturbation in the allowed range of K for our setup.

As noted earlier, it is reasonable to anticipate related properties emerging at the fixed points generated by single-Z versus ZZ measurements, given the similar spin configurations promoted in the two cases (e.g., $|\uparrow \ldots \uparrow\rangle$ in the former and $\{|\uparrow \ldots \uparrow\rangle, |\downarrow \ldots \downarrow\rangle\}$ in the latter). Explicit symmetry breaking by the single-Z measurement clearly induces $\langle Z_{j,1}\rangle \neq 0$—implying long-range Z correlations in the measured top chain as in property (i) enumerated for the ZZ case. In the projective measurement limit, we can establish a stronger result. There, the post-Z-measurement state is $\left|\psi^{\text{post-}Z}\right\rangle = \mathcal{P}_{\uparrow\cdots\uparrow} |\psi_\Delta\rangle$, while the post-$ZZ$-measurement wavefunction can be written as $\left|\psi^{\text{post-}ZZ}\right\rangle = \frac{1}{\sqrt{2}}(\mathcal{P}_{\uparrow\cdots\uparrow} |\psi_\Delta\rangle + \mathcal{P}_{\downarrow\cdots\downarrow} |\psi_\Delta\rangle)$. Notice that $\mathcal{P}_{\uparrow\cdots\uparrow} |\psi_\Delta\rangle$ and $\mathcal{P}_{\downarrow\cdots\downarrow} |\psi_\Delta\rangle$ represent the same wavefunction for the lower-chain degrees of freedom, because neither the pre-measurement state $|\psi_\Delta\rangle$ nor the ZZ measurement breaks the $\mathbb{Z}_2$ spin-flip symmetry in the upper chain. Thus the expectation value of any operator O_2 in the lower chain is the same for the two post-measurement wavefunctions, $\left\langle\psi^{\text{post-}Z}|O_2|\psi^{\text{post-}Z}\right\rangle = \left\langle\psi^{\text{post-}ZZ}|O_2|\psi^{\text{post-}ZZ}\right\rangle$. Figure 7.4(a) verifies for $K = 1.5$ that properties (ii) and (iii) indeed hold under projective single-Z measurement—including with the same exponents. Finally, Fig. 7.4(b) confirms property (iv) for the single-Z case, i.e., area-law entanglement of the post-measurement state. We have also verified the same properties for $K = 1/2$ and 1 (not shown). Since Z measurement induces a relevant perturbation, we expect (i) through (iv) to persist also in the weak measurement regime.

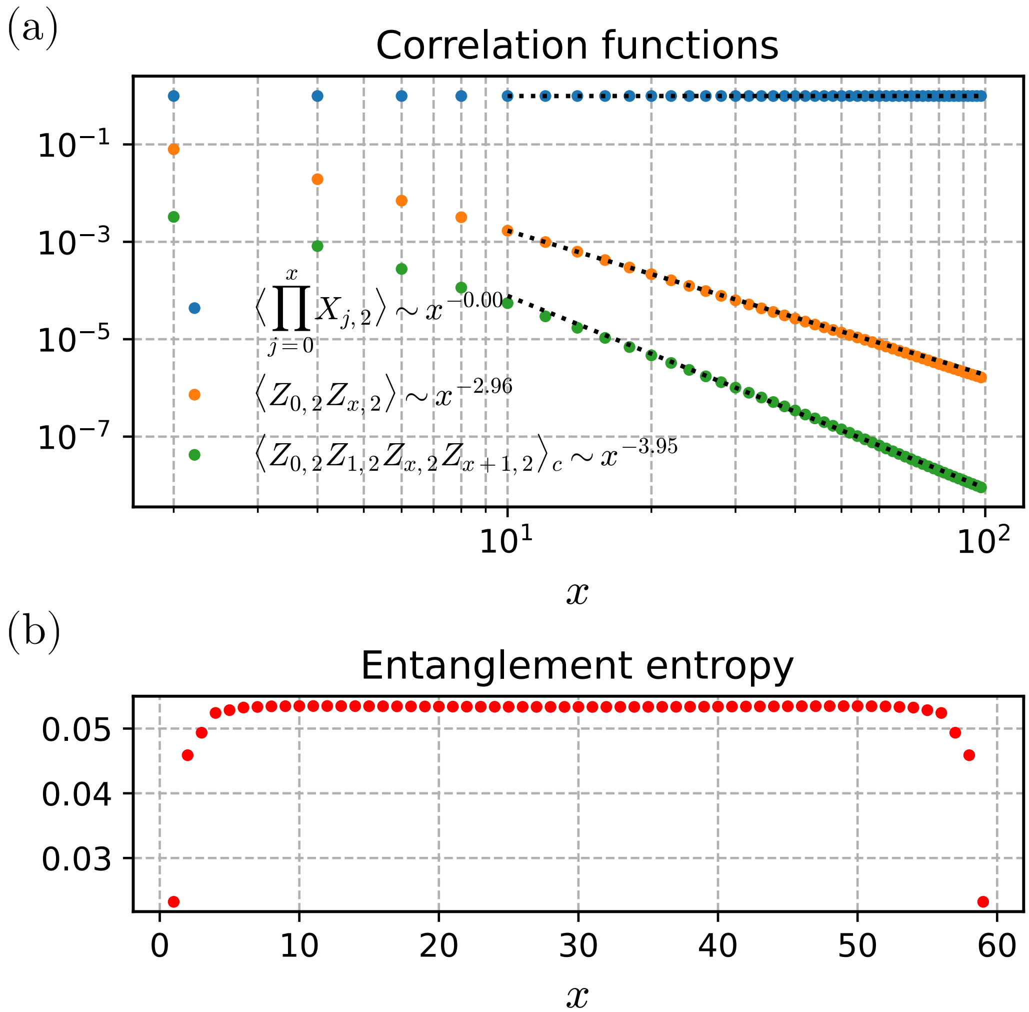

Figure 7.4: Same as Fig. 7.3, but after projective measurement of Z in the upper chain. The fitted power-laws in (a) agree well with analytical predictions in Eqs. (7.35) and (7.36). For both (a) and (b), we have numerically checked that the results for finite measurement strength $\beta = 0.3, 0.5, 1$ are similar to the projective limit.

7.4 Decoding protocol for the gapless parent

For the canonical cluster state with partial projective measurements, we reviewed in Sec. 7.1 how combining classical information with quantum correlations reveals GHZ correlations without resorting to post-selection; recall in particular Eq. (7.7). In this section we show that a similar protocol applied to the gapless parent of the cluster state reveals nontrivially measurement-altered power-law correlations.

Specifically, we take the gapless parent wavefunction $|\psi_\Delta\rangle$ as the initial state and projectively measure $\{X_{j,1}\}$ on the top chain. The measurement outcome $\boldsymbol{s} = \{s_j\}$

and correlations $\langle Z_{j,2}Z_{k,2}\rangle_{\boldsymbol{s}}$ on the bottom chain of the post-measurement state are recorded. Just as for the canonical cluster state in Eq. (7.7), we define the *decoded* ZZ correlator as the following average over all measurement outcomes weighted by the Born probability $p_{\boldsymbol{s}}$:

$$\langle Z_{j,2}Z_{k,2}\rangle_{\mathrm{d}} \equiv \sum_{\boldsymbol{s}} p_{\boldsymbol{s}} \langle Z_{j,2}Z_{k,2}\rangle_{\boldsymbol{s}} s_{j+1}s_{j+2}\cdots s_k. \tag{7.39}$$

Contrary to the cluster state, however, the right-hand side does not simply evaluate to 1. Upon transforming to the $\mathcal{XY}$ basis using Eq. (7.9), this average instead reduces to the 2-point $\mathcal{XX}$ correlator of the initial *pre-measurement* state,

$$\langle Z_{j,2}Z_{k,2}\rangle_{\mathrm{d}} = \langle \mathcal{X}_j\mathcal{X}_k\rangle . \tag{7.40}$$

One can efficiently obtain this rewriting by bringing the s_j factors inside of the expectation value and replacing them with $X_{j,1}$ operators. Note that this step relies only an operator identity and is thus independent of the particular initial state under consideration. For the case of our gapless parent state, Eq. (7.14) yields decoded power-law correlations

$$\langle Z_{j,2}Z_{k,2}\rangle_{\mathrm{d}} \sim |j-k|^{-\frac{1}{2K}}. \tag{7.41}$$

As an illuminating reference, ZZ correlations in the pre-measurement gapless parent state take a very different form compared to Eq. (7.40):

$$\langle Z_{j,2}Z_{k,2}\rangle = \begin{bmatrix} & \mathcal{X}_{j+1} & \mathcal{X}_{j+2} & \cdots & \mathcal{X}_k \\ \tilde{\mathcal{X}}_j & \tilde{\mathcal{X}}_{j+1} & \tilde{\mathcal{X}}_{j+2} & \cdots & \end{bmatrix} \sim |j-k|^{-\frac{1}{2}}. \tag{7.42}$$

The power-law on the right follows from the discussion after Eq. (7.38) and in Sec. 8.5. At $K = 1$ the decoded and unmeasured correlators coincidentally exhibit the same exponent, though at $K \neq 1$ the former are nontrivially measurement altered as claimed.

7.5 More properties of the canonical cluster state SPT

Measurement on generic $\mathbb{Z}_2 \times \mathbb{Z}_2$ SPTs

In Sec. 7.1 we primarily reviewed properties of the $\mathbb{Z}_2 \times \mathbb{Z}_2$ cluster state SPT by specializing to the zero-correlation limit. There we recalled how projective measurement of $X_{j,1}$ for all j in the upper chain yields long-range ordered correlations with $|\langle Z_{j,1}Z_{k,1}\rangle| = 1$ in the lower chain. Here we show that such measurement also induces long-range order in generic $\mathbb{Z}_2 \times \mathbb{Z}_2$ SPTs with finite correlation length.

Let $|\psi_{\mathrm{SPT}}\rangle$ denote a generic ground state in the $\mathbb{Z}_2 \times \mathbb{Z}_2$ SPT phase. We continue to view $|\psi_{\mathrm{SPT}}\rangle$ as living on the ladder from Fig. 7.1(a); moreover, we assume that the two $\mathbb{Z}_2$ symmetries protecting the order are generated by the spin-flip operators in Eq. (7.2). By assumption, one of the SPT string order parameters evaluated with respect to $|\psi_{\mathrm{SPT}}\rangle$ gives

$$\left\langle \begin{bmatrix} & X_{j+1} & \cdots & X_{k-1} & X_k \\ Z_j & & & & Z_k \end{bmatrix} \right\rangle \neq 0 \text{ as } |j-k| \to \infty. \tag{7.43}$$

Applying the string order parameter directly to $|\psi_{\mathrm{SPT}}\rangle$, we can write the resulting wavefunction as

$$\begin{bmatrix} & X_{j+1} & \cdots & X_{k-1} & X_k \\ Z_j & & & & Z_k \end{bmatrix} |\psi_{\mathrm{SPT}}\rangle = c\,|\psi_{\mathrm{SPT}}\rangle + c_\perp \left|\psi_{\mathrm{SPT}}^\perp\right\rangle, \tag{7.44}$$

where $\left|\psi_{\mathrm{SPT}}^\perp\right\rangle$ lives in the orthogonal complement space of $|\psi_{\mathrm{SPT}}\rangle$, i.e., $\left\langle\psi_{\mathrm{SPT}}^\perp|\psi_{\mathrm{SPT}}\right\rangle = 0$. The coefficients c and $c_\perp$ generally depend on j and k. Compatibility with Eq. (7.43), however, requires that $c \neq 0$ for $|j-k| \to \infty$.

Now consider measuring $\{X_{j,1}\}$ with outcome $\boldsymbol{s} = \{s_j\}$. Applying the associated projector

$$\mathcal{P}_{\boldsymbol{s}} = \prod_{j=1}^{N} \left(\frac{1 + s_j X_{j,1}}{2}\right) \tag{7.45}$$

to the left of Eq. (7.44), one obtains

$$\begin{aligned} &\mathcal{P}_{\boldsymbol{s}} \begin{bmatrix} & X_{j+1} & \cdots & X_{k-1} & X_k \\ Z_j & & & & Z_k \end{bmatrix} |\psi_{\mathrm{SPT}}\rangle \\ &= s_{j+1} \cdots s_k Z_{j,2} Z_{k,2} \mathcal{P}_{\boldsymbol{s}} |\psi_{\mathrm{SPT}}\rangle \\ &= c\mathcal{P}_{\boldsymbol{s}} |\psi_{\mathrm{SPT}}\rangle + c_\perp \mathcal{P}_{\boldsymbol{s}} \left|\psi_{\mathrm{SPT}}^\perp\right\rangle. \end{aligned}$$

The $Z_{j,2}Z_{k,2}$ correlator of the post-measurement state is therefore

$$\begin{aligned} \left\langle Z_{j,2} Z_{k,2} \right\rangle_{\boldsymbol{s}} &\equiv \frac{\left\langle \psi_{\mathrm{SPT}} | \mathcal{P}_{\boldsymbol{s}} Z_{j,2} Z_{k,2} \mathcal{P}_{\boldsymbol{s}} | \psi_{\mathrm{SPT}} \right\rangle}{\langle \psi_{\mathrm{SPT}} | \mathcal{P}_{\boldsymbol{s}} | \psi_{\mathrm{SPT}} \rangle} \\ &= s_{j+1} \dots s_k \left(c + c_\perp \frac{\left\langle \psi_{\mathrm{SPT}} | \mathcal{P}_{\boldsymbol{s}} | \psi_{\mathrm{SPT}}^\perp \right\rangle}{\langle \psi_{\mathrm{SPT}} | \mathcal{P}_{\boldsymbol{s}} | \psi_{\mathrm{SPT}} \rangle} \right). \end{aligned} \tag{7.46}$$

For the canonical cluster state, $c = 1$ and $c_\perp = 0$, so one immediately gets $\left\langle Z_{j,2} Z_{k,2} \right\rangle_{\boldsymbol{s}} = s_{j+1} \dots s_k$ in agreement with Eq. (7.5). For generic SPT states, since c remains non-zero even at $|j-k| \to \infty$, $|\langle Z_{j,2} Z_{k,2} \rangle_{\boldsymbol{s}}|$, or alternatively

$s_{j+1}\ldots s_k \left\langle Z_{j,2}Z_{k,2}\right\rangle_{\boldsymbol{s}}$, generically exhibits long-range order in the post-measurement state, regardless of the particular measurement outcome $\boldsymbol{s}$.

The decoding protocol reviewed in Sec. 7.1 also extends straightforwardly to the finite-correlation-length regime. Consider again the generic SPT string order parameter expectation value from Eq. (7.43). Upon inserting X-basis resolutions of the identity for chain 1, one can exactly write

$$\left\langle\begin{bmatrix} & X_{j+1} & \cdots & X_{k-1} & X_k \\ Z_j & & & & Z_k \end{bmatrix}\right\rangle = \sum_{\boldsymbol{s}} p_{\boldsymbol{s}} \left\langle Z_{j,2}Z_{k,2}\right\rangle_{\boldsymbol{s}} s_{j+1}\cdots s_k. \tag{7.47}$$

Since the left side exhibits long-range order (again by assumption), so too must the right side, i.e.,

$$\sum_{\boldsymbol{s}} p_{\boldsymbol{s}} \left\langle Z_{j,2}Z_{k,2}\right\rangle_{\boldsymbol{s}} s_{j+1}\cdots s_k \neq 0 \;\text{ as }\; |j-k|\to\infty. \tag{7.48}$$

The finite correlation length merely reduces the nonzero constant from its maximal value of 1; cf. Eq. (7.7).

Weak measurements in a tilted basis

For the remainder of this Sec. we return to the zero-correlation-length SPT ground state, $|\psi_0\rangle$, defined with periodic boundary conditions. Suppose now that we *weakly* measure the 'tilted' operator $\cos\omega X_{j,1} + \sin\omega Z_{j,1}$ for all sites j in the top chain, post-selecting for simplicity on a spatially uniform measurement outcome. We are interested in the fate of the two-point ZZ correlator for the lower chain in this generalized scenario. The correlator explicitly reads

$$\left\langle Z_{j,2}Z_{k,2}\right\rangle_{\text{uni}} = \frac{\left\langle\psi_0|Z_{j,2}Z_{k,2}e^{2\beta\sum_j(\cos\omega X_{j,1}+\sin\omega Z_{j,1})}|\psi_0\right\rangle}{\left\langle\psi_0|e^{2\beta\sum_j(\cos\omega X_{j,1}+\sin\omega Z_{j,1})}|\psi_0\right\rangle}, \tag{7.49}$$

where β parameterizes the weak measurement strength. Using the fact that

$$Z_{j,2}X_{j+1,1}\ldots X_{k,1}Z_{k,2} = 1 \tag{7.50}$$

when acting on the zero-correlation-length ground state, we can rewrite Eq. (7.49) in terms of expectation values of operators exclusively acting on the top chain:

$$\left\langle Z_{j,2}Z_{k,2}\right\rangle_{\text{uni}} = \frac{\left\langle\psi_0|\left(\prod_{i=j+1}^{k} X_{i,1}\right)e^{2\beta\sum_j(\cos\omega X_{j,1}+\sin\omega Z_{j,1})}|\psi_0\right\rangle}{\left\langle\psi_0|e^{2\beta\sum_j(\cos\omega X_{j,1}+\sin\omega Z_{j,1})}|\psi_0\right\rangle}, \tag{7.51}$$

Reference [78] showed that such expectation values in the $|\psi_0\rangle$ state are nonvanishing only if the operator under consideration commutes with all ZXZ terms in the

Hamiltonian; for an operator living exclusively on one chain, as in the case above, it must be either the identity or a symmetry generator. We then obtain

$$\left\langle Z_{j,2} Z_{k,2} \right\rangle_{\text{uni}} = \frac{(\tanh 2\beta \cos\omega)^{|j-k|} + (\tanh 2\beta \cos\omega)^{N-|j-k|}}{1 + (\tanh 2\beta \cos\omega)^{N}}, \tag{7.52}$$

where N is the number of sites in each chain and we used the fact that $\langle \prod_{i=1}^{N} X_{i,1} \rangle = +1$. With $\omega = 0$ and in the projective-measurement limit $\beta \to \infty$, the right side of Eq. (7.52) becomes unity, recovering the standard long-range-order result. Suppose instead that β is finite and/or $\omega \neq 0$. Taking $|j - k| \ll N$ and then $N \to \infty$, here we find

$$\left\langle Z_{j,2} Z_{k,2} \right\rangle_{\text{uni}} \approx (\tanh 2\beta \cos\omega)^{|j-k|} \equiv e^{-|j-k|/\xi}. \tag{7.53}$$

Above we defined a finite correlation length

$$\xi = \frac{1}{\ln\left(\frac{1}{\tanh 2\beta \cos\omega}\right)} \tag{7.54}$$

that signals the exponential decay of the ZZ correlator. Therefore, long-range order only appears when the measurement is projective *and* when the tilt angle is $\omega = 0$ [78].

Chapter 8

MEASUREMENT-INDUCED BOUNDARY TRANSITIONS

Chapter 7 identified the gapless cluster-state parent and described how uniform measurements act as defect-line or boundary perturbations. Here the measurement basis itself becomes a tuning parameter. The resulting transition is not present in the descendant gapped cluster state: it relies on the gapless parent and is naturally interpreted as a boundary RG flow.

8.1 Tilted measurements and intermediate fixed points

Section 7.3 showed that weakly measuring $X_{j,1}$ in the gapless parent of the cluster state and post-selecting the uniform outcome $X_{j,1} = +1$ yields long-range order in the second chain; i.e., the two-point function $\langle Z_{j,2} Z_{k,2} \rangle_{\text{uni}}$ tends to a nonzero constant as $|j - k| \to \infty$. This result reflects the fact that weak $X_{j,1}$ measurements generate a relevant perturbation to the Luttinger liquid fixed point in this post-selection sector, revealing distinct behavior from the gapped cluster state SPT. Indeed in the gapped SPT, long-range Z order arises only when projectively measuring $X_{j,1}$ (recall Sec. 7.5). This section investigates whether measurement-induced long-range order in the gapless parent state persists upon rotating the measurement basis away from X toward Z. Here too we will uncover richer behavior than for the gapped SPT, where long-range Z order induced by projective X measurements immediately disappears upon tilting the measuring basis [78] (see also Sec. 7.5).

One can partially address the impact of tilting the measuring basis by studying the stability of fixed points driven by X- or Z-type weak measurements. In particular, if both fixed points are stable, then (i) long-range Z order induced by X measurements persists over a finite tilt-angle regime and (ii) an intermediate (unstable) fixed point naturally occurs at some nontrivial critical tilt angle. Therefore, this sets up the stage for exploring possible measurement-induced boundary transitions.

As a warm-up related to the start of Sec. 7.3, in Sec. 8.1 we study weak measurements of the $\mathbb{Z}_2$-preserving operators $\cos(\omega) X_{j,1} + \sin(\omega) Z_{j,1} Z_{j+1,1}$, where $\omega \in [0, \pi/2]$ denotes the tilt angle. In Sec. 8.1, we then consider an on-site tilted measurement basis $\cos(\omega) X_{j,1} + \sin(\omega) Z_{j,1}$ that generically breaks $\mathbb{Z}_2$ spin-flip symmetry for the measured chain. Both subsections focus on uniform post-selection sectors. For both types of tilted measurement bases, we present numerical and analytical evidence that $\omega = 0$ and $\omega = \pi/2$ indeed correspond to stable fixed points separated by an intervening fixed point at a critical ω_c. Section 8.1 analyzes non-linear averages over measurement outcomes and argues that signatures of such intermediate fixed points persist as measured by such quantities.

$\mathbb{Z}_2$-preserving measurement basis

Consider a weak measurement enacted by the non-unitary operator

$$M_{\mathrm{sym}}(\omega) = \prod_{j \in \mathrm{even}} e^{\beta[\cos(\omega) X_{j,1} + \sin(\omega) Z_{j,1} Z_{j+1,1}]}, \tag{8.1}$$

which preserves the $\mathbb{Z}_2$ symmetry in the first chain. Each term in the product represents local weak measurement of a two-site operator $\cos(\omega) X_{j,1} + \sin(\omega) Z_{j,1} Z_{j+1,1}$ whose eigenvalues are ± 1. Note that the product runs over all *even* sites, such that all the local measurements mutually commute. The operator $M_{\mathrm{sym}}(\omega)$ corresponds to a weak measurement outcome that uniformly amplifies contribution from the $+1$ eigenvalues for each constituent two-site operator. Since both $X_{j,1}$ and $Z_{j,1} Z_{j+1,1}$ admit a local representation in terms of the $\mathcal{XXZ}$ spin chains [Eq. (7.11)], it is easier to understand the transition between different fixed points compared to the case (examined later) where we weakly measure single-spin operators in a tilted basis.

We essentially already studied the extreme cases $\omega = 0$ and $\omega = \pi/2$ in Secs. 7.3 and 7.3, respectively. The sole difference is that the weak measurement operator $M_{\mathrm{sym}}(\omega)$ covers only half the sites, which does not affect the leading contribution to the measurement-induced boundary term in the action. For $\omega = 0$ the boundary term again takes the form of Eq. (7.23), which generates long-range order in the disorder operator for the upper chain, long-range Z order for the lower chain, and area-law entanglement. For $\omega = \pi/2$, the boundary term is given in Eq. (7.33) and generates dual behavior: long-range Z order for the upper chain and long-range order in the disorder operator for the lower chain, again with area-law entanglement. If the fixed points arising from measurements in these extreme limits are stable, it is natural to expect an intervening unstable fixed point at a critical tilt angle ω_c—which we indeed establish below. The duality transformation in Eq. (7.34) sends $\omega \to \frac{\pi}{2} - \omega$ and hence fixes the critical angle exactly to $\omega_c = \pi/4$.

We can access the intermediate fixed point from a field-theoretic viewpoint as follows. For general tilt angles ω, the measurement encoded in Eq. (8.1) induces a boundary term

$$\delta S_{\text{meas}} \propto \beta \int_{x,\tau} \delta(\tau)\,[\cos\omega\cos\theta\cos\tilde{\theta} + \sin\omega\sin\theta\sin\tilde{\theta}], \tag{8.2}$$

which is relevant for $K > 1/2$. Upon passing to symmetric and antisymmetric field combinations $\theta_\pm$ and $\phi_\pm$—defined below Eq. (7.23)—we equivalently obtain

$$\delta S_{\text{meas}} \propto \beta \int_{x,\tau} \delta(\tau)\left[\sin\left(\frac{\pi}{4} - \omega\right)\cos\theta_+ + \cos\left(\frac{\pi}{4} - \omega\right)\cos\theta_-\right]. \tag{8.3}$$

For $0 \le \omega < \pi/4$, both relevant cosines have nonzero, positive prefactors, thus pinning θ_+ and θ_- to minima of the boundary perturbation. In this tilt-angle regime we expect the system to flow to the same boundary fixed point as in the limiting case with $\omega = 0$ (pure X measurement). For $\pi/4 < \omega \le \pi/2$, both cosines again have nonzero coefficients, though the $\cos\theta_+$ prefactor exhibits the opposite sign, pinning θ_+ to distinct minima compared to the preceding regime. Here we expect the system to flow to the same boundary fixed point that arises with $\omega = \pi/2$ (pure ZZ measurement).

We check the stability of these two fixed points by computing the correlation functions of several $\mathbb{Z}_2$-preserving operators and extracting their scaling dimensions. In particular, a symmetry-allowed operator O with scaling dimension less than 1 would constitute a relevant perturbation and indicate instability of the underlying fixed point; conversely, if the scaling dimensions of all such operators are larger than 1, then the fixed point is stable. As reported in Table 8.2, we find that with $\omega = 0$ all scaling dimensions for the $\mathbb{Z}_2$-preserving operators that we extracted indeed exceed 1 for any $K > 1/2$—evidencing that this fixed point is stable against symmetry-allowed perturbations. Duality implies that the $\omega = \pi/2$ fixed point has the same stability as the $\omega = 0$ fixed point.

Exactly at $\omega = \pi/4$, the θ_- sector remains pinned while the θ_+ sector becomes unpinned (due to vanishing of the relevant cosine term), indicating an analytically tractable measurement-induced boundary transition in the $\mathbb{Z}_2$-preserving measurement basis. One can crudely view the pinned θ_- sector as contributing area-law entanglement while the unpinned θ_+ sector underlies logarithmic entanglement scaling with an associated effective central charge $c_{\text{eff}} = 1$.Formally, c_{eff} follows by fitting the system's overall entanglement entropy to $S = \frac{c_{\text{eff}}}{3}\log[\frac{L}{\pi}\sin\frac{\pi l}{L}] + \text{const.}$ We indeed numerically extract an effective central charge $c_{\text{eff}} \approx 1$ following this procedure as shown in Fig. 8.1.

The intermediate fixed point is unstable, as one can infer from the scaling dimension $[X_{j,1}] = \frac{1}{2K} < 1$ for $K > \frac{1}{2}$; see Sec. 8.5 for the derivation. Physically, adding a

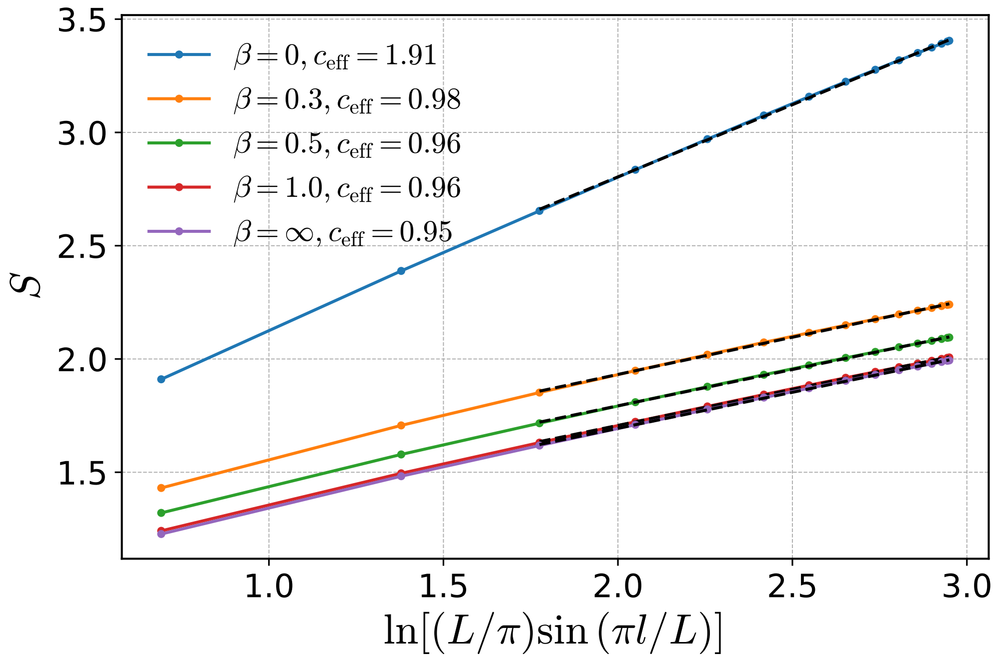

Figure 8.1: Entanglement entropy scaling at the measurement-induced boundary transition for the $\mathbb{Z}_2$-preserving case [$\omega = \pi/4$ in Eq. (8.1)]. Data were obtained from DMRG with bond dimension $\chi = 2000$ assuming $K = 1.5$, $L = 60$, and periodic boundary conditions. In the horizontal axis l is the subsystem size. The effective central charge c_{eff} is extracted by fitting to $S = \frac{c_{\text{eff}}}{3} \ln[(L/\pi)\sin(\pi l/L)] + \text{const}$ (see black dashed lines). For all non-zero measurement strengths shown, we obtain $c_{\text{eff}} \approx 1$ in harmony with field-theory predictions. We verified that the fitted effective central charge is essentially unchanged for $K = 1$.

relevant term composed of $X_{j,1}$ operators to the boundary action has the same effect as changing the tilt angle away from $\omega = \pi/4$—driving the system into one of the two stable fixed points depending on the sign of the coefficient.

We numerically examine the measurement-induced boundary transition by probing order and disorder operators as a function of tilt angle. More precisely, for a system of length L, we find that in the post-measurement wavefunction, the derivative of order and disorder operator correlations,

$$\frac{d}{d\omega}\left\langle Z_{\frac{L}{4},2} Z_{\frac{3L}{4},2}\right\rangle_{\text{uni}} \quad \text{and} \quad \frac{d}{d\omega}\left\langle \prod_{j=L/4}^{3L/4} X_{j,2}\right\rangle_{\text{uni}}, \tag{8.4}$$

both exhibit a peak near $\omega = \pi/4$ that sharpens as L increases—consistent with onset of a divergence in the thermodynamic limit. Figure 8.2 plots the two quantities above in the projective measurement limit; we have checked that similar results also arise for weak measurements, e.g., with $\beta = 0.5$ (see Sec. 8.5). Because of duality, the two panels in Fig. 8.2 are related by $\omega \to \frac{\pi}{2} - \omega$, up to a minus sign.

Table 8.1: Operators with long-range order in two distinct measurement-tilt-angle regimes, $0 \leq \omega < \frac{\pi}{4}$ and $\frac{\pi}{4} < \omega \leq \frac{\pi}{2}$, for the case with $\mathbb{Z}_2$-preserving tilted measurement operators. At $\omega = \pi/4$ the measurement-induced boundary transition is described by a $c = 1$ boson CFT.

	$0 \leq \omega < \frac{\pi}{4}$	$\frac{\pi}{4} < \omega \leq \frac{\pi}{2}$
upper chain	$\left\langle \prod_{j=0}^{x} X_{j,1} \right\rangle$	$\langle Z_{0,1} Z_{x,1} \rangle$
lower chain	$\langle Z_{0,2} Z_{x,2} \rangle$	$\left\langle \prod_{j=0}^{x} X_{j,2} \right\rangle$

To summarize, the measurement in Eq. (8.1) yields a transition between two stable fixed points when the tilt angle ω varies from 0 to $\pi/2$ (see Table 8.1). The transition is described by a $c = 1$ boson CFT that one can view as a two-channel Luttinger liquid in which weak measurements pin a field at $\tau = 0$ for one channel but not the other. As an aside, the same low-energy theory in Eq. (8.3) alternatively arises from measurement of both $X_{j,1}$ and $X_{j,2}$:

$$M'_{\text{sym}}(\omega) = \prod_j e^{\beta \cos(\omega) X_{j,1}} e^{\beta \sin(\omega) X_{j,2}}. \tag{8.5}$$

We explore this measurement operator in Sec. 8.5 and find a similar intermediate fixed point with $c_{\text{eff}} = 1$.

$\mathbb{Z}_2$-breaking measurement basis

The example above was analytically tractable thanks to duality arguments and bosonization. Next we address the more subtle case of tilted on-site measurements implemented by

$$M(\omega) = e^{\beta \sum_j [\cos(\omega) X_{j,1} + \sin(\omega) Z_{j,1}]}. \tag{8.6}$$

The limits $\omega = 0$ and $\omega = \pi/2$ correspond to two different fixed points that we analyzed in Sections 7.3 and 7.3, respectively. For intermediate ω values, the relevant $X_{j,1}$ and $Z_{j,1}$ measurements compete with each other, and the winner determines the long-distance physics. We will show that, as in the previous subsection, these fixed points are separated by an intervening unstable fixed point at an intermediate critical tilt angle ω_c (which here becomes β dependent).

To investigate the stability of the $\omega = 0, \pi/2$ fixed points, we compute the scaling dimension of several different operators. Tables 8.2 and 8.3 in Sec. 8.5 report our

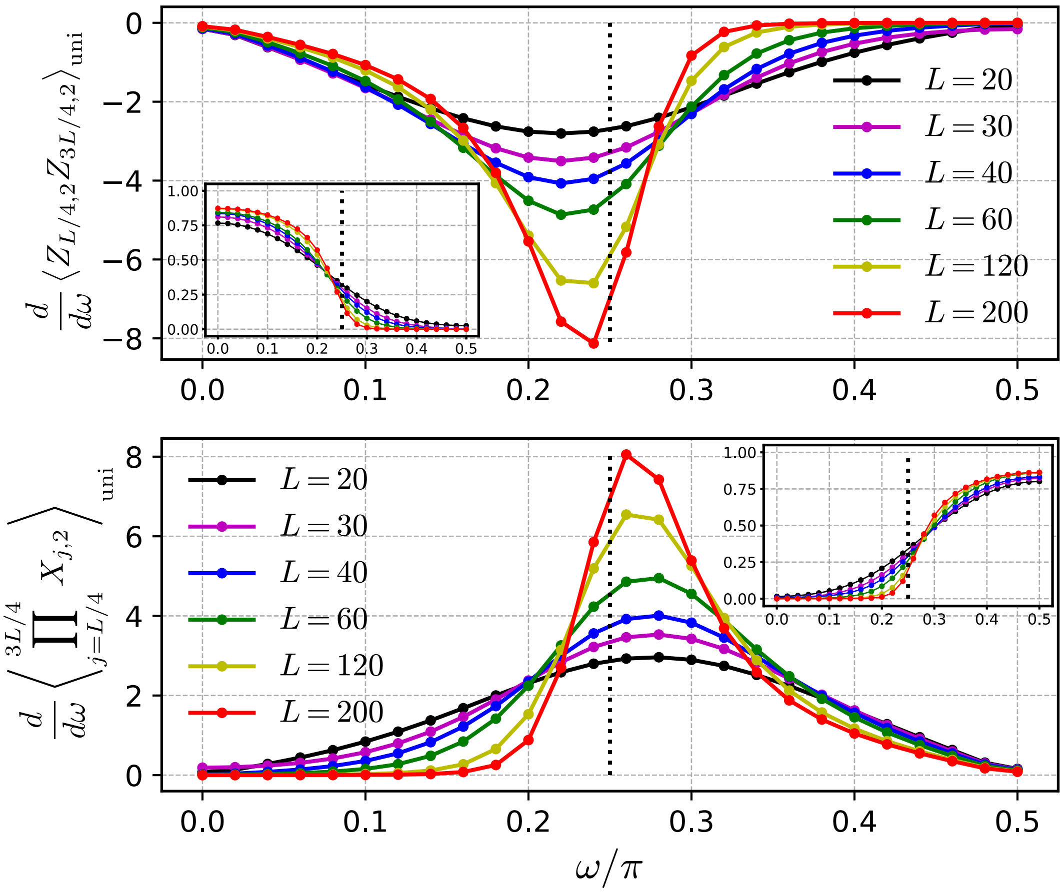

Figure 8.2: Derivative of order and disorder parameter correlations for the lower chain of the post-measurement gapless parent of the cluster state with $K = 1.5$ as a function of the measurement tilt angle ω in the $\mathbb{Z}_2$-preserving case [Eq. (8.1)]. Black dotted lines mark the measurement-induced boundary transition at $\omega_c = \pi/4$. Insets: order parameter correlations $\left\langle Z_{\frac{L}{4},2}Z_{\frac{3L}{4},2}\right\rangle_{\text{uni}}$ (upper panel) and disorder parameter correlations $\left\langle \prod_{j=L/4}^{3L/4} X_{j,2}\right\rangle_{\text{uni}}$ (bottom panel) as a function of ω/π. The gapless parent state is obtained using DMRG with open boundary conditions and bond dimension $\chi = 1200$.

results for the $\omega = 0$ and $\omega = \pi/2$ cases, respectively. Unlike the previous subsection, it is now essential to consider operators that break $\mathbb{Z}_2$ in the first chain, since the tilted measurement operator in Eq. (8.6) explicitly breaks that symmetry. In particular, we find numerically that at $K = 1$, $Z_{j,1}$ is a marginal operator at the $\omega = 0$ fixed point; in this case we can not infer the stability of that fixed point by a simple scaling dimension analysis. However, for $K > 1$, all the operators we have checked have scaling dimension larger than 1 for both fixed points, indicating that they are likely stable and hence that a transition exists at a nontrivial critical tilt angle ω_c.

Figure 8.3 corroborates this picture by plotting correlations of the order and the disorder operators for the lower chain at different system sizes L with $K = 1.5$. Note the striking similarity to Fig. 8.2 obtained for a fully $\mathbb{Z}_2$ preserving measurement. The breaking of $\mathbb{Z}_2$ symmetry for the upper chain combined with the loss of duality in the present case pushes the critical tilt angle ω_c slightly below $\pi/4$; an intermediate fixed point nevertheless clearly still arises—representing a second example of a measurement-induced boundary transition.

Unlike the symmetry-preserving measurement in the previous section, it is hard to analytically assess the entanglement scaling at the intermediate fixed point due to the nonlocality of the $\mathbb{Z}_2$-breaking measurement operator in the $\mathcal{XXZ}$ basis. Nonetheless, we numerically compute the effective central charge at the transition for systems with different Luttinger parameters. As an example, in Fig. 8.4(a) we observe that the entanglement entropy peaks at the intermediate fixed point $\omega_c \approx 0.22\pi$ for $K = 1.5$, and we can extract the effective central charge $c_{\text{eff}} \approx 0.52$ using the relation between half-chain entanglement entropy and system size for one interval attached to the boundary, $S_{L/2} = \frac{c_{\text{eff}}}{6} \log(L) + \text{const}$ [see Fig. 8.4(b)]. Using the same procedure for systems with different Luttinger parameters, we also observe that c_{eff} varies as a function of K; see Fig. 8.4(c).

To understand the relation between intermediate fixed points from $\mathbb{Z}_2$-preserving and $\mathbb{Z}_2$-breaking measurements, we note that the former is not stable against symmetry-breaking measurements. More specifically, the $\mathbb{Z}_2$-breaking operator $Z_{j,1}$ is relevant at the $\mathbb{Z}_2$-preserving intermediate fixed point, as shown in Sec. 8.5. It is therefore expected that a weak $Z_{j,1}$ measurement drives an RG flow away from the $\mathbb{Z}_2$-preserving intermediate fixed point to the $\omega = \pi/2$ fixed point in Eq. (8.6). Meanwhile, adding a small $X_{j,1}$ measurement to the $\mathbb{Z}_2$-preserving intermediate fixed point forces the system to flow to the $\omega = 0$ fixed point. With some fine-tuned combination of $Z_{j,1}$ and $X_{j,1}$ measurements, we expect a flow from the $\mathbb{Z}_2$-preserving intermediate fixed point to the $\mathbb{Z}_2$-breaking one. Recall that in the $\mathbb{Z}_2$-preserving case, the effective central charge is $c_{\text{eff}} = 1$ because one of the bosonic modes is gapped while the other remains gapless (and the central charge of a single Luttinger liquid is 1 for any value of K). The origin and significance of the continuous dependence of c_{eff} on K in the $\mathbb{Z}_2$-breaking measurement remains an intriguing question for future work.

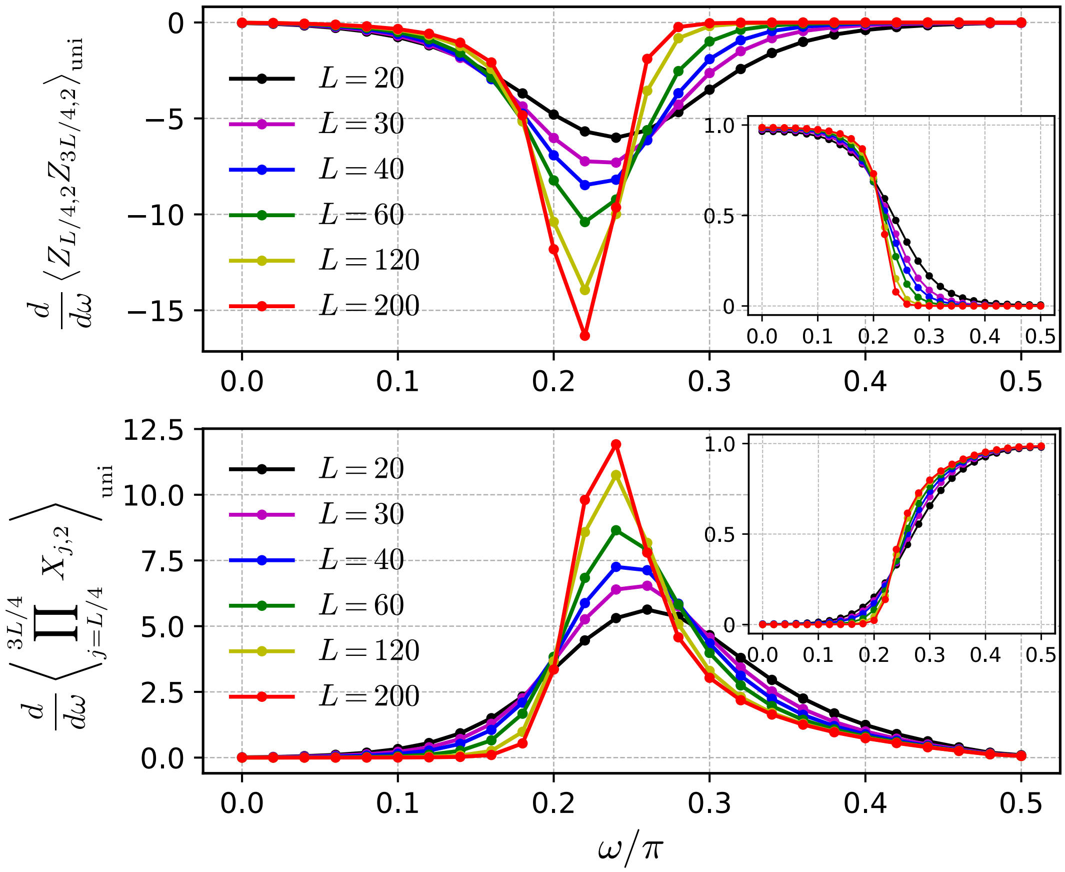

Figure 8.3: Same as Fig. 8.2 but for the $\mathbb{Z}_2$-breaking measurement operator [Eq. (8.6)]. Here the critical tilt angle for the measurement-induced boundary transition is around $\omega_c \approx 0.22\pi$.

Intermediate fixed point from an ensemble of measurement outcomes

So far in this section we focused only on post-selecting for uniform measurement outcomes—which generically require exponentially many trials in system size to capture with reasonable probability. Another way to observe the measurement-induced effect is to average quantities that are nonlinear in the density matrix $\rho_s = |\psi_s\rangle\langle\psi_s|$ [16, 58, 57]. For instance, one can take advantage of "non-linear observables" defined as

$$\langle\langle\Gamma\rangle\rangle \equiv \frac{\sum_s p_s^2 \langle\Gamma\rangle_s}{\sum_s p_s^2}, \tag{8.7}$$

where Γ is any operator on the second chain of our gapless parent of the cluster state. By doing so we effectively weight each set of measurement outcomes s by the probability distribution p_s^2, thereby favoring the most likely outcomes. Experimentally determining the right-hand side remains nontrivial, however: One would need to repeatedly measure Γ and record the results for different outcomes

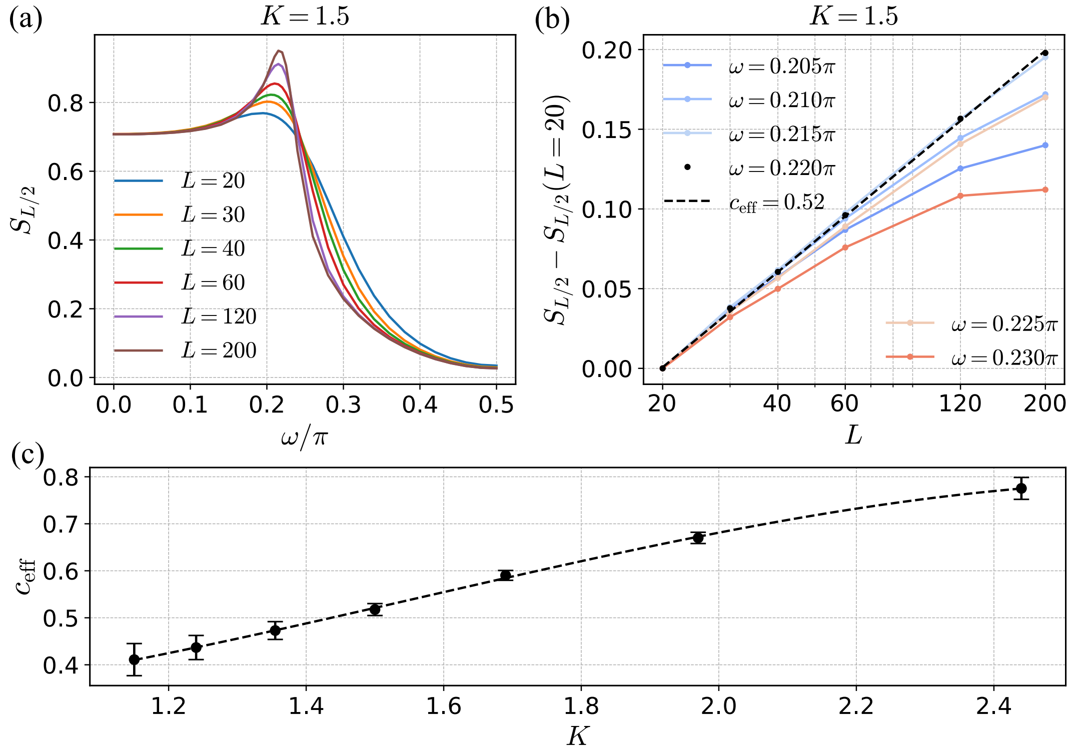

Figure 8.4: (a,b) Dependence of half-chain entanglement entropy $S_{L/2}$ on tilt angle ω and system size L for the $\mathbb{Z}_2$-breaking measurement protocol [Eq. (8.6)], assuming $K = 1.5$. At the intermediate fixed point $\omega = \omega_c \approx 0.22\pi$ [see black dots in (b)] the data fit well to $S_{L/2} = \frac{c_{\text{eff}}}{6}\log(L) + \text{const}$ with $c_{\text{eff}} \approx 0.52$. (c) Effective central charge obtained obtain by the same procedure in (b) but for different Luttinger parameters. The dashed line is simply a guide to the eye. Data were obtained from DMRG with bond dimension $\chi = 1200$; see Sec. 8.5 for numerical details.

$\boldsymbol{s}$, collecting sufficient data to estimate the associated probabilities $p_{\boldsymbol{s}}$—which also requires exponentially many trials. The main point of this section is that Eq. (8.7) is easy to compute analytically, manifestly involves all measurement outcomes, and yet still reveals measurement-altered properties. Following Refs. [58, 57], we show in Sec. 8.3 that these nonlinear, measurement-averaged observables are exactly equivalent to observables evaluated in a replicated theory—i.e., describing four chains instead of two—with uniform post-selection. The price we pay in considering a replicated version of the model is thus balanced by the simplicity of focusing on uniform measurement outcomes.

Suppose that in some original (un-replicated) model we measure operators O_j with strength β and perform a non-linear average over measurement outcomes. Sec. 8.3

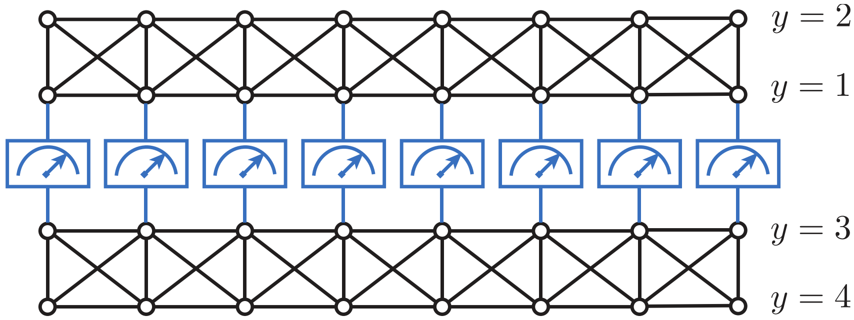

Figure 8.5: Graphical representation of the setup considered to compute the non-linear averages in Eq. (8.7). The replicated system consists of four chains: Chains 1 and 2 are the original gapless parent of the cluster state (swapped relative to Fig. 7.1), while chains 3 and 4 form an identical copy of 1 and 2, respectively. To compute the non-linear observables in Eq. (8.7), a weak measurement of $O_{j,1}O_{j,3}$ is applied at all sites with post-selection for a uniform outcome.

recasts Eq. (8.7) as

$$\langle\langle\Gamma\rangle\rangle = \frac{\langle\psi_\Delta^A| \langle\psi_\Delta^B| \Gamma^A e^{2\beta' \sum_j O_j^A O_j^B} |\psi_\Delta^A\rangle |\psi_\Delta^B\rangle}{\langle\psi_\Delta^A| \langle\psi_\Delta^B| e^{2\beta' \sum_j O_j^A O_j^B} |\psi_\Delta^A\rangle |\psi_\Delta^B\rangle}, \tag{8.8}$$

where the superscripts (A, B) denote the copy of the replicated theory, $|\psi_\Delta\rangle$ is the unmeasured Hamiltonian ground state, and $\tanh(2\beta') = \tanh^2(2\beta)$. Notice that, as stated above, the right side of Eq. (8.8) does not involve an explicit sum over measurement outcomes, but rather takes the form of a normalized expectation value involving the joint state $|\psi_\Delta^A\rangle |\psi_\Delta^B\rangle$ modified by a uniform weak-measurement operator $e^{\beta' \sum_j O_j^A O_j^B}$ acting on both copies. Numerically, Eq. (8.8) provides a straightforward way of computing non-linearly averages from a many-body state (obtained from, e.g., tensor networks), in contrast to Eq. (8.7) which requires summing over exponentially many outcomes.

In our setup, $|\psi\rangle$ is the ground state of the Hamiltonian (7.11) defined on a two-chain system; in the replicated theory we associated copy A with chains $y = 1, 2$, and copy B with chains $y = 3, 4$ (see Fig. 8.5). Measurement of the tilted operator $\cos(\omega)X_{j,1} + \sin(\omega)Z_{j,1}$ in the un-replicated theory translates into a uniform weak measurement operator

$$e^{\beta' \sum_j [\cos(\omega)X_{j,1}+\sin(\omega)Z_{j,1}][\cos(\omega)X_{j,3}+\sin(\omega)Z_{j,3}]} \tag{8.9}$$

in the replica problem specified on the right side of Eq. (8.8). We are specifically interested in ω dependence of correlations $\langle\langle Z_{j,2}Z_{k,2}\rangle\rangle$ and $\left\langle\left\langle \prod_{i=j}^k X_{i,2}\right\rangle\right\rangle$ of the order and disorder operators, respectively, in the unmeasured chain 2. Computing these quantities analytically is complicated, so we content ourselves with the numerical evaluation presented in Fig. 8.6. We observe behavior very similar to that shown in Fig. 8.3 for an un-replicated system with uniform post-selection. Even though the finite size effects are more pronounced in the replicated theory because of the reduced maximum system size we can achieve using DMRG, an intermediate fixed point at some nontrivial ω_c clearly persists when non-linearly averaging over measurement outcomes, suggesting that a measurement-induced boundary transition occurs also in this case.

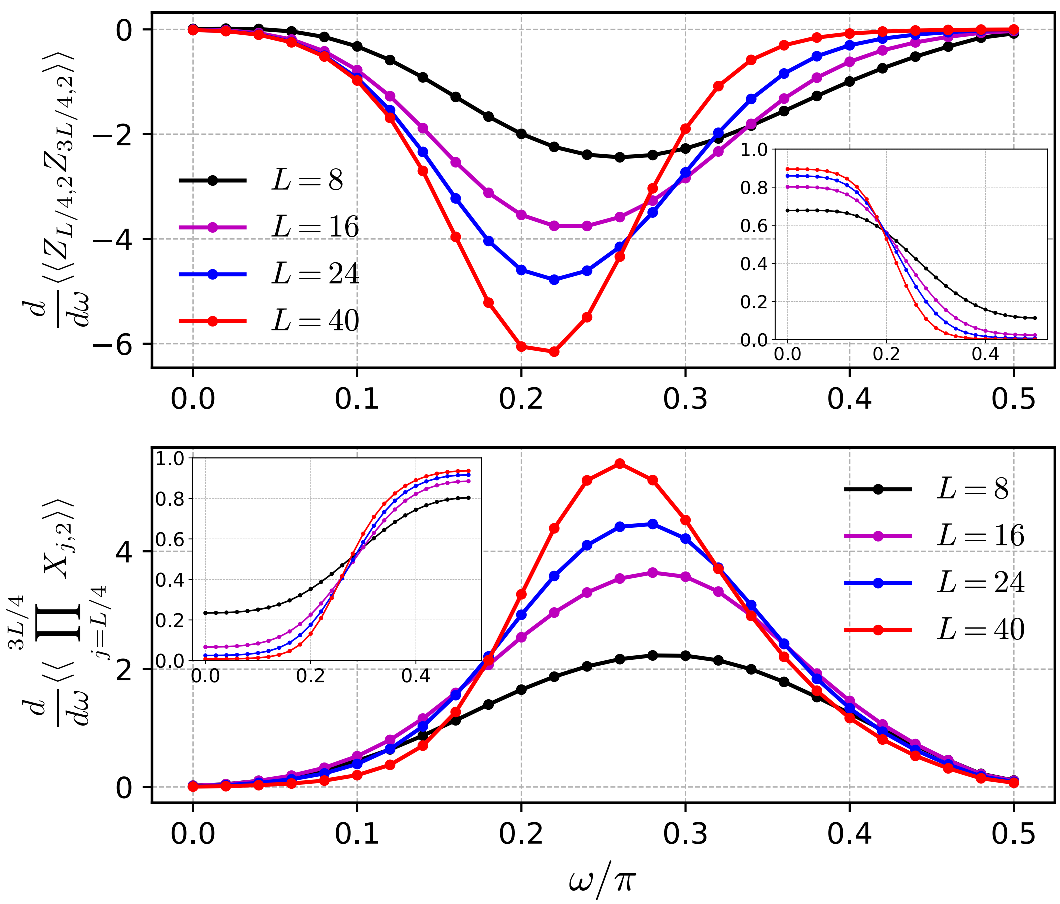

Figure 8.6: Derivative of order and disorder parameter correlations in the $y = 2$ chain of the post-measurement replicated gapless parent of the cluster state as a function of the tilting angle ω. A measurement-induced boundary transition remains visible at a critical value of around $\omega_c \approx 0.2\pi$. Insets: order parameter correlations $\left\langle\!\left\langle Z_{\frac{L}{4},2}Z_{\frac{3L}{4},2}\right\rangle\!\right\rangle$ and disorder parameter correlations $\left\langle\!\left\langle \prod_{j=L/4}^{3L/4} X_{j,2}\right\rangle\!\right\rangle$ as a function of ω/π. The replicated gapless parent of the cluster state is obtained using DMRG with open boundary conditions and bond dimension $\chi = 1600$, assuming $K = 1.5$. Sec. 8.5 analyzes different K values.

8.2 Perturbative approach in the projective measurement limit

In this technical section, we focus on the $\mathcal{X}$ measurement, $e^{\sum_j \beta \mathcal{X}_j}$, in a single $\mathcal{XXZ}$ chain

$$H = -\sum_j (\mathcal{X}_j \mathcal{X}_{j+1} + \mathcal{Y}_j \mathcal{Y}_{j+1} + \Delta \mathcal{Z}_j \mathcal{Z}_{j+1}). \tag{8.10}$$

Since the $\mathcal{X}$ measurement and post-selection of the uniform measurement outcome induce a relevant perturbation for every $\Delta \in (-1, 1)$, any weak measurement with finite measurement strength β flows to the projective-measurement fixed point with $\beta \to \infty$. Therefore, we can expand the wavefunction around the projective limit [4]

$$|\psi\rangle_{\text{uni}} \propto e^{\sum_j \beta \mathcal{X}_j} |\psi_c\rangle \propto |\Omega\rangle + u \sum_j a_j |j\rangle + u^2 \sum_{j,k} a_{jk} |j, k\rangle + O(u^3) \tag{8.11}$$

where $u = \exp(-2\beta)$, $|\psi_c\rangle$ is the ground state of the Hamiltonian (8.10), $|\psi\rangle_{\text{uni}}$ is the post-measurement wavefunction, $|\Omega\rangle$ is the product state $\bigotimes_j \left|\mathcal{X}_j = +1\right\rangle$ corresponding to the uniform outcome, $|j, k, l, \ldots\rangle = \mathcal{Z}_j \mathcal{Z}_k \mathcal{Z}_l \ldots |\Omega\rangle$, and $a_{j,k,l,\ldots}$ is the *strange correlator*

$$a_{j,k,l,\ldots} \equiv \frac{\left\langle \Omega | \mathcal{Z}_j \mathcal{Z}_k \mathcal{Z}_l \ldots | \psi_c \right\rangle}{\langle \Omega | \psi_c \rangle}. \tag{8.12}$$

The strange correlator has been studied for SPT states [80], but here it is computed for a critical state. In general $|\psi_0\rangle$ can be any critical state, and one can replace $\mathcal{X}$ by any local operator $\mathcal{O}$ and $\mathcal{Z}$ by $\mathcal{O}^{\perp}$ such that $\{\mathcal{O}, \mathcal{O}^{\perp}\} = 0$. In the large β (i.e. $u \ll 1$) limit, the $O(u^3)$ terms in Eq. (8.11) can be neglected and the correlation functions can be computed from the truncated wavefunction

$$|\psi_{\text{trunc}}\rangle = |\Omega\rangle + u \sum_j a_j |j\rangle + u^2 \sum_{j,k} a_{jk} |j, k\rangle. \tag{8.13}$$

In the cases of interest, we observe that a_j and a_{jk} take the following form,

$$a_j = m, \quad a_{jk} - a_j a_k \sim \frac{const.}{|j-k|^{\eta}}. \tag{8.14}$$

We remark that the expansion (8.11) is well-behaved only if $\eta > 1$: for the examples analyzed in this work, this is always true when the measurement corresponds to a relevant operator. The correlators of the truncated wavefunction can thus be computed as,

$$\begin{aligned}
\left\langle \mathcal{X}_j \right\rangle_{\text{trunc}} &\sim 1 - c_1 u^2 m^2 \quad (\text{if } m \neq 0) \\
&\sim 1 - c_2 u^4 \qquad\;\; (\text{if } m = 0) \\
\left\langle \mathcal{X}_0 \mathcal{X}_j \right\rangle_{c,\text{trunc}} &\sim u^4 m^4 |j|^{-\eta} \quad (\text{if } m \neq 0) \\
&\sim u^4 |j|^{-2\eta} \qquad (\text{if } m = 0) \\
\left\langle \mathcal{Y}_0 \mathcal{Y}_j \right\rangle_{\text{trunc}} &\sim \left\langle \mathcal{Z}_0 \mathcal{Z}_j \right\rangle_{\text{trunc}} \sim u^2 |j|^{-\eta}
\end{aligned} \tag{8.15}$$

where $c_{1,2}$ are non-universal constants. For the ground state of the $\mathcal{XXZ}$ model, $m = 0$. The exponents above do not depend on the measurement strength and should be consistent with the power-law decay of correlators found from BCFT. Comparing Eq. (8.15) with Eq. (7.18), we conclude that the exponent of $a_{jk} - a_j a_k$ should be exactly $\eta = 2$ in the $\mathcal{XXZ}$ model. In Fig. 8.7 we numerically compute $a_{jk} - a_j a_k$ using DMRG and indeed observe $\eta = 2$ for different Δ.

In fact, this perturbative approach is generic and $|\psi_c\rangle$ can be any critical state. One can also compute the second Rényi entropy of the truncated wavefunction in Eq. (8.15),

$$S_A^{(2)} \simeq 2u^4 \sum_{j\in A} \sum_{k\in \bar{A}} (a_{jk} - a_j a_k)^2 + O(u^6), \tag{8.16}$$

where A is a subsystem consisting of l consecutive sites and $\bar{A}$ is the complement. It is shown in Ref. [4] that the scaling of $S_A^{(2)}$ depends on the exponent of the strange correlator,

$$S_A^{(2)} \sim \begin{cases} \text{area law.} & \text{if } \eta > 1, \\ \ln(l(L-l)/l) & \text{if } \eta = 1. \end{cases} \tag{8.17}$$

The perturbative approach breaks down when $\eta < 1$.

8.3 Non-linear observables

In this technical section, we derive the relation between non-linear observables (Eq. (8.8)) and expectation values of the replica system. The weak measurement on site j is described by the Kraus operators,

$$K_{s_j=\pm} = \frac{e^{s_j \beta O_j}}{\sqrt{2\cosh 2\beta}} \tag{8.18}$$

where O_j is a linear combination of Pauli matrices s.t. $O_j^2 = \mathbb{I}$ and β is the measurement strength. Let's consider weak measurements on N sites of the initial state $|\psi_\Delta\rangle$ with outcome $\boldsymbol{s} = \{s_1, \ldots, s_N\}$. The post-measurement state is

$$|\psi_{\boldsymbol{s}}\rangle = \frac{K_{\boldsymbol{s}} |\psi_\Delta\rangle}{\sqrt{\langle K_{\boldsymbol{s}}^2\rangle_0}} \tag{8.19}$$

where $K_{\boldsymbol{s}} = \prod_j K_{s_j}$ and $\langle\cdot\rangle_0 \equiv \langle\psi_\Delta| \cdot |\psi_\Delta\rangle$. We are interested in the non-linear observable

$$\frac{\sum_{\boldsymbol{s}} p_{\boldsymbol{s}}^n \langle\Gamma\rangle_{\boldsymbol{s}}}{\sum_{\boldsymbol{s}} p_{\boldsymbol{s}}^n} = \frac{\sum_{\boldsymbol{s}} \langle K_{\boldsymbol{s}}^2\rangle_0^{n-1} \langle K_{\boldsymbol{s}}^2 \Gamma\rangle_0}{\sum_{\boldsymbol{s}} \langle K_{\boldsymbol{s}}^2\rangle_0^n} \tag{8.20}$$

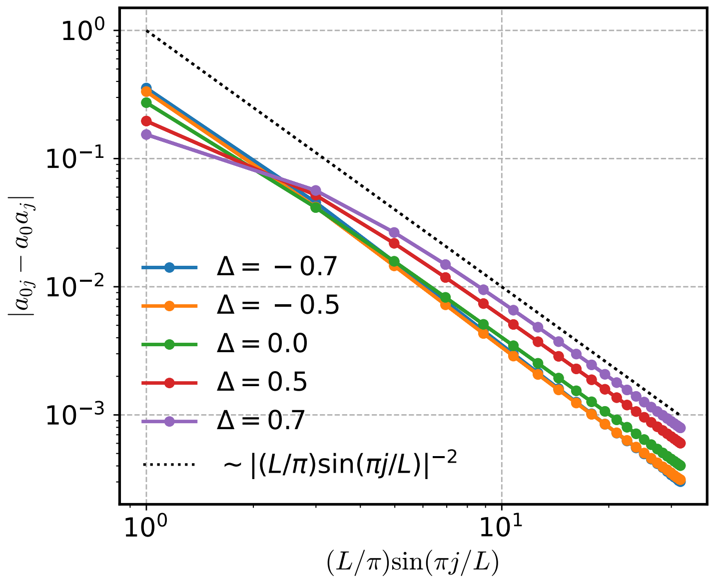

Figure 8.7: The strange correlator $a_{0j} - a_0 a_j$ of an $\mathcal{XXZ}$ chain as a function of chord length $(L/\pi)\sin(\pi j/L)$. The data for different interaction strength Δ is obtained by DMRG simulations with periodic boundary conditions and system size $L = 50$, using bond dimension $\chi = 300$. The BCFT analysis of Sec. 7.3 predicts that $a_{0j} - a_0 a_j$ decays as a power law with exponent -2 for any $\Delta \in (-1, 1)$, which is consistent with the numerical data.

where $p_{\boldsymbol{s}} = \langle K_{\boldsymbol{s}}^2 \rangle_0$ is the probability of the outcome $\boldsymbol{s}$ and Γ is the observable of interest such that $[\Gamma, K_{\boldsymbol{s}}] = 0$.

On the other hand, let us consider the n-replica version of the initial wavefunction, $\left|\psi_\Delta^n\right\rangle \equiv \left|\psi_\Delta^{(1)}\right\rangle \otimes \cdots \otimes \left|\psi_\Delta^{(n)}\right\rangle$. The superscript refers to the index of replicas. The terms in the numerator and denominator can be expressed in terms of expectation values of the replica wavefunction. For example,

$$\begin{aligned}
\sum_{\boldsymbol{s}} \langle K_{\boldsymbol{s}}^2 \rangle_0^n &= \sum_{\boldsymbol{s}} \left\langle \psi_\Delta^n \right| \left(K_{\boldsymbol{s}}^2\right)^{(1)} \otimes \cdots \otimes \left(K_{\boldsymbol{s}}^2\right)^{(n)} \left|\psi_\Delta^n\right\rangle \\
&= \left\langle \psi_\Delta^n \right| \sum_{\boldsymbol{s}} \left(K_{\boldsymbol{s}}^2\right)^{(1)} \otimes \cdots \otimes \left(K_{\boldsymbol{s}}^2\right)^{(n)} \left|\psi_\Delta^n\right\rangle \\
&= \left\langle \psi_\Delta^n \right| \prod_j \left[\sum_{s_j = \pm} \left(K_{s_j}^2\right)^{(1)} \otimes \cdots \otimes \left(K_{s_j}^2\right)^{(n)} \right] \left|\psi_\Delta^n\right\rangle
\end{aligned} \tag{8.21}$$

and also,

$$\sum_{\vec{s}} \left\langle K_{\vec{s}}^2 \right\rangle_0^{n-1} \left\langle K_{\vec{s}}^2 \Gamma \right\rangle_0 = \left\langle \psi_\Delta^n | \Gamma^{(1)} \prod_j \left[\sum_{s_j=\pm} \left(K_{s_j}^2 \right)^{(1)} \otimes \cdots \otimes \left(K_{s_j}^2 \right)^{(n)} \right] | \psi_\Delta^n \right\rangle . \tag{8.22}$$

In the $n = 2$ case, we have

$$\sum_{s_j=\pm} \left(K_{s_j}^2 \right)^{(1)} \otimes \left(K_{s_j}^2 \right)^{(2)} \propto e^{2\beta' O_j^{(1)} O_j^{(2)}}, \tag{8.23}$$

where $\tanh(2\beta') = \tanh^2(2\beta)$. Therefore we have proven Eq. (8.8),

$$\frac{\sum_{\boldsymbol{s}} p_{\boldsymbol{s}}^2 \langle \Gamma \rangle_{\boldsymbol{s}}}{\sum_{\boldsymbol{s}} p_{\boldsymbol{s}}^2} = \frac{\left\langle \psi_\Delta^2 | \Gamma^{(1)} \prod_j e^{2\beta' O_j^{(1)} O_j^{(2)}} | \psi_\Delta^2 \right\rangle}{\left\langle \psi_\Delta^2 | \prod_j e^{2\beta' O_j^{(1)} O_j^{(2)}} | \psi_\Delta^2 \right\rangle}. \tag{8.24}$$

8.4 Correlation functions of the post-measurement state from BCFT

The low-energy and long-distance theory of an $\mathcal{XXZ}$ chain is described by the TLL theory whose action is reported in Eq. (7.12). This model is also known as a compact boson, and the compactification radius is related to the Luttinger parameter K. The action can be expressed in terms in terms of the field θ, or its dual, ϕ. Let us start by analyzing some relevant features of the θ field, which can be helpful to derive part of the results we have presented in the main text.

An important class of primary fields for this model are the vertex operators, $e^{ia\theta}$ (here we implicitly assume that all the fields are normal ordered), whose expectation value is given by

$$\left\langle \prod_j e^{ia_j \theta(z_j, \bar{z}_j)} \right\rangle = \prod_{j<k} |z_j - z_k|^{a_j a_k/(2K)} \text{ (if } \sum_j a_j = 0) \tag{8.25}$$

where we have used the complex coordinates $z = x + i\tau$, $\bar{z} = x - i\tau$.

As we discussed in Sec. 7.3, the weak measurement of $X \sim \cos(\theta)$ induces a defect-line perturbation at $\tau = 0$ which is relevant in the RG analysis for $K > 1/4$. It effectively cuts the full 1+1D plane into two halves and pins $\theta(\tau^*) = 0$ at all x and at a β-dependent τ^*. To simplify the following computations, in this Sec. we assume that the field will be pinned at $\tau^* = 0$, having in mind that the final result could be always translated by $\tau \to \tau - \tau^*$.

Thus, the correlation functions of the post-measurement wavefunction in the long-distance limit can be computed by studying the Luttinger liquid on the upper half-plane (UHP), $\tau > 0$, with Dirichlet boundary condition, $\theta(x, \tau = 0) = 0$. Under the parity transformation $\tau \to -\tau$, in the presence of DBC, the θ field transforms as

$$\theta(z, \bar{z}) \to -\theta(\bar{z}, z). \tag{8.26}$$

It was shown by Cardy [13] that an n-point function on the UHP satisfies the same differential equation as the (holomorphic) $2n$-point function on the entire complex plane $\mathbb{C}$. By exploiting this doubling trick, we can find that the vertex operators at $z_1 = x_1 + i\tau_1$ and $z_2 = x_2 + i\tau_2$ satisfy [9]

$$\begin{aligned}
&\left\langle e^{ia\theta(z_1,\bar{z}_1)} e^{-ib\theta(z_2,\bar{z}_2)} \right\rangle_{\text{UHP}} = \left\langle e^{ia\theta(z_1)} e^{-ia\theta(\bar{z}_1)} e^{-ib\theta(z_2)} e^{ib\theta(\bar{z}_2)} \right\rangle_{\mathbb{C}} \\
&= \frac{1}{(\text{Im}z_1)^{a^2/(4K)} (\text{Im}z_2)^{b^2/(4K)}} \left| \frac{z_1 - z_2}{z_1 - \bar{z}_2} \right|^{-ab/(2K)} \\
&= \tau_1^{-a^2/(4K)} \tau_2^{-b^2/(4K)} \left[1 - \frac{4\tau_1\tau_2}{(\tau_1 + \tau_2)^2 + (x_1 - x_2)^2} \right]^{-ab/(4K)} .
\end{aligned} \tag{8.27}$$

In the second line, we have used the holomorphic part of Eq. (8.25). From the result above, we can also easily derive the one-point correlator

$$\left\langle e^{ia\theta(0,\tau)} \right\rangle_{\text{DBC}} = \tau^{-a^2/(4K)}. \tag{8.28}$$

As we mentioned earlier, the action Eq. (7.12) is also written in a dual representation, in terms of the field ϕ. If $\theta(z, \bar{z})$ satisfies DBC, the dual field $\phi(z, \bar{z})$ obeys Neumann boundary condition and, under the parity transformation $\tau \to -\tau$, behaves as

$$\phi(z, \bar{z}) \to \phi(\bar{z}, z). \tag{8.29}$$

Therefore, the correlation function of vertex operators $e^{ia\phi}$ in the presence of NBC reads [9]

$$\begin{aligned}
&\left\langle e^{ia\phi(z_1,\bar{z}_1)} e^{-ib\phi(z_2,\bar{z}_2)} \right\rangle_{\text{UHP}} = \left\langle e^{ia\phi(z_1)} e^{ia\phi(\bar{z}_1)} e^{-ib\phi(z_2)} e^{-ib\phi(\bar{z}_2)} \right\rangle_{\mathbb{C}} \\
&= \delta_{ab} \left(\frac{\text{Im}z_1 \, \text{Im}z_2}{|z_1 - z_2|^2 |z_1 - \bar{z}_2|^2} \right)^{a^2K/4} \\
&= \delta_{ab} \left\{ \frac{\tau_1\tau_2}{[(\tau_1 - \tau_2)^2 + (x_1 - x_2)^2][(\tau_1 + \tau_2)^2 + (x_1 - x_2)^2]} \right\}^{\frac{a^2K}{4}} ,
\end{aligned} \tag{8.30}$$

where again we have used the holomorphic part of Eq. (8.25). The Eq. (8.27) has been used in Sec. 7.3 to derive the post-measuremnet correlation function (7.17) and they were also useful to extrapolate a relationship between the measurement strength β and the imaginary-time evolution τ. In particular, we can perform an

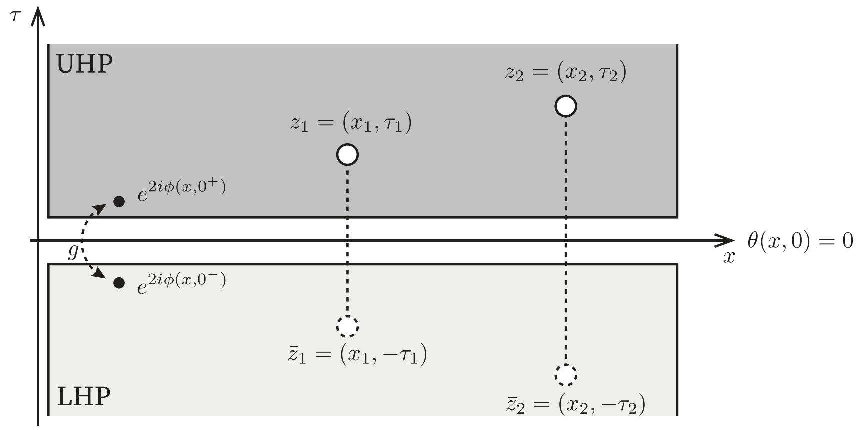

Figure 8.8: BCFT and method of images. The measurement pins $\theta(0, \tau = 0) = 0$, and the remnant interaction between UHP and LHP is modeled by $g\cos[2\phi(x, 0^+) - 2\phi(x, 0^-)]$, as depicted by the black dots on the left. We are interested in the two-point correlators at z_1 and z_2 in the UHP, which can be computed as holomorphic four-point correlators involving $z_1, z_2, \bar{z}_1, \bar{z}_2$ as shown by the hollow circles [13]. The two circles $\bar{z}_1$ and $\bar{z}_2$ in the LHP represent the mirror images of z_1 and z_2.

expansion around $\tau = 0$, then shift the final result as $\tau \to \tau - \tau^*$, and finally set $\tau = 0$ to recover Eq. (7.17).

Despite BCFT provides a powerful tool to compute the correlation functions in the presence of relevant perturbations, we need to be very careful about the periodicity of the weak measurement in Eq. (7.16). In the large measurement strength limit, the field θ can tunnel from one minimum of the cosine to the other [117], so the field θ is not really blocked. A similar problem is already discussed in [16] computing the correlator $\langle \partial_x\phi(x)\partial_{x'}\phi(x')\rangle$ in the presence of the weak measurement $\int_x \cos[2\phi(x)]$. Also in that case, a naïve analysis based on BCFT would predict that $\langle \partial_x\phi(x)\partial_{x'}\phi(x')\rangle \sim |x - x'|^{-4}$, while Ref. [16] has shown that $\langle \partial_x\phi(x)\partial_{x'}\phi(x')\rangle \sim |x - x'|^{-2/K}$. This result can be obtained by taking into account that $\cos[2\phi(x)]$ is maximized for $\phi(x) = p\pi$, with p integer and the tunneling among the different saddle points of the action determines the behavior of the correlator $\langle \partial_x\phi(x)\partial_{x'}\phi(x')\rangle$.

By taking into account the necessity of a careful treatment of the cosine perturbation in Eq. (7.16), in the second part of this section, we compute the two-point correlation function $\langle \mathcal{Y}_0\mathcal{Y}_x\rangle \sim \langle \sin(\theta(0))\sin(\theta(x))\rangle$. If we map the measurement problem into the Kane and Fisher study of an isolated defect in a TLL [118], we can use their analysis of the strong coupling regime in order to get the correct behavior of our correlation functions in the presence of the relevant perturbation (7.16). In the defect problem, the impurity is spatially local, i.e. it acts at all (imaginary) time steps but $x = 0$. If the field $\theta(x = 0)$ was totally blocked, the chain would be cut into two disconnected pieces. As we mentioned above, this cannot be true if the coupling of the impurity is not infinite, so to analyze the strong coupling regime, one has to take into account the possibility of adding a tunneling term jumping across the impurity. Therefore, in our measurement problem, the effective action that we should consider when θ is pinned around $\theta(x, \tau = 0) = 0$ is

$$\begin{aligned} S' = \frac{K}{2\pi} \int_x \int_0^{\infty} d\tau \, \left[(\partial_\tau \theta_1)^2 + (\partial_x \theta_1)^2\right] \\ + \frac{K}{2\pi} \int_x \int_{-\infty}^{0} d\tau \, \left[(\partial_\tau \theta_2)^2 + (\partial_x \theta_2)^2\right] + g \int_x O(x). \end{aligned} \tag{8.31}$$

where $O(x) = \cos[2\phi_1(x) - 2\phi_2(x)]$, $\phi_1(x) = \phi(x, 0^+)$ and $\phi_2(x) = \phi(x, 0^-)$ are copies of the fields on the upper and lower half plane, respectively, and similarly for θ_j, $j = 1, 2$. We stress that the choice of the Hermitian perturbation $O(x)$ is compatible with the symmetries of our problem and with the fact that it is the first irrelevant operator for $K > 1/4$, which is the regime where the weak measurement (7.16) is relevant.

Let us analyse how the tunneling term present in Eq. (8.31) changes the behavior of the correlation functions.

By expanding the action, we get that

$$\begin{aligned} \langle \sin[\theta_1(z)] \sin[\theta_1(z')] \rangle = \langle \sin[\theta_1(z)] \sin[\theta_1(z')] \rangle_{g=0} \\ + g^2 \int_{x_1, x_2} \Big\langle \sin[\theta_1(z)] \sin[\theta_1(z')] \times O(x_1) O(x_2) \Big\rangle_{g=0} + o(g^4). \end{aligned} \tag{8.32}$$

From the computation of the correlation functions close to a boundary in Eq. (7.17), we learn that $\langle \sin[\theta_1(x)] \sin[\theta_1(x')] \rangle_{g=0} \sim |x' - x|^{-2}$ and the scaling dimension of $O(x)$ is $4K$. Computing the integral in Eq. (8.32) is far from being trivial. We observe that the integrand is proportional to

$$\begin{aligned} \Big\langle e^{i[\theta_1(z) - \theta_1(z')]} e^{2i[\phi_1(x_1) - \phi_1(x_2)]} e^{-2i[\phi_2(x_1) - \phi_2(x_2)]} \Big\rangle \\ = \Big\langle e^{i[\theta_1(z) - \theta_1(z')]} e^{2i[\phi_1(x_1) - \phi_1(x_2)]} \Big\rangle \Big\langle e^{-2i[\phi_2(x_1) - \phi_2(x_2)]} \Big\rangle. \end{aligned} \tag{8.33}$$

The correlator $\left\langle e^{-2i[\phi_2(x_1) - \phi_2(x_2)]} \right\rangle$ can be found in Eq. 8.30 and it is $|x_1 - x_2|^{-4K}$. However, the first correlator is less trivial to be computed. We can ask what is the operator product expansion between $e^{i\theta}$ and $e^{i\phi}$ and, to address this question, it can be useful to write down both ϕ and θ in terms of the right and left chiral components. In particular, $\phi = \varphi_R + \varphi_L$ and $\theta = \varphi_R - \varphi_L$. We can use that (we are implicitly assuming that all the operators of the form $e^{i\alpha\varphi_{L/R}}$ are normal ordered [9])

$$e^{i\alpha\varphi_L(x)}e^{i\beta\varphi_L(x')} = e^{i\alpha\varphi_L(x)+i\beta\varphi_L(x')}(x-x')^{\alpha\beta K/2}, \tag{8.34}$$

such that, by multiplying the chiral and antichiral parts again, we get

$$e^{i[\theta_1(z)-\theta_1(z')]}e^{2i[\phi_1(x_1)-\phi_1(x_2)]} \sim \frac{e^{i[\varphi_R(x_2)-\varphi_L(x_2)]}e^{-i[\varphi_R(x_1)-\varphi_L(x_1)]}}{(z-x_1)^K(z-x_2)^K(z'-x_1)^K(z'-x_2)^K}. \tag{8.35}$$

By recalling that $\varphi_R - \varphi_L = \theta$, and $\left\langle e^{i\theta(x_1)}e^{-i\theta(x_2)}\right\rangle \sim |x_1 - x_2|^{-2}$ we have to evaluate the following integral

$$\begin{aligned}\langle\sin[\theta_1(z)]\sin[\theta_1(z')]\rangle &= \langle\sin[\theta_1(z)]\sin[\theta_1(z')]\rangle_{g=0}\\ &+ g^2\int_{x_1,x_2}\frac{|x_1-x_2|^{-2-4K}}{(z-x_1)^K(z-x_2)^K(z'-x_1)^K(z'-x_2)^K} + o(g^4).\end{aligned} \tag{8.36}$$

Without explicitly solving the integral above, we observe that the scaling dimension of the second term is $|x - x'|^{-8K}$ and we can conclude that

$$\langle\sin[\theta_1(z)]\sin[\theta_1(z')]\rangle \sim (z-z')^{-\min(8K,2)}. \tag{8.37}$$

Eq. (8.37) holds as far as the perturbation (7.16) is relevant, i.e. $K > 1/4$. We can therefore conclude that $\left\langle \mathcal{Y}_j\mathcal{Y}_k\right\rangle \sim |j-k|^{-2}$.

Given this analysis, we can now also understand the result in Eq. (7.28). In this case, we are interested in the correlation function $\left\langle \mathcal{Y}_j\tilde{\mathcal{Y}}_j\mathcal{Y}_k\tilde{\mathcal{Y}}_k\right\rangle$ when we measure $\mathcal{X}_j\tilde{\mathcal{X}}_j$, which in the bosonic language amounts to add the weak measurement $\int_x \cos[\theta(x)]\cos[\tilde{\theta}(x)]$ (Eq. (7.23)). In order to evaluate the correlation functions above, it is useful to consider the $+,-$ sectors, with $\theta_\pm = \theta \pm \tilde{\theta}$. In this way, the two Luttinger theories coupled through $\int_x \cos[\theta(x)]\cos[\tilde{\theta}(x)]$ can be written as in Eq. (7.24), i.e. a sum of two TLL with $\theta_\pm$ pinned around 0. The scaling dimension of $\cos(\theta_\pm)$ is $1/(2K)$.

In order to evaluate the correlation function we are interested in, we must add a term

$$\delta S = g\int_x O(x) \tag{8.38}$$

where $O(x) = \cos[2\phi_1^+(x) - 2\phi_2^+(x)]$. Here we focus on only one single TLL, for instance in the $+$ sector. We remind that

$$\begin{aligned}\left\langle \mathcal{Y}_j\tilde{\mathcal{Y}}_j\mathcal{Y}_k\tilde{\mathcal{Y}}_k\right\rangle &\sim \left\langle \sin[\theta(j)]\sin[\tilde{\theta}(j)]\sin[\theta(k)]\sin[\tilde{\theta}(k)]\right\rangle\\ &\sim \langle\cos[\theta_+(j)]\cos(\theta_+(k))\rangle + \langle\cos[\theta_-(j)]\cos[\theta_-(k)]\rangle\\ &- \langle\cos[\theta_+(j)]\rangle\langle\cos[\theta_-(k)]\rangle - \langle\cos[\theta_-(j)]\rangle\langle\cos[\theta_+(k)]\rangle,\end{aligned} \tag{8.39}$$

and taking into account the presence the tunneling term (8.38), we need to evaluate

$$\begin{aligned}&\left\langle\cos[\theta_{+,1}(z)]\cos[\theta_{+,1}(z')]\right\rangle = \left\langle\cos[\theta_{+,1}(z)]\cos[\theta_{+,1}(z')]\right\rangle_{g=0}\\&+g^2\int_{x_1,x_2}\left\langle\cos[\theta_{+,1}(z)]\cos[\theta_{+,1}(z')]O(x_1)O^\dagger(x_2)\right\rangle + o(g^4).\end{aligned}\tag{8.40}$$

We can expand the second term, such that we get

$$\begin{aligned}&\int_{x_1,x_2}\left\langle\cos[\theta_{+,1}(z)]\cos[\theta_{+,1}(z')]O(x_1)O^\dagger(x_2)\right\rangle =\\&\frac{1}{4}\int_{x_1,x_2}[\left\langle e^{i\theta_{+,1}(z)}e^{-i\theta_{+,1}(z')}O(x_1)O^\dagger(x_2)\right\rangle + \left\langle e^{-i\theta_{+,1}(z)}e^{i\theta_{+,1}(z')}O(x_1)O^\dagger(x_2)\right\rangle].\end{aligned}\tag{8.41}$$

At the strong coupling fixed point, the dimension of $O(x)$ is $2K$. In order to compute the large distance behavior of the correlator (8.41), we can again use a decomposition similar to Eq. (8.34), together with a scaling dimension analysis. Therefore, we can deduce that each integral above behaves as $|x-x'|^{-4K}$. Given that $\left\langle\cos[\theta_{+,1}(x)]\cos[\theta_{+,1}(x')]\right\rangle_{g=0} \sim const + |x-x'|^{-4}$ (see Eq. (7.17)), we find that

$$\left\langle\mathcal{Y}_j\tilde{\mathcal{Y}}_j\mathcal{Y}_k\tilde{\mathcal{Y}}_k\right\rangle \sim |j-k|^{-\min(4K,4)}.\tag{8.42}$$

We cross-check the result above against numerics in Fig. 8.9.

8.5 Numerical and analytical details on the gapless parent of 1D cluster state

In this technical section, we provide some additional numerical evidence of the findings we have presented in Sections 7.3-8.1 of the main text.

Power-law exponent of $\left\langle\prod_{j=0}^{x} X_{j,2}\right\rangle_{\text{uni}}$ after uniform projective measurement of $X_{j,1}$

In the gapless parent of the cluster state, if one performs $X_{j,1}$ measurement and post-select the uniform outcome $X_{j,1}=1, \forall j$, it is shown in Sec. 7.3 that we expect $\langle\prod_{j=0}^{x} X_{j,2}\rangle_{\text{uni}} \sim x^{-2K}$. We examine this in Fig. 8.10 using infinite DMRG (iDMRG) simulations for systems with different Luttinger parameters.

Scaling dimension of $Z_{j,1}$

In the decoupled-$\mathcal{XXZ}$-chain representation, we have

$$Z_{j,1}Z_{k,1} = \begin{bmatrix} & \mathcal{Y}_{j+1} & \cdots & \mathcal{Y}_k & \mathcal{Y}_{k+1}\\ \tilde{\mathcal{Y}}_j & \tilde{\mathcal{Y}}_{j+1} & \cdots & \tilde{\mathcal{Y}}_k & \end{bmatrix}, \qquad \left\langle Z_{j,1}Z_{k,1}\right\rangle = \left(\left\langle\prod_{i=j}^{k}\mathcal{Y}_i\right\rangle\right)^2. \tag{8.43}$$

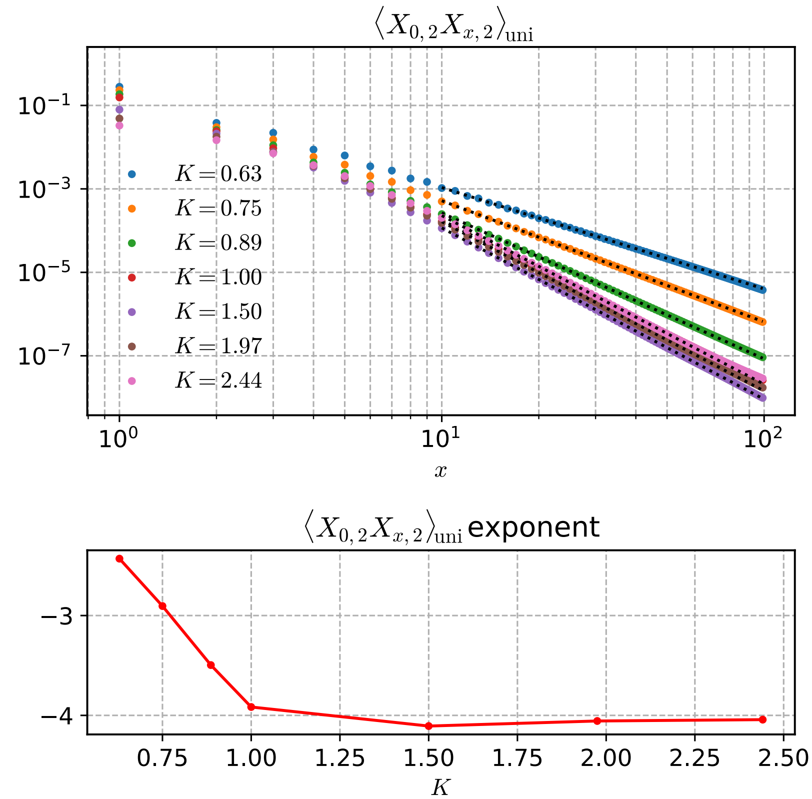

Figure 8.9: Top panel: the correlation function $\left\langle \mathcal{Y}_0\tilde{\mathcal{Y}}_0\mathcal{Y}_x\tilde{\mathcal{Y}}_x\right\rangle_{\text{uni}} \equiv \left\langle X_{0,2}X_{x,2}\right\rangle_{\text{uni}}$ of the gapless parent of the cluster state with different Luttinger parameter K after $X_{j,1} = 1, \forall j$ measurement. The power-law exponents are extracted by fitting the data (see the black dotted lines). Bottom panel: the power-law exponent as a function of K, which is consistent with $-\min(4K, 4)$. Data obtained by iDMRG with bond dimension $\chi = 2000$.

Thus we can compute the correlation function from $\langle \prod_{i=j}^{k} \mathcal{Y}_i \rangle$ of a single $\mathcal{XXZ}$ chain. Numerically, we use DMRG to obtain the ground state of an $\mathcal{XXZ}$ chain with $L = 50$ and periodic boundary conditions, and then compute $\left\langle Z_{j,1}Z_{k,1}\right\rangle$ using Eq. 8.43. The numerical data for different Luttinger parameters K is shown in Fig. 8.11. The results suggest that $[Z_{j,1}] = 1/4$ for all values of K. Even though, in general, the lack of a bosonic representation for Eq. (8.43) prevents us from predicting this scaling dimension, we are able to analytically derive this result for two special cases, $K = 1/2$ and $K = 1$. For $K = 1/2$, the symmetry of the $\mathcal{XXZ}$ spin chain is enhanced to $SU(2)$, and therefore we can use the following equality among correlators $\left\langle \prod_{x=j}^{k} \mathcal{Y}_x \right\rangle = \left\langle \prod_{x=j}^{k} \mathcal{Z}_x \right\rangle$. By using the bosonization dictionary $\mathcal{Z} \sim -\frac{2}{\pi}\partial_x\phi$ in Eq. (7.13), we observe that $\left\langle \prod_{x=j}^{k} \mathcal{Z}_x \right\rangle \sim$

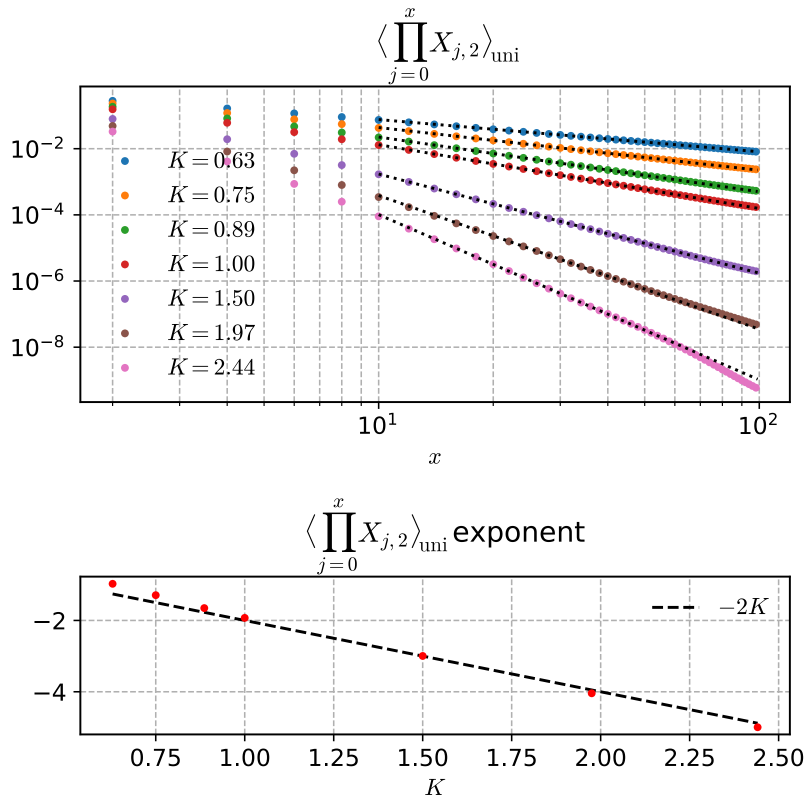

Figure 8.10: Top panel: the expectation value $\langle \prod_{j=0}^{x} X_{j,2} \rangle_{\rm uni}$ of the gapless parent of the cluster state with different Luttinger parameter K after $X_{j,1} = 1, \forall j$ measurement. The power-law exponents are extracted by fitting the data (see the black dotted lines). Bottom panel: the power-law exponent as a function of K. Data obtained by iDMRG with bond dimension $\chi = 2000$.

$\left\langle e^{i\frac{\pi}{2}\sum_{x=j}^{k}\mathcal{Z}_x}\right\rangle \sim \left\langle e^{-i\int_j^k dx\partial\phi}\right\rangle = \left\langle e^{-i\phi(k)}e^{i\phi(j)}\right\rangle \sim |j-k|^{-K/2}$. Therefore, when $K = 1/2$, $\left\langle \prod_{x=j}^{k}\mathcal{Y}_x\right\rangle \sim |j-k|^{-1/4}$ and, after taking into account also the contribution of $\tilde{\mathcal{Y}}$, we can conclude that $[Z_{j,1}] = \frac{1}{4}$.

When $K = 1$, the coupling Δ in Eq. (7.11) vanishes, so we get two copies of the $\mathcal{XY}$ spin chain. Each of them can be rewritten as

$$H = -\sum_j [(\mathcal{X}_{2j-1}\mathcal{X}_{2j} + \mathcal{Y}_{2j-1}\mathcal{Y}_{2j}) + (\mathcal{X}_{2j}\mathcal{X}_{2j+1} + \mathcal{Y}_{2j}\mathcal{Y}_{2j+1})], \tag{8.44}$$

where we have split odd-even and even-odd couplings. We can now define

$$\mathcal{X}_j = \sigma_j^x\sigma_{j+1}^x, \quad \mathcal{Y}_j\mathcal{Y}_{j+1} = \sigma_j^y, \tag{8.45}$$

such that Eq. (8.44) becomes

$$H = -\sum_j [(\sigma^x_{2j-1}\sigma^x_{2j+1} + \sigma^y_{2j-1}) + (\sigma^x_{2j}\sigma^x_{2j+2} + \sigma^y_{2j})], \tag{8.46}$$

i.e. it becomes the sum of two transverse-field Ising Hamiltonians defined on odd and even lattice sites. Notice that, in principle, we could have applied a rotation $e^{i\pi/4\mathcal{X}_j}$ in Eq. (8.44) to send $\mathcal{Y}_j \to \mathcal{Z}_j$ and recover the more canonical form of the Ising Hamiltonian, but it is more convenient for us to work with a transverse field along the y-direction. Indeed, we are interested in the operator $\prod_{k=j}\mathcal{Y}_k$, and in particular

$$\prod_{k=2j}\mathcal{Y}_k = \prod_{k=2j,\mathrm{even}}\sigma^y_k = \mu_{2j}P^{\mathrm{even}}, \qquad \prod_{k=2j-1}\mathcal{Y}_k = \prod_{k=2j-1,\mathrm{odd}}\sigma^y_k = \mu_{2j-1}P^{\mathrm{odd}} \tag{8.47}$$

where $P^{\mathrm{even}} = \prod_{2j}\sigma^y_{2j}$ is the parity operator of the Ising chain defined on the even sites (and similarly for P^{odd}), while μ is the disorder operator with scaling dimension $1/8$ (note that the parity operator is dimensionless). If we now take into account also the $\tilde{\mathcal{X}}\tilde{\mathcal{Y}}$ spin chain, then we get that the total scaling dimension for $\prod_{k=2j}\mathcal{Y}_k\tilde{\mathcal{Y}}_{k-1}$ or $\prod_{k=2j+1}\mathcal{Y}_k\tilde{\mathcal{Y}}_{k-1}$ is $1/8 + 1/8 = 1/4$, which is consistent with the scaling dimension of the operator $Z_{j,1}$.

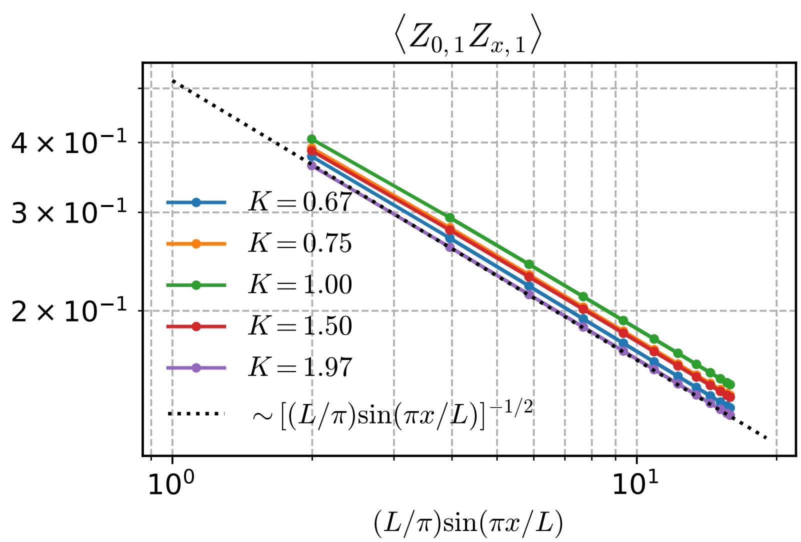

Figure 8.11: Two-point correlation function of $Z_{x,1}$ as a function of the chord length. Data have been obtained using the decoupled $\mathcal{XXZ}$ representation. We simulate the $\mathcal{XXZ}$ chain with $L = 50$ and periodic boundary conditions using DMRG with bond dimension $\chi = 300$. The data for different values of K show that the scaling dimension $[Z_{x,1}]$ is always $1/4$.

More numerical results on the weak $\mathbb{Z}_2$-preserving measurements

In Sec. 8.1, Fig. 8.2 shows numerically the behavior of the order parameter in the lower chain of the post-measurement wavefunction as a function of the parameter ω in the projective measurement limit. In Fig. 8.12 we check that for the weak measurement with $\beta = 0.5$, the long-range order and disorder parameters remain the same as those presented in Table 8.1: when $0 \leq \omega < \frac{\pi}{4}$, $\left\langle \prod_{j=0}^{x} X_{j,1} \right\rangle_{\text{uni}}$ and $\left\langle Z_{0,2} Z_2 \right\rangle_{\text{uni}}$ have long-range order; when $\omega = \frac{\pi}{4}$, the system is gapless; when $\frac{\pi}{4} < \omega \leq \frac{\pi}{2}$, $\left\langle Z_{0,1} Z_{x,1} \right\rangle_{\text{uni}}$ and $\left\langle \prod_{j=0}^{x} X_{j,2} \right\rangle_{\text{uni}}$ have long-range order.

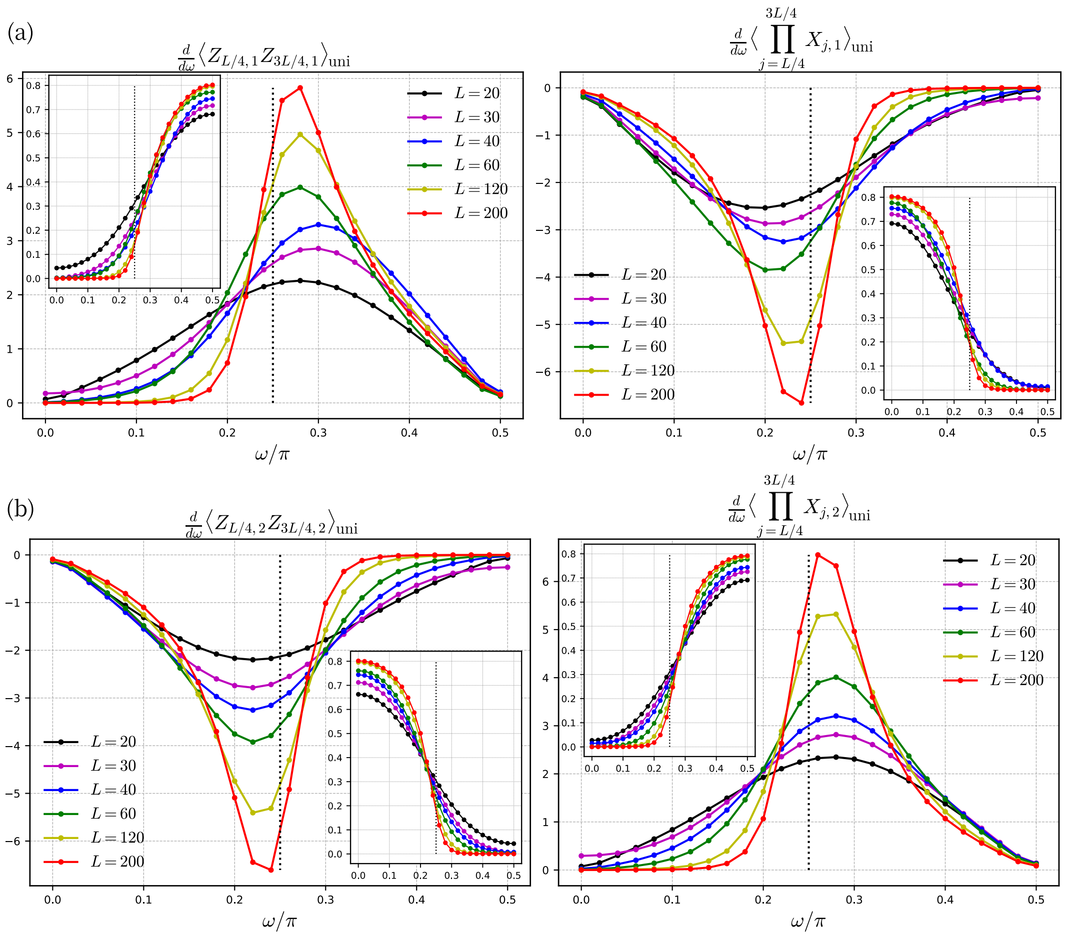

Figure 8.12: The derivative of order and disorder parameters in the (a) upper and (b) lower chain of the post-measurement gapless parent of the cluster state with $K = 1.5$ as a function of the parameter ω. The measurement strength is $\beta = 0.5$. The black dotted lines mark the transition at $\omega_c = \pi/4$. Insets: order and disorder parameters without derivative. The gapless parent state in obtained using DMRG with open boundary conditions and bond dimension $\chi = 1200$.

Uniform weak measurement of $X_{j,1}$ and $X_{j,2}$

As another example of $\mathbb{Z}_2$-preserving measurements, we consider weak measurement of both $X_{j,1}$ and $X_{j,2}$ as described in Eq. (8.5). Since the low-energy theory is still described by Eq. (8.3), we expect that the results to be similar to those in Sec. 8.1. In Fig. 8.13 we apply the weak measurement in Eq. (8.5) with $\beta = 0.5$ to the gapless parent state, and probe the order and disorder parameters of the post-measurement wavefunction, $\left\langle Z_{\frac{L}{4},2} Z_{\frac{3L}{4},2} \right\rangle_{\text{uni}}$ and $\left\langle \prod_{j=L/4}^{3L/4} X_{j,2} \right\rangle_{\text{uni}}$, as a function of ω for different system sizes L. The divergence of the derivative of the order/disorder parameter with respect to ω suggests a phase transition at $\omega = \pi/4$, as expected from Sec. 8.1.

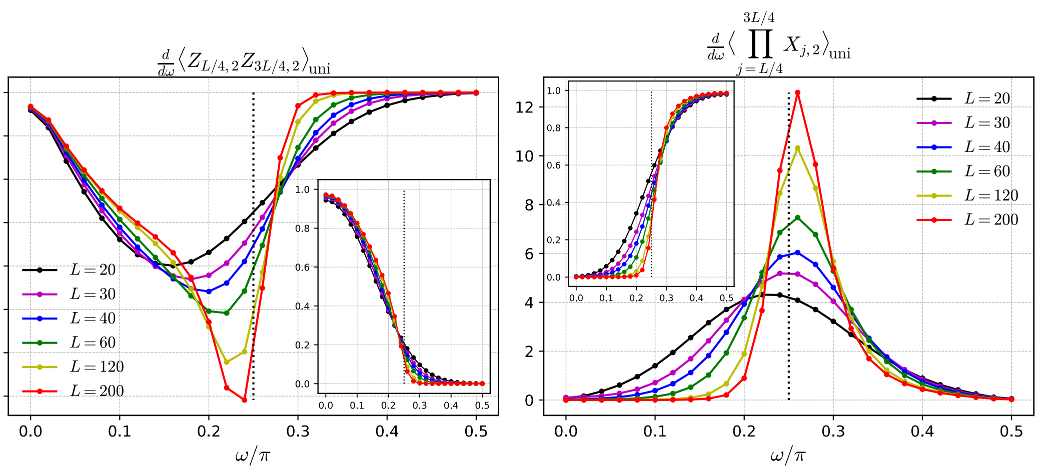

Figure 8.13: The derivative of order and disorder parameters in the lower chain of the post-measurement gapless parent of the cluster state with $K = 1.5$ as a function of the parameter ω. The black dotted lines mark the transition at $\omega_c = \pi/4$. Insets: the order parameter , $\left\langle Z_{\frac{L}{4},2} Z_{\frac{3L}{4},2} \right\rangle_{\text{uni}}$, and disorder parameter, $\left\langle \prod_{j=L/4}^{3L/4} X_{j,2} \right\rangle_{\text{uni}}$, as a function of ω. The gapless parent of the cluster state in obtained using DMRG with open boundary conditions and bond dimension $\chi = 1200$.

At the transition, the post-measurement wavefunction is $e^{\frac{\beta}{\sqrt{2}} \sum_j (X_{j,1}+X_{j,2})} |\psi_\Delta\rangle$, and we now compute its correlation functions. Since the measurement induces a relevant perturbation in the RG sense, we focus on the large β limit. Using the bosonization form, we can compute the XX correlation function,

$$\begin{aligned} \left\langle X_{0,1} X_{x,1} \right\rangle_c = \left\langle \mathcal{X}_0 \tilde{\mathcal{X}}_0 \mathcal{X}_x \tilde{\mathcal{X}}_x \right\rangle_c &= \left\langle \cos\theta(0) \cos\tilde{\theta}(0) \cos\theta(x) \cos\tilde{\theta}(x) \right\rangle_c \\ &\sim \langle \cos\theta_+(0) \cos\theta_+(x) \rangle_c + \langle \cos\theta_-(0) \cos\theta_-(x) \rangle_c \sim x^{-\frac{1}{K}}, \end{aligned} \tag{8.48}$$

where in the last line we have used the fact that the θ_- field is pinned at $\tau = 0$, while the θ_+ field remains gapless. Using the analogy with Eq. (8.15), we conclude that

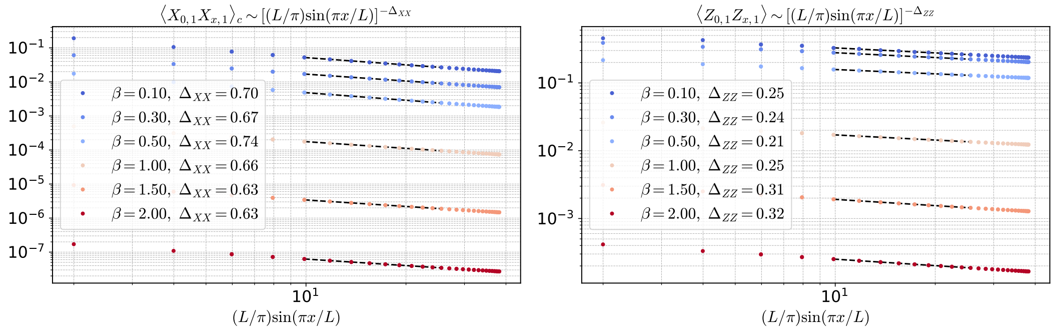

Figure 8.14: Correlation functions of $e^{\beta\sum_j(X_{j,1}+X_{j,2})}\,|\psi_\Delta\rangle$ with Luttinger parameter $K=1.5$. The gapless parent state $|\psi_\Delta\rangle$ with length $L=60$ and periodic boundary conditions is obtained using DMRG with bond dimension $\chi=2000$. In the large β limit, the theoretical power-law exponents of $\langle X_{0,1}X_{x,1}\rangle_c$ and $\langle Z_{0,1}Z_{x,1}\rangle$ are $\frac{1}{K}\approx 0.67$ and $\frac{1}{2K}\approx 0.33$ respectively, which are close to the numerical fittings: 0.63 and 0.32 (see the black dashed lines).

the strange correlator decays as

$$a_{0x} - a_0 a_x \sim x^{-\frac{1}{2K}}, \tag{8.49}$$

and correspondingly, for large β, the correlators of Y and Z Pauli operators are

$$\langle Y_{0,1}Y_{x,1}\rangle \sim \langle Z_{0,1}Z_{x,1}\rangle \sim x^{-\frac{1}{2K}}. \tag{8.50}$$

We numerically check the above results in Fig. 8.14 by DMRG. Besides, in Fig. 8.15 we check that the transition at $\omega=\pi/4$ has an effective central charge $c_{\text{eff}}=1$ which corresponds to the gapless θ_+ mode.

Power-law exponents of specific operators

In this short section, we compute power-law exponents of several operators in the gapless parent state after $e^{\beta\sum_j X_{j,1}}$ measurement. Then we use the duality argument to find the exponents of $e^{\beta\sum_j Z_{j,1}}$ measurement.

For the $e^{\beta\sum_j X_{j,1}}$ measurement, the arguments of Sec. 7.3 give the following representative scaling estimates for connected or uniform-sector correlators:

$$\begin{aligned}
\langle Z_{0,2}Z_{x,2}\rangle_{\text{uni}} &\sim \text{LRO},\\
\langle X_{0,2}X_{x,2}\rangle_{\text{uni}} &\sim x^{-\min(4,4K)},\\
\langle X_{0,1}X_{x,1}\rangle_{s} &\sim x^{-\min(4,4K)},\\
\langle X_{0,1}X_{0,2}X_{x,1}X_{x,2}\rangle_{\text{uni}} &\sim x^{-\min(4,4K)}.
\end{aligned} \tag{8.51}$$

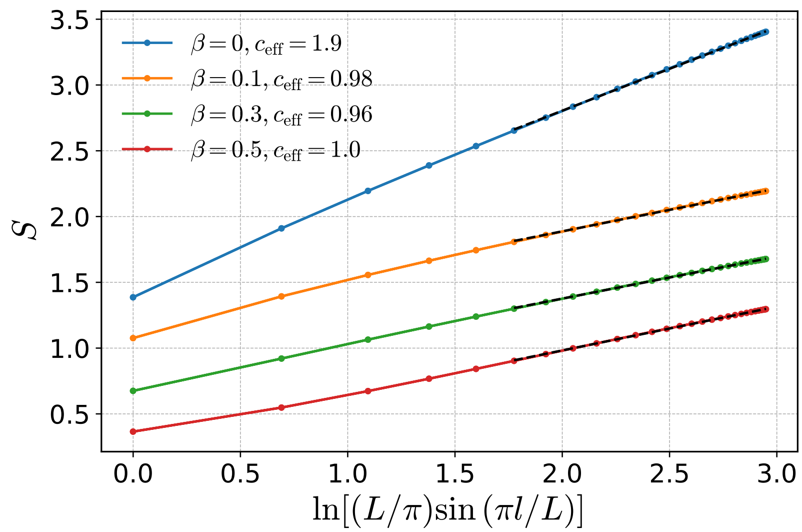

Figure 8.15: The entanglement entropy S as a function of $\ln[(L/\pi)\sin(\pi l/L)]$ where l is the subsystem size, after weak measurement of $e^{\beta\sum_j(X_{j,1}+X_{j,2})}$ in the gapless parent of the cluster state of size $L = 60$ with periodic boundary conditions. The effective central charge c_{eff} is extracted by fitting the data with $S = \frac{c_{\text{eff}}}{3}\ln[(L/\pi)\sin(\pi l/L)] + const.$ (see the black dashed lines) for different measurement strength β.

The four-Z correlators follow from the identifications $Z_{x,1}Z_{x+1,1} \sim \tilde{\mathcal{Y}}_j\mathcal{Y}_{j+1} \sim X_{x,2}$ and the corresponding chain-exchanged relation. We summarize the resulting exponents in Table 8.2. When $K > 1$, the scaling dimensions of the selected operators are larger than one.

Table 8.2: Power-law exponents of selected operators (connected part) after $e^{\beta\sum_j X_{j,1}}$ measurement.

Correlators	$\langle X_{0,1}X_{x,1}\rangle$	$\langle Z_{0,1}Z_{x,1}\rangle$	$\langle X_{0,2}X_{x,2}\rangle$	$\langle Z_{0,2}Z_{x,2}\rangle$	$\langle Z_{0,1}Z_{1,1}Z_{x,1}Z_{x+1,1}\rangle$	$\langle Z_{0,2}Z_{1,2}Z_{x,2}Z_{x+1,2}\rangle$	$\langle X_{0,1}X_{0,2}X_{x,1}X_{x,2}\rangle$
Exponents	$\min(4,4K)$	$2K$	$\min(4,4K)$	LRO	$\min(4,4K)$	$\min(4,4K)$	$\min(4,4K)$

For the $e^{\beta\sum_j Z_{j,1}}$ measurement, using the argument in Sec. 7.3, we expect the nature of this fixed point is similar to the fixed point of the measurement of $e^{\beta\sum_j Z_{j,1}Z_{j+1,1}}$. Since in terms of the bosonic representation, $Z_{j,1}Z_{j+1,1} \sim X_{j,2}$, one can immediately obtain the post-measurement power-law exponents by swapping $1 \leftrightarrow 2$ in the previous paragraph. The only difference is that, since measuring $Z_{\cdot,1}$ does not result in a "cat" state as in the measurement of $Z_{j,1}Z_{j+1,1}$, now the connected part of $\langle Z_{0,1}Z_{x,1}\rangle_{\text{uni},c}$ does not exhibit long-range order, as opposed to $\langle Z_{0,2}Z_{x,2}\rangle_{\text{uni},c} \sim const.$ in the $e^{\beta\sum_j X_{j,1}}$ measurement. Using the same arguments as in Sec. 8.4, we expect that $\langle Z_{0,1}Z_{x,1}\rangle_{\text{uni},c} \sim x^{-\min(4,4K)}$. We summarize the results in Table 8.3. Also note that when $K > 1$, the scaling dimensions are larger than 1. Therefore, we expect that both X and Z measurements of the first chain flow to stable fixed points when $K > 1$.

Table 8.3: Power-law exponents of select operators (connected part) after $e^{\beta \sum_j Z_{j,1}}$ measurement.

Correlators	$\langle X_{0,1}X_{x,1}\rangle$	$\langle Z_{0,1}Z_{x,1}\rangle$	$\langle X_{0,2}X_{x,2}\rangle$	$\langle Z_{0,2}Z_{x,2}\rangle$	$\langle Z_{0,1}Z_{1,1}Z_{x,1}Z_{x+1,1}\rangle$	$\langle Z_{0,2}Z_{1,2}Z_{x,2}Z_{x+1,2}\rangle$	$\langle X_{0,1}X_{0,2}X_{x,1}X_{x,2}\rangle$
Exponents	$\min(4, 4K)$	$\min(4, 4K)$	$\min(4, 4K)$	$2K$	$\min(4, 4K)$	$\min(4, 4K)$	$\min(4, 4K)$

We numerically check the irrelevance of selected operators for $K = 1.5$ in Fig. 8.16.

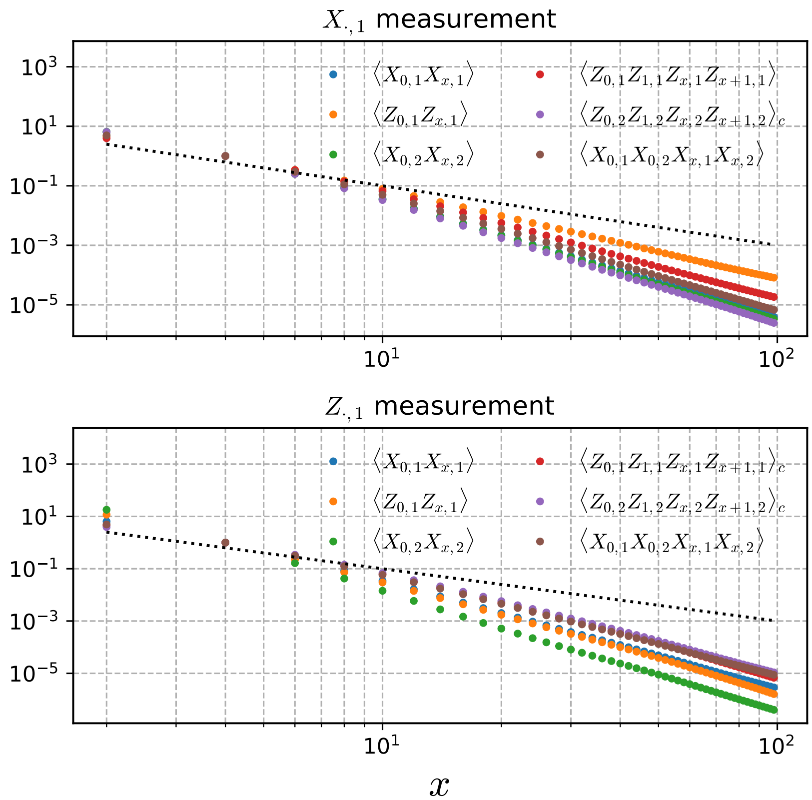

Figure 8.16: Two-point correlation functions of selected operators in the gapless parent of the cluster state with Luttinger parameter $K = 1.5$ after (a) $e^{\beta \sum_j X_{j,1}}$ and (b) $e^{\beta \sum_j Z_{j,1}}$ measurement with $\beta = 1$. The correlators are rescaled for a better visualization of the data. As a guide-line, the black dotted line has exponent -2. An operator is irrelevant if the two-point correlator decays faster than the reference line, as in the case presented here.

Details of DMRG simulations for the entanglement entropy at the intermediate fixed point

In Fig. 8.4, we investigate the entanglement scaling at the intermediate fixed point. The numerical data are obtained using finite-size DMRG with open boundary conditions and bond dimension $\chi = 1200$. By fitting the post-measurement half-chain entanglement entropy with the system size using $S_{L/2} = \frac{c_{\text{eff}}}{6} \log(L) + const.$ for $L = [20, 40, 60, 120, 200]$, we obtain the effective central charge c_{eff} in Fig. 8.4(c). The error bars in Fig. 8.4(c) is three times the standard deviation of c_{eff} from the linear fitting $S_{L/2}$ - $\log(L)$.

To check whether $\chi = 1200$ is enough for DMRG convergence, we plot in Fig. 8.17 entanglement entropy at the transition for $K = 1.24, 1.5, 1.97$ obtained using bond dimension $\chi = 600, 800, 1200, 1600$. Due to lack of computer memory, we do not have data for $L = 200, \chi = 1600$. From Fig. 8.17 we conclude that $\chi = 1200$ is enough for convergence at least for $L \lesssim 120$.

It is known that the numerical error in extracting c_{eff} from an XXZ chain can be large in the limit $K \to \infty$ [120]. In the above discussion, however, we are free from this problem because we always consider $K \sim O(1)$. Also, since we focus on post-selection of the uniform measurement outcome, our simulation is numerically simpler than for other non-Hermitian processes like dissipation (see e.g. [121]).

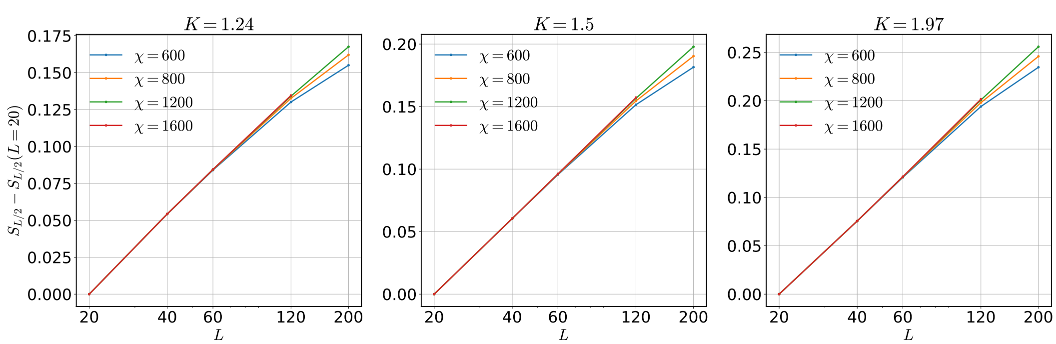

Figure 8.17: Entanglement entropy obtained by DMRG with different bond dimensions $\chi = 600, 800, 1200, 1600$.

Replica model with different values of K

Since it is difficult to study analytically the replica model of Section 8.1, we add more numerical results for the tilted measurement basis with different values of K. In Fig. 8.18 we plot the order parameter , $\left\langle\!\left\langle Z_{\frac{L}{4},2} Z_{\frac{3L}{4},2} \right\rangle\!\right\rangle$, and disorder parameter,

$\left\langle\!\left\langle \prod_{j=L/4}^{3L/4} X_{j,2} \right\rangle\!\right\rangle$ for $K = 0.75$ and $K = 2.44$, as an addition to the case shown in Fig. 8.5 for $K = 1.5$.

For $K = 0.75$ in Fig. 8.18(a), $X_{j,1}$ is irrelevant so at $\omega = 0$ the long-range physics is still described by the pristine Luttinger liquid theory, and we do not find a significant sign of phase transition in the order and disorder parameters. For $K = 2.44$ in Fig. 8.18(b), however, we find the crossing point in the order and disorder parameter curves with different system sizes, which, similar to Fig. 8.5, signals the presence of the measurement-induced boundary transition discussed in Sec. 8.1.

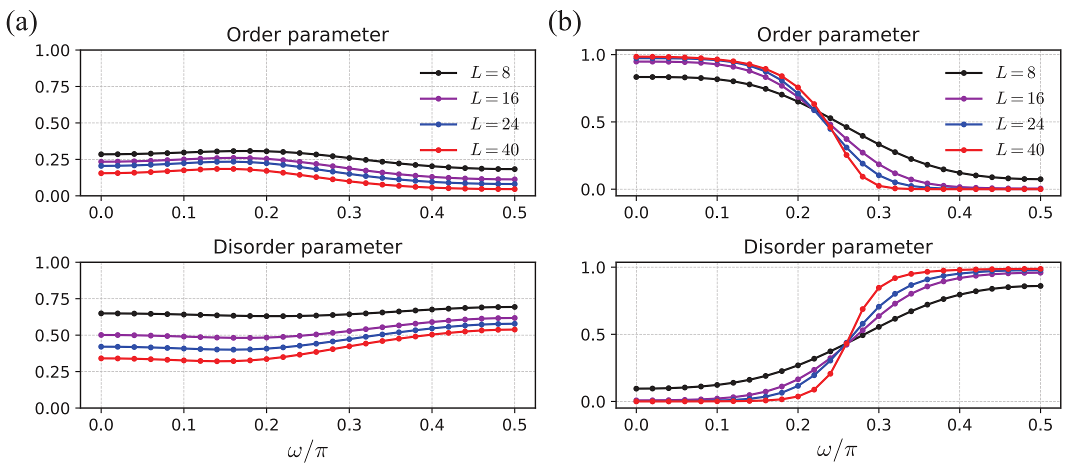

Figure 8.18: Order and disorder parameters as a function of the tilting angle for (a) $K = 0.75$ and (b) $K = 2.44$.

Chapter 9

BEYOND ISING: MINIMAL MODELS AND OTHER UNIVERSALITY CLASSES

9.1 Measurement-induced boundary transitions in minimal models

The previous section established that tilted weak measurements on the gapless parent of the cluster state generate a measurement-induced boundary transition. The key ingredient was the generation of multiple competing relevant perturbations under weak measurement—a property that can certainly arise in broader contexts. Armed with this insight, we now investigate alternate setups involving minimal models that indeed host similar transitions: namely, ground states of the tricritical Ising model and the three-state Potts model after a single round of measurements that yield a uniform outcome.

Tricritical Ising

The tricritical Ising CFT—realized by various systems including Rydberg atom arrays [32, 21] and spin chains [122]—provides an experimentally relevant example of a minimal model that exhibits a measurement-induced boundary transition. The CFT is characterized by a central charge $c = 7/10$ and hosts six primary fields of scaling dimensions $0, 3/40, 1/5, 7/8, 6/5$, and 3. Particularly relevant here are the spin field σ (dimension $3/40$) and the energy field ε (dimension $1/5$).

We consider O'Brien and Fendley's microscopic implementation that arises upon adding a self-dual 3-spin interactions to the critical transverse-field Ising model [122]:

$$H = -\sum_j [Z_j Z_{j+1} + X_j - \lambda(Z_{j-1}Z_j X_{j+1} + X_{j-1}Z_j Z_{j+1})] \tag{9.1}$$

with a parameter $\lambda \geq 0$. (Upcoming work will examine similar physics in the Rydberg array context [6].) For $\lambda < \lambda_c \approx 0.428$, the low-energy physics is simply governed by an Ising CFT that describes a continuous transition between ferromagnetic and paramagnetic phases. Increasing λ beyond λ_c generates a spectral gap and renders the transition first order. At the critical value $\lambda = \lambda_c$, the transition belongs to the tricritical Ising universality class; there we can relate the microscopic spin operators to the CFT fields as $Z \sim \sigma$, $X \sim \varepsilon$.

Suppose that we prepare the ground state of Eq. (9.1) at the tricritical Ising point, and then perform a uniform-post-selection weak measurement associated with the non-unitary operator

$$e^{\beta \sum_j [\cos(\omega) X_j + \sin(\omega) Z_j]}. \tag{9.2}$$

At $\omega = 0$, the measurement operator $X \sim \varepsilon$ induces a relevant defect-line perturbation to the CFT that triggers an RG flow to free boundary conditions. [Here we assume $\beta > 0$, which at $\omega = 0$ amplifies configurations favored by the transverse field in Eq. (9.1).] Post-measurement correlation functions exhibit power-law decay with exponents that can be obtained from BCFT calculations [123, 124] (see Sec. 9.4 for details); for example, one finds

$$\langle Z_0 Z_x \rangle_{\text{uni}} \sim \langle Y_0 Y_x \rangle_{\text{uni}} \sim x^{-3}. \tag{9.3}$$

The power-law exponent above is sufficiently large that both Z and Y operators comprise irrelevant perturbations to the free boundary condition fixed point, suggesting local stability. Similarly, at $\omega = \pi/2$, the measurement operator $Z \sim \sigma$ induces a relevant defect-line perturbation that triggers a flow to fixed boundary conditions with post-measurement correlations

$$\langle X_0 X_x \rangle_{\text{uni}} \sim \langle Y_0 Y_x \rangle_{\text{uni}} \sim x^{-4}, \tag{9.4}$$

again suggesting local stability of the corresponding fixed point.

In fact, both fixed points are known in the tricritical Ising BCFT and are stable against any local perturbations [124]. Interestingly, in the boundary RG flow—illustrated in Fig. 9.1(a)—there exists an unstable intermediate fixed point between the free (0) and fixed (+) boundary conditions, corresponding to the “partially polarized” boundary condition (0+) of the tricritical Ising theory. In our weak measurement protocol, this intermediate fixed point arises at a critical tilt angle ω_c, and can be identified by a second-order transition in the order parameter $\langle Z \rangle_{\text{uni}}$; see Fig. 9.1(b). This agreement highlights the robustness of our results within the established theoretical framework of BCFT. From a perturbative analysis, we note that at the intermediate fixed point, the post-measurement entanglement entropy obeys an area law, in contrast to the case of the gapless parent of the 1D cluster state. In Sec. 9.4, we numerically verify that, at the intermediate fixed point, the scaling dimension of the σ-field is compatible with the flow to the 0+ boundary condition. Beyond the theoretical relevance of this example, a protocol to realize the measurement-induced boundary transitions in Rydberg arrays is shown in later chapters. The protocol relies on post-selection, but with remarkably high success probabilities of O(10%) in a system of O(100) atoms.

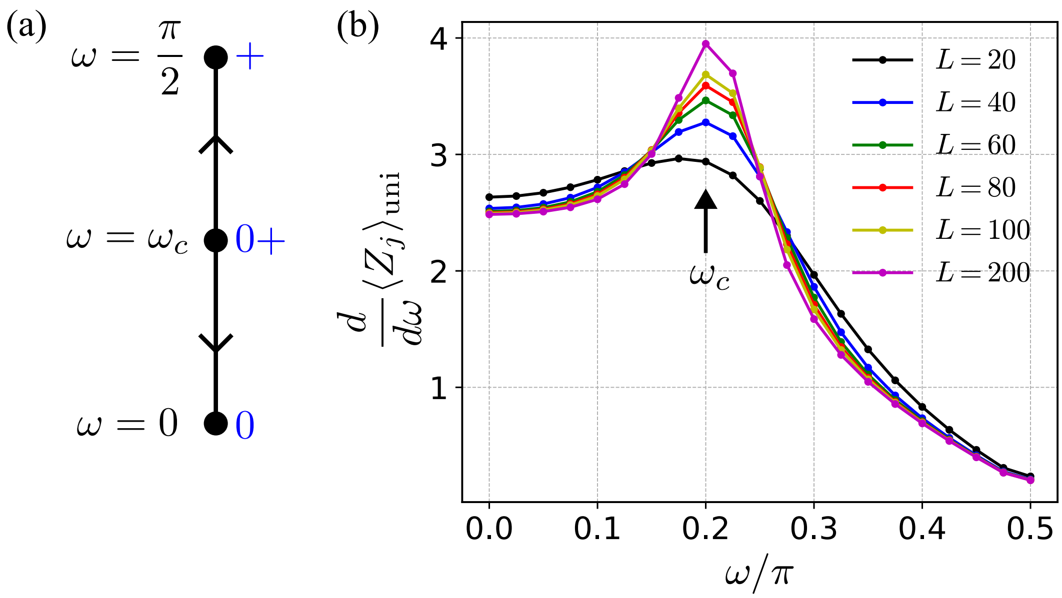

Figure 9.1: (a) Boundary renormalization group flow involving select fixed points for the tricritical Ising CFT, corresponding to free (0), fixed (+), and partially polarized (0+) boundary conditions. The unstable 0+ fixed point represents a measurement-induced boundary transition obtained at a fine-tuned measurement-basis tilt angle ω_c. (b) Derivative of the post-measurement 1-point function $\langle Z_j \rangle_{\text{uni}}$ versus tilt angle. Data were obtained by DMRG using periodic boundary conditions and bond dimension $\chi = 1000$. The measurement strength is $\beta = 0.5$.

Three-state Potts

The BCFT analysis capturing possible interesting measurement-induced transitions generalizes to other critical theories as well. A further example is the three-state Potts model, described by a CFT with central charge $c = 4/5$ and six primary fields with scaling dimensions $0, 2/15, 4/5, 4/3, 14/5, 6$. We are also primarily interested in the spin field σ (dimension $2/15$) and energy field ε (dimension $4/5$).

For a microscopic realization, let us define on-site operators

$$U_j = \begin{pmatrix} 1 & 0 & 0 \\ 0 & e^{i2\pi/3} & 0 \\ 0 & 0 & e^{-i2\pi/3} \end{pmatrix}, \quad V_j = \begin{pmatrix} 0 & 0 & 1 \\ 1 & 0 & 0 \\ 0 & 1 & 0 \end{pmatrix}. \tag{9.5}$$

The eigenvalues of U_j label three local spin states—which we denote by A, B, C—while V_j cycles the spin among those three values. A lattice Hamiltonian realizing the $c = 4/5$ CFT reads

$$H = -\sum_j \left(U_j U_{j+1}^\dagger + U_j^\dagger U_{j+1} + V_j + V_j^\dagger \right). \tag{9.6}$$

Notice that H preserves a $\mathbb{Z}_3$ symmetry that sends $U_j \to e^{i2\pi/3} U_j$. The rich operator content of this model gives rise to various possible boundary conditions [123, 125], some of which we can readily realize via weak measurement. Exploring the impact of weak measurements is facilitated by the dictionary between lattice operators and CFT fields derived in Ref. [126]: one finds $U_j \sim \sigma$ and $V_j + V_j^\dagger \sim \varepsilon$. Note that in this context σ is not a Hermitian field.

Consider first the weak measurement operator

$$e^{\beta \sum_j (V_j + V_j^\dagger)}, \tag{9.7}$$

which generates a relevant defect-line action involving the ε field. (Here too we assume $\beta > 0$ such that the measurement amplifies configurations favored by the V_j terms in H.) The perturbation induces a flow to a BCFT corresponding to free boundary conditions. There we find power-law correlations (see Sec. 9.4)

$$\left\langle U_0 U_j^\dagger \right\rangle \sim |j|^{-4/3}, \quad \left\langle V_0 V_j^\dagger \right\rangle \sim |j|^{-8/3}. \tag{9.8}$$

The fact that the scaling dimension of U_j is smaller than one indicates instability of this fixed point under $\mathbb{Z}_3$-breaking measurement operators.

Next we consider a family of such $\mathbb{Z}_3$-symmetry breaking operators given by

$$e^{-\beta \sum_j (V_j + V_j^\dagger)(e^{i\omega} U_j + e^{-i\omega} U_j^\dagger)(V_j + V_j^\dagger)} \quad (\beta > 0), \tag{9.9}$$

which generates a defect-line action involving $e^{i\omega}\sigma + e^{-i\omega}\sigma^\dagger$, up to irrelevant $\mathbb{Z}_3$ breaking operators. [The $(V + V^\dagger)$ terms do not change the symmetry of the measurement, but produce the expected boundary fixed points numerically.] Here ω plays the role of a tilt angle for the measurement basis. When ω varies, the measurement operator favors different Potts states, or certain superposition of them. At $\omega = 0$, for example, the measurement operator (weakly) projects each site to a state close to A, while $\omega = \pi$ equally favors B and C states. We find that when $\omega \in (-\pi/3, \frac{\pi}{3})$, $(\frac{\pi}{3}, \pi)$ and $(\pi, \frac{5\pi}{3})$, the perturbation induces a flow to A, B and C fixed boundary conditions, respectively, with power-law correlations,

$$\left\langle U_0 U_j^\dagger \right\rangle \sim |j|^{-4}, \quad \left\langle V_0 V_j^\dagger \right\rangle \sim |j|^{-4}. \tag{9.10}$$

At $\omega = \frac{\pi}{3}$, π and $\frac{5\pi}{3}$, the measurement induces a flow to mixed boundary conditions labeled by CA, BC, and AB respectively, featuring power-law correlations,

$$\left\langle U_0 U_j^\dagger \right\rangle \sim |j|^{-4/5}, \quad \left\langle V_0 V_j^\dagger \right\rangle \sim |j|^{-4/5}. \tag{9.11}$$

These mixed boundary condition fixed points are unstable against fixed boundary conditions and thus can be viewed as measurement-induced boundary transitions between A, B, C fixed points; see Fig. 9.2.

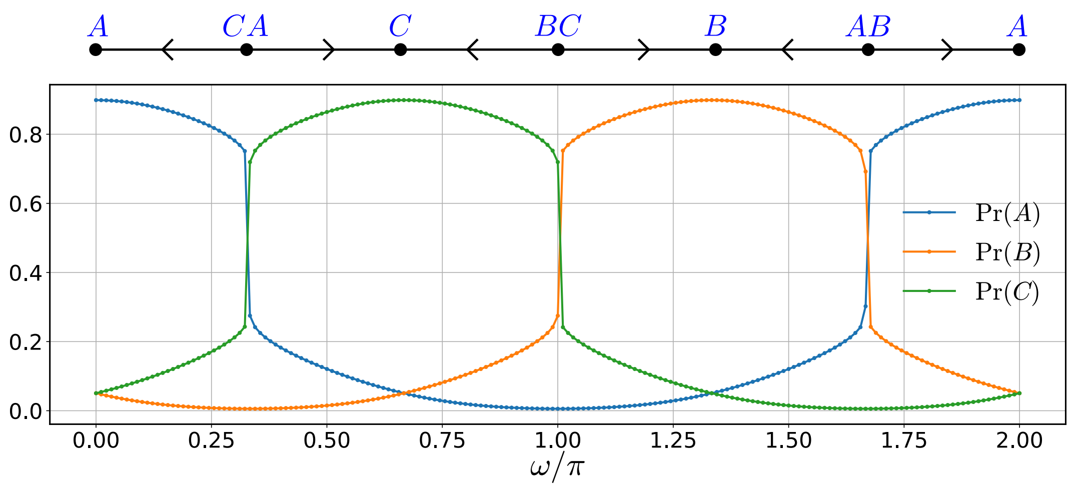

Figure 9.2: Boundary RG flow between fixed and mixed boundary conditions of the three-state Potts model. The three fixed boundary conditions are labeled by A, B, C and the mixed boundary conditions are labeled by AB, BC, CA. We plot the post-measurement probability of observing each Potts state as a function of tilt angle ω specified in Eq. (9.9). Data were obtained with iDMRG using bond dimension $\chi = 300$ and measurement strength $\beta = 0.1$.

9.2 Discussion and outlook

We have introduced a gapless parent of the 1D cluster state SPT that exactly maps to two decoupled Luttinger liquids. Local measurements together with post-selection of the uniform outcome introduce a defect line in the CFT action that triggers an RG flow to various BCFT fixed points—allowing us to derive universal properties of the post-measurement wavefunction. We uncovered richer behavior compared to the descendant gapped cluster state SPT, including nontrivial correlations persisting under weak measurements and measurement-induced boundary transitions accessed by tilting the measurement basis.

It is useful to additionally contrast with several previous works exploring measurement-altered quantum critical states—which can also be understood within BCFT. For instance, Ref. [16] investigated weak measurement of the density operator $\cos(2\phi)$ in a single-channel Luttinger liquid [in spin language, Z-basis measurement in an $\mathcal{XXZ}$ spin chain governed by the first line of Eq. (7.11)]. By post-selecting the outcome $s = \{(-1)^j\}$, the weak measurement induces a boundary condition

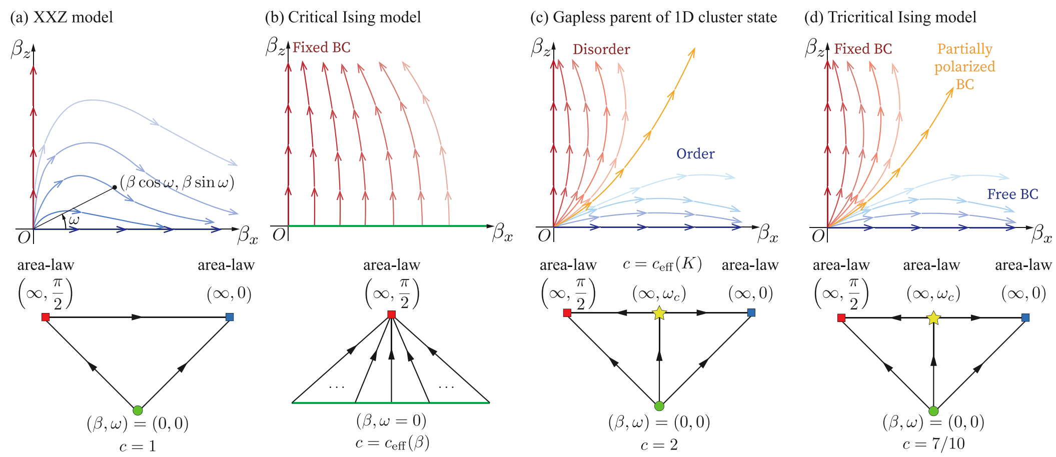

Figure 9.3: Upper row: Schematic RG flow induced by measurements enacted by $\exp[\beta \sum_j (\cos\omega X_j + \sin\omega Z_j)]$ in different gapless models; ω specifies the measurement-basis tilt angle, while $\beta_x = \beta\cos\omega$ and $\beta_z = \beta\sin\omega$. Lower row: Phase diagram of different boundary fixed points located at (β, ω) values specified in the parentheses. Green circles represent the pristine unmeasured CFTs; red (blue) squares show the boundary fixed points induced by measurement in the Z (X) basis; and yellow stars represent intermediate fixed points realizing measurement-induced boundary transitions [present in (c,d) but not (a,b)]. In (b) the green line is a line of fixed points. All fixed points feature power-law correlations and thus have infinite correlation length.

$\phi = n\pi, n \in \mathbb{Z}$. References [3, 58, 57, 4] studied weak measurements in the critical Ising chain described by the Hamiltonian $H = -\sum_j Z_j Z_{j+1} - \sum_j X_j$; here different measurement bases yield significantly different behaviors. The underlying low-energy theory is a $c = 1/2$ Ising CFT with three primary fields, $1, \sigma, \varepsilon$ with respective scaling dimensions $0, 1/8, 1$. After post-selection of the uniform outcome, X-basis measurements induce a marginal perturbation $\sim \varepsilon$ that yields a series of fixed points whose features depend on the measurement strength; Z-basis measurements, however, generate a relevant perturbation $\sim \sigma$ and a flow to the fixed boundary condition of the Ising CFT. In all these previous setups exhibiting measurement-altered criticality, tilting the measurement basis away from the Z-direction does not lead to a boundary transition, contrary to the gapless parent of the cluster state SPT.

Indeed, we can generalize the protocol of Ref. [16] by applying a tilted-basis weak measurement operator, $e^{\beta\sum_j[\cos\omega X_j + \sin(\omega)(-1)^j Z_j]}$, similarly to what we did for the gapless parent state in Section 8.1. We focus on the $K < 1$ case where the measurement of $(-1)^j Z_j$ induces a relevant perturbation to the pristine Luttinger liquid. By computing the scaling dimension of $X_j, Y_j, (-1)^j Z_j$ operators, we can study the stability of the two fixed points corresponding to $(\beta, \omega) = (\infty, 0)$ and $(\beta, \omega) = (\infty, \pi/2)$. The former is stable against any perturbation, while the latter is unstable against uniform X perturbations (or Y by symmetry). Relevance of weak X measurement in the second case follows from the fact that, after Z-basis measurements, the correlator $\langle X_0 X_x \rangle$ decays as $\sim x^{-1/K}$. Figure 9.3(a) illustrates the RG flow: by tuning ω from 0 to $\pi/2$, the system flows to $(\beta, \omega) = (\infty, 0)$, without any intermediate fixed point.

Similar logic applies to the critical Ising chain under tilted weak measurements enacted by $e^{\sum_j \beta[\cos(\omega) X_j + \sin(\omega) Z_j]}$. The series of fixed points induced by X measurement at $\omega = 0$ is always unstable to a σ perturbation induced by finite ω, while the fixed point arising at $\omega = \pi/2$ is stable to arbitrary perturbations. Therefore, for any $\omega > 0$, the long-range physics is determined by the latter. In BCFT language, the boundary fixed points of the Ising model that preserve the conformal symmetry and the RG flow between them are known [13, 123] (see also Fig. 9.3(b)). Interested readers may wonder what happens when tilting the measurement basis in the (Y, Z) instead of the (X, Z) plane, since symmetry does not relate the two problems in this case. Reference [4] shows that, at the CFT level, weak measurements in the Y basis generate a marginal ε perturbation—similar to X but with reduced coupling strength. Consequently, weak measurements in a basis chosen arbitrarily in the (X, Y) plane are always unstable to rotating the basis towards Z. The main difference between the Ising CFT and the other minimal models is that an ε-defect line is a marginal perturbation, while the flow to a boundary conformal field theory occurs only if the perturbation is relevant. In this sense there is not a competition between X and Z weak measurements.

One goal of this work was to identify protocols that, after a single round of measurements on critical systems, induce a non-trivial transition between two fixed points. Such measurement-induced boundary transitions can arise when different types of measurements yield at least two *stable* boundary fixed points, which in the gapless parent of the cluster state correspond to $\omega = 0$ and $\omega = \pi/2$ in Eqs. (8.1) and (8.6). These two fixed points are disconnected in the sense that any path in the parameter space connecting them goes across an intermediate fixed point. If the measurement preserves the $\mathbb{Z}_2$ symmetry of the gapless parent state, the intermediate fixed point is a critical theory with central charge $c = 1$. On the other hand, if we consider a $\mathbb{Z}_2$ symmetry-breaking measurement operator, surprisingly the intermediate fixed point appears to show an effective central charge that continuously varies with the Luttinger parameter K. Figure 9.3(c) illustrates the resulting schematic RG flow diagram indicating the competition between the two relevant measurement-induced perturbations. Other measurement-induced boundary transitions can be found by studying tilted measurements on the ground state of minimal models such as tricritical Ising (see Fig. 9.3(d)) and the three-state Potts model, whose rich operator content also enables non-trivial transitions between different fixed points.

We mainly focused our analysis of measurement-induced boundary transitions by post-selecting for uniform measurement outcomes (but see Sec. 8.1). Can analogous transitions persist when post-selecting for *typical* outcomes, i.e., those obtained by sampling according to the Born probability distribution $p_{\boldsymbol{s}}$? Following Kadanoff's decimation argument, Refs. [16, 4] found that if the scaling dimension of the leading perturbation generated by the measurement operator is less than $1/2$, then the *disordered* defect-line perturbation emerging with typical outcomes remains relevant. Critical theories supporting multiple measurement operators with dimensions below $1/2$ might then support novel measurement-induced boundary transitions for typical outcomes—provided the fixed points generated by each operator are also stable. The minimal models studied in Sec. 9.1 provide potentially fruitful test cases. For tricritical Ising, tilting between X (dimension $1/5$) and Z (dimension $3/40$) measurements would potentially yield interesting typical-outcome boundary transitions. In the three-state Potts case, the Hermitian operators $U+U^\dagger$ and $i(U-U^\dagger)$ both carry dimension $2/15$, potentially fulfilling the above criterion as well. Further investigation along these lines would be worthwhile.

Our work also highlights various other interesting future directions. For instance, can one connect the $c = 1$ intermediate fixed point studied in Sec. 8.1 to that of Sec. 8.1 by adding a $\mathbb{Z}_2$-breaking perturbation, and gain an analytical understanding of the K-dependent effective central charge found in the latter case? Is it possible to induce additional boundary conditions via measurements beyond those studied here, and possibly new measurement-induced boundary transitions, in minimal models such as the tricritical Ising and three-state Potts examples? Are there metrological applications of the measurement-altered critical states studied in this work? And finally, can one devise generalized decoding protocols (extending that of Sec. 7.4) to a more general class of measurement bases, ideally to probe intermediate fixed points without post-selection?

9.3 $\mathbb{Z}_2 \times \mathbb{Z}_2$ SPT phase with interaction reflection symmetry and its relation with a spin-1 chain

In Sec. 7.2, we have shown that the cluster state SPT can be obtained by breaking the interchain reflection symmetry of the gapless parent state, i.e., taking $\alpha \neq \pi/4$ in Eq. (7.8). A natural question to ask is whether it is possible to obtain an inter-chain-reflection symmetric $\mathbb{Z}_2 \times \mathbb{Z}_2$ SPT by gapping out the gapless parent state. We will show that the answer is yes.

We begin with the $\mathcal{X}\mathcal{Y}$ representation of the gapless parent of the cluster state with central charge $c = 2$,

$$H = -\sum_j \left[\mathcal{X}_j\mathcal{X}_{j+1} + \mathcal{Y}_j\mathcal{Y}_{j+1} + \tilde{\mathcal{X}}_j\tilde{\mathcal{X}}_{j+1} + \tilde{\mathcal{Y}}_j\tilde{\mathcal{Y}}_{j+1}\right]. \tag{9.12}$$

For simplicity, we only focus on the $K = 1$ case. The interchain-reflection symmetry transforms as follows,

$$\mathcal{X}_j \to \mathcal{Y}_j G_2, \quad \tilde{\mathcal{X}}_j \to \tilde{\mathcal{Y}}_j G_2 \tag{9.13}$$

where the $\mathbb{Z}_2$ symmetry generators $G_{1,2}$ are defined in Eq. 7.2. The ground state $|\psi_\Delta\rangle$ satisfies $G_{1,2} = 1$ and the reflection transformation is just $\mathcal{X}_j \leftrightarrow \mathcal{Y}_j$ and $\tilde{\mathcal{X}}_j \leftrightarrow \tilde{\mathcal{Y}}_j$.

Now consider adding interchain coupling terms to the Hamiltonian,

$$\begin{aligned} H_\perp &= -\lambda \sum_j (\mathcal{X}_j\tilde{\mathcal{X}}_j + \mathcal{Y}_j\tilde{\mathcal{Y}}_j + \mathcal{Z}_j\tilde{\mathcal{Z}}_j), \quad (\lambda > 0) \\ &= -\lambda \sum_j (X_{j,1} + X_{j,2} - X_{j,1}X_{j,2}) \quad \text{(in the } ZXZ \text{ basis).} \end{aligned} \tag{9.14}$$

In terms of boson fields, $H + H_\perp$ can be decomposed using symmetric (+) and antisymmetric (−) fields $\phi_\pm = \frac{1}{\sqrt{2}}(\phi \pm \tilde{\phi})$ and $\theta_\pm = \frac{1}{\sqrt{2}}(\theta \pm \tilde{\theta})$ [117],

$$\begin{aligned} H + H_\perp &= H_+ + H_- \\ H_+ &= \int_x \frac{1}{2\pi}\left[K_+(\nabla\theta_+)^2 + \frac{1}{K_+}(\nabla\phi_+)^2\right] + g_+ \int_x \cos(\sqrt{8}\phi_+) \\ H_- &= \int_x \frac{1}{2\pi}\left[K_-(\nabla\theta_-)^2 + \frac{1}{K_-}(\nabla\phi_-)^2\right] + g_-^{(1)} \int_x \cos(\sqrt{8}\phi_-) \\ &\quad + g_-^{(2)} \int_x \cos(\sqrt{2}\theta_-) \end{aligned} \tag{9.15}$$

where $g_+, g_-^{(1,2)} \propto \lambda$, and

$$K_\pm = K\left(1 \mp \frac{K\lambda a}{2\pi u}\right) \tag{9.16}$$

with a being the lattice spacing and u the Fermi velocity. The antisymmetric part is always gapped once $H_\perp$ is added. For the symmetric part, $\cos(\sqrt{8}\phi_+)$ is relevant when $K_+ < 1$. At the $\mathcal{XY}$ point ($K = 1$), we have $K_+ > 1$ when $\lambda > 0$. Therefore the symmetric part remains gapless and one should expect an effective central charge $c = 1$.

Another useful way to understand the effect of $H_\perp$ is to consider the $\lambda \to \infty$ limit, where $H_\perp$ projects the two spin-1/2's on the same rung, $(\mathcal{X}, \mathcal{Y}, \mathcal{Z})_j$ and $(\tilde{\mathcal{X}}, \tilde{\mathcal{Y}}, \tilde{\mathcal{Z}})_j$, onto the triplet subspace with spin-1 operators $\mathbf{S}_j = \frac{1}{2}[(\mathcal{X}_j + \tilde{\mathcal{X}}_j)\hat{\mathbf{x}} + (\mathcal{Y}_j + \tilde{\mathcal{Y}}_j)\hat{\mathbf{y}} + (\mathcal{Z}_j + \tilde{\mathcal{Z}}_j)\hat{\mathbf{z}})]$. Within the triplet subspace, the Hamiltonian $H + H_\perp$ acts like a spin-1 xy chain,

$$H_1 = -\sum_j (S^x_j S^x_{j+1} + S^y_j S^y_{j+1}), \tag{9.17}$$

which is also gapless but with central charge $c = 1$. The interchain reflection transforms as $x \leftrightarrow y$. The correlations in the ground state of H_1 are (see Fig. 9.4 for DMRG simulations),

$$\left\langle S^x_j S^x_k \right\rangle = \left\langle S^y_j S^y_k \right\rangle \sim \frac{1}{|j-k|^{\frac{1}{4}}}, \quad \left\langle S^z_j S^z_k \right\rangle \sim \frac{1}{|j-k|^2}. \tag{9.18}$$

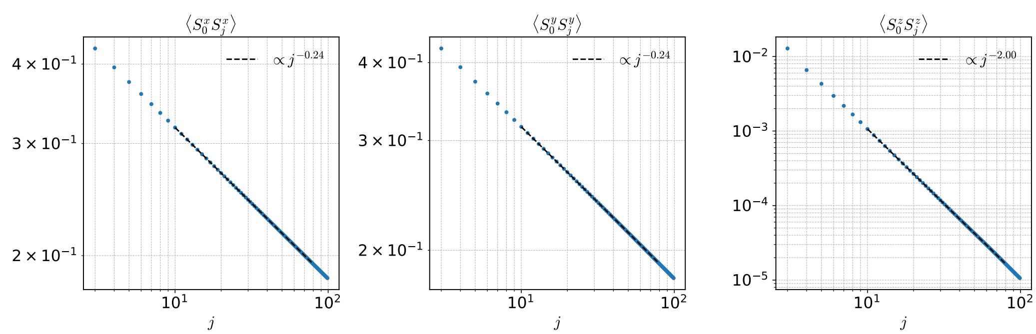

Figure 9.4: The correlation functions of the ground state of a spin-1 xy chain. The power-law exponents are obtained by fitting the data in log-log scale (see the black dashed lines). The wavefunction is obtained by iDMRG with bond dimension $\chi = 450$.

The interchain-reflection symmectric $\mathbb{Z}_2 \times \mathbb{Z}_2$ SPT phase of the spin-1/2 ladder corresponds to the ferromagnetically ordered phase in the effective spin-1 chain with $\left\langle S^x_j S^x_k \right\rangle \sim \left\langle S^y_j S^y_k \right\rangle \sim const.$, which can be obtained by further adding a next-nearest-neighbor perturbation to the spin-1 xy chain, e.g.,

$$H' = J' \sum_j \sum_{\mu=x,y} S^\mu_{j-1}[2(S^\mu_j)^2 - 1]S^\mu_{j+1} \tag{9.19}$$

with $J' > 0$. In the $\mathcal{XXZ}$ basis, the perturbation term can be written as

$$H' = J' \sum_j (\mathcal{X}_j \mathcal{X}_{j+1} \tilde{\mathcal{X}}_{j+1} \tilde{\mathcal{X}}_{j+2} + \mathcal{Y}_j \mathcal{Y}_{j+1} \tilde{\mathcal{Y}}_{j+1} \tilde{\mathcal{Y}}_{j+2}), \tag{9.20}$$

and in the original ZXZ basis, H' represents next-nearest-neighbor interactions,

$$H' = J' \sum_j (X_{j,1} Z_{j,2} X_{j+2,1} Z_{j+2,2} + Z_{j,1} X_{j,2} Z_{j+2,1} X_{j+2,2}). \tag{9.21}$$

In Ref. [112], it is shown that such next-nearest-neighbor couplings yield the interchain-reflection symmetric $\mathbb{Z}_2 \times \mathbb{Z}_2$ SPT phase.

One can also study the measurement problem in the spin-1 represeatation. Numerically, DMRG simulation of the spin-1 chain requires less computational resource than that of the gapless parent of the cluster state. Within the triplet subspace, $X_{j,1} = \mathcal{X}_j \tilde{\mathcal{X}}_j = 2(S_j^x)^2 - 1$, the uniform projective measurement with $X_{j,1} = +1$ is equivalent to applying $\prod_j \frac{1+X_{j,1}}{2} = \prod_j (S_j^x)^2$ to the ground state.

The $Z_{j,2} Z_{k,2}$ correlation within the triplet subspace is equivalent to the string operator,

$$\left\langle Z_{j,2} Z_{k,2} \right\rangle \sim (-1)^{k-j-1} \left\langle S_j^x \left[\prod_{l=j+1}^{k} \exp(i\pi S_l^x) \right] S_k^x \right\rangle \tag{9.22}$$

which is short-ranged in the ferromagnetic phase of the spin-1 chain and decays algebraically at the gapless point. Once the uniform outcome $s = \{X_{j,1} = +1\}$ is post-selected, one can simplify Eq. (9.22) by $-\exp(i\pi S_l^x) = 2(S_l^x)^2 - 1 = 1$ and obtain,

$$\left\langle Z_{j,2} Z_{k,2} \right\rangle_{\text{uni}} \sim \left\langle S_j^x S_k^x \right\rangle_{\text{uni}}, \tag{9.23}$$

which is analogous to Eq. (7.27). Also, the counterpart of Eq. (7.28) is

$$\left\langle X_{j,2} X_{k,2} \right\rangle_{\text{uni}} \sim \left\langle (S_j^y)^2 (S_k^y)^2 \right\rangle_{\text{uni}}. \tag{9.24}$$

From DMRG calculations (see Fig. 9.5), we see that

$$\left\langle Z_{j,2} Z_{k,2} \right\rangle_{\text{uni}} \sim const, \quad \left\langle X_{j,2} X_{k,2} \right\rangle_{\text{uni}} \sim |j-k|^{-4}, \tag{9.25}$$

which are consistent with Eq. (7.27) and Eq. (7.28) at $K = 1$.

9.4 Boundary fixed points and RG flows

In BCFT, the conformal invariant boundary conditions (BCs) and the corresponding boundary fixed points are characterized by Cardy states [123]. The operator content

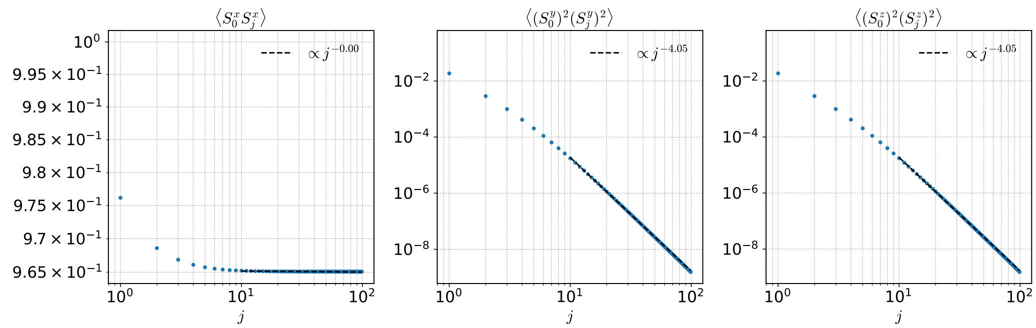

Figure 9.5: Select correlation functions of the spin-1 xy chain after applying $\prod_j (S_j^x)^2$. The power-law exponents are obtained by fitting the data in log-log scale (see the black dashed lines). The wavefunction is obtained by infinite DMRG with bond dimension $\chi = 450$.

and conformal spectrum can be obtained by the fusion rules of the primary operators corresponding to the Cardy states. As an example, in the 2D Ising CFT there are three primary fields, I (identity), ε (energy), and σ (spin). One can associate the free BC (denoted by "0") with a Cardy state corresponding to the spin field, $|0\rangle \equiv |\tilde{\sigma}\rangle$. The operator content can be obtained by the fusion rule, $\sigma \times \sigma = I + \varepsilon$. There are also two fixed BCs obtained by applying an external boundary field h_b that breaks the $\mathbb{Z}_2$ symmetry. We denote them by "+" and "−", depending on the sign of h_b. The Cardy states of these two BCs are $|+\rangle \equiv \left|\tilde{I}\right\rangle$ and $|-\rangle \equiv |\tilde{\varepsilon}\rangle$, and in their operator contents only the identity I appears, because both $I \times I$ and $\varepsilon \times \varepsilon$ fuse to I. Therefore, the conformal spectrum of free BC is $\{0, \frac{1}{2}, \frac{3}{2}, 2, \frac{5}{2}, 3, \frac{7}{2}, 4, 4, \frac{9}{2}, \frac{9}{2}, \dots\}$, and those of fixed BCs are $\{0, 2, 3, 4, 4, 5, 5, \dots\}$.

The scaling dimension of local boundary operators, such as the spin in the Ising model example, can be extracted from the conformal spectrum and generally differs from that of the same operator when located far from the boundary. In the measurement problem discussed in the main text, the scaling dimension of local operators in the post-measurement wavefunction should also take value in the conformal spectrum, at least when the relevant measurement operator flows to a specific BCFT. For example, let $|\psi_0\rangle$ be the ground state of a critical transverse-field Ising chain $H = -\sum_j (Z_j Z_{j+1} + X_j)$. Then the post-measurement state $e^{\beta \sum_j X_j} |\psi_0\rangle$, $\beta \to \infty$, corresponds to the free BC and the post-measurement scaling dimension $[Z]_{\text{uni}} = 1/2$ can be read off from the free BC conformal spectrum. Similarly, $e^{\beta \sum_j Z_j} |\psi_0\rangle$ corresponds to fixed BC and $[Z]_{\text{uni}} = 2$ is also consistent with the first gap in the fixed BC conformal spectrum. After measurements of relevant operators, an alternative way to find these scaling dimensions is by exploiting the power-law decay of the strange correlator $a_{jk} - a_j a_k$ defined in Eq. (8.14).

Table 9.1: The conformally invariant boundary conditions, Cardy states, and corresponding operator contents of a 2D tricritical Ising CFT. The boundary conditions are labeled by symbols in the parentheses: 0, +, −, etc.

Boundary condition	Cardy state	Operator content	Conformal spectrum
Free (0)	$\lvert 0\rangle \equiv \lvert\tilde{\sigma'}\rangle$	$I + \varepsilon''$	$\{0, \frac{3}{2}, 2, \frac{5}{2}, 3, \frac{7}{2}, \frac{7}{2}, \dots\}$
Fixed (+)	$\lvert +\rangle \equiv \lvert\tilde{I}\rangle$	I	$\{0, 2, 3, 4, 4, 5, 5, \dots\}$
Fixed (−)	$\lvert -\rangle \equiv \lvert\tilde{\varepsilon''}\rangle$	I	$\{0, 2, 3, 4, 4, 5, 5, \dots\}$
Partially polarized (0+)	$\lvert 0+\rangle \equiv \lvert\tilde{\varepsilon}\rangle$	$I + \varepsilon'$	$\{0, \frac{3}{5}, \frac{8}{5}, 2, \frac{13}{5}, \frac{13}{5}, 3, \dots\}$
Partially polarized (0−)	$\lvert 0-\rangle \equiv \lvert\tilde{\varepsilon'}\rangle$	$I + \varepsilon'$	$\{0, \frac{3}{5}, \frac{8}{5}, 2, \frac{13}{5}, \frac{13}{5}, 3, \dots\}$
degenerate (d)	$\lvert d\rangle \equiv \lvert\tilde{\sigma}\rangle$	$I + \varepsilon + \varepsilon' + \varepsilon''$	$\{0, \frac{1}{10}, \frac{3}{5}, \frac{11}{10}, \frac{3}{2}, \frac{8}{5}, 2, \dots\}$
Fixed (+&−)	$\lvert +\&-\rangle \equiv \lvert +\rangle + \lvert -\rangle$	$2(I + \varepsilon'')$	$\{0, 0, \frac{3}{2}, \frac{3}{2}, 2, 2, \frac{5}{2}, \frac{5}{2}, \dots\}$

The boundary fixed points and Cardy states of the 2D tricritical Ising CFT are more complicated. As we have already reviewed in the main text, there are six primary fields in this case. Four of them preserve the $\mathbb{Z}_2$ spin-inversion symmetry, I, ε, ε, ε' and ε'', while two of them break it, σ and σ'. We list the Cardy states and corresponding BCs in Table. 9.1. The RG flow between the boundary fixed points has been studied in Refs. [127, 124], and is summarized in Fig. 9.1(a).

In the measurement problem, if $|\psi_0\rangle$ is the ground state of Eq. (9.1), the weak measurement $e^{\beta\sum_j X_j}|\psi_0\rangle$, $\beta > 0$ flows to the free BC, and the strange correlator decays as $a_{jk} - a_j a_k \sim |j-k|^{-3}$, whose exponent is just twice the first gap of the conformal spectrum we can read from the first line of Table 9.1. This result justifies the power-law decay of Eq. (9.3). The measurement $e^{\beta\sum_j Z_j}$, $\beta > 0$, flows to the fixed + BC, and one immediately gets Eq. (9.4) by looking at the second line of Table 9.1. When the measurement angle is tilted between the X and Z axes, it will go across a transition corresponding to the partially polarized 0+ BC, where the strange correlator decays as $a_{jk} - a_j a_k \sim |j-k|^{-6/5}$. We numerically analyze these results in Fig. 9.6: in the left panel ($\omega = 0$), we verify that the order parameter decays as x^{-3}, as we would expect from free BCs, in the middle panel ($\omega = \pi/2$) we show the decay of the order parameter as x^{-4}, consistently with the flow to fixed BCs. Finally, the right panel ($\omega = \omega_c$) corresponds to the measurement-induced boundary transition described by the intermediate fixed point 0+, in agreement with the order parameter decay $x^{-6/5}$. As discussed in Sec. 8.2, the post-measurement wavefunction is expected to obey an area law entanglement since the exponent $6/5$ exceeds 1.

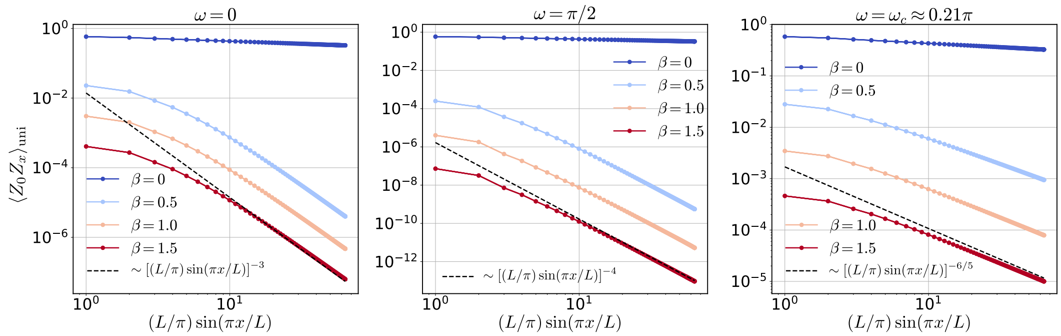

Figure 9.6: Post-measurement correlation functions of $e^{\beta\sum_j[\cos(\omega)X_j+\sin(\omega)Z_j]}\,|\psi_0\rangle$, where $|\psi_0\rangle$ is the ground state of Eq. (9.1) at the tricritical Ising point. Data obtained using DMRG with system size $L = 200$, bond dimension $\chi = 1000$ and periodic boundary conditions. In this figure, $\omega = 0$ and $\omega = \pi/2$ correspond to free (0) and fixed (+) BC respectively, and $\omega = \omega_c \approx 0.21\pi$ corresponds to the intermediate fixed point — partially polarized (0+) BC.

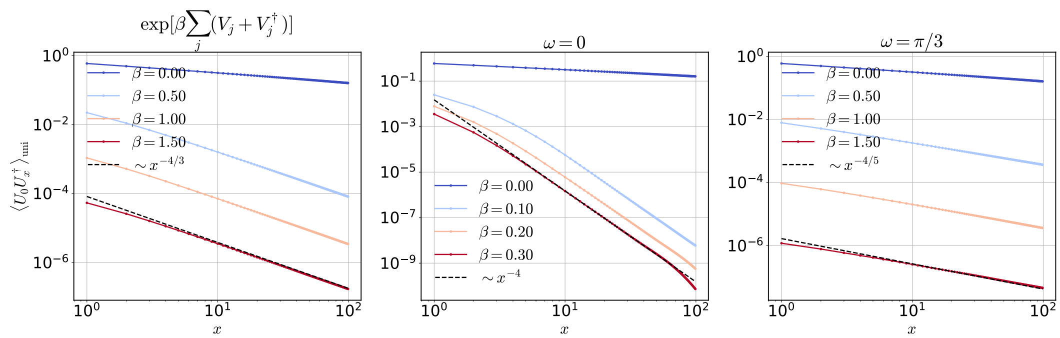

Figure 9.7: Correlation functions of three-state Potts model after measurement of $e^{\beta\sum_j[V_j+V_j^\dagger]}$ (left panel) and measurement in Eq. 9.9 with $\omega = 0$ (middle panel) or $\omega = \pi/3$ (right panel). Data obtained using iDMRG with bond dimension $\chi = 500$.

We conclude this Section by observing that also the three-state Potts model has six primary fields. In the previous chapters, we have mainly focused on σ and ε, whose scaling dimensions are respectively $2/15$ and $4/5$. We have observed that the measurement $e^{\beta\sum_j(V_j+V_j^\dagger)}$, with $\beta > 0$, flows to the free boundary condition, and the power-law exponent of $\left\langle U_0 U_j^\dagger\right\rangle_{\text{uni}}$ can be read off from the boundary conformal spectrum, and it is equal to $4/3$, as we also show in the left panel of Fig. 9.7. Then, we have shown how the measurement operator in Eq. (9.9) is responsible for a flow to fixed boundary conditions, A, B or C, while by tuning $\omega = \pi/3, \pi, 5/\pi$, the measurement flows to mixed boundary conditions, CA, BC or AB. The first energy gap of the BCFT with fixed boundary conditions suggests that $[U + U^\dagger]_{\text{uni}} = 2$, while for mixed boundary conditions $[U + U^\dagger]_{\text{uni}} = 2/5$. These predictions are supported by the middle and right panels of Fig. 9.7.

Part V

Experimental Realization in Rydberg Arrays

"If you can walk a mile in someone else's shoes, you totally should. Free shoes for a whole mile, maaan!"

— Pascal, *Animal Crossing: New Horizons*

Chapter 10

RYDBERG ARRAYS AS A PLATFORM FOR MEASUREMENT-ALTERED CRITICALITY

10.1 Motivation for an ancilla-free experimental protocol

Experimental exploration of measurement-altered criticality requires a versatile platform capable of initializing a critical ground state with high fidelity, measuring to appropriately modify the wavefunction, and detecting the resulting changes in universal properties. Wavefunction modifications are commonly studied theoretically using weak measurements [55, 56, 58, 57, 60, 128, 62, 129, 5], e.g., mediated by ancillae that are unitarily entangled with the critical degrees of freedom and then projectively measured [16, 3]. Weak measurements can modestly restructure the amplitudes in the critical wavefunction, facilitating field-theoretic predictions for the impact on long-distance behavior [16, 3, 56, 55, 58, 57, 5, 128, 62, 129, 60, 130, 131, 132]. Verifying these predictions poses an intrinsic problem, however, since measurements restructure the wavefunction in a manner dependent on the information gleaned—which is inherently probabilistic. Revealing measurement-altered criticality requires either post-selecting for specific target outcomes—whose probability generically decreases exponentially with system size—or non-standard averaging procedures [16, 3, 64, 128, 58].

We provide a practical roadmap for addressing these challenges using a single chain of laser-excited Rydberg atoms trapped in optical tweezers, which can realize Ising and tricritical Ising quantum critical wavefunctions [32, 133, 134, 21, 33, 135, 136, 137] (among other universality classes [138, 139, 140, 141, 142, 143, 144, 145]) via adiabatic state preparation; see Fig. 10.1(a). We develop an ancilla-free protocol that is useful to conceptually divide into two stages. First, projectively measure the state of the atoms at a *subset* of sites.

Judiciously choosing both the pattern of measured sites and post-selected measurement outcomes, e.g., as indicated by the solid measurement icons in Fig. 10.1(b,c), controls universal modifications to critical correlations. These modifications manifest with either open or periodic boundary conditions and can be probed via subsequently measuring the remainder of the chain [faded measurement icons in Fig. 10.1(b,c)]. We show that the post-selection probabilities for the target measurement outcomes

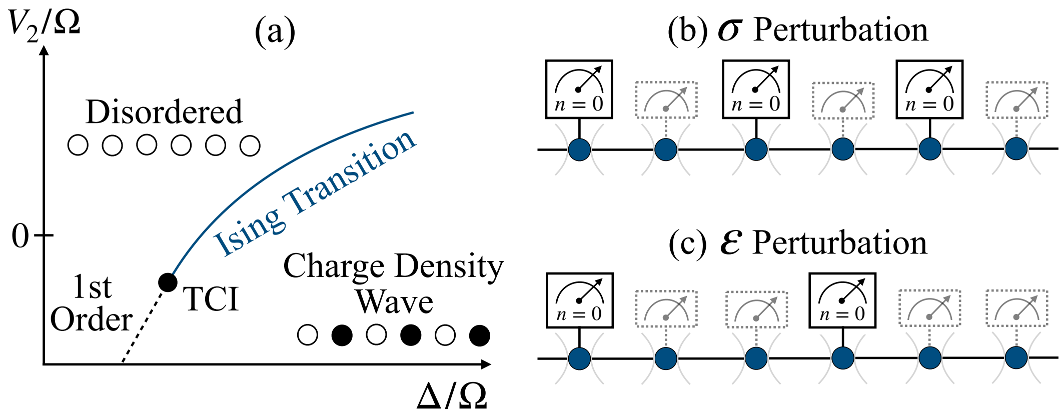

Figure 10.1: **Phase diagram and measurement protocols.** (a) Schematic phase diagram of the blockaded Rydberg chain Hamiltonian, Eq. (10.1), featuring charge density wave and disordered states separated by an Ising transition line terminating at a tricritical Ising (TCI) point. (b,c) Example protocols for measurement-altered criticality associated with (b) σ and (c) ε CFT perturbations. Modified correlations follow by simply measuring all sites simultaneously, and averaging over outcomes subject to the post-selection conditions indicated in the solid measurement icons.

yielding the most dramatic effects are surprisingly high for experimentally relevant system sizes; see Fig. 12.1. More practically, the same measurement-altered correlations emerge upon projectively measuring *all* sites simultaneously and simply averaging over a restricted set of measurement outcomes (instead of all outcomes, which would return correlations from the unmeasured theory). Our scheme thus entails minimal overhead beyond that required to probe pristine quantum critical correlations. Near-term realization appears particularly promising given recently released experimental signatures of Ising and tricritical Ising criticality in Rydberg arrays [137].

10.2 Rydberg-chain Hamiltonian and pure criticality

We model a length-L Rydberg chain with the minimal Hamiltonian [32]

$$\hat{H} = \sum_j \left[\frac{\Omega}{2}(\hat{b}_j + \hat{b}_j^\dagger) - \Delta \hat{n}_j + V_1 \hat{n}_j \hat{n}_{j+1} + V_2 \hat{n}_j \hat{n}_{j+2} \right], \tag{10.1}$$

where $\hat{b}_j$ is a hard-core boson operator and $\hat{n}_j = \hat{b}_j^\dagger \hat{b}_j$ with eigenvalues 0 (ground state) and 1 (Rydberg excited state). The first two terms encode, within the rotating wave approximation, driving of the atoms with Rabi frequency Ω and detuning Δ from resonance; $V_{1,2}$ represent first- and second-neighbor interactions mediated by the Rydberg excited states. We assume that $V_1 > 0$ dominates all couplings, energetically imposing the blockade constraint that no two neighboring atoms can simultaneously enter the Rydberg state. Within the blockaded subspace, one can effectively realize either sign of V_2 in experiment [21, 33]. Unless specified otherwise we consider an even-length, periodic chain for which $\hat{H}$ preserves both translation T_x and bond-reflection R_x symmetries that transform the occupation numbers via $\hat{n}_j \to \hat{n}_{j+1}$ and $\hat{n}_j \to \hat{n}_{L-j+1}$, respectively.

The phase diagram of $\hat{H}$ [Fig. 10.1(a)] features a trivial symmetric phase and a two-fold degenerate charge density wave (CDW) phase wherein Rydberg excitations occur predominantly on every other site, doubling the unit cell and spontaneously breaking T_x and R_x. Starting from $V_2 > 0$, these phases are separated by a continuous Ising transition that, on decreasing V_2, terminates at an integrable tricritical Ising (TCI) point [32] and then becomes first-order. Throughout we consider a Rydberg chain prepared into the ground state $|\psi_c\rangle$ of either the Ising or TCI transitions, which are respectively governed by conformal field theories (CFTs) with central charge $c = 1/2$ and $7/10$.

Symmetries allow one to relate microscopic operators to CFT fields that govern their leading long-distance correlations [21]. Lattice operators that transform trivially under T_x and R_x generically map to the 'thermal perturbation' ε that one must fine-tune away to reach criticality, e.g.,

$$\hat{\varepsilon}_{j+1/2} \equiv (\hat{n}_j + \hat{n}_{j+1})/2 \sim c_1 + c_2\varepsilon + \cdots \tag{10.2}$$

with non-universal $c_{1,2}$ and subleading terms indicated by the ellipsis. Equation (10.2) implies that connected two-point correlations exhibit universal power-law decay: $\langle \hat{\varepsilon}_{j+1/2}\hat{\varepsilon}_{j'+1/2}\rangle_c \sim \langle \varepsilon(x)\varepsilon(x')\rangle_c \sim |j-j'|^{-2\Delta_\varepsilon}$ with scaling dimension $\Delta_\varepsilon = 1$ (Ising) or $1/5$ (TCI) dictated by the underlying CFT.

Moreover, the microscopic CDW order parameter maps to the CFT 'spin field' σ,

$$\hat{\sigma}_{j+1/2} \equiv (-1)^j(\hat{n}_j - \hat{n}_{j+1})/2 \sim \sigma + \cdots . \tag{10.3}$$

Both $\hat{\sigma}_{j+1/2}$ and σ acquire a minus sign under T_x and R_x, and hence symmetry dictates that $\langle\hat{\sigma}_{j+1/2}\rangle = \langle\sigma\rangle = 0$. Two-point order-parameter correlations, however, also decay as a power-law, but with scaling dimension $\Delta_\sigma = 1/8$ (Ising) or $\Delta_\sigma = 3/40$ (TCI). Chains with open boundaries explicitly break T_x, seeding CDW order at the edges [21]. Consequently, even in an otherwise uniform critical chain, $\langle\hat{\sigma}_{j+1/2}\rangle$ and $\langle\sigma\rangle$ become finite and decay towards zero into the bulk with a functional form dependent on Δ_σ; see Ref. [146] for details. Open chains thereby enable extraction of scaling dimensions via relatively simple one-point expectation values.

10.3 Preparing critical ground states

To obtain the critical states used in our numerics, we employ the two-site density matrix renormalization group (DMRG) algorithm to prepare the ground state of the Hamiltonian defined in Eq. (10.1) in the main text. Since our goal is to investigate measurement-altered critical states, it is essential to first accurately prepare the unmeasured critical states within DMRG.

To realize a Rydberg chain at the Ising critical point, we begin by identifying suitable Hamiltonian parameters along the critical line shown in Fig. 10.1 in the main text. Following the curve-crossing procedure introduced in Ref. [21], we sweep the detuning parameter Δ while fixing the remaining parameters to $\Omega = 1$, $V_1 = 100$ (accounting for the blockaded regime), and $V_2 = 0$. For each value of Δ and for multiple system sizes with open boundary conditions, we compute the rescaled observable $\langle \hat{\sigma}_{L/2} \rangle \cdot \sin(\pi/(L+2))^{-1/8}$, which exhibits scale invariance at criticality. More precisely, the critical point is identified as the value of $\Delta = \Delta_c$ where this quantity becomes independent of system size, as shown in Fig. 10.2(a). We further verify criticality with periodic boundary chains in Fig. 10.2(b) (with additional details provided in Fig. 10.3(a)) by examining the power-law decay of the connected order parameter correlator at this point in parameter space.

In the case of the TCI point, the critical parameters are known exactly for the closely related integrable model [32] with the Hilbert space constraint $n_j n_{j+1} = 0$ on all sites. These parameters, as provided in Refs. [32, 21], are $(\Delta/\Omega)_{\mathrm{TCI}} = -\frac{1}{2}(5\sqrt{5} - 2)$ and $(V_2/\Omega)_{\mathrm{TCI}} = -\frac{1}{2}\left(\frac{1+\sqrt{5}}{2}\right)^{5/2}$. Although we do not explicitly enforce the Hilbert space constraint in our simulations, we approximate it by setting $V_1 = 1000$. Using these parameters places the system close to the TCI point of the constrained model, which we verify in Fig. 10.3(b) (blue data points) showing a scaling of $\langle \hat{\sigma}^{\mathbf{n}}_{\ell_1} \hat{\sigma}^{\mathbf{n}}_{\ell_2} \rangle_c$ with the (chord) distance $|\ell_2 - \ell_1|$ consistent with a power-law dependence, with exponent $\Delta_\sigma = 3/40$.

In our DMRG simulations, we terminate the algorithm only when the change in entropy and energy between successive sweeps satisfy $\Delta S < 10^{-5}$ and $\Delta E < 10^{-7}$, respectively. To ensure convergence with respect to the bond dimension χ, we examine the connected correlation function $\langle \hat{\sigma}^{\mathbf{n}}_{\ell_1} \hat{\sigma}^{\mathbf{n}}_{\ell_2} \rangle_c$ as χ is doubled (see numerical agreement between "x" and "o" markers in Fig. 10.3). This analysis is performed for the pre-measurement states in both the TCI and Ising critical points, as well as for the lowest-probability post-measurement states we consider ($\{n_{3j}, n_{3j+1} = 0\}$ and $\{n_{4j}, n_{4j+1} = 0\}$ for Ising and TCI, respectively), which we expect to be the most

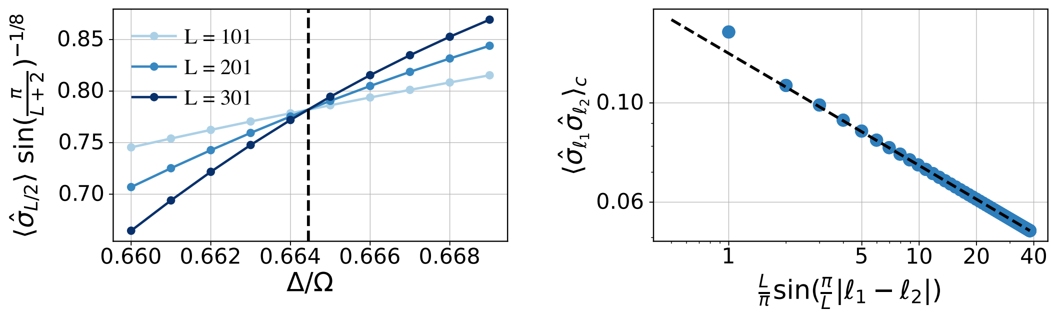

Figure 10.2: Identification of the critical detuning Δ_c at $V_2 = 0$ along the Ising critical line. The vertical dashed line in panel (a) marks the value of detuning $\Delta_c = 0.66445$ where $\langle\hat{\sigma}_{L/2}\rangle \cdot \sin(\pi/(L+2))^{-1/8}$ exhibits a curve-crossing for open chains of different sizes. Panel (b) shows the order parameter connected correlator with respect to the ground state of a Hamiltonian prepared at these extracted critical parameters. The dashed line is the predicted critical scaling for $\Delta_\sigma = 1/8$.

demanding in χ among those examined.

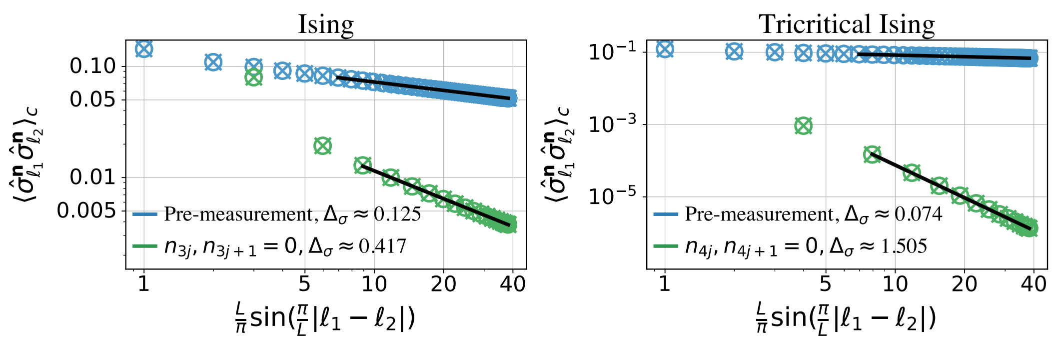

Figure 10.3: Verification of DMRG convergence in bond dimension. We observe how the observable $\langle\hat{\sigma}^{\mathbf{n}}_{\ell_1}\hat{\sigma}^{\mathbf{n}}_{\ell_2}\rangle_c$ changes as we double our bond dimension from $\chi = 250$ (denoted by 'o' markers) to $\chi = 500$ (denoted by 'x' markers). We do this for the pre-measurement state (blue symbols), as well as the post-measurement state with the least likely measurement outcome (green symbols). The black line shows a fit of the longest-range 90% of points used to calculate the approximate Δ_σ's shown in the legends. Universal predictions are that $\Delta_\sigma = 1/8,\ 3/40$ for the pre-measurement states in Ising, TCI respectively.

10.4 Projective measurements in the Rydberg occupation basis

We examine changes in universal properties of the critical state $|\psi_c\rangle$ after measuring a fraction of sites $\{i_1, i_2, \ldots, i_K\}$ in the Rydberg occupation number basis with post-selected outcomes $\mathbf{n} = \{n_{i_1}, n_{i_2}, ..., n_{i_K}\}$. Measurements generically break translation symmetry T_x, though we always consider choices of $\mathbf{n}$ that enlarge the unit cell to

p sites, preserving a subgroup $(T_x)^p$ on periodic chains; see, e.g., Figs. 10.1(b,c). Bond reflections R_x may either be broken or preserved, as in Figs. 10.1(b) and (c), respectively. The (unnormalized) post-measurement state reads

$$|\psi_c^{\mathbf{n}}\rangle = e^{-\frac{\beta}{2}\hat{\mathcal{H}}_{\mathbf{n}}}|\psi_c\rangle, \quad \hat{\mathcal{H}}_{\mathbf{n}} = \sum_{a=1}^{K}(-1)^{n_{i_a}}\hat{n}_{i_a} \tag{10.4}$$

with β parametrizing the measurement strength. Our experimental protocol and numerical simulations always invoke the projective limit $\beta \to \infty$, corresponding to $e^{-\frac{\beta}{2}\hat{\mathcal{H}}_{\mathbf{n}}} \propto \prod_{j=1}^{K} |n_{i_j}\rangle\langle n_{i_j}|$. We evaluate measurement-induced changes to critical correlations by probing microscopic operators $\hat{\sigma}_\ell^{\mathbf{n}}$ and (for protocols that preserve R_x) $\hat{\varepsilon}_\ell^{\mathbf{n}}$ that respectively map onto the CFT fields σ and ε after measurement; see End Matter for details.

Complementary analytical insights follow from the weak-measurement limit $0 < \beta \ll 1$. At $\beta = 0$, expectation values $\left\langle\psi_c^{\mathbf{n}}\right| \cdots \left|\psi_c^{\mathbf{n}}\right\rangle$ can be recast as a path integral weighted by a 'pure' Euclidean CFT action S_{CFT} defined over space-time coordinates (x, τ), such that the imaginary time intervals $\tau > 0$ and $\tau < 0$ respectively prepare the quantum critical bra $\langle\psi_c|$ and ket $|\psi_c\rangle$. Turning on weak β perturbs S_{CFT} with a 'defect line' action S_{meas} that acts at all x but only $\tau = 0$ [16]. Given measurement data $\mathbf{n}$, the action S_{meas} is constrained by symmetry and explicitly follows from coarse-graining $\beta\hat{\mathcal{H}}_{\mathbf{n}}$ using the field decompositions specified in Eqs. (10.2) and (10.3). The most general form we will need for either the Ising or TCI cases is

$$S_{\text{meas}} \sim \beta \int_x [a_\sigma \sigma(x, \tau = 0) + a_\varepsilon \varepsilon(x, \tau = 0)], \tag{10.5}$$

where we neglected subleading terms, e.g., involving derivatives. Coefficients a_σ and a_ε are coarse-grained over a length scale large compared to the unit cell size and are therefore position-independent; their magnitudes and relative size do, however, depend on $\mathbf{n}$, and consequently the choice of measured sites and post-selected outcomes controls the defect-line action and consequences thereof. Measurement patterns that preserve $(T_x)^{p\in\text{odd}}$ and/or R_x, for instance, constrain $a_\sigma = 0$, while otherwise both a_σ and a_ε are generically non-zero. Renormalization group and boundary CFT techniques predict modifications of long-distance correlations stemming from weak measurements generating Eq. (10.5). We will see that, in all cases, partial projective measurements implemented by our protocol ($\beta \to \infty$ at fixed L) are consistent with expectations based on these field-theoretic treatments valid at small β.

10.5 Post-measurement operator dictionary

The post-measurement states we consider (characterized by post-selected outcomes **n**) always exhibit simple unit cells that one can organize as a set of measured sites followed by a set of unmeasured sets. For all such states the microscopic operator

$$\hat{\sigma}_\ell^{\mathbf{n}} \equiv \frac{1}{|\Lambda_\ell^{\mathbf{n}}|} \sum_{k \in \Lambda_\ell^{\mathbf{n}}} (-1)^k \hat{n}_k \sim \sigma + \cdots , \tag{10.6}$$

with $\Lambda_\ell^{\mathbf{n}}$ the set of unmeasured sites within a unit cell labeled by the 'center of mass' position ℓ, yields the CFT field σ as the leading long-distance contribution. As an example, for $\mathbf{n} = \{n_{5j} = 0\}$ the $\Lambda_\ell^{\mathbf{n}}$'s take the form

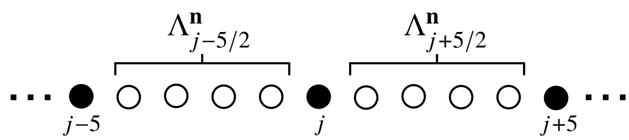

While certainly not unique, the mapping in Eq. (10.6) democratically incorporates all unmeasured sites within a unit cell into the order-parameter operator.

When the post-measurement state lacks bond reflection symmetry R_x, the ε field generically appears as the next-leading term represented by the ellipsis in Eq. (10.6). Preservation of R_x, however, allows one to cancel off the ε contribution—leaving an even less relevant next-leading term and thus streamlining extraction of properties related to σ. If the bond-reflection center resides within the set of unmeasured sites (as is the case in the $\mathbf{n} = \{n_{5j} = 0\}$ example), then the above $\Lambda_\ell^{\mathbf{n}}$ prescription automatically removes the ε contribution since $\hat{\sigma}_\ell^{\mathbf{n}}$ is odd under R_x. For $\mathbf{n} = \{n_{3j}, n_{3j+1} = 0\}$ where the reflection center resides between consecutive measured sites, our usual $\Lambda_\ell^{\mathbf{n}}$ choice leaves an oscillatory $(-1)^\ell \varepsilon$ contribution to $\hat{\sigma}_\ell^{\mathbf{n}}$. For this special case we cancel the oscillatory ε term by extending $\Lambda_\ell^{\mathbf{n}}$ to include adjacent unit cells as follows:

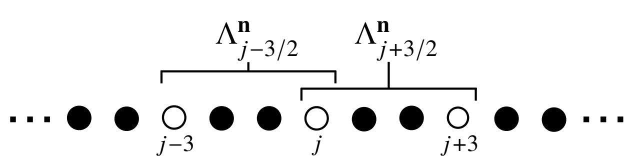

Outcomes that preserve R_x additionally enable a symmetry-based construction of microscopic operators that yield ε as the leading contribution (modulo a trivial identity factor). In particular, we define

$$\hat{\varepsilon}_\ell^{\mathbf{n}} \equiv \frac{1}{|\Lambda_\ell^{\mathbf{n}}|} \sum_{k \in \Lambda_\ell^{\mathbf{n}}} \hat{n}_k \sim c_1^{\mathbf{n}} + c_2^{\mathbf{n}} \varepsilon + \cdots \quad (R_x\text{-symmetric } \mathbf{n}) \tag{10.7}$$

using exactly the same $\Lambda_\ell^{\mathbf{n}}$ choices used for $\hat{\sigma}_\ell^{\mathbf{n}}$, which precludes a σ contribution to the right side by R_x symmetry. For many post-selected outcomes, even when R_x is broken, one could in principle isolate ε by searching for a fine-tuned combination of $\hat{n}_k$ operators that cancels off σ, but we will not pursue such an extraction here.

10.6 Extracting scaling dimensions

Equipped with microscopic mappings that represent σ and (in some cases) ε after applying a variety of measurement protocols, we now discuss the extraction of post-measurement scaling dimensions via DMRG simulations.

For periodic chains, Δ_σ was calculated via a power-law fit of the longest-range 80% of post-measurement connected correlators, $\langle \hat{\sigma}_{\ell_1}^{\mathbf{n}} \hat{\sigma}_{\ell_2}^{\mathbf{n}} \rangle_c$, shown in the insets of Figs. 11.1 and 11.2 in the main text. For chains with open boundary conditions, translation symmetry is explicitly broken at the edges; $\langle \sigma \rangle$ consequently obtains a spatially dependent expectation value that decays towards zero in the bulk. Reference [21] provides the universal scaling of this expectation value from the boundary of an (unmeasured) odd-length open Rydberg chain:

$$\langle \hat{\sigma}_{j+1/2} \rangle \sim \left[\sin\left(\pi \frac{j+1}{L+2} \right) \right]^{-\Delta_\sigma} . \tag{10.8}$$

In our post-measurement setting, we use the above equation modified by taking $j + 1/2 \to \ell$ and $\hat{\sigma}_{j+1/2} \to \hat{\sigma}_\ell^{\mathbf{n}}$.

10.7 Relation to the ancilla-assisted Ising and boundary-CFT viewpoints

The Rydberg protocol uses a single number-basis measurement rather than the ancilla-assisted weak measurements of Chapter 3. Nevertheless, the field-theory structure is the same: after coarse graining, the measurement generates a defect-line action whose allowed terms are fixed by lattice symmetries and by the selected outcome sector. The same relevant-versus-marginal distinction that controlled Chapters 3–6 therefore reappears in an experimentally accessible setting, while the boundary-condition language of Chapters 7–9 explains the fixed points reached by strong projective measurements.

Chapter 11

ALTERED ISING AND TRICRITICAL ISING CRITICALITY IN RYDBERG CHAINS

11.1 Measurement-altered Ising criticality in Rydberg arrays

Suppose now that $|\psi_c\rangle$ represents a quantum critical state tuned to the Ising transition line in Fig. 10.1(a). In the Ising CFT, the ε term from Eq. (10.5) is marginal whereas σ is strongly relevant. Provided $a_\sigma \neq 0$, the latter thus dominates—inducing a flow to a new stable fixed point described by a boundary CFT with fixed boundary conditions at $\tau = 0$ [13, 123]. Here measurements (i) generate order-parameter condensation, (ii) non-perturbatively modify the $\tau = 0$ σ and ε scaling dimensions to $\Delta_\sigma = \Delta_\varepsilon = 2$, and (iii) produce area-law entanglement in the post-measurement wavefunction [3, 57]. The marginal ε term controls the long-distance physics, however, if a_σ vanishes due to symmetry; measurements then leave Δ_ε unchanged, while both the scaling dimension Δ_σ and effective central charge (quantified by the entanglement entropy) vary continuously with the measurement strength β [3, 57, 58, 26, 27].

To test these predictions with more practical projective measurements, we employ density matrix renormalization group (DMRG) simulations to extract correlations of a critical Rydberg chain before and after measuring. Specifically, we simulate a finite-size chain and perform projective measurements on a subset of sites corresponding to various choices of $\mathbf{n}$ at $V_2 = 0$ in periodic chains and with open boundaries. Scaling dimensions are extracted from power-law fits of two-point correlators or, with open boundaries, from the decay of one-point σ correlators away from edges [21]. Pre-measurement correlators simply return scaling dimensions in excellent agreement with those of the 'pure' Ising CFT—a useful diagnostic for the fidelity of the critical state (see Fig. 11.1, left). The middle (blue) and right (green) regions of Fig. 11.1 summarize our post-measurement results for the $\tau = 0$ scaling dimension Δ_σ arising in $\mathbf{n}$ sectors specified on the horizontal axis. (See Ref. [146] for results on Δ_ε.)

Middle data correspond to measurements that preserve neither $(T_x)^{p\in\text{odd}}$ nor R_x, thus permitting a nontrivial σ perturbation in Eq. (10.5). For intuition, consider the case where we measure sites $\{2, 4, 6, \ldots, L\}$ with outcomes $\{0, 0, 0, \ldots, 0\}$, i.e., post-selecting for the atomic ground state on every other site. Hereafter we

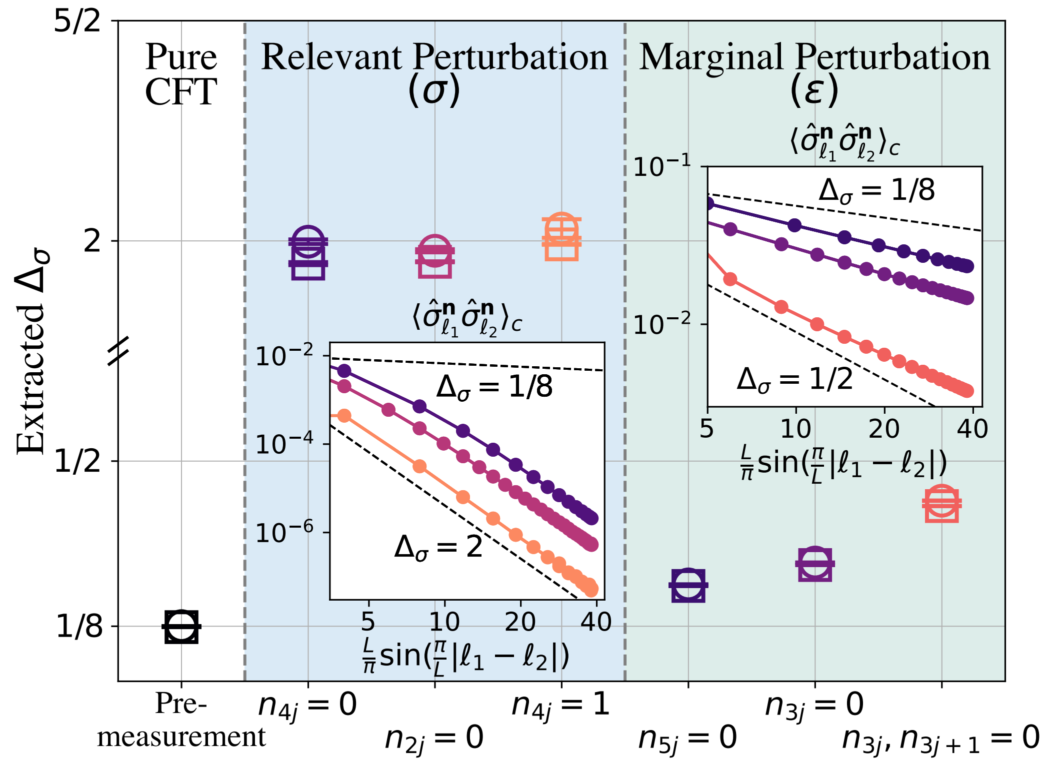

Figure 11.1: **Altered Ising criticality.** Extracted scaling dimension of σ (Δ_σ) at Ising criticality before (left region) and after (middle and right regions) projective measurements. Horizontal axis indicates various measurement protocols, including the subset of measured sites and their outcomes. Circles (squares) correspond to chains with periodic (open) boundary conditions. *Insets:* Post-measurement order parameter correlators for periodic chains, which were used to determine the circular markers of the same color in the main panel. The dependence on chord distance (horizontal axis) arises from the conformal mapping from an infinite line to a circle of circumference L [9]. Corresponding open-chain correlators and DMRG implementation details appear in Ref. [146].

adopt shorthand notation $\mathbf{n} = \{n_{2j} = 0\}$ for this protocol (and similarly for other outcomes). This measurement sector reduces translation symmetry in a manner that accommodates only one of the two CDW ordered patterns. Analogous logic holds for the sectors with $\mathbf{n} = \{n_{4j} = 0\}$ or $\mathbf{n} = \{n_{4j} = 1\}$, albeit with weaker ordering bias because fewer sites are measured. For all these cases our DMRG simulations recover $\Delta_\sigma \approx 2$, which agrees with the intuition that these CDW-order-seeding measurements act as a σ deformation.

The right section of Fig. 11.1 corresponds to measurements that preserve $(T_x)^{p\in\text{odd}}$ and R_x, leaving only the ε perturbation in Eq. (10.5). Measurements with $\mathbf{n} = \{n_{3j} = 0\}$, for instance, do not discriminate between the two adjacent CDW orders; instead order-parameter correlations are simply suppressed given the ground-state atomic configuration imposed on every third site. One can control this suppression by choosing $\mathbf{n}$'s with the same symmetry but different densities of measured sites. Consistent with the intuition above as well as predictions from the weak-measurement limit, our DMRG results reveal $\mathbf{n}$-dependent Δ_σ's exceeding the pre-measurement value of $1/8$. This agreement supports extrapolating $\beta \ll 1$ analytic predictions to the $\beta \to \infty$ projective protocol, as previously discussed.

11.2 Measurement-altered tricritical Ising criticality

Next we examine the critical ground state $|\psi_c\rangle$ at the TCI point. Here both the σ *and* ε terms from Eq. (10.5) constitute strongly relevant perturbations. When a_σ dominates, the system again flows to a stable fixed point with the same characteristics highlighted earlier for the Ising case (including modified $\tau = 0$ dimensions $\Delta_\sigma = \Delta_\varepsilon = 2$). Measurements yielding dominant a_ε,[1] in contrast, now induce a flow to a different stable fixed point exhibiting free boundary conditions—non-perturbatively modifying the $\tau = 0$ dimensions to $\Delta_\sigma = 3/2, \Delta_\varepsilon = 2$ [147]. At some critical value of a_σ/a_ε, measurements drive a flow to an intervening unstable fixed point corresponding to a boundary CFT with partially polarized boundary conditions and $\Delta_\sigma = \Delta_\varepsilon = 3/5$ [123, 124].

Numerical simulations are consistent with these predictions for the TCI chain; see Fig. 11.2 for periodic systems (Ref. [146] includes additional details for open boundary conditions). The green region on the right once again corresponds to measurement outcomes for which symmetry dictates $a_\sigma = 0$, in this case yielding $\Delta_\sigma \approx 3/2$ as expected for the TCI point. The blue region on the left represents outcomes with $n_j = 1$ on every fourth, sixth, or eighth site. Because of the blockade constraint enforcing $n_{j-1} = n_{j+1} = 0$ on the adjacent sites, such outcomes clearly inject CDW order, acting as a σ deformation to indeed yield $\Delta_\sigma \approx 2$ as expected from the a_σ-driven fixed point. In principle, one could tune a_σ/a_ε to cross the intermediate unstable fixed point by considering measurement patterns that intermix the two types of outcomes above in varying proportions. Interestingly, however, the End Matter provides numerical evidence that simple outcomes with $n_{2j} = 0$ place the system at or very near the intermediate fixed point.

[1]We assume a sign of a_ε such that the ε term opposes CDW order, which is always the case for $\mathbf{n}$'s that we have studied.

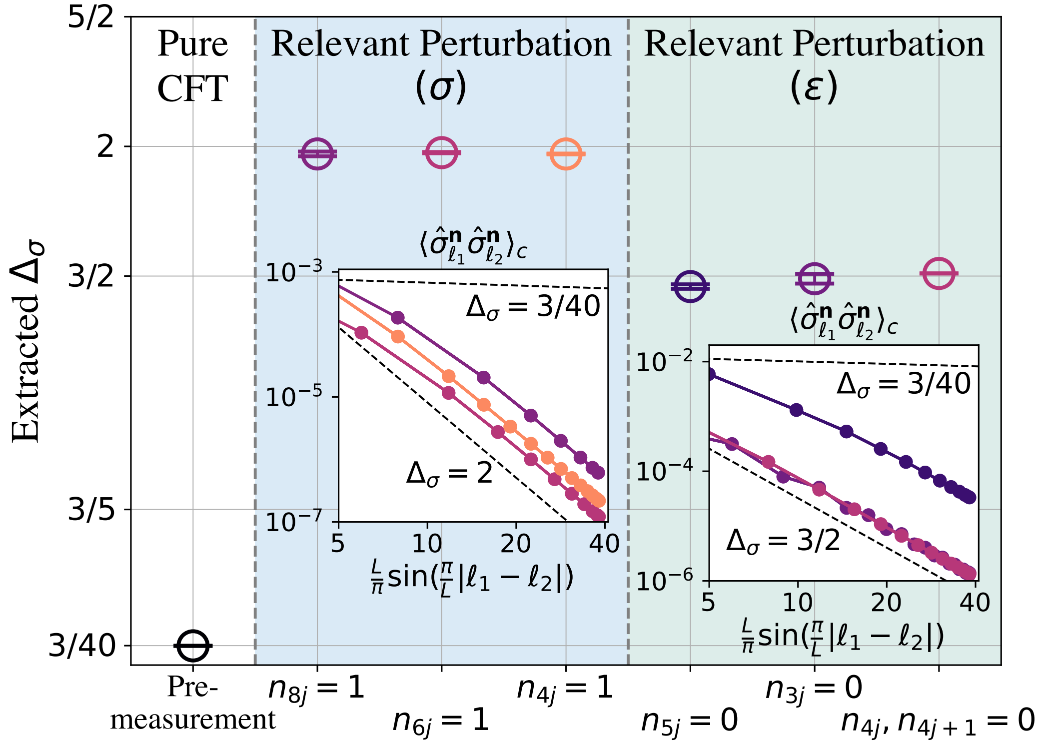

Figure 11.2: **Altered tricritical Ising.** Extracted scaling dimension of σ (Δ_σ) at TCI before (left region) and after (middle and right regions) projective measurements (patterns of which are indicated on the horizontal axis) with periodic boundary conditions. *Insets:* Chord distance dependence of the post-measurement order parameter correlators. Additional data for open boundary conditions and the intermediate fixed point can be found in Ref. [146], respectively.

11.3 Open-boundary diagnostics and finite-size scaling

Figure 11.3 examines the open-boundary-condition scaling behavior of the one-point σ correlator under various measurement protocols applied to critical Ising and TCI chains. Panel (a) shows $\langle \hat{\sigma}^{\mathbf{n}}_{\ell} \rangle$ for $\mathbf{n}$'s that preserve R_x symmetry, corresponding to marginal perturbations to the Ising CFT. As the density of measured sites increases, the numerical results reveal a smooth increase of Δ_σ relative to the pre-measured value of $1/8$. The extracted Δ_σ values agree well with those obtained from two-point correlators in periodic chains; see Table 11.1, which provides a summary of the exponents extracted for various measurement outcomes on both open and periodic chains. Panel (b) shows numerical results for R_x-symmetric measurement outcomes on the TCI wavefunction generating, in this case, a relevant (symmetric) ε perturbation. While the analytical prediction is $\Delta_\sigma = 3/2$, we observe a slight numerical drift (with the deviation from the predicted Δ_σ reaching as large as 12%

for the measurement outcome $\{n_{5j} = 0\}$) with the measurement strength. We attribute this dependence to finite-size effects (we observe a light improvement with increasing system size, although we are then limited by bond dimension). Moreover, unlike for the σ-perturbation, the power-law dependence of the correlator for measurement outcomes $n_{5j} = 0$ and $n_{3j} = 0$, is only observed at sufficiently large distances, preventing us from extracting an accurate power-law exponent. Outcomes $\mathbf{n}$ that break R_x symmetry correspond to relevant CFT perturbations that drive a non-zero $\langle\sigma\rangle$ value in the bulk even in the thermodynamic limit. To mod out this bulk contribution and isolate the scaling behavior away from the edges, panels (c) and (d) show the spatial derivative of $\langle\sigma_\ell^{\mathbf{n}}\rangle$ with respect to the horizontal-axis parameterization. The fitted slope ν on the log-log plot yields a scaling dimension $\Delta_\sigma = -\nu - 1$. For both critical Ising and TCI chains, we find $\Delta_\sigma \approx 2$ independent of the measurement protocol—consistent with both analytical predictions and numerical results for periodic chains.

Ising							
	Pure CFT	Relevant Perturbation (σ)			Marginal Perturbation (ε)		
	Predic. $\Delta_\sigma = \frac{1}{8}$	Prediction $\Delta_\sigma = 2$			Prediction Δ_σ increases w/ meas. strength		
$\mathbf{n}$	N/A	$\{n_{4j} = 0\}$	$\{n_{2j} = 0\}$	$\{n_{4j} = 1\}$	$\{n_{5j} = 0\}$	$\{n_{3j} = 0\}$	$\{n_{3j}, n_{3j+1} = 0\}$
PBC	0.125233(5)	1.998(5)	1.978(3)	2.03(2)	0.2199(1)	0.26968(4)	0.4101(4)
OBC	0.12302(5)	1.948(3)	1.952(3)	1.9921(8)	0.2165(3)	0.2639(1)	0.3978(3)
R_x	N/A	No	No	No	Yes	Yes	Yes
$(T_x)^{p\in\text{odd}}$	N/A	No	No	No	Yes	Yes	Yes

Tricritical Ising							
	Pure CFT	Relevant Perturbation (σ)			Relevant Perturbation (ε)		
	Predic. $\Delta_\sigma = \frac{3}{40}$	Prediction $\Delta_\sigma = 2$			Prediction $\Delta_\sigma = \frac{3}{2}$		
$\mathbf{n}$	N/A	$\{n_{8j} = 1\}$	$\{n_{6j} = 1\}$	$\{n_{4j} = 1\}$	$\{n_{5j} = 0\}$	$\{n_{3j} = 0\}$	$\{n_{4j}, n_{4j+1} = 0\}$
PBC	0.074158(8)	1.971(9)	1.976(2)	1.971(2)	1.460(8)	1.49(2)	1.5101(3)
OBC	0.0711(3)	1.914(2)	1.887(2)	1.856(3)	1.68(4)	1.63(1)	1.529(7)
R_x	N/A	No	No	No	Yes	Yes	Yes
$(T_x)^{p\in\text{odd}}$	N/A	No	No	No	Yes	Yes	No

Table 11.1: Numerically extracted scaling dimensions Δ_σ for Ising and TCI chains in both periodic and open boundary conditions. The uncertainty values (parentheses) are the standard errors from linear regression fits used to obtain Δ_σ and are shown as error bars in Figs. 11.1 and 11.2 from the main text. Note that these uncertainties do not account for finite-size effects or slight deviations from exact critical tuning, both of which we expect contribute to discrepancies from theoretical predictions. The bottom rows of each table indicate whether each protocol respects or breaks the R_x or $(T_x)^{p\in\text{odd}}$ symmetries.

For R_x-preserving measurement outcomes, we can additionally extract the ε scaling dimension via Eq. (10.7) in the main text. Figure 11.4 demonstrates this extraction

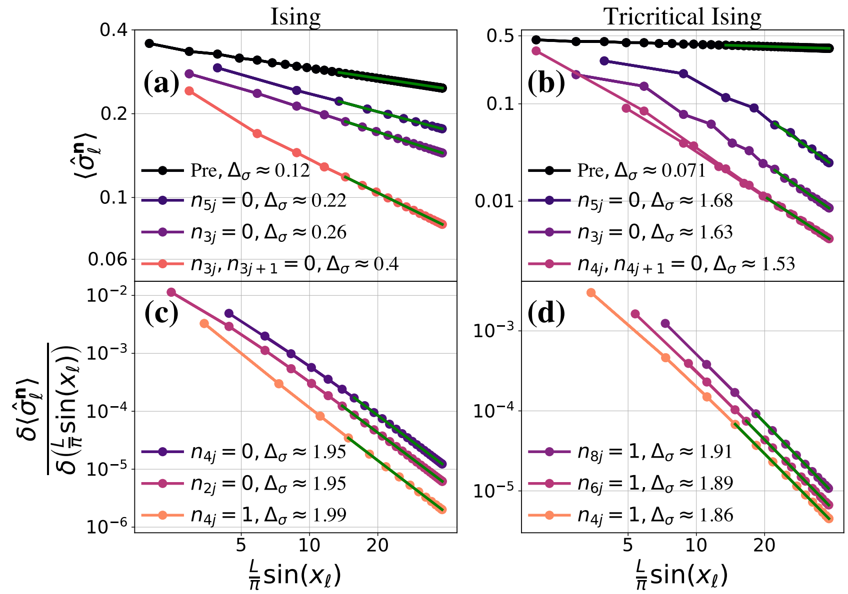

Figure 11.3: One-point order parameter correlations following measurements of an $L = 121$-site open chain tuned to Ising (left) or tricritical Ising (right) criticality. To give best agreement with boundary CFT predictions, right panels employ a detuning shift, $\Delta \to \Delta - V_2$, on the first and last sites of Eq. (10.1) of the main text, as detailed in Ref. [21]. Data represent measurement protocols yielding ε (top) and σ (bottom) CFT perturbations, with $x_\ell \equiv \pi\frac{\ell+1/2}{L+2}$ on the horizontal axis. Bottom panels show the spatial derivative of the one-point correlator to effectively cancel off a finite $\langle\sigma\rangle$ bulk contribution. The furthest 80% of data from the boundary is used in all cases to fit the corresponding power-law exponent, with the exception of the post-measurement correlators in panel (b) where finite-size effects encourage us to fit only the furthest 2/3 of sites.

through the power-law scaling of the connected correlator $\langle\hat{\varepsilon}^{\mathbf{n}}_{\ell_1}\hat{\varepsilon}^{\mathbf{n}}_{\ell_2}\rangle_c$ in a periodic chain prepared at (a) the Ising transition and (b) the TCI point. In (a) we perform a local spatial average over adjacent pairs of unit cells to suppress a pronounced oscillatory component, which we attribute to a closely subleading, symmetry-allowed term of the form $(-1)^\ell\partial_x\sigma$ appearing in the ellipsis of Eq. (10.7). In contrast, this averaging is unnecessary for the TCI case in (b), where ε is significantly more relevant than $\partial_x\sigma$. In both the Ising and TCI case, we find consistency with the CFT predictions of $\Delta_\varepsilon = 1$ and $\Delta_\varepsilon = 2$, respectively.

Analysis of $\langle\varepsilon\varepsilon\rangle_c$ for the $\{n_{3j}, n_{3j+1} = 0\}$ outcome

We provide here the analysis of the ε scaling dimension in the $\{n_{3j}, n_{3j+1} = 0\}$ post-measurement state. We employ the following microscopic operator mapping,

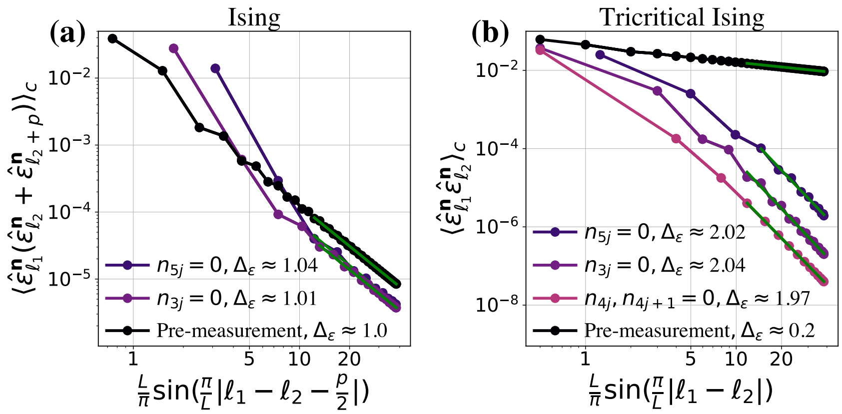

Figure 11.4: Connected two-point ε correlators following R_x-symmetric measurement protocols in an $L = 120$-site periodic critical chain tuned to (a) Ising criticality and (b) the TCI point. The SM analyzes data for the $n_{3j}, n_{3j+1} = 0$ Ising measurement protocol, which suffers from more severe finite-size effects.

closely related to the originally prescribed ε mapping:

$$\hat{\varepsilon}^{\mathbf{n},Z_2}_{\ell} \equiv \frac{1}{2}\left(\hat{\varepsilon}^{\mathbf{n}}_{\ell-3/2} + \hat{\varepsilon}^{\mathbf{n}}_{\ell+3/2}\right) = \frac{1}{4}\left(\hat{n}_{\ell-3} + 2\hat{n}_{\ell} + \hat{n}_{\ell+3}\right) \tag{11.1}$$

This choice preserves the symmetries $R_xT_x^3$ and site-reflection $R_xT_x^{-1}$, ensuring that the fields σ and $(-1)^{\ell}\partial_x\sigma$, respectively, do not appear in the field-theoretic description. Eliminating the sub-leading field $(-1)^{\ell}\partial_x\sigma$ is crucial due to its pronounced oscillatory effects, which stem from its scaling dimension being very closely sub-leading to that of ε in the $\{n_{3j}, n_{3j+1} = 0\}$ post-measurement setting. We provide evidence of numerical agreement with theoretically predicted scaling in Fig. 11.5.

11.4 Intermediate fixed point for tricritical Ising

As discussed in the main text, σ and ε in Eq. (10.5) are both relevant at the TCI point and thus compete nontrivially when the symmetry of the measurement outcome permits both terms. Here we explore a possible Rydberg array realization of the transition region where these terms compete to a draw—driving a flow to an intervening unstable fixed point. To this end, we study generalized post-measurement states $|\psi(\beta,\theta)\rangle = e^{-\frac{\beta}{2}\hat{\mathcal{H}}(\theta)}|\psi_c\rangle$ with $|\psi_c\rangle$ the TCI ground state and

$$\hat{\mathcal{H}}(\theta) = \sum_j \left[(-1)^j \sin(\theta) + \cos(\theta)\right]\hat{n}_j. \tag{11.2}$$

At $\theta = 0$, the measurement drives a flow to the ε-driven fixed point for any finite $\beta > 0$, since the translation symmetry exhibited by $\hat{\mathcal{H}}$ disallows σ from the action. At

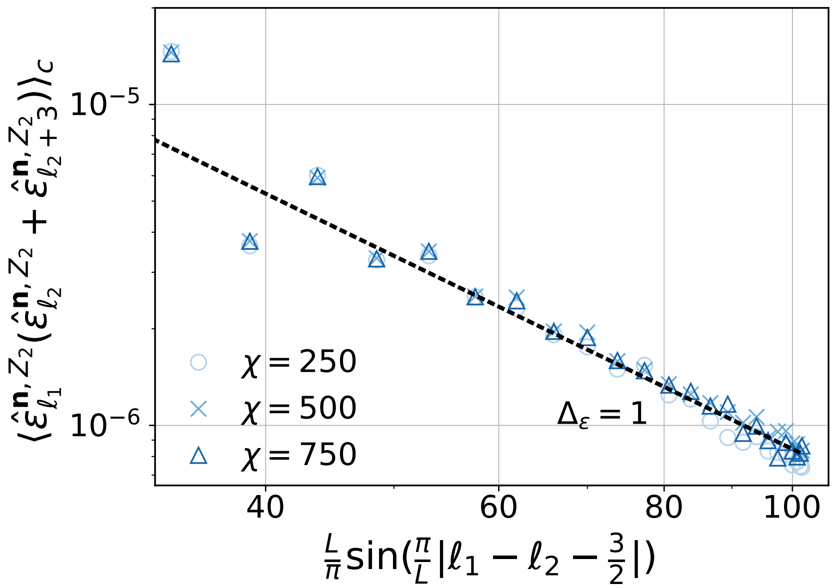

Figure 11.5: Two-unit-cell average of connected correlators of $\hat{\varepsilon}_\ell^{\mathbf{n},Z_2}$ after applying the $\mathbf{n} = \{n_{3j}, n_{3j+1} = 0\}$ measurement protocol on an $L = 180$ Ising critical Rydberg chain with PBC. The dashed line shows the boundary CFT prediction of $\Delta_\varepsilon = 1$.

$\theta = \pi/2$ by contrast, the measurement promotes CDW configurations by enhancing amplitudes with $n_{2j} = 0$ and $n_{2j+1} = 1$—naturally yielding the σ-driven fixed point. Sweeping θ between these extremes may then cross the intermediate fixed point at some β-dependent critical angle θ_c.

We confirm this scenario by analyzing the observable $\langle\hat{\sigma}_{1/2}\rangle \equiv \langle\psi(\beta,\theta)|\hat{\sigma}_{1/2}|\psi(\beta,\theta)\rangle$ across various β and θ assuming periodic boundary conditions (hence the results do not depend on the evaluation point). Figure 11.6(a) shows $\langle\hat{\sigma}_{1/2}\rangle$ versus θ at $\beta = 1$, which realizes an increasingly step-like curve as system size L increases. The inset zoom-in reveals a scale-invariant point at $\theta \approx 0.221\pi$ that we identify as θ_c. Figure 11.6(b) illustrates the β dependence of θ_c determined analogously.

Interestingly, as $\beta \to \infty$, θ_c appears to asymptotically approach $\pi/4$—which is intuitive from the following perspective. In the projective-measurement regime ($\beta = \infty$), $e^{-\frac{\beta}{2}\hat{\mathcal{H}}(\theta)}$ projects the TCI wavefunction onto a symmetric, trivial product state with all $n_j = 0$ for $0 \leq \theta < \pi/4$, but instead projects all sites onto a CDW product state for $\pi/4 < \theta \leq \pi/2$. A nontrivially entangled post-measurement state survives uniquely at $\theta = \pi/4$, which intervenes between the adjacent trivial and CDW states (just like the intermediate fixed point expected from the CFT). Examining Eq. (11.2) with $\theta = \pi/4$, one sees that this limit corresponds to our usual projective

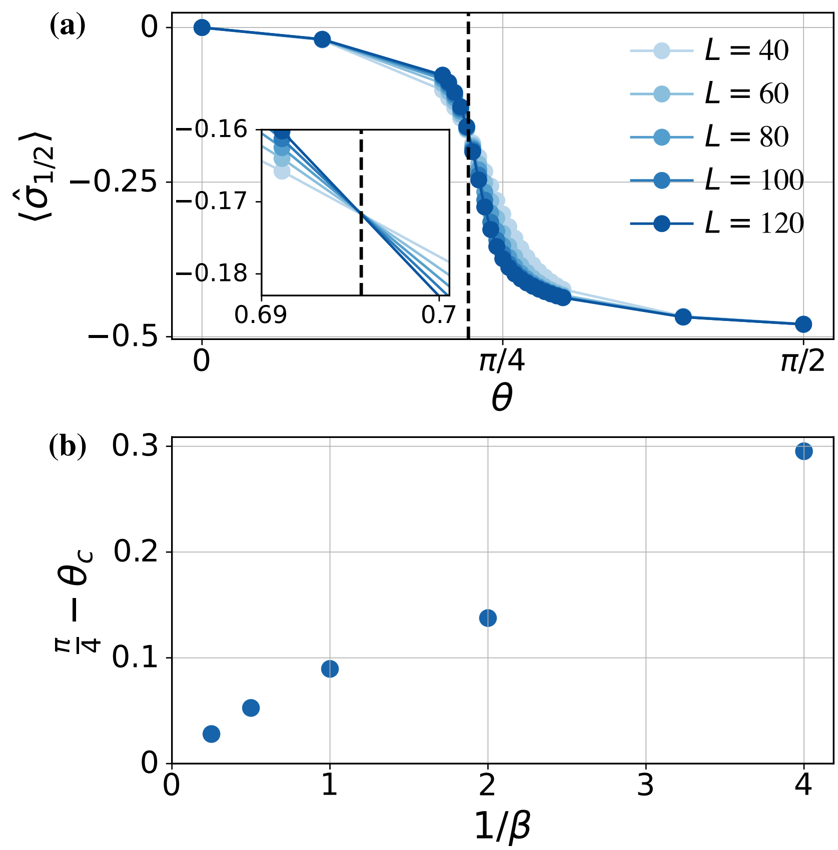

Figure 11.6: **Evidence for measurement-induced intermediate fixed point.** (a) Expectation value $\langle\hat{\sigma}_{1/2}\rangle$ versus θ at $\beta = 1$ for various system sizes. *Inset:* Zoom-in revealing a scale-invariant point at $\theta_c \approx 0.221\pi$ (vertical dashed line) indicating the unstable intermediate fixed point. (b) Extracted θ_c values at various β. Axes are chosen to highlight the apparent asymptotic trend, $\theta_c \to \pi/4$ as $\beta \to \infty$.

measurement protocol with $\mathbf{n} = \{n_{2j} = 0\}$—suggesting that this relatively high probability outcome may realize (or very nearly realize) the intermediate unstable fixed point with $\Delta_\sigma = 3/5$. We further test this possibility by computing the connected order-parameter correlators of the $\{n_{2j} = 0\}$ projective post-measurement state. Despite strong finite-size effects, the results in Fig. 11.7 decay much more slowly compared to either the σ- or ε-driven fixed points (cf. Fig. 11.2). Scaling with system size, however, indicates that the scaling dimension extracted from our simulations exceeds the expected $\Delta_\sigma = 3/5$ value as L increases—possibly stemming from imperfect tuning to the TCI point due to finite V_1.

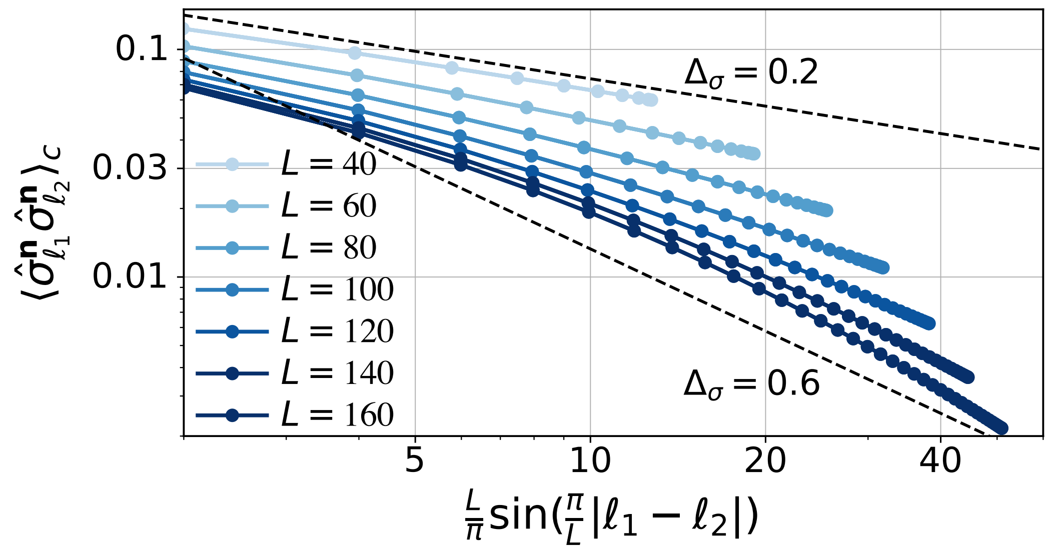

Figure 11.7: Connected order-parameter correlations after applying the projective-measurement protocol with $\mathbf{n} = \{n_{2j} = 0\}$ to TCI ground states on periodic chains.

11.5 Extrapolating from weak measurements to the projective limit

In the main text, our analytical treatment relies on the $L \to \infty$, weak-measurement limit $0 < \beta \ll 1$, whereas the experimentally relevant protocol corresponds to the projective limit $\beta \to \infty$ on a finite-sized system. To connect these two limits, here we study a family of post-measurement states obtained by applying the weak-measurement operator

$$\hat{M} \propto e^{-\frac{\beta}{2}\sum_j \hat{n}_{2j}} \tag{11.3}$$

that interpolates between the weak-measurement regime and the projector onto the outcome $\mathbf{n} = \{n_{2j} = 0\}$. For any $\beta > 0$, this protocol breaks the same lattice symmetries as the fully projective measurement, and therefore is expected to induce the same σ-dominated deformation. Figure 11.8 provides a representative numerical check of this expectation. As β is increased from the weak-measurement regime to large values, the connected two-point correlator evolves smoothly toward the fully projective result, and its long-distance behavior approaches the same field-theory-predicted post-measurement scaling. Note that, for very small β, this predicted scaling is not yet visible at the numerically accessible system size. Physically, one may view this as a finite-size crossover effect: when the perturbation is too weak, the available length scales are insufficient for the system to fully flow to the σ-induced fixed point. More quantitatively, a simple RG analysis characterizes the crossover regime to occur when $\beta L^{7/8} \sim$ constant [148].

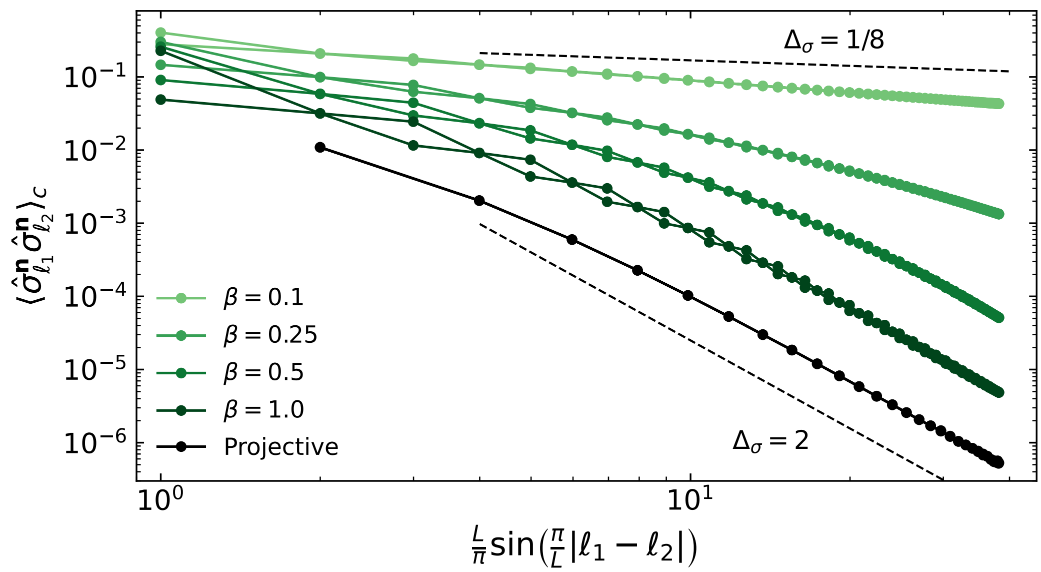

Figure 11.8: Comparison of two-point correlators of σ for an $L = 120$-site periodic Ising critical chain after applying weak measurements of $n = 0$ on every even site. Green curves correspond to finite measurement strengths β, while the black curve denotes the fully projective post-selected state with $\mathbf{n} = \{n_{2j} = 0\}$.

11.6 Boundary-CFT derivation of the modified σ scaling dimension

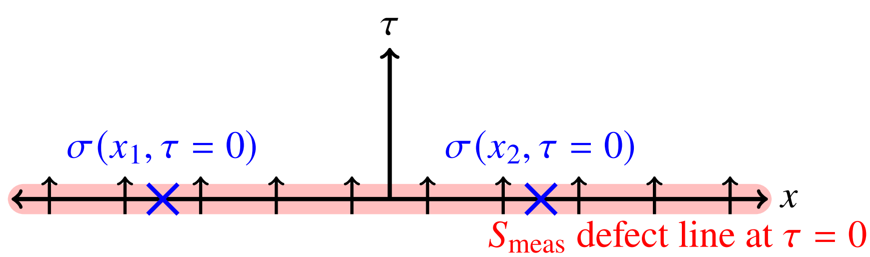

Figure 11.9: Schematic boundary-CFT description of the post-measurement fixed point. A relevant measurement defect at $\tau = 0$ flows to the fixed conformal boundary condition with all spins aligned. The two $\times$ symbols indicate σ insertions brought to the boundary, whose connected correlator realizes the defect scaling dimension.

The aim of this section is to demonstrate how one arrives at the modified $\Delta_\sigma = 2$ scaling dimension in the presence of a relevant measurement defect. As discussed in the main text, the weak measurement introduces a $\tau = 0$ 'defect-line' action S_{meas} that acts at all x, but only $\tau = 0$. For relevant deformations, S_{meas} will grow under RG flow and pin the spins along $\tau = 0$. The pinned spins cause a decoupling between $\tau = 0^+$ and $\tau = 0^-$. In this decoupled setting, we can consider correlators on only the upper half plane (UHP). Such correlators can be calculated using the "method of images" where n-point correlators on the UHP with uniform, conformally invariant boundary conditions are related to $2n$-point correlation functions on the full plane [13]. The case that we are interested in, corresponding to two-point correlator of σ in the UHP with spins pinned to + at $\tau = 0$ (see Fig. 11.9), has been calculated through this method of images by Ref. [103] as

$$\langle \sigma(x_1, \tau_1)\sigma(x_2, \tau_2)\rangle_c = (4\tau_1\tau_2)^{-1/8}\left[(\chi_{12} + \chi_{12}^{-1})^{1/2} - \sqrt{2}\right] \tag{11.4}$$

with

$$\chi_{12} = \left(1 + \frac{4\tau_1\tau_2}{r^2}\right), \qquad r^2 = (x_1 - x_2)^2 + (\tau_1 - \tau_2)^2. \tag{11.5}$$

Since we are interested in equal-time correlators at the boundary we consider $\tau_1 = \tau_2 \to \epsilon$ where ϵ is small. Expanding to lowest order in ϵ we recover

$$\langle \sigma(x_1)\sigma(x_2)\rangle_c \approx \frac{\epsilon^{15/4}}{2^{7/4}}|x_1 - x_2|^{-4} + O(\epsilon^{23/4}) \sim |x_1 - x_2|^{-2\Delta'_\sigma} \tag{11.6}$$

with $\Delta'_\sigma = 2$ being the modified scaling dimension. Note, while Eq. (11.6) shows the result of the two-point correlator corresponding to an infinite 1D line, one can perform a conformal transformation to recover the correlator along a finite circle geometry. Upon doing so, one recovers the chord distance dependence as shown in the numerical results of the manuscript.

11.7 Comparison with the boundary-transition framework

The Rydberg results are naturally read as a projective-measurement realization of the boundary-CFT phenomena developed in Part IV. Outcome sectors that seed one of the two CDW patterns behave like σ deformations and flow toward fixed-boundary behavior. Symmetry-preserving sectors remove the σ perturbation and expose either the Ising marginal ε deformation or, at the tricritical Ising point, a relevant ε deformation that drives a distinct boundary condition. The intermediate fixed point discussed above is the Rydberg-array counterpart of the partially polarized boundary fixed point in the tricritical Ising boundary theory.

Chapter 12

POST-SELECTION, RESTRICTED AVERAGES, AND EXPERIMENTAL IMPERFECTIONS

12.1 Why post-selection is the experimental bottleneck

Our approach to observing measurement-altered criticality requires repeatedly obtaining target states $\left|\psi_c^{\mathbf{n}}\right\rangle$ by post-selectively measuring a finite fraction $k \equiv K/L$ of sites. Although the success probability $P_{\mathbf{n}} \sim e^{-kL/\xi_{\mathbf{n}}}$ generically decays exponentially with L, we find that $k/\xi_{\mathbf{n}}$ can be quite small for certain outcomes—implying a relatively benign post-selection problem that can be further tamed by reducing the density of measured sites k.

Figure 12.1 presents $P_{\mathbf{n}}$ for various $\mathbf{n}$ sectors extracted from DMRG simulations of both critical Ising and TCI wavefunctions. Panel (a) reveals encouragingly high probabilities for the $\{n_{2j} = 0\}$ outcome even for fairly large systems of order 100 sites, which we attribute to several factors: Among protocols that measure every other site, the outcome $\{n_{2j} = 0\}$ maximizes the subspace dimension of the unmeasured sites (any site measured to have $n_j = 1$ pins the adjacent sites to $n_{j-1} = n_{j+1} = 0$ due to Rydberg blockade). The Fig. 12.1(a) inset moreover shows that the conditional probability for obtaining $n_{2k} = 0$ given prior measurements of $n_{2k-2} = n_{2k-4} = \cdots = n_0 = 0$ rapidly reaches near unity as k increases—consistent with the observed slow decay with L. Finally, the relatively high probability for $\{n_{2j} = 0\}$ is rather natural given that this outcome accommodates both CDW $(\ldots 010101 \ldots)$ and disordered $(\ldots 000000 \ldots)$ configurations that are associated with the adjacent gapped phases and thus heavily weighted in the critical wavefunction—particularly at the TCI point beyond which the transition becomes first order.

Probabilities for additional outcomes shown in panel (b) decay much faster with L. Nevertheless, even those outcomes remain feasible for chains with a few tens of sites. Note that degeneracy factors would enhance their success probability by a few times; e.g., obtaining $\{n_{3j} = 0\}$, $\{n_{3j+1} = 0\}$, or $\{n_{3j+2} = 0\}$ yield symmetry-equivalent measurement-altered states, at least on a periodic chain.

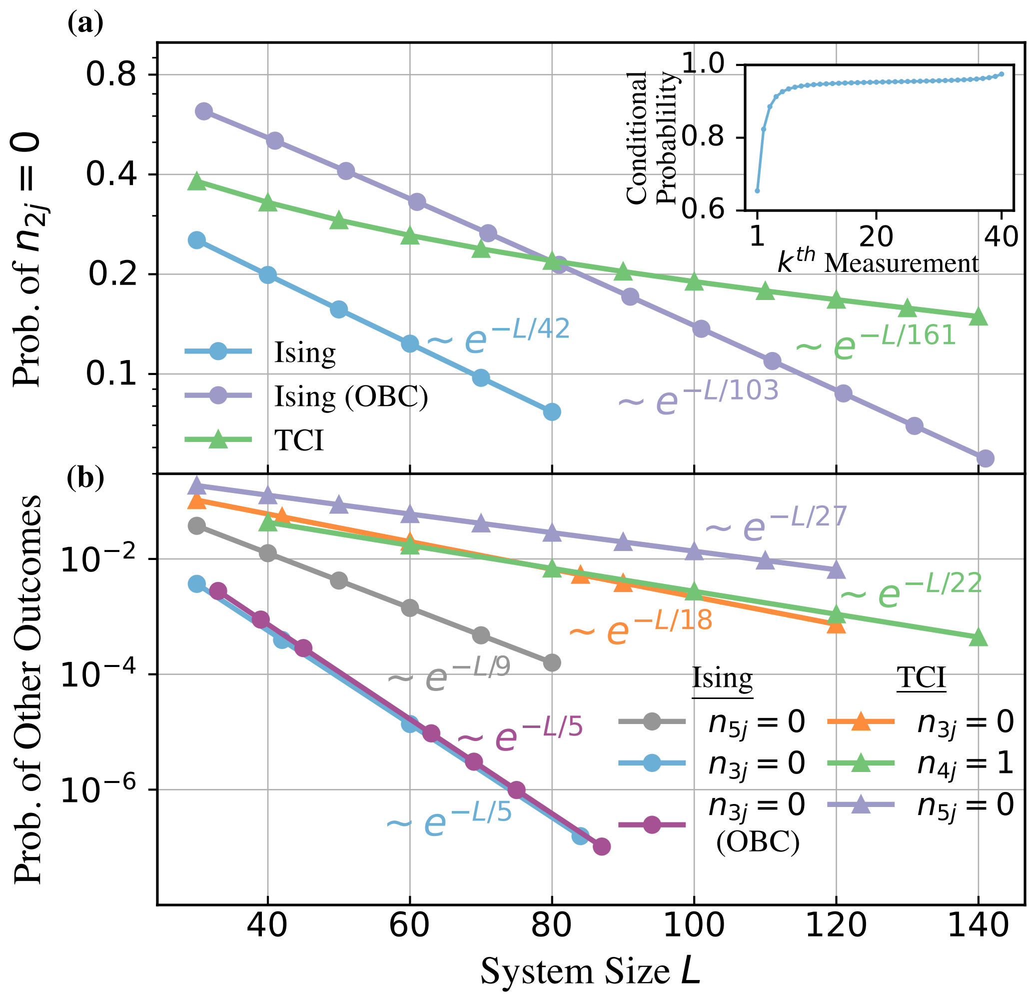

Figure 12.1: **Enhanced probability outcomes.** Post-selection probabilities for (a) $\{n_{2j} = 0\}$ and (b) other outcomes in critical Ising and TCI Rydberg chains. *Panel (a) inset:* conditional probability of measuring $n_{2k} = 0$, given prior $n_{2(j<k)} = 0$ outcomes for an $L = 80$ critical Ising chain with periodic boundaries.

12.2 Restricted averages from full-chain measurement data

In the pre-measurement quantum critical state $|\psi_c\rangle$, expectation values of generic operators $f(\{\hat{n}_j\})$ diagonal in the number basis can be recast as an unrestricted sum over eigenvalues $f(\{n_j\})$ weighted by the corresponding Born probabilities. To evaluate such quantities in practice, one would repeatedly prepare $|\psi_c\rangle$ and then projectively measure all sites simultaneously to sample the Born probability distribution.

Precisely the same data set encodes measurement-altered correlations. Indeed expectation values in the post-measurement state $\left|\psi_c^{\mathbf{n}}\right\rangle$ take an identical form but where the sum is restricted over occupation numbers compatible with a target post-selection sector $\mathbf{n}$. Additional overhead for probing measurement-altered criticality only comes from an increased number of experimental runs needed to access target sectors with sufficient statistics to back out measurement-altered correlations, whose amplitudes are typically reduced compared to their pre-measurement counterparts. While this increase is generically exponential in system size, we showed that relevant post-selection probabilities are enhanced in part by the Rydberg blockade. Another virtue of the Rydberg setup is that measurements in a *single basis* suffice to not only probe different CFT fields [recall Eqs. (10.2) and (10.3)], but also to access distinct measurement-induced modifications by simply tailoring the post-selected outcomes $\mathbf{n}$. This feature reflects the fact that the CDW ordered states break translation symmetry, rather than a purely on-site symmetry. The transverse-field Ising model with local spin-flip symmetry, for instance, would require measurements in two different bases [3, 58, 57].

Looking ahead, it will be important to characterize decoherence and finite-temperature effects occurring in the experimental setup (see Ref. [146] for an analysis of the effects of off-critical state preparation), as well as possible error correction and decoding protocols to further facilitate the demonstration of measurement-altered criticality. Additionally, Kibble-Zurek-like protocols that incorporate measurements, whether applied before, after, or continuously during the ramp, provide an interesting direction for future study and may offer alternative routes to extracting altered scaling dimensions. The Rydberg setup may further allow realizing predictions from Ref. [128] on the same CFTs studied here, regarding non-linear quantities in the density matrix; devising practical algorithms to that end poses another interesting future direction.

12.3 Possible experimental imperfections

The protocols described in this work provide a concrete route to observing measurement-altered criticality in Rydberg arrays assuming idealized preparation of the initial critical state. In practice, however, various experimental imperfections may hinder their realization. One possible source of imperfection is disorder arising from spatial variation in the local detuning and Rabi frequency. If sufficiently strong, such disorder sources could drive the system away from the clean Ising CFT fixed point and toward disorder-dominated behavior [149]. Recent works suggest that random positional deviations in the optical tweezers manifest in a more constrained fashion, leading to a 'psuedo-critical' disordered fixed point [150, 151]. A recent Rydberg-array experiment that spectroscopically revealed excitation spectra predicted by a clean Ising-critical theory, suggests that such disorder is not dominant, even in currently available experimental platforms [137].

Another possible imperfection is off-critical state preparation. Below we consider states prepared slightly away from the critical point and examine their pre-measurement and post-measurement correlations, as well as the modifications to the post-selection probabilities shown in Fig. 12.1 of the main text. Additional experimental imperfections include errors accumulated during the quasi-adiabatic ramp, decoherence due to coupling with the environment, and atom loss arising from finite Rydberg lifetime and imaging imperfections [134, 33, 135, 152]. A recent experiment treated such perturbations phenomenologically through an exponential envelope multiplying the critical power-law correlations to recover the pure Ising CFT order-parameter scaling dimension [135]. In what follows, we adopt a similar philosophy and model perturbations that move the system away from the pure critical ground state by phenomenologically introducing a finite temperature that modifies the form of the universal prediction.

Off-critical state preparation

To characterize the robustness of correlations to off-critical state preparation, we consider the Hamiltonian of main text Eq. (10.1) with periodic boundary conditions, $V_2 = 0$, and $\Delta = \Delta_c - \delta\Delta$, where $\delta\Delta$ parametrizes deviations from the critical detuning. Due to translation invariance, this imperfection can be treated as a bulk ε deformation to the Ising CFT which, from standard renormalization group scaling arguments, induces a correlation length that scales as $\xi \sim 1/|\delta\Delta|$ [153]. We expect the pre- and post-measurement correlation functions to be largely insensitive to such imperfections provided $\xi \gtrsim L$. Figure 12.2(a) shows the pre-measurement connected correlator of σ for several detuning shifts. We consider off-critical states only on the disordered side, $\delta\Delta > 0$, to avoid GHZ-like states that appear on finite sizes. To extract the correlation length of the off-critical states, we adopt the same phenomenological form as Ref. [135] and fit the corresponding correlators to

$$\langle\hat{\sigma}_{1/2}\hat{\sigma}_{d+1/2}\rangle_c \sim \sin(\frac{\pi d}{L})^{-1/4} e^{-\frac{L}{\pi\xi}\sin(\frac{\pi d}{L})}. \tag{12.1}$$

In Fig. 12.2(b), we show the connected σ correlators after modding out the fitted exponential, recovering the critical power-law scaling. At small detuning shifts, where the CFT description is expected to hold most closely, the correlation length is found (see Fig. 12.2(c)) to scale inversely proportional to $\delta\Delta$, as predicted. In particular, the scaling suggests that experiments such as Ref. [137] which prepare near-critical states with $L \approx 20, 30$ should realize only mild finite-ξ effects for off-critical thresholds of $\delta\Delta/\Omega \approx 0.04, 0.03$, respectively.

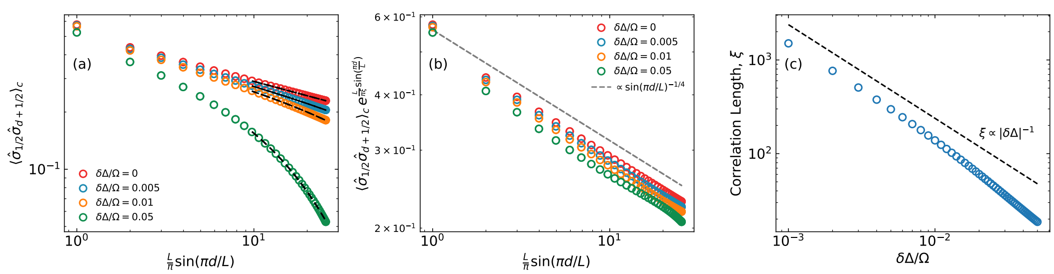

Figure 12.2: (a) Two-point correlator of σ for an $L = 80$ periodic Rydberg chain prepared at various distances from criticality. For $\delta\Delta/\Omega = 0.0,\ 0.005,\ 0.01$ and 0.05 the fits of Eq. (12.1) (dashed curves) yield $\xi \approx 530,\ 165,\ 93.1$ and 16.8, respectively. (b) Modified correlation functions after modding out the exponential prefactor. The black dashed line indicates expected scaling directly at the critical point. (c) Extracted correlation length ξ as a function of detuning distance from criticality $\delta\Delta/\Omega$; the dashed line indicates the expected scaling $\xi \propto |\delta\Delta|^{-1}$.

One may also consider how measurements alter states prepared at off-critical detunings. In Fig. 12.3(a), we show connected correlators of σ after post-selectively measuring $\mathbf{n} = \{n_{2j} = 0\}$ on states prepared at varying distances from criticality. In this case, the strong σ deformation dominates over the off-critical perturbation (for the system sizes simulated), and we see less dramatic deviation from the ideal scaling than in the measurement-free case. Additionally, Fig. 12.3(b) shows that the post-selection probability for this outcome decreases away from criticality, but remains appreciable for the detuning range considered. This decrease reflects the sign of $\delta\Delta$ that we assumed—which pushes the system into the trivial phase, where CDW order is suppressed.

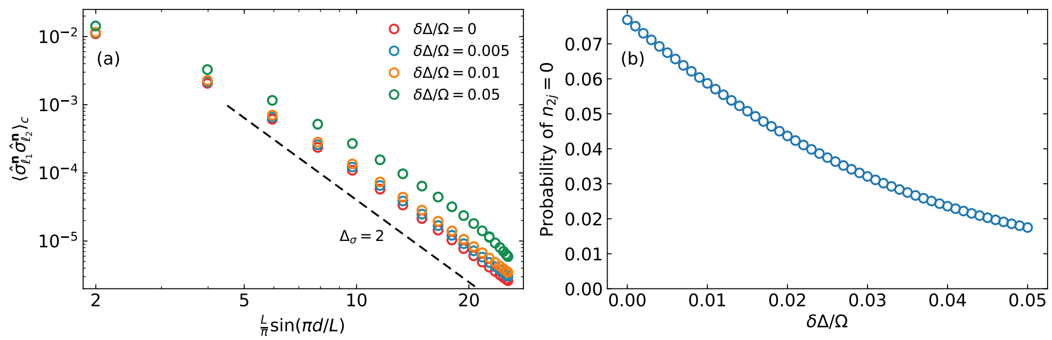

Figure 12.3: (a) Post-measurement $\mathbf{n} = \{n_{2j} = 0\}$ connected correlators of σ for an $L = 80$ periodic Rydberg chain prepared at various distances from criticality. The dashed line shows the predicted scaling at the σ-induced fixed point. (b) The post-selection probability of the $\mathbf{n} = \{n_{2j} = 0\}$ outcome as a function of distance from criticality.

Phenomenological finite-temperature effects in critical Rydberg arrays

Next we model imperfect critical ground-state preparation—i.e., setting $\delta\Delta = 0$ but allowing for diabatic errors, decoherence, or atom loss—by incorporating a phenomenological finite temperature. A virtue of this modeling choice is that conformal field theory can still be employed to make universal predictions. As a simple example, we consider a finite periodic critical chain of length L prepared at inverse temperature β_T. The corresponding Euclidean path integral is defined on a torus with spatial coordinate $x \in [0, L]$ and imaginary time $\tau \in [0, \beta_T]$. For the Ising CFT, the two-point correlator of the spin field σ on the torus is known to take the form [9]

$$\langle \sigma(u)\sigma(0)\rangle \propto \left|\frac{\partial_u \theta_1(0|\tau_{\text{tor}})}{\theta_1(u|\tau_{\text{tor}})}\right|^{\frac{1}{4}} \frac{\sum_{\nu=1}^{4} |\theta_\nu(\frac{u}{2}|\tau_{\text{tor}})|}{\sum_{\nu=2}^{4} |\theta_\nu(0|\tau_{\text{tor}})|}, \qquad \tau_{\text{tor}} = i\frac{v\beta_T}{L} \tag{12.2}$$

where v is the non-universal velocity, $u = \pi x/L$, and θ_ν denotes a Jacobi theta function.

In the low-temperature limit defined by $\beta \gg L/v$, one has $\tau_{\text{tor}} \to +i\infty$, and the expression above simplifies to

$$\langle \sigma(u)\sigma(0)\rangle \propto \sin(u)^{-1/4}\left(1 + 2e^{-\pi v\beta_T/(4L)}\sin^2(u/4) + O(e^{-\pi v\beta_T/(2L)})\right). \tag{12.3}$$

Here thermal corrections are exponentially suppressed, and the correlator retains the algebraic decay $\sin(u)^{-1/4}$. In the opposite limit where $\tau_{\text{tor}} \to 0$ ($\beta_T \ll L/v$), keeping x fixed, we can perform a modular transformation of the θ-functions. In

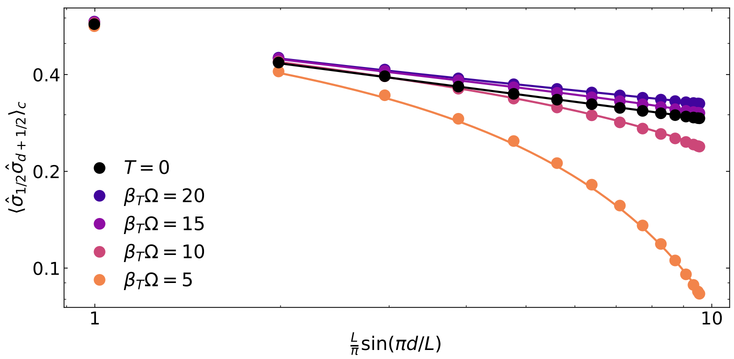

Figure 12.4: Connected σ-correlators for the Ising CFT at finite temperature versus chord distance, $\frac{L}{\pi}\sin(\pi d/L)$. Markers show data calculated from ED for an $L = 30$ periodic Rydberg chain prepared along the $V_2 = 0$ point of the Ising critical line at finite temperature $\beta_T\Omega$. Colored lines are fits of the form of Eq. (12.2). In total, for all the colored lines, only 2 fit parameters were used: the velocity $v = 0.915(2)$ and the overall prefactor $A = 0.7183(3)$.

this way, they can be rewritten as a function of the modular parameter $e^{-\pi L/(v\beta_T)}$, yielding the $\tau_{\text{tor}} \to 0$ expression

$$\langle\sigma(u)\sigma(0)\rangle \propto \left(\frac{\pi/(v\beta_T)}{\sinh\left(Lu/(v\beta_T)\right)}\right)^{1/4}. \tag{12.4}$$

Instead of exhibiting power law scaling with distance, as in the low-temperature limit, Eq. (12.4) crosses over to exponential decay and, in the limit of $Lu/(v\beta_T) \gg 1$, possesses a thermal correlation length, $\xi \propto v\beta_T$.

Figure 12.4 compares numerically calculated connected σ-correlators at several values of β_T with the finite-temperature CFT prediction of Eq. (12.2). The fact that all datasets are accurately captured, using only a single velocity and single overall prefactor for the CFT fits, indicates good agreement at a variety of temperatures, even at the experimentally relevant system size, $L = 30$. Additionally, at moderate temperatures, the correlators retain an almost pristine form over an extended window of chord distance before eventually crossing over to stronger thermal suppression, suggesting that states with sufficiently large β_T/L may still be treated with the $T = 0$, pristine power-law ansatz.

Equation (12.2) applies only to finite-temperature observables in the absence of measurements. Extending the analysis to measurement-altered critical states would require evaluating correlators on geometries with both finite imaginary-time extent and measurement-induced boundary conditions or defect insertions. We leave such calculations for future work.

12.4 Experimental workflow for detecting altered scaling dimensions

The practical workflow suggested by the preceding chapters is direct. First prepare a near-critical Rydberg chain at the Ising transition or TCI point. Second, measure either a prescribed subset of sites or all sites in the Rydberg occupation basis. Third, restrict the resulting measurement records to the outcome sector of interest, construct the post-measurement operators described in Chapter 10, and extract scaling dimensions using the finite-size forms summarized there. The success of this workflow depends on the enhanced probabilities of favorable sectors and on the fact that the same measurement basis gives access to several distinct post-measurement fixed points.

12.5 Why decoding becomes useful

The restricted-average viewpoint makes clear why the next part of the thesis turns to learning-based decoders. Even when the relevant outcome sectors are unusually probable, post-selection still discards data. Decoder methods aim to use the full measurement record more efficiently by learning conditional observables or nonlinear Born-weighted moments, thereby turning the experimental bottleneck of this chapter into the statistical-learning problem studied in Part VI.

Part VI

Post-Selection-Free Measurement-Altered Criticality

"Everything changes. Sometimes it's scary, sometimes it's a relief, and sometimes it means dinner's ready."

— Pascal, *Animal Crossing: New Horizons*

Chapter 13

NONLINEAR OBSERVABLES AND THE STATISTICAL LEARNING PROBLEM

The previous parts of the thesis repeatedly encountered the same practical obstacle. The clearest theoretical signatures of measurement-altered criticality often appear in a conditioned post-measurement ensemble: one fixes or reweights the measurement record, computes an expectation value in that conditioned state, and then diagnoses how the resulting object scales. Experiments, however, naturally produce unpost-selected snapshots. This chapter explains why nonlinear conditioned observables can nevertheless be estimated from those snapshots by turning the problem into supervised learning.

13.1 Why post-selection-free decoding is needed

Measurements provide a powerful new control knob for quantum many-body dynamics. While projective measurements on the entire system erases quantum coherence and yields a trivial post-measurement state, measurements on a partial system can reshape the state of the unmeasured degrees of freedom in a nontrivial manner, offering an avenue for engineering quantum states and observing novel phenomena. A prominent example is the measurement-induced phase transition (MIPT), which occurs in the competition between unitary dynamics and random measurements applied to a trivial initial state. On the other hand, starting with a nontrivial initial state, partial/weak measurements can also non-perturbatively alter quantum correlations and entanglement. Recently, there have been extensive studies on measurement-altered criticality (MAC) in 1D quantum systems where some correlation power-law exponents can be non-perturbatively modified by measurements. Existing probes of MAC typically focus on post-selecting certain measurement outcomes or computing nonlinear functionals of the density matrix, both of which appear to demand an exponential number of snapshot samples and form an obstacle for experimental observation of MAC.

To circumvent this issue, previous works have proposed to use methods like quantum-classical correlations or physics-informed decoders to postprocess the experimental snapshot data. However, these methods relies on additional information of the underlying physics or has limited applicability. In this part, we propose using statistical learning models as a general and efficient decoder to extract the critical exponents of MAC from snapshot data only. We prove that the number of snapshots required to get converged estimation only scales with the model capacity and the desired accuracy. In critical Ising chains, we demonstrate numerically that polynomial-capacity models accurately recover MAC exponents from unpostselected measurement records, making measurement-altered criticality experimentally accessible.

13.2 Measurement records, snapshots, and conditioned states

We consider a chain of L qubits initialized into a quantum critical ground state ρ_0 whose universal long-distance properties are governed by a conformal field theory. Weak measurements are implemented by pairwise entangling the critical spins with L ancillary qubits and then projectively measuring the ancillas with outcome $\mathbf{s} = \{s_1, s_2, \ldots, s_L\}$ arising with Born probability $p(\mathbf{s})$. Conditioned on $\mathbf{s}$, the system enters the non-unitarily modified state

$$\rho_{\mathbf{s}} = \frac{M_{\mathbf{s}}\rho_0 M_{\mathbf{s}}^\dagger}{p(\mathbf{s})}, \quad p(\mathbf{s}) = \mathrm{Tr}(M_{\mathbf{s}}\rho_0 M_{\mathbf{s}}^\dagger) \tag{13.1}$$

with $M_{\mathbf{s}}$ the Kraus operator that imposes the information gleaned from the measurement. In field-theory language, the weak measurement generates a sub-dimensional perturbation—acting at a single imaginary-time slice but all positions—that we crucially assume is relevant for generic outcomes $\mathbf{s}$. In the thermodynamic limit such measurements *non-perturbatively* alter the critical spin chain's properties for any typical $\mathbf{s}$ and any non-zero measurement strength.

Our goal is to harness data from either experiments or simulations to *efficiently* extract the resulting qualitative changes in measurement-altered observables judiciously averaged over $\mathbf{s}$. For any operator O, a standard linear average of conditional expectation values reproduces the expectation value of the pre-measured state,

$$\sum_{\mathbf{s}} p(\mathbf{s}) \langle O \rangle_{\mathbf{s}} = \langle O \rangle , \tag{13.2}$$

and thus discards the outcome-to-outcome variations that encode measurement-altered behavior of interest. Nontrivial measurement effects can, however, survive upon averaging higher moments and/or utilizing probabilities $w(\mathbf{s})$ that differ from the Born probabilities $p(\mathbf{s})$ when summing over measurement outcomes. We therefore focus on nonstandard averages of the form

$$A_q[O_1, O_2, \ldots] \equiv \sum_{\mathbf{s}} w(\mathbf{s}) \langle O_1 \rangle_{\mathbf{s}}^q \langle O_2 \rangle_{\mathbf{s}}^q \cdots \tag{13.3}$$

for some operators $O_{1,2,\ldots}$ and an exponent q specifying the moment of the expectation values. Such quantities are natural theoretical objects as they can be formulated in terms of replicated path integrals. From an experimental standpoint, however, their direct estimation appears extremely difficult at first glance. The conditional expectation values $\langle O\rangle_{\mathbf{s}}$ require many repetitions with the same measurement record $\mathbf{s}$, but typical records occur with Born probability that decays exponentially with system size L; moreover, nonstandard $w(\mathbf{s}) \neq p(\mathbf{s})$ probabilities introduce an additional re-weighting problem. Thus extracting A_q from raw data faces a severe post-selection bottleneck, motivating more efficient strategies that we turn to next.

Throughout this part we examine Z-basis weak measurements, encoded through $M_{\mathbf{s}} \propto \exp[\beta \sum_j s_j Z_j]$, that explicitly break the global $Z \to -Z$ symmetry preserved by H. In the thermodynamic limit, for any non-zero measurement strength β and for any outcome $\mathbf{s}$, such measurements *non-perturbatively* alter critical properties of the spin chain by modifying the underlying Ising conformal field theory with a relevant perturbation. We are interested in efficiently extracting the resulting qualitative changes to Z-basis observables, e.g., the spatial profile of the magnetization given some particular $\mathbf{s}$ and suitable averages of related quantities over measurement outcomes.

In experimental settings such as the Rydberg array platform, however, one does not have direct access to the post-measurement state $\rho_{\mathbf{s}}$ itself. Instead, in each run, both the system and the ancilla are measured projectively, yielding a snapshot pair $\{\mathbf{z}; \mathbf{s}\}$ where $\mathbf{z}$ ($\mathbf{s}$) is a list of ± 1 outcomes for the system (ancilla) spins. Throughout this work, we assume that both the system and ancilla are measured in the z basis. The experimentally available data therefore consist of i.i.d. samples drawn from a joint distribution $p(\mathbf{z}, \mathbf{s})$, rather than direct access to the conditioned quantum state.

A natural question is then how to extract the physics of measurement-altered phenomena directly from these snapshot data. More precisely, how much information about an observable O of the system is encoded in the ancilla outcome $\mathbf{s}$? For simplicity, we only consider the operators that are diagonal in the z basis and therefore can be written as a function of the system snapshot $O(\mathbf{z})$. This class already includes local magnetizations and z-basis correlations. We define the conditional expectation value $\langle O\rangle_{\mathbf{s}} \equiv \mathbb{E}[O(\mathbf{z})|\mathbf{s}]$ given a certain ancilla configuration $\mathbf{s}$, where $\mathbb{E}$ denotes the average over repeated experimental runs. This is exactly the expectation value in the post-measurement state associated with outcome $\mathbf{s}$.

A key observation is that a linear average of conditional expectation values is just the expectation value of the pre-measured state, and thus discards the outcome-to-outcome fluctuations that encode measurement-altered physics, $\sum_{\mathbf{s}} p(\mathbf{s}) \langle O \rangle_{\mathbf{s}} = \langle O \rangle_0$

$$\sum_{\mathbf{s}} p(\mathbf{s}) \langle O \rangle_{\mathbf{s}} = \mathbb{E}\left[\mathbb{E}[O|\mathbf{s}]\right] = \mathbb{E}[O] = \langle O \rangle \tag{13.4}$$

where $p(\mathbf{s})$ is the Born probability. This motivates us to study higher moments of the conditional expectation,

$$A_q[O] \equiv \sum_{\mathbf{s}} p(\mathbf{s}) \langle O \rangle_{\mathbf{s}}^q = \mathbb{E}[\mathbb{E}[O|\mathbf{s}]^q]. \tag{13.5}$$

These nonlinear quantities retain information about how strongly the ancilla record predicts the response of the system and are therefore natural probes of measurement-altered criticality. Specifically, the second moment $A_2[O]$ quantifies the fraction of fluctuations explainable by the best possible predictor (see Section 16).

13.3 Variational estimation of nonlinear observables

A natural strategy to estimate $A_2[O]$ is to estimate $\mathbb{E}[O|\mathbf{s}]$ separately for each ancilla outcome **s**and then average the square. Given N experimental snapshots $\{(\mathbf{z}_i, \mathbf{s}_i)\}_{i=1}^N$, let $N_{\mathbf{s}}$ be the number of snapshots in sector **s**. The direct estimator is written as,

$$\hat{A}_2^{\mathrm{dir}}[O] = \sum_{\mathbf{s}:N_{\mathbf{s}}>0} \frac{N_{\mathbf{s}}}{N} \left(\frac{\sum_{i:\mathbf{s}_i=\mathbf{s}} O(\mathbf{z}_i)}{N_{\mathbf{s}}} \right)^2. \tag{13.6}$$

Although asymptotically correct, i.e., $\hat{A}_2^{\mathrm{dir}}[O] \to A_2[O]$ at $N \to \infty$, this estimator is biased with finite samples. Section 16 shows that its expected error cannot be made small unless $N \gtrsim O(e^{\alpha L})$, where α is some non-zero constant. Therefore this strategy encounters the *post-selection problem*.

The key observation is that the same nonlinear quantity admits a post-selection-free variational representation,

$$A_2[O] = \sup_f \mathbb{E}\left[2O(\mathbf{z}) f(\mathbf{s}) - f(\mathbf{s})^2\right], \tag{13.7}$$

where O and f are assumed to be bounded. Conditioning on **s** gives $\mathbb{E}[2Of - f^2] = A_2[O] - \mathbb{E}_{\mathbf{s}}[(f(\mathbf{s}) - \langle O \rangle_{\mathbf{s}})^2]$, so the unrestricted optimizer is the Bayes predictor $f^\star(\mathbf{s}) = \langle O \rangle_{\mathbf{s}}$. Thus estimating $A_2[O]$ is equivalent to learning the conditional response $\mathbf{s} \mapsto \langle O \rangle_{\mathbf{s}}$ from raw snapshot pairs, without resolving each post-selected sector separately.

In practice, we choose a hypothesis class $\mathcal{F}$ and minimize the empirical square loss

$$\hat{\mathcal{L}}_N(f) = \frac{1}{N}\sum_{i=1}^{N}\left[O(\mathbf{z}_i) - f(\mathbf{s}_i)\right]^2 \tag{13.8}$$

over $f \in \mathcal{F}$. Denoting the learned decoder by $\hat{f} = \arg\min_{f\in\mathcal{F}} \hat{\mathcal{L}}_N(f)$, we estimate

$$\hat{A}_2[O] = \frac{1}{N}\sum_{i=1}^{N}\left[2O(\mathbf{z}_i)\hat{f}(\mathbf{s}_i) - \hat{f}(\mathbf{s}_i)^2\right]. \tag{13.9}$$

Standard statistical-learning theory then implies that the number of snapshots needed to estimate the best-in-class value to additive error ϵ scales as

$$N = O\left(\frac{\mathrm{Pdim}(\mathcal{F})\log \mathrm{Pdim}(\mathcal{F}) + \log(1/\delta)}{\epsilon^2}\right) \tag{13.10}$$

with probability at least $1-\delta$, where $\mathrm{Pdim}(\mathcal{F})$ is the pseudo-dimension of the decoder class which roughly counts the number of free parameters in $\mathcal{F}$; see Chapter 16. The sample cost is therefore controlled by the decoder capacity rather than by the exponentially many possible ancilla strings. For example, a linear decoder $f(\mathbf{s}) = c_0 + \sum_{j=1}^{L} c_j s_j$ where c's are parameters has $\mathrm{Pdim}(\mathcal{F}) = L + 1$ before imposing additional symmetries.

The interest of this approach is thus twofold. Experimentally, it provides a post-selection-free route to extracting measurement-altered physics directly from snapshot data. Conceptually, it turns the nonlinear quantity $A_2[O]$ into a controlled inference problem: machine learning enters not as a black-box add-on, but as a structured ansatz for the conditional response $\mathbf{s} \mapsto \langle O\rangle_{\mathbf{s}}$.

Once learned, the decoder can also be used as a plug-in representation of the conditioned ensemble. For example,

$$A_q[O] = \sum_{\mathbf{s}} p(\mathbf{s})\,\langle O\rangle_{\mathbf{s}}^q \approx \frac{1}{N}\sum_{i=1}^{N}\hat{f}(\mathbf{s}_i)^q, \tag{13.11}$$

and, given site-resolved decoders $f_j(\mathbf{s}) \approx \langle O_j\rangle_{\mathbf{s}}$ and $f_k(\mathbf{s}) \approx \langle O_k\rangle_{\mathbf{s}}$, disconnected conditioned correlators can be estimated as

$$A_q[O_j, O_k] \equiv \sum_{\mathbf{s}} p(\mathbf{s})\,\langle O_j\rangle_{\mathbf{s}}\langle O_k\rangle_{\mathbf{s}} \approx \frac{1}{N}\sum_{i=1}^{N} f_j(\mathbf{s}_i) f_k(\mathbf{s}_i). \tag{13.12}$$

In this sense, $f(\mathbf{s})$ is not merely an estimator for A_2; it is a compact, post-selection-free representation of the conditioned ensemble.

13.4 Conceptual summary

The essential point is that a measurement record $\mathbf{s}$ is not only an outcome to be post-selected; it is also a classical feature vector that carries information about the conditional state. The Bayes-optimal predictor of an observable $O(\mathbf{z})$ from $\mathbf{s}$ is precisely the conditioned expectation value $\langle O\rangle_{\mathbf{s}}$. Learning this predictor therefore gives a compact, post-selection-free representation of the conditioned ensemble. Nonlinear quantities such as $A_2[O]$ are then estimated from the learned response rather than from repeated occurrences of the same exponentially rare record.

Chapter 14

DECODER ARCHITECTURES FOR MEASUREMENT-ALTERED CRITICALITY

Chapter 13 reduced post-selection-free measurement-altered criticality to a regression problem: learn the conditional response $\mathbf{s} \mapsto \langle O \rangle_{\mathbf{s}}$ from snapshot pairs. This chapter describes the decoder classes used in the Ising-chain benchmarks. The main text emphasizes the physical inductive biases—translation covariance, Ising symmetry, bounded outputs, and multiscale receptive fields—while Chapter 17 records implementation and hyperparameter details.

14.1 Decoder task

For the numerical examples below, both ancilla and system spins are measured in the z basis. A training example is therefore a pair $(\mathbf{z}^{(a)}, \mathbf{s}^{(a)})$ drawn from the joint distribution generated by the weak-measurement protocol. For site-resolved magnetization, the decoder targets

$$f_j(\mathbf{s}) \approx \left\langle Z_j \right\rangle_{\mathbf{s}} = \mathbb{E}[z_j|\mathbf{s}], \tag{14.1}$$

where the right-hand side is exactly the conditional expectation in the post-measurement state. The same logic applies to local energy-density observables or disconnected conditioned correlations once suitable site-resolved decoders are trained.

14.2 Decoder families for one-point functions

We train three types of machine-learning decoders for the one-point function in the measurement basis, $f_j(\mathbf{s}) \approx \left\langle Z_j \right\rangle_{\mathbf{s}}$. The simplest models are linear and logistic regressions (see Fig. 14.1(a,b)),

$$f_j^{\mathrm{lin}}(\mathbf{s}) = c_0 + \sum_{k=1}^{L} c_k s_k, \; f_j^{\mathrm{log}}(\mathbf{s}) = \tanh\left(c_0 + \sum_{k=1}^{L} c_k s_k\right). \tag{14.2}$$

These models have $\mathrm{Pdim}(\mathcal{F}) = O(L)$ and thus require only $O(L)$ snapshots. For a periodic chain, this number can be further reduced to $O(1)$ due to translational symmetry. Specifically, the linear model is expected to capture the leading dependence on $\mathbf{s}$ in the perturbative regime: $\left\langle Z_j \right\rangle_{\mathbf{s}} \approx 2\beta \sum_k s_k \left\langle Z_j Z_k \right\rangle_0$ for $\beta \ll 1$. We also

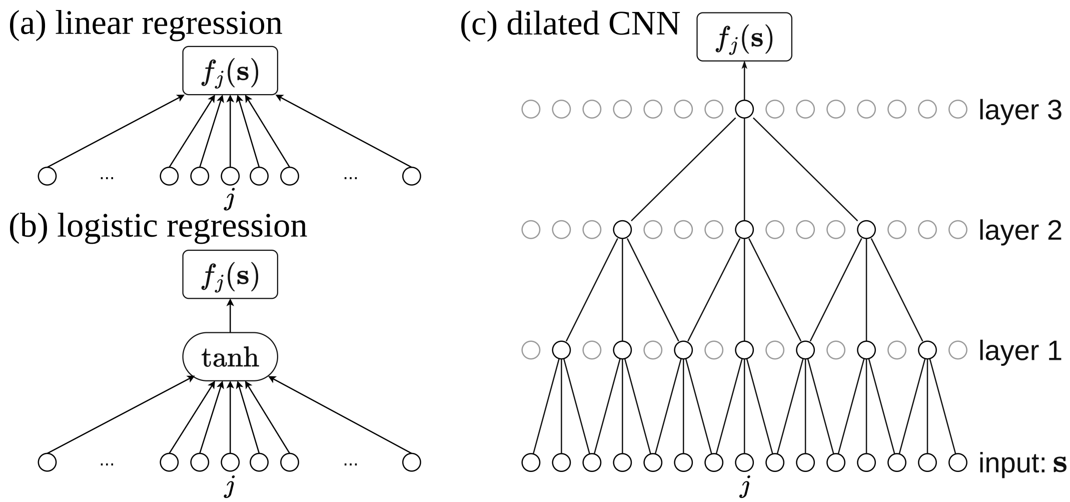

Figure 14.1: Schematic comparison of the three architectures used for one-point-function decoders. Circles denote site-resolved measurement outcomes or hidden neurons.

train a translation-covariant dilated convolutional neural network (CNN) [154]. The neural network consists of $O(\log(L))$ convolution layers with dilation $2^0, 2^1, 2^2 \ldots$, capturing multi-scale dependence on $\mathbf{s}$ (see Fig. 14.1(c)). This is reminiscent of coarse graining and multiscale entanglement renormalization ansatz [155]. The exact architecture is given in Chapter 17.

All these three models are trained using 80000 i.i.d. snapshot pairs sampled from the joint distribution $p(\mathbf{z}, \mathbf{s})$ and tested using another 20000 snapshots. Figure 14.2 shows that all three decoders learn the conditioned magnetization from snapshots, and the dilated CNN gives the smallest validation error. The top panel illustrates an example of random outcome and shows that ML-decoded one-point functions are close to the true $\langle Z_j \rangle_{\mathbf{s}}$ computed from MPS. The bottom panels show the validation mean-squared error of three models as a function of training-set size N, which saturates at $N \gtrsim O(10)$ for linear and logistic regression and decreases with N for CNN. This indicates that these decoders can reach high accuracy with far fewer than exponentially many samples. We leave the numerical details in Chapter 17.

14.3 Training data, validation, and error estimates

The training data consist of independent snapshot pairs, with held-out validation snapshots used to evaluate the variational objective and the corresponding estimate of $A_2[Z_j]$. For the MPS reference curves, measurement records are sampled independently from the Born distribution and the exact conditional means are

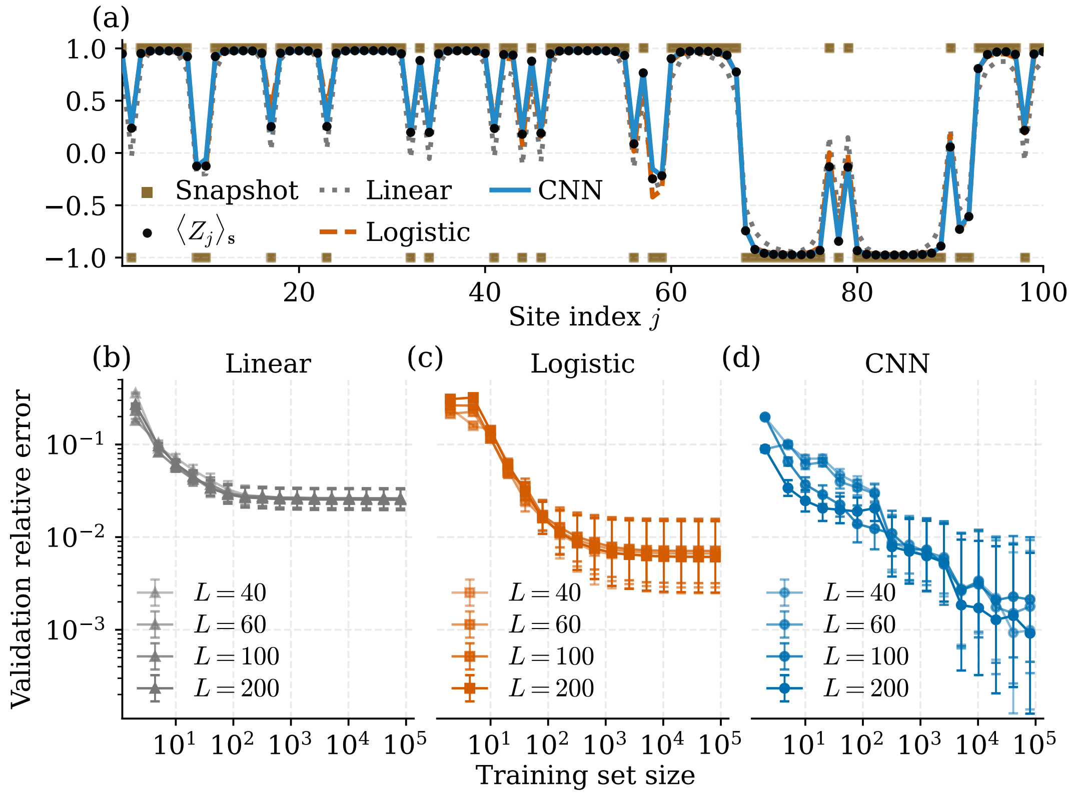

Figure 14.2: Decoder benchmark for $\langle Z_j \rangle_{\mathbf{s}}$. (a): a representative record for $L = 100$, $\beta = 0.5$, comparing exact MPS conditional means (black dots) with linear, logistic and dilated CNN predictions. (b,c,d): relative validation error versus training-set size for $\beta = 0.5$ and several L. Errors saturate with far fewer than exponentially many samples.

computed by tensor-network contraction. The detailed data sizes, translational pooling convention, symmetry augmentation, optimizer choices, and error-bar formulas are collected in Chapter 17.

14.4 Why multiscale architectures are natural near criticality

The critical input state has correlations on all length scales. In the weak-measurement regime, the leading perturbative decoder already sums over the two-point function $\langle Z_j Z_k \rangle_0$, so distant measurement outcomes can contribute algebraically rather than exponentially. Dilated convolutions provide a simple way to encode this multiscale dependence: each layer enlarges the receptive field by a factor set by the dilation, while translation covariance keeps the number of independent parameters under control. This is why the CNN architecture used here is a natural compromise between expressive nonlinear decoding and the restricted-capacity assumptions needed for the learning-theory bounds.

Chapter 15

LEARNING MEASUREMENT-ALTERED FIXED POINTS

The decoder is useful only if it recovers universal physics, not merely local correlations in a finite data set. This chapter uses the learned one-point-function decoders as plug-in estimators for nonlinear observables that diagnose measurement-altered fixed points. The first result is a finite-size scaling collapse of $A_2[Z]$ governed by the weak-measurement crossover length. The second and third results use higher moments and uniform-outcome averages to probe the locked-replica and zero-replica boundary/defect limits.

15.1 Born-weighted replica theory and finite-size scaling

The Born-weighted measurement ensemble admits a useful replica-field-theory description that controls both the weak-measurement scaling of $A_2[Z_j]$ and the long-distance moment correlations. For a fixed measurement record, define $\mathcal{Z}(\mathbf{s}) = \left\langle e^{2\beta \sum_j s_j Z_j} \right\rangle_0$. For integer R, the replicated weight $\mathcal{Z}(\mathbf{s})^R$ is represented by R copies of the Ising CFT coupled to the same record, with $S_{\mathbf{s},R} = \sum_a S^{(a)}_{\text{Ising}} - 2\beta \int dx\, s(x) \sum_a \sigma_a(x,0)$, where a is the replica index. The measurement outcome average is performed on the Boltzmann weight, $\sum_{\mathbf{s}} e^{-S_{\mathbf{s},R}}$, where $\sum_{\mathbf{s}} \equiv \prod_j \sum_{s_j=\pm 1}$. This gives the replicated action

$$S_R = \sum_{a=1}^{R} S^{(a)}_{\text{Ising}} - \int dx\, \log\left[2\cosh\left(2\beta \sum_{a=1}^{R} \sigma_a(x,0)\right)\right], \tag{15.1}$$

with physical continuation $R \to 1$ due to the Born weight.

Expanding Eq. (15.1) at small β generates a defect perturbation $-g \int dx \sum_{a<b} \sigma_a \sigma_b + \cdots$ with $g \propto \beta^2$. Since this operator has defect scaling dimension $2\Delta_\sigma$, the RG eigenvalue is $y_g = 1 - 2\Delta_\sigma$, implying a crossover length $\xi(\beta) \sim g^{-1/y_g} \sim \beta^{-2/(1-2\Delta_\sigma)}$. For the Ising CFT $\Delta_\sigma = 1/8$, this perturbation is relevant. Thus the unmeasured Ising fixed point controls length scales below $\xi(\beta)$, whereas the long-distance behavior is governed by a strong-coupling, locked-replica fixed point.

We now use this crossover scale to analyze $A_2[Z_j]$. Expanding the conditional mean gives

$$\left\langle Z_j \right\rangle_{\mathbf{s}} = \frac{\left\langle Z_j e^{2\beta \sum_k s_k Z_k} \right\rangle_0}{\left\langle e^{2\beta \sum_k s_k Z_k} \right\rangle_0} \xrightarrow{\beta \ll 1} 2\beta \sum_k s_k \left\langle Z_j Z_k \right\rangle_0 + O(\beta^3), \tag{15.2}$$

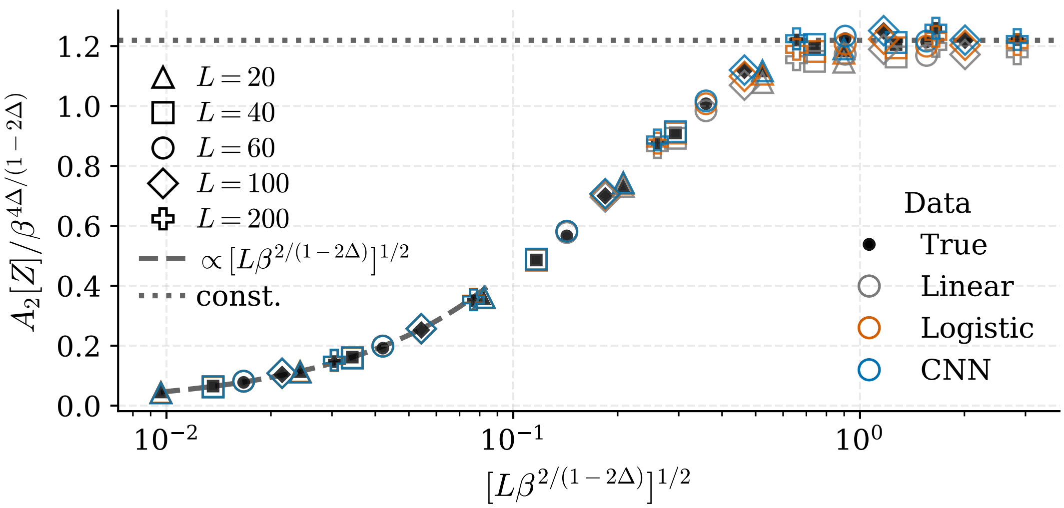

Figure 15.1: Finite-size scaling collapse of $A_2[Z]$ for $\beta \leq 0.3$. The MPS reference and the learned linear, logistic and CNN estimators follow Eq. 15.4.

and thus

$$A_2[Z_j] = \sum_{\mathbf{s}} p(\mathbf{s}) \left\langle Z_j \right\rangle_{\mathbf{s}}^2 = 4\beta^2 \sum_k \left\langle Z_j Z_k \right\rangle_0^2 + O(\beta^4). \tag{15.3}$$

Using $\left\langle Z_j Z_{j+r} \right\rangle_0 \sim r^{-2\Delta_\sigma}$ yields the perturbative scaling $A_2[Z_j] \sim \beta^2 L^{1-4\Delta_\sigma}$ for $L \ll \xi(\beta)$, while for $L \gtrsim \xi(\beta)$ the sum is cut off at $|j-k| \sim \xi(\beta)$. Matching the two regimes gives

$$A_2[Z_j] = \beta^{\frac{4\Delta_\sigma}{1-2\Delta_\sigma}} \, C\left(L\beta^{\frac{2}{1-2\Delta_\sigma}}\right), \tag{15.4}$$

with $C(x) \sim x^{1-4\Delta_\sigma} = x^{1/2}$ for $x \ll 1$ and $C(x) \to$ const. for $x \gtrsim 1$. Figure 15.1 shows that all the learned decoders reproduce this finite-size collapse without exponential sample complexity.

15.2 Locked-replica fixed point and moment correlations

We now turn to the long-distance regime $r \gg \xi(\beta)$, where the same measurement-induced perturbation flows to the locked-replica fixed point. The higher moments of disconnected conditioned two-point functions provide direct probes of this fixed point. We consider $A_q[Z_j, Z_k] \equiv \sum_{\mathbf{s}} p(\mathbf{s}) \left\langle Z_j \right\rangle_{\mathbf{s}}^q \langle Z_k \rangle_{\mathbf{s}}^q$, with integer $q > 0$. For integer $R \geq 2q$, the replicated representation uses two disjoint groups of replicas: q spin insertions at site j and another q spin insertions at site k. Equivalently,

$$\begin{gathered} \mathcal{G}_{q,R}(j,k) = \left\langle \prod_{a=1}^{q} \sigma_a(j,0) \prod_{a=q+1}^{2q} \sigma_a(k,0) \right\rangle_{S_R}, \\ A_q[Z_j, Z_k] = \lim_{R \to 1} \mathcal{G}_{q,R}(j,k). \end{gathered} \tag{15.5}$$

Replica permutation symmetry makes the particular choice of labels unimportant.

At the locked fixed point, the composite insertion in Eq. (15.5) behaves as the qth power of the single locked spin field. Hence odd q lies in the diagonal Ising-odd sector and has leading overlap with σ, while even q lies in the even sector and contains an identity component. The leading nontrivial even correction comes from the energy field ϵ. Therefore, on a ring with $d_L(r) = (L/\pi)\sin(\pi r/L)$,

$$A_q[Z_j, Z_{j+r}] \sim \begin{cases} b_q\, d_L(r)^{-1/4}, & q \text{ odd}, \\ c_q + a_q\, d_L(r)^{-2}, & q \text{ even}, \end{cases} \tag{15.6}$$

where a_q, b_q, c_q are nonuniversal. The powers follow from $\Delta_\sigma = 1/8$ and $\Delta_\epsilon = 1$ of the Ising CFT.

Figure 15.2 tests the odd/even structure predicted by the locked-replica picture. The odd moments with $q = 1, 3, 5, 7$ show a common algebraic decay consistent with the Ising-odd channel, $A_q[Z_j, Z_{j+r}] \sim d_L(r)^{-1/4}$. For even q, the most robust feature is the approach to a nonzero constant, as expected from the identity component in the even sector. The dashed curves show the theory-motivated form $c_q + a_q d_L(r)^{-2}$, corresponding to the energy-field correction in Eq. (15.6). Given the limited scaling window and the small size of the subleading term, however, we regard the exponent -2 fit as a consistency check rather than an independent numerical determination. Higher moments emphasize outcomes with larger conditional response, so the agreement between MPS and CNN data provides a nontrivial check that the learned decoder captures the measurement-conditioned order-parameter field, not only its local variance.

An alternative way to estimate the scaling is to use a mean-field approximation of the nonlinear observable. Denoting $m_i(s) = \langle Z_i \rangle_s$, for odd q we can write $m_i(s)^q = m_i(s) m_i(s)^{q-1}$, and replace the even factor by its typical value. Thus $m_i(s)^q$ flows to a linear order-parameter observable, $m_i(s)^q \sim A_q m_i(s)$, giving

$$\sum_s p_s\, m_i(s)^q m_j(s)^q \sim \sum_s p_s\, m_i(s) m_j(s) \sim \left\langle Z_i Z_j \right\rangle . \tag{15.7}$$

At the critical Ising point, this correlator decays as $|i-j|^{-1/4}$. For even q, instead, $m_i(s)^q$ is even under the Ising $\mathbb{Z}_2$ symmetry and its leading projection is the identity, so the averaged correlator approaches a constant. The first correction comes from the lowest nontrivial even operator, the Ising energy density ε, with scaling dimension 1. Therefore one expects

$$\sum_s p_s\, m_i(s)^q m_j(s)^q = C_0^{(q)} + C_1^{(q)} |i-j|^{-2} + \cdots , \qquad q \text{ even}, \tag{15.8}$$

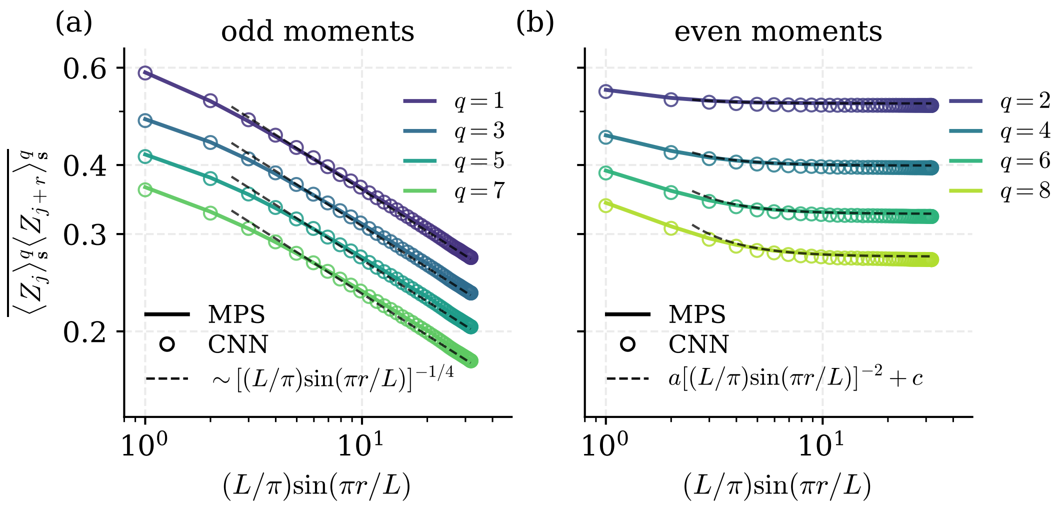

Figure 15.2: Higher moments of disconnected conditioned two-point functions for the critical Ising chain at $L = 100$ and $\beta = 0.5$. The horizontal axis is the chord distance $d_L(r)$. MPS data are computed from 10000 randomly sampled conditioned post-measurement states, while CNN data use the learned decoder $f_j(\mathbf{s}) \simeq \langle Z_j \rangle_{\mathbf{s}}$ as a plug-in estimate (80000 training trials). Odd moments are consistent with the locked-replica prediction $d_L(r)^{-1/4}$, whereas even moments approach a constant; the dashed curves show the theory-motivated correction $c_q + a_q d_L(r)^{-2}$.

where $C_0^{(q)}$ is the identity contribution and the $|i-j|^{-2}$ term is the leading connected correction.

15.3 Uniform-outcome correlations and the zero-replica limit

The Born-weighted observables above are tied to the physical $R \to 1$ continuation of the replicated measurement defect. We now consider a different ensemble of measurement records, the uniform-outcome average

$$B(j,k) \equiv \frac{1}{2^L} \sum_{\mathbf{s}} \langle Z_j \rangle_{\mathbf{s}} \langle Z_k \rangle_{\mathbf{s}} . \tag{15.9}$$

This quantity is not directly sampled by the Born distribution, but it is a useful theoretical companion because it removes the extra factor $p(\mathbf{s}) \propto \mathcal{Z}(\mathbf{s})$ that selected the $R \to 1$ limit. In practice, after training $f_j(\mathbf{s}) \simeq \langle Z_j \rangle_{\mathbf{s}}$, we estimate Eq. (15.9) by evaluating $f_j f_k$ on uniformly generated records.

Using $\mathcal{Z}_j(\mathbf{s}) = \langle Z_j e^{2\beta \sum_l s_l Z_l} \rangle_0$ and $\langle Z_j \rangle_{\mathbf{s}} = \mathcal{Z}_j(\mathbf{s})/\mathcal{Z}(\mathbf{s})$, the integer-replica object for $R \geq 2$ places the two insertions in different replicas. Analytic continuation gives

$$B(j,k) = \lim_{R \to 0} \langle \sigma_1(j,0) \sigma_2(k,0) \rangle_{S_R} , \tag{15.10}$$

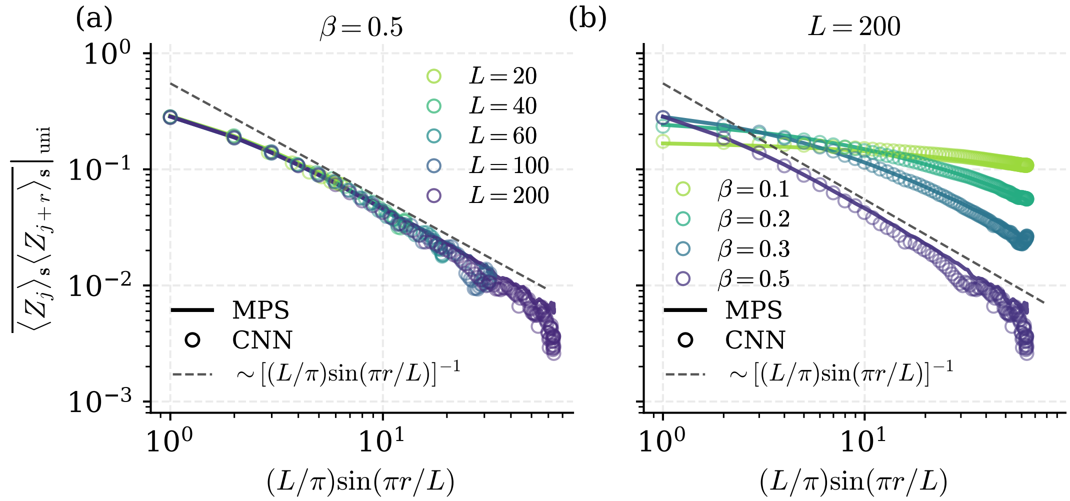

Figure 15.3: Uniform-outcome disconnected conditioned correlations, $B(j, j + r) = 2^{-L} \sum_{\mathbf{s}} \langle Z_j \rangle_{\mathbf{s}} \langle Z_{j+r} \rangle_{\mathbf{s}}$. The horizontal axis is the chord distance $d_L(r) = (L/\pi)\sin(\pi r/L)$. MPS data are computed directly from conditioned post-measurement states, while CNN data use the learned decoder $f_j(\mathbf{s}) \simeq \langle Z_j \rangle_{\mathbf{s}}$ evaluated on uniformly sampled records. (a) Fixed $\beta = 0.5$ with varying L. (b) Fixed $L = 200$ with varying measurement strength. The dashed line is a guide to the free-boundary form $d_L(r)^{-1}$ expected for the zero-replica random-field defect.

with the same replicated action S_R as in Eq. (15.1). The denominator becomes $\sum_{\mathbf{s}} \mathcal{Z}(\mathbf{s})^R \to \sum_{\mathbf{s}} 1 = 2^L$, so the uniform average is the zero-replica counterpart of the Born-weighted problem [156].

It is useful to note a similar object — the same-replica correlator $B_{\mathrm{sr}}(j, k) = 2^{-L} \sum_{\mathbf{s}} \langle Z_j Z_k \rangle_{\mathbf{s}} = \lim_{R\to 0} \langle \sigma_1(j, 0)\sigma_1(k, 0)\rangle_{S_R}$ which is addressed in the random-boundary-field CFT literature. In the Ising case, a quenched random magnetic field along a defect line is argued to flow to two decoupled half-plane Ising models with free boundary conditions [157, 158]. The boundary spin at the free Ising boundary has dimension $h_\sigma^{\mathrm{free}} = 1/2$ [159, 158], leading to the familiar free-boundary decay $B_{\mathrm{sr}}(j, j + r) \sim d_L(r)^{-1}$. The long-range contribution to the averaged correlator can be understood from the effective boundary problem produced by the replica construction. The replicas are glued together along the measured region, and this gluing line acts as a boundary defect. The large-distance decay is then controlled by the scaling dimension of the spin operator close to this defect. For the Ising chain, Ref. [160] argued that, for $R < 1$, this defect flows under RG to free boundary conditions. Thus, in the regime $R < 1$, the asymptotic behavior of the long-range contribution is expected to be controlled by the free-boundary fixed point. At this fixed point, the boundary spin has scaling dimension $h_\sigma^{\rm free} = \frac{1}{2}$, which gives

$$B(j, j+r) \sim \tilde{b}_0(\beta)\, d_L(r)^{-2h_\sigma^{\rm free}} = \tilde{b}_0(\beta)\, d_L(r)^{-1}. \tag{15.11}$$

This scaling form has been rigorously found in the replica geometry corresponding to $R = 1/2$ in Ref. [161]. Our numerical results suggest that the same free-boundary scaling also describes the continuation toward $R \to 0$, consistent with the RG picture of Ref. [160].

Our observable B is instead the inter-replica, disconnected counterpart. Thus the free-boundary result is not a direct theorem for Eq. (15.9). Nevertheless, the same zero-replica random-field flow suggests that its leading algebraic envelope should be governed by boundary spin insertions at the free-boundary fixed point. Provided the inter-replica amplitude generated by the random-field flow is nonzero, one expects

$$B(j, j+r) \sim \tilde{b}_0(\beta)\, d_L(r)^{-1}, \tag{15.12}$$

up to nonuniversal amplitudes and possible logarithmic corrections associated with random surface fields [157, 162]. We therefore regard Eq. (15.12) as a free-boundary-motivated prediction for the disconnected uniform average, to be checked numerically.

Figure 15.3 shows that B is consistent with this expectation. At fixed β, different system sizes follow a common $d_L(r)^{-1}$ trend over the accessible scaling window. At fixed L, the same trend appears for several measurement strengths, with stronger crossover effects at smaller β where the measurement length scale is larger. The dashed line is a guide with power-law exponent -1. The agreement between MPS and CNN estimates indicates that the learned one-point-function decoder captures conditioned magnetization correlations even under the non-Born reweighting of measurement records.

15.4 Decoder-assisted experiments and future directions

We have shown that nonlinear observables of measurement-conditioned states can be extracted from unpostselected snapshot pairs $(\mathbf{z}, \mathbf{s})$ by variational regression. For $A_2[O]$, the optimal decoder is the conditional mean $f^\star(\mathbf{s}) = \langle O \rangle_{\mathbf{s}}$, so the sample cost is controlled by decoder capacity rather than by the exponentially many measurement records. In the critical Ising chain, translation-covariant decoders reproduce the finite-size scaling of $A_2[Z_j]$ and, used as plug-in estimators, capture higher-moment and uniform-outcome correlations associated with the $R \to 1$ locked-replica and $R \to 0$ random-defect limits.

The method is naturally suited to Rydberg arrays. Recent work proposed realizing MAC by projectively measuring subsets of atoms in Rydberg chains tuned to Ising or tricritical-Ising criticality [6], and experiments have begun resolving finite-size CFT spectra and dynamical response in such systems [137]. There the measured atoms provide $\mathbf{s}$ and the remaining readout provides $\mathbf{z}$, allowing order-parameter or energy-density decoders to use all shots and complement outcome-selective postselection.

There are potential interesting future directions. One is to replace purely classical post-processing by circuit decoders: the record $\mathbf{s}$ could control a shallow feed-forward unitary $U_\theta(\mathbf{s})$ before the final readout, or parametrized quantum circuits could be used as structured hybrid representations of the map $\mathbf{s} \mapsto \langle O \rangle_{\mathbf{s}}$. Optimizing the same variational objective may then extend post-selection-free probes to non-diagonal observables, connected conditioned correlators, adaptive measurement bases, and other Rydberg-accessible universality classes.

Chapter 16

STATISTICAL LEARNING THEORY: SAMPLE-COMPLEXITY BOUNDS

In this section we give a self-contained derivation of the sample-complexity statements used in Sec. 13.3. We keep the notation of the previous chapter: a single experimental run gives a system snapshot and an ancilla record, $(z, s) \sim p(z, s)$, and $O(z)$ is a diagonal observable of the system. We assume throughout the proof that

$$|O(z)| \leq 1. \tag{16.1}$$

This is the natural normalization for Pauli observables and their products. If instead $|O(z)| \leq B$, all statements below remain true with only changes of numerical constants by powers of B.

For a fixed measurement record s, define

$$m_O(s) := \mathbb{E}[O(z) \mid s] = \langle O \rangle_s \,. \tag{16.2}$$

The nonlinear observable considered in the previous chapter is

$$A_2[O] := \mathbb{E}_s\, m_O(s)^2 = \sum_s p(s)\, \langle O \rangle_s^2 \,. \tag{16.3}$$

All expectations below are taken with respect to the joint snapshot distribution $p(z, s)$ unless otherwise stated.

16.1 What is measured by $A_2[O]$?

The linear average of the conditional expectation does not retain outcome-to-outcome information,

$$\mathbb{E}_s\, m_O(s) = \mathbb{E}[\mathbb{E}[O(z) \mid s]] = \mathbb{E}[O(z)] = \langle O \rangle \,. \tag{16.4}$$

The second moment $A_2[O]$, by contrast, measures the fluctuations of the Bayes-optimal prediction of $O(z)$ from the ancilla record. Indeed,

$$A_2[O] - \langle O \rangle^2 = \mathrm{Var}_s(m_O(s)) \,. \tag{16.5}$$

The normalized quantity

$$\eta^2(O \mid s) := \frac{\mathrm{Var}_s(m_O(s))}{\mathrm{Var}(O(z))} \tag{16.6}$$

is the correlation ratio of $O(z)$ on the record s. It is the fraction of fluctuations of $O(z)$ explained by the best possible, generally nonlinear, predictor built from s. The law of total variance gives

$$\mathrm{Var}(O(z)) = \mathbb{E}_s[\mathrm{Var}(O(z) \mid s)] + \mathrm{Var}_s(m_O(s)), \tag{16.7}$$

and therefore $0 \le \eta^2(O \mid s) \le 1$.

Relation to linear regression. If one restricts the predictor to be linear in the ancilla bits, the explained variance reduces to the usual linear-regression R^2. For instance, if the bits s_j are treated as real random variables and O is centered, the best linear predictor has explained fraction

$$R^2 = \rho^T C^{-1} \rho, \tag{16.8}$$

where $\rho_j = \mathrm{Corr}(O, s_j)$ and $C_{jk} = \mathrm{Corr}(s_j, s_k)$, assuming C is nonsingular. Since η^2 optimizes over all measurable functions of s, one always has $R^2 \le \eta^2(O \mid s)$. The learning approach in the previous chapter should be viewed as an interpolation between these two extremes: the decoder class $\mathcal{F}$ is richer than a fixed analytic ansatz, but much smaller than the set of all functions on 2^L ancilla records.

Asymmetry and information. The correlation ratio is directional: in general $\eta^2(O \mid s) \neq \eta^2(s \mid O)$. It asks specifically how well the system observable $O(z)$ can be inferred from the measurement record s. It also gives a useful information-theoretic diagnostic. If $\rho_m(O; s)$ denotes the Hirschfeld–Gebelein–Renyi maximal correlation between the scalar random variable $O(z)$ and the record s, then

$$\eta^2(O \mid s) \le \rho_m(O; s)^2. \tag{16.9}$$

Using the standard inequality $\rho_m(O; s)^2 \le 1 - e^{-2I(O;s)}$, one obtains the lower bound

$$I(O; s) \ge -\frac{1}{2} \log\left[1 - \eta^2(O \mid s)\right]. \tag{16.10}$$

Thus a nonzero correlation ratio implies nonzero mutual information between $O(z)$ and the record s. In the present work we use $A_2[O]$ and $\eta^2(O \mid s)$ not primarily as information measures, but as experimentally accessible probes of the measurement-conditioned ensemble.

16.2 Direct estimator and exponential cost

Suppose we collect N independent snapshots $\{(z_i, s_i)\}_{i=1}^{N}$. For a fixed ancilla record s, define

$$N_s := \sum_{i=1}^{N} \mathbf{1}\{s_i = s\}, \qquad\qquad S_s := \sum_{i:s_i=s} O(z_i), \tag{16.11}$$

$$\hat{m}_O(s) := \begin{cases} S_s/N_s, & N_s > 0, \\ 0, & N_s = 0. \end{cases} \tag{16.12}$$

The direct estimator in Sec. III is

$$\widehat{A}_2^{\mathrm{dir}}[O] = \sum_{s:N_s>0} \frac{N_s}{N} \hat{m}_O(s)^2 \tag{16.13}$$

$$= \frac{1}{N} \sum_s \frac{S_s^2}{N_s} \mathbf{1}\{N_s > 0\}. \tag{16.14}$$

This estimator explicitly estimates $\langle O \rangle_s$ separately in every post-selected sector that appears in the data.

Let

$$\sigma_O^2(s) := \mathrm{Var}(O(z) \mid s). \tag{16.15}$$

Conditioned on $N_s = n > 0$, the n samples entering $\hat{m}_O(s)$ are i.i.d. draws from $p(z \mid s)$. Hence

$$\mathbb{E}\big[\hat{m}_O(s)^2 \mid N_s = n\big] = m_O(s)^2 + \frac{\sigma_O^2(s)}{n}. \tag{16.16}$$

Using Eq. (16.16) inside Eq. (16.14) gives

$$\mathbb{E}\, \widehat{A}_2^{\mathrm{dir}}[O] = A_2[O] + \frac{1}{N} \sum_s \sigma_O^2(s) \Pr(N_s > 0). \tag{16.17}$$

Thus the direct estimator is upward biased at finite N, although it becomes unbiased as $N \to \infty$ at fixed L.

Since $|O| \le 1$ implies $\sigma_O^2(s) \le 1$, Eq. (16.17) gives the worst-case upper bound

$$0 \le \mathbb{E}\, \widehat{A}_2^{\mathrm{dir}}[O] - A_2[O] \tag{16.18}$$

$$\le \frac{1}{N} \sum_s \Pr(N_s > 0) = \frac{\mathbb{E} D_N}{N} \le \frac{|\mathcal{S}|}{N}, \tag{16.19}$$

where $\mathcal{S}$ is the support of the ancilla record and

$$D_N := \#\{s \in \mathcal{S} : N_s > 0\} \tag{16.20}$$

is the number of distinct records observed in the sample. For an L-qubit ancilla, $|\mathcal{S}| \le 2^L$. Thus making the bias term smaller than an additive accuracy ϵ requires $N \gtrsim 2^L/\epsilon$ in the worst case.

The exponential obstruction is the post-selection bias, not an anomalously large fluctuation around the mean. To see this, write

$$\widehat{A}_2^{\mathrm{dir}}[O] = \frac{1}{N}\sum_s a(N_s, S_s), \tag{16.21}$$

$$a(n,u) := \begin{cases} u^2/n, & n > 0, \\ 0, & n = 0. \end{cases} \tag{16.22}$$

Changing one snapshot affects at most two ancilla sectors. For $|O| \le 1$, one has $|a(n,u) - a(n',u')| \le 8$ for each affected sector under a single sample replacement, and therefore

$$\left|\widehat{A}_2^{\mathrm{dir}}(S) - \widehat{A}_2^{\mathrm{dir}}(S^{(i)})\right| \le \frac{16}{N}. \tag{16.23}$$

McDiarmid's inequality then gives

$$\Pr\!\left(\left|\widehat{A}_2^{\mathrm{dir}}[O] - \mathbb{E}\,\widehat{A}_2^{\mathrm{dir}}[O]\right| \ge \epsilon\right) \le 2\exp\!\left(-\frac{N\epsilon^2}{128}\right). \tag{16.24}$$

Equivalently, with probability at least $1-\delta$,

$$\left|\widehat{A}_2^{\mathrm{dir}}[O] - A_2[O]\right| \le \frac{1}{N}\sum_s \sigma_O^2(s)\Pr(N_s > 0) \tag{16.25}$$

$$+ \sqrt{\frac{128\log(2/\delta)}{N}}. \tag{16.26}$$

The first term is the post-selection bias; the second is the ordinary concentration term.

One can also prove a lower bound showing that the exponential scaling is not just an artifact of Eq. (16.19). Assume that the conditional variance is uniformly nonzero,

$$\sigma_O^2(s) \ge v > 0 \qquad \text{for every } s \in \mathcal{S}. \tag{16.27}$$

Then Eq. (16.17) implies

$$\mathbb{E}\,\widehat{A}_2^{\mathrm{dir}}[O] - A_2[O] \ge \frac{v}{N}\mathbb{E}D_N. \tag{16.28}$$

Furthermore,

$$D_N \sum_s N_s^2 \ge \left(\sum_s N_s\right)^2 = N^2. \tag{16.29}$$

Using Jensen's inequality and

$$\mathbb{E}\sum_s N_s^2 = N + N(N-1)\sum_s p(s)^2, \tag{16.30}$$

one obtains

$$\mathbb{E}D_N \geq \frac{N}{1+(N-1)\sum_s p(s)^2}. \tag{16.31}$$

Therefore

$$\mathbb{E}\left|\widehat{A}_2^{\mathrm{dir}}[O] - A_2[O]\right| \geq \frac{v}{1+(N-1)\sum_s p(s)^2}. \tag{16.32}$$

Let

$$H_2(s) := -\log\sum_s p(s)^2 \tag{16.33}$$

be the second Renyi entropy of the ancilla record. A necessary condition for the expected error of the direct estimator to be at most $\epsilon < v$ is

$$N \geq 1 + \left(\frac{v}{\epsilon} - 1\right) e^{H_2(s)}. \tag{16.34}$$

Since $\sum_s p(s)^2 \leq p_{\max}$, where $p_{\max} := \max_s p(s)$, the weaker but simpler bound

$$N \geq 1 + \left(\frac{v}{\epsilon} - 1\right)\frac{1}{p_{\max}} \tag{16.35}$$

also follows. In the measurement protocols studied in the previous chapter, the measurement record has exponentially large effective support, so $H_2(s) = \alpha L + o(L)$ for some $\alpha > 0$. Equation (16.34) then gives $N \geq \Omega(e^{\alpha L})$ for the direct post-selection estimator.

16.3 Variational representation of $A_2[O]$

The post-selection-free approach starts from the identity

$$A_2[O] = \sup_f J(f), \tag{16.36}$$

$$J(f) := \mathbb{E}\left[2O(z)f(s) - f(s)^2\right], \tag{16.37}$$

where the supremum is over bounded measurable functions of the ancilla record. Conditioning on s gives

$$J(f) = \mathbb{E}_s\left[2m_O(s)f(s) - f(s)^2\right] \tag{16.38}$$

$$= \mathbb{E}_s\, m_O(s)^2 - \mathbb{E}_s\left[f(s) - m_O(s)\right]^2. \tag{16.39}$$

Thus the optimal decoder is the Bayes predictor

$$f^\star(s) = m_O(s) = \langle O\rangle_s, \tag{16.40}$$

and the maximum value is $A_2[O]$.

Equivalently,

$$2O(z)f(s) - f(s)^2 = O(z)^2 - [O(z) - f(s)]^2 . \tag{16.41}$$

Therefore maximizing $J(f)$ is the same as minimizing the mean-squared prediction loss

$$L(f) := \mathbb{E}[O(z) - f(s)]^2 . \tag{16.42}$$

This is the precise sense in which the nonlinear observable $A_2[O]$ is converted into a supervised-learning problem.

In practice the decoder is restricted to a hypothesis class $\mathcal{F}$ of functions $f : \mathcal{S} \to [-1, 1]$. Define the best-in-class value

$$J^\star_{\mathcal{F}} := \sup_{f\in\mathcal{F}} J(f) \tag{16.43}$$

$$= A_2[O] - \inf_{f\in\mathcal{F}} \mathbb{E}_s[f(s) - \langle O\rangle_s]^2 . \tag{16.44}$$

The second term is the approximation error of the decoder class. Thus the learning method is not a no-free-lunch procedure: if the map $s \mapsto \langle O\rangle_s$ is completely unstructured, a small decoder class will not approximate it. The gain comes from using the physical structure of measurement-conditioned states, encoded either explicitly or through the inductive bias of the model, to choose a class $\mathcal{F}$ whose capacity is much smaller than 2^L.

16.4 Uniform convergence and sample complexity

Given data $\{(z_i, s_i)\}_{i=1}^N$, define the empirical objective

$$\widehat{J}_N(f) := \frac{1}{N}\sum_{i=1}^{N}\left[2O(z_i)f(s_i) - f(s_i)^2\right] \tag{16.45}$$

and choose

$$\hat{f}_N \in \arg\max_{f\in\mathcal{F}} \widehat{J}_N(f). \tag{16.46}$$

Equivalently, $\hat{f}_N$ minimizes the empirical mean-squared loss

$$\widehat{L}_N(f) := \frac{1}{N}\sum_{i=1}^{N}[O(z_i) - f(s_i)]^2 . \tag{16.47}$$

The estimator reported in Sec. III is

$$\widehat{A}_{2,\mathcal{F}}[O] := \widehat{J}_N(\hat{f}_N) \tag{16.48}$$

$$= \frac{1}{N}\sum_{i=1}^{N}\left[2O(z_i)\hat{f}_N(s_i) - \hat{f}_N(s_i)^2\right]. \tag{16.49}$$

Let

$$\mathcal{H}_{\mathcal{F}} := \left\{h_f(z,s) = 2O(z)f(s) - f(s)^2 : f \in \mathcal{F}\right\} \tag{16.50}$$

be the induced objective-function class, and let

$$d_{\mathrm{obj}} := \mathrm{Pdim}(\mathcal{H}_{\mathcal{F}}) \tag{16.51}$$

be its pseudo-dimension. The pseudo-dimension is the real-valued analogue of VC dimension: it is the largest number of inputs that can be threshold-shattered by functions in the class. For the decoder classes used in the previous chapters, d_{obj} is of the same order as the pseudo-dimension of the decoder class itself. In scaling estimates we therefore write $d_{\mathrm{obj}} = \Theta(\mathrm{Pdim}(\mathcal{F}))$.

Because $|O| \le 1$ and $|f| \le 1$, every h_f lies in an interval of length at most 4. Standard uniform-convergence bounds for bounded real-valued function classes imply that, for a universal constant C, with probability at least $1-\delta$,

$$\Delta_N := \sup_{f\in\mathcal{F}}\left|\widehat{J}_N(f) - J(f)\right| \tag{16.52}$$

$$\le C\left[\frac{d_{\mathrm{obj}}\log(eN/d_{\mathrm{obj}}) + \log(1/\delta)}{N}\right]^{1/2}, \tag{16.53}$$

for $N \ge d_{\mathrm{obj}}$.

Let $f^\star_{\mathcal{F}} \in \arg\max_{f\in\mathcal{F}} J(f)$. On the event where Eq. (16.53) holds,

$$J(\hat{f}_N) \ge \widehat{J}_N(\hat{f}_N) - \Delta_N \tag{16.54}$$

$$\ge \widehat{J}_N(f^\star_{\mathcal{F}}) - \Delta_N \tag{16.55}$$

$$\ge J(f^\star_{\mathcal{F}}) - 2\Delta_N. \tag{16.56}$$

Thus the learned decoder has excess objective value bounded by

$$0 \le J^\star_{\mathcal{F}} - J(\hat{f}_N) \le 2\Delta_N. \tag{16.57}$$

The empirical optimum itself is also close to the best-in-class value:

$$\widehat{J}_N(\hat{f}_N) \ge \widehat{J}_N(f^\star_{\mathcal{F}}) \ge J^\star_{\mathcal{F}} - \Delta_N, \tag{16.58}$$

$$\widehat{J}_N(\hat{f}_N) \le J(\hat{f}_N) + \Delta_N \le J^\star_{\mathcal{F}} + \Delta_N. \tag{16.59}$$

Therefore

$$\left|\widehat{A}_{2,\mathcal{F}}[O] - J^{\star}_{\mathcal{F}}\right| \le \Delta_N. \tag{16.60}$$

Combining Eqs. (16.44) and (16.60) yields the decomposition

$$\left|\widehat{A}_{2,\mathcal{F}}[O] - A_2[O]\right| \le \Delta_N + \inf_{f\in\mathcal{F}} \mathbb{E}_s[f(s) - \langle O\rangle_s]^2 . \tag{16.61}$$

The first term is the statistical estimation error, and the second term is the approximation error.

Solving Eq. (16.53) for $\Delta_N \le \epsilon$ gives

$$N = O\left(\frac{\mathrm{Pdim}(\mathcal{F}) \log \mathrm{Pdim}(\mathcal{F}) + \log(1/\delta)}{\epsilon^2}\right), \tag{16.62}$$

up to universal constants and mild logarithmic factors. This is the sample-complexity estimate quoted in Sec. III. The number of snapshots is controlled by the decoder capacity rather than by the number of possible ancilla strings.

Examples of capacities. For the linear decoder

$$f(s) = c_0 + \sum_{j=1}^{L} c_j s_j, \tag{16.63}$$

the pseudo-dimension is $L + 1$ before imposing additional symmetries or bounds. If a translation-covariant ansatz with a fixed number of shared parameters is used, the parameter count, and hence the capacity entering the bound, can be reduced accordingly. For neural-network decoders, standard pseudo-dimension bounds scale polynomially in the number of trainable weights; a common bound is of the form

$$\mathrm{Pdim}(\mathcal{F}) = O(W\ell \log W), \tag{16.64}$$

where W is the number of trainable parameters and ℓ is the number of layers. Thus a decoder whose number of parameters grows polynomially with system size has polynomial sample complexity. Conversely, if $\mathcal{F}$ is taken to be the set of all functions on L ancilla bits, then $\mathrm{Pdim}(\mathcal{F}) = 2^L$, and Eq. (16.62) reproduces the exponential post-selection scaling.

Training and evaluation on the same data. Equation (16.60) is a uniform-convergence result, so it allows the same data to be used both to train $\hat{f}_N$ and to evaluate $\widehat{J}_N(\hat{f}_N)$. A more conservative experimental protocol is to train $\hat{f}_N$ on one set of snapshots and evaluate Eq. (16.49) on an independent validation set. Conditioned on the trained decoder, the validation estimate is an ordinary average of bounded random variables and is therefore controlled directly by Hoeffding's inequality. The scaling with the capacity of $\mathcal{F}$ enters only through the training step.

16.5 Plug-in estimates for other conditioned observables

The proof above is stated for $A_2[O]$ because the square loss gives the exact variational identity Eq. (16.37). Once a decoder $f(s) \approx m_O(s)$ has been learned, however, the same function can be used as a representation of the conditioned ensemble.

Let

$$e_O(f) := \mathbb{E}_s\left[f(s) - m_O(s)\right]^2 \tag{16.65}$$

be the mean-squared decoder error. If $|f| \leq 1$ and $|m_O| \leq 1$, then for integer $q \geq 1$,

$$|f(s)^q - m_O(s)^q| \leq q|f(s) - m_O(s)|. \tag{16.66}$$

Therefore

$$\left|\mathbb{E}_s f(s)^q - A_q[O]\right| \leq q\sqrt{e_O(f)}. \tag{16.67}$$

The same bound applies to absolute moments $\mathbb{E}_s|m_O(s)|^q$ for $q \geq 1$ after replacing f^q by $|f|^q$.

For two observables $O_a(z)$ and $O_b(z)$, define $m_a(s) = \langle O_a\rangle_s$ and $m_b(s) = \langle O_b\rangle_s$. Suppose f_a and f_b are bounded decoders with errors e_a and e_b in the sense of Eq. (16.65). Then the disconnected conditioned correlator obeys

$$|\mathbb{E}_s f_a(s) f_b(s) - \mathbb{E}_s m_a(s) m_b(s)| \tag{16.68}$$

$$\leq \sqrt{e_a} + \sqrt{e_b}. \tag{16.69}$$

This justifies the plug-in estimates used in the previous chapters, such as

$$\sum_s p(s)\,\langle O_a\rangle_s\,\langle O_b\rangle_s \approx \frac{1}{N}\sum_{i=1}^{N} f_a(s_i) f_b(s_i), \tag{16.70}$$

with the usual additional sampling error if the right-hand side is evaluated on a finite validation set.

16.6 Connected conditional correlators

The same variational idea can be applied to connected conditional correlators. Let $O_a(z)$ and $O_b(z)$ be two bounded observables and define

$$C_{ab}(s) := \langle O_a O_b\rangle_s - \langle O_a\rangle_s\,\langle O_b\rangle_s\,, \tag{16.71}$$

$$B_{ab} := \mathbb{E}_s\, C_{ab}(s)^2. \tag{16.72}$$

If the one-point conditional means $m_a(s) = \langle O_a \rangle_s$ and $m_b(s) = \langle O_b \rangle_s$ were known exactly, then the residual variable

$$R_{ab}(z,s) := [O_a(z) - m_a(s)]\,[O_b(z) - m_b(s)] \tag{16.73}$$

satisfies

$$\mathbb{E}[R_{ab}(z,s) \mid s] = C_{ab}(s). \tag{16.74}$$

Hence

$$B_{ab} = \sup_g \mathbb{E}\left[2R_{ab}(z,s)g(s) - g(s)^2\right], \tag{16.75}$$

with optimizer $g^\star(s) = C_{ab}(s)$. This is the same square-loss identity as before, applied to the bounded target R_{ab}.

With finite data, a clean implementation uses sample splitting. First, use one subset of snapshots to learn $\hat{m}_a(s)$ and $\hat{m}_b(s)$. Second, on an independent subset, form

$$\widehat{R}_{ab,i} := [O_a(z_i) - \hat{m}_a(s_i)]\,[O_b(z_i) - \hat{m}_b(s_i)]\,. \tag{16.76}$$

Third, learn a decoder $g(s)$ for $\widehat{R}_{ab}$ by maximizing

$$\frac{1}{N}\sum_i \left[2\widehat{R}_{ab,i}\,g(s_i) - g(s_i)^2\right]. \tag{16.77}$$

Conditioned on the first subset, the functions $\hat{m}_a$ and $\hat{m}_b$ are fixed on the second subset. If

$$e_a(s) := \hat{m}_a(s) - m_a(s), \qquad e_b(s) := \hat{m}_b(s) - m_b(s), \tag{16.78}$$

then the conditional mean of the residual target used in the second stage is

$$\mathbb{E}[\widehat{R}_{ab}(z,s) \mid s] = C_{ab}(s) + e_a(s)e_b(s). \tag{16.79}$$

Thus the first-stage bias in the connected target is quadratic in the one-point decoder errors. The sample complexity of the last step is again controlled by the pseudo-dimension of the decoder class for g, with additional approximation terms inherited from the first-stage decoders. This construction is not needed for the main numerical results, but it shows that genuinely connected conditioned observables can also be treated without explicit sector-by-sector postselection.

16.7 Other losses and related conditional quantities

The square loss is special because it learns the conditional mean, which is the quantity entering $A_2[O]$. Other losses learn other conditional summaries and can be useful diagnostics of the same measurement record.

Absolute loss and conditional medians. For a real random variable X, the minimizer of $\mathbb{E}[|X - a|]$ over constants a is a median of X. Therefore minimizing

$$\mathbb{E}\left[|O(z) - f(s)|\right] \tag{16.80}$$

over functions f learns the conditional median of $O(z)$ given s, rather than the conditional mean. For binary observables $O(z) \in \{\pm 1\}$, this conditional median is the majority-vote predictor $\operatorname{sign} m_O(s)$, up to ties.

For binary $O(z) \in \{\pm 1\}$, the first absolute moment of the conditional mean can be obtained from the optimal classification accuracy. For a classifier $h(s) \in \{\pm 1\}$,

$$\operatorname{Acc}(h) := \Pr[h(s) = O(z)] \tag{16.81}$$

$$= \mathbb{E}\left[\frac{1 + O(z)h(s)}{2}\right] = \frac{1 + \mathbb{E}_s[m_O(s)h(s)]}{2}. \tag{16.82}$$

Maximizing over all classifiers gives $h^\star(s) = \operatorname{sign} m_O(s)$ and

$$\mathbb{E}_s|m_O(s)| = 2\operatorname{Acc}^\star - 1. \tag{16.83}$$

Restricting h to a classifier class gives a post-selection-free estimator whose sample complexity is governed by the VC dimension, or an analogous capacity measure, of that class.

Cross entropy and conditional entropy. If a coarse-grained system label $\chi(z)$ takes values in $\{1, \ldots, K\}$, a probabilistic decoder $q_\theta(k \mid s)$ trained by cross entropy learns the conditional distribution of χ given s. For any candidate conditional distribution $q(k \mid s)$,

$$\mathbb{E}\left[-\log q(\chi(z) \mid s)\right] = H(\chi \mid s) \tag{16.84}$$

$$+ \mathbb{E}_s\, D_{\mathrm{KL}}(p(\cdot \mid s) \| q(\cdot \mid s)) \tag{16.85}$$

$$\geq H(\chi \mid s), \tag{16.86}$$

with equality for $q(k \mid s) = p(\chi = k \mid s)$. Thus the optimum cross entropy is the conditional entropy, and $I(\chi; s) = H(\chi) - H(\chi \mid s)$ gives the mutual information between the label and the measurement record. Unlike the bounded square-loss setting used for Eq. (16.62), the logarithmic loss is unbounded unless the predicted probabilities are clipped away from zero. With such clipping, analogous uniform-convergence bounds can be applied, with constants depending on the clipping scale.

Chapter 17

DECODER ARCHITECTURES AND NUMERICAL TRAINING PROTOCOL

This chapter gives the architectural and training details for the decoders used in Sec. 15.1. We keep the notation of the previous chapters. A snapshot is a pair (z, s) sampled from the joint Born distribution $p(z, s)$, where $z_j, s_j \in \{\pm 1\}$ are the system and ancilla outcomes. For the one-point function we train a decoder

$$f_j(s) \simeq m_j(s), \qquad m_j(s) := \mathbb{E}[z_j \mid s] = \left\langle Z_j \right\rangle_s, \tag{17.1}$$

for every site j. The decoders are trained only on raw snapshot pairs (z, s). The exact conditional values $m_j(s)$ computed by MPS are not used as training labels; they are used only for the reference curves and for the error estimates described below.

17.1 Implementation conventions for the hyperparameters

Several names used below are implementation flags in the numerical code rather than standard machine-learning terminology. We define them here before listing the numerical choices for each decoder.

The option `fit_intercept` specifies whether an affine bias b is included in the linear or logistic map. In the notation of the previous chapters, this is the constant term c_0 in Eqs. 14.2 and 14.2. The option `pbc_shared` enforces the periodic translation symmetry at the level of the trainable parameters. Instead of fitting independent coefficients $\{b_j, w_r^{(j)}\}$ for each output site j, it fits one reference-site decoder g with a single set of coefficients $\{b, w_r\}$ and predicts every other site by translating the ancilla record to the reference frame,

$$f_j(s) = g(T_{-j} s), \tag{17.2}$$

where T_{-j} shifts the target site j to a fixed reference position. Equivalently, with periodic indices understood modulo L, the linear shared-PBC model has the form $f_j(s) = b + \sum_r w_r s_{j+r}$. Thus the parameters are translation invariant in relative coordinates, while the site-resolved output is translation covariant, or equivariant: $f_{j+a}(T_a s) = f_j(s)$. If `pbc_shared` is not used, one instead fits independent site-wise models with independent parameter vectors. Finally, `augment_z2` denotes augmentation by the global Ising symmetry: for each training example (s, z) we also include $(-s, -z)$. This enforces, or at least strongly biases the fit toward, the physically expected odd response $f_j(-s) = -f_j(s)$.

For the logistic regression, `solver` is the numerical optimizer, `max_iter` is its maximum number of iterations, and C is the inverse strength of the standard ℓ_2 penalty in the logistic objective. Thus larger C corresponds to weaker regularization. For the CNN, the parameters listed below are the number of hidden channels, convolution kernel size, dilation base, learning rate, batch size, and number of training epochs.

17.2 Data sets and translational averaging

For each pair (L, β) used in the figures, we generated independent snapshot pairs $(z^{(a)}, s^{(a)})$ from the MPS representation of the measured critical Ising chain. In the convergence and validation plots, the data set contains

$$N_{\text{tot}} = 10^5 \tag{17.3}$$

raw snapshot pairs. We used a fixed random split with

$$N_{\text{val}} = 2 \times 10^4, \qquad N_{\text{train}}^{\text{max}} = 8 \times 10^4. \tag{17.4}$$

The validation set is disjoint from the training set. When the training-size dependence is plotted, the training set of size N_{train} is chosen as a nested subset of the fixed training pool, with

$$\begin{aligned} N_{\text{train}} \in \{&2, 5, 10, 20, 40, 80, 160, 320, 640, \\ &1280, 2560, 5120, 10240, 20480, \\ &40960, 80000\}. \end{aligned} \tag{17.5}$$

Thus different points in a convergence curve are evaluated on the same validation set.

The chain is periodic in the numerical experiments. For the linear and logistic decoders, we use the shared-PBC construction defined in Eq. (17.2). Equivalently, the shared training set is

$$\mathcal{D}_{\text{sh}} = \{(T_{-j} s^{(a)}, z_j^{(a)}) : \; a = 1, \ldots, N_{\text{train}}, \; j = 1, \ldots, L\}. \tag{17.6}$$

This realizes the statement in Sec. 15.1 that translation symmetry can reduce the number of independent parameters relative to fitting an unrelated model at every site. The shared linear and logistic maps still have $L + 1$ coefficients, but a single snapshot supplies labels for all L translated sites, so translation averaging reduces the number of independent snapshot records needed in practice. For the convolutional neural network, translation covariance is built into the architecture by weight sharing and circular padding, so no explicit shifted data set is required.

We also use the global Ising symmetry in the data augmentation step. Whenever a training snapshot (s, z) is used, we include its symmetry partner

$$(s, z) \mapsto (-s, -z). \tag{17.7}$$

For the convex linear and logistic objectives this makes the optimal intercept zero up to numerical tolerance. For the neural network it acts as symmetry augmentation and strongly biases the learned decoder toward $f_j(-s) = -f_j(s)$.

17.3 Linear decoder

The linear decoder is the translationally shared version of Eq. 14.2 of the previous chapters. With periodic indices understood modulo L, it can be written as

$$f_j^{\mathrm{lin}}(s) = \mathrm{clip}_{[-1,1]}\left(b + \sum_{r=0}^{L-1} w_r s_{j+r}\right). \tag{17.8}$$

The clipping is applied only at prediction time to keep the output in the physical range $[-1, 1]$. The fit itself is ordinary least-squares regression on the augmented shared data set in Eq. (17.6). Numerically, the linear runs include the affine bias b, impose the shared-PBC translation-covariant form, use the global $\mathbb{Z}_2$ data augmentation, and apply no explicit regularization. No separate cyclic-shift augmentation is used beyond the shared-PBC pooling. In the code notation defined above, this is `fit_intercept=True`, `pbc_shared=True`, and `augment_z2=True`. The number of trainable parameters in the shared PBC implementation is $L + 1$ before the $\mathbb{Z}_2$ symmetry sets the intercept to zero. Without the shared-PBC constraint, a separate linear model for every site would have $L(L + 1)$ parameters.

17.4 Logistic decoder

The logistic decoder uses the same shared-PBC feature map as the linear decoder, but it learns the conditional probability of a positive system outcome. For $u = T_{-j}s$, define

$$p_+(u) = \frac{1}{1 + \exp[-(b + \sum_{r=0}^{L-1} w_r u_r)]}. \tag{17.9}$$

The magnetization prediction is

$$f_j^{\log}(s) = 2p_+(T_{-j}s) - 1 = \tanh\left[\frac{1}{2}\left(b + \sum_{r=0}^{L-1} w_r s_{j+r}\right)\right]. \tag{17.10}$$

After a harmless rescaling of b and w_r, this is the bounded logistic form shown in Eq. 14.2 of the previous chapters.

The model is trained by binary cross entropy on the labels $(z_j + 1)/2 \in \{0, 1\}$. The Bayes optimum of this classification problem is $p_+(s) = \Pr(z_j = +1 \mid s)$, and therefore the corresponding magnetization is $2p_+(s) - 1 = \langle Z_j \rangle_s$. Thus the logistic loss and the squared loss have the same target conditional mean, although they weight finite-sample errors differently.

Numerically, the logistic runs use the same shared-PBC and $\mathbb{Z}_2$-augmented data convention as the linear runs, with an affine bias included and the shared-PBC pooling. The optimizer is `lbfgs`, the maximum number of optimizer iterations is 400, and $C = 1.0$ is the inverse strength of the standard ℓ_2 regularization in the logistic objective. In the code notation defined above, this is `solver=lbfgs`, `C=1.0`, `max_iter=400`, `fit_intercept=True`, `pbc_shared=True`, and `augment_z2=True`. The shared model has $L + 1$ trainable parameters before the symmetry constraint on the intercept.

17.5 Dilated convolutional neural network

The neural-network decoder is a one-dimensional dilated convolutional neural network with periodic padding. Unlike the linear and logistic baselines, it outputs all sites simultaneously,

$$f_\theta(s) = \big(f_{\theta,1}(s), \ldots, f_{\theta,L}(s)\big) \in [-1, 1]^L. \tag{17.11}$$

The input is viewed as a one-channel signal of length L. The architecture is:

1. A circular convolutional stem with one input channel, $C = 64$ hidden channels, kernel size $K = 3$, dilation 1, followed by the SiLU activation $\mathrm{SiLU}(x) = x/(1 + e^{-x})$.

2. A stack of B residual dilated convolutional blocks. The ℓth block, with $\ell = 0, \ldots, B - 1$, has dilation

$$d_\ell = 2^\ell, \tag{17.12}$$

   $C = 64$ input and output channels, kernel size $K = 3$, and circular padding. If $h^{(\ell)}$ is the hidden representation entering the block, the update is

$$h^{(\ell+1)} = h^{(\ell)} + \mathrm{SiLU}\Big(\mathrm{Conv}^{\mathrm{circ}}_{K=3,d_\ell} h^{(\ell)}\Big). \tag{17.13}$$

3. A pointwise readout convolution with kernel size 1, mapping the $C = 64$ hidden channels to one output channel at each site, followed by a final tanh nonlinearity,
$$f_\theta(s) = \tanh\left(\mathrm{Conv}_{K=1} h^{(B)}\right). \tag{17.14}$$

The final tanh enforces the physical bound $f_{\theta,j}(s) \in [-1, 1]$.

The number of residual blocks is chosen automatically so that the receptive field covers the periodic chain. With the stem included, the receptive-field length after B residual blocks is
$$R_B = 3 + 2\sum_{\ell=0}^{B-1} 2^\ell = 2^{B+1} + 1. \tag{17.15}$$
We choose the smallest B such that $R_B \geq L$. Thus $B = O(\log L)$, and with fixed channel number the number of trainable weights also scales as $O(\log L)$. For the hyperparameters used here, the parameter count is
$$\begin{aligned} W_{\mathrm{CNN}} &= 64(3+1) + B(64^2 \cdot 3 + 64) + (64+1) \\ &= 321 + 12352B. \end{aligned} \tag{17.16}$$

For the system sizes used in the figures this gives the values in Table 17.1.

Table 17.1: Number of dilated residual blocks and trainable parameters for the CNN with $C = 64$, $K = 3$, and dilation base 2.

L	B	receptive field R_B	trainable parameters
20	4	33	49729
40	5	65	62081
60	5	65	62081
100	6	129	74433
200	7	257	86785

The CNN is trained as a Bernoulli decoder for all sites. Its magnetization output is converted to a probability
$$p_{\theta,j}(+ \mid s) = \frac{f_{\theta,j}(s) + 1}{2}, \tag{17.17}$$
and the target is $y_j = (z_j + 1)/2$. The training loss is the site-averaged binary cross entropy
$$\begin{aligned} \mathcal{L}_{\mathrm{BCE}}(\theta) = -\frac{1}{N_{\mathrm{train}} L} \sum_{a=1}^{N_{\mathrm{train}}} \sum_{j=1}^{L} \Big[& y_j^{(a)} \log p_{\theta,j}(+ \mid s^{(a)}) \\ & + (1 - y_j^{(a)}) \log(1 - p_{\theta,j}(+ \mid s^{(a)})) \Big]. \end{aligned} \tag{17.18}$$

with the probabilities clipped to the interval $[10^{-6}, 1 - 10^{-6}]$ for numerical stability. The optimizer is Adam with learning rate 10^{-3}, batch size 256, and 20 epochs. No dropout or weight decay is used.

Hyperparameter summary. The numerical settings used for the three decoders in Sec. IV are as follows. The implementation-specific names in parentheses are defined in Sec. 17.1.

Linear decoder

Ordinary least-squares regression; affine bias included (`fit_intercept`); translationally shared PBC model (`pbc_shared`); global Ising-symmetry augmentation (`augment_z2`); no explicit regularization.

Logistic decoder

Bernoulli logistic regression for $\Pr(z_j = +1 \mid s)$; affine bias included; translationally shared PBC model; global Ising-symmetry augmentation; `lbfgs` optimizer; inverse ℓ_2 regularization strength $C = 1.0$; maximum iteration count 400.

Dilated CNN

Circular one-dimensional residual CNN with hidden channels $C = 64$, kernel size $K = 3$, dilation base 2, and automatic number B of residual blocks chosen from Eq. (17.15); SiLU activations; final tanh output; binary-cross-entropy loss; Adam optimizer; learning rate 10^{-3}; batch size 256; 20 epochs; global Ising-symmetry augmentation; no dropout and no weight decay.

17.6 Validation estimator and reference MPS error bars

The validation set is used to estimate the variational objective in Sec. 13.3 without reusing the training data. For a trained model $\mathcal{M}$, define the site-averaged validation mean-squared error

$$\widehat{\mathcal{L}}^{\mathcal{M}}_{\mathrm{val}} := \frac{1}{N_{\mathrm{val}} L} \sum_{a=1}^{N_{\mathrm{val}}} \sum_{j=1}^{L} \left[z_j^{(a)} - f_j^{\mathcal{M}}(s^{(a)}) \right]^2 . \tag{17.19}$$

Because $z_j^2 = 1$, the corresponding validation estimate of the site-averaged second moment is

$$\widehat{\overline{A}}{}^{\mathrm{val}}_{2,\mathcal{M}} = 1 - \widehat{\mathcal{L}}^{\mathcal{M}}_{\mathrm{val}}, \tag{17.20}$$

where

$$\overline{A}_2[Z] := \frac{1}{L} \sum_{j=1}^{L} A_2[Z_j] = \frac{1}{L} \sum_{j=1}^{L} \mathbb{E}_s \left\langle Z_j \right\rangle_s^2 . \tag{17.21}$$

Indeed, if $f_j^{\mathcal{M}}(s) = \langle Z_j \rangle_s$ is the Bayes decoder, then

$$\mathbb{E}\left[(z_j - f_j^{\mathcal{M}}(s))^2\right] = 1 - A_2[Z_j]. \tag{17.22}$$

Thus the irreducible validation MSE is $1 - \overline{A}_2[Z]$.

For the MPS reference, we independently sample

$$N_{\text{MPS}} = 10^4 \tag{17.23}$$

measurement records from the Born distribution and compute the true conditional expectation values $m_j^{\text{MPS}}(s) = \langle Z_j \rangle_s$ by MPS contraction. The reference value is

$$\widehat{\overline{A}}_2^{\text{MPS}} = \frac{1}{N_{\text{MPS}} L} \sum_{a=1}^{N_{\text{MPS}}} \sum_{j=1}^{L} \left[m_j^{\text{MPS}}(s^{(a)})\right]^2, \tag{17.24}$$

or, equivalently, the reference irreducible MSE is

$$\widehat{\mathcal{L}}_{\text{MPS}} = 1 - \widehat{\overline{A}}_2^{\text{MPS}}. \tag{17.25}$$

Part VII

Summary and Outlook

"The sun never really sets. It just stands there doing its thing while we run circles around it."

— Pascal, *Animal Crossing: New Horizons*

Chapter 18

THEORY OF MEASUREMENT-ALTERED QUANTUM CRITICALITY

The preceding parts of this thesis develop measurement-altered quantum criticality from several directions: ancilla-assisted weak measurements of the Ising CFT, imperfect teleportation of critical wavefunctions, boundary transitions generated by single-shot measurements on gapless states, projective-measurement protocols in Rydberg arrays, and statistical-learning methods for extracting conditioned observables without explicit post-selection. The examples differ in microscopic implementation, but they are organized by the same theoretical pattern. One begins with a critical wavefunction, applies a measurement map or an operation equivalent to one, and studies the universal properties of the conditioned, averaged, decoded, or replicated ensemble that results. This chapter collects the common lessons.

18.1 Measurement protocols as non-unitary deformations

A measurement-conditioned state can be written schematically as

$$|\psi_s\rangle = \frac{K_s\,|\psi_0\rangle}{\sqrt{p_s}}, \qquad p_s = \langle\psi_0|\,K_s^\dagger K_s\,|\psi_0\rangle\,, \tag{18.1}$$

where $|\psi_0\rangle$ is a critical state and K_s is the Kraus operator associated with outcome record s. The central observation of the thesis is that, for many physically relevant protocols, K_s can be reinterpreted as a non-unitary deformation of the critical wavefunction. In a continuum description this deformation takes the form

$$K_s \sim \exp[-S_{\text{meas}}(s)], \qquad S_{\text{meas}}(s) = \sum_a \int \mathrm{d}^d x\, \lambda_a(x;s)\, O_a(x) + \cdots\,, \tag{18.2}$$

where O_a are fields of the underlying CFT. The ellipsis contains higher-order and less relevant terms. The fate of the measured state is controlled by the symmetry, scaling dimension, spatial profile, and the couplings λ_a.

This language simultaneously describes several limits encountered earlier. In the ancilla-assisted Ising protocol, perturbative measurement strength generates local couplings to Ising fields. In imperfect teleportation, imperfect entangling gates act as effective weak measurements of the would-be teleported critical state. In the boundary-transition construction, a single measurement round creates a boundary condition or defect whose RG flow determines long-distance correlations. In Rydberg arrays, partial projective measurement of atoms implements an experimentally accessible version of the same deformation. In the decoder chapters, one no longer fixes a single s; instead, one learns the map $s \mapsto \langle O \rangle_s$, thereby probing the ensemble of deformations.

18.2 Relevant, marginal, and irrelevant measurement perturbations

The simplest classification is the RG classification of the induced operator. If a measurement-induced operator has scaling dimension Δ below the dimension of the integration manifold, it is relevant and can drive the measured state away from the original critical fixed point. If it is marginal, one expects logarithmic flow or a continuously varying response. If it is irrelevant, the measured state retains the same leading universal behavior, although subleading corrections may still be measurable.

This classification is visible throughout the thesis. In Chapters 3 and 4, different measurement bases and outcome sectors select different Ising fields, changing whether the dominant response is order-parameter condensation, altered spin correlations, or symmetry-resolved nonlinear behavior. In Chapters 5 and 6, teleportation imperfections fall into relevant, marginal, and disguised marginal categories, showing that noisy transfer of a critical state can preserve, alter, or hide universal data depending on microscopic structure. In Chapters 7–9, the language becomes that of boundary RG: measurement basis and outcome ensemble tune boundary perturbations, sometimes producing an intermediate fixed point. In Chapters 10–12, projective Rydberg measurements realize these ideas with a microscopic Hamiltonian that is experimentally motivated rather than designed only for theoretical convenience.

A useful way to summarize the classification is

$$\begin{aligned} \text{measurement protocol} \quad &\longrightarrow \quad \{O_a, \lambda_a(s)\} \\ &\longrightarrow \quad \text{RG flow of conditioned or ensemble observables.} \end{aligned} \tag{18.3}$$

The same microscopic protocol may therefore have multiple universal interpretations, because different observables and different outcome ensembles probe different combinations of the induced perturbations.

18.3 Outcome dependence and symmetry constraints

Measurements introduce two ingredients that ordinary Hamiltonian perturbations do not usually have: stochastic outcome dependence and ensemble choice. The outcome record s can explicitly break a microscopic symmetry, preserve it only statistically, or select a symmetry sector. This is why a single protocol can produce fixed-outcome order, symmetry-resolved averages, Born-weighted averages, or learned conditional responses.

Symmetry determines which perturbations are allowed in Eq. (18.2). If an outcome sector is invariant under a symmetry, fields odd under that symmetry are absent from the leading effective action. If an outcome breaks the symmetry, the corresponding order-parameter field can appear and may be relevant. If an ensemble sums over symmetry-related outcomes, ordinary linear averages may cancel the order parameter even though nonlinear observables remain singular. This explains why quantities such as

$$A_q[O] = \sum_s p_s \, \langle O \rangle_s^q \tag{18.4}$$

play such a prominent role. They are not auxiliary diagnostics; they are the natural observables of measurement-conditioned criticality when the fixed-outcome state is not directly accessible.

This point also clarifies the role of decoding. A decoder does not change the underlying physics; it changes the experimentally accessible representation of it. Rather than requiring exponentially rare exact post-selection, the decoder estimates the conditional response $\langle O \rangle_s$ from samples of (z, s). The statistical-learning formulation therefore sits on top of the same symmetry and outcome structure that appears in the field-theory chapters.

18.4 Defect-line versus boundary-condition viewpoints

The same measurement deformation can be described either as a defect line inserted into a Euclidean path integral or as a boundary condition of the corresponding CFT. The first viewpoint is natural for weak measurements of a critical wavefunction, because the measurement acts on a time slice and can be represented by a defect operator. The second viewpoint is natural for single-round *relevant* measurements that leave behind a BCFT. The defect-line viewpoint emphasizes local operator content. One asks which CFT fields appear in the defect action and whether their couplings are relevant. The boundary-condition viewpoint emphasizes endpoint data of the RG flow, usually a BCFT.

The two viewpoints are complementary rather than competing. A relevant defect perturbation can flow to a boundary fixed point. A boundary fixed point can be diagnosed by the scaling dimensions of operators that also appear in a defect expansion. The high-level picture is therefore a web of equivalent descriptions:

$$\text{Kraus map} \;\leftrightarrow\; \text{non-unitary defect} \;\leftrightarrow\; \text{boundary condition} \tag{18.5}$$

18.5 Fixed-outcome, Born-weighted, restricted, and uniform ensembles

Measurement-altered criticality is not specified by the microscopic operation alone; it is also specified by the ensemble through which the operation is probed. Four ensembles recur throughout this thesis.

A *fixed-outcome ensemble* studies a target record $s = s_\star$. It is the cleanest theoretical object because it has a definite effective action. It is also the most experimentally demanding when $p_{s_\star}$ is exponentially small. A *Born-weighted ensemble* averages over measurement outcomes with their physical probabilities. It is experimentally natural but may wash out symmetry-breaking signatures. A *restricted ensemble* averages over a subset of outcomes that are symmetry equivalent, experimentally common, or selected by simple classical rules. A *uniform or reweighted ensemble* is useful theoretically and in some decoder formulations because it exposes the geometry of outcome space rather than the Born distribution alone.

The differences are not merely technical. Different ensembles can correspond to different effective replica theories and therefore different universal exponents. For example, Born-weighted nonlinear moments probe locked-replica physics, while uniform-outcome correlations can probe a zero-replica or random-defect limit. Post-selected Rydberg sectors, restricted averages over symmetry-related sectors, and learned decoder outputs are therefore different experimental or computational cuts through a larger ensemble landscape.

18.6 Nonlinear observables and replica descriptions

Nonlinear observables are the common bridge between theory and access. The fixed-outcome expectation $\langle O \rangle_s$ may show an altered scaling law, but a laboratory generally samples s. The Born-weighted average $\sum_s p_s \langle O \rangle_s$ can vanish by symmetry. The moment $A_2[O]$, by contrast, can remain nonzero and universal.

One useful identity behind the decoder chapters is the variational representation

$$A_2[O] = \max_f \left[2\,\mathbb{E}\{f(s)O(z)\} - \mathbb{E}\{f(s)^2\} \right], \tag{18.6}$$

where the maximum is over functions of the measurement record. The optimizer is the conditional expectation $f_\star(s) = \mathbb{E}[O(z) \mid s]$. This equation makes precise why supervised learning is natural: a decoder trained from snapshots approximates the function that realizes the nonlinear observable. Thus the decoder is not an ad hoc post-processing tool; it is a variational representation of a universal ensemble quantity.

Replica language gives another interpretation. Moments such as A_q couple several copies of the system through a shared measurement record. In favorable regimes these replicas lock, generating scaling behavior distinct from that of the original single-copy critical state. Uniform or reweighted ensembles instead resemble random-defect averages and can lead to different limits.

18.7 Experimental access: post-selection, restricted averages, and learned decoders

The experimental question is how to see altered criticality without assuming ideal access to a chosen outcome. The thesis develops several answers, ordered from direct to indirect.

First, if the target outcome has sufficiently high probability, one may post-select directly. Rydberg blockade can enhance useful target-sector probabilities, making this route less hopeless than it would be for independent unbiased measurements. Second, if symmetry-related sectors are available, restricted averages can combine many records that share the same universal response. Third, nonlinear Born-weighted observables can reveal fixed-outcome physics even when the linear average vanishes. Fourth, decoder-assisted protocols learn conditional observables from raw snapshots and avoid explicitly estimating each sector separately.

These strategies should be viewed as complementary. Direct post-selection gives the clearest comparison to field theory. Restricted averages exploit microscopic symmetries and constraints. Nonlinear moments define universal observables of the ensemble. Decoders provide scalable estimators for those observables. A realistic experiment may use several of these ideas simultaneously: choose a favorable measurement pattern, group symmetry-related outcomes, measure many snapshots, and train a decoder to extract the relevant conditioned response.

Chapter 19

OUTLOOK

This thesis develops measurement-altered quantum criticality in one-dimensional systems where conformal field theory, boundary CFT, tensor-network numerics, and statistical-learning tools can be combined in detail. The resulting framework is already broad: it includes weak and projective measurements, teleportation errors, boundary transitions, Rydberg experiments, and decoder-assisted nonlinear observables. Still, the work should be viewed as an initial map rather than a closed theory. This chapter outlines directions in which the ideas can be extended.

19.1 Higher-dimensional measurement-altered criticality

The most direct theoretical extension is to higher-dimensional critical points. In one spatial dimension, the power of CFT and BCFT makes it possible to identify measurement-induced perturbations, boundary fixed points, and scaling dimensions with high precision. In higher dimensions the same conceptual questions remain, but the tools are less complete. A measurement can still generate a non-unitary defect, boundary condition, or random surface; the problem is to determine which operators are induced and how they flow.

Several qualitative changes should occur in higher dimensions. First, measured submanifolds can have nontrivial geometry: lines, surfaces, corners, and fractal sets of measured degrees of freedom may define different universality classes. Second, boundary and defect operator spectra are richer and less constrained. Third, numerical access is more challenging, so decoder-based methods may become more important rather than less. Finally, experiments on two-dimensional Rydberg arrays, superconducting qubit arrays, trapped ions, or photonic systems may naturally realize measurement geometries that are unavailable in strictly one-dimensional chains.

19.2 Other CFTs and universality classes

The Ising and tricritical Ising theories are natural starting points because their operator content is simple and their lattice realizations are well controlled. The boundary-transition chapters already show that the measurement-altered framework extends to other minimal models and SPT-related critical states. A systematic next step is to classify measurement-induced deformations across larger families of CFTs.

Important targets include compact bosons and Luttinger liquids with tunable radius, parafermion CFTs, Wess–Zumino–Witten models, nonunitary CFTs, and multicritical points with several relevant fields. In each case one can ask which measurement bases couple to which primary fields, which outcome sectors preserve symmetries, which boundary fixed points are accessible, and which nonlinear observables remain experimentally visible. Such a classification would turn the examples in this thesis into a more general dictionary between measurement protocols and CFT data.

19.3 Continuous monitoring and hybrid dynamics

This thesis focuses primarily on single-round or effectively static measurements. Continuous monitoring introduces a time direction and connects measurement-altered criticality to hybrid quantum circuits and measurement-induced phase transitions. The distinction is important. Measurement-induced transitions in monitored dynamics are often transitions between volume-law and area-law entanglement phases. Measurement-altered criticality instead asks how measurements reshape the universal data of an already critical wavefunction. Nevertheless, the two subjects should have overlapping regimes.

A continuously monitored critical system may exhibit both effects: the monitoring can alter the instantaneous critical correlations while also driving a dynamical entanglement transition. Understanding the interplay between static measurement-induced defects and dynamical measurement histories is an open problem. A useful first step would be to study weakly monitored versions of the Ising and Rydberg protocols in this thesis, asking whether the single-round boundary or defect fixed points survive as preasymptotic regimes of a monitored dynamics.

19.4 Adaptive measurements and feedback

Another natural extension is adaptivity. In the protocols studied here, the measurement basis and target sectors are chosen before or independent of the measured outcomes. Adaptive protocols can choose later measurements or feedback operations based on earlier records. This could be used to steer a critical wavefunction toward a desired boundary fixed point, increase the probability of favorable outcome sectors, or implement a real-time decoder at the quantum-control level rather than only in classical post-processing.

Adaptivity also raises theoretical questions. A nonadaptive measurement corresponds to a fixed set of Kraus operators. An adaptive protocol corresponds to a measurement tree, and the effective deformation depends on a history-dependent classical control rule. Field-theoretically, this may generate new classes of nonlocal or temporally correlated defects. Experimentally, adaptive measurement could be a practical way to interpolate between post-selection and feedback-controlled state engineering.

19.5 Quantum decoders and circuit-based post-processing

The decoder chapters treat decoding as a classical supervised-learning problem. A broader perspective is to ask whether decoder logic can be implemented by a quantum circuit or hybrid quantum-classical protocol. Instead of learning $s \mapsto \langle O \rangle_s$ after the fact, one might use a circuit that coherently processes measurement records, applies conditional corrections, or maps an ensemble of conditioned states into a common representative.

This possibility connects measurement-altered criticality to quantum error correction. In error correction, syndrome measurements reveal information about errors without directly measuring logical degrees of freedom, and a decoder infers a correction. In measurement-altered criticality, the measurement record reveals information about how the critical wavefunction was deformed, and a decoder infers the conditioned observable or effective fixed point. The analogy is not exact, but it suggests that quantum-information methods may be useful for designing protocols that preserve or deliberately transform critical universal data.

19.6 Relation to quantum teleportation and state engineering

The teleportation chapters show that measurement-altered criticality is not only a matter of measurement protocols designed to study critical systems. It also appears as a robustness question for quantum information tasks. Imperfect teleportation of a critical state can generate relevant or marginal measurement-like perturbations. Thus universal critical data can be a sensitive diagnostic of state-transfer quality.

This suggests using critical states as structured probes of quantum devices. A device that teleports, stores, or processes a critical wavefunction may reveal coherent imperfections through altered scaling dimensions or entanglement diagnostics. Conversely, measurement-induced deformations can be used constructively to engineer states with desired boundary conditions or order-parameter responses. The boundary between “error” and “resource” is therefore protocol dependent: a measurement-like perturbation may be harmful for preserving a pristine critical state, but useful for preparing a new universal state.

19.7 Toward a classification of measurement-altered universality

A long-term goal is a classification of measurement-altered universality classes. Such a classification would specify an underlying critical theory, a measured submanifold, a measurement basis, a set of accessible outcome ensembles, and a family of observables. The output would be a list of stable fixed points, relevant measurement-induced perturbations, nonlinear ensemble exponents, and experimentally viable diagnostics.

The examples in this thesis suggest that this classification is feasible at least in one dimension. Minimal models, compact bosons, SPT critical states, and constrained Rydberg chains provide a testing ground. The classification should not be limited to post-selected pure states; it should include mixed states, Born-weighted moments, restricted averages, learned conditional observables, and possibly adaptive protocols.

BIBLIOGRAPHY

[1] Yaodong Li, Xiao Chen, and Matthew P. A. Fisher. "Quantum Zeno Effect and the Many-Body Entanglement Transition". In: *Physical Review B* 98 (2018), p. 205136. DOI: 10.1103/PhysRevB.98.205136.

[2] Brian Skinner, Jonathan Ruhman, and Adam Nahum. "Measurement-Induced Phase Transitions in the Dynamics of Entanglement". In: *Physical Review X* 9 (2019), p. 031009. DOI: 10.1103/PhysRevX.9.031009.

[3] Sara Murciano, Pablo Sala, Yue Liu, Roger S. K. Mong, and Jason Alicea. "Measurement-Altered Ising Quantum Criticality". In: *Physical Review X* 13 (2023), p. 041042. DOI: 10.1103/PhysRevX.13.041042. arXiv: 2302.04325.

[4] Pablo Sala, Sara Murciano, Yue Liu, and Jason Alicea. "Quantum Criticality Under Imperfect Teleportation". In: *PRX Quantum* 5 (2024), p. 030307. DOI: 10.1103/PRXQuantum.5.030307. arXiv: 2403.04843.

[5] Yue Liu, Sara Murciano, David F. Mross, and Jason Alicea. "Boundary Transitions from a Single Round of Measurements on Gapless Quantum States". In: *Physical Review Research* 7 (2025), p. 023293. DOI: 10.1103/l4b7-h5cd. arXiv: 2412.07830.

[6] Stephen Naus, Yue Liu, Sara Murciano, Pablo Sala, Manuel Endres, and Jason Alicea. "Practical Roadmap to Measurement-Altered Criticality in Rydberg Arrays". arXiv preprint. 2025. DOI: 10.48550/arXiv.2506.21963. arXiv: 2506.21963.

[7] Yue Liu, Nandagopal Manoj, Stephen Naus, Zack Weinstein, Sara Murciano, David F. Mross, and Jason Alicea. "Post-Selection-Free Measurement-Altered Criticality via Statistical Learning". In preparation. 2026.

[8] A. A. Belavin, A. M. Polyakov, and A. B. Zamolodchikov. "Infinite Conformal Symmetry in Two-Dimensional Quantum Field Theory". In: *Nuclear Physics B* 241 (1984), pp. 333–380. DOI: 10.1016/0550-3213(84)90052-X.

[9] Philippe Di Francesco, Pierre Mathieu, and David Sénéchal. *Conformal Field Theory*. Springer, 1997.

[10] John Cardy. *Scaling and Renormalization in Statistical Physics*. Cambridge University Press, 1996.

[11] Pierre Pfeuty. "The One-Dimensional Ising Model with a Transverse Field". In: *Annals of Physics* 57 (1970), pp. 79–90. DOI: 10.1016/0003-4916(70)90270-8.

[12] Pasquale Calabrese and John Cardy. "Entanglement Entropy and Quantum Field Theory". In: *Journal of Statistical Mechanics: Theory and Experiment* 2004 (2004), P06002. DOI: 10.1088/1742-5468/2004/06/P06002.

[13] John L. Cardy. “Conformal Invariance and Surface Critical Behavior”. In: *Nuclear Physics B* 240 (1984), pp. 514–532. DOI: `10.1016/0550-3213(84)90241-4`.

[14] Steven R. White. “Density Matrix Formulation for Quantum Renormalization Groups”. In: *Physical Review Letters* 69 (1992), pp. 2863–2866. DOI: `10.1103/PhysRevLett.69.2863`.

[15] Guifré Vidal. “Efficient Classical Simulation of Slightly Entangled Quantum Computations”. In: *Physical Review Letters* 91 (2003), p. 147902. DOI: `10.1103/PhysRevLett.91.147902`.

[16] Samuel J. Garratt, Zack Weinstein, and Ehud Altman. “Measurements Conspire Nonlocally to Restructure Critical Quantum States”. In: *Phys. Rev. X* 13 (2 2023), p. 021026. DOI: `10.1103/PhysRevX.13.021026`. URL: `https://link.aps.org/doi/10.1103/PhysRevX.13.021026`.

[17] Michael A. Nielsen and Isaac L. Chuang. *Quantum Computation and Quantum Information: 10th Anniversary Edition*. 10th. USA: Cambridge University Press, 2011.

[18] Johannes Hauschild and Frank Pollmann. “Efficient numerical simulations with Tensor Networks: Tensor Network Python (TeNPy)”. In: *SciPost Phys. Lect. Notes* (2018). Code available from `https://github.com/tenpy/tenpy`, p. 5. DOI: `10.21468/SciPostPhysLectNotes.5`. arXiv: `1805.00055`. URL: `https://scipost.org/10.21468/SciPostPhysLectNotes.5`.

[19] I. P. McCulloch. *Infinite size density matrix renormalization group, revisited*. 2008. arXiv: `0804.2509 [cond-mat.str-el]`.

[20] Sergey Bravyi, David P. Divincenzo, Roberto Oliveira, and Barbara M. Terhal. “The Complexity of Stoquastic Local Hamiltonian Problems”. In: *Quantum Info. Comput.* 8.5 (2008), pp. 361–385. URL: `https://dl.acm.org/doi/10.5555/2011772.2011773`.

[21] Kevin Slagle, David Aasen, Hannes Pichler, Roger S. K. Mong, Paul Fendley, Xie Chen, Manuel Endres, and Jason Alicea. “Microscopic characterization of Ising conformal field theory in Rydberg chains”. In: *Phys. Rev. B* 104 (23 2021), p. 235109. DOI: `10.1103/PhysRevB.104.235109`. URL: `https://link.aps.org/doi/10.1103/PhysRevB.104.235109`.

[22] J. I. Latorre, E. Rico, and G. Vidal. “Ground State Entanglement in Quantum Spin Chains”. In: *Quantum Info. Comput.* 4.1 (2004), pp. 48–92. URL: `https://arxiv.org/abs/quant-ph/0304098`.

[23] Jacopo Surace and Luca Tagliacozzo. “Fermionic Gaussian states: an introduction to numerical approaches”. In: *SciPost Phys. Lect. Notes* 54 (2022). URL: `https://doi.org/10.21468/scipostphyslectnotes.54`.

[24] H. Widom. "Asymptotic behavior of block Toeplitz matrices and determinants". In: *Adv. in Math.* 13.3 (1974), pp. 284–322. ISSN: 0001-8708. DOI: https://doi.org/10.1016/0001-8708(74)90072-3. URL: https://www.sciencedirect.com/science/article/pii/0001870874900723.

[25] Barry M. McCoy and Jacques H. H. Perk. "Spin Correlation Functions of an Ising Model with Continuous Exponents". In: *Phys. Rev. Lett.* 144 (1980), p. 840. DOI: 10.1103/PhysRevLett.44.840. URL: https://link.aps.org/doi/10.1103/PhysRevLett.44.840.

[26] D. Cabra and C. Naó. "2D Ising model with a defect line". In: *Mod. Phys. Lett. A* 09 (1994), p. 2017. DOI: 10.1142/s0217732394001969. URL: https://doi.org/10.1142/s0217732394001969.

[27] Carlos Naón and Marta Trobo. "The spin correlation function in 2D statistical mechanics models with inhomogeneous line defects". In: *J. Stat. Mech.* 2011.02 (2011), P02021. DOI: 10.1088/1742-5468/2011/02/p02021. URL: https://doi.org/10.1088/1742-5468/2011/02/p02021.

[28] P. Sala, S. Murciano, Y. Liu, and J. Alicea. *Future work on measurement-altered criticality*. In preparation.

[29] Thomas Koffel, M. Lewenstein, and Luca Tagliacozzo. "Entanglement Entropy for the Long-Range Ising Chain in a Transverse Field". In: *Phys. Rev. Lett.* 109.26 (Dec. 2012), p. 267203. DOI: 10.1103/PhysRevLett.109.267203.

[30] Davide Vodola, Luca Lepori, Elisa Ercolessi, and Guido Pupillo. "Long-range Ising and Kitaev models: phases, correlations and edge modes". In: *New J. Phys.* 18.1 (Dec. 2015), p. 015001. ISSN: 1367-2630. DOI: 10.1088/1367-2630/18/1/015001.

[31] G.M.P. van Kempen and L.J. van Vliet. "Mean and variance of ratio estimators used in fluorescence ratio imaging". In: *Cytometry* 39.4 (2000), pp. 300–305. DOI: https://doi.org/10.1002/(SICI)1097-0320(20000401)39:4<300::AID-CYTO8>3.0.CO;2-O. URL: https://onlinelibrary.wiley.com/doi/abs/10.1002/%28SICI%291097-0320%2820000401%2939%3A4%3C300%3A%3AAID-CYTO8%3E3.0.CO%3B2-O.

[32] Paul Fendley, K. Sengupta, and Subir Sachdev. "Competing density-wave orders in a one-dimensional hard-boson model". In: *Phys. Rev. B* 69 (7 2004), p. 075106. DOI: 10.1103/PhysRevB.69.075106. URL: https://link.aps.org/doi/10.1103/PhysRevB.69.075106.

[33] Pascal Scholl, Adam L. Shaw, Richard Bing-Shiun Tsai, Ran Finkelstein, Joonhee Choi, and Manuel Endres. "Erasure conversion in a high-fidelity Rydberg quantum simulator". In: *Nature* 622.7982 (Oct. 2023), pp. 273–278. ISSN: 1476-4687. DOI: 10.1038/s41586-023-06516-4. URL: http://dx.doi.org/10.1038/s41586-023-06516-4.

[34] Reza Haghshenas, Eli Chertkov, Matthew DeCross, Thomas M. Gatterman, Justin A. Gerber, Kevin Gilmore, Dan Gresh, Nathan Hewitt, Chandler V. Horst, Mitchell Matheny, and *et al. Probing critical states of matter on a digital quantum computer*. 2023. arXiv: `2305.01650 [quant-ph]`.

[35] C. H, G, C, R, A, and W. K. *Teleporting an unknown quantum state via dual classical and einstein-podolsky-rosen channels*. Phys. Rev. Lett. 1993. DOI: `10.1103/PhysRevLett.70.1895`.

[36] S and J. *Unitarity of black hole evaporation in final-state projection models*. JHEP. 2014. DOI: `10.1007/JHEP08(2014)126`.

[37] Robert Raussendorf and Hans J. Briegel. "A One-Way Quantum Computer". In: *Phys. Rev. Lett.* 86 (22 2001), pp. 5188–5191. DOI: `10.1103/PhysRevLett.86.5188`. URL: `https://link.aps.org/doi/10.1103/PhysRevLett.86.5188`.

[38] X.-M, Y, B.-H, C.-F, and G.-C. *Progress in quantum teleportation*. Nature Reviews Physics. 2023. DOI: `10.1038/s42254-023-00588-x`.

[39] S, J, C, A, and S. L. *Advances in quantum teleportation*. Nature Photonics. 2015. DOI: `10.1038/nphoton.2015.154`.

[40] M, M, R, M, and S. *A review and prospects of quantum teleportation*. 2009. DOI: `10.1109/ICCAE.2009.77`.

[41] D, J, and K. e. a. *Experimental quantum teleportation*. Nat. Physics. 1997. DOI: `10.1038/37539`.

[42] S. L and H. J. *Teleportation of continuous quantum variables*. Phys. Rev. Lett. 1998. DOI: `10.1103/PhysRevLett.80.869`.

[43] H, I, W, H, D, and N. *Long distance quantum teleportation in a quantum relay configuration*. Phys. Rev. Lett. 2004. DOI: `10.1103/PhysRevLett.92.047904`.

[44] e. a. *Quantum teleportation on a photonic chip*. Nat. Photonics. 2014. DOI: `10.1038/nphoton.2014.217`.

[45] T, T, M, J, B, R, and A. *Teleportation of entanglement over 143 km*. PNAS. 2015. DOI: `10.1073/pnas.1517007112`.

[46] J.-G, P, H.-L, L, S.-K, J, W.-Y, W.-Q, et al. *Ground-to-satellite quantum teleportation*. Nature. 2017. DOI: `10.1038/nature23675`.

[47] D and E. *Measurement-induced dynamics of many-body systems at quantum criticality*. Phys. Rev. B. 2020. DOI: `10.1103/PhysRevB.102.035119`.

[48] T.-C, L. A, I. H, and T. H. *Measurement as a shortcut to long-range entangled quantum matter*. PRX Quantum. 2022. DOI: `10.1103/PRXQuantum.3.040337`.

[49] A, R. M, M, and G. *Unitary-projective entanglement dynamics*. Phys. Rev. B. 2019. DOI: 10.1103/PhysRevB.99.224307.

[50] X, A, and A. D. *Entanglement in a fermion chain under continuous monitoring*. SciPost Phys. 2019. DOI: 10.21468/SciPostPhys.7.2.024.

[51] Y, X, A. W. W, and M. P. A. *Conformal invariance and quantum nonlocality in critical hybrid circuits*. Phys. Rev. B. 2021. DOI: 10.1103/PhysRevB.104.104305.

[52] Aaron J. Friedman, Chao Yin, Yifan Hong, and Andrew Lucas. *Locality and error correction in quantum dynamics with measurement*. 2022. DOI: 10.48550/arXiv.2206.09929. arXiv: 2206.09929 [quant-ph].

[53] C.-J, W, Y, S, and T. H. *Probing sign structure using measurement-induced entanglement*. 2023. DOI: 10.22331/q-2023-02-02-910.

[54] C. L and M. P. A. *Transport in a one-channel luttinger liquid*. Phys. Rev. Lett. 1992. DOI: 10.1103/PhysRevLett.68.1220.

[55] Xinyu Sun, Hong Yao, and Shao-Kai Jian. *New critical states induced by measurement*. 2023. arXiv: 2301.11337 [quant-ph]. URL: https://arxiv.org/abs/2301.11337.

[56] Yuto Ashida, Shunsuke Furukawa, and Masaki Oshikawa. "System-environment entanglement phase transitions". In: *Phys. Rev. B* 110 (9 2024), p. 094404. DOI: 10.1103/PhysRevB.110.094404. URL: https://link.aps.org/doi/10.1103/PhysRevB.110.094404.

[57] Zhou Yang, Dan Mao, and Chao-Ming Jian. "Entanglement in a one-dimensional critical state after measurements". In: *Phys. Rev. B* 108 (16 2023), p. 165120. DOI: 10.1103/PhysRevB.108.165120. URL: https://link.aps.org/doi/10.1103/PhysRevB.108.165120.

[58] Zack Weinstein, Rohith Sajith, Ehud Altman, and Samuel J. Garratt. "Nonlocality and entanglement in measured critical quantum Ising chains". In: *Phys. Rev. B* 107 (24 2023), p. 245132. DOI: 10.1103/PhysRevB.107.245132. URL: https://link.aps.org/doi/10.1103/PhysRevB.107.245132.

[59] R. *Exploring critical systems under measurements and decoherence via Keldysh field theory*. arXiv e-prints. 2023. DOI: 10.48550/arXiv.2304.08277.

[60] Alessio Paviglianiti, Xhek Turkeshi, Marco Schirò, and Alessandro Silva. "Enhanced Entanglement in the Measurement-Altered Quantum Ising Chain". In: *Quantum* 8 (2024), p. 1576. DOI: 10.22331/q-2024-12-23-1576. arXiv: 2310.02686 [quant-ph].

[61] X and S.-K. *Holographic Weak Measurement*. arXiv e-prints. 2023. DOI: 10.48550/arXiv.2309.15896.

[62] Jong Yeon Lee, Chao-Ming Jian, and Cenke Xu. "Quantum Criticality Under Decoherence or Weak Measurement". In: *PRX Quantum* 4 (3 2023), p. 030317. DOI: 10.1103/PRXQuantum.4.030317. URL: https://link.aps.org/doi/10.1103/PRXQuantum.4.030317.

[63] Yijian Zou, Shengqi Sang, and Timothy H. Hsieh. "Channeling Quantum Criticality". In: *Phys. Rev. Lett.* 130 (25 2023), p. 250403. DOI: 10.1103/PhysRevLett.130.250403. URL: https://link.aps.org/doi/10.1103/PhysRevLett.130.250403.

[64] Samuel J. Garratt and Ehud Altman. "Probing post-measurement entanglement without post-selection". In: *arXiv e-prints*, arXiv:2305.20092 (May 2023), arXiv:2305.20092. DOI: 10.48550/arXiv.2305.20092. arXiv: 2305.20092 [quant-ph].

[65] M and M. *Shadow tomography from emergent state designs in analog quantum simulators*. Phys. Rev. Lett. 2023. DOI: 10.1103/PhysRevLett.131.160601.

[66] M. *Postselection-free learning of measurement-induced quantum dynamics*. arXiv e-prints. 2023. DOI: 10.48550/arXiv.2310.04156.

[67] Y, Y, P, E, and M. P. A. *Cross Entropy Benchmark for Measurement-Induced Phase Transitions*. 2023. DOI: 10.1103/PhysRevLett.130.220404.

[68] Y, X, and M. P. A. *Measurement-driven entanglement transition in hybrid quantum circuits*. Phys. Rev. B. 2019. DOI: 10.1103/PhysRevB.100.134306.

[69] E. V. H, Y, I. V, A. D, and D. G. *Evolution of many-body systems under ancilla quantum measurements*. Phys. Rev. B. 2023. DOI: 10.1103/PhysRevB.107.214203.

[70] D and J. *Steering-induced phase transition in measurement-only quantum circuits*. Phys. Rev. B. 2024. DOI: 10.1103/PhysRevB.109.024301.

[71] S, Z, T. H, and B. *Ultrafast entanglement dynamics in monitored quantum circuits*. PRX Quantum. 2023. DOI: 10.1103/PRXQuantum.4.040332.

[72] P, I. V, and Y. *Measurements on an anderson chain*. Phys. Rev. B. 2023. DOI: 10.1103/PhysRevB.107.174203.

[73] X, B, and A. *Measurement-induced phase transitions on dynamical quantum trees*. PRX Quantum. 2023. DOI: 10.1103/PRXQuantum.4.030333.

[74] Ruben Verresen, Nathanan Tantivasadakarn, and Ashvin Vishwanath. *Efficiently preparing Schrödinger's cat, fractons and non-Abelian topological order in quantum devices*. 2021. DOI: 10.48550/arXiv.2112.03061. arXiv: 2112.03061 [quant-ph].

[75] Nathanan Tantivasadakarn, Ryan Thorngren, Ashvin Vishwanath, and Ruben Verresen. "Long-range entanglement from measuring symmetry-protected topological phases". In: *Physical Review X* 14 (2024), p. 021040. DOI: 10.1103/PhysRevX.14.021040. arXiv: 2112.01519 [cond-mat.str-el].

[76] N, A, and R. *Hierarchy of topological order from finite-depth unitaries, measurement, and feedforward*. PRX Quantum. 2023. DOI: 10.1103/PRXQuantum.4.020339.

[77] Sergey Bravyi, Isaac Kim, Alexander Kliesch, and Robert Koenig. *Adaptive constant-depth circuits for manipulating non-Abelian anyons*. 2022. DOI: 10.48550/arXiv.2205.01933. arXiv: 2205.01933 [quant-ph].

[78] Jong Yeon Lee, Wenjie Ji, Zhen Bi, and Matthew P. A. Fisher. "Decoding Measurement-Prepared Quantum Phases and Transitions: from Ising model to gauge theory, and beyond". In: *arxiv* (Aug. 2022). DOI: 10.48550/arXiv.2208.11699.

[79] G.-Y, N, A, S, and R. *Nishimori's cat: Stable long-range entanglement from finite-depth unitaries and weak measurements*. Phys. Rev. Lett. 2023. DOI: 10.1103/PhysRevLett.131.200201.

[80] Yi-Zhuang You, Zhen Bi, Alex Rasmussen, Kevin Slagle, and Cenke Xu. "Wave Function and Strange Correlator of Short-Range Entangled States". In: *Phys. Rev. Lett.* 112 (24 2014), p. 247202. DOI: 10.1103/PhysRevLett.112.247202. URL: https://link.aps.org/doi/10.1103/PhysRevLett.112.247202.

[81] E, A, R, and M. *Full counting statistics as probe of measurement-induced transitions in the quantum Ising chain*. SciPost Phys. 2023. DOI: 10.21468/SciPostPhys.15.3.096.

[82] Tsung-Cheng Lu, Zhehao Zhang, Sagar Vijay, and Timothy H. Hsieh. "Mixed-State Long-Range Order and Criticality from Measurement and Feedback". In: *PRX Quantum* 4 (3 2023), p. 030318. DOI: 10.1103/PRXQuantum.4.030318. URL: https://link.aps.org/doi/10.1103/PRXQuantum.4.030318.

[83] V, Z, and F. *Magnetization distribution in the transverse ising chain with energy flux*. Phys. Rev. E. 2003. DOI: 10.1103/PhysRevE.67.056129.

[84] A and P. *Order parameter statistics in the critical quantum ising chain*. Phys. Rev. Lett. 2008. DOI: 10.1103/PhysRevLett.100.165706.

[85] E. *Constraints on supersymmetry breaking*. Nuclear Physics B. 1982. DOI: https://doi.org/10.1016/0550-3213(82)90071-2.

[86] E, B. M, and M. *Statistical mechanics of the XY model. i*. Phys. Rev. A. 1970. DOI: 10.1103/PhysRevA.2.1075.

[87] E and B. M. *Statistical mechanics of the xy model. ii. spin-correlation functions*. Phys. Rev. A. 1971. DOI: 10.1103/PhysRevA.3.786.

[88] B, D, and C. P. *Correlations at PT-symmetric quantum critical point*. Physical Review Letters. 2022. DOI: 10.1103/physrevlett.128.146804.

[89] Tomotaka Kuwahara and Keiji Saito. "Area law of noncritical ground states in 1D long-range interacting systems". In: *Nat. Commun.* 11.4478 (Sept. 2020), pp. 1–7. ISSN: 2041-1723. DOI: 10.1038/s41467-020-18055-x.

[90] V and I. *Entanglement in fermionic chains with interface defects*. Annalen der Physik. 2010. DOI: https://doi.org/10.1002/andp.201000055.

[91] X and M. *Entanglement and correlation spreading in non-hermitian spin chains*. Phys. Rev. B. 2023. DOI: 10.1103/PhysRevB.107.L020403.

[92] F, J. G, F, and A. R. *Entanglement entropy in the long-range kitaev chain*. Phys. Rev. A. 2018. DOI: 10.1103/PhysRevA.97.062301.

[93] Milton Abramowitz and Irene A. Stegun. *Handbook of Mathematical Functions with Formulas, Graphs, and Mathematical Tables*. New York: Dover Publications, 1964.

[94] O. A and L. *Ordering in spatially anisotropic triangular antiferromagnets*. Phys. Rev. Lett. 2007. DOI: 10.1103/PhysRevLett.98.077205.

[95] L. P. *Scaling laws for ising models near T_c*. Physics Physique Fizika. 1966. DOI: 10.1103/PhysicsPhysiqueFizika.2.263.

[96] A. *Separability criterion for density matrices*. Phys. Rev. Lett. 1996. DOI: 10.1103/PhysRevLett.77.1413.

[97] G and R. F. *Computable measure of entanglement*. Phys. Rev. A. 2002. DOI: 10.1103/PhysRevA.65.032314.

[98] L, G, and J. I. *Quantum circuits assisted by local operations and classical communication: Transformations and phases of matter*. Phys. Rev. Lett. 2021. DOI: 10.1103/PhysRevLett.127.220503.

[99] N, R, and A. *Shortest route to non-abelian topological order on a quantum processor*. Phys. Rev. Lett. 2023. DOI: 10.1103/PhysRevLett.131.060405.

[100] J, K, N, J. I, and F. *Gauging quantum states: From global to local symmetries in many-body systems*. Phys. Rev. X. 2015. DOI: 10.1103/PhysRevX.5.011024.

[101] G.-Y and G.-M. *Gapless coulomb state emerging from a self-dual topological tensor-network state*. Phys. Rev. Lett. 2019. DOI: 10.1103/PhysRevLett.122.176401.

[102] T. W and T. *Conformal invariance and critical systems with mixed boundary conditions*. Nuclear Physics B. 1991. DOI: https://doi.org/10.1016/0550-3213(91)90370-D.

[103] Theodore W. Burkhardt and Ihnsouk Guim. "Conformal theory of the two-dimensional Ising model with homogeneous boundary conditions and with disordred boundary fields". In: *Phys. Rev. B* 47 (21 1993), pp. 14306–14311. DOI: 10.1103/PhysRevB.47.14306. URL: https://link.aps.org/doi/10.1103/PhysRevB.47.14306.

[104] U. *The density-matrix renormalization group in the age of matrix product states*. Ann. Phys. 2011. DOI: 10.1016/j.aop.2010.09.012.

[105] M. B. *An area law for one-dimensional quantum systems*. Journal of Statistical Mechanics: Theory and Experiment. 2007. DOI: 10.1088/1742-5468/2007/08/p08024.

[106] I and V. *Reduced density matrices and entanglement entropy in free lattice models*. Journal of Physics A: Mathematical and Theoretical. 2009. DOI: 10.1088/1751-8113/42/50/504003.

[107] E. L. *A localization theorem for toeplitz determinants*. Indiana University Mathematics Journal. 1979.

[108] E. L and K. E. *The fisher-hartwig conjecture and toeplitz eigenvalues*. Linear Algebra and its Applications. 1994. DOI: https://doi.org/10.1016/0024-3795(94)90187-2.

[109] F, S, A. M, and J. E. *Theory of finite-entanglement scaling at one-dimensional quantum critical points*. Physical Review Letters. 2009. DOI: 10.1103/physrevlett.102.255701.

[110] P, J, and E. *Entanglement negativity in extended systems: a field theoretical approach*. J. Stat. Mech. 2013. DOI: 10.1088/1742-5468/2013/02/P02008.

[111] Ruben Verresen, Roderich Moessner, and Frank Pollmann. "One-dimensional symmetry protected topological phases and their transitions". In: *Phys. Rev. B* 96 (16 2017), p. 165124. DOI: 10.1103/PhysRevB.96.165124. URL: https://link.aps.org/doi/10.1103/PhysRevB.96.165124.

[112] Yue Liu, Nathanan Tantivasadakarn, Kevin Slagle, David F. Mross, and Jason Alicea. "Assembling Kitaev honeycomb spin liquids from arrays of one-dimensional symmetry-protected topological phases". In: *Phys. Rev. B* 108 (18 2023), p. 184406. DOI: 10.1103/PhysRevB.108.184406. URL: https://link.aps.org/doi/10.1103/PhysRevB.108.184406.

[113] Tom Kennedy and Hal Tasaki. "Hidden symmetry breaking and the Haldane phase inS=1 quantum spin chains". In: *Commun. Math. Phys.* 147.3 (July 1992), pp. 431–484. ISSN: 1432-0916. DOI: 10.1007/BF02097239.

[114] Tom Kennedy and Hal Tasaki. "Hidden $Z_2 \times Z_2$ symmetry breaking in Haldane-gap antiferromagnets". In: *Phys. Rev. B* 45 (1 1992), pp. 304–307. DOI: 10.1103/PhysRevB.45.304. URL: https://link.aps.org/doi/10.1103/PhysRevB.45.304.

[115] Linhao Li, Masaki Oshikawa, and Yunqin Zheng. "Noninvertible duality transformation between symmetry-protected topological and spontaneous symmetry breaking phases". In: *Phys. Rev. B* 108 (21 2023), p. 214429. DOI: 10.1103/PhysRevB.108.214429. URL: https://link.aps.org/doi/10.1103/PhysRevB.108.214429.

[116] Linhao Li, Masaki Oshikawa, and Yunqin Zheng. "Intrinsically/Purely Gapless-SPT from Non-Invertible Duality Transformations". In: *arxiv* (2023). arXiv: 2307.04788 [cond-mat.str-el]. URL: https://arxiv.org/abs/2307.04788.

[117] Thierry Giamarchi. *Quantum Physics in One Dimension*. Oxford University Press, 2003. DOI: 10.1093/acprof:oso/9780198525004.001.0001. URL: https://doi.org/10.1093/acprof:oso/9780198525004.001.0001.

[118] C. L. Kane and Matthew P. A. Fisher. "Transmission through barriers and resonant tunneling in an interacting one-dimensional electron gas". In: *Phys. Rev. B* 46 (23 1992), pp. 15233–15262. DOI: 10.1103/PhysRevB.46.15233. URL: https://link.aps.org/doi/10.1103/PhysRevB.46.15233.

[119] F. Verstraete, M. M. Wolf, D. Perez-Garcia, and J. I. Cirac. "Criticality, the Area Law, and the Computational Power of Projected Entangled Pair States". In: *Phys. Rev. Lett.* 96.22 (June 2006), p. 220601. DOI: 10.1103/PhysRevLett.96.220601.

[120] Pochung Chen, Zhi-long Xue, I. P. McCulloch, Ming-Chiang Chung, Miguel Cazalilla, and S.-K. Yip. "Entanglement entropy scaling of the XXZ chain". In: *J. Stat. Mech.: Theory Exp.* 2013.10 (Oct. 2013), P10007. ISSN: 1742-5468. DOI: 10.1088/1742-5468/2013/10/P10007.

[121] Kazuki Yamamoto, Masaya Nakagawa, Masaki Tezuka, Masahito Ueda, and Norio Kawakami. "Universal properties of dissipative Tomonaga-Luttinger liquids: Case study of a non-Hermitian XXZ spin chain". In: *Phys. Rev. B* 105.20 (May 2022), p. 205125. DOI: 10.1103/PhysRevB.105.205125.

[122] Edward O'Brien and Paul Fendley. "Lattice Supersymmetry and Order-Disorder Coexistence in the Tricritical Ising Model". In: *Phys. Rev. Lett.* 120 (20 2018), p. 206403. DOI: 10.1103/PhysRevLett.120.206403. URL: https://link.aps.org/doi/10.1103/PhysRevLett.120.206403.

[123] John L. Cardy. "Boundary conditions, fusion rules and the Verlinde formula". In: *Nucl. Phys. B* 324.3 (Oct. 1989), pp. 581–596. ISSN: 0550-3213. DOI: 10.1016/0550-3213(89)90521-X.

[124] Ian Affleck. "Edge critical behaviour of the two-dimensional tri-criticalIsing model". In: *J. Phys. A: Math. Gen.* 33.37 (Sept. 2000), p. 6473. ISSN: 0305-4470. DOI: 10.1088/0305-4470/33/37/301.

[125] H. Saleur and M. Bauer. “On some relations between local height probabilities and conformal invariance”. In: *Nuclear Physics B* 320.3 (1989), pp. 591–624. ISSN: 0550-3213. DOI: https://doi.org/10.1016/0550-3213(89)90014-X. URL: https://www.sciencedirect.com/science/article/pii/055032138990014X.

[126] Roger S K Mong, David J Clarke, Jason Alicea, Netanel H Lindner, and Paul Fendley. “Parafermionic conformal field theory on the lattice”. In: *Journal of Physics A: Mathematical and Theoretical* 47.45 (Oct. 2014), p. 452001. ISSN: 1751-8121. DOI: 10.1088/1751-8113/47/45/452001. URL: http://dx.doi.org/10.1088/1751-8113/47/45/452001.

[127] Leung Chim. “BOUNDARY S MATRIX FOR THE TRICRITICAL ISING MODEL”. In: *Int. J. Mod. Phys. A* 11.25 (Oct. 1996), pp. 4491–4512. ISSN: 0217-751X. DOI: 10.1142/S0217751X9600208X.

[128] Rushikesh A. Patil and Andreas W. W. Ludwig. *Highly complex novel critical behavior from the intrinsic randomness of quantum mechanical measurements on critical ground states – a controlled renormalization group analysis*. 2024. arXiv: 2409.02107 [cond-mat.stat-mech]. URL: https://arxiv.org/abs/2409.02107.

[129] Qicheng Tang and Xueda Wen. *A critical state under weak measurement is not critical*. 2024. arXiv: 2411.13705 [cond-mat.stat-mech]. URL: https://arxiv.org/abs/2411.13705.

[130] Masahiro Hoshino, Masaki Oshikawa, and Yuto Ashida. “Entanglement swapping in critical quantum spin chains”. In: *Phys. Rev. B* 111.15 (2025), p. 155143. DOI: 10.1103/PhysRevB.111.155143. arXiv: 2406.12377 [quant-ph].

[131] Adam Nahum and Jesper Lykke Jacobsen. *Bayesian critical points in classical lattice models*. 2025. arXiv: 2504.01264 [cond-mat.stat-mech].

[132] Malte Pütz, Samuel J. Garratt, Hidetoshi Nishimori, Simon Trebst, and Guo-Yi Zhu. *Learning transitions in classical Ising models and deformed toric codes*. 2025. arXiv: 2504.12385 [cond-mat.stat-mech].

[133] Hannes Bernien, Sylvain Schwartz, Alexander Keesling, Harry Levine, Ahmed Omran, Hannes Pichler, Soonwon Choi, Alexander S. Zibrov, Manuel Endres, Markus Greiner, Vladan Vuletić, and Mikhail D. Lukin. “Probing many-body dynamics on a 51-atom quantum simulator”. In: *Nature* 551.7682 (Nov. 2017), pp. 579–584. ISSN: 1476-4687. DOI: 10.1038/nature24622. URL: http://dx.doi.org/10.1038/nature24622.

[134] Alexander Keesling, Ahmed Omran, Harry Levine, Hannes Bernien, Hannes Pichler, Soonwon Choi, Rhine Samajdar, Sylvain Schwartz, Pietro Silvi, Subir Sachdev, Peter Zoller, Manuel Endres, Markus Greiner, Vladan Vuletić, and Mikhail D. Lukin. “Quantum Kibble–Zurek mechanism and critical dynamics on a programmable Rydberg simulator”. In: *Nature* 568.7751 (Apr.

2019), pp. 207–211. ISSN: 1476-4687. DOI: 10.1038/s41586-019-1070-1. URL: http://dx.doi.org/10.1038/s41586-019-1070-1.

[135] Fang Fang, Kenneth Wang, Vincent S. Liu, Yu Wang, Ryan Cimmino, Julia Wei, Marcus Bintz, Avery Parr, Jack Kemp, Kang-Kuen Ni, and Norman Y. Yao. *Probing critical phenomena in open quantum systems using atom arrays*. 2024. arXiv: 2402.15376 [quant-ph]. URL: https://arxiv.org/abs/2402.15376.

[136] Hanteng Wang, Xingyu Li, and Chengshu Li. *Tricritical Kibble-Zurek Scaling in Rydberg Atom Ladders*. 2025. arXiv: 2505.12979 [cond-mat.quant-gas]. URL: https://arxiv.org/abs/2505.12979.

[137] Xiangkai Sun, Yuan Le, Stephen Naus, Richard Bing-Shiun Tsai, Lewis R. B. Picard, Sara Murciano, Michael Knap, Jason Alicea, and Manuel Endres. *Experimental observation of conformal field theory spectra*. 2026. DOI: 10.48550/arXiv.2601.16275. arXiv: 2601.16275 [quant-ph].

[138] Seth Whitsitt, Rhine Samajdar, and Subir Sachdev. "Quantum field theory for the chiral clock transition in one spatial dimension". In: *Physical Review. B* 98.20 (2018). ISSN: ISSN 2469-9950. DOI: 10.1103/physrevb.98.205118. URL: https://www.osti.gov/biblio/1613073.

[139] Natalia Chepiga and Frédéric Mila. "Floating Phase versus Chiral Transition in a 1D Hard-Boson Model". In: *Phys. Rev. Lett.* 122 (1 2019), p. 017205. DOI: 10.1103/PhysRevLett.122.017205. URL: https://link.aps.org/doi/10.1103/PhysRevLett.122.017205.

[140] Natalia Chepiga and Frédéric Mila. "Kibble-Zurek exponent and chiral transition of the period-4 phase of Rydberg chains". In: *Nature Communications* 12.1 (Jan. 2021). ISSN: 2041-1723. DOI: 10.1038/s41467-020-20641-y. URL: http://dx.doi.org/10.1038/s41467-020-20641-y.

[141] Rhine Samajdar, Soonwon Choi, Hannes Pichler, Mikhail D. Lukin, and Subir Sachdev. "Numerical study of the chiral Z_3 quantum phase transition in one spatial dimension". In: *Phys. Rev. A* 98 (2 2018), p. 023614. DOI: 10.1103/PhysRevA.98.023614. URL: https://link.aps.org/doi/10.1103/PhysRevA.98.023614.

[142] Natalia Chepiga. "Tunable Quantum Criticality in Multicomponent Rydberg Arrays". In: *Physical Review Letters* 132.7 (Feb. 2024). ISSN: 1079-7114. DOI: 10.1103/physrevlett.132.076505. URL: http://dx.doi.org/10.1103/PhysRevLett.132.076505.

[143] Chengshu Li, Shang Liu, Hanteng Wang, Wenjun Zhang, Zi-Xiang Li, Hui Zhai, and Yingfei Gu. "Uncovering Emergent Spacetime Supersymmetry with Rydberg Atom Arrays". In: *Phys. Rev. Lett.* 133 (22 2024), p. 223401. DOI: 10.1103/PhysRevLett.133.223401. URL: https://link.aps.org/doi/10.1103/PhysRevLett.133.223401.

[144] Jin Zhang, Sergio H Cantú, Fangli Liu, Alexei Bylinskii, Boris Braverman, Florian Huber, Jesse Amato-Grill, Alexander Lukin, Nathan Gemelke, Alexander Keesling, et al. "Probing quantum floating phases in Rydberg atom arrays". In: *Nature Communications* 16.1 (2025), p. 712.

[145] Jose Soto and Natalia Chepiga. *Numerical investigation of quantum phases and phase transitions in a two-leg ladder of Rydberg atoms*. 2025. arXiv: `2411.05494 [cond-mat.quant-gas]`. URL: `https://arxiv.org/abs/2411.05494`.

[146] *Supplemental Material*.

[147] Per Fröjdh and Henrik Johannesson. "The two-dimensional tricritical Ising model in restricted domains with free boundaries". In: *Nucl. Phys. B* 366.3 (1991), pp. 429–466. ISSN: 0550-3213. DOI: `https://doi.org/10.1016/0550-3213(91)90026-T`. URL: `https://www.sciencedirect.com/science/article/pii/055032139190026T`.

[148] Abhijat Sarma, Nayan Myerson-Jain, Yue Liu, Nandagopal Manoj, Jason Alicea, Roger G. Melko, and Cenke Xu. "Probing Defects with Quantum Simulator Snapshots". In: *Physical Review Letters* 136 (2026), p. 020603. DOI: `10.48550/arXiv.2507.05379`. arXiv: `2507.05379 [quant-ph]`.

[149] Y. Imry and S.-k. Ma. "Random-Field Instability of the Ordered State of Continuous Symmetry". In: *Physical Review Letters* 35.21 (Nov. 1975), pp. 1399–1401. DOI: `10.1103/PhysRevLett.35.1399`.

[150] Xingyu Li, Shuyan Zhou, Xue Chen, Chengshu Li, and Hanteng Wang. "Random displacements in critical Rydberg atom arrays". In: *Physical Review B* 112 (2025), p. L180202. DOI: `10.1103/dpn8-63p6`.

[151] J. Soto-Garcia and N. Chepiga. "Infinite Randomness Criticality and Localization of the Floating Phase in Disordered Rydberg Atom Arrays". In: *Physical Review Letters* (2026). DOI: `10.1103/tmyk-b1yv`.

[152] Hannah J. Manetsch, Gyohei Nomura, Elie Bataille, Xudong Lv, Kon H. Leung, Manuel Endres, et al. "A tweezer array with 6,100 highly coherent atomic qubits". In: *Nature* 647 (Sept. 2025), pp. 60–67. DOI: `10.1038/s41586-025-09641-4`.

[153] Subir Sachdev. *Quantum Phase Transitions*. 2nd ed. Cambridge: Cambridge University Press, 2011. DOI: `10.1017/CBO9780511973765`.

[154] Aaron van den Oord, Sander Dieleman, Heiga Zen, Karen Simonyan, Oriol Vinyals, Alex Graves, Nal Kalchbrenner, Andrew Senior, and Koray Kavukcuoglu. "WaveNet: A Generative Model for Raw Audio". In: *arxiv* (Sept. 2016). DOI: `10.48550/arXiv.1609.03499`. eprint: `1609.03499`.

[155] V. Giovannetti, S. Montangero, and Rosario Fazio. "Quantum Multiscale Entanglement Renormalization Ansatz Channels". In: *Phys. Rev. Lett.* 101.18 (Oct. 2008), p. 180503. DOI: `10.1103/PhysRevLett.101.180503`.

[156] Chao-Ming Jian, Hassan Shapourian, Bela Bauer, and Andreas W. W. Ludwig. "Measurement-induced entanglement transitions in quantum circuits of non-interacting fermions: Born-rule versus forced measurements". In: *arXiv e-prints* (2023), arXiv:2302.09094. DOI: 10.48550/arXiv.2302.09094. arXiv: 2302.09094 [cond-mat.stat-mech].

[157] John L. Cardy. "The Ising model in a random boundary field". In: *J. Phys. A: Math. Gen.* 24.22 (1991), pp. L1315–L1319. DOI: 10.1088/0305-4470/24/22/003.

[158] Monwhea Jeng and Andreas W. W. Ludwig. "Random defect lines in conformal minimal models". In: *Nuclear Physics B* 594.3 (2001), pp. 685–712. DOI: 10.1016/S0550-3213(00)00639-8. arXiv: cond-mat/9910181.

[159] John L. Cardy. "Boundary Conditions in Conformal Field Theory". In: *Integrable Systems in Quantum Field Theory and Statistical Mechanics*. Vol. 19. Advanced Studies in Pure Mathematics. 1989, pp. 127–148. DOI: 10.2969/aspm/01910127.

[160] Michael P. Zaletel, Jens H. Bardarson, and Joel E. Moore. "Logarithmic Terms in Entanglement Entropies of 2D Quantum Critical Points and Shannon Entropies of Spin Chains". In: *Phys. Rev. Lett.* 107 (2 2011), p. 020402. DOI: 10.1103/PhysRevLett.107.020402. URL: https://link.aps.org/doi/10.1103/PhysRevLett.107.020402.

[161] Jean-Marie Stéphan. "Shannon and Rényi mutual information in quantum critical spin chains". In: *Phys. Rev. B* 90 (4 2014), p. 045424. DOI: 10.1103/PhysRevB.90.045424. URL: https://link.aps.org/doi/10.1103/PhysRevB.90.045424.

[162] M. Pleimling, F. A. Bagaméry, L. Turban, and F. Iglói. "Logarithmic corrections in the two-dimensional Ising model in a random surface field". In: *Journal of Physics A: Mathematical and General* 37.37 (2004), pp. 8801–8809. DOI: 10.1088/0305-4470/37/37/003. arXiv: cond-mat/0402188.